GEOMETRY, KINEMATICS, MICROSTRUCTURE, STRAIN ANALYSIS, AND P-T CONDITIONS OF THE SHEAR ZONES AND ASSOCIATED DUCTILE THRUSTS IN THE SOUTHERN MT. LOFTY RANGES/ADELAIDE HILLS AREA; SOUTH AUSTRALIA

ALI YASSAGHI

B.Sc. in Geology 1986, Mashhad University

M.Sc. in Structural Geology and Tectonics 1989,
Tarbiet-Modarress University

Thesis submitted for the degree of
Doctor of Philosophy in Geology

THE UNIVERSITY OF ADELAIDE
Department of Geology and Geophysics

January 1998

CONTENTS

Table of Content.....I
List of Figures.....VI
List of Tables.....XI
Abstract.....XII
Statement.....XV
Acknowledgments.....XVI
Dedication.....XVII

CHAPTER ONE: **INTRODUCTION**

1.1. Preamble.....1
1.2. Foreland fold-thrust belts 2
1.2.1. Definition and general characteristics 3
1.2.2. The formation of fault/shear zones in thrust belts 5
1.2.3. Mechanisms of fold-thrust belt formation 8
1.3. Adelaide Fold-Thrust Belt 10
1.3.1. Tectonic setting of the Adelaide Fold-Thrust Belt 11
1.3.2. Regional setting of the southern Adelaide Fold-Thrust Belt 13
1.3.3. Previous structural interpretation of the southern Adelaide Fold-Thrust Belt 14
1.4. Study objectives 16
1.5. Methods of study 17

CHAPTER TWO: **GEOLOGICAL SETTING OF THE SOUTHERN MT. LOFTY RANGES/ADELAIDE HILLS AREA**

2.1. Introduction.....19
2.2. Stratigraphy 20
2.2.1. Gneissic basement.....20
2.2.2. Burra Group.....20
2.3 Structural geometry 22
2.3.1. Shear zones 23
2.3.2. Ductile thrusts 25
2.3.3. Mesoscopic folds 26
2.4. Summary 27

CHAPTER THREE: GEOMETRIC AND KINEMATIC ANALYSIS OF THE SHEAR ZONES

3.1. Introduction 29
3.2. The Morialta area 30
3.2.1. Structural geometry and fabric development in the Morialta shear zone 31
3.3. The Montacute Heights area 34
3.3.1. Structures and fabrics of the Montacute Heights shear zone 35
3.4. The Greenhill area.....36
3.4.1. The Greenhill shear zone 37
3.4.2. The Norton Summit shear zone 38
3.5. The Pole Road area 39
3.5.1. Structural geometry of the Pole Road shear zone 41
3.6. The Clarendon area 43
3.6.1. Geometrical features of the Clarendon shear zone 44
3.7. The Mt. Bold area 46
3.7.1. Geometrical features of the Mt. Bold shear zone 48
3.7.1.1. Fabrics 48
3.7.1.2. Minor folds 49
3.7.1.3. Veins 50
3.8. Discussion 51
3.8.1. Bedding parallel nature of the shear zones 51
3.8.2. Movement direction of the shear zones 52
3.8.3. Development of cleavages in the shear zones 54
3.8.3.1. Regional cleavages 54
3.8.3.2. Crenulation and continuous cleavages 55
3.8.3.3. Extensional crenulation cleavages and general non-coaxial nature of the shear zones 56
3.8.4. Developments of folds 57
3.8.5. Structural model for the development of the shear zones 59
3.9. Conclusions 62

CHAPTER FOUR: SECTION BALANCING AND STRAIN ANALYSIS

4.1. Introduction 64
4.2. Construction and balancing of cross sections 65
4.3. Restoration of the sections 66
4.4. Finite strain analysis 68
4.4.1. Objects 68
4.4.2. Analytical methods 68

4.4.3. Results 69
4.4.4. Sources of error 70
4.5. Discussion 70
4.5.1. Thrust system 70
4.5.2. Restoration of balanced sections and internal deformation 71
4.5.3. Finite strain variation across the sheets 72
4.5.4. Finite longitudinal strain components 73
4.5.5. Shortening and volume loss across the sheets 74

CHAPTER FIVE: **MICROSTRUCTURES OF CLEAVAGES IN THE SHEAR ZONES**

5.1. Introduction.....76
5.2. Mineralogy and microstructures of psammites.....78
5.2.1. Introduction.....78
5.2.2. Description of cleavage types in psammites.....78
5.2.3. Microstructural development of rough cleavages in pasmmites from within the shear zones.....80
5.3. Mineralogy and microstructures of pelites.....82
5.3.1. Introduction.....82
5.3.2. Description of cleavage types in pelites.....82
5.3.3. Microstructural development of continuous cleavages in pelites from within the shear zones.....83
5.3.4. Microstructures of crenulation cleavages in the shear zones.....84
5.3.5. Development of crenulation cleavages in the shear zones.....85
5.4. Microscopic shear sense indicators.....86
5.4.1. Asymmetric pressure fringes.....86
5.4.2. Displaced broken grains.....88
5.4.3. Other criteria used to deduce the sense of shear in the shear zones.....88
5.5. Discussion.....89
5.5.1. The mechanism of formation of cleavages in psammites from within the shear zones.....89
5.5.2. The mechanism of formation of crenulation cleavages in pelites from within the shear zones.....90

CHAPTER SIX: **QUANTITATIVE/STATISTICAL ANALYSIS OF QUARTZITE MICROSTRUCTURES**

6.1. Introduction.....92
6.2. The deformational behaviour of quartz and felspar from within the shear zones.....93
6.2.1. Mt. Bold shear zone.....94
6.2.2. Pole Road shear zone.....96
6.2.3. Morialta shear zone.....97

6.2.4. Summary of the deformational behaviour of quartz and feldspar from within the shear zones....99
6.3. Qualitative analysis of microstructural quartz grain geometry....100
6.3.1. Grain size analysis....101
6.3.2. grain shape (aspect ratio) analysis....102
6.3.3. Shape-preferred orientation (Ø) analysis....102
6.4. Quantitative statistical analysis of the quartz grain configuration data....103
6.4.1. Results....105
6.4.1.1. Grain size....105
6.4.1.2. Grain shape (aspect ratio)....105
6.4.1.3. Shape-preferred orientation....106
6.5. Discussion....106
6.5.1. Microstructural development within quartzites in the shear zones....106
6.5.2. Environment conditions and deformation mechanisms of the shear zones..107
6.5.3. Statistical interpretation of the microstructural data....109
6.5.4. Temporal evolution of the shear zones....112

CHAPTER SEVEN: PRESSURE AND TEMPERATURE CONDITIONS OF THE SHEAR ZONES

7.1. Introduction....114
7.2. Fluid inclusion analysis....115
7.2.1. Microstructure of quartz veins....115
7.2.2. Types of fluid inclusions....116
7.2.3. Analytical methods....118
7.2.3.1. Freezing....11
7.2.3.2. Heating....120
7.2.4. Salinity-T_H relationship....121
7.2.5. Interpretation of homogenisation temperature....122
7.2.6. Estimation of temperatures of entrapment....124
7.2.7. Estimation of pressure of trapping....126
7.3. Geobarometric analysis using electron microprobe data....127
7.3.1. Sample petrography and microstructures....127
7.3.2. Mineral chemistry....128
7.3.3. Estimation of pressures and temperatures....129
7.3.3.1. Estimation of average pressures....129
7.3.3.2. Estimation of average temperatures....131
7.3.3.3. Estimation of average pressure and temperature....132
7.3.4. Estimation of average pressure and temperature of peak metamorphism....132
7.4. Discussion....133

7.4.1. Microstructural analysis and fluid inclusions data.....133
7.4.2. P-T paths and conditions of deformation based on fluid inclusion data.....134
7.4.3. Pressure and temperature conditions of peak metamorphism.....136
7.5. Conclusions.....138

CHAPTER EIGHT: **DISCUSSION OF STRUCTURAL EVOLUTION, DEFORMATION MECHANISMS, AND P-T CONDITIONS OF THE SHEAR ZONES**

8.1. Introduction.....140
8.2. Structural geometry of the shear zones.....141
8.3. The relative significance of ductile thrusts versus shear zones.....143
8.4. Strain and displacement of the shear zones.....146
8.5. Deformation mechanisms operating during development of the shear zones.....147
8.6. Temperature variations of the shear zones.....150
8.7. Ductile-brittle transition conditions in the shear zones.....151
8.8. Exhumation of the shear zones.....152
8.9. Mechanisms of formation of the shear zones.....154
8.10 Conclusions.....158

REFERENCES.....163

APPENDICES:

Appendix A: Sample location map.

Appendix B: Graphical Rf/Ø plots of quartzites from the Stonyfell Quartzites

Appendix C: Method of quantitative analysis of microstructural quartz grain geometry

Appendix D: Results of the f-test statistic

Appendix E: Spreadsheets of fluid inclusion data

Appendix F: Representative P-T estimates using Thermocalc Program and the approach of Powell and Holland (1988) with the expanded, internally consistent datset of Holland and Powell (1990).

LIST OF FIGURES

Page numbers of the figures refer to the number of previous pages in the text.

CHAPTER ONE

Fig. 1.1: Generalised map of the Alpine-Iranian Orogen.....2

Fig. 1.2: Principal elements of the Delamerian Orogen in south Australia.....10

Fig. 1.3: Simplified geological map of the southern Adelaide Fold-Thrust Belt.....12

CHAPTER TWO

Fig. 2.1: Stratigraphic column of the Adelaide Hills area.....20

Fig. 2.2: Geological map of the Adelaide Hills area.....23

Fig. 2.3: Cartoons showing a typical ductile shear zone with a maximum displacement gradient in the shear zone centre and a typical asymmetric shear zone.....23

CHAPTER THREE

Fig. 3.1: Geological map of the Morialta area.....30

Fig. 3.2: (a) Photograph of a major antiformal structure in the Morialta are. (b) Minor folds in the deformation zone of the HW_1 ductile thrust in the Morialta area. (c) Cleavage refraction within the interlayered psammoplites and psammites of the Stonyfell Quartzite. (d) ECC-Fabrics in sheared Stonyfell Quartzite within the Morialta shear zone. (e) En-echelon quartz veins in the Stonyfell Quartzites.....31

Fig. 3.3: Progressive development of overprinting cleavages from the upper transitional zone toward the lower boundary thrust in the Morialta shear zone.....32

Fig. 3.4: Scketches of main geometrical features of the Morialta area.....33

Fig. 3.5: (a) Transposed layering and minor asymmetric folds with top to NW sense of asymmetry in the Woolshed Flat Shale within the Morialta shear zone. (b) Folded and mullion like structures, trending SE, in the Stonyfell Quartzite within the deformation zone of the FW_1 ductile thrust in the Montacute Heights area. (c) Photograph and sketch (rectangle area in the photograph) of minor asymmetric folds along with micro-scale thrusts in the pelites of the Woolshed Flat shale within the Norton Summit shear zone in the Greenhill area.....34

Fig. 3.6: Geological map of the Montacute-Heights area.....35

Fig. 3.7: Geological map of the Greenhill area.....36

Fig. 3.8: Sketch map of fault-propagation folds along the HWII ductile thrust in the hangingwall of the Greenhill shear zone in the Greenhill area.....37

Fig. 3.9: (a) Fault-propagation fold along the HW_{2w} ductile thrust within the Greenhill area. (b) Sheared off overturned forelimb of the minor asymmetric folds along the ductile thrusts in the Ackland Hill Road. (c) Synclinal breakthrough fault-propagation fold within the deformation zone of the Aldgate thrust. (d) Photograph and sketch of extensional crenulation cleavage (ECC-Fabric) from within the Pole Road shear zone.....39

Fig. 3.10: Geological map of the Poll Road area.....39

Fig. 3.11: (a) Simplified geological map of the Pole Road area showing subareas A, B, C, and D of different angles between bedding and regional cleavage. (b) A sketch cross section across the subareas.....41

Fig. 3.12: Geological map of the Clarendon area.....43

Fig. 3.13: (a) Photograph and sketch showing development of cleavages from S_{1a} to S_{1c} in phyllonites of the Woolshed Flat Shale from within the Clarendon shear zone. (b) Slickensides lineation on the movement plane (bedding) and as growth fibres (arrow) in the quartz veins from within the Clarendon shear zone. (c) Folded and boudinaged quartz veins in the phyllonites of the Woolshed Flat Shale from within the Clarendon shear zone. (d) Extensional crenulation cleavages (ECC-Fabrics) in the phyllonite from within the Clarendon shear zone.....44

Fig. 3.14: Geological map of the Mt. bold area.....46

Fig. 3.15: (a) Minor asymmetric folds in pelites of the Woolshed Flat Shale from within the Mt. Bold shear zone. (b) Transposition of bedding within psammites of the Woolshed Flat Shale within the Mt. Bold shear zone. (c) Asymmetrical extension shear bands (arrows) and deformed quartz veins in the phyllonites of the Woolshed Flat Shale from within the Mt. Bold shear zone. (d) Sheared Stonyfell quartzite with development of boudinaged quartz veins from within the Mt. Bold shear zone. (e) Truncation of minor to mesoscopic recumbent isoclinal folds by out-of-sequence T_3 thrusting in the Mt. Bold shear zone.....47

Fig. 3.16: (a) Isoclinal recumbent sheath-like folds (Type I) in the Woolshed Flat shale from within the Mt. Bold shear zone. Note that its upper limb is truncated by T_3 thrusting. Also note superposition of minor asymmetric folds of Type II on the lower limb (arrow). (b) Photomicrograph of Type I fold geometry showing sheath-like nature of these fold types. Notice eye fold closure in the upper part of photomicrograph. (c) Truncation of the upper limbs of Type I fold by T_3 thrusting from within the Mt. Bold shear zone. (d) Minor asymmetric Type II fold geometry in the Woolshed Flat Shale from within the Mt. Bold shear zone. (e) Out of syncline thrust geometry of T_1 thrusting within the Mt. Bold shear zone. (f) Asymmetric boudinaged quartz veins from within the Mt. Bold shear zone.....49

Fig. 3.17: Sketches showing cleavage vergence analysis, after Bell (1981).....53

Fig. 3.18: Vergence direction analysis of the shear zones in the study area.....53

Fig. 3.19: Stereograms showing transport direction analysis of the shear zones in study area.....54

Fig. 3.20: Sketches showing development of folds in shear zones of the study area.....54

Fig. 3.21: Proposed strain fields for deformational history of the study area.....60

Fig. 3.22: Schematic diagrams showing development of the shear zones and associated ductile thrusts in the study area.....61

CHAPTER FOUR

Fig. 4.1: Balanced cross-sections and geometrical restorations of four sections across the Adelaide Hills area.....64

Fig. 4.2: Enlarged geometry of mesoscopic fold in the hangingwall of the Morialta shear zone.....66

Fig. 4.3: Flinn diagram for finite strain geometry of the Stonyfell Quartzite samples across the shear zones in the study area.....74

Fig. 4.4: Logarithmic Flinn diagram of the Stonyfell Quartzite data.....74

CHAPTER FIVE

Fig. 5.1: Sketch showing general location of sub-zones in the shear zones.....77

Fig. 5.2: Morphological classification of cleavages using an optical microscope.....78

Fig. 5.3: (a) Weakly developed rough cleavage in psammites of the Woolshed Flat Shale from the upper transitional zone of the Mt. Bold shear zone. (b) Well developed rough cleavages in psammites of the Woolshed Flat Shale from within the Mt. Bold shear zone. (c) Very thin, flattened presolved quartz grains "F" and less modified detrital grains "M" with development of beards of overgrowth "B". (d) Overgrowths of quartz and small-scale mica in shadows of bent detrital mica oriented sub-orthogonal to the cleavage. (e) Detrital mica oriented sub-parallel to the cleavage domains. Note the deformation of the mica along the (001) cleavage. (f) Deformation band and to a lesser extent subgrain formation in detrital quartz grains from the lower boundary thrust to the Mt. Bold shear zone.....79

Fig. 5.4: Microstructural development of rough cleavages from the upper transitional zone towards the lower boundary thrusts within the Mt. Bold shear zone.....81

Fig. 5.5: (a) Continuous cleavage in the pelites from the Woolshed Flat Shale defined by fine-grained micaceous material. (b) Development of cleavage domains in sandy pelites of the Woolshed Flat Shale. (c) Transposition cleavage in sandy unit of a pelite of the Woolshed Flat Shale which is parallel to the continuous cleavage described in the text. (d) Discrete crenulation cleavage (subhorizontal dark traces) overprinting an early slaty cleavage (steep crenulated mica and quartz grains) in pelites of the Clarendon shear zone. (e) Development of zonal crenulation cleavage by concentration of phyllosilicates in cleavage domains (subhorizontal traces). (f) Development of discrete crenulation cleavages (solution seams where the micas are also oriented in parallel) in sandy pelites from the Mt. Bold shear zone.....82

Fig. 5.6: Photomicrographs and sketches showing development of crenulation cleavages from the upper transitional zone towards the lower boundary thrusts within the shear zones of the study area.....85

Fig. 5.7: Microscopic shear sense indicators in samples from within the shear zones. (a) Pressure fringes developed in silty pelites of the Woolshed Flat Shale in the Clarendon shear zone. (b) Pressure fringes in psammites from within the Mt. Bold shear zone. (c) Displaced broken feldspar in quartzite from within the Mt. Bold shear zone. (d) Antithetic microfaults developed in the basal (001) cleavage and displaced the mica fragments oblique to the mesoscopic shear plane and orientation of cleavage in matrix; the sense of shear is to NW (to the left). (e) Asymmetric sheared folds in a sandy unit of the Woolshed Flat Shale from within the Pole Road shear zone; the top to NW (to the left) sense of asymmetry defines the sense of shear in the shear zone. (f) Curved fibre quartz veins in dolomites of the Montacute Dolomites from within the Mt. Bold shear zone; the curved geometry of the fibres defines the sense of displacement in the shear zone which is to the NW (to the left).....87

CHAPTER SIX

Fig. 6.1: Photomicrographs of quartzite collected from the Mt. Bold shear zone. Thin sections cut parallel to the stretching lineation and perpendicular to the cleavage. (a) Slightly deformed quartzite from sub-zone I. (b) More deformed quartzite from sub-zone II. (c) More highly deformed quartz from sub-zone III.....95

Fig. 6.2: Photomicrographs of quartzite collected from the Pole Road shear zone. Thin sections cut parallel to the stretching lineation and perpendicular to the cleavage. (a) Undeformed to slightly deformed quartzite from sub-zone I. Note random intracrystalline extinction (UN) and development of overgrowths (arrows). (b) More deformed quartzite from sub-zone II. Here, quartz grains are more deformed to develop small recrystallised grains (RE) which shows initiation of core and mantle structures. (c) More highly deformed quartz from sub-zone III. Note greater

development of core and mantle structure and also development of phyllosilicates to form spaced cleavage.....96

Fig. 6.3: Photomicrographs of deformed quartzite collected from within the Morialta shear zone and associated hangingwall ductile thrust. (a) Slightly deformed quartzite from sub-zone I. Note low intensity of intracrystalline deformation and weak development of phyllosilicates which define initiation of a spaced cleavage. (b) More deformed quartzite with greater development of pressure solution products from sub-zone II. Note development bearded overgrowths (BO) and truncation of grains boundaries (T) by oriented phyllosilicates. (c) More highly developed pressure solution process in phyllosilicate rich layer of a sample from sub-zone III. Note increasing development of cleavage domains and bearded overgrowths (BO). (d) Highly deformed quartz grains in quartz rich layer of a sample from sub-zone III. Note development of small recrystallised grains due to subgrain rotation recrystallisation (SRR) around the margin of original grains. (e) Fractured feldspar with development of slight intracrystalline deformation in sample from sub-zone III. (f) Intracrystalline fracturing in quartz from the hangingwall ductile thrust of the shear zone.....97

Fig. 6.4: Histograms and scattergrams of the distribution of grain sizes and grain shapes of the quartzite from within: (a) the Mt. Bold and Pole Road shear zone and: (b) the Norton Summit, Greenhill, and Morialta shear zones.....101

Fig. 6.5: linegraphs of the aspect ratio of the grains and histograms of the shape-preferred orientation of the grains in samples of quartzite from sub-zone I towards sub-zone III within: (a) the Mt. Bold and Pole Road shear zones and: (b) the Norton Summit, Greenhill, and Morialta shear zones.....102

Fig. 6.6: Descriptive statistics and 3-D histogram of the grain size variations along with the results of the statistical test (t-Test) on grain size variations for samples from within: (a) the Mt. Bold shear zone; (b) the pole Road shear zone; and: (c) the Morialta shear zone.....104

Fig. 6.7: Descriptive statistics and 3-D histogram of the grain shape (aspect ratio) variation analysis along with the results of the statistical test (t-Test) on aspect ratio variations for samples from within: (a) the Mt. Bold shear zone; (b) the pole Road shear zone; and: (c) the Morialta shear zone.....105

Fig. 6.8: Descriptive statistics and 3-D histogram of the shape-preferred orientation analysis along with the results of the statistical test (t-Test) on shape-preferred orientation variations for samples from within: (a) the Mt. Bold shear zone; (b) the pole Road shear zone; and: (c) the Morialta shear zone.....106

Fig. 6.9: Scattergrams showing the relationship between aspect ratio (ellipticity) and grain size in samples from sub-zone I towards sub-zone III from within the Mt. Bold, Pole Road, and Morialta shear zones.....111

CHAPTER SEVEN

Fig. 7.1: (a) Photograph of folded and boudinaged quartz veins in the phyllonites of the Woolshed Flat Shale from within the Clarendon shear zone. (b) Type I and III fluid inclusions in quartz veins collected from the Pole Road shear. (c) Rounded (R) to negative crystal (NC) Type II fluid inclusions in quartz vein sample from the Mt. Bold shear zone. (d) Type II fluid inclusion with negative crystal (NC) shape along sub-grain boundaries.....115

Fig. 7.2: Sketches of main fluid inclusion types.....116

Fig. 7.3: (a) Photomicrograph of Type IV fluid inclusions developed as healed fractures. (b) Photomicrograph of Type IV fluid inclusions cutting grain (GB) and sub-grain (SG) boundaries. (c) Photomicrograph of Type IV fluid inclusions in a sample from the Morialta shear zone. (d) Necking in type III inclusions (arrow) along healed microfractures showing reequilibrated fluid inclusions. (e) Decrepitated inclusions

surrounded by a halo of smaller inclusions along grain boundaries in a quartz vein sample from the Mt. Bold shear zone. (f) Showing arrangement of fluid inclusions along grain and subgrain boundaries.....117

Fig. 7.4: Histogram showing the distribution of last melting temperature and CO_2 clathrate melting temperature for all fluid inclusion types.....119

Fig. 7.5: Temperature-composition diagram for the system H_2O-NaCl (after Crawford 1981).....119

Fig. 7.6: Histogram showing the distribution of CO2 homogenisation temperature and total homogenisation temperature for all fluid inclusion types.....120

Fig. 7.7: Scattergram of homogenisation temperature vs salinity data of all fluid inclusions.....121

Fig. 7.8: Scattergram of aspect ration of carbonic fluid inclusions of Types I an II.....121

Fig. 7.9: Histograms of homogenisation temperature and descriptive statistics of all fluid inclusion types.....123

Fig. 7.10: P-V-T graphs and P-T paths of the shear zones.....127

Fig. 7.11: (a) Photomicrograph and backscatter image of the phyllosilicate aggregates from within the Morialta shear zone, showing a cluster of green biotite (bold circle in the image) and chlorite (white cross in the image). (b) Photomicrograph and backscatter image of a sample from within the Mt. Bold shear zone, showing clusters of brown biotite (white cross in the image). (c) Cleavage domains in pelites from the lower boundary thrust to the Pole Road shear zone.....128

Fig. 7.12: Diagrams showing the distribution of minimum, maximum, and average temperatures and pressures of peak metamorphism in samples from the shear zones.....136

CHAPTER EIGHT

Fig. 8.1: Schematic cartoon showing progressive development of deformation fabrics, structures, and microstructures from outside towards lower boundary thrusts to the shear zones in study area.....142

Fig. 8.2: Sketches showing development of fault-propagation folds along the ductile thrusts in the Adelaide Hills area.....145

Fig. 8.3: (a) Schematic diagram showing the geometry of a taper orogenic wedge. (b) Behaviour of a Columb wedge in response to changes in certain geological parameters.....156

Fig. 8.4: Initiation of thrust sheets in region of high basin taper.....156

Fig. 8.5: Sketches showing evolution of thrust/shear zones in the Adelaide Hills area wedge.....157

Fig. 8.6: Trajectories of three rocks from three main shear zones in the southern Adelaide Fold-Thrust belt.....157

LIST OF TABLES

Page numbers of the tables refer to the number of previous pages in the text.

CHAPTER FOUR

Table 4.1: Finite and longitudinal strain results of the Stonyfell Quartzites samples across the study area.....69

CHAPTER SIX

Table 6.1: General description of the microstructures of quartz and feldspars in quartzite from within the shear zones. Labels; Qtz: quartz, F: feldspar, DB: deformation bands; GBMR: grain boundary migration recrystallisation; SRR: subgrain rotation recrystallisation; SS: subgrain structures, SUE: sweeping undulatory extinction, and SMT: solution mass-transfer. **I, II,** and **III** are the sub-zones of the shear zones...94

CHAPTER SEVEN

Table 7.1: Summary of fluid inclusion data.....119

Table 7.2: Summary data of bulk composition, bulk density, and estimated pressure and temperature of trapment of all types of fluid inclusions.....126

Table 7.3: Representative probe analyses of minerals in samples from the Morialta, Pole Road, and Mt. Bold shear zones.....128

Table 7.4: Average pressure calculations on samples from the Morialta, Pole Road, and Mt. Bold shear zones.....130

Table 7.5: Average temperature calculations on samples from the Morialta, Pole Road, and Mt. Bold shear zones.....131

Table 7.6: Average pressure and temperature calculations on samples from the Morialta, Pole Road, and Mt. Bold shear zones.....130

ABSTRACT

Strain partitioned into the shear zones and associated ductile thrusts forms the main locus of deformation in the southern Adelaide Fold-Thrust belt. The shear zones reveal a concentration of deformed fabrics and structures within narrow subparallel high deformation zones, separated by larger less deformed area. These zones provide an opportunity to examine the geometry, kinematic and microstructural processes which resulted in the formation and structural evolution of such high deformational zones in the southern Mt. Lofty Ranges/Adelaide Hills study.

Structural mapping across the area has revealed six major stacked high deformation zones or shear zones, with generally NE-SW trends and shallow- to moderate SE dips. These shear zones, which are uniformly bounded by emergent lower boundary thrusts at the base and by upper transitional zones at the top, are named the *Morialta*, *Greenhill-Montacute Heights*, *Norton Summit*, *Pole Road-Summertown, Clarendon* and *Mt. Bold* shear zones, from NW to SE respectively. All of the shear zones anastomose and include minor ductile thrusts that form imbricate fans propagating to the NW. These ductile thrusts developed either within the shear zones or in the footwalls and hangingwalls to the shear zones. They are in fact narrow zones of ductile deformation in which, like the shear zones, fabrics and deformed structures with the same geometry and kinematics as the shear zones are developed.

Detailed structural mapping and analysis of the area has documented that outside the shear zones and associated ductile thrusts original bedding, open folding, and to lesser extent regional slaty cleavage are the main geometrical elements. Within the shear zones an array of deformation fabrics (stretching lineations, crenulation/spaced cleavages, and shear bands) and structures (minor folds, veins, and transposed layering) occur. The minor folds, the most prominent structural features of the shear zones, are generally disharmonic structures forming open-to-tight, buckle-style folds, plunging shallowly to SE. Two types of minor fold geometries have been recognised. The first type is formed by gently to moderately curvilinear-to-isoclinal recumbent folds with axes sub-parallel to the local stretching

lineation, whereas the second fold type is formed by gentle-to-tight, asymmetric, NW verging folds with axes mostly oblique to the local stretching lineation. Where both of them occur together, the second type of folds are superposed on first type.

Crenulation cleavages are another set of notable structures found within the shear zones. These are initiated as open zonal crenulations at the upper transitional zones, but intensify to develop discrete crenulation cleavages within the shear zones and are even more intensified to form new continuous cleavages close to the lower boundary thrusts. Superposition of folds and development of new continuous cleavages in the shear zones appears to have occurred during a single progressive deformation.

Geometrical restoration of balanced cross-sections across the area indicates an average of 34% for geometrical shortening, which is close to the estimated average shortening of many fold-thrust belts and implies that the area is mainly deformed by displacement along the shear zones/thrusts and folding. Similarly, finite strain analyses of quartzite using the Rf/Ø method shows relatively low strain values in samples across much of the area. Strain increases in the shear zones and especially at the lower boundary thrusts. This indicates that most strain is concentrated in the shear zones and especially at the lower boundary thrusts. Deformation microstructures developed in cleavage from psammites within the shear zones and at the lower boundary thrusts further confirms that much of the strain is concentrated at these boundaries.

Microstructures of quartz in quartzite from within the shear zones show evidence of intracrystalline deformation in the form of undulatory extinction, deformation bands, and sub-grain formation, which increase in intensity from the upper transitional zones toward the lower boundary thrusts. At these boundaries grain boundary migration recrystallisation and sub-grain rotation recrystallisation occur and to form core and mantle structures. Comparison of the microstructures across the shear zones shows that the amount of intracrystalline deformation features and core and mantle structures decreases from within the shear zones closest to the foreland toward the shear zones closest to hinterland. Such a decrease in crystal plastic deformation products across the shear zones occur within brittle-

ductile transitional conditions of deformation. Similarly, quantitative/statistical evaluation of the quartz-grain configuration data on a number of quartzite samples from within the shear zones indicates that from the upper transitional zones toward the lower boundary thrusts the grain size decreases, the aspect ratio increases, and the shape-preferred orientation of grains is modified. This is also confirmed by the relatively high statistical confidence value (t-test) of the quartz grains and provides further evidence to constrain the development of grain configuration in the shear zones during shearing/thrusting.

P-T conditions and deformation paths have been determined using microprobe and fluid inclusion data. This has been carried out to determine the pressure and temperature of peak metamorphism and to recognise the burial and exhumation history of rocks in the shear zones of the study area and of the southern Adelaide Fold-Thrust Belt. The results of calculations of average pressure and temperature of peak metamorphism show temperatures around 400°C and pressures of about 2.5 kbar, which represent deformation conditions at or near the brittle-ductile transition and further support the results of studies on microstructures. The higher temperature of peak metamorphism was considered mainly to be due to advection of magmatic activity in the more internal portion of the belt and to a lesser extent to the effects of internal frictional heating within the deforming wedge of the southern Adelaide Fold-Thrust belt during syntectonic metamorphism. Similarly, detailed analyses of fluid inclusion data recorded fairly similar P-T conditions, but also showed that the inclusions were modified during the exhumation of the area, most likely along the lower boundary thrusts to the shear zones. This further provides data to propose a deformation path for development of the shear zones. The amount of inclusion modification and/or exhumation also decreased toward the more forelandward shear zones.

NAME: ..... Ali Yassaghi COURSE: ..... Geology .....

This work contains no material which has been accepted for the award of any other degree or diploma in any university or other tertiary institution and, to the best of my knowledge and belief, contains no material previously published or written by another person, except where due reference has been made in the text.

I give consent to this copy of my thesis, when deposited in the University Libraries, being available for photocopying and loan.

SIGNATURE: ..... DATE: ..... 5/1/98 .....

ACKNOWLEDGMENTS

This research was made possible by a scholarship from the Ministry of Culture and Higher Education of the Islamic Republic of Iran, for which I am most grateful.

Sincere thanks are due to my supervisors Dr. Patrick James and Dr. Thomas Flöttmann for their friendly suggestions and advice and their invaluable reviews of drafts of the manuscript.

Discussions with Dr. Mike Sandiford, who was also a member of my thesis committee, Dr. Robin Oliver, Dr. Martin Hands, and Dr. Peter Brooker about different aspects of the project are acknowledged. Assistance by Dr. Yvonne Bone and Dr. Ross Both on study of fluid inclusions are also acknowledged.

Staff members of the University of Adelaide provided technical support throughout the study, in particular from the Department of Geology and Geophysics I especially acknowledge Dr. John Foden, Dr. Victor Gostin, Gerald Buttfield, Sophia Craddock, Kim Crawford for their friendly assistance, Wayne Mussared and Geoff Trevelyan for preparation of thin sections, Sherry Proferes for advice and help on drafting; and from the Centre for Electron Microscopy and Microstructure analysis (CEMMSA) John Terlet and Huw Rosser for their assistance with the electron microprobe.

The logistic support of Mines and Energy South Australia (MESA) is gratefully acknowledged.

My special thanks to Dr. Reza Moussavi-Harami, my former teacher and colleges in Mashhad Uni., and his family for their warm friendship and helpfulness; and also due to, Dr. Hossain Rahimpour-Bonab, Hassan Baghian-Yazd, and Lal Mendis for their warm friendship and company over the years of university life in Adelaide.

As ever, my deepest gratitude goes to my parents for their support through all stages of my education. Certain thanks to my wife Fatemeh for her endless support during all these years far from home; and to the little Hamed and Uness for giving up many evenings and weekends.

I dedicate this thesis

to

my wife *Fatemeh*

and

my sons *Hamed* & *Uness*

Chapter one

INTRODUCTION

1.1 Preamble

Thrust faults and shear zones contain a comprehensive record of the tectonism of fold-thrust belts. Therefore the study of thrust faults and shear zones is one of the key subjects to understand the external parts (fold-thrust belts) of major orogenic belts (Mitra & Fisher 1992). Detailed structural mapping and concomitant studies of the development and regional significance of minor structures associated with thrust faults and shear zones have contributed much to the understanding of development of classical fold-thrust belts such as the Appalachian Valley and Ridge province (e.g. Mitra & Wojtal 1988) and Canadian Rocky Mountains (e.g. Price 1981). Current research on fold-thrust belts is focused on the structural geometry and kinematics, regional structural studies, and mechanics and mechanisms of their evolution (Mitra & Fisher 1992). Microstructures, strain and displacement, and P-T-t data are also considered as essential tools in the interpretation of the processes operating during thrust/shear zone formation (McClay 1992).

This thesis provides the first detailed examination of the geometry and kinematics, microstructures and deformation mechanisms, and P-T conditions of thrusts and shear zones in the southern Mt. Lofty Ranges/Adelaide Hills area. The main concept is to provide data to improve our understanding of the development of the southern Adelaide Fold-Thrust belt. This also contributes to our overall knowledge of the evolution of fold-thrust belts.

In this chapter, firstly an overall definition and description of the general characteristics, and mechanisms of formation of fold-thrust belts are presented. Then, the regional tectonic setting of the southern Adelaide Fold-Thrust belt and previous studies of the interpretation and development of the belt are addressed. Finally, the objectives of the study and methods used to resolve the objectives are presented. A detailed study of a small area in the southern

Adelaide Fold-Thrust belt (southern Mt. Lofty Ranges/Adelaide Hills area) is presented in following chapters.

The general geological setting of the study area (southern Mt. Lofty Ranges/Adelaide Hills area) is presented along with the distribution and features of the mapped major shear zones and associated ductile thrusts (chapter 2). The geometry and kinematics of deformational fabrics and structures from both outside of and from within the thrust/shear zones are examined and discussed in chapter 3. Chapter 4 presents an interprets balanced and geometrical restorations of cross sections which are accompanied by the results of finite strain analysis on selected quartzite samples. Microstructural analysis of cleavage development in psammites and pelites and microscopic kinematic indicators are discussed in chapter 5. Chapter 6 examines qualitative and quantitative analysis of quartz grain microstructures in quartzites and discusses the operating deformation mechanisms. The results of fluid inclusions and microprobe studies to assess pressure and temperature conditions of the shear zones are addressed in chapter 7. Finally, a model for the development of the thrust/shear zones in the area of study, and in general, in the southern Adelaide Fold-Thrust belt are presented and discussed in chapter 8.

1.2 Foreland fold-thrust belts

Orogenic belts coincide, not accidentally, with some of the earth's major continental mountain chains. It is clear that no single map or cross section can provide a universal model of an orogenic belt. Nevertheless, although many orogens are asymmetric, most orogens have a number of features in common. These features include a rough bilateral structural symmetry, with undeformed crust on either side, foredeeps, fold-thrust belts or outer part/external orogenic zones, and an internal crystalline core zone of metamorphosed and deformed sedimentary and volcanic rocks, mafic-ultramafic complexes and granitic plutons (Fig. 1.1) (Hsü 1981, Twiss & Moore 1992).

In this section, the very general characteristics and mechanisms of formation of fold-thrust belts are presented and discussed with examples from the main well known and studied

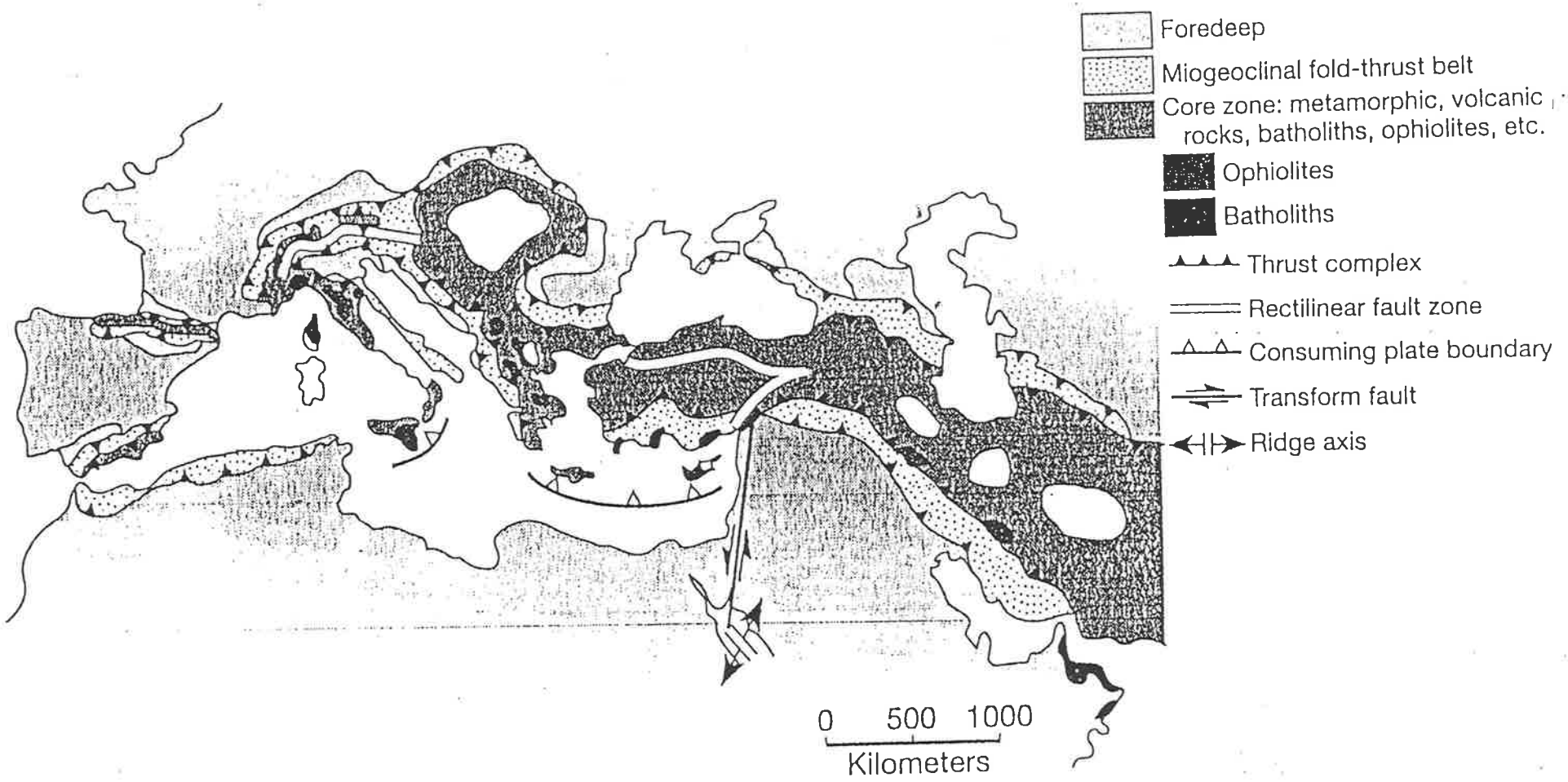

Fig. 1.1: Generalised map of the Alpine-Iranian or western segment of the Alpine-Himalayan Orogen (after Twiss & Moores 1992).

ancient (e.g. Appalachian Blue Ridge) and more recent (e.g. Taiwan) fold-thrust belts. This has been done in order to highlight the most common features of these belts.

1.2.1 Definition and general characteristics of fold-thrust belts

On the outer margins of most orogenic belts, there is commonly a wide deformational belt, with distributed deformation of a thick prism of sedimentary rocks that were deposited upon the margins of a stable craton and sediments thicken dramatically from the cratonal edge to the internal part of the belt (e.g. Rodgers 1970, Roeder *et al.* 1978, and Price 1981). These sedimentary rocks, which are not, or are at most very mildly metamorphosed, are commonly shortened into long parallel folds generally cut by parallel thrust faults of large displacement (Rodgers 1991a). The vergences of both folds and thrust faults are fairly consistently directed towards the craton. A well known and well documented example of such a fold-thrust belt is the US Appalachian Valley and Ridge province (e.g. Rodgers 1970, 1981, Boyer 1978, and Wojtal & Mitra 1988). Fold-thrust belts like the Appalachian Valley and Ridge province are widespread on earth and have been forming since at least the early Proterozoic. Other well known examples are the Cordilleran overthrust belt, especially north of the Basin and Range province (e.g. Price & Mountjoy 1970, Elliott 1976 & Chapple 1978), the Jura mountains north of the European Alps (e.g. Laubscher 1965, 1987 in Rodeger), the Zagros mountains of Iran (e.g. Berberian 1983), the western Taiwan fold-thrust belt (e.g. Suppe 1987, and Dahlen & Barr 1989), and of importance to this study, the southern Adelaide fold-thrust belt (e.g. Flöttmann *et al.* 1994, 1995, and Flöttmann & James 1997).

Characteristically, the deformation of such belts is comprised of thin-skinned tectonics, that is, the folds and thrusts terminate downwards in a main décollement within the cover sequence above the cratonic basement. However, some particular kinds of thrust sheets exhibit thin-skinned behaviour in which the basal thrusts or décollement are rooted within the crystalline basement (Hatcher & Hooper 1992).

Fold-thrust belts differ in a wide variety of ways, for example, in the geometry of their margins. In some regions the outermost margin of the belt is quite sharp, with a single major

sole thrust separating strongly deformed rocks in the fold-thrust belt from nearly flat or only locally deformed strata in the foreland basin (e.g. the Maranon & Subandean fold-thrust belt in Peru, Megard 1981 in Rodgers 1991). The inner margins may also vary in different fold-thrust belts. In some regions (e.g. the Appalachian, western Alps, and Urals; Rodgers 1991) the fold-thrust belt is backed by a basement anticlinorium or a line of such anticlinoria, commonly located along a steep metamorphic gradient. In the other regions, however, the fold-thrust belt may merge into a more internal belt where rocks of the same age but often of contrasting sedimentary facies, are more metamorphosed (e.g. the slate belt of N. Wales, Twiss & Moores 1992).

Another source of variability is the nature of the stratigraphy of the sediments involved. The stratigraphic sequences of fold-thrust belts as defined in the literature range from carbonate-dominated sequences (e.g. the Jura fold-thrust belt, Laubscher 1965) to clastic-dominated sequences (e.g. western Taiwan, Suppe 1987). According to the classification of Rodgers (1991) the southern Adelaide fold-thrust belt (Mt. Lofty Ranges) is transitional between these extremes, because in the southern Adelaide fold-thrust belt there is a combination of clastic and carbonate rocks.

Most rocks in fold-thrust belts are only weakly or are unmetamorphosed. In some regions, however, low grade metamorphism (up to greenschist facies) is present, where clay minerals for example are recrystallised to chlorites and micas. Slaty cleavage is characteristic of argillaceous sediments and may be cut by a second generation of spaced or crenulation cleavage formed by solution transfer during deformation (Passchier & Trouw 1995, p. 71).

The most typical and characteristic structural feature of foreland fold-thrust belts is that they consist of a set of low-angle listric thrust faults that have a consistent general strike and dip. These thrust faults are the most common examples of large thrust systems (Boyer & Elliott 1982). Similarly, fold-thrust belts characteristically overlie undeformed basement or involve basement along a décollement surface or sole thrust. In this case, significant deformation and shearing in the thrust systems are confined to the rocks above the décollement. The décollement cuts up through the stratigraphic section toward the foreland to give the thrust

sheet a wedge-shaped geometry. Above the sole thrust, there may be several décollements, all of which ultimately branch-off from the main sole thrust and like the sole thrust tend to rise through the stratigraphic section toward the foreland and produce propagating imbricate fans or duplexes (e.g. Boyer & Elliott 1982, Butler 1982).

Most fold-thrust belts exhibit spatial variation in overall shape, thrust spacing, and internal imbrication. For example, the Sawtooth thrust belt in Montana has a maximum width of 28 km and contains 15 to 20 closely spaced imbricate faults (Mudgo & Earhart 1983) whereas the Wyoming thrust belt is approx 145 km wide and generally consists of 4 or 5 major thrust sheets exhibiting only minor internal imbrication (Coogan 1993). There are also differences in relative thrust timing among thrust belt segments. Synchronous thrusting occurs within the Sawtooth Range (Boyer 1992), whereas the Wyoming thrust belt appears to have developed generally in a relatively simple hinterland-to-foreland sequence with the exception of minor out-of-sequence imbrication and reactivation of existing thrusts (Coogan 1993). Similarly, in many other foreland fold-thrust belts, pervasive arrays of minor faults are the primary thrust zone structures. These thrust sheets alternately shorten and elongate during sheet movement (Woodward *et al.* 1989) or deformation is more localised and is associated with a softening process and shearing along the bases of the thrust sheets (Wojtal & Mitra 1988). The latter is more likely to happen in more internal portions of orogenic belts where softening processes lead to the formation of mylonites (Gilotti & Kumpulanien 1986). However, studies of the external portions of orogenic belts, i.e. fold-thrust belts, shows that deformation can be localised along the base of thrust sheets (Wojtal 1986) which is presented and discussed in the more detail in next section.

1.2.2 The formation of fault/shear zones in thrust belts

A discussions of the formation of fault/shear zones in thrust belts is presented in this section in order to determine how deformation may be localised within such narrow zones to produce these most common features of fold-thrust belts. Fault rocks in fault/shear zones may be examined in two ways. Fault rocks may be studied by determining how undeformed rocks near a fault are transformed into tectonites (Sibson 1977, Schmid 1983, and Gilotti &

Kumpulainen 1986), or alternatively by examining rock masses at different points adjacent to a fault to determine how changes in temperature, and pressure affected the fault history (e.g. Wojtal & Mitra 1988). The first approach is akin to the Lagrangian approach to fluid flow problems, while the second is analogous to a Eulerian treatment of fluid flow problems (Batchelor 1976, p71). Both approaches have merit in thrust belts because thrust faults form under a range of conditions and may evolve along several different paths. By using the first approach of the study of fault rock types, two principal fault zone types have been distinguished in thrust belts (Wojtal & Mitra 1988). These are analogous to Mean's (1984) two types of shear zones. In a Type I fault/shear zone, the deformation zone develops from the centre to the margin by work-hardening (White *et al.* 1980) throughout the development of the zone. In a Type II fault/shear zone, rocks at the centre of the zone strain-soften throughout the evolution of the zone, commonly to culminate in the development of a discrete fault. In thrust faults from internal and external portions of orogenic belts, both types of fault/shear zones may evolve and from, or into, each other. This may occur with continued movement or as physical conditions change during fault displacement (Wojtal & Mitra 1986, 1988).

At the pressures and temperatures typically formed in the internal portions of orogenic belts, large, weakly to moderately deformed sheets of rock move by concentrating shear strain in a narrow zone at their base, which leads to the formation of mylonites (e.g. Schmid 1983, Gilotti & Kumpulanien 1986). Sharp strain gradients across internal thrust zones, apparent because of their distinctive pattern of curving foliations, are typical of these fault/shear zones (Ramsay & Graham 1970, Ramsay 1980) and crystal plastic deformation mechanisms, as defined by Passchier & Trouw (1995), are dominant. These mechanisms are instrumental in restricting shearing to thin zones of continuous deformation (White *et al.* 1980, Schmid 1983, Gilotti & Kumpalanien 1986). In such zones dislocation creep (Vernon 1976) is dominant and is accompanied by dynamic recrystallisation (Knipe & White 1979). This process which confines shearing within these zones at the onset of deformation has been referred to as Type I fault/shear zone formation (Wojtal & Mitra 1988). Strain softening processes cause further deformation to be confined to the mylonite zone, which may lead to fault/shear zones changing from Type I to Type II by a change from a dislocation creep deformation mechanism to a grain

size-sensitive creep (Mitra 1978, Wojtal & Mitra 1988). Shearing within the zone is recognised to enhance perturbations in the layering, giving rise to minor-scale isoclinal folding of banded mylonites (Hudleston 1977). Examples of such fault/shear zones were described from the Moine thrust zone in Scotland (Elliott & Johnson 1980, Kelley & Powell 1985), the Glarus thrust zone in the Helvetic Alps (Schmid 1983) and the Blue Ridge thrust sheets in the southern Appalachians (Boyer & Elliott 1982, Wojtal & Mitra 1988).

Detailed studies of fault rocks in thrust/shear zones from the external portions of orogenic belts (especially fold-thrust belts) are not as common as they are from the internal portions. This may be in part because of the continued argument about the nature of these zones. The traditional idea is that external thrusts are discrete and clean faults because they initiated as brittle fractures (Hubbert & Ruby 1959, Hsü 1969, and Muller & Hsü 1980). Another view, however, considers that external thrust faults form by slow forcing of ductile deformation through deformed rocks (Elliott 1976, Chapple 1978). Field evidence in well studied fold-thrust belts like the Appalachian Valley and Ridge has revealed that emplacement of thrust sheets evolves by the development of penetrative arrays of minor faults at the base of the sheets (Harris & Milici 1977, and Wojtal 1986). As displacement increases, the spacing of minor fault changes to be most closely spaced immediately adjacent to the thrust, but remains at or above a minimum value of fault spacing which reflects an overall strengthening in pervasively faulted rocks, i.e., thrusts exhibit Type I behaviour (Wojtal & Mitra 1986, 1988). The numbers of microfaults, fractures, and extension veins that occur in fault/shear zones adjacent to large displacement thrusts are usually greater than the numbers of microfaults, fractures, and extension veins in rocks adjacent to small displacement thrusts (Wojtal 1986). However, where evidence for continuous (quasi-plastic) deformation can be seen, deformation in the external portion of orogenic belts does not cease and can have occurred even when a deformed zone attains minimum fault spacing (Wojtal & Mitra 1988). In the presence of sufficiently fine-grained matrix and fluids, diffusion-accommodated deformation mechanisms such as pressure solution and grain-boundary migration cause strain-softening and concentration of deformation along the fault/shear zone (Mitra 1984, Wojtal & Mitra 1986). Thus, as in the internal portions of the belts, softening processes leading to continuous

deformation are at work to change thrust/shear zones from Type I mode to Type II mode in nearly all large displacement faults, where pore fluids are often essential components in the process (Mitra 1984, Wojtal & Mitra 1986, 1988).

Nevertheless, although thrust/shear zones in fold-thrust belts are described as deformation zones of plastic yield (Chapple 1978), the rock fabrics which might support that inference are not necessarily easy to document. This is because in such zones arrays of mesoscopic brittle riedel shears, microfaults and shear bands all display heterogenous shearing (Woodward *et al.* 1989). Such heterogenous simple shear zones are abundant at the base of almost all large displacement thrust sheets but their abundance commonly decreases away from the thrust surfaces (Yonkee & Bruhn 1989, Woodward *et al.* 1989).

It appears therefore from the literature that there are no substantial differences between thrust/shear zones of fold-thrust belts and thrust/shear zones from the internal portions of orogenic belts. Different deformation mechanisms, however, control deformation in both portions of orogenic belts, but the over-all distribution of deformation indicates that rocks follow similar paths through strain-hardening and strain-softening deformation. Therefore, it is not surprising that similar large-scale geometries are found in the two types of area (Wojtal & Mitra 1988).

1.2.3 Mechanisms of fold-thrust belt formation

The formation of fold-thrust belts is now generally believed to be driven, in a broad sense, by the taper of critical orogenic wedges (Davis *et al.* 1983). Historically, however, three main hypotheses were invoked to explain the mechanics of fold-thrust belt deformation. They are gravity sliding, gravity spreading and tangential compression (Smith 1981). The adjacent internal basement anticlinoria to these belts (where present) have been called on as the uplifted source for the sliding, the uplifted mass that spread, or the compressing plunger, depending on the hypothesis invoked. Meanwhile, many structural geologists appear to favour "The Push" as the driving force of fold-thrust belt formation even though mechanical constraints indicate that gravity should play the dominant role (e.g. Elliott 1976, 1980). However,

Hubbert & Rubey (1959) argued that the coefficient of friction in foreland fold-thrust belts is too high to allow the emplacement of large thrust sheets under horizontal compression. Therefore, they considered gravity sliding as a more practicable explanation for the emplacement of thrust sheets.

Recently, the critical-tapered coulomb wedge model proposed by Davis *et al.* (1983), Dahlen (1984) and Dahlen *et al.* (1984), together with subsequent modifications and developments (e.g. Davis & Engelder 1985, Dahlen & Barr 1989, and Dahlen 1990) produced a coherent explanation for the geometry and kinematics of thrust sheets in foreland fold-thrust belts and returned "The Push" to favour. The key point in this model is that thrust sheets are not tabular as Hubbert and Rubey (1959) assumed, but they are instead wedge shaped.

According to the critical wedge model (Davis *et al.* 1983), an active fold-thrust belt is analogous to a wedge of soil or snow that forms in front of a moving bulldozer. Such a wedge deforms internally until it attains a critical taper which is governed by the relative magnitudes of the frictional resistance along the base and coulomb strength of the material within the wedge under a given shortening regime (Davis *et al.* 1983). The rate of erosion and the accretionary influx rate of fresh material controls the width of a critically-tapered wedge and produces a steady state fold-thrust belt. A dynamic steady state fold-thrust belt is one in which the accretionary influx is balanced by the erosive efflux (Suppe 1981, Dahlen & Suppe 1988). Rocks are accreted at the toe and then horizontally shortened as they are transported toward the rear of the wedge. Material that enters at a lower level in the accreted section is more deeply buried before being uplifted by erosion.

The dynamic steady-state conditions which apply to active fold-thrust belts result in a characteristic map pattern of low grade metamorphism on the surface. Metamorphic isograds are generally parallel to the regional strike of a fold-thrust belt, with the grade increasing progressively from unmetamorphosed and zeolitic facies near the deformation front or toe of the wedge up to greenschist facies in the thickened part of the wedge (Barr & Dahlen 1989). The thermal structure of such dynamic steady state fold-thrust belts is influenced by frictional heating, both on the basal décollement and to a lesser extent within the deforming brittle

wedge. Such frictional heating that accompanies the deformation is responsible for the formation and degree of syntectonic metamorphism in an active fold thrust belt (Barr & Dahlen 1989, Barr *et al.* 1991).

A dynamic study of such an active fold-thrust belt in Taiwan has showed that in a fold-thrust belt with nearly lithostatic pore fluid pressure, approximately 60% of the work of steady state mountain building is being dissipated against friction on the décollement fault, and about 25% is being dissipated against internal friction, thus only 15% is available to do useful work against gravity (Dahlen & Barr 1989). An alternative description is provided by the equation $W'_B = W_D + W_S + W'_G$. The quantity of W'_B is the rate at which work is performed on the back of the wedge by "The Push", W_D is the rate at which energy is dissipated against friction on the décollement fault, W_S is the rate at which energy is dissipated against the internal frictional process within the deforming wedge, and W_G is the rate of work performed against gravity. The latter quantity is always positive for any critically tapered fold-thrust belt whose décollement fault dips towards its rear, in contrast to the gravity spreading theory of fold-and-thrust tectonics (e.g. Dahlen & Barr 1989).

Overall, the presently deforming fold-thrust belts like Taiwan show that the uplift which powers the gravity spreading is itself being produced by tangential compression or in other words by "The Push" from the rear (Dahlen & Barr 1989, Rodgers 1991, and Boyer 1995).

1.3. The Adelaide Fold-Thrust Belt

The Adelaide Fold-Thrust Belt (AF-TB) is mainly located in south Australia (see Fig. 1.2 for the location of the belt) and includes Kangaroo Island, the Mt. Lofty Ranges (which includes the Fleurieu Peninsula and the Adelaide Hills), the southern Flinders Ranges, the Central Flinders Ranges, and the Northern Flinders Ranges (Fig. 1.2). The structures exposed in the belt are Cambro-Ordovician in age, based on cross-cutting relations with igneous bodies (Foden *et al.* 1994, Sandiford *et al.* 1992, Jenkins & Sandiford 1992). The present topography, however, was initiated during the Cenozoic, based on stratigraphic relations in bordering basins (Sprigg 1946, Campana 1954, and Lemon 1989). To the west of the AF-TB

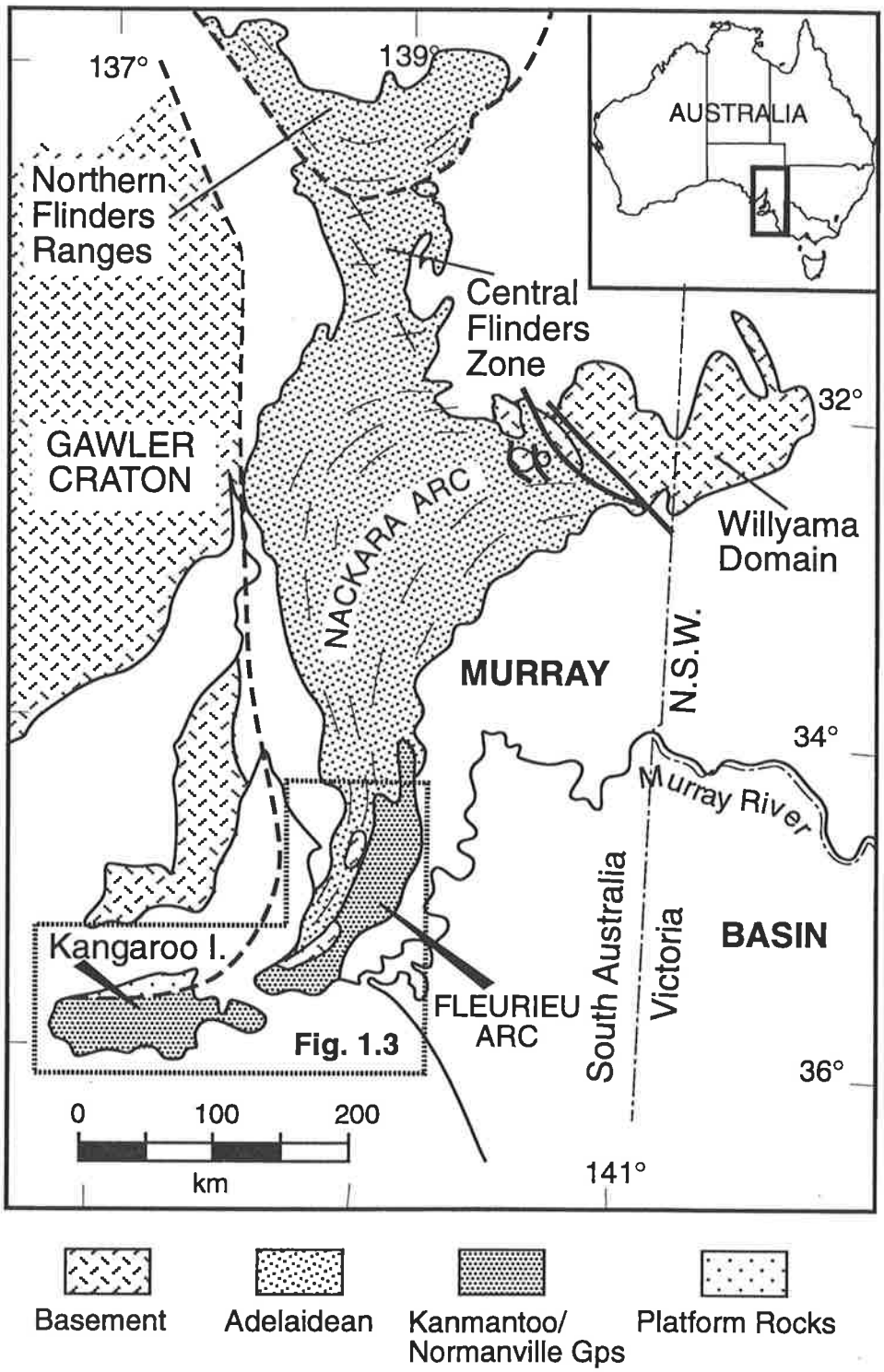

Fig. 1.2: Principal elements of the Delamerian Orogen in south Australia. Box shows the location of the Southern Adelaide Fold-Thrust Belt. For more detail see figure 1.3.

is the Gawler craton, a Precambrian shield (2500 Ma old gneiss and schist, Webb *et al.* 1987), and the Stuart Shelf (a region in which Precambrian basement is covered by thin undeformed sediments of late Proterozoic and Paleozoic age, Preiss 1987). To the east of the AF-TB is the Cenozoic Murray basin (Fig. 1.2).

In the following sections a summary of the tectonic setting of the belt is presented and a brief review of previous structural interpretations of the southern part of the belt (Southern Adelaide Fold-Thrust Belt, Figs 1.2 & 1.3) where the study area is located (the Adelaide Hills), are also presented. The main problems that resulted from earlier interpretations which in part lead to this study are discussed.

1.3.1 Tectonic setting of the Adelaide Fold-Thrust Belt

The early evolution of the Adelaide Fold-Thrust Belt (AF-TB, Fig. 1.2) is recorded by sediments deposited during repeated rift and sag phases and subsequent deformation, metamorphism and felsic magmatism during compressional events during the late Proterozoic and the Paleozoic (e.g. Jenkins & Sandiford 1991, Flöttmann *et al.* 1994). The Neoproterozoic extensional events caused a fundamental rift/drift phase which presumably separated the North America and eastern Gondwana cratons and thereby formed the continental margin of eastern Australia and Antarctica (Moores 1991, Dalziel 1991). Deposition of thick sequences of well stratified, glaciomarine Adelaidean rocks on the Mesoproterozoic basement in south Australia attests to Neoproterozoic (between ~ 800 and ~ 540 Ma; Cooper *et al.* 1992) rift and sag phases (Jenkins 1990). Localised early Cambrian platformal rocks were deposited subsequently followed rapidly by deposition of marine turbidites of the Middle Cambrian Kanmantoo Group at the southeastern exposed margin of the Adelaidean rocks in the Kanmantoo Trough (Daily & Milnes 1973). The extensional event was followed by the contraction orogenic of the Delamerian Orogen (Thomson 1969) in the Cambrian and earliest Ordovician. The Delamerian Orogeny in Australia and the formerly contiguous Ross Orogeny in Antarctica record the onset of Palaeozoic convergence along the proto-pacific margin of Gondwana (Flöttmann *et al.* 1993).

The deformational style of the Delamerian Orogeny varies along the strike of the AF-TB. In the Nackara Arc (Fig. 1.2) which forms the northern part of the AF-TB (Rutland *et al.* 1980, Marshak & Flöttmann 1996), the Delamerian Orogeny is characterised by distributed strain and open folds which formed above a basal detachment (Flöttmann *et al.* 1994), and no basement was involved in the deformation of the Arc (Marshak & Flöttmann 1996). The southern part of the belt is named the Southern Adelaide Fold-Thrust Belt (SAF-TB) by Flöttmann *et al.* (1994) which is more or less coincident with the occurrence of the Kanmantoo Group (Fig. 1.2). The SAF-TB, however, includes a zone of exposed basement inliers, which form an elongate culmination (Jenkins 1990). Similarly, in this part of the belt, there is a spatial coincidence between the depositional style of the Kanmantoo Group, emergent thrusting, basement involvement and to a lesser extent high metamorphic grade. Nevertheless, characteristically, there is an asymmetry in stratigraphy, structure and metamorphic grade across the Southern Adelaide Fold-Thrust Belt which has allowed its subdivision into an external zone, bounded along the western and northwestern margins of the SAF-TB, and a more internal strongly metamorphosed zone of high grade metasediments and gneisses in the eastern and southeastern parts of the belt (e.g. Jenkins & Sandiford 1992). The Williamstown-Meadows Fault (Fig. 1.3), where an abrupt change in metamorphic grade is recorded, has been considered as the boundary between the internal and external part of the SAF-TB (e.g. Jenkins & Sandiford 1992).

In the internal portion of the SAF-TB, the deformed Kanmantoo Group sequence was intruded by syn- to post kinematic granites which occur only in the eastern part of the Belt (e.g. Milnes *et al.* 1977, Foden *et al.* 1990). In aureoles of these synkinematic granite intrusions, higher-grade metamorphism, up to amphibolite grade exits (e.g. Jenkins & Sandiford 1992). To the east of the Williamstown-Meadows fault (Fig. 1.3), metamorphism is characteristically biotite grade or higher with sillimanite and migmatite grades attained in the vicinity of the deformed granitic intrusive bodies (Offler & Fleming 1968, Manketelow 1990, and Dymoke & Sandiford 1992). Towards the external portion of the SAF-TB in the western Mt. Lofty Ranges the degree of metamorphism decreases to chlorite or, at most, biotite grade (Jenkins & Sandiford 1992).

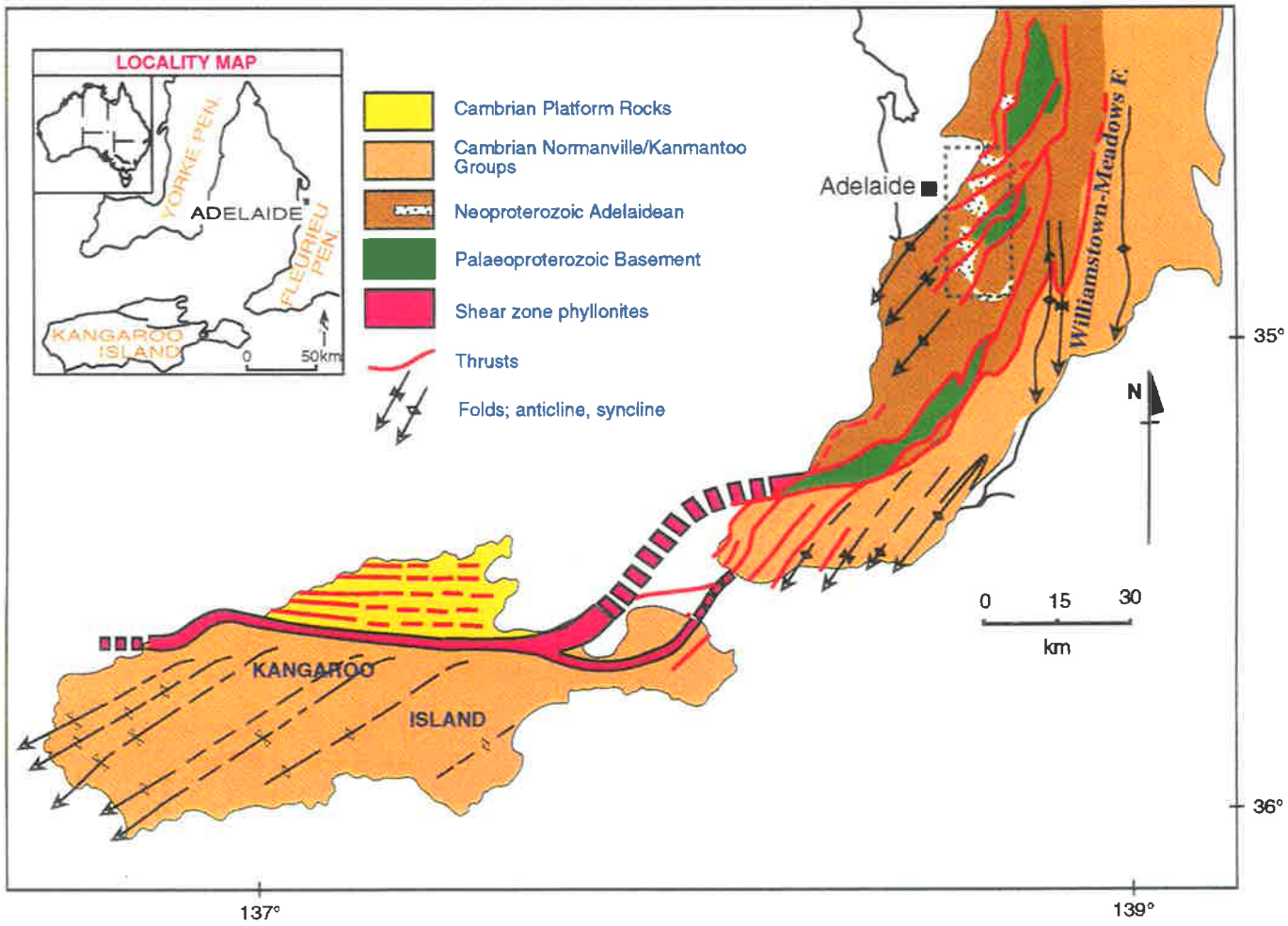

Fig. 1.3: Simplified geological map of the southern Adelaide Fold-and-Thrust Belt; modified after Flöttmann *et al.* (1994). The location of the southern Mt. Lofty ranges/Adelaide Hills area is shown within the dashed quadrangle (see Fig. 2.2 for more detail).

1.3.2 Regional setting of the Southern Adelaide Fold-Thrust Belt

The Southern Adelaide Fold-Thrust Belt (SAF-TB) is the southern extension of the AF-TB and is a narrow (approximately 80 km wide) north-south trending zone, east of Adelaide, gradually changing strike in a sweeping curve along the Fleurieu Peninsula and across the Backstairs passage to an east-west trend on Kangaroo Island (Figs 1.2 & 1.3). The SAF-TB forms a major foreland fold-thrust belt to the Cambro/Ordovician Delamerian Orogeny of southeast Australia (e.g. Flöttmann *et al.* 1994, Marshak & Flöttmann 1996, and Flöttmann and James 1997).

In the SAF-TB, the cratonic basement is overlain by thick sequences of late Proterozoic sedimentary rocks of The Burra Group (e.g. Preiss 1987). The Burra Group consists of repeated sandstone, supratidal dolomites and thick siltstone of shelf aspect. Such patterns of deposition are consistent with the rapid accumulation of shallow marine sediments during development of an intracratonic stretch basin (Preiss 1987, Jenkins 1990). The Burra Group is partly transgressive and overlain conformably by a much thinner Lower-Middle Cambrian fossiliferous carbonate platform sequence (the Normanville Group). The Normanville Group is in turn overlain by the Mid-Upper Cambrian Kanmantoo Group which consists of very thick deep-water flysch-like clastic sediments in a sequence of unfossilifereous immature greywacke, sands and muds (Daily & Milnes 1973). The deposition of the Adelaidean Supergroup and Normanville Group reflects a shallow-water sedimentation and delineates the edge of cratonic Australia in Cambrian time, while the very thick deep-water Kanmantoo Group is the first evidence of turbidite terrain outboard of cratonic Australia (e.g. Clark & Powell 1989). Jenkins (1990) attributes this to lithospheric stretching by considerable crustal attenuation of the underlying basement. Recent work by Flöttmann *et al.* (1994), however, suggests that the Kanmantoo Group was deposited during southeastward increasing subsidence controlled by growth faults which were subsequently reactivated during the Delamerian Orogeny.

The overall cumulative thickness of the sediments within the belt is difficult to estimate because the oldest part of succession are situated in regions with tectonic margins (Dalgarno

1986, in Jenkins 1990) and contain many thrusts which repeat parts of the sequence. Mawson and Sprigg (1950) estimated sedimentary thicknesses of the Adelaidean strata in the Mt. Lofty Ranges of up to 8500 m while the thicknesses of the Kanmantoo Group sediments was reported as over 10000 m by Daily and Milnes (1973), but more recently has been estimated by Flöttmann and James (1997) to be not in excess of 8 km.

The western margin of the SAF-TB is defined by the Torrens Hinge Zone (Thomson 1969), which represents both the edge of the Gawler Craton and the transitional zone between thick, folded and thrusted Neoproterozoic sediments of the belt and their very thin flat-lying platformal counterparts on the Sturt Shelf (Sprigg 1951). This zone strikingly marks the boundary and also controls the differences between the strongly deformed Adelaidean sedimentary rocks of the belt and mainly undeformed platformal sequences of the Stuart Shelf overlying the Gawler Craton in the west.

1.3.3 Previous structural interpretation of the southern Adelaide Fold-Thrust Belt

Tectonic activity within orogenic belts has classically been described in terms of either thick-skinned or thin-skinned behaviour. Thick-skinned tectonics are characterised by vertical movement on deep-seated, steeply dipping reverse faults which penetrate through cover sequences and are rooted in crystalline basement. Thin-skinned tectonics generally implies detachment of a sedimentary sequence from a crystalline basement. In such belts strain is concentrated in shallow dipping thrust faults and shear zones. These interpretations of orogenic belts are thus entirely based on the involvement or not of basement. The strict division of thrust systems into thin- or thick-skinned tectonics based only on this involvement of basement has recently been challenged following the recognition that crystalline thrust sheets may themselves exhibit a thin-skinned tectonic style (Hatcher & Hooper 1992).

Sprigg (1946) first mapped mostly the northern part of the SAF-TB in the Mt. Lofty Ranges, where he described small overthrusts in the overturned limbs of folds. He further considered the area as a major regional anticlinorium with north-south trending axial traces which he

inferred developed during a major deformation with an east-west maximum compressional stress direction. Similarly, in the southern part of the SAF-TB (Fleurieu Peninsula) limited thrusting was reported from the Normanville area by Anderson (1975) whilst within the SAF-TB, the western boundary of the Kanmantoo Group was described as a near bedding-parallel fault by Daily and Milnes (1971). Later, a more detailed regional study was carried out by Manktelow (1979, 1981, 1990) who described the belt as having a relatively simple classical evolutionary model with one major orogenic contraction which affected the thick sedimentary prism making up the belt. He regarded the SAF-TB as a foreland fold belt, governed by a single large-scale folding event with involvement of basement in the cores of major anticlines (e.g. Mancktelow 1981, 1990), that is classical thick-skinned tectonics. He also mentioned that thrust faults in the belt are minor structures with less than 100 m displacement, and only occur on the steep to overturned west facing limbs of the major asymmetric F_1 folds which formed during the D_1 regional folding. Thrusting was not recognised as an important process. This was partly due to the deficiency of evidence for emergent faults and large scale displacements (high strain zones or shear zones) at the surface; but thrusting is now conceived because of an improved understanding of the evolution of the crystalline thrust sheets (Hatcher & Hopper 1992) as well as the recognition of fault related folding in such foreland fold-thrust belts (e.g. Boyer & Elliott 1982).

Other problems inherent in earlier interpretations of the evolution of the belt include the lack of a recognised thrust system so common to other, similar foreland fold-thrust belts, include significant variations in formation thickness, stratigraphic repetition, unusual thickness and the nature of the basal contact of the Kanmantoo Group and the apparently inverted and telescoped character of the metamorphic facies, all of which implied that the belt should contain some major thrust faults or shear zones (eg. Offler & Fleming 1968, Jenkins 1990).

In an attempt to resolve these problems, three more recent publications independently presented reinterpretations of the belt, each involving large scale displacement on intermediate to low angle thrust faults (Clarke & Powell 1989, Jenkins 1990, and Steinhardt 1991). These publications were the first to propose a comprehensive evolutionary model of thin-skinned

thrusting and nappe formation. However, their individual interpretations differ, were mostly speculative and were not substantiated by field evidence (James 1989). Similarly, the location of mapped thrusts in each of these three works and the amount of strain and geometry were controversial and uncertain.

Subsequently, detailed studies by Flöttmann and James (1993, 1997), James and Flöttmann (1994), and Flöttmann *et al.* (1994 & 1995) based on regional mapping of the northern Kangaroo Island and southern part of the Fleurieu Peninsula and by construction of balanced and restored cross sections from two major transects across the belt, in conjunction with strain and kinematic analysis, determined the precise location and distribution of many thrust faults and shear zones. They further proposed qualitatively, that from the west to east, i.e. from foreland to hinterland, the strain varies, being low in the foreland but higher in a central imbricate fan and in the metamorphosed hinterland. These features are characteristic of thin-skinned tectonics and common in foreland fold-and thrust belts.

1.4 Study objectives

The regional mapping and the construction of balanced and restored sections on the Fleurieu Peninsula (Flöttmann *et al.* 1994) and on Kangaroo Island (Flöttmann *et al.* 1995) were carried out to address the existence of thrust/shear zones with large displacements and also to document the general structural geometry of the SAF-TB. There was, however, uncertainty as to the location and/or continuation of the mapped thrust/shear zones in the northern part of the Belt (southern Mt. Lofty Ranges/Adelaide Hills area). Moreover, the physical processes inherent in the development of deformed fabrics and microstructural changes in individual thrust sheet of rocks from near to and within the thrust/shear zones remained unanswered in detail. In addition, the conditions of deformation (P-T conditions), and possible changes in pressure and temperature, across the external portion of the southern Adelaide Fold-Thrust Belt were also not determined. Finally, the mechanism of thrusting/shearing and/or formation of the SAF-TB had not been addressed clearly.

In this study therefore, it is aimed to:

1) Define the possible existence and/or location of thrust/shear zones in the northern part of the SAF-TB and their continuation to the south on to the Fleurieu Peninsula.

2) Investigate in detail the physical characteristics of deformation fabrics and structures across the thrust and/or shear zones and analyse them descriptively and statistically in order to document the existence of the thrust/shear zones, and to depict their geometry and kinematics.

3) Detail the distribution, pattern, components, and quantify finite strain across the thrust/shear zones.

4) Determine the conditions and history of deformation (P-T conditions) and deformation mechanisms (microstructural analysis) acting on the shear zones and their possible changes using qualitative and quantitative analyses.

5) Define and/or propose a dynamic model for the deformation of the area and for the mechanisms of development of the thrust/shear zones.

6) Provide further evidence for general development of thrust/shear zones in fold-thrust belts.

To achieve these aims, the southern Mt. Lofty Ranges/Adelaide Hills area which is situated in the northern part of the southern Adelaide Fold-Thrust Belt (the dashed quadrangle in Fig. 1.3) was selected to study in more detail the geometry, kinematics, microstructures, and thermodynamics of the rocks from in particular the thrust/shear zones. Similarly, some parts of the Fleurieu Peninsula were also studied to a lesser extent and mostly for comparison.

1.5 Methods of study

Detailed geological and structural mapping was carried out in the southern Mt. Lofty Ranges/Adelaide Hills area. Since the area is mainly covered by vegetation and housing, mapping was confined to transects along a few accessible roads and along the perimeter of the Mt. Bold reservoir where low water levels revealed excellent outcrops. No aerial photographs were used, rather the geological and topographic maps of the Mt. Lofty Ranges (Adelaide, Noarlunga, and Onkaparinga 1:50 000 maps) were used as a base for the mapping. Six smaller areas, each about 3 km x 3 km, were also mapped in more detail to indicate the precise location, size, and scale of the shear zones, to measure the orientations and to find out the

relations between the main deformation fabrics and minor structures, and to collect oriented samples systematically from different rock types and quartz veins across the areas.

Following the detailed mapping, a general structural map of the area was drafted at 1: 50 000 scale (see later Fig. 2.2). Larger scale (1: 13 000) structural maps of the small selected areas across the shear zones, which were mapped in more detail, were also drafted in the same way and supplemented with all mapped fabrics and structures. Stereographic analysis techniques were also used to analyse the orientation of fabrics and minor structures.

Oriented thin-sections (in the XZ and YZ planes of the local finite strain ellipsoid) were made to investigate microstructural development and their changes across the area from outside into the shear zones and also to determine deformation conditions of the shear zones. Movement directions of the shear zones were also investigated using kinematic indicators to document in more detail the proposed movement directions for the Belt overall.

Balanced and geometrical restorations of four cross-sections across the area were constructed to provide better illustrations of the geometry of the area. Strain data collected from the (XZ) plane of the section of a key bed (Stonyfell Quartzite) were also plotted to investigate the finite strain pattern across the area.

Geothermometric and geobarometric analyses of the shear zones were carried out on selected samples of quartz veins and phyllite from within the shear zones, using fluid inclusion and electron microprobe data. These analyses have been done in order to determine the P-T conditions of the shearing/thrusting and to provide data to propose a dynamic model for the development of thrust/shear zones in the southern Adelaide Fold-Thrust Belt which has also been used to further develop information about mechanisms of thrusting/shearing in similar fold-thrust belts in general.

Chapter 2

GEOLOGICAL SETTING OF THE SOUTHERN MT. LOFTY RANGES/ADELAIDE HILLS AREA

2.1. Introduction

The southern Mt. Lofty Ranges/Adelaide Hills area is sited east of the city of Adelaide and in the northern part of the SAF-TB (Fig. 1.3). The area was first mapped by Sprigg (1946), who considered the southern Mt. Lofty Ranges as a major anticlinorial fold sequence with small steeply dipping overthrusts on the overturned limbs of these regional folds. Later, Forbes (1979, 1980, 1983) compiled 1:50000 geological maps of the Mt. Lofty Ranges, published by South Australian Department of Mines and Energy (SADME). Mapping and interpreted cross-sections across the Mt. Lofty Ranges (e.g. Forbes 1980, 1983) were based on the earlier mapping and interpretation of Sprigg (1946). Sprigg (1946) was the first point out the presence of high deformation on the overturned limbs of his interpreted regional folds. Jenkins (1990) also summarised data on the existence of high strain zones in the area based on his investigation of some isolated localities at Scott Bottom and Clarendon and from the preparation of a regional cross section (refer to Fig. 7 in Jenkins 1990). Kapetas (1993) also described briefly the presence of another major high deformation zone at the Mt. Bold reservoir.

The geological setting of the southern Adelaide Fold-Thrust belt and its structural interpretation were described in the previous chapter. In this chapter, firstly a summary of the stratigraphy of the southern Mt. Lofty Ranges/Adelaide Hills area is presented. The general characteristics of the structural geometry of the area, based on mapping and investigation of the high deformation zones and their margins, is also described and discussed. For convenience, hereafter, the area is named as the Adelaide Hills area. Further detail on the geometry and kinematics of the structures within these high deformation zones is presented on the succeeding chapter 3.

2.2. Stratigraphy

2.2.1. Gneissic basement

A number of discrete early Proterozoic basement inliers named the Aldgate Inliers (eg. Preiss 1987, Drexel *et al.* 1993) comprise the oldest rocks in the Adelaide Hills. These areas of basement consist of metamorphic rocks known collectively as the Barossa Complex. The basement rocks were originally of moderately high metamorphic grade (upper amphibolite facies) but have been variably affected by the Delamarian Orogeny and have undergone extensive retrograde metamorphism (greenschist facies) and shearing (e.g. Mills 1973 and Preiss 1987, 1993). The bulk of the basement inliers are metasediments with a strong layering or banding, although the precise distribution of rock types throughout all the inliers is uncertain (Drexel 1993). Several fold noses, which are shown on the Mt. Lofty Ranges 1:50 000 geological maps (SADME 1980-1983), at the lateral termination of the inliers, are poorly exposed. The western margins of these inliers are invariably faulted and sheared, whereas an overlying unconformity is usually preserved on the eastern flanks (Mills 1972, and Preiss 1987). The basement inliers are overlain unconformably by a sequence of late Precambrian Adelaidean metasedimentary rocks which, following Preiss (1987), are recognised as clastic sediments of the Burra Group (Fig. 2.1).

2.2.2. Burra Group

The Burra Group forms the lower part of the Adelaidean Supergroup and is of Torrensian age (i.e. 800-900 Ma) (Preiss 1987). Based on the previously published geological maps (Forbes 1980, 1983), the Burra Group in the Adelaide Hills area comprises mainly multiple units of competent quartzite formed by the Aldgate Sandstone and Stonyfell Quartzite interleaved with incompetent dolomitic, pelitic, and phyllite rocks [the lower and upper slate of Mawson & Sprigg (1950)] of the Woolshed Flat and Saddleworth Formations, followed at the top by the Belair subgroup (Fig. 2.1). This sequence of alternating pelitic and psammitic rocks significantly affects the distribution of a range of minor structures during the deformation. The Burra Group is inferred to have a maximum thickness of about 3000 m, much of which belongs to the Aldgate Sandstone which directly overlays the basement. These thicknesses, however,

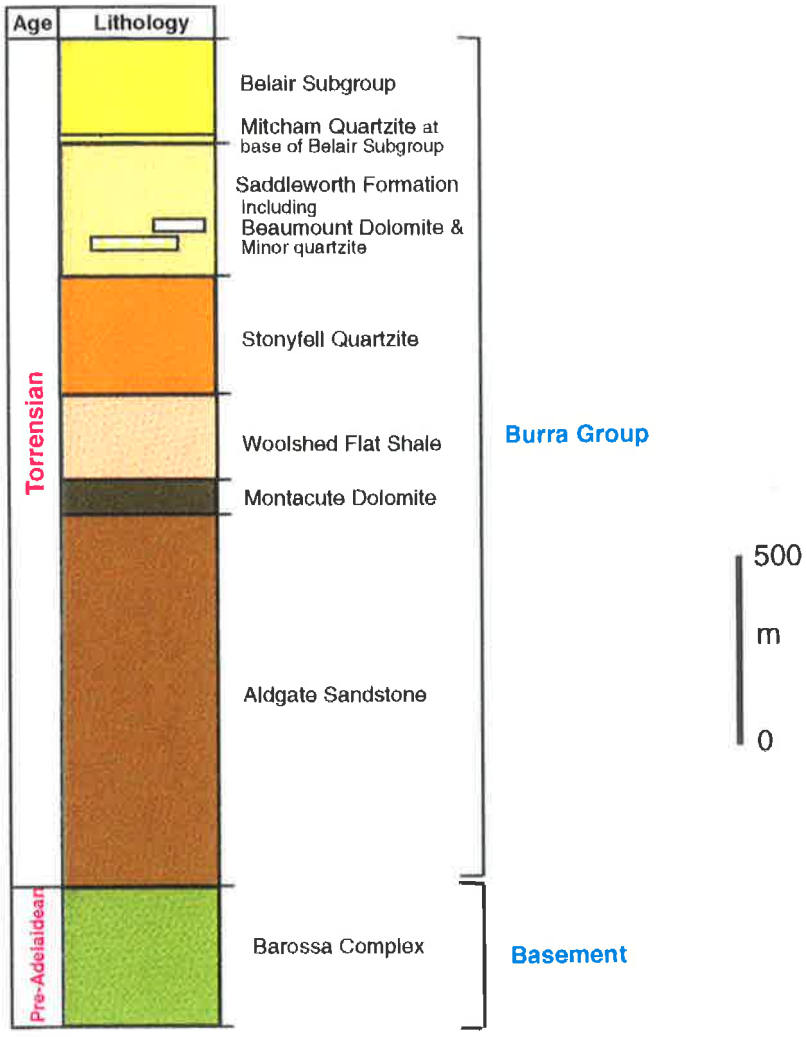

Fig. 2.1: Stratigraphic column of the Adelaide Hills area

might be overestimated due to the previously unidentified major high strain zones. The base of the Burra Group in the area and in most other areas across the belt is deformed and faulted against crystalline basement (e.g. Warren Inlier, Mills 1973), except for occasional outcropping angular unconformity surfaces outlined by basal conglomerate (e.g. Aldgate Railway Station and Kangaroo Creek Dam).

Aldgate Sandstone

The lower parts of the Burra Group are named differently in different part of the Adelaide Fold-Thrust belt but in the Adelaide Hills area the Aldgate Sandstone represent the basal unit (Mawson & Sprigg 1950). This unit consists mainly of feldspathic sandstone with heavy-mineral cross-bedded laminations. Conglomerate is dominant at the base, graphitic pelite in the middle part and silty sandstone at the upper part. The thickness of the Aldgate Sandstone in the Adelaide Hills area is about 1000 m (e.g. Preiss 1987, see also Fig. 2.1).

Montacute Dolomite

This unit, which overlies the Aldgate Sandstone, is dominantly comprised of blue-grey fine-grained dolomite with interbeds of dolomitic sandstone, quartzite and dolomitic phyllite. The Montacute Dolomite is a thinner stratigraphic marker unit across the area and its thickness is never greater than 130 m (e.g. Preiss 1987, see also Fig. 2.1).

Woolshed Flat Shale

The Woolshed Flat Shale mostly consists of pale-grey laminated siltstone, shale and sandy shale overlying the Montacute Dolomite. In the northern part of the area the distinction between Montacute Dolomite and Woolshed Flat Shale is not easy since the Montacute Dolomite lenses out into Woolshed Flat Shale (Wilson 1952 in Preiss 1987, see also Fig. 2.2). This unit is estimated as about 250 m thick in the Adelaide Hills area (Fig. 2.1).

Stonyfell Quartzite

This is a thick quartzite which forms a prominent part of the western Mt. Lofty Ranges and in the Adelaide Hills area is mainly feldspathic quartzite with interbedded feldspathic sandstone (greywacke). These cleaner quartzites, outcrop mainly in the southern part of the area, and are well sorted with well rounded grains commonly cemented by silica. However, in the northern most part of the area, especially within the Morialta Conservation Park, interbedded, somewhat schistose and poorly sorted greywacke also exists. The thickness of this unit is estimated at about 300 m (Fig. 2.1 and also see Preiss 1987) and it overlies Woolshed Flat Shale.

Saddleworth Formation

The dominant lithologies within this unit are dark-grey siltstone, shale and phyllite. Grey-blue dolomite and minor quartzite forms a minor sub-unit within the Saddleworth Formation which is named as the Beaumont Dolomite. The thickness of the Saddleworth Formation in the Adelaide Hills area is estimated at about 300 m (e.g. see Preiss 1987 and also Fig. 2.1).

Belair Subgroup

The Belair Subgroup is dominated by a sequence of feldspathic sandstone and laminated siltstone at the top of the Burra Group. The thickness of this subgroup in the area is estimated at about 270 m (e.g. Preiss 1987 also see Fig. 2.1). A 30 m thick, coarse to medium-grained highly feldspathic, cross-bedded quartzite is present at the base of the Belair Subgroup. The contact of this unit with the rest of the Belair Subgroup is well exposed in several of the Glen Osmond quarries on the Glen Osmond Road (see Adelaide 1:50 000 geological map sheet). This subgroup overlies the Saddleworth Formation conformably.

2.3. Structural geometry

Detailed structural mapping including many transects has been carried out across the Adelaide Hills area mostly along the few accessible roads, as the area is both vegetated and populated. During this mapping major shear zones, ductile thrusts, mesoscopic folds, stretching lineations, fabrics and minor structures were recognised and analysed from various localities throughout

the mapped area and their distributions are summarily presented in figure 2.2. During the preparation of this map, the basic geology and stratigraphy of the area was compiled from the Onkaparinga, Adelaide and Noarlunga 1:50 000 geological maps, which were prepared by (1979, 1980 & 1983, respectively).

The general structural geometry of the shear zones, ductile thrusts and mesoscopic folds is presented in proceeding sub-sections. Studies on the structural geometry of the shear zones and associated ductile thrusts based on more detailed mapping and measurement of selected localities (see rectangular areas ***I-VI*** in Fig. 2.2) across the shear zones is presented, analysed and discussed in the chapter 3.

2.3.1. Shear zones

The most notable deformation feature of the Adelaide Hills area is a concentration of deformation fabrics and structures in narrow subparallel high deformation zones, separated by larger low deformed zones with less concentration and intensity of deformation features. Structural mapping across the area has revealed six major stacked parallel examples of such high deformation zones, hereafter named shear zones. They are the *Morialta, Greenhill-Montacute Heights, Norton Summit, Pole Road-Summertown, Clarendon and Mt. Bold* shear zones, from NW to SE respectively (Fig. 2.2). The geometry of these shear zones are not precisely the same as the geometry of typical ductile shear zones commonly found in deformed crystalline basement rocks (eg. gneisses) as typified in the literature (e.g. Ramsay & Graham 1974, Ramsay 1980). Such typical ductile shear zones show a maximum displacement gradient in the shear zone centre (the gradient decreases towards the margin) and demonstrate that the tectonically induced planar fabrics in the shear zones generally show a characteristic sigmoid form, where the angle between the planar fabrics (i.e. cleavages) and shear zone walls decreases from a high angle (45°) to shear parallel towards the shear zone centre (Fig. 2.3a). No evidence of such symmetric displacement gradients is seen in the mapped high deformation zones (shear zones) of the Adelaide Hills area, which are rather asymmetric with distinct basal discontinuties or thrusts (Fig. 2.3b). However, the presence of asymmetric minor folds, stretching lineations subparallel

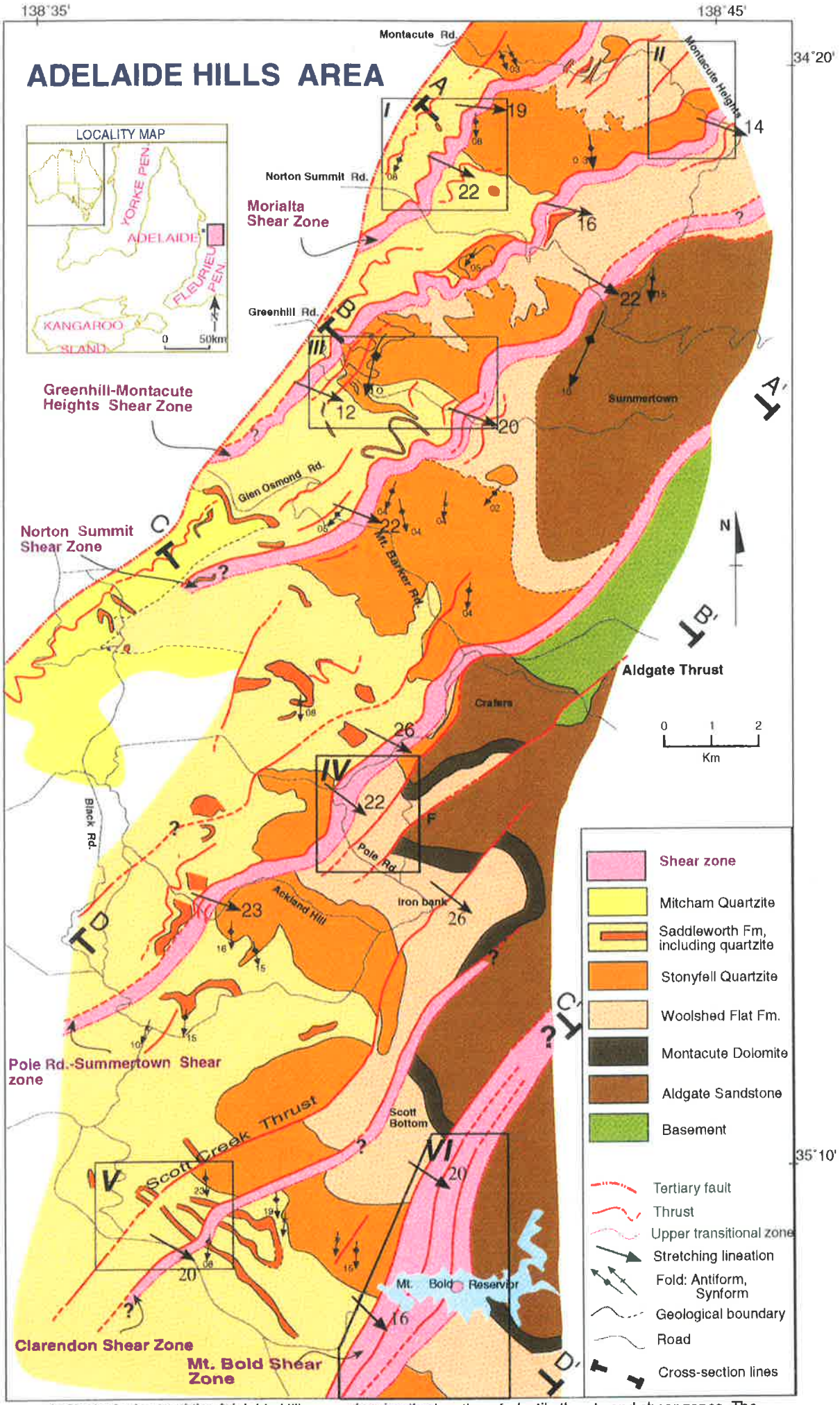

Fig 2.2: Geological map of the Adelaide Hills area showing the location of ductile thrusts and shear zones. The rectangles show detailed maps of *I:* Morialta area, *II:* Montacute area, *III*: Greenhill area, *IV*: Pole Road area, *V:* Clarendon area and *VI*: Mt. Bold area.

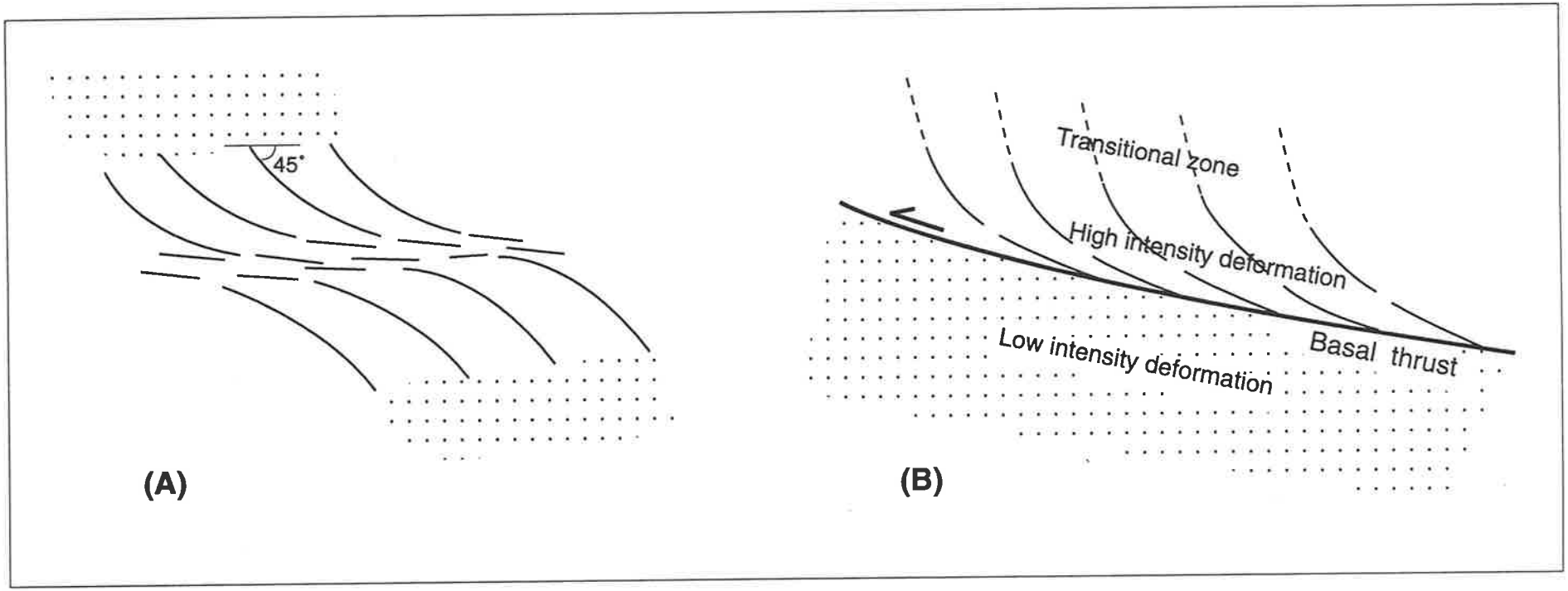

Fig. 2.3: Cartoons showing (a) a typical ductile shear zone with a maximum displacement gradient in the shear zone centre; (b) a typical asymmetric shear zone of Adelaide Hills area with a distinct basal thrust.

to intersection lineations, asymmetric boudinaged veins and shear bands all imply that these high deformation zones are governed by non-coaxial deformation regimes.

The shear zones strike generally NE-SW (N-040 to N-050) and dip shallow- to moderately SE ($25\text{-}40^0$). Their mapped strike-lengths range from 8 to 20 km. The poor outcrops of the shear zones creates some difficulty in following their lateral continuation to the NE or SW. Thus, the extent of the Norton Summit and Clarendon shear zone are especially not well defined. Road sections provide the best outcrops of the shear zones, although most sections are weathered.

Although the exposure of the shear zones in the Adelaide Hills area is generally poor, there are some excellent outcrops of the Morialta, Pole Road, Clarendon, and Mt. Bold shear zones. In the Morialta Conservation Park (Fig. 2.2), walking trails within the park reveal good outcrops to study the Morialta shear zone. The best outcrop of sheared Stonyfell Quartzite with the development of shear bands is also seen in this area. The Norton Summit Road where it crosses the Morialta shear zone (Fig. 2.2) also provides a good section to study the development of composite foliations from slaty cleavage (outside the shear zone) to discrete crenulation cleavage (within the shear zone, see sections 3.1 & 4.3 for more detail). A very narrow road-cut across the Pole Road shear zone reveals another significant exposure of the shear zones and is especially useful to study bedding-cleavage angle variation across the shear zone (for more detail see section 3.5 and Fig. 3.12).

Similarly small exposures of the Clarendon shear zone at the foot of the Clarendon Weir provide another good outcrop of folded and boudinaged quartz veins and extensional crenulation cleavages. In the Mt. Bold reservoir (Fig. 2.2), the perimeter of the reservoir, while the water level is low, and a few existing trails around the reservoir, enabled detail study of this shear zone. The variety of intense deformational features in this the most major shear zone provided the best evidence for the study of the geometrical and kinematic evolution of the shear zones.

The map widths of the shear zones vary from 250 m (Clarendon) to more than one kilometre (Mt. Bold), depending mainly upon the competence of the rock units and localisation of deformation. The upper boundaries to the shear zones are transitional where it is mostly difficult

to constrain a distinct boundary, whilst the lower boundaries to the shear zones are generally sharp and bounded by discrete thrusts which make up the base of the shear zones (see also Fig. 2.3b). All the lower boundary thrusts reach the surface and, following the definition of Boyer and Elliott (1982), they are thus emergent lower boundary thrusts.

The stretching lineations in the shear zones (Fig. 2.2) generally trend southeast, which together with overthrust kinematic indicators imply northwestward displacement across the shear zones. The orientation of this lineation is slightly different between competent and incompetent units, where in competent units the stretching lineations trend more easterly.

The shear zones display several features analogous to those recognised in conventional thrust zones (e.g. Boyer & Elliott 1982, Evans 1989) and in most cases thrust rules are obeyed with higher grades and older rocks being emplaced over younger rocks. The shear zones also make up the main structural elements of the area and cause apparent right lateral offset to the rock units, especially to the major competent Stonyfell Quartzite (Fig. 2.2).

As will be detailed and described more fully later in the thesis, the shear zones are most likely to represent the lines of emergence of a major crustal discontinuity or detachment possibly extending to the middle crust (see also Fig. 4.1), which may be responsible for the emergence of the basement inliers and for their involvement in the shearing throughout the SAF-TB. Although good outcrops of the basement can't be seen in the Adelaide Hills area, observation of an outcrop of sheared basement on the Mt. Barker Road within the area, and more extensively in the Houghton inlier, 10-15 km to the north (Forbes 1979, Preiss 1987) and in the Little Gorge area, 60 km to the south of the Adelaide Hills (Steinhardt 1991), further support this argument. The basement inliers are also thought to make up the unexposed cores of major ramp anticlines formed by large areas of exposed Aldgate Sandstone, mainly seen in the eastern part of the area around Summertown, Crafers, and east of Mt. Bold (Fig. 2.2).

2.3.2 Ductile thrusts

All of the shear zones anastomose and bifurcate to produce a separate and distinct array of minor ductile thrusts that form propagating imbricate fans verging to the NW. Ductile thrusts in the

Adelaide Hills area are actually narrow zones of ductile deformation in which, like the shear zones, fabrics and deformation structures with the same geometry and kinematics as the shear zones are developed. The term ductile thrust was used in this study for these narrow zones of deformation in order to differentiate them from the shear zones. This term has been utilised elsewhere for highly deformed and sheared mylonitic rocks (e.g. Holdsworth 1990; Martino *et al.* 1993) or for thrust zones invaded by fluids associated with plutonism (e.g. McNulty 1995). The deformation geometry along the ductile thrusts in the study area is not necessarily compatible with the deformation style associated with those ductile thrusts mentioned above. The deformation style and spatial geometry of the ductile thrusts in the Adelaide Hills area is similar to those of the fault rocks from the Appalachian thrusts (Wojtal & Mitra 1988).

The ductile thrusts in the Adelaide Hills area are formed either within the shear zones (see for example the Mt. Bold shear zone, Fig. 2.2) or in the footwalls and hangingwalls to the shear zones (see for example Greenhill and Norton Summit shear zones, Fig. 2.2). The lengths, widths, and intensity of deformation of these ductile thrust are different but are generally considerably less than those of the shear zones. The longest ductile thrusts (eg. Scott Creek Thrust & Aldgate Thrust in Fig. 2.2) have a wider deformation zone than the smaller ones with also greater development of fabrics and structures. The orientations of the stretching lineations, fabrics and minor folds across these ductile thrusts are the same as for the shear zones (for detail see chapter 3). The minor folds are almost always asymmetric with top to the NW sense of asymmetry and their geometry is similar to the geometry of fault-propagation folds (for more detail on the kinematic development of these fault-propagation folds refer to section 8.3 and Fig. 8.2).

2.3.3 Mesoscopic folds

Mesoscopic folds, the majority of which are anticlines with overturned western limbs, are characteristic of the hangingwall deformation of the lower boundary thrusts to the shear zones and along the associated ductile thrusts (e.g. see mesoscopic anticlines in the hangingwall of the Morialta shear zone, Figs 2.2 & 3.2a). However, there are mesoscopic folds which are not developed on the hangingwall of the shear zones or along associated ductile thrusts (Fig. 2.2).

The mesoscopic folds are almost all plunges shallowly (usually less than 10°) south-southwest and are best seen in more competent quartzite units. The geometry of these mesoscopic folds (see also figures 3.2a and 3.8) are close to the geometry of fault-propagation folds and in almost all cases the shear zones and associated ductile thrusts were developed on the steep to overturned forelimb of these folds (Figs 3.2a and 3.9a) and produce a structure quite similar to the geometry of synclinal break-through fault propagation folds (Suppe & Medwedeff 1990). Similarly, based on these observation it is more likely the mesoscopic folds which developed areas with low deformation intensity between the shear zones which were developed on the tips of blind ductile thrusts at depth.

2.4. Summary

The Adelaide Hills area forms the northern part of the southern Adelaide Fold-Thrust Belt and is sited east of the city of Adelaide. The Barossa Complex which consists of early Proterozoic metamorphic rocks comprises exposed basement to the area and is overlain unconformably by Late Precambrian Adelaidean metasedimentary rocks. The lower part of the Adelaidean rocks consists of clastic sediments of the Burra Group. The Burra Group comprises multiple quartzites with interleaved with pelites and phyllites.

Structural mapping across the Adelaide Hills area has revealed six major stacked parallel shear zones, together with ductile thrusts, and mesoscopic folds. The shear zones which strike generally N-NE and dip shallow to moderately SE are bounded by upper transitional zones and by lower boundary thrusts. Unlike the upper transitional zones which are mostly difficult to constrain as distinct boundaries, the lower boundary thrusts are generally sharp and bounded by discrete thrusts.

The shear zones are associated with minor imbricated ductile thrusts which were developed either within the shear zones or on the hangingwall or footwall to the shear zones. The geometry and kinematics of these ductile thrusts are similar to the shear zones but their intensity of deformation is considerably less than those of the shear zones.

Mesoscopic folds which are most characteristic of the hangingwall deformation of the shear zones and their associated ductile thrusts are also seen in the less deformed zones between the

shear zones. Mesoscopic folds are almost always asymmetric with steep to overturned forelimb and low dipping back limb. In almost all cases the shear zones and associated ductile thrusts were developed on the forelimb of the folds and produce structures similar to the geometry of synclinal break through fault-propagation folds. Based on this observation it is considered that the mesoscopic folds in the low deformed areas were developed above the tips of blind ductile thrusts and/or shear zones at depth.

Chapter 3

GEOMETRIC AND KINEMATIC ANALYSIS OF SHEAR ZONES IN THE ADELAIDE HILLS

3.1. Introduction

Having recognised the existence of shear zones, the first questions to resolve concern the physical processes inherent in the development of the structures (geometrical and kinematic analysis) (Hanmer & Passchier 1991). Moreover, the kinematic history of a shear zone can be more fully resolved by geometrical analysis of structures (folds and veins) and fabrics (foliations, lineations and composite planar fabrics) formed within it.

Description of the variation of fabrics and deformed structures from the outside to within a shear zone not only define the characteristics of the shear zone boundaries, but also qualitatively demonstrate the intensity of shearing. This is indicated by a uniform attitude of foliations and lineations, frequency and intensity of composite planar fabrics, the presence of asymmetric boudinage at different scales, and the existence of sheath folds (e.g. Naruk 1986, Gaudemer & Tapponnier 1987, Malavieille 1987). However, varying fabric orientation and development, lack of composite planar fabrics, and open crenulations all indicate less intense shearing. Thus, a geometrical study of the variation of fabrics, folds and veins provides information regarding the geometric and kinematic evolution of the shear zones.

To better understand the geometrical architecture and mechanics of ductile thrusts and shear zones of the Adelaide Hills area, the geometrical features of the shear zones from a number of small areas have been analysed. In particular, the characteristics of their fabrics and minor structures have been studied in detail and are presented in figure 2.2. For convenience the areas are named as the Morialta, Montacute Heights, Greenhill, Pole Road, Clarendon, and Mt. Bold shear zones from north to south or from the foreland side to the hinterland side, respectively (Fig. 2.2). Consequently, the sequential development of the main geometrical features across

each of the shear zones has also been studied and synthesised to allow a more comprehensive understanding of the geometric and kinematic evolution of this complex array of SAF-TB shear zones. A structural model for the evolution and development of the shear zones is then presented based on the geometric and kinematic features, previously outlined.

For the purpose of this study, the following abbreviations are used in describing deformation fabrics and structures:

S_0= bedding.

S_{1a}= low angle (less than 30°) regional cleavage which is developed more pervasively within incompetent units.

S_{1b}= medium angle (less than 45°) fault related cleavage and/or crenulation cleavage which is well developed within phyllites and to a lesser extent in pelites.

S_{1c}= intensely deformed variety of the S_{1b} cleavage formed only along the lower boundary thrusts to the shear zones.

L_x= stretching lineations.

3.2. The Morialta area

The Morialta area is located in the NW of the Adelaide Hills area and NE of the city of Adelaide (Fig. 2.2). This area reveals the best exposures of the Morialta shear zone (MSZ). Outcrops of the shear zone within two different lithological units were identified by detailed mapping of the area across the Morialta Conservation Park and along the New Norton Summit road (Fig. 3.1). The units, which comprise all of the outcropping road in the area, include Saddleworth Formation and Stonyfell Quartzite and these provide an opportunity to study details of the structural variation within these units from outside of and into this shear zone.

The map width of the MSZ varies from about 400 m in the Saddleworth Formation to about 200 m in the Stonyfell Quartzite. The shear zone in both units is bounded by a lower boundary thrust to the NW and by a transitional zone to the SE. In the Morialta Conservation Park this lower boundary thrust also forms the contact between the lithological units and causes the older Stonyfell Quartzite to over ride the younger Saddleworth Formation. This thrusting is

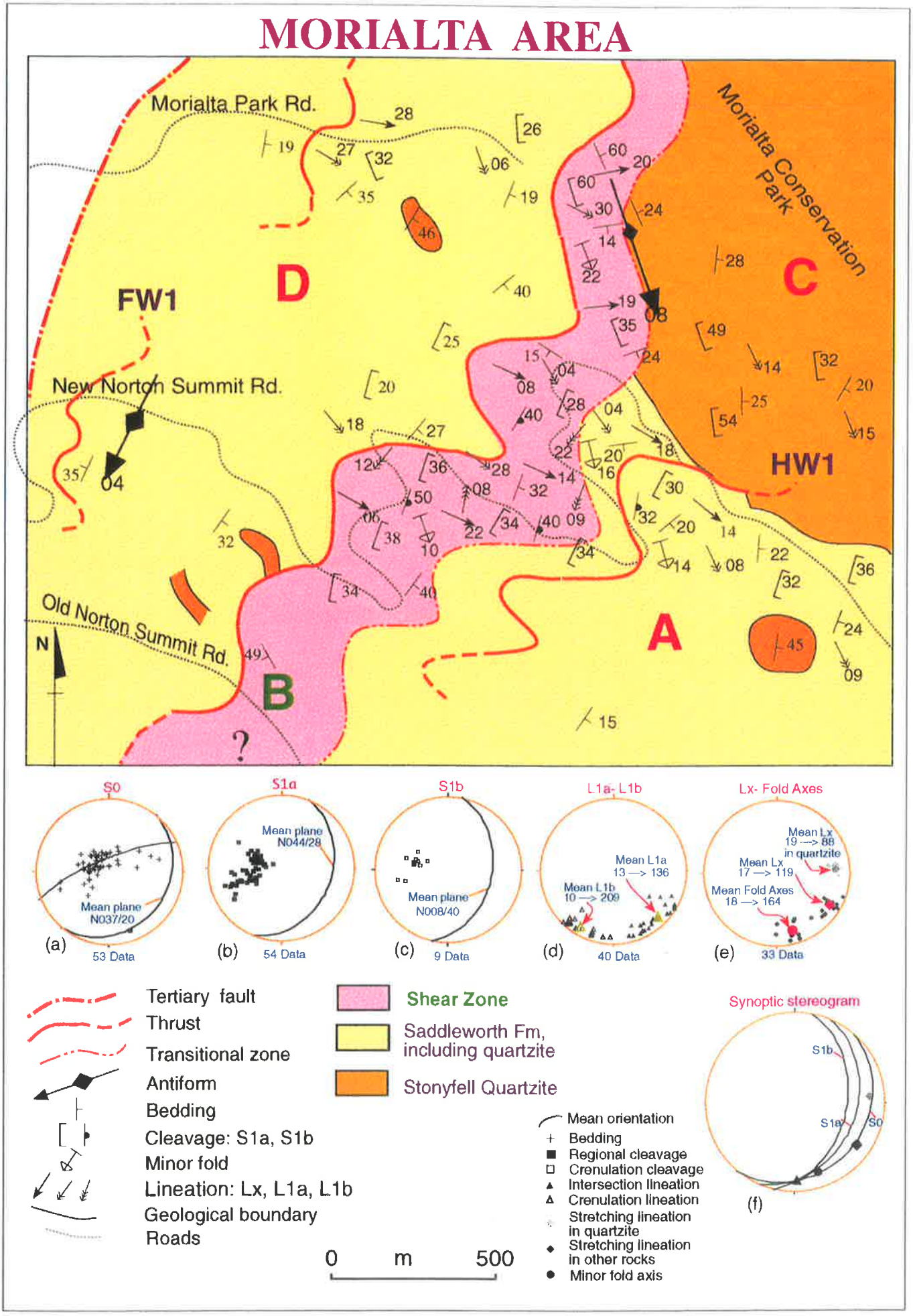

Fig. 3.1: Geological map of the Morialta area showing distribution of the main lithological units, location of the Morialta shear zone and associated ductile thrusts, and orientation of deformed fabrics and structures. Symbols: S0: bedding, S1a: regional cleavage, S1b; crenulation and/or fault-related cleavage, L1a: intersection lineation, L1b: crenulation lineation, Lx: stretching lineation.

accompanied by the development of a major antiform in the hangingwall, which the shear zone was most likely propagated through it's overturned limb (Fig. 3.2a). In contrast, along the Norton Summit Road, the Saddleworth Formation was thrust along a lower boundary thrust over the other parts of the same formation (refer to Fig. 3.1). Although no comparable major antiform was mapped across this road, it is most likely that it was developed but eroded off after deformation. The transitional zone within both units is gradational and has been mapped where the first evidence of deformation structures and fabrics appears to develop.

Two ductile thrusts (HW_1 & FW_1) were also mapped in this area (Fig. 3.1). The HW_1 ductile thrust is situated in the hangingwall of the shear zone while the FW_1 ductile thrust is located in the footwall to the shear zone. In both ductile thrusts evidence of minor fault propagation folds (Fig. 3.2b) and fault related cleavages/crenulation cleavages (S_{1b}) can also be seen. However, the width of the HW_1 deformation zone is about 50 m which is greater than the FW_1 (about 20 m).

3.2.1. Structural geometry and fabric development in the Morialta shear zone

Bedding (S_0) and to a lesser extent the regional cleavage (S_{1a}) are the main structures and fabrics formed outside the MSZ and associated ductile thrusts. The S_{1a} cleavage is most strongly developed within incompetent pelites and phyllonites. In the Stonyfell Quartzite, S_{1a} is only recognised by an alignment of phylosilicates in thin incompetent psammitic and pelitic units interbedded within thick to massive quartzite. In these incompetent units the cleavage is not pervasive and refracts from pelites to psammites (Fig. 3.2c). In the Saddleworth Formation, this cleavage appears as a continuous or penetrative cleavage especially in pelites (see also Fig. 3.2c). Here, the mean cleavage attitude is also refracted somewhat in sandy units and psammites.

As the upper transitional zone is approached, the shearing is characterised in the Stonyfell Quartzite by the development of a weak disjunctive cleavage which is spaced at intervals of about 2-5 cm with cleavage domains occupying less than 10% of the rock. Minor folds are also developed where interlaying of psammite and pelite bands exist. In pelites and phyllonites of the Saddleworth Formation, the shearing is identified by the development of weak (open)

Figures opposite:

Fig. 3.2a: Photograph of a major antiformal structure (located at 357902 AMG reference, Australian Mercator Grid) in the Morialta area where the Morialta shear zone is developed on its steeper forelimb dipping NW; width of view= 600m.

Fig. 3.2b: Minor folds in the deformation zone of the HW_1 ductile thrust in the Morialta area (357902 AMG reference). This photograph and some of the others in this chapter (as indicated by the word "Mirrored" in their captions) are printed in reverse/reflection mode in order to be easier for the reader to note the kinematics and vergence of the structures towards the west which is in all cases shown to the left side of each photograph.

Fig. 3.2c: Interlayered psammopelites and psammites in thick quartzite of the Stonyfell Quartzite in the Morialta area (354904 AMG reference). Note that the cleavage dies out on entering the thick quartzites on both sides. In the sketch also note the refraction of S_{1a} from psammopelites into quartzitic psammites; the coin diameter is 1.5 cm.

Fig. 3.2d: Sheared Stonyfell Quartzite about 50 m from the lower boundary thrust to the Morialta shear zone in the Morialta Conservation Park (353902 AMG reference); note the development of the shear bands or ECC-Fabrics (dashed lines) which cause extension of the lozenge-shape domains to the NW; the coin diameter is 1.5 cm (photograph is mirrored).

Fig. 3.2e: Development of en-echelon quartz veins in the Stonyfell Quartzite within the Morialta shear zone (353902 AMG reference). Note that the veins were deformed progressively in a semi-ductile manner in which more than one generation of the veins can be seen (photograph is mirrored).

W

E

a

b

c

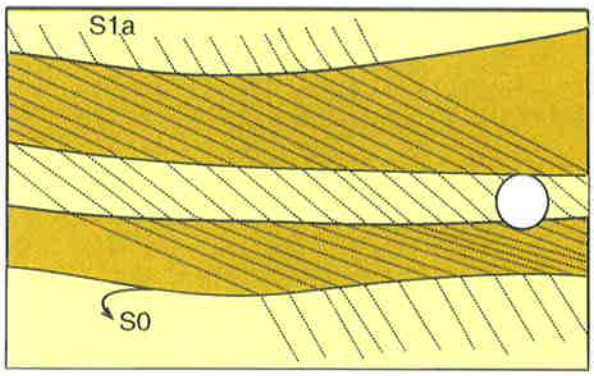

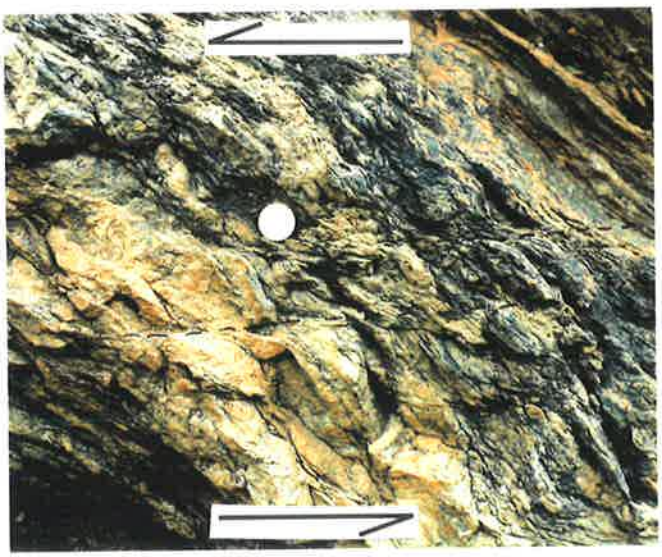

d

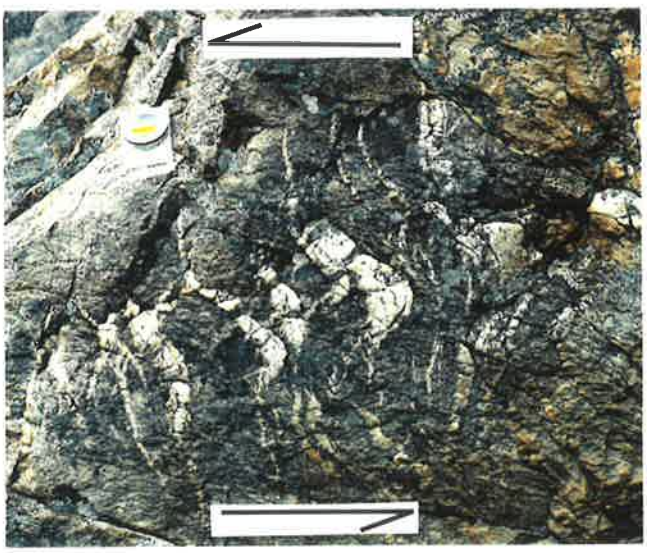

e

crenulation folds with asymmetric shapes and linear spaced axes at intervals of about 10-20 cm (Fig. 3.3a).

Within the shear zone, over about 150 m from the transitional zone towards the lower boundary thrust, in the Stonyfell Quartzite unit, the weak S_{1b} cleavage is more intensely developed by an alignment of detrital quartz grains to form a spaced cleavage. The spacing between the cleavage surfaces is generally about 2 cm but is not strikingly regular. At about 50 m from the lower boundary thrust this spaced cleavage is more strongly developed and foliates the thick layered quartzite. Here this cleavage is intensely developed with about 5mm spacing (Fig. 3.2d). In thinner quartzite and associated psammite units, these spaced cleavage planes are anastomosing and divide the rocks into lozenge-shaped domains. These domains are separated along shear planes and show the geometry of shear bands (Fig. 3.2d). En-echelon quartz veins are also present in quartzites (Fig. 3.2e).

Similarly, in pelites and phyllonites of the Saddleworth Formation, open zonal crenulation folds with linear spaced axes at intervals of about 10-20 cm are seen at the transitional zone (Fig. 3.3a). These are more intensely developed over about 200 m within the shear zone to form crenulation folds (Fig. 3.3b). These crenulation folds which are defined by microfolding or crenulation of the preexisting slaty cleavage (S_{1a}) are asymmetric and have linear spaced axes at intervals of about 5-10 cm. The micro-fold limbs of the crenulations are sheared off and show evidence of some pressure solution and redistribution of minerals. These dissolution surfaces (see Fig. 3.3b) which almost always grow on the steep to overturned short limbs of the asymmetrical microfolds, and sometimes cut across some axial planes, define a weak cleavage similar to the crenulation cleavage (S_{1b}). Crenulation folds are more frequently developed in finely laminated pelites and to a lesser extent in psammites. Closer, at about 20 m, from the lower boundary thrust, the crenulation folds are further intensified to develop strong crenulation cleavages or S_{1b} (Fig. 3.3c). As is shown, the microfolding and/or crenulation folds are intensely developed with more strongly developed discrete solution surfaces which clearly define typical crenulation cleavages (e.g. Hobbs *et al.* 1976). These dissolution surfaces which are spaced at intervals of 1-2 cm, refract, anastomose, bifurcate and displace the

Figures opposite:

Fig. 3.3: Progressive development of overprinting cleavages from the upper transitional zone toward the lower boundary thrust in the Morialta shear zone. Because of weak development of the S_{1a} cleavage in pelites, it is not easy to see S_{1a} in these photographs. All photographs were taken from the transects along the New Norton Summit road with 340900 AMG reference; the diameter of the coins are 1.5 cm.

Fig. 3.3a: Development of weakly (open) crenulation folds at the upper transitional zone where earlier regional cleavage (S_{1a}) is deformed to incipient a new crenulation cleavage (S_{1b}).

Fig. 3.3b: Crenulation folds and cleavages within the shear zone; note the initiation of dissolution surfaces on the short steeper forelimbs of the crenulation folds.

Fig. 3.3c: Typical crenulation cleavages (S_{1b}) in the phyllonites about 20m from the lower boundary thrust where the dissolution surfaces were well developed (see also the sketch).

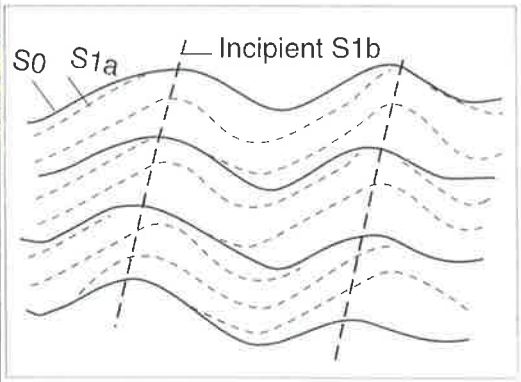

a

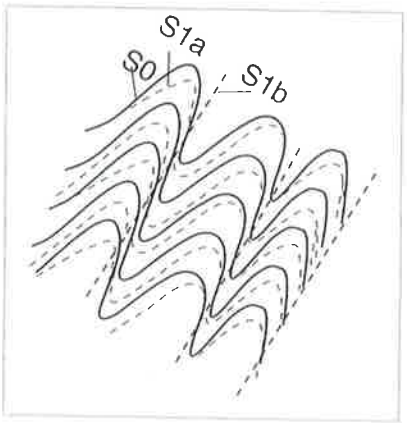

b

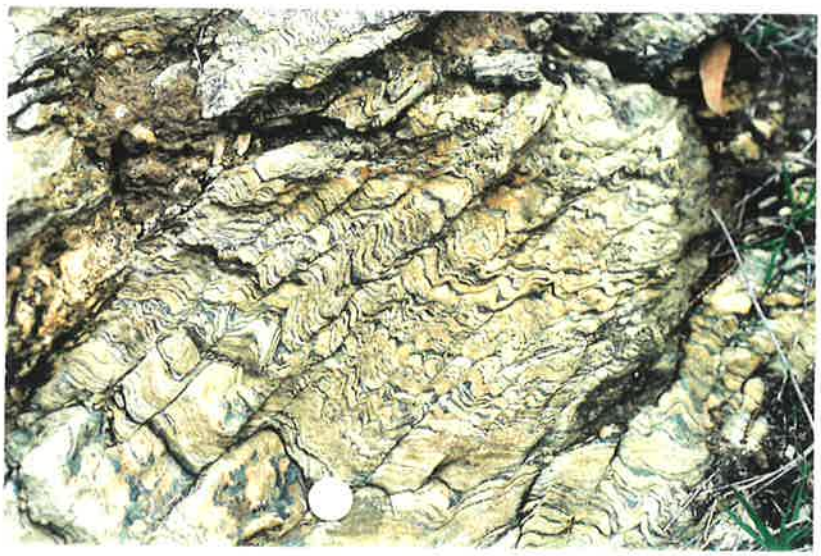

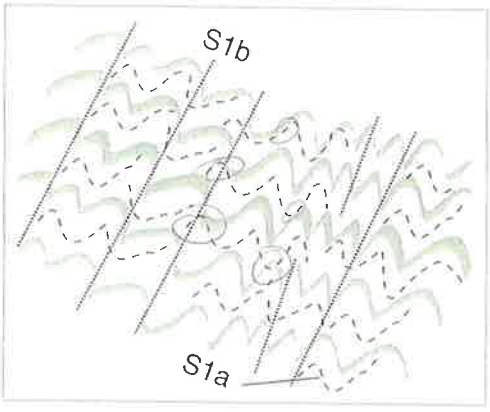

c

crenulation-fold limbs. The apparent displacement of the crenulation-fold limbs along these surface (Fig. 3.3c) is due to dissolution of the limbs (e.g. Cosgrove 1976).

Nevertheless, in more sandy units of the Saddleworth Formation, where interbedded pelites and psammites are present, minor asymmetric folds with a top-to-NW sense of asymmetry, and transposition of psammitic bands to form transposed layering, can also be seen (Fig. 3.5a). The orientation of the transposed layering and the axial planes of the minor folds are sub-parallel and are almost the same as the orientation of fault-related cleavages/crenulation cleavages (S_{1b}).

Stereograms showing the orientation of the S_0, S_{1a} and S_{1b} surfaces across the area are shown in figure 3.1. As shown on the map and stereograms (a, b and c in Fig. 3.1), these structures and fabrics strike N-S, NE-SW or NW-SE, but all dip shallowly to moderately in southeastly direction. The mean orientation of these structures and fabrics, however, all strike NE-SW. As stereogram e in figure 3.1 shows, the minor folds plunge shallowly S-SE but the stretching lineations are widespread and show two separate orientations. One group of lineations plunges shallowly E and another group plunges to the SE. The inferred fold axis, constructed from the pole to the profile plane (see stereogram a in Fig. 3.1) has roughly the same orientation as the orientation of minor folds measured from within the shear zone and associated HW_1 ductile thrust (compare stereograms a and e in Fig. 3.1). A synoptic stereogram of mean values of all major structures and fabrics was also constructed to analyse their spatial relationship (stereogram f in Fig. 3.1). As can be seen, the cyclographic trace of the mean value of the bedding has a close similarity to the plane defining the variation in orientations of minor folds and stretching lineations.

To better understand the spatial distribution of the structural geometry within and outside the shear zone but in the same geological units, four separate sketch maps of the Morialta area have been drawn (Fig. 3.4). On each sketch map, the area is separated into four different sub-areas, that is, A: hangingwall to the shear zone in the Saddleworth Formation; B: shear zone; C: hangingwall to the shear zone in the Stonyfell Quartzite; and D: footwall to the shear zone in the Saddleworth Formation. The orientations of bedding and regional cleavage change slightly as

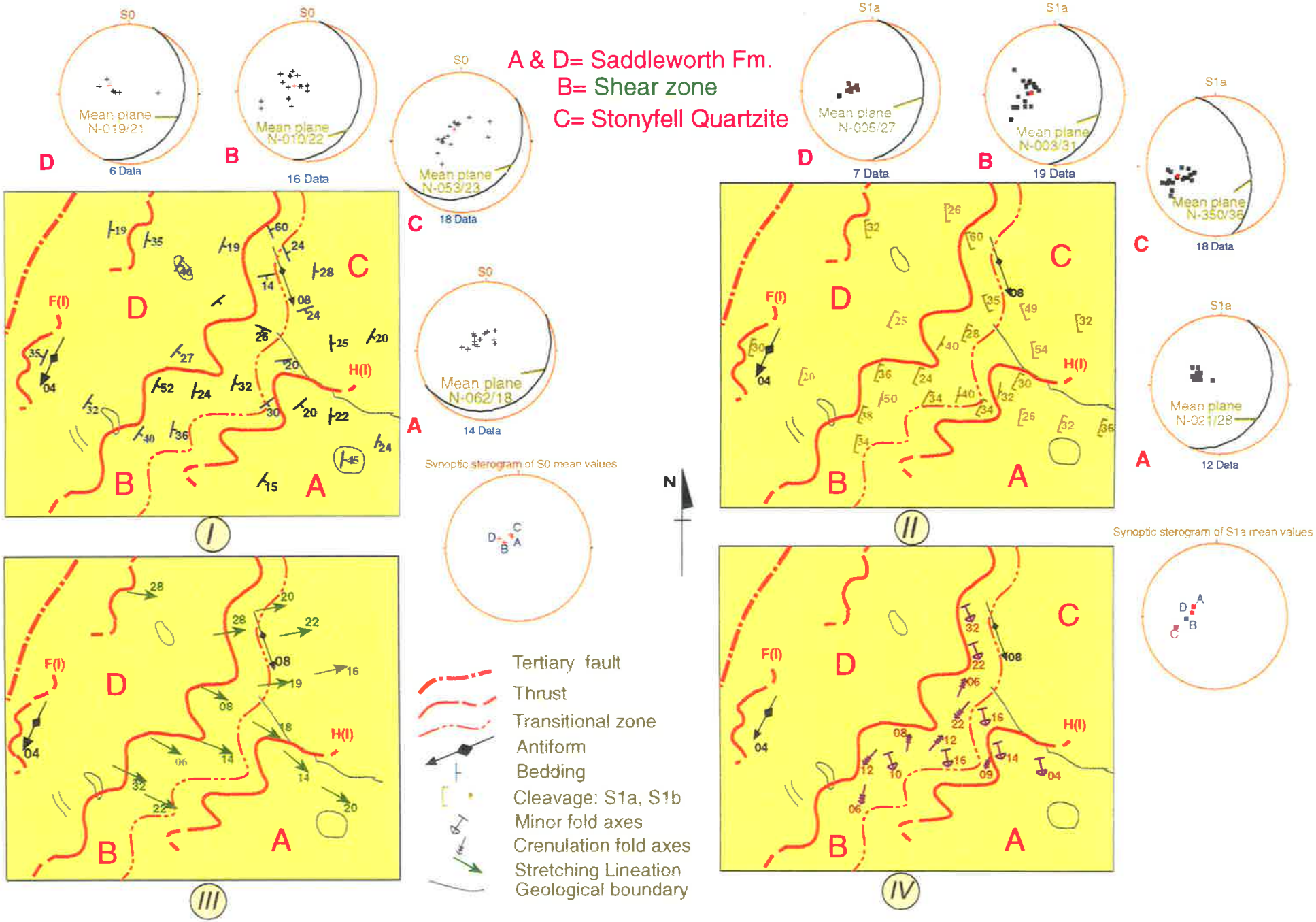

Fig. 3.4: Sketches of main geometrical features of the Morialta subareas including *(I)* : bedding (S0); *(II)* : regional cleavage (S1a) and fault related cleavag (S1b); *(III)* : stretching lineation; *(IV)*: minor and crenulation folds. For explanation see text. See also figure 3.1.

they progress into the shear zone. As the stereograms in figure 3.4 show, this change can be seen in the orientation of mean values of these fabrics and structures. In the Saddleworth Formation the mean values of orientation of the bedding change from 062/18 SE to 010/22 SE from area A to B. Similarly, the mean orientation of the regional cleavage (S_{1a}) also changes from 021/28 SE to 003/31 SE from area A to B. This variation can also be seen in the Stonyfell Quartzite where the mean orientation of the bedding changes from 053/23 SE to 010/22 SE from area C to B and where the orientation of S_{1a} also varies from 350/36 SE to 003/31 SE (see the synoptic stereograms in Fig. 3.4). Although these changes in the orientation of bedding and the S_{1a} cleavage is not as significant as might be expected from within classical shear zones, small changes in the mean orientation of bedding and the regional cleavage as shown in the synoptic stereograms (Fig. 3.4), from area A to B within the Saddleworth formation and from area C to B within the Stonyfell Quartzite show the effect of the shear zone development, i.e. may suggests a component of oblique lateral slip.

There is little evidence of minor and crenulation folds outside of the shear zone and its associated ductile thrusts (see sketch map *IV* in Fig. 3.4). Within the shear zone and in the associated ductile thrusts, the stretching lineations reveal a different orientation between sheared Stonyfell Quartzite and pelites and phyllonites of the Saddleworth Formation. As stereogram e of figure 3.1 and also sketch map *III* of figure 3.4 shown, this lineation in the Stonyfell Quartzite plunges shallowly E (about 090), while in the Saddleworth Formation it plunges closer to SE (about 120). The significance of the variations of the stretching lineations will be discussed further in section 3.8.2.

3.3. The Montacute Heights area

The location of the Montacute Heights area within the Adelaide Hills is shown in figure 2.2. Figure 3.6 shows the distribution of the lithological units, main fabrics and deformation structures together with the location of the Montacute Heights shear zone (MHSZ) and its associated ductile thrusts in more detail. Outcrops are mainly exposed along the roads and tracks and therefore study of the area was confined to these. Detailed mapping of the area in early 1995 lead to the discovery of the MHSZ along road-cuts of the Montacute Heights Road

Figures opposite:

Fig. 3.5a: Transposed layering and minor asymmetric folds with top to NW sense of asymmetry in the Woolshed Flat Shale within the Morialta shear zone (340900 AMG reference); the coin diameter is 1.5 cm. In sketch also note the development of transposition cleavage in thicker psammite bands in the upper part of the photograph and development of minor folds in thinner psammite bands in the lower part of the photograph.

Fig. 3.5b: Folded and mullion like structures, trending SE, in the Stonyfell Quartzite within the deformation zone of the FW_1 ductile thrust in the Montacute Heights area (370940 AMG reference) (see also Fig. 3.6 for the location).

Fig. 3.5c: Photograph and sketch (rectangle area in the photograph) of minor asymmetric folds along with micro-scale thrusts in the pelites of the Woolshed Flat shale within the Norton Summit shear zone in the Greenhill area (290905 AMG reference); the coin diameter is 1.5 cm (photograph is mirrored).

W

E

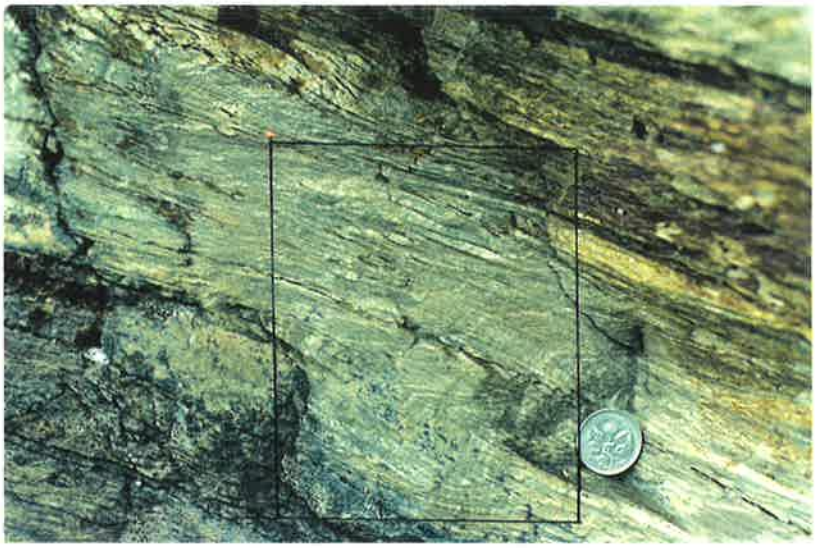

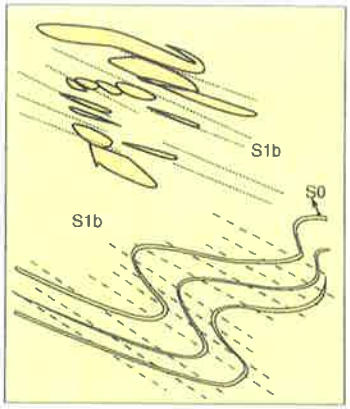

a

b

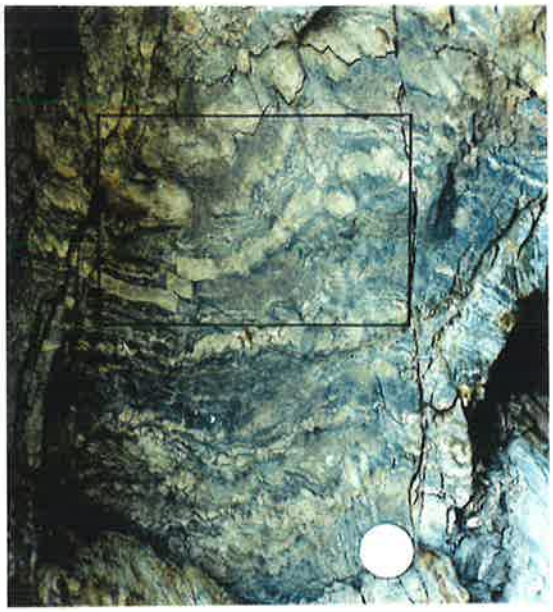

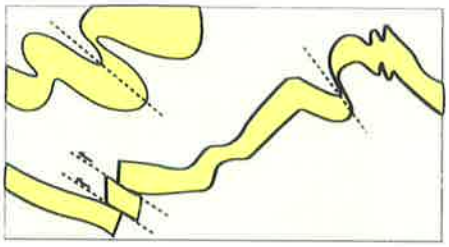

c

(see Fig. 3.6) where the best exposures of the Greenhill-Montacute Heights shear zone in the Adelaide Hills exists. As can be seen in figure 3.6, the shear zone is located within both the Woolshed Flat Shale and the Stonyfell Quartzite, but most parts of the shear zone are developed in the Woolshed Flat Shale. The map width of the shear zone is about 460 m on figure 3.6 and it is bounded by a lower boundary thrust in the Stonyfell Quartzite to the NW and by an upper transitional zone (over 30-50 m) in the Woolshed Flat Shale to the SE. The upper transitional zone unlike the lower boundary thrust is gradational and its precise location is located by the position where deformed structures and fabrics are seen to begin to develop.

Three ductile thrust were also mapped in the area and are labelled as HW_1 in the hangingwall of the MHSZ and FW_1 & FW_2 in the footwall to the shear zone (see Fig. 3.6). The width of deformation associated with these ductile thrusts is substantially less than that of the main shear zone and is about 20 m across strike in each. HW_1 and FW_2 which are located in the Woolshed Flat Shale, develop minor and crenulation folds and crenulation cleavage, but in FW_1 the Stonyfell Quartzite develops folded and mullion structures (Fig. 3.5b).

3.3.1. Structures and fabrics of the Montacute Heights shear zone

The structural geometry and fabric development of the MHSZ is similar to that of the Morialta shear zone (MSZ) but these are not as well exposed due to poor outcrops of the shear zone in this area (see description of these fabrics and structures in the Morialta shear zone in section 3.2). Like the MSZ, bedding (S_0) and to a lesser extent regional cleavage (S_{1a}) are the main structures in the area outside the shear zone. Within the shear zone, this cleavage is more intensely developed within incompetent pelites and phyllites of the Woolshed Flat Shale and this is also itself deformed to form a crenulation cleavage (S_{1b}). This crenulation cleavage is more intensely developed closer to the lower boundary thrust (about 80 m from this boundary within the shear zone). About 40 m from the lower boundary thrust, deformed quartz veins and a weak spaced fault related cleavage (S_{1b}) are also developed in the Stonyfell Quartzite. No evidence of high intensity deformation is seen in the Stonyfell Quartzite at the lower boundary thrust because of the poor outcrops of this boundary and/or less intense development of the shearing here.

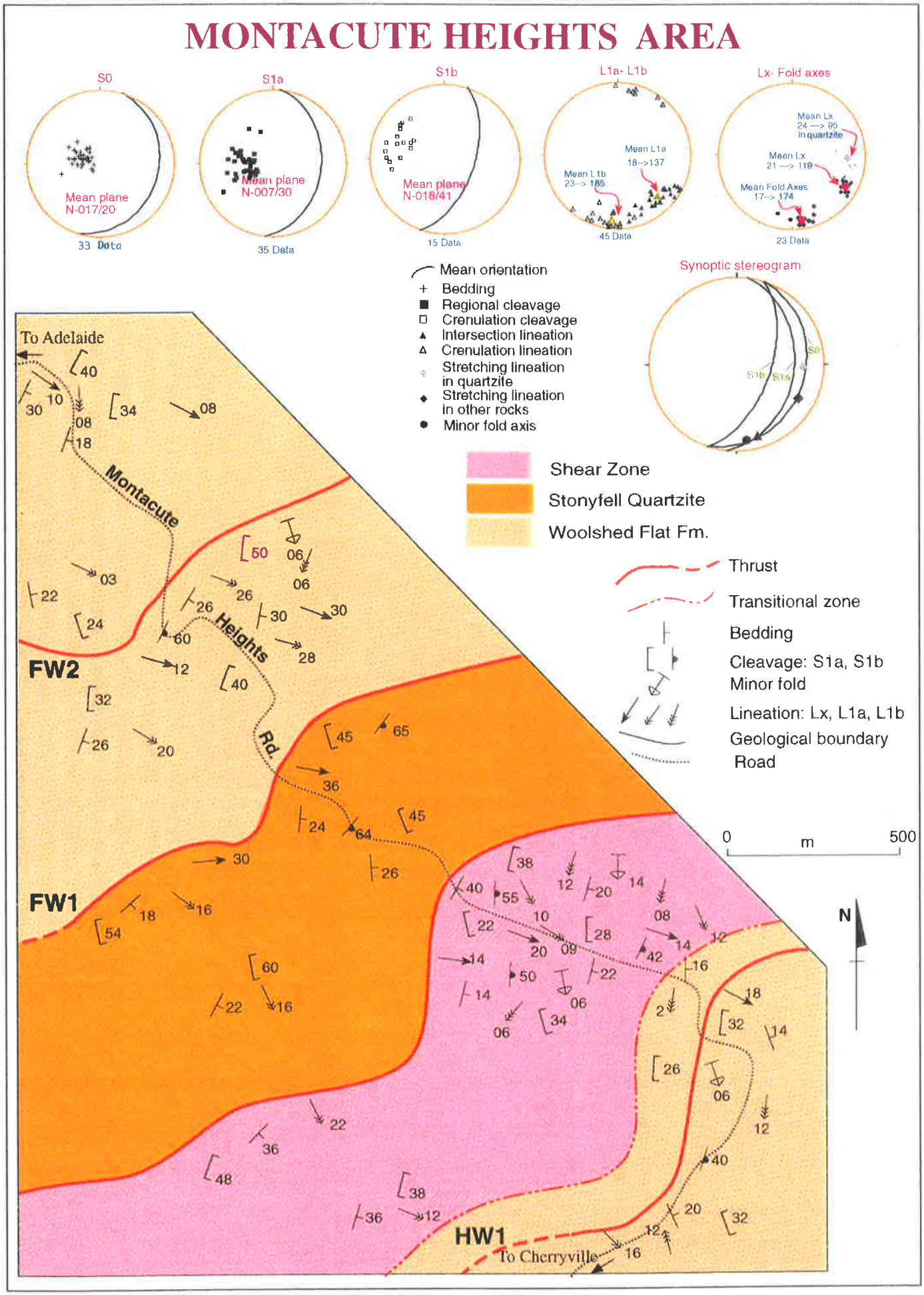

Fig. 3.6: Geological map of the Montacute-Heights area showing distribution of the main lithological units, location of the Montacute Heights shear zone and associated ductile thrusts, and orientation of deformed fabrics and structures. Symbols: S0: bedding, S1a: regional cleavage, S1b; crenulation and/or fault-related cleavage, L1a: intersection lineation, L1b: crenulation lineation, Lx: stretching lineation.

The orientations of structures and fabrics are shown on separate stereograms in figure 3.6. Like the Morialta shear zone (compare the stereograms in Fig. 3.6 with Fig. 3.1), the mean orientations of bedding (S_0) and the cleavages (S_{1a} & S_{1b}) all strike N-NNE and dip shallowly to moderately E-SSE, though S_{1a} is consistently steeper than S_0, and S_{1b} is likewise consistently steeper than S_{1a}. Similarly, minor folds which are seen to develop only within the shear zone and along the ductile thrusts plunge shallowly (15-20°) toward the S-SSE. As in the Morialta shear zone the stretching lineations have two slightly different orientations. In the Stonyfell Quartzite, they plunge (about 25°) to the E, while in the Woolshed Flat Shale they plunge (about 20°) to the SE (see the stereogram in Fig. 3.6).

A synoptic stereogram of the mean orientation of all the data has also been constructed (Fig. 3.6), which like the Morialta shear zone shows that the great circle representing the mean orientation of bedding is a best fit to the mean orientations of minor folds and stretching lineations. The implication of these relationships are fully discussed in section 3.8.1 and indicate an interrelationship between bedding and shear plane orientation.

3.4. The Greenhill area

This area is situated in the central part of the Adelaide Hills area (Fig. 2.2). Since most of the Greenhill area is covered by vegetation and because of the poor outcrop on the foothill slopes, detailed mapping of the area was confined to road cuts along Greenhill Road. From this mapping of the area the two major shear zones and associated ductile thrusts (shown on Fig. 3.7) were identified. The shear zones are the Greenhill shear zone (GSZ) in the west and the Norton Summit shear zone (NSSZ) in the east. Both shear zones are bounded by lower boundary thrusts to the west and upper transitional zones to the east. The general characteristics of the boundaries of these shear zones are like the other shear zones and have been recognised by the gradual occurrence of shear zone structures and fabrics across the transitional zone which then become more developed and intensified towards the lower boundary thrusts.

As is shown on figure 3.7, in the GSZ the Stonyfell Quartzite is thrust over the Saddleworth Formation but in the NSSZ the Woolshed Flat Shale is thrust over both the Stonyfell Quartzite and Saddleworth Formation.

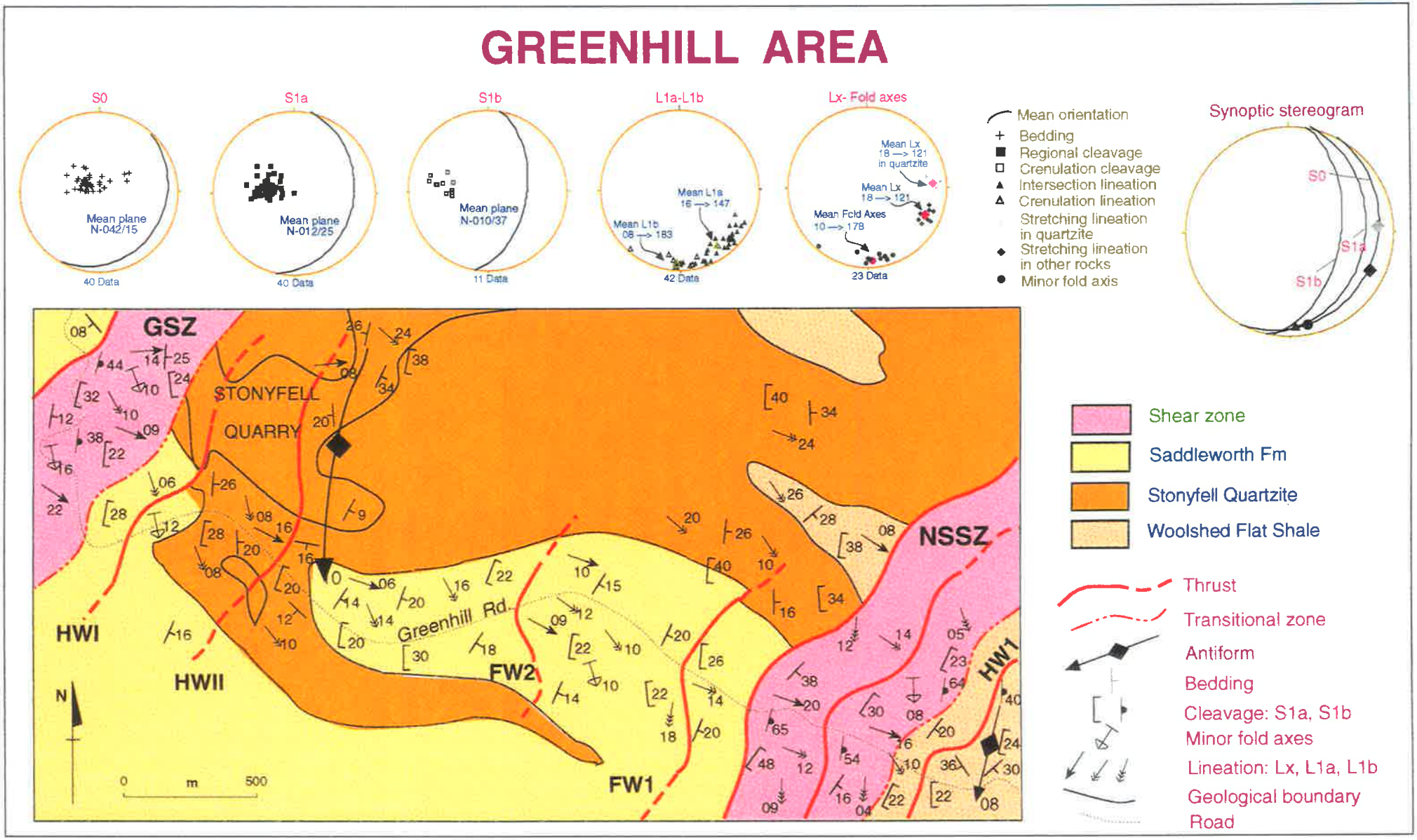

Fig. 3.7: Geological map of the Greenhill Area including GSZ: Greenhill Shear Zone and NSSZ: Norton Summit Shear Zone and their associated ductile thrusts. Symbols: S0: bedding, S1a: regional cleavage, S1b: crenulation and/or fault-related cleavage, L1a: intersection lineation, L1b: crenulation lineation, Lx: stretching lineation.

The orientations of the main structures and fabrics measured across the area are also plotted in figure 3.7. Like the other previously mentioned shear zones in the Adelaide Hills area the orientation of the regional (S_{1a}) and fault related and/or crenulation (S_{1b}) cleavages, minor folds, and stretching lineations are roughly the same as in the other shear zones. However, the S_{1b} cleavage in the NSSZ has a steeper dip (from 54° to 64°, Fig. 3.7) not only than the same fabrics in the Greenhill shear zone (from 38° to 44°, Fig. 3.7) but also than those in the Morialta (from 40° to 50°, Fig. 3.1) and Montacute Heights (from 40° to 55°, Fig. 3.6) shear zones. Similarly, the orientations of the mesoscopic antiforms in the hangingwalls of the HW_I and HW_{II} ductile thrusts are approximately the same as the orientations of the minor folds (Fig. 3.7). To provide a better understanding of the structural features of this area, the characteristics of the two shear zones are described separately.

3.4.1. The Greenhill shear zone

The Greenhill shear zone forms the southern extension of the major Montacute Heights-Greenhill shear zone (Fig. 2.2). Because of the highly weathered nature of the outcrop of sheared rocks, the Montacute Heights-Greenhill shear zone is overall very poorly exposed. However, the two major road cut sections of Greenhill Road and Montacute Heights Road (Fig. 2.2) provide the best exposure of the Greenhill-Montacute Heights shear zone in the Adelaide Hills.

The map width of the Greenhill shear zone where it includes Saddleworth Formation is about 450 m, but it is reduced in width when it cuts through the Stonyfell Quartzite. Two associated ductile thrusts have also been mapped (HW_I and HW_{II}) in the hangingwall of the shear zone (see Fig. 3.7). The HW_{II} ductile thrust is accompanied by a major hangingwall antiform which plunges shallowly SSE and superficially resembles a fault propagation fold. As mentioned in the preceding chapter, these types of structures are widespread along the shear zones and ductile thrusts in the Adelaide Hills. The very good exposure of these structures in the Greenhill area can be seen in the Stonyfell Quarry (see Fig. 3.7), where it displays the geometry of cut-through fault propagation fold (Fig. 3.8).

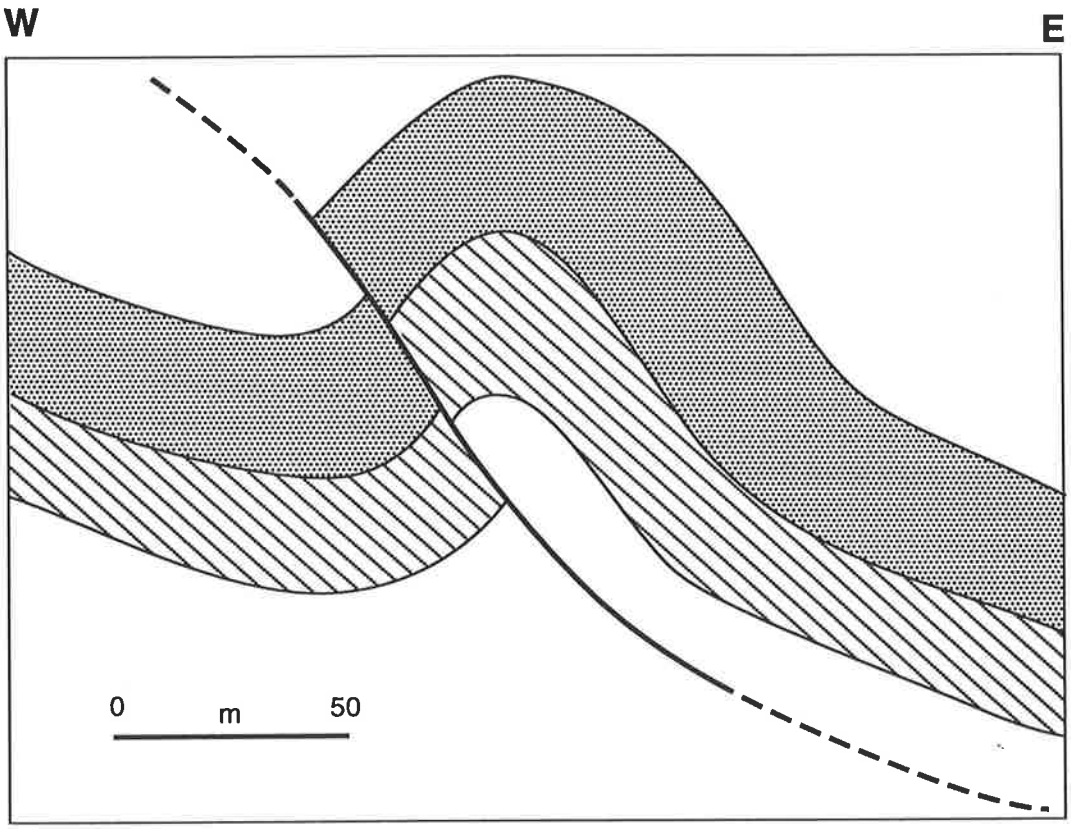

Fig. 3.8: Sketch map of a cut through fault-propagation fold along the HWII ductile thrust in the hangingwall of the Greenhill shear zone in the Greenhill area (see Fig. 3.7 for the location).

The general characteristics of structures and fabrics from within this shear zone are quite similar to the Morialta and Montacute Heights shear zones, MSZ and MHSZ respectively. In the Saddleworth Formation, as in the MSZ, crenulation folds and crenulation cleavages (S_{1b}) in phyllite units, transposed layering in interbedded pelite and psammite units, and deformed quartz veins, mostly at the lower boundary thrust, are developed. Similarly, in the Stonyfell Quartzite a weak cleavage begins to develop at the transitional zone and increases in intensity within the shear zone and toward the lower boundary thrust.

3.4.2. The Norton Summit shear zone

The road cuts along the Greenhill Road (Figs 2.2 & 3.7) provide the best exposure of this shear zone although this transect is itself partly weathered. Most of the Norton Summit shear zone occurs in the Stonyfell Quartzite where thick bedded quartzites contain a spaced cleavage and deformed quartz veins. This cleavage is mainly manifest by alignment of detrital quartz grains. The spacing between the cleavage surfaces is generally about 1-2 cm. Cleavage spacing as well as that of the quartz veins, is narrower toward the lower boundary thrust. The map width of this shear zone is about 600 m and this is likely to be underestimated since the lower boundary thrust and the upper transitional zone were not clearly identifiable due to the weathered nature of outcrops.

The Norton Summit shear zone is characterised by the occurrence of transposed layering and the development of minor asymmetric folds with a top to the NW sense of displacement. These structures are seen in interbeds of carbonate pelites, phyllites and sandy shales (Fig. 3.5c). The detailed sketch of part of figure 3.5c shows a sandy bed, which is consistently folded in the lower half but faulted and also transposed along microfaults in the upper half. All of these microfolds are mostly asymmetric with top-to-the-NW sense of asymmetry. Their overturned limbs are sheared off and/or apparently displaced probably due to the effects of dissolution processes. Similarly, transposition of the sandy layers along small-scale thrusts (Fig. 3.5c) also occurs in the same direction as the sense of microfold asymmetry. These structures therefore also provide good evidence for the movement direction and sense of the shear zone. The axial surfaces of these minor folds, as shown in the sketch of figure 3.5c), are sub-parallel

to the small-scale thrusts which produced the transposition and they are also sub-parallel to the fault related cleavages (S_{1b}) developed mostly in the phyllonite units within the shear zone. The dip of this cleavage is steeper than the ones in the Morialta and Montacute Heights shear zones. The abundance and intensity of these fabrics like the Morialta and Montacute Heights shear zones increases toward the lower boundary thrust where folded and boudinaged quartz veins are also developed.

The Norton Summit shear zone is associated with several ductile thrusts which are formed within the shear zone or in both the hangingwall (HW_1) and footwall (FW_1 & FW_2) to the shear zone (Fig. 3.7). The occurrence of ductile thrusts within the shear zone may indicate that the ductile thrusts developed later than or progressively after the shearing. In the hangingwall of the HW_1 ductile thrust, which has about a 30 m wide zone of deformation, a SE plunging antiform occurs. In the footwall to the shear zone two major ductile thrusts (FW_1 & FW_2) were also mapped (Fig. 3.7). The width of the deformation zone produced by each of these thrusts varies from about 50 m for FW_1 to less than 10 m for FW_2. In both of these ductile thrusts, like the major shear zone, asymmetric minor folds and transposed layering were also developed.

The FW_2 ductile thrust has small ductile thrusts in the hangingwall (for convenience named here FW_{2W}) but these are too small scale to map (Fig. 3.9a). The FW_{2W} ductile thrust which is located in a quartzite unit of the Saddleworth Formation is accompanied in its hangingwall by a fault-propagation fold (Fig. 3.9a) which clearly reveals the geometry and kinematics of this ductile thrust. This also allows the comparison of such geometries with the other ductile thrusts and shear zones which do not exhibit good outcrops to show their geometries. Sketches showing the possible development of these ductile thrusts and a full analysis of their formation are shown in figure 8.2 and discussed on section 8.3.

3.5. The Pole road area

The location of the Pole Road area is shown in figure 2.2. Detailed mapping of the area was carried out, especially along the Pole Road which provides a good transect of road-cut outcrops. From this mapping, a major shear zone, hereafter named the Pole Road shear zone and the two associated ductile thrusts in its hangingwall, have been identified (Fig. 3.10).

Figures opposite:

Fig. 3.9a: Fault-propagation fold along the HW_{2w} ductile thrust within the Greenhill area (297890 AMG reference).

Fig. 3.9b: Sheared off overturned forelimb of the minor asymmetric folds along the ductile thrusts in the Ackland Hill Road (198850 AMG reference). Note the long shallow-dipping normal limbs and short steeper overturned limbs.

Fig. 3.9c: Synclinal breakthrough fault-propagation fold within the deformation zone of the Aldgate thrust (198885 AMG reference). Note the parallelism of the thrust (large arrow) and fault related cleavage (small arrow).

Fig. 3.9d: Photograph and sketch of extensional crenulation cleavage (ECC-Fabric) from within the Pole Road shear zone (210875 AMG reference). Note the extensional nature of these fabrics from separation of asymmetric quartz boudins and the sense of movement which is to the NW (photograph is mirrored).

W

E

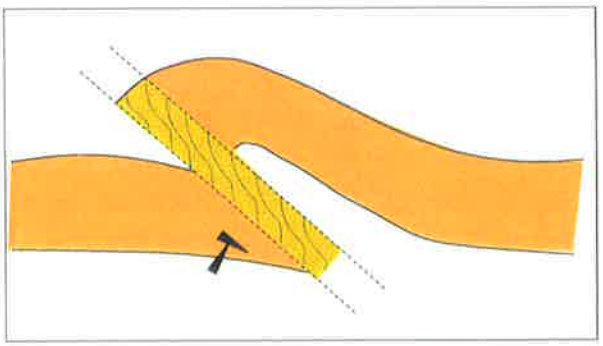

a

b

c

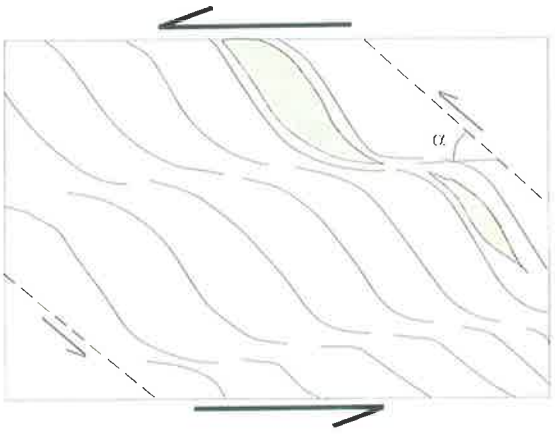

d

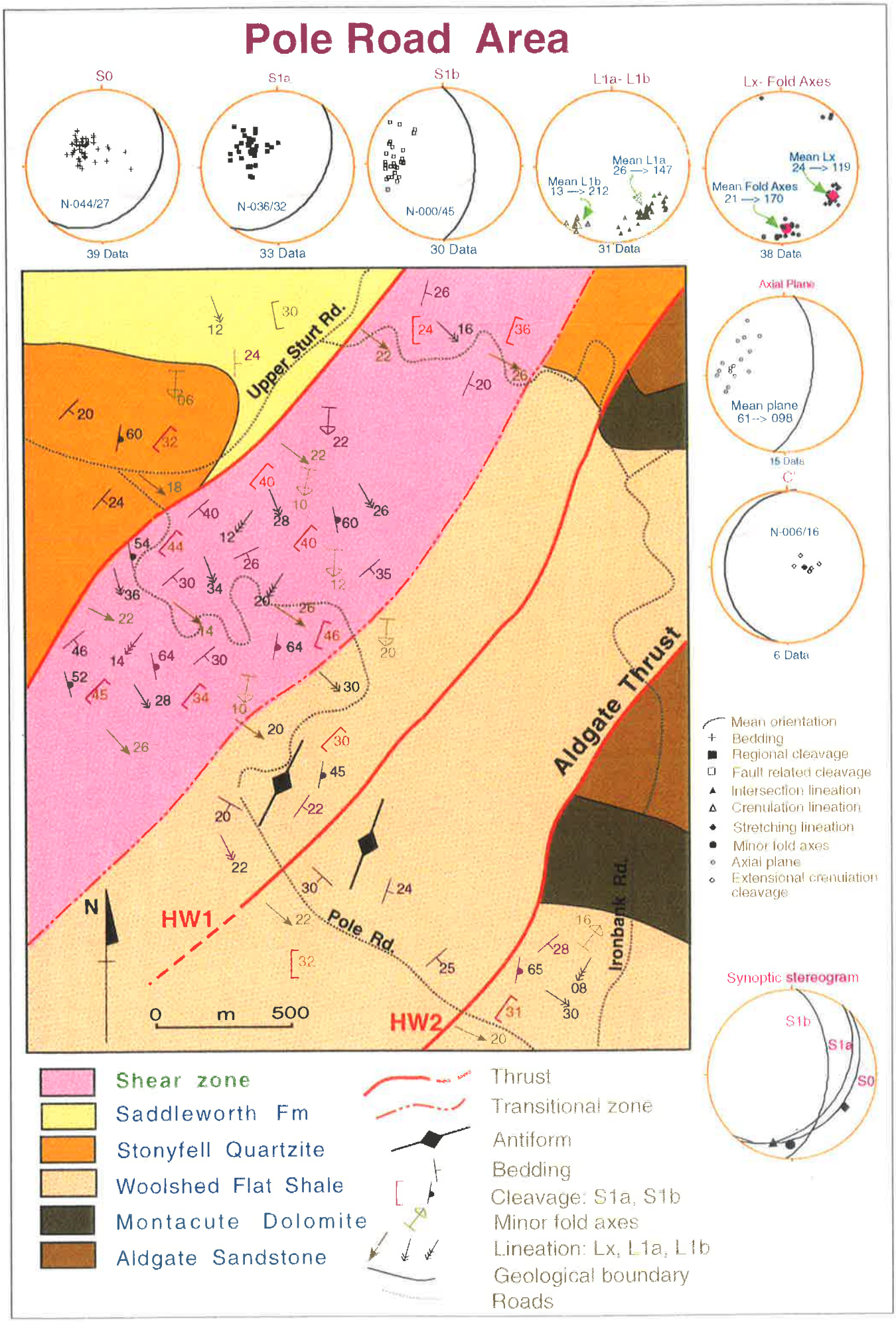

Fig. 3.10: Geological map of the Pole Road area showing distribution of the main lithological units, location of the Pole Road shear zone and associated ductile thrusts, and orientation of deformed fabrics and structures. Symbols: S0: bedding, S1a: regional cleavage, S1b; crenulation and/or fault-related cleavage, L1a: intersection lineation, L1b: crenulation lineation, Lx: stretching lineation and C': extentional crenulation cleavages.

In the Adelaide Hills area, the continuation of this shear zone to the north has been identified on the Mt. Barker Road where an outcrop of highly sheared basement exists north of Crafers (Fig. 2.2). Further to the north, a weathered outcrop of the sheared basement was also mapped in the area east of Summertown (Fig. 2.2). However, the contact of the basement with the overlying Burra Group is not exposed and the exact location of the lower boundary thrust to the Summertown shear zone remains equivocal. To the south of the Pole Road area, on Acland Hill Road, an outcrop of sheared Stonyfell Quartzite contains several ductile thrusts which are considered to be the continuation of the Pole Road shear zone. Four main ductile thrusts can be seen in this section each with antiforms developed in their hangingwalls and showing geometries similar to those of figure 3.8. These ductile thrusts are accompanied by several minor folds (Fig. 3.9b) and S-C band structures. As can be seen in figure 3.9b, all the minor folds are asymmetric with long shallow-dipping east limbs and short steeper dipping and sheared-off overturned west limbs. The hinge zones of the folds are almost always thicker than the limbs and show class II similar styles of folding, which is characteristic of shear or passive folding (Ramsay 1967-1987, Hudleston 1973, 1986, 1993). Further to the south, across Black Road (Fig. 2.2), there is a weathered outcrop of sheared Saddleworth Formation which may be considered as a further continuation of the Pole Road-Summertown shear zone.

The width of the shear zone in the Pole Road area (Fig. 3.10) is about 600 m in the Woolshed Flat Shale but to the NE this width decreases when the shear zone cuts through the competent Stonyfell Quartzite. Like the other shear zones, the Pole Road shear zone is bounded by an upper transitional zone to the SE and by a lower boundary thrust to the NW, in which older rocks are thrust over younger units (Fig. 3.10).

In the hangingwall of the Pole Road shear zone two ductile thrusts were mapped (Fig. 3.10) and named as HW_1 and HW_2. The HW_1 ductile thrust is characterised by a small deformation zone about 10 m wide in which evidence of weak S_{1b} and small-scale minor folds were seen. In the hangingwall of this ductile thrust, a mesoscopic antiform was also present. In the NE of the Pole Road area (Fig. 3.10), the older Montacute Dolomite and Aldgate Sandstone are exposed in the core to this antiform. The HW_2 ductile thrust and its continuation was also mapped

towards the Aldgate area and across the Mt. Barker Road (Fig. 2.2) and has been named the Aldgate Thrust in this study.

The deformation zone accompanying the Aldgate thrust is more than 50 m wide, although this might be greater due to limited exposure and weathered outcrops. This deformation zone is characterised by the development of fault related cleavages (S_{1b}) and minor folds with geometries similar to the geometry of synclinal breakthrough fault propagation folds (Fig. 3.9c), where the fault has propagated through the sheared-off limb of the synform. These minor folds are associated with the S_{1b} fabric which is sub-parallel to the axial plane of the folds. The exposure of the basement in the hangingwall of the Aldgate thrust implies that the thrust is deeply rooted. The steeper dip angle of S_{1b} (65°, Fig. 3.10) may further support this inference.

3.5.1. Structural geometry of the Pole Road shear zone

Stereograms showing the orientation of the main geometrical features of the Pole Road shear zone are displayed in figure 3.10. These include both fabrics (S_{1a}, S_{1b} and extensional crenulation cleavages) and minor structures (minor folds, transposed layering). The stereograms of bedding and regional cleavage show an average NE strike and SE dip. The angle between S_0 and S_{1a}, however, is not constant and changes across the shear zone (Fig. 3.11a). The shear zone has been subdivided into four shear zone parallel sub-areas depending on this change in the bedding-regional cleavage angle. This angle is low (about 5°) in sub-area A, which is coincident with the hangingwall transition into the shear zone. In sub-area B, this angle increases to 12° while in sub-area D, it again decreases to 6° where crenulation folds and cleavages are also well developed. Sub-area C is a transitional area between sub-areas B and D but like sub-area D shows low angle between bedding and regional cleavage. The main reason for separation of this sub-area from sub-area D is that the crenulation folds are initiated as open crenulation folds in this sub-area.

Steepening and shallowing of cleavage in such narrow zones has been referred to as a process of ramp folding along thrust sheets (Rattey & Sanderson 1982, Sanderson 1982). As is shown in Fig. 3.11, in sub-area A, the cleavage is shallow which may be coincident with the position

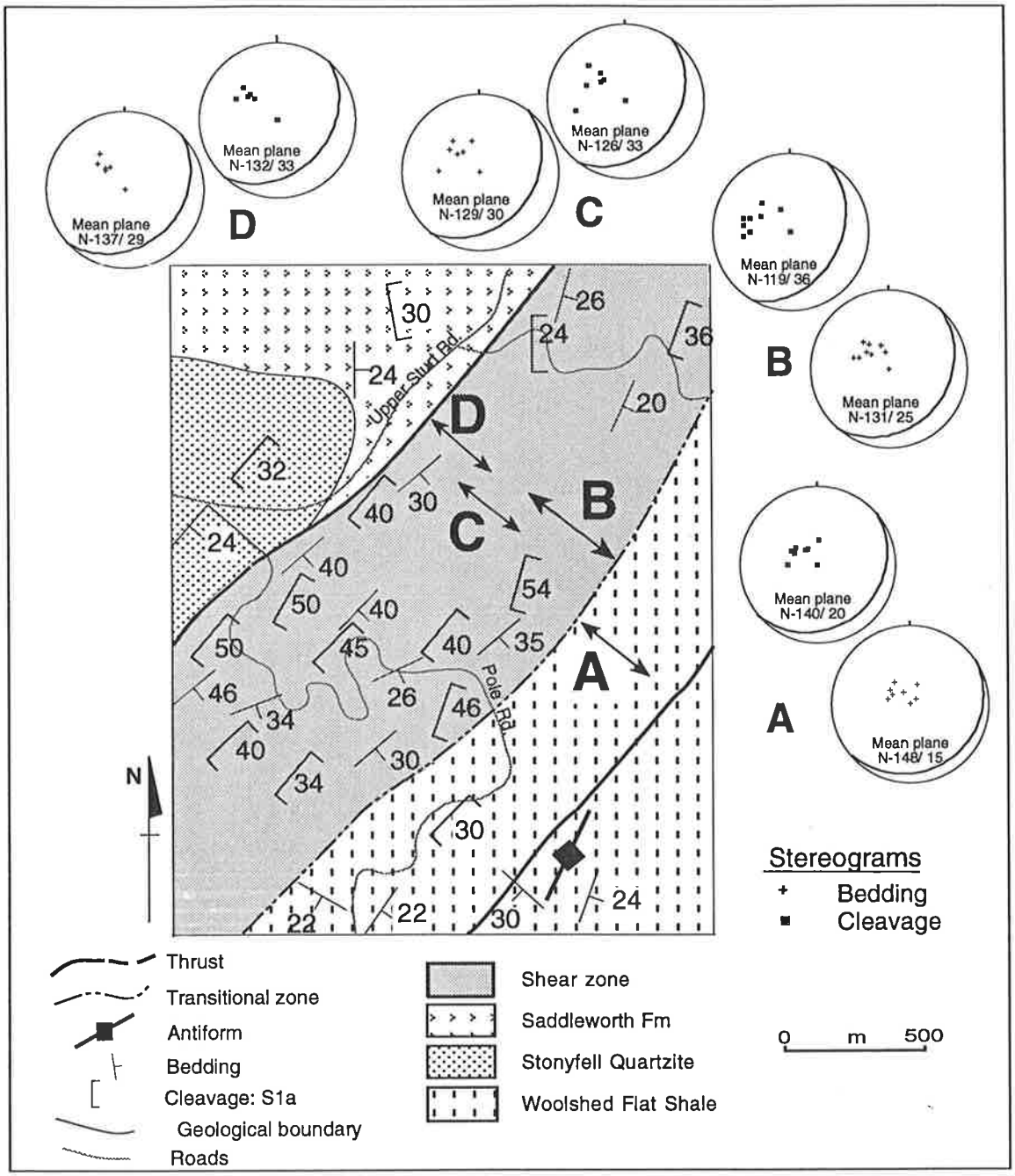

(a)

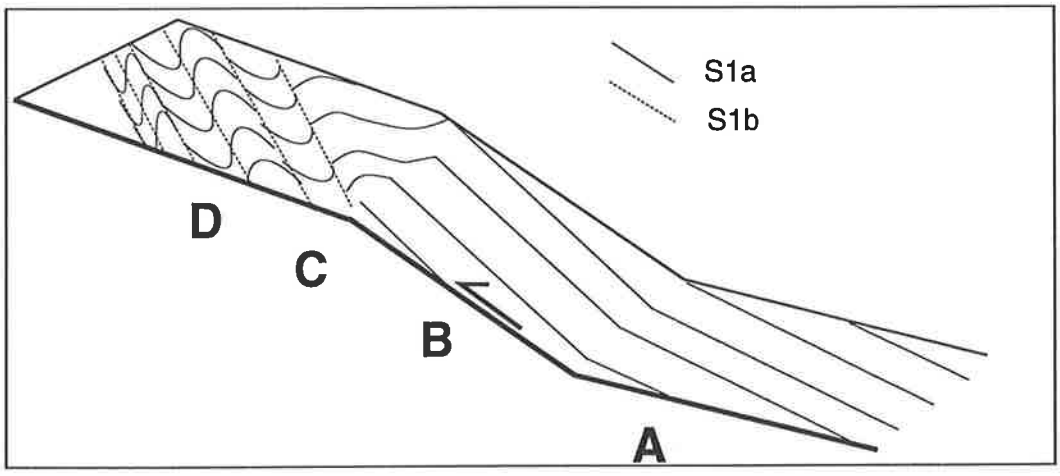

(b)

Fig. 3.11: (a): Simplified geological map of the Pole Road area showing subareas A, B, C & D defined by different angles between bedding and regional slaty cleavage; (b): a sketch cross section across the subareas showing cleavage orientation and development in different parts of a fault-bend fold. For more detail see text.

of a lower flat. Progressing towards sub-area B, the cleavage steepens and this may represent the climb from the lower flat up a ramp. In sub-area D, the cleavage again shallows and crenulation folds and cleavages (S1b) are also developed. Here it can be inferred that the thrust sheet passes from the ramp to the upper flat (see also cross-section sketch in Fig. 3.11b).

Stretching lineations and minor folds plunge shallowly SE and S-SE, respectively (see stereograms in Fig. 3.10). Minor folds occur within the shear zone but are more strongly developed over a distance of about 200 m from the lower boundary thrust where crenulation folds and cleavages (S_{1b}) are also developed. These cleavages are also sub-parallel to the axial planes of the minor folds (see stereograms in Fig. 3.10).

Composite planar fabrics in the form of the extensional crenulation cleavages (ECC-fabrics of Passchier 1991) are the other notable geometrical structures formed in the Pole Road shear zone (Fig. 3.9d). The stereogram showing the orientation of these fabrics in figure 3.10 shows that they all strike N-NE and dip shallowly W-NW. From this dip direction, the sense of shearing can be defined (e.g. Simpson & Schmid 1982, Lister & Snoke 1984, and Hanmer & Passchier 1991) and is consistently toward W-NW. Figure 3.9d, shows the magnitude of typical ECC-fabrics at up to 20 cm in length. They also displace boudinaged quartz veins, which further shows their extensional nature (see also the sketch in Fig. 3.9d).

The geometry of the ECC-fabrics in figure 3.9d are the same as those of extensional crenulation cleavages previously described elsewhere (e.g. Platt & Vissers 1980, Hanmer & Passchier 1991, and Passchier 1991). In this shear zone, the angle between the shear plane, which is considered to be sub-parallel to the bedding (see section 3.8.1 for more detail), and the ECC-fabrics is about 40°. This angle is important because it shows the intensity of shearing and therefore can be used to contrast the intensity of the shearing in this shear zone against that of the others in the Adelaide Hills area. Distribution of the ECC-fabrics are not widespread across the shear zone and are mostly confined to the SE, that is the upper parts of the shear zone and closer to the transitional zone.

3.6 The Clarendon area

The Clarendon area is situated in the south western part of the Adelaide Hills area (Fig. 2.2). Figure 3.12 shows in more detail the geological features of the area including the Clarendon shear zone, the Scott Creek ductile thrust and both of their hangingwall antiforms. The main lithological units of the Clarendon area are the Stonyfell Quartzite and Saddleworth Formation. The latter is interbedded with a few thick (1-2m) beds of quartzite (see Fig. 3.12).

The only outcrop of the Clarendon shear zone outside the Clarendon area was mapped along the Scott Creek road at Scott Bottom (see Fig. 2.2 for its location). This outcrop was first recognised by Jenkins (1990) as the location of the Scott Bottom shear zone. Based on the general trend of the shear zones in the Adelaide Hills area, this outcrop is considered to represent a continuation of the Clarendon shear zone to the NE but this is difficult to confirm due to the poor outcrop across the area.

Kapetas (1993) first mapped the Clarendon shear zone in the Clarendon area but he could not confirm the precise boundaries and continuation of the shear zone. Detailed mapping of the Clarendon area along Grants Road and Potter Road shows more precisely the location of the shear zone and its associated footwall ductile thrust (Fig. 3.12). Like the other shear zones, this shear zone is bounded by a lower boundary thrust to the NW and by an upper transitional zone to the SE. The best outcrops of the shear zone are adjacent to the Clarendon Weir, on the main road near to the Weir and at the Clarendon oval (see Fig. 3.12 for the location). The Clarendon Weir (Fig. 3.12) shows one major excellent outcrop of intensely sheared phyllonite which allows a detailed study of the geometrical features of the shear zone.

Outside the shear zone and in the footwall to the shear zone to the NW, a major ductile thrust (the Scott Creek Thrust) was mapped on Grants Road to the south (Fig. 3.12). Crenulation folds and cleavages (S_{1b}), and minor asymmetric folds also occur along this ductile thrust. The orientations of these structures are roughly the same as the orientations of their equivalents in the Clarendon shear zone, described in the next section. The continuation of this ductile thrust was also mapped along Potter Road. The exposure of the thrust in this road suggests that the

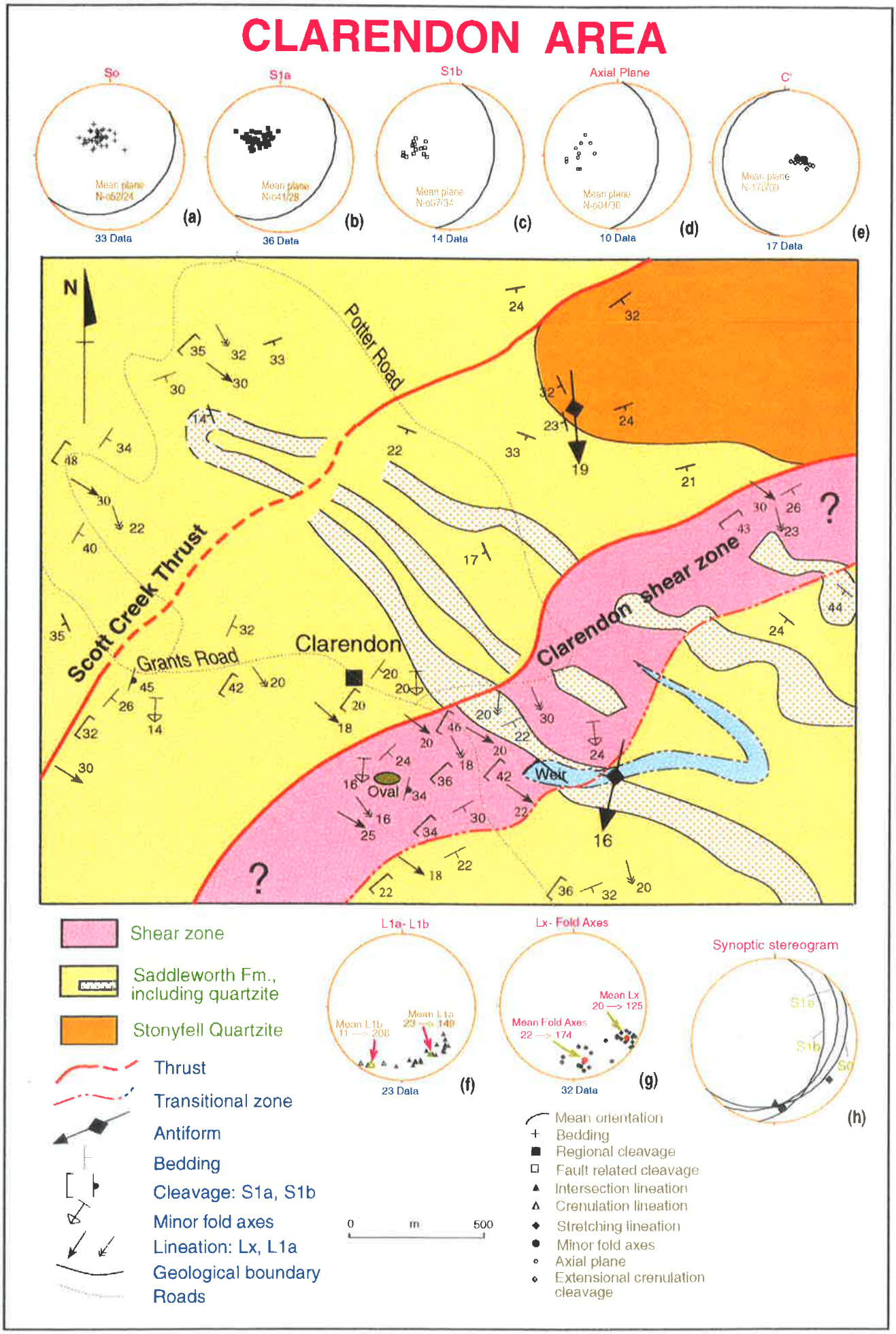

Fig. 3.12: Geological map of the Clarendon area showing distribution of the main lithological units, location of the Clarendon shear zone and associated ductile thrust, and orientation of deformed fabrics and structures. Symbols: S0: bedding, S1a: regional cleavage, S1b; crenulation and/or fault-related cleavage, L1a: intersection lineation, L1b: crenulation lineation, Lx: stretching lineation, and C': extensional crenulation cleavages.

thrust may connect with the Scott Creek thrust which was mapped in the Adelaide Hills area to the NE (Fig. 2.2).

The Scott Creek ductile thrust is one of the major ductile thrusts in the Adelaide Hills area showing the same orientation as the orientation of the shear zones. Outcrops of this thrust can be seen at a few localities in the area (in the Ironbank area and NW of the Scott Bottom area, Fig. 2.2) and are accompanied by development of stretching lineations, minor asymmetric folds, crenulation folds and cleavages (S_{1b}). The width of the deformation zone across the thrust is about 80 m in the Ironbank area but is less than this (about 50 m in width) in the NW of the Scott Bottom area.

3.6.1. Geometrical features of the Clarendon shear zone

The main geometrical features of the Clarendon shear zone are bedding (S_0), S_{1a} and S_{1b} fabrics, minor asymmetric folds, extensional crenulation cleavages (ECC-fabrics of Passchier 1991), and deformed quartz veins. A detailed study of the orientation of these structures is shown in the stereograms of figure 3.12. The S_0 bedding and S_{1a} fabric are sub-parallel and both strike NE and dip (about 30°) SE. Close to the lower boundary thrust, S_{1a} is crenulated to develop crenulation cleavages (S_{1b}). This cleavage is intensified and further deformed at the lower boundary thrust, especially in phyllonites, to initiate a new cleavage, S_{1c}, (Fig. 3.13a). This S_{1c} cleavage, which is sub-parallel to bedding shows a geometry similar to that of transposition cleavage (Fig. 3.13a) and also displaces layering in the overturned limbs of the minor asymmetric folds which are developed in more pelitic bands.

Minor asymmetrical folds with a top-to-the-NW sense of asymmetry are another geometrical feature of the shear zone. These plunge shallowly SE-SW (Fig. 3.12) and are seen to occur usually closer (about 50 m in distance) to the lower boundary thrust. Almost no evidence of these structures was seen at the upper transitional zone. The orientation of S_{1b} is sub-parallel to the orientation of the axial plane of the minor folds (see Fig. 3.13a and the stereograms of the S_{1b} & axial plane of the minor folds).

Figures opposite:

Fig. 3.13a: Photograph and sketch showing development of cleavages from S_{1a} to S_{1c} in phyllonites of the Woolshed Flat Shale from within the Clarendon shear zone (120840 AMG reference) (looking SW).

Fig. 3.13b: Slickensides lineation on the movement plane (bedding) and as growth fibres (arrow) in the quartz veins from within the Clarendon shear zone (118843 AMG reference). Note that they both have similar trend (looking SW).

Fig. 3.13c: Folded and boudinaged quartz veins in the phyllonites of the Woolshed Flat Shale from within the Clarendon shear zone (118843 AMG reference); the coin diameter is 2.2 cm (photograph is mirrored).

Fig. 3.13d: Extensional crenulation cleavages (ECC-Fabrics) in the phyllonite from within the Clarendon shear zone (118843 AMG reference); the coin diameter is 1.5 cm. In the sketch note the angle α= 30 which is between bedding or C plane (dashed lines) and shear band (photograph is mirrored).

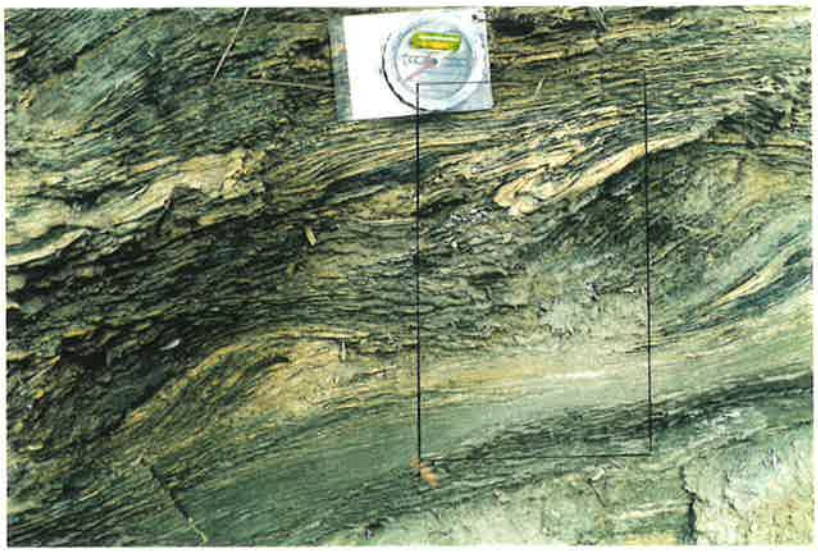

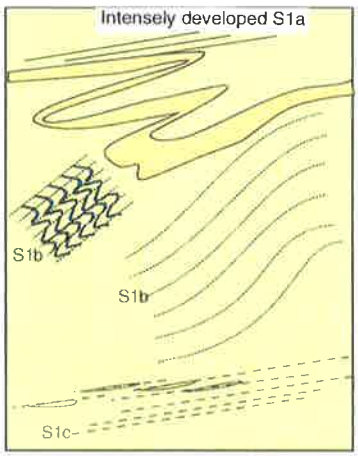

a

b

c

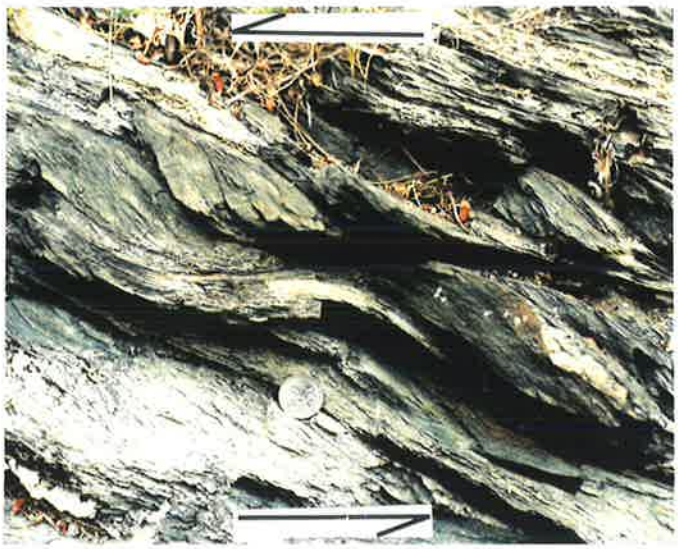

d

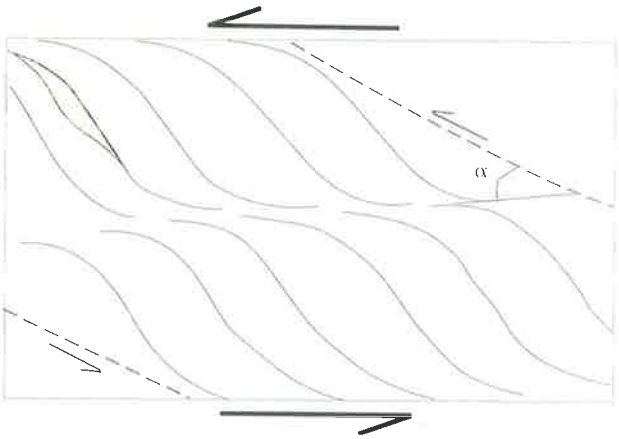

Slip lineations are the other geometrical feature of the Clarendon shear zone. Like the other shear zones these plunge uniformly and gently to the SE (stereogram in g Fig. 3.12). They occur as slickensides on the movement surfaces of the S_0 and/or S_{1a} or as growth fibres of quartz in the quartz veins (Fig. 3.13b). As can be seen, both are sub-parallel and show the consistent movement direction of the shear zone.

The quartz veins, which are the other notable structures in the area, are developed more extensively in the Clarendon shear zone than in the other shear zones. They occur normally as lens-shaped bodies in which the major and intermediate axes are almost always parallel to the bedding and/or foliation planes. The maximum thickness of the veins is 30 cm, while their length varies and is not easy to estimate due to the intensity of the deformation. The veins are almost always deformed to form folded and boudinaged vein systems (Fig. 3.13c). The individual boudinaged veins are asymmetric with almost always top to the northwest sense of asymmetry. The coincidence in orientation of the growth fibres in the quartz veins with the orientation of the stretching lineations (Fig. 3.13b) implies a similar genetic origin for the quartz veins.

The most intensely developed fabrics in the Clarendon shear zone are asymmetrical extension shear bands or ECC-fabrics. These fabrics strike N-S and dip shallowly (<10°) to the NW (see stereogram e on Fig. 3.12). They occur mostly in phyllonite on centimetre scales (up to 15 cm) within the shear zone (Fig. 3.13d). The ECC-fabrics make an angle of 30° to S_0 which dips (about 40°) to the SE. The ECC-fabrics themselves dip to the NNW (see stereogram e in Fig. 3.12) and cause extension of S_{1a} which dips to the SE (see stereogram b in Fig. 3.12). The geometry of these fabrics in the Clarendon shear zone is the same as their geometry in the Pole Road shear zone which was demonstrated in detail in figure 3.9d. In the Clarendon shear zone, however, these fabrics are more intensely developed, which is shown by a decrease in the α angle (the angle between bedding and ECC-fabrics) from about 40° (in the Pole Road shear zone, see sketch of Fig. 3.9d) to less than 30° (in the Clarendon shear zone, see sketch of Fig. 3.13d). The best outcrop of the ECC-fabrics in the shear zone can be seen at the Clarendon Weir (Fig. 3.12) although evidence of these structures was also mapped in the Scott Bottom

area. At the Clarendon Weir outcrop, within 30 meters of the weir, the magnitude and frequency of these structures substantially decreases toward the lower boundary thrust where the minor folds and crenulation cleavages are more intensely developed.

A synoptic stereogram for the all structures and fabrics of the Clarendon shear zone and its associated ductile thrust shows that the bedding is parallel to the great circle which joins the minor folds and stretching lineations (see stereogram h in Fig. 3.12). Considering the fact that this great circle represent the orientation of the shear plane, it is most likely confirmation that the shear is statistically bedding parallel.

3.7. The Mt. Bold area

This area is situated between the southern edge of the Adelaide Hills and the northern part of the Fleurieu Peninsula (Fig. 2.2). The area is mainly covered by vegetation, so the mapping and data collection were carried out on the outcrops along the perimeter of the Mt. Bold reservoir and along a few access roads. Low water levels in the reservoir enabled a detailed study of two traverses across the northern and southern floor of the Mt. Bold reservoir.

The basic geological map of the area (Fig. 3.14) shows in detail the main lithological units, the mapped shear zone and associated ductile thrusts and detailed geometrical orientations of the deformation fabrics and structures. The shear zone is bounded by a lower boundary thrust in the NW and an upper transitional zone to the SE. Two other ductile thrusts within the shear zone were also mapped. Within the shear zone, the older Aldgate Sandstone, Montacute Dolomite and Woolshed Flat Shale are thrust over the younger Stonyfell Quartzite and Saddleworth Formation. This has also caused apparent right lateral offset on the Stonyfell Quartzite and Montacute Dolomite units. The map width of the shear zone across the reservoir and within the Woolshed Flat Shale is more than 1 km but this decreases toward the north and south when the shear zone crosses the more competent Aldgate Sandstone and Stonyfell Quartzite (Fig. 3.14).

The Mt. Bold shear zone was described first briefly by Kapetas (1993) who mapped the perimeter of the Mt. Bold reservoir. The exact location and the continuation of the shear zone to the north and south were mapped during this study. Further continuation of the shear zone to

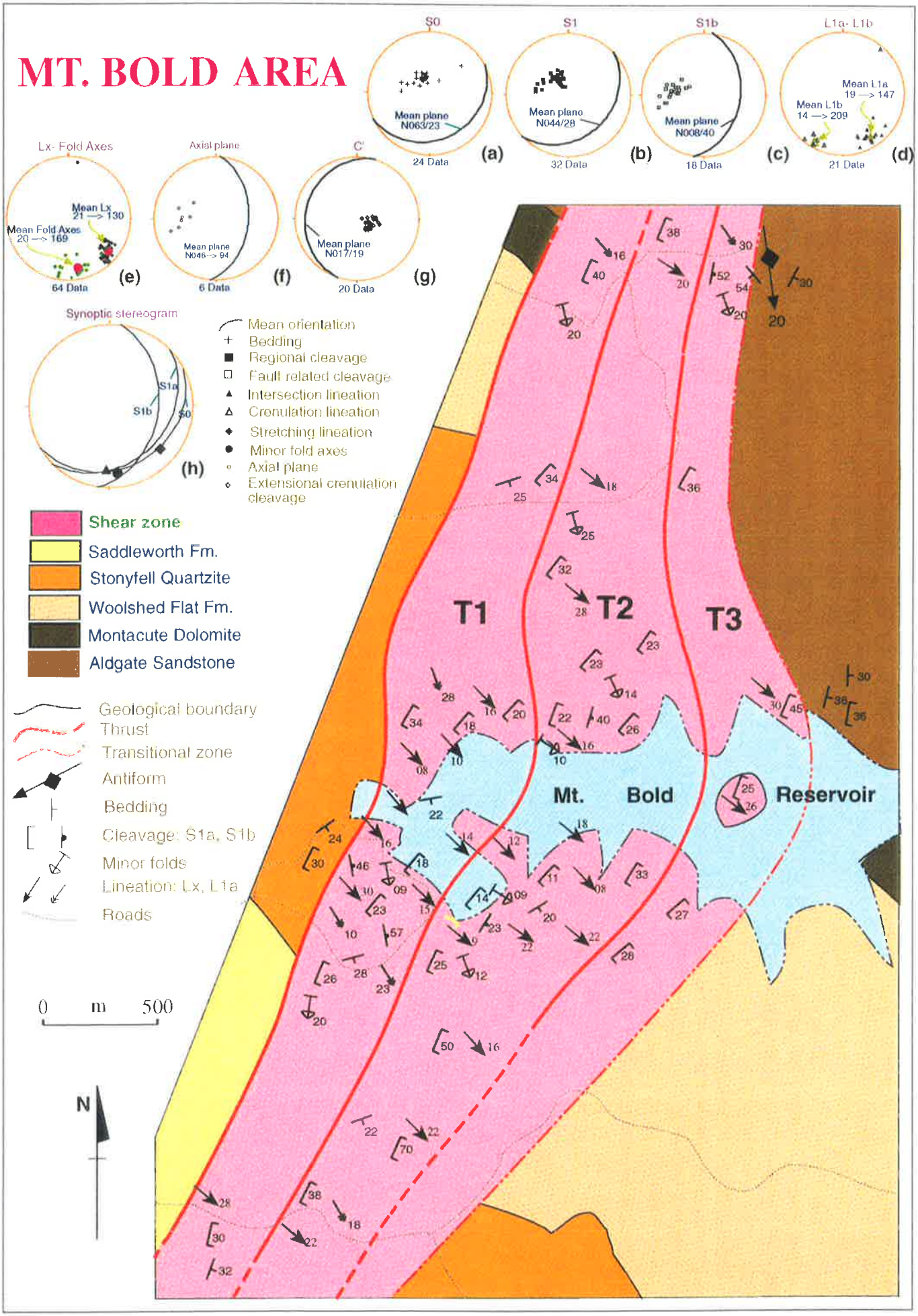

Fig. 3.14: Geological map of the Mt. Bold area showing distribution of the main lithological units, location of the Mt. Bold shear zone and associated ductile thrusts, and orientation of deformed fabrics and structures. Symbols: S0: bedding, S1a: regional cleavage, S1b; crenulation and/or fault related cleavage, L1a: intersection lineation, L1b: crenulation lineation, Lx: stretching lineation, and C': extentional crenulation cleavages. The map is modified after Kapetas (1993).

the north in the Adelaide Hills area is difficult to assess due to thick vegetation. To the south, on the Fleurieu Peninsula, it is likely that the shear zone connects with the high deformation zone across the Myponga River in the Sellicks Hill area which was mapped by Buhrer (1995).

In the Woolshed Flat Shale the shear zone is characterised by development of minor folds in more pelitic units (Fig. 3.15a), transposition of psammitic bands (Fig. 3.15b), and crenulation cleavage, shear bands and deformed quartz veins in phyllonite (Fig. 3.15c). In the Stonyfell Quartzite, the shear zone is characterised by the development of sheeted quartz in psammitic quartzite in the transitional zone. Within the shear zone sheared quartzite is developed toward the lower boundary thrust where deformed and boudinaged quartz veins are also developed (Fig. 3.15d).

Based on the presence of the three major mapped thrusts, the shear zone can be divided into three thrust sheets named from west to east as T_1, T_2 and T_3 (Fig. 3.14). Normally, in packets of thrust sheets a piggy back sequence (T_3 over T_2 and T_2 over T_1) might be expected. However, evidence of truncation of the upper limbs of minor-recumbent folds (Fig. 3.15e) from within the T_2 thrust sheet may imply that the T_3 thrust sheet is likely to be responsible for this event. Therefore, it is unlikely that the T_3 thrust sheet was thrust over the T_2 thrust sheet in a piggy back fashion. Two possibilities can be considered for the development of the T_3 thrust sheet. One is that it developed as a hangingwall ductile thrust to the shear zone and another scenario is that the thrust sheet occurred later as an out-of-sequence thrust (e.g. McClay 1992). Evidence of upper limb truncations of minor recumbent folds (Fig. 3.15e) provides some support for the latter possibility.

The greater concentration of deformation structures and fabrics in the hangingwall of T_2 thrust sheet and the absence of minor-recumbent folds, which are cross-cut by T_3 thrust sheet (Fig. 3.15e), may support the suggestion that the T_1 thrust sheet acts as the footwall imbricate ductile thrust. This may also provide evidence that the lower boundary thrust to the T_2 thrust sheets may be considered as the lower boundary thrust to the shear zone and therefore the T_1 thrust sheets and T_3 thrust sheet would be associated ductile thrusts.

Figures opposite:

Fig. 3.15a: Minor asymmetric folds in pelites of the Woolshed Flat Shale from within the Mt. Bold shear zone (105887 AMG reference) (photograph is mirrored); the vergence direction is top to the NW.

Fig. 3.15b: Transposition of bedding within psammites of the Woolshed Flat Shale within the Mt. Bold shear zone (108886 AMG reference). The asymmetric geometry of the boudin like structure is consistent with the NW sense of movement (photograph is mirrored).

Fig. 3.15c: Asymmetrical extension shear bands (arrows) and deformed quartz veins in the phyllonites of the Woolshed Flat Shale from within the Mt. Bold shear zone (113887 AMG reference).

Fig. 3.15d: Sheared Stonyfell quartzite with development of boudinaged quartz veins from within the Mt. Bold shear zone (092883 AMG reference).

Fig. 3.15e: Truncation of minor to mesoscopic recumbent isoclinal folds by out-of-sequence T_3 thrusting in the Mt. Bold shear zone (113887 AMG reference); width of view= 200 m. For more detail see text.

W

a

E

b

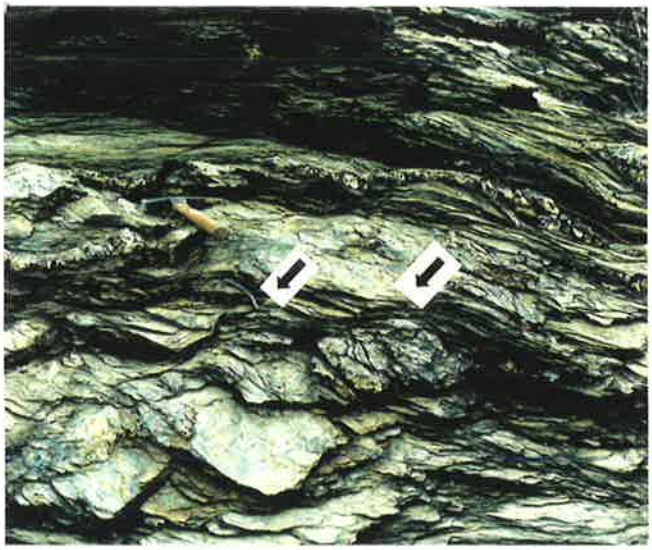

c

d

e

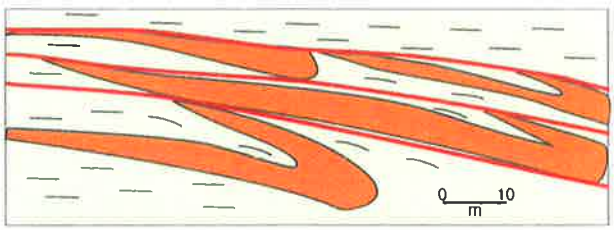

3.7.1. Geometrical features of the Mt. Bold area

Outside the Mt. Bold shear zone, the main geometrical feature of the area is bedding and to a lesser extent the regional cleavage (S_{1a}). The latter is better developed in pelites and phyllites in the incompetent units. In the shear zone, the main geometrical features are deformation fabrics (S_{1a}, S_{1b}, stretching lineation and shear bands) and structures (minor folds, veins and transposed layering). The stereograms of the orientations of these main features are shown in figure 3.14. Detailed geometrical features of the shear zone are described separately as fabrics, minor folds and veins in the next sections.

3.7.1.1. fabrics

The orientations of the main fabrics in the Mt. Bold shear zone are shown in figure 3.14. The stretching lineation, which is the most prominent fabric element in the shear zone plunges shallowly (<30°) SE (see also stereogram e in Fig. 3.14). This orientation is roughly constant across the Mt. Bold shear zone (130°, Fig. 3.14) and is nearly identical to the orientation of the stretching lineation in incompetent units from within the other shear zones in the Adelaide Hills area. For example the mean value for the orientations of stretching lineations in the Morialta, Montacute Heights, and Norton Summit shear zones trends towards 120° and in the Clarendon shear zone it is trending towards 125° (compare the mean value of this fabric in stereogram e of figure 3.14 with its counterparts in the other shear zones).

Crenulation cleavage and transposition of layering are other fabrics formed across the shear zone. The crenulation cleavage (S_{1b}) which strikes N-NE and dips moderately S-SE (see stereogram c in Fig. 3.14) is well developed in the phyllonite close to the lower boundary thrust to the shear zone and along the associated ductile thrusts (T_1 & T_3). Transposition of layering, however, is developed more strongly in pelites which are interbedded with sandy and silty units (Fig. 3.15b). The orientation of these fabrics is nearly the same as the orientation of S_{1b} and like those they are also well developed closer to the lower boundary thrust to the shear zone and along associated ductile thrusts.

The another significant group of fabrics in the Mt. Bold shear zone are asymmetrical extensional shear bands (ECC-fabrics). Like S_{1b}, these fabrics are well developed in the phyllonite (Fig. 3.15c) within the shear zone and associated ductile thrust sheets, but closer (about 150m) to the upper transitional zone to the shear zone (T_2 thrust sheet, Fig. 3.14) and associated ductile thrust sheets (T_1 & T_3). They strike N-NE and dip shallowly W-NW (see stereogram g in Fig. 3.14). From this orientation, the sense of shear, which is toward the NW, can be confirmed (e.g. Platt 1984 and Hanmer & Passchier 1991). In figure 3.15c, the ECC-fabrics lie about 25° away from the shear plane (C). They are also seen affecting the boudinaged veins where boudinaged segments are displaced to produce a normal-sense riedel shear as so called "foliation boudinage" (Lacassin 1989).

3.7.1.2. Minor folds

Minor folds are the most prominent structures in the Mt. Bold shear zone. They occur only within the shear zone and associated ductile thrusts whilst no minor folds are found outside the shear zone. In the shear zone and associated ductile thrusts, minor folds are generally developed in almost all units except the Stonyfell Quartzite and they are also developed where the rocks have a layered anisotropy due to interbanding of psammite and pelite layers. Their geometry, however, is not constant across the shear zone and two types of minor fold geometry has been distinguished.

The first type (Type I) are gently to moderately curvilinear, close-to-isoclinal recumbent fold types with fold axes sub-parallel or at low angles to the local stretching lineation (Fig. 3.16a). This fold type which plunges shallowly SE (see stereogram e in Fig. 3.14) has a sheath-like geometry (Fig. 3.16b). These folds are only seen within this shear zone (T_2 sheet) and no evidence of these folds were recorded in the associated ductile thrusts (T_1 & T_2). The upper limbs of this type of fold geometry are consistently truncated and cut-off by small-scale minor imbricate ductile thrusts (Figs 3.15e & 3.16c), which are possibly related to the occurrence of the out-of-sequence T_3 ductile thrust sheet.

The second fold type (Type II) are gentle-to-tight asymmetric NW verging folds with long gently dipping SE limbs and short steeply overturned NW limbs (Fig. 3.20b). This fold type

Figures opposite:

Fig. 3.16a: Isoclinal recumbent sheath-like folds (Type I) in the Woolshed Flat shale from within the Mt. Bold shear zone (113887 AMG reference). This fold is actually one of the folds in figure 3.15e, in which, like those folds, its upper limb is truncated by T_3 thrusting. Also note superposition of minor asymmetric folds of Type II on the lower limb (arrow).

Fig. 3.16b: Photomicrograph of Type I fold geometry showing sheath-like nature of these fold types. Notice eye fold closure in the upper part of photomicrograph.

Fig. 3.16c: Truncation of the upper limbs of Type I fold by T_3 thrusting from within the Mt. Bold shear zone (looking SE) (124896 AMG reference).

Fig. 3.16d: Minor asymmetric Type II fold geometry in the Woolshed Flat Shale from within the Mt. Bold shear zone (113887 AMG reference). Note the sub-parallelism of the axial plane with the S_{1b}.

Fig. 3.16e: Out of syncline thrust geometry of T_1 thrusting within the Mt. Bold shear zone (photograph is mirrored); see text for more detail (looking SW) (106880 AMG reference).

Fig. 3.16f: Asymmetric boudinaged quartz veins from within the Mt. Bold shear zone (photograph is mirrored) (108886 AMG reference). From the asymmetric tails of the boudins the sense of movement can be defined which is towards NW.

W

a

E

b

c

d

e

f

plunges shallowly S-SE (see stereogram e in Fig. 3.14) and their axial planes consistently dip moderately SE and are sub-parallel to S_{1b} (compare stereograms c with f in Fig. 3.14 and also see Fig. 3.16d). These folds display little or no detectable hinge line curvature and the fold axes are almost always oblique to the local stretching lineation. The length ratio of long limbs to short limbs of these asymmetric folds varies across the shear zones. Within the shear zones, this ratio is between 1.0:0.67 to 1.0:0.75 but the folds are still asymmetric. Near to the lower boundary thrusts, this ratio increases to 1.0:0.45 to 1.0:0.5 and the short limbs of the folds are almost always sheared-off. At the lower boundary thrust (T_2) and along T_1 and T_3, ductile thrusts propagate through these sheared-off limbs carrying the antiforms some distance from the syncline in the footwall (Fig. 3.16e) creating small-scale out-of-syncline thrust geometries (e.g. Coward 1988).

The Type II folds are superimposed on the earlier isoclinal-recumbent Type I folds (see the arrow on the lower left side of Fig. 3.16a). This suggests that progressive superposed folding of these fold types took place during the evolution of the shear zone. However, the lack of the presence of gently to moderately curvilinear folds of Type I in the other shear zones may also indicate that the folds in the other shear zones in the Adelaide Hills were not developed in such progressive manner.

3.7.1.3. Veins

Quartz veins are the other structures formed in the shear zone and are almost always sub-parallel to S_0 and/or S_{1a}. They are mostly seen in the phyllonite and to some extent in the quartzite close to the lower boundary thrust of the shear zone and associated ductile thrusts (Figs 3.15c & d). They are often deformed to form boudinaged veins. These boudinaged veins are almost always asymmetric and from the asymmetric tails of these boudins (Fig. 3.16f), which is toward the NW, the sense of shear can also be defined (e.g. Hanmer & Passchier 1991).

3.8. Discussion

3.8.1. Bedding parallel nature of the shear zones in the study area

The concentration of minor folds within the shear zones and associated ductile thrusts provides compelling evidence that these structures were most likely developed due to processes of shearing. Therefore, in a given stereographic plot, the cyclographic projection of the plane (a great circle) which contains these minor folds and stretching lineations should define the shear plane orientation (e.g. Hansen 1971, Roering & Smit 1987). A detailed study of the synoptic stereograms from within the shear zones (see the synoptic stereograms in Figs 3.1, 3.6, 3.7, 3.10, 3.12 & 3.14) shows that the great circle representing the mean value of the bedding has a close coincidence with the orientation of the minor folds and stretching lineations, and is thus parallel to the shear plane. This also shows that the bedding planes within the shear zones are also likely to be parallel to the shear plane which acted as movement or shear plane throughout the deformation.

The quartz veins, which are spatially confined to the shear zones and associated ductile thrusts, are mostly parallel to the bedding planes. They are almost always formed as lense-shaped bodies between bedding surfaces especially in the phyllonites, where they are also deformed (e.g. Fig. 3.13a). On the bedding surfaces, movement horizons are marked by quartz veins in which slickenfiber lineations on the surface record the slip direction. Bedding parallel veins are a type of vein that formed between bedding surfaces where differential movement is considered to be subparallel to bedding. The origin of this type of vein is attributed to various settings such as: flexural slip during folding (eg. Tanner 1989), post-diagenetic fluid over-pressuring of detachments in sediments buried to depths of several hundred metres prior to cleavage development and folding (Fitches *et al.* 1986), hydraulic pumping either during folding (e.g. Cosgrove 1993) or syntectonic vein formation (Mawer 1987, Henderson & Henderson 1990). Spatial development of deformed veins within the shear zones and especially closer to the lower boundary thrusts, along with sub-parallelism of fibre growth surface with the stretching lineations on the vein, may support a syntectonic origin of the bedding-parallel quartz veins in the shear zones.

3.8.2. Movement direction of the shear zones

It is accepted that the orientation of stretching lineations and shear bands reliably indicate the direction and sense of movement in shear zones and thrust sheets (e.g. Hanmer & Passchier 1991, and Aller & Bastida 1993). The shear bands in the shear zones dip about 15° to the W-WNW (e.g. the stereograms e & g in Figs 3.12 & 3.14, respectively). The orientation of the stretching lineation in almost all the shear zones varies in detail, by about 20-30°, between competent and incompetent units (e.g. Fig. 3.4). Unlike the quartz-fibre slickensides in competent Stonyfell Quartzite which trend to the E, the stretching lineation on bedding surfaces of incompetent units of the Saddleworth and Woolshed Flat Shale Formations trend towards the SE. The trend of stretching lineations also changes slightly (from 109° to 130° average) from the northwestern shear zone (the Morialta Shear Zone) to the southeastern one (the Mt. Bold Shear Zone).

Ridely (1986) studied the stretching lineations on the Island of Syros (Greece) using detailed analysis of the relationships between curved lineations, which vary in trend throughout this layered sequence, with competency contrasts. He showed that in the case of different layers with different viscosities, representing a planar anisotropy, the orientations of the linear structures may alternatively differ between competent and incompetent units. He also stated that the orientation of the stretching lineation within the incompetent layers lies closer to the transport direction.

Neither substantial variation in the trend of stretching lineations nor extensive evidence of parallelism of stretching lineations and fold hinges have been found within the shear zones in the Adelaide Hills. It seems therefore that there is no spatial evidence to support the existence of a significant wrench component in stretching lineations during overthrust shearing as was described by Ridely (1986). If there was a low ratio of wrench component to thrust shear, it may have caused the development of minor oblique folds within different competent and incompetent lithological units in all the shear zones and their associated ductile thrusts. There is, however, no change in the orientation of minor folds between these competent and incompetent units. Therefore, it seems that the planar anisotropy proposal of Ridely (1986) for

layers with different competency does not fully support the differences in the orientation of the stretching lineations in the Adelaide Hills shear zones.

To resolve the precise transport direction of the Adelaide Hills shear zones, the vergence analysis technique of Bell (1981) has been applied (Fig. 3.17). In this technique, cleavage vergence is defined on cleavage-bedding and/or cleavage-cleavage relationship as a horizontal direction. This can be determined within the plane normal to the fabric intersection lineation, towards which a younger fabric needs to be rotated so that it becomes parallel to the older fabric. In all cases the younger fabric should be rotated through the acute not the obtuse angle. Three steps were made for the analysis (see Fig. 3.17): 1) the plane normal to the intersection lineation of bedding-fabrics and/or two fabrics was defined, 2) in that plane normal to the bedding or earlier fabrics, an upwards direction in space was projected and 3) the direction towards which the normal would have to be rotated to lie parallel to the later fabrics was deduced to define the direction of vergence of the later fabric.

Some selected pairs of bedding and regional cleavage from outside and inside all the shear zones have been used to analyses the vergence direction of the regional cleavage (S_{1a}). The rose diagrams of S_{1a} for outside and inside all the shear zones show a fairly constant vergence direction toward the WSW (257°) or W (276°) (Figs. 3.18a & b), respectively. This consistency of the vergence direction may also indicate that this cleavage is not an axial planar fabric related to folding but rather developed due to overthrust shearing (e.g. Roering & Smit 1987). In addition, the result also shows that the mean vector of the vergence direction is slightly rotated toward the N from outside to inside the shear zones.

Another attempt to resolve the transport direction was carried out by constructing the vergence direction of fault-related cleavage (S_{1b}) using some selected pairs of S_{1a} and S_{1b} (Fig. 3.18c). As this rose diagram shows, the vergence direction is toward the W-NW (azimuth 284°). The slight rotation of the mean value of the vergence direction towards the NW from outside into the shear zone and from older fabrics to younger ones more likely be due to progressive development of the fabrics during shearing.

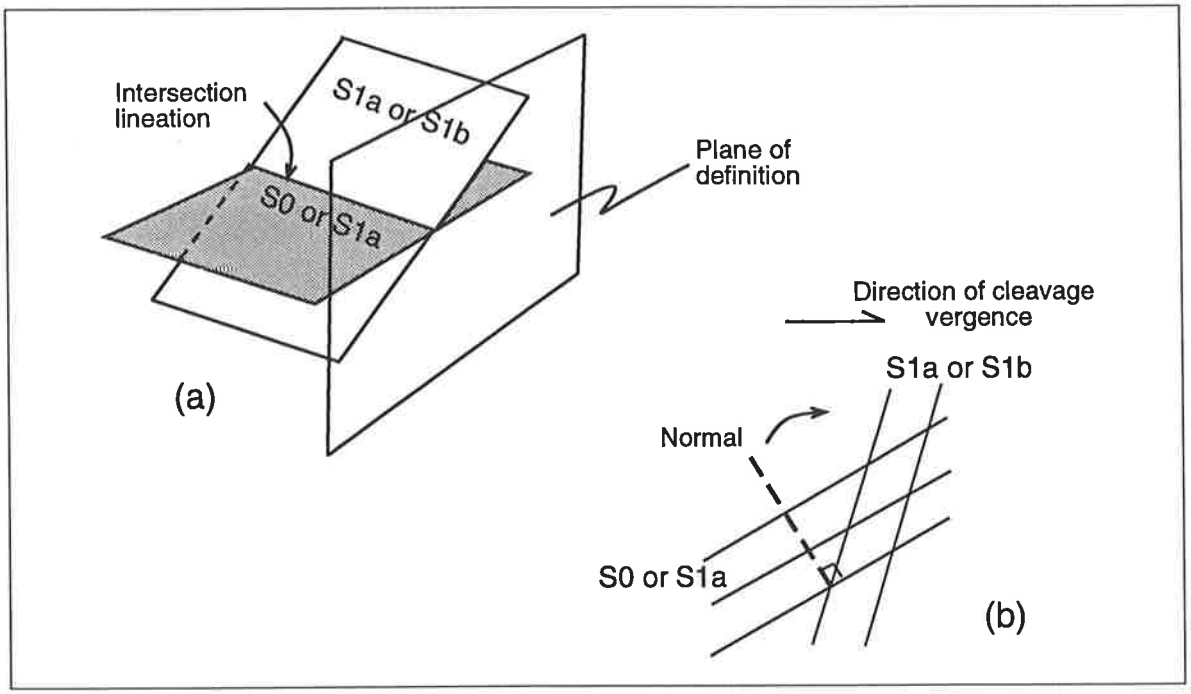

Fig. 3.17: Cleavage vergence analysis, after Bell (1981). (a) plane of definition normal to intersection of bedding-cleavage or cleavage-cleavage. (b) direction of cleavage vergence in the plane of definition. See text for more detail.

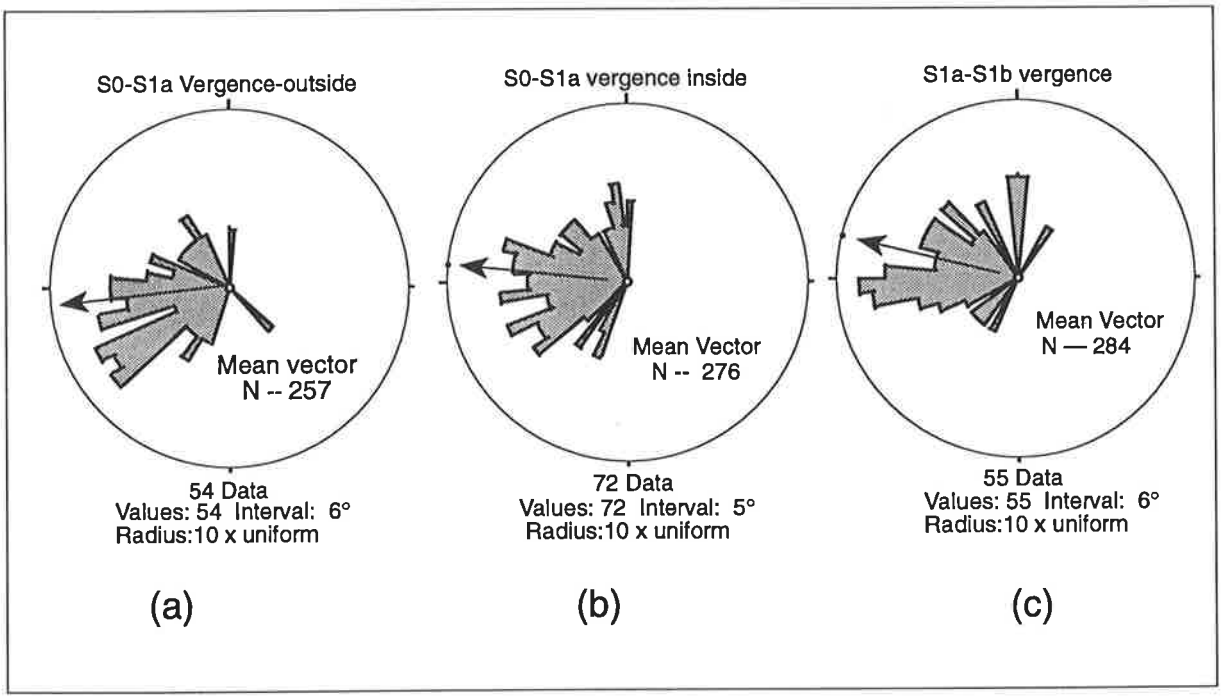

Fig. 3.18: Vergence direction analysis of the shear zones. a: vergence direction analysis of S1a outside the shear zone; b: vergence direction analysis of S1a within the shear zones; and c: vergence direction analysis of the S1b within the shear zone. Development of the mean Value of the vergence direction towards the NW from a to c indicate progressive development of the fabrics from early shortening event (a) to initiation of shearing phase (b) and to development of shearing process (c).

It is widely considered that shear bands are a reliable indicator of the relative movement direction of shear zones (e.g. Simpson & Schmid 1983, Lister & Snoke 1984, and Hanmer & Passachier 1991). As bedding is roughly coincident with the shear plane (refer to previous section) and as shear bands show the sense of shear, the orthogonal line to the intersection of the mean value of bedding and shear bands on the bedding plane can also be used as a movement direction indicator (Fig. 3.19). The result of this analysis also shows, the movement direction is toward WNW, i.e. towards 290°.

The interpretations of vergence direction and shear plane analyses confirm that the transport direction of the shear zones is toward WNW (with an average of 287°). This movement direction is coincident with the movement direction implied from the orientation of the stretching lineations in incompetent units which is toward the NW. This further confirms the interpretation of Ridely (1986) that in an area where a planar anisotropy of layers with different competency is present, the orientation of stretching lineations in incompetent units are closer to the transport direction. These interpretations are also in accordance with the NW sense of movement obtained from the asymmetric minor folds (e.g. Fig. 3.16d), asymmetric tails of boudinaged quartz veins (e.g. Fig. 3.16f) and extensional crenulation cleavages or shear bands (e.g. Fig. 3.13d).

3.8.3. Development of cleavages in the shear zone

3.8.3.1. Regional cleavages

The S_{1a} cleavage is a regional structure outside the shear zones and ductile thrusts. This cleavage, which forms as a slaty or phyllitic cleavage of variable intensity (e.g. Fig. 3.2c), is well developed within incompetent units of phyllite, pelite, carbonate and occasionally psammitic rocks. The S_{1a} cleavage, which forms an axial plane fabric to the regional shallow inclined folds and is similar to the geometry of weak to moderate continuous cleavages described by Powell (1979), is the earliest recognisable tectonic structure. This fabric generally trends N-NE to S-SW and dips (less than 30°) SE and often lies at a low angle (less than 10°) to the bedding (see the synoptic stereograms in Figs 3.1, 3.6, 3.7, 3.10, 3.12 & 3.14).

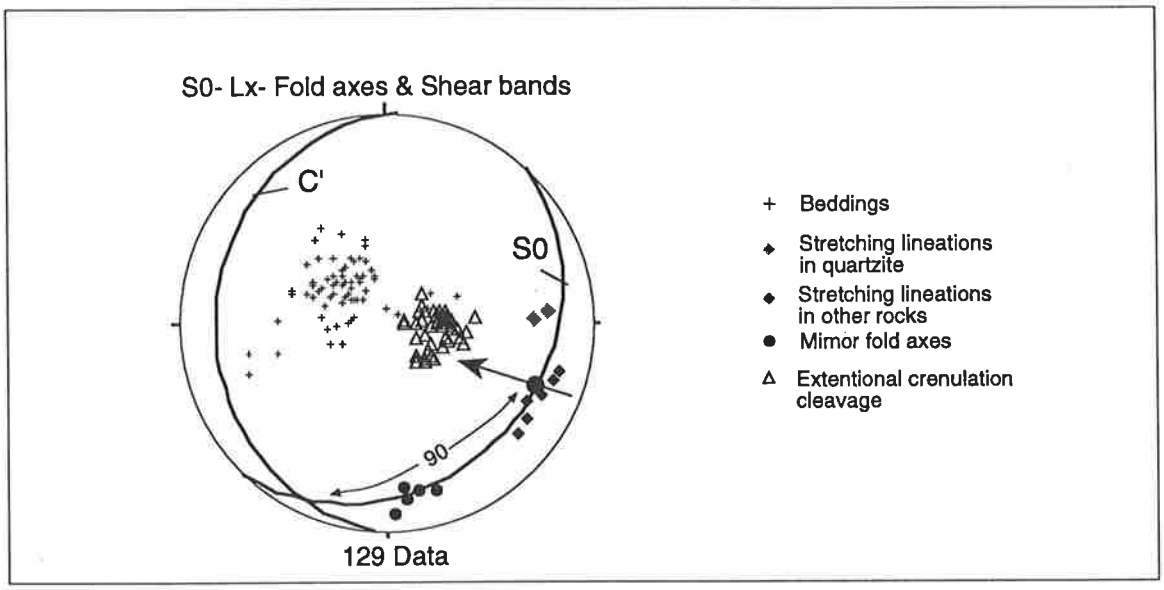

Fig. 3.19: Sterograms showing transport direction analysis of the shear zones. The arrow shows constructed movement direction of the shear zone based on the intersection of the great circles of mean orientations of the shear bands (C') and bedding planes (S0) which represent orientation of shear planes. For more explanation see text.

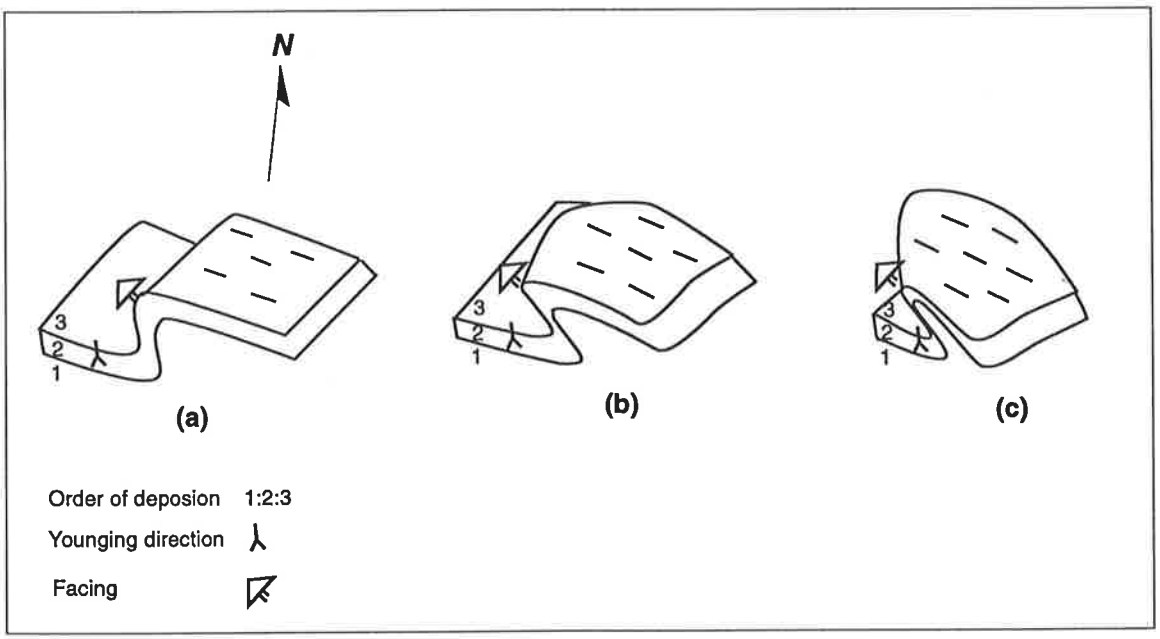

Fig. 3.20: Development of folds in shear zones of the Adelaide Hills area. (a:) initiation of folds as asymmetric NW facing folds, (b): weakly curvilinear asymmetric Type I fold geometry, and (c): moderately curvilinear to isoclinal Type II fold geometry.

The origin and significance of near bedding-parallel cleavages have been a topic of some debate. They have previously been interpreted as primary fabrics forming during deposition, or as enhanced primary fabrics developed during metamorphism (e.g. Keighin *et al.* 1972, and Ojakangas 1972 in Holst 1985). Powell and Rickard (1985), however, from a detailed study of deformed turbidites named these near parallel cleavages as S* in contrast to S_1. They considered that S* can be a tectonic foliation rather than simply depositional fabric if it cuts across the bedding. There is little evidence to support the existence of S* in the Adelaide Hills area. Bedding-parallel cleavage may also form as a result of deformation which may be quite intense and lead to transposition of bedding (Hobbs *et al.* 1976, PP. 252-264), which is the situation that is most likely within the Adelaide Hills shear zones.

Within the shear zones, the regional cleavages are intensified and more strongly developed in all lithological units but more significantly enhanced in incompetent units. They are also deformed to form crenulation cleavages in pelites and phyllites and/or transposition cleavages in pelites and psammites (e.g. Fig. 3.15b and also see Hobbs *et al.* 1976, PP. 252-264).

Overall, the S_{1a} cleavage is a low angle regional cleavage formed as an axial plane fabric to regional shallow inclined folds. This cleavage developed at low metamorphic grades and was intensely produced by the beginning of the progressive shear deformation which eventually lead to shearing and thrusting.

3.8.3.2. Crenulation and continuous cleavages

The S_{1a} cleavage formed in incompetent units within all of the shear zones and ductile thrusts is often crenulated to develop a crenulation cleavage or fault-related cleavage (S_{1b}). As was described in section 3.2.1 (see also Fig. 3.3), these always develop near (within about 50 m) to the lower boundary thrust of the shear zones. This fault-related cleavage initiates as a weakly zonal crenulation cleavage near to the transitional zones within the shear zones (Fig. 3.3a). Within the shear zones, the interlimb angles of the crenulations become smaller to form crenulation folds (Fig. 3.3b). Close to the lower boundary thrusts, crenulation folds intensify to form strong crenulation cleavages or S_{1b} (Fig. 3.3c) with orientations close to that of the S_{1a}, but steeper (see for example the stereograms e in Figs 3.10 & 3.14). As can be seen in figure

3.3c, S_{1b} is a dissolution cleavage (Gray 1979) and in some exposures, where the rate of this dissolution is higher, S_{1a} has simply rotated to form S_{1b} without intervening crenulation phases (see also Tobisch & Patterson 1988). At the lower boundary thrusts to the shear zones, the crenulation cleavages (S_{1b}) are completely transposed into a new continuous cleavage or S_{1c} (e.g. Fig. 3.13a) whose orientation is sub-parallel to S_{1a} (see sketch map of Fig. 3.13a). This cleavage is occasionally indistinguishable from the initial slaty cleavage outcropping in the field and sometimes even in thin sections.

Progressive development of cleavages from S_{1a} to S_{1b} and finally to S_{1c} within the shear zones appears to be uniform through all the shear zones, although it is not possible in most cases to recognise this development due to lack of continuous exposure. Since these cleavages show groups of surfaces where their components share almost similar orientations, it is preferred to refer to them as "composite foliations" (Tobisch & Patterson 1988 and the references therein). The processes generating this composite foliation in shear zones can involve complex rotation of early foliations by passing through a crenulation cleavage phase, accompanied by transposition of layers or pre-existing cleavages with differentiation due to solution transfer (Tobisch & Patterson 1988). The presence of crenulation folds and cleavages in all the shear zones which are considered to develop due to solution transfer (Cosgrove 1976, Gray 1979, Gray & Durney 1979, and Ho *et al.* 1996), along with the processes of transposition of bedding or early cleavages (S_{1a} or S_{1b}) supports the development of these composite foliations in the shear zones and associated ductile thrusts of the Adelaide Hills during the processes of shearing and thrusting.

3.8.3.3. Extensional crenulation cleavages and general non-coaxial nature of the shear zones

Besides small-scale contractional structures (like minor folds & crenulation folds) within the shear zones, extensional shear bands occur and truncate S_{1a} at regular intervals. These shear bands which occur on a centimetre scale (up to 10 cm) dip gently (about 15°) WNW (e.g. stereograms e and g in Figs 3.12 & 3.14, respectively) and are best observed in regions where the minor folds are almost absent. That is, in the shear zones, they almost all develop closer to the upper transitional zone whilst the minor folds develop closer to the lower boundary thrusts.

The shear bands are common in both sheared quartzite (e.g. Fig. 3.2d) and phyllonite (e.g. Fig. 3.9d) and their geometries are almost the same. Within both units, shear bands or ECC-fabrics displace finite strain cleavages or S planes and form minor discrete shear zones (Figs 3.2d &. 3.9d). In the phyllonites the C'-planes form a typical extensional crenulation cleavage type of shear band or ECC-fabrics (White 1979, Platt & Vissers 1980, and Passchier 1991). In both units, unlike the C-planes, which are sub-parallel to the main shear zone boundaries, ECC-fabrics or shear bands are normally oblique to the trend of the margin of the shear zone in which they are generated and provide reliable data to deduce the sense of shear (e.g. Platt & Vissers 1980, Platt 1984, Hanmmer & Passchier 1991, and Passciher 1991). From the orientation of the shear bands or ECC-fabrics, the sense of shear can therefore be deduced and is consistently toward the NW (refer to stereograms d & g in Figs 3.12 & 3.14, and also see Fig. 3.10).

Since the orientation of asymmetric extensional crenulation cleavages (ECC-fabrics) is not directly related to the axes of the finite strain (like an S surface), i.e. oriented at about 15-25° to the bulk simple shear (e.g. Platt 1984), it is considered that these structures are generated in the later stages of deformation compared to the early fabrics (S_{1a} & S_{1b}) (e.g. Platt 1984, Passchier 1991). Two reasons are cited for this relationship: 1) that they do not propagate parallel to the direction of flow and 2) that the strain deviates from simple shear because of superposition of coaxial stretching components on simple shear components at the zone of failure (e.g. Platt 1984). Hanmer and Passchier (1991) considered the nature of general non-coaxial flow for the rocks which contain these cleavages. This implies that the kinematics of flow in the Adelaide Hills shear zones, containing extensional crenulation cleavages departs from progressive inhomogenous simple shear (see also Stock 1992), a feature that is commonly assumed (e.g. Ramsay 1980, and Ramsay & Huber 1987) in shear zones.

3.8.4. Development of folds

Minor folds, the most prominent structural features of the shear zones and ductile thrusts, are generally disharmonic structures forming open-to-tight buckle-style folds (e.g. 3.15a & 3.16d) plunging shallowly (mostly less than 15°, see Figs 2.2, 3.1 & 3.7) to the SSE. They are

generally developed where the rocks have an anisotropy, due to the interlaying of psammites and pelites. Two types of minor fold geometries have been recognised in almost all the shear zones and associated ductile thrusts. The first type are gently to moderately curvilinear, close-to-isoclinal recumbent folds with axes sub-parallel to the local stretching lineation and are formed only in the Mt. Bold shear zone (e.g. Fig. 3.16a). The second type of folds are gentle-to-tight asymmetric NW verging folds with axes which vary but are mostly oblique to the local stretching lineation (e.g. Fig. 3.16d).

The geometry of the two fold types and the general non-coaxial nature of the deformation (discussed in the previous section) that affected the shear zones, suggest that a considerable part of the fold development resulted from either the passive rotation of pre-existing folds during non-coaxial flow (Sanderson 1973, Escher & Waterson 1974), or as a consequence of the passive amplification of small irregularities in the bedding plane, or flow during intense non-coaxial deformation, i.e. shear strain $\gamma>10$, (Cobbold & Qinquis 1980). Although no extensive evidence of intense non-coaxial deformation is seen in the shear zones, evidence for a distributed non-coaxial progressive deformation operating during at least the latter stage of deformation is provided by the presence of sheath-like folds of Type I geometry (isoclinal recumbent folds, see also section 3.7.1.2 and Fig. 3.16a) and by the existence of oblique folds of Type II geometry (asymmetrical folds, see also section 3.7.1.2 and Fig. 3.16d).

The presence of a strong anisotropy, due to the interlaying (about 10-20 cm) of competent and incompetent rocks, suggests that buckling is most likely to be the fold initiation mechanism. The weakly curvilinear (asymmetric folds, Type II) to moderately curvilinear (isoclinal folds, Type I) geometry of the folded layers may indicate a kinematic amplification during development of the folds (Fig. 3.20). Because thrusting and shearing is the dominant deformation in the area, it is unlikely for the folds to form only by buckling within a simple shear dominated regime. The low angle between the bedding and cleavage in the shear zones creates a difficulty for bedding to lie within the finite shortening field of the local strain ellipsoid, which is necessary for the generation of buckle folds (Flinn 1962). Therefore, it is

likely that after initiation of buckling, subsequent modifications of the folds may have produced the curvilinear geometry of the folded layers.

It seems that the folds initiated as west or northwestward-facing inclined to overturned structures with more intense strains on the overturned limbs and with their axes orthogonal to the movement direction (Fig. 3.20). The folds presumably developed as buckle folds within the ductile thrusts and the shear zones. The very similar geometry of these minor folds to the geometry of fault-propagation folds may imply that the folds developed in this fashion (see Figs 2.3 & 3.9a). The steeper cleavages within the shear zones (e.g. the Pole Road Shear Zone, Fig. 3.12) and the development of crenulation folds and cleavages closer to the lower boundary thrusts within the shear zones, however, may suggest that they also developed as fault-bend folds, especially in the hangingwall of the lower boundary thrusts to the Pole Road and Clarendon shear zones. Therefore it is likely that many of the minor and mesoscopic folds in the shear zones and associated ductile thrusts were developed as consequence of the accommodation of the folds during non-planar thrusting. This is further supported by the absence of downward or eastward facing relationships of these folds and the consistency of the vergence direction of the folds to the WNW (see Figs 3.9b & 3.16d).

The fact that in almost all the shear zones the minor folds are oblique to or sub-parallel to the stretching lineations imply that the folds in the shear zones were rotated after their initiation and during shearing (Fig. 3.20) (e.g. Sanderson 1973, Escher & Watterson 1974). This passive rotation of the folds toward the finite extension direction can be further constrained by the presence of orthogonal minor and mesoscopic folds along some associated ductile thrusts. Similarly, such distribution of orthogonal folds along ductile thrusts may also indicate that the processes of shearing was not strongly developed along these ductile thrusts.

3.8.5 Structural model for the development of the shear zones and associated ductile thrusts

The spatial concentration of fabrics and structures in the shear zones and their associated ductile thrusts suggests that the deformation in the Adelaide Hills area is clearly heterogeneous on a large scale and is partitioned into zones of high strain ductile deformation sub-parallel to the S_0

and/or S_{1a}. This relationship suggests that a "banded deformation" model similar to that of Sanderson (1982) may be cited as a first possible deformation style. The near parallelism of regional cleavage (S_{1a}) within and outside the shear zones and associated ductile thrusts, the consistency of vergence direction of regional and fault-related cleavages, the roughly constant orientation of the stretching lineations and the preservation of minor, asymmetric shear-sense criterion suggest the shear zones were subjected to significant non-coaxial strains.

The near parallelism of S_{1a} within and outside the shear zones also suggests that the deformation should not be modelled as a classical heterogenous simple shear. This is due to the requirement of marked variation in cleavage orientation which parallels the XY plane of finite strain between different domains of strain intensity (Ramsay & Graham 1970). The presence of shear bands in the shear zones which are recognised to develop in the later stages of deformation during general non-coaxial flow (Platt & Vissers 1980, Platt 1984, and Hanmer & Passchier 1991) may further constrain this argument. Furthermore, the extensive evidence of oblique to sub-parallel folds (Type I) along with the presence of recumbent folds (Type II) cross-cut by ductile thrusts or shear zone branches (e.g. Fig. 3.16c), also implies that the structures in the area developed in a progressive manner rather than during single, short lived events.

Similarly, the WNW-overturned character of the folds and the fault-propagation and fault-bend fold geometry of the minor and mesoscopic folds implies the existence of a component of overthrusting in this direction. The simplest explanation for the coexisting evidence of non-coaxial deformation and overthrusting would be that there was an early phase of WNW directed layer-parallel shortening and thrusting (Fig. 3.21a), possibly due to a decrease in thrust movement near thrust tips (e.g. Coward 1984 and Coward *et al* 1992). This strain field is a combination of homogenous pure shear and heterogenous simple shear (e.g. Sanderson 1982). This early deformation was progressively overprinted by a deformation which would have caused, for instance, passive rotation of early buckle folds to produced oblique to sub-parallel folds (e.g. Hansen 1971, and Escher & Watterson 1974). This later deformation is formed by layer-parallel extension and shearing (Fig. 3.21b) which caused the rocks stretch and flatten sub-parallel to the shear plane (e.g. Sanderson 1982, and Passchier 1991). In the case of the

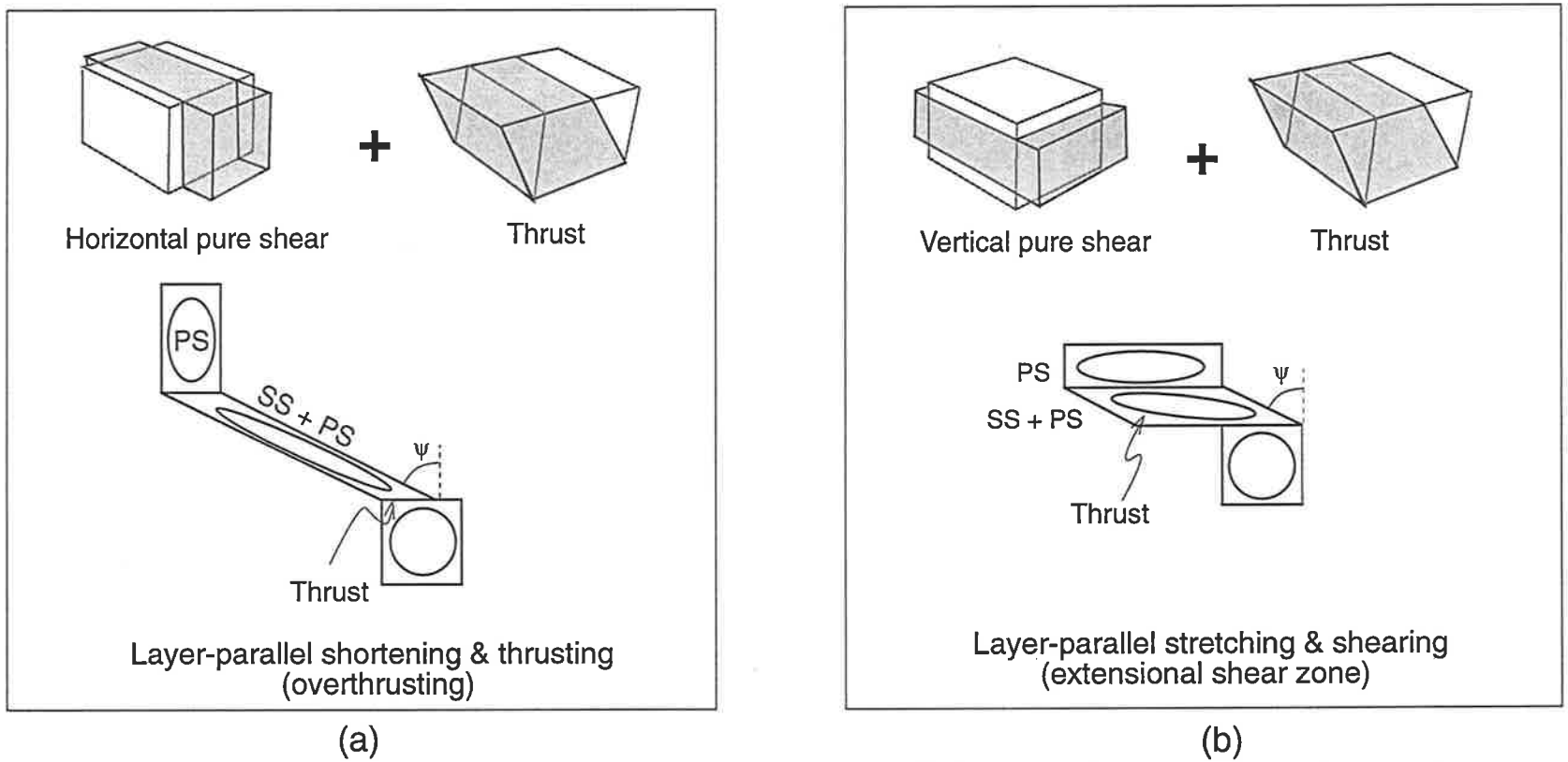

Fig. 3.21: Proposed strain fields for deformational history of the area (modified after Sanderson 1982). (a): Combined layer-parallel shortening and thrusting; (b): Combined layer parallel stretching and shearing (extensional shear zone of Passchier 1991).

Adelaide Hills area, the lower boundary thrusts to the shear zones form the shear planes during localisation of deformation or development of shear zones. The presence of extensional crenulation cleavages which are considered to have developed in extensional shear zones (Passchier 1991) may further constrain the progressive superposition of this later phase. Similar strain fields across thrust zones have also been proposed elsewhere, for instance, in the Betic Cordillera of SE Spain (Platt & Behrmann 1986), in northern Scotland (Holdsworth 1989, 1990), and in central Australia (Kirschner & Teyssier 1992).

The Adelaide Hills area lies in the northern part of the Southern Adelaide Fold-Thrust Belt which is proposed to form a foreland to the Cambro/Ordovician of Delamerian Orogenic Belt of South Australia (Flöttmann *et al.* 1994). Within the belt, the Neo-Proterozoic Adelaidean Supergroup and Cambrian Normanville/Kanmantoo Groups were reactivated and their sedimentary rocks were inverted and thrust toward the Australian craton (Flöttmann & James 1993), located to the west. During this reactivation, a master décollement within the basement of the Barossa Complex may have simultaneously propagated towards the foreland of the Stuart Shelf. This provides a possibility that an individual crystalline megathrust sheets (Hatcher & Hooper 1992) may have developed (Fig. 3.22a). Similar developments of ductile thrusts within basement were also reported from the Caledonian (e.g. Holdsworth 1989, 1990 and Coward *et al.* 1992) and the Appalachian (e.g. Evans 1989 and Hatcher & Hooper 1992) fold and thrust belts. The propagation of this basal thrust in a WNW direction toward the foreland was accomplished by overthrusting which caused the development of fold-thrust interaction buckle folds (fault-propagation folds and fault-bend folds) in the hangingwall of the propagated ductile thrusts (Fig. 3.22b).

As the layer-parallel shortening and thrusting migrated toward the foreland due to propagation of the master crystalline megathrust (Fig. 3.22), layer-parallel extension and shearing was gradually substituted. This strain field of combined flattening and shearing (Sanderson 1982, and Ratty & Sanderson 1982) was probably formed when thrusts cut through the more deformed and sheared, steeply dipping fold limbs and when sub-vertical flattening due to loading of the rocks in the hinterland (possibly Kanmantoo Group) concurrently stretched folds (antiforms) forward on the hangingwall (Fig. 3.22c). It is at this stage that the extensional

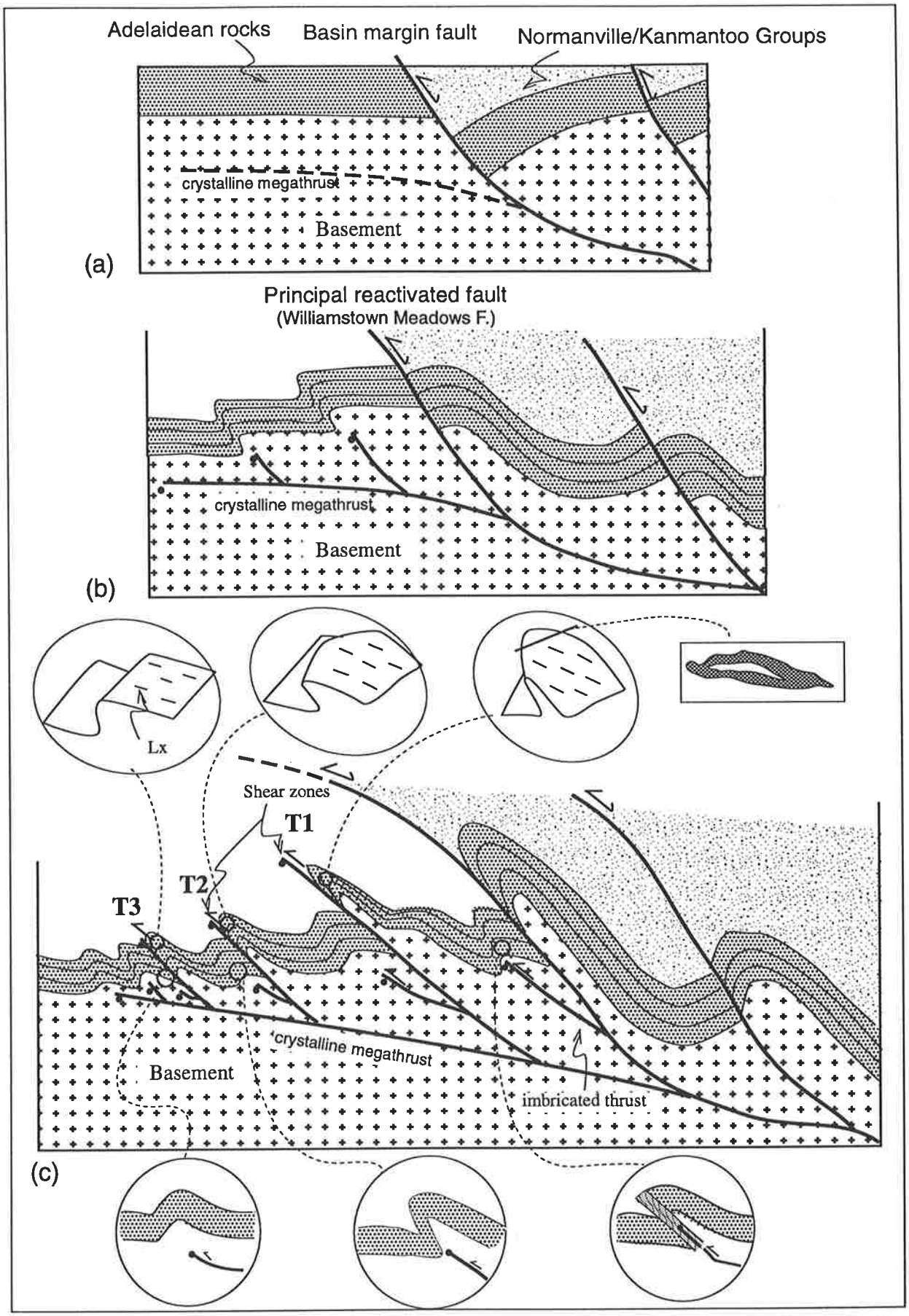

Fig. 3.22: Schematic diagrams showing development of the shear zones and associated ductile thrusts. (a): Initiation of crystalline megathrust in basement during basin reactivation; (b): Continued reactivation and further development of megathrust in basement and its propagation into the cover. At this time combined layer-parallel shorthening and thrusting occured; (c): With further propagation of the thrusts toward the foreland, the strain field of combined layer-parallel stretching and shearing is superposed which caused development of the shear zones. For further explanation see text.

crenulation cleavages (ECC-fabrics) or shear bands formed and the folds amplified to produce curvilinear or sheath-like geometries in the shear zones.

Further propagation of the basal crystalline megathrusts toward the foreland occurred synchronously with uplift and erosion which progressively reduced the depth at which later thrusts formed (T_3 & T_4 in Fig. 3.22c) and therefore lessened the amount of sub-vertical flattening. This also caused the amount of shearing to decrease toward these later thrust sheets and the deformation to be more localised along the lower boundary of the pre-existing thrust sheets to develop more intense shear zones (T_1 & T_2 in Fig. 3.22c). This is constrained by the decrease in the frequency and intensity of the shear bands (ECC-fabrics) along with the absence of curvilinear folds from the Mt. Bold shear zone toward the Morialta shear zone. The localisation of deformation along the lower boundary thrusts was developed during layer-parallel extension and shearing deformation. Nevertheless, such localisation of deformation due to layer-parallel extension and shearing deformation did not occur along associated imbricate thrusts which propagated in both the hangingwall and the footwall to the shear zones. Therefore, ductile deformation of these thrusts was only developed due to layer-parallel shortening and thrusting deformation to produce ductile thrusts (Fig. 3.22c). For these reasons, these minor imbricate thrusts are considered as ductile thrusts in contrast to the shear zones. This is also justified by the absence of the shear bands and by the very narrow width of the deformation zones along these ductile thrusts in comparison with major the shear zones.

3.9. Conclusions

1- The spatial, geometric and kinematic distribution of highly deformed fabrics and structures within the shear zones and their associated ductile thrusts show that these fabrics and structures in the Adelaide Hills area are restricted to these shear zones and ductile thrusts. As the deformation increases into the shear zones and towards the lower boundary thrusts and as the parallelism of all planar fabric elements concentrates at the lower boundary thrusts, the overall shortening in the area appears to have been largely accomplished by slip along the base of the major mapped discrete shear zones and their associated ductile thrusts.

2- Despite the discrepancy in the orientation of the stretching lineations within competent and incompetent units, vergence and trend analysis of movement directions in the shear zones and ductile thrusts show that they were propagated and overthrust toward the WNW.

3- The strain field development of the shear zones consists of two distinct but progressive deformations which are; layer-parallel shortening and thrusting, and layer-parallel extension and shearing. The investigation of sheath-like folds in the Mt. Bold shear zone along with decrease in the frequency of curvilinear geometry of the folds and of the intensity of the ECC-fabrics toward the Morialta shear zone show that the amount of layer-parallel extension and shearing decreases toward the northwest.

4- The shear zones more likely propagated from a crystalline megathrust within the basement toward the foreland to form a foreland imbricate fan of shear zones and associated ductile thrusts.

5- The absence of shear bands and curvilinear folds associated with the ductile thrusts implies that these thrusts were developed by a strain field of layer-parallel shortening and thrusting alone. Thus, the processes of localisation of deformation and development of shear zones which happened during the development of layer-parallel extension and shearing was not developed along the ductile thrusts.

Chapter 4

SECTION BALANCING AND STRAIN ANALYSIS

4.1. Introduction

Balanced geological sections are an important aid to understanding fold-thrust belt evolution (Woodward *et al.* 1986, DePaor 1988). Similarly, section balancing has been used to draw well-constrained illustrations of the three-dimensional geometry of many fold-thrust belts (Woodward *et al.* 1989, Geiser 1988b, and Mitra 1994). The procedure of cross-section balancing has become popular in recent years as a means of helping to analyse and improve cross sections. It also provides the tools to draw admissible and viable sections; that is, structures and their styles used in section balancing are the ones observed in the field (*e.g.* Elliott 1983, Marshak & Woodward 1989) and should be "retrodeformable" (Suppe 1985) from the deformed to a pre-deformational state.

The large- to small-scale (macro to minor) geometry of the structures in the shear zones and associated ductile thrusts of the study area were described in the previous chapter. The techniques of balanced cross-section construction (Dahlstrom 1969, Elliott 1983, and Woodward *et al.* 1989), together with mapped surface geometry have been used to draw four principal cross sections across the area (Fig. 4.1, see also Fig. 2.2 for their locations). The admissibility criteria of the sections were met by applying the observed and dominant style of fault propagation folds on to the sections.

Restoration of the sections was also done to support their geometric viability. Only a geometrical restoration of the sections was carried out. This is because contrasting rheological properties of the stratigraphic units would require very comprehensive analysis of internal strain for each lithology (Mitra 1994, Von Winterfeld & Oncken 1995). Some strain data was,

Figures opposite and in next 3 pages:

Fig. 4.1: Partially balanced cross-sections and geometric restorations of four sections [AA´ (opposite), BB´, CC´, and DD´ (next pages)] across the Adelaide Hills area. For the location of the section lines see figure 2.2. Depicted ellipsoids on each section show shape and orientation of finite strain ellipses in plane of sections for samples of Stonyfell Quartzite units. The graphs shown on top of each section represent the finite strain variations in the plane of sections (XZ).

The orientation of the stretching lineation changes between different competent and incompetent units across the area. As discussed in section 3.8.2, the orientation of the stretching lineation in incompetent units is considered to be closer to the orientation of the movement direction of the shear zones. Therefore, the cross-section lines are drawn subparallel to this orientation, which ranges from 125° to 135° in azimuth.

Since no finite thickness can be attributed to the basement in the area of study, only the sedimentary units have been balanced. Consequently, the cross-sections are not fully balanced with regard to the basement. Similarly, the exact depth to the detachment also can not be shown on the sections. Therefore, the estimated location of the detachment in the sections is displayed by an arbitrarily stippled signature.

The loose lines in the balanced sections show irregular (non-straight) geometries which reflect inhomogeneous strain distribution and accommodation during simple shear strain deformation.

Because of the general geometry of fault-propagation folding in the hangingwall of the shear zones (refer to 2.3.3) and also to the poor quality of outcrop east of the basement, the fault-propagation fold geometry of the sedimentary units on the eastern part of the AA' and BB' sections are extrapolated. Therefore, the eastern end of the AA' and BB' sections show more detail than is shown on figure 2.2.

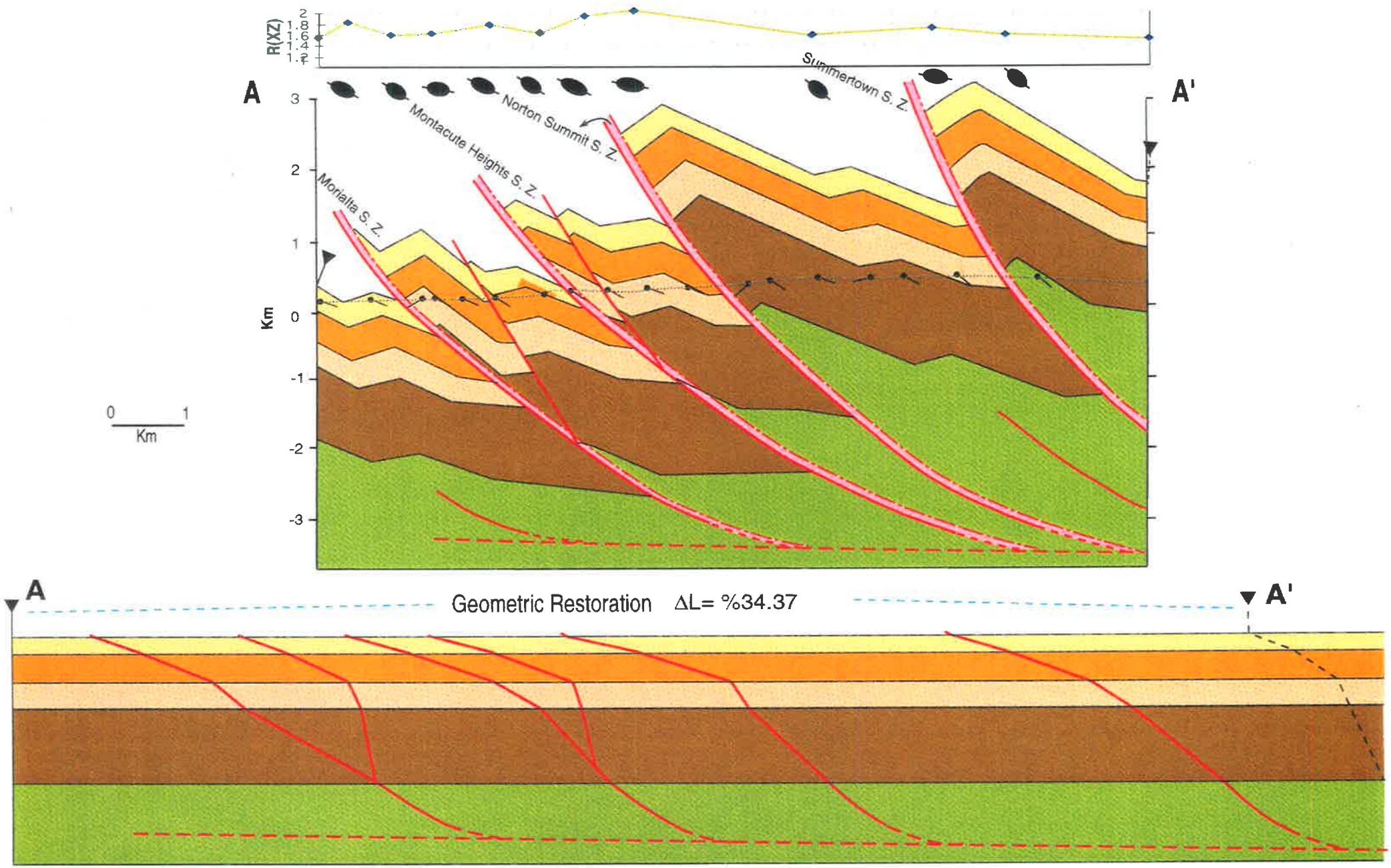
R(XZ)
2
1.8
1.6
1.4
1.2
A
A'
Summertown S. Z.
Norton Summit S. Z.
Montacute Heights S. Z.
Morialta S. Z.
3
2
1
0
-1
-2
-3
Km
0
1
Km
A
Geometric Restoration ΔL= %34.37
A'

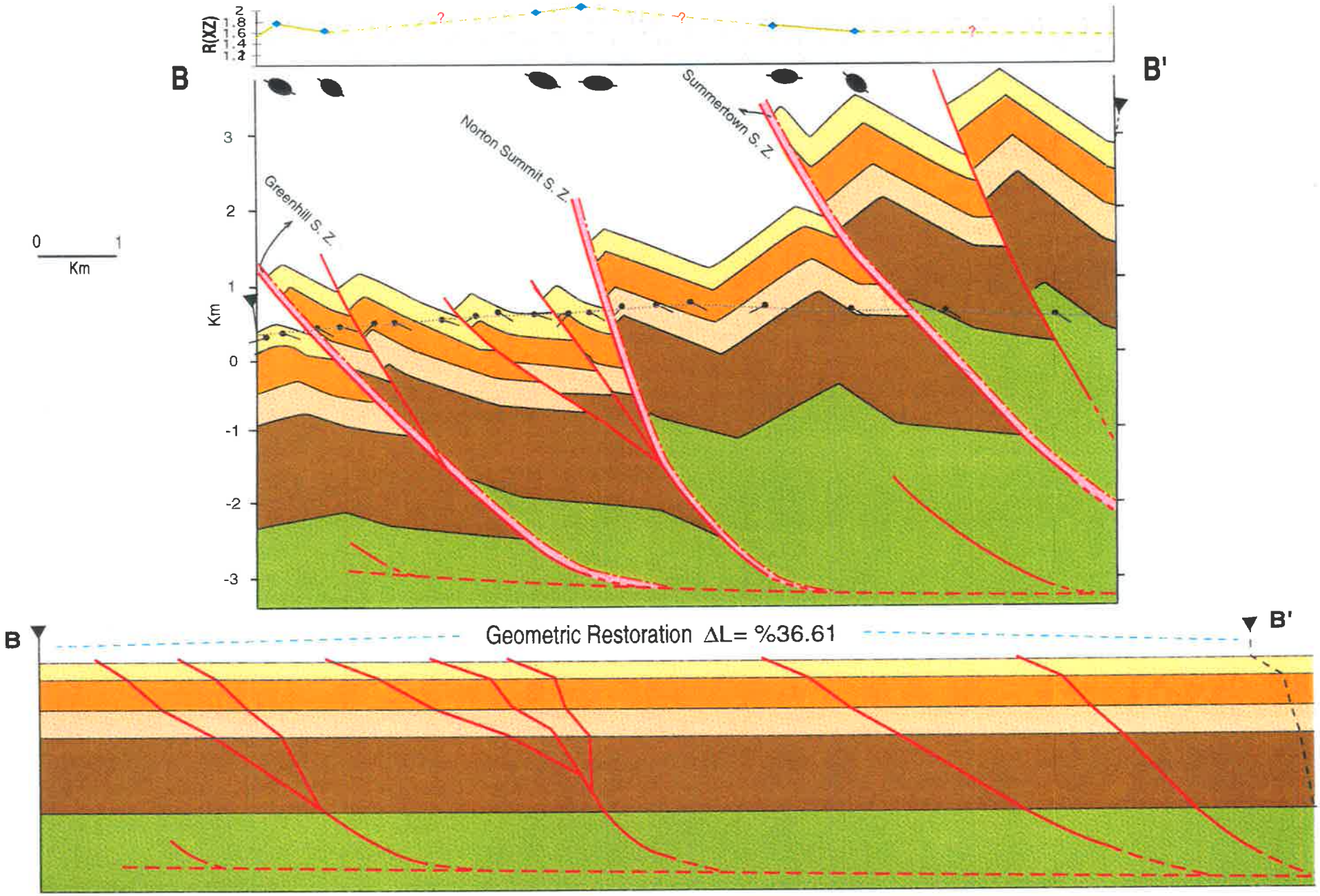

Fig. 4.1: Continued.

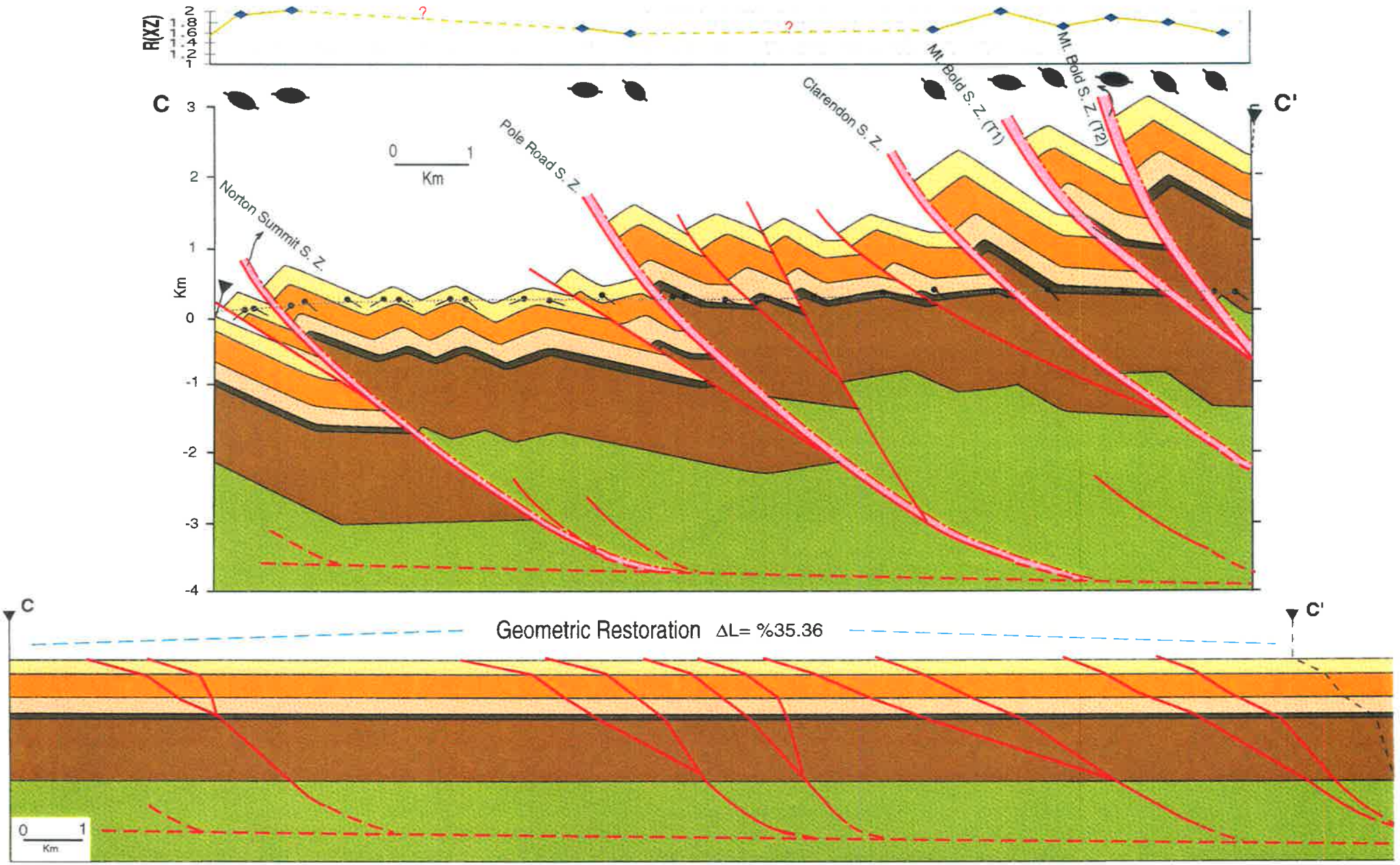

Fig. 4.1: Continued.

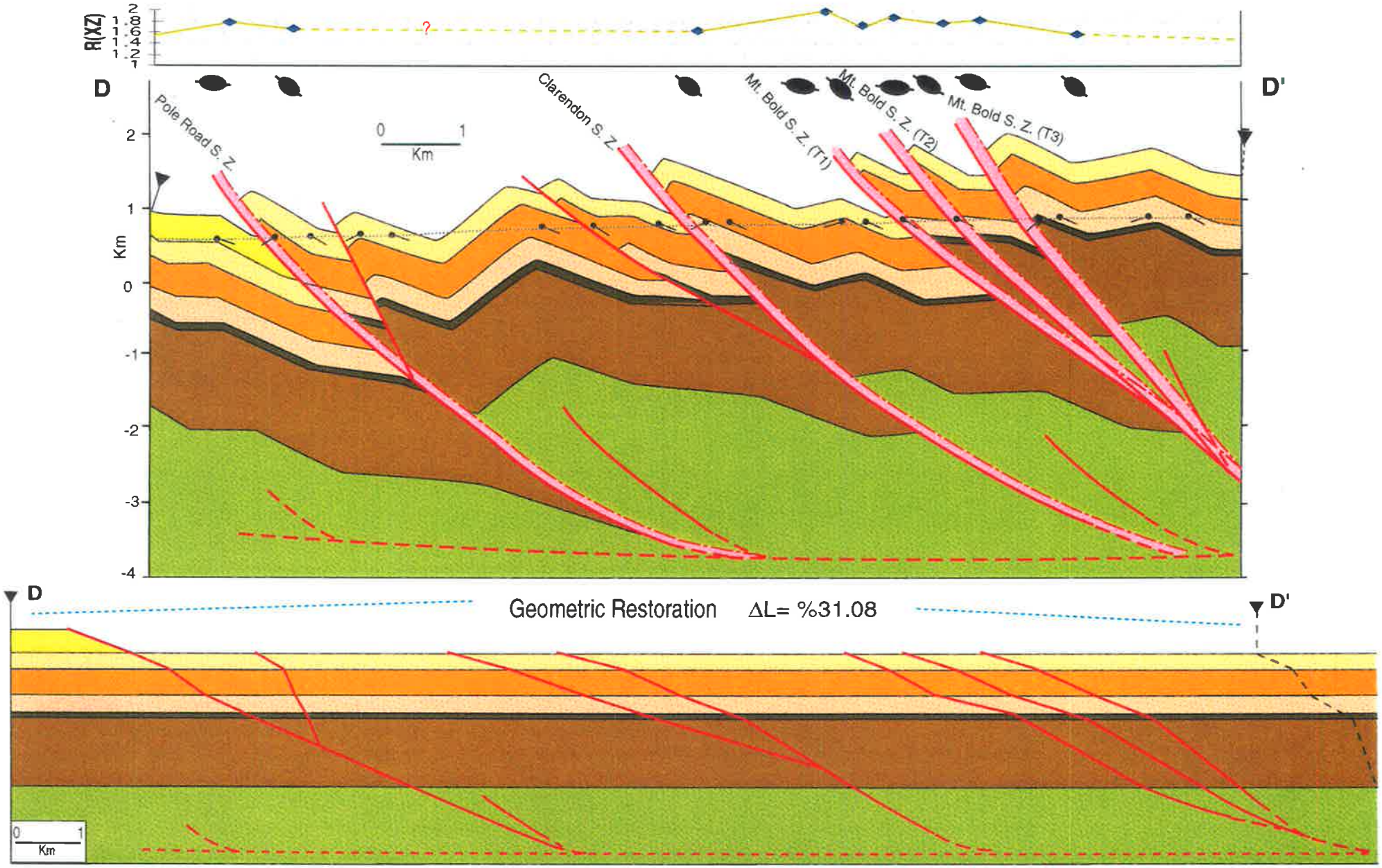

Fig. 4.1: Continued.

however, collected from outcrops along the plane of the cross sections, so the average orientation and magnitude of finite strain ellipses was also incorporated into the sections.

This strain analysis was carried out on selected samples of the Stonyfell Quartzite unit across each thrust sheet. They were used to determine the general distribution of the amount of strain and geometry of the finite strain ellipses within and across the thrust sheets and to compare the amount of line-length change of the samples from the outside the shear zones toward the lower boundary thrusts. They also help to interpret and differentiate possible components of finite strain during development of the shear zones.

4.2. Construction and balancing of cross sections

The section balancing process begins by drawing deformed sections which follow the rules of thrusting and then measuring bed-lengths to restore faults and folds in the undeformed state (Woodward *et al.* 1989). Some assumptions were made before section drawing commenced. Since most of the shortening was accommodated by folds and to a lesser extent by cleavage formation, plane strain deformation was considered to be dominant. Similarly, the bed thickness was assumed as constant.

The cross-section lines were drawn parallel to the movement direction which was defined by consistently oriented stretching lineations (AA′, BB′, CC′, and DD′ in Figs 2.2 and 4.1) in shear zones and associated ductile thrusts. A stratigraphic template was constructed based on stratigraphic thicknesses of the units, which was determined from the direct measurement of the units on the geological map of figure 2.2 where possible (stratigraphic column in Fig. 2.1) or which was estimated by recent workers (Preiss 1987, 1995, and Flöttmann *et al.* 1994). Depth to basement within the thrust sheets was also calculated from this stratigraphic template.

Data collected for construction of the sections was gathered from the surface structures on the line of sections or from the surrounding region. These include mainly geological boundaries, key beds (e.g. Stonyfell Quartzite), dip data, orientation of cleavages, fold geometry, and ductile thrusts, which were either seen in road cuts or projected, using orthographic projection (e.g. Marshak & Mitra 1989), from the adjacent area. Since the folds are plunging at a low

angle (mostly less than 10°), their projection up and down the sections does not provide a source of error. Where bedding was poorly constrained, major-scale folds were constructed to mirror minor-scale folds, a relationship which was generally observed in outcrop and discussed in chapter 3. Since the lower boundary thrust surfaces were not generally observed in outcrop, their surface inclination was assumed to be subparallel to their fault related cleavages (S_{1b}).

The recognition of the dominance of cut-through fault propagation folds with mostly kink style geometry (Suppe 1983, 1985) across the area was the basic tool for the construction of the balanced sections and for the determination of the structure of the thrust sheets both up and down the sections. Because of the scale problem, the steep to overturned limbs of most of the mesoscopic folds at the lower boundary thrust to the shear zones could not be shown on the sections (see for example the mesoscopic fold in the hangingwall of the Morialta shear zone in Fig. 4.2).

Incorporation of the geometric and kinematic analyses of the shear zones and associated ductile thrusts to the section balancing and the assumption that the thrusts (shear zones) are dipping hindward, implies that thrust propagation is toward the foreland or to the NW (Fig. 4.1). As can be seen, in all the cross sections, the hindward thrust sheets have moved structurally on to the top of more forelandward thrust sheets. Each sheet shows reverse displacement with movement on individual thrusts varying from less than 100 m to more than 1700 m. Displacement was measured between cut off points on the hangingwall and footwall of each particular thrust/shear zone. Similarly, measured total relative vertical displacement across each cross section varies from 2800 m to 3000 m.

4.3. Restoration of the sections

To confirm the viability of the constructed balanced sections, restoration of each section was also done and is shown along with the sections in figure 4.1. The western or foreland sides of the sections were used to place the pin lines for making the restored and balanced sections. The loose lines therefore were drawn at the trailing edges of the cross sections. Since bedding thickness is assumed to be constant, the bed-length or sinuous-bed balancing method

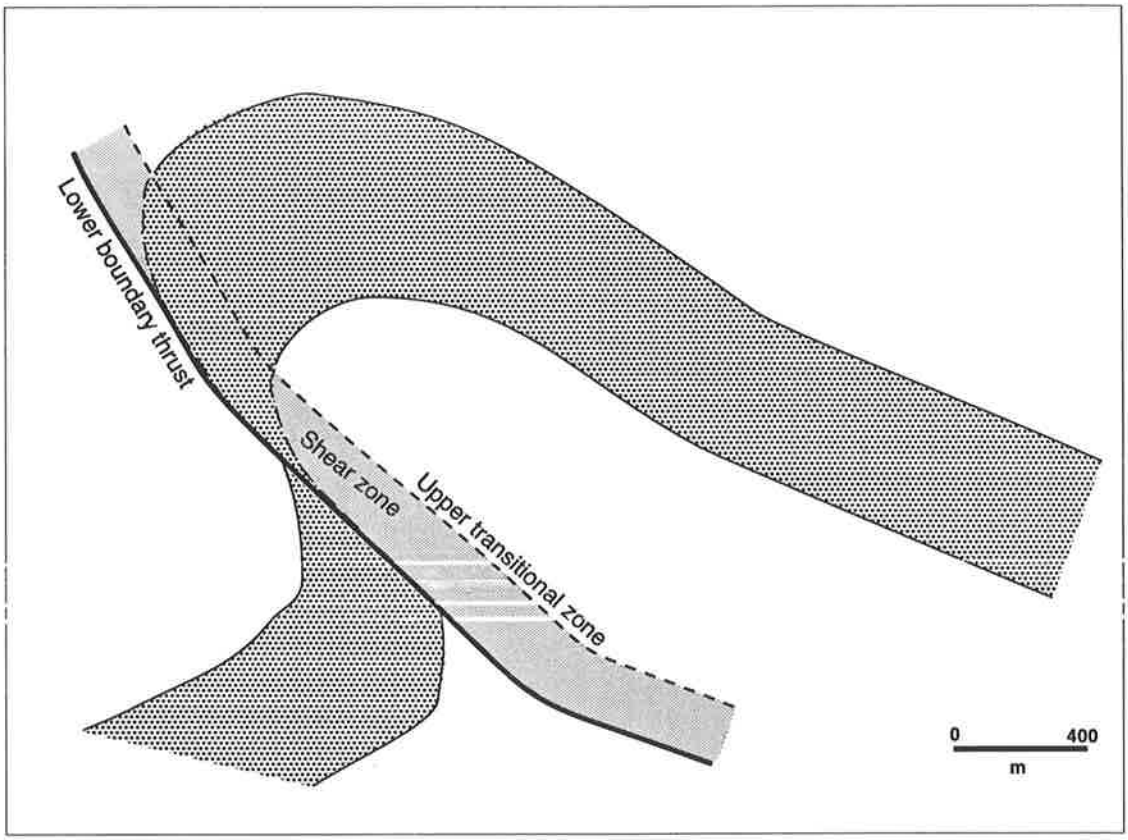

Fig. 4.2: Enlarged geometry of the mesoscopic fold in the hangingwall of the Morialta shear zone (see also AA' balanced cross-section in Fig. 4.1). Note steep to overturned limb of the fold in the shear zone especialy closer to and/or at the lower bounday thrust.

(Woodward *et al.* 1986, 1989) was used to restore the balanced sections by measuring the bed-lengths to relocate the faults in the undeformed state (Fig. 4.1). The restoration was carried out starting from the youngest thrusts on the foreland side to the oldest one in the hinterland side. The restored sections show that the more hindward thrusts demonstrate steeper dips which is a common feature in fold-thrust belts with several imbricate fans (Woodward *et al.* 1989).

The strain data were not integrated into the restoration of the cross-sections because the collected strain data were confined to a single lithological unit, i.e. Stonyfell Quartzite, (Table 4.1). To calculate the shortening in the entire thrust sheets, it is necessary to project strain data to depth, assuming that the vertical strain gradient is zero. This condition is unlikely in the area of study and for most parts of the SAF-TB since the thrust sheets consist of different lithological units with different and lithologically controlled finite strains (see also Flöttmann & James 1997).

The shapes of the resultant loose lines, which were drawn as straight lines in the deformed-state sections, become changed in the undeformed state (Fig. 4.1). Loose lines are allowed to change when restored to the undeformed state . Their analysis, however, provides a means to investigate whether a constructed deformed state geometry is compatible with finite strain (Geiser 1988a). An undeformed state loose line creates a displacement profile which gives information on the state of strain within thrust sheets (Geiser 1988a). In an area with inhomogenous strain within thrust sheets, the initially orthogonal loose line will have a curved trajectory. The change to the tangent for the angle between the undeformed state loose lines and the sliding surface in the deformed state (in the case of the area of study these are bedding planes, based on the argument as to shear being parallel to bedding in section 3.8.2) allows the calculation of the angular shear strain (Geiser 1988a). Taking this into account, a shear strain equal to γ=0.45 to 0.7 can be inferred from the geometry of the loose lines in the undeformed state sections (see the restored sections in Fig. 4.1 for the shear angles).

Shortening values calculated from the geometrical restoration of the sections show 34%, 36%, 35% and 31% total shortening for AA´, BB´, CC´, and DD´ cross sections, respectively (Fig. 4.1).

4.4. Finite strain analysis

4.4.1 Objects

Finite strain analysis was carried out to determine the magnitude and distribution of the finite strain within and across the shear zones. It was mainly carried out on detrital quartz grains of the Stonyfell Quartzite unit. The less matrix-supported, uniform and purer quartzite, which is clearly representative of the unit, was chosen to avoid possible partitioning of finite strain between grains and matrix. Some 20 oriented samples were collected generally from outside (at about 400-600 m from the lower boundary thrusts), within the shear zones (at about 100-300 m from the lower boundary thrusts) and at the lower boundary thrusts to the shear zones (see the ellipses on the sections in Fig. 4.1 and appendix A for their locations). These samples are also the same samples that were used in the microstructural analysis (chapter 6). Although most samples collected from the lower boundary thrusts were marginally recrystallised, this has not obscured the original shape of the detrital grains.

4.4.2. Analytical method

Strain determination was performed using the Rf/Ø method of strain analysis for elliptical objects (Ramsay 1967, Dunnet 1969). The choice of method was determined by the rock type and the nature of the strain markers (almost all quartz grains were non-spherical) from the Stonyfell Quartzite unit, which comprised grain supported fabrics in largely monomineralic rock. The markers have undergone predominantly crystal plastic deformation (see chapter 6 for more detail) and show a weak sedimentary preferred orientation. In the case of more deformed grains which contained a core and mantle structure, measurements were made on grains whose outlines could be clearly identified.

All samples were cut roughly perpendicular to regional cleavage (S_{1a}) and parallel to the stretching lineation (XZ plane of the finite strain) or almost perpendicular to both the stretching lineation and S_{1a} (YZ plane of the finite strain). Enlarged photomicrographs of the XZ and YZ thin sections provided the raw data. The axial ratio (Rf) of the detrital quartz grains in each section was measured using the numerical software package DIGITIZE (RockWare, Inc. 1989). A minimum of 40 measurements were digitised from each photomicrograph. Analyses and calculations were performed on the data sets using an automated procedure with the INSTRAIN package (Erslev 1988) to produce graphical Rf/Ø plots (see appendix B for the plots). The values of Ø (the angle between the long axes of the marker and maximum extension direction in the final or deformed state) and the harmonic means of the aspect ratios of the grains were finally gathered from the plots and tabulated in table 4.1. The harmonic values of the aspect ratios of the grains were taken by many workers to be closely similar to the Rf/Ø values (e.g. Ramsay & Huber 1983, PP. 110-113, and Dittmar *et al.* 1994).

4.4.3. Results

The values obtained for the XZ and YZ principal planes of strain range between 1.4 to about 2.0 which indicate relatively low strains (Table 4.1). The axial ratio of the third plane (XY) was estimated by the equation $R_{xz}= R_{xy}* R_{yz}$ (Ramsay & Huber 1983, pp. 170) (Table 4.1). The Flinn K-parameter was also calculated for each sample (Table 4.1). By plotting the YZ and XY axial ratios in the Flinn diagram the geometry of the strain ellipsoids for each sample was obtained (Fig. 4.3). This shows that samples have a general trend to apparent flattening strain geometries.

Similarly, the values of all principal axes of strain were calculated from the values of principal planes of the strain ellipsoid using equations from Von Winterfeld & Oncken (1995). Moreover, from these data longitudinal strains (shortening or extension; negative or positive values of dL[%] in Table 4.1 respectively) were also calculated with respect to the bedding co-ordinate system (i.e. shortening of bed-length) (Table 4.1).

Samples	Shear Zones	ϕ	XZ	YZ	XY	K=Ln(XY/YZ)	1+e1	1+e2	1+e3	dL[%]
MO1	Morialta (HT)	10.8	1.6	1.61	1.00	0.00	1.17	1.17	0.73	13.65
MO5	# # (W)	-34	1.58	1.47	1.07	0.19	1.19	1.11	0.76	-1.54
MO4	# # (L)	28.8	1.86	1.62	1.15	0.29	1.29	1.12	0.69	2.73
H8	Greenhill(W)	32.9	1.64	1.61	1.02	0.04	1.19	1.16	0.72	-3.08
H9	# # (L)	-26.1	1.78	1.51	1.18	0.40	1.28	1.09	0.72	7.43
G6	Norton Su. (L)	-4.72	1.99	1.87	1.06	0.09	1.28	1.21	0.65	26.71
G7	# # (FT)	24.2	1.95	1.75	1.11	0.19	1.29	1.16	0.66	6.78
U10	Pole Road (W)	-38.7	1.59	1.45	1.10	0.25	1.20	1.10	0.76	-4.78
AC3	# # (W)	40	1.65	1.62	1.02	0.04	1.19	1.17	0.72	-9.13
AC2	# # (L)	-5.8	1.78	1.94	0.92	0.13	1.18	1.28	0.66	16.46
U9	# # (L)	-3.5	1.71	1.81	0.94	0.10	1.17	1.24	0.69	16.90
M39	Mt. Bold (T)	36.6	1.54	1.42	1.08	0.23	1.19	1.09	0.77	-2.73
M17	# # (T)	-38.6	1.57	1.55	1.01	0.03	1.17	1.15	0.74	-6.86
M9I	# # (W)	42	1.82	1.61	1.13	0.26	1.27	1.13	0.70	-10.86
M11	# # (W)	-36.4	1.68	1.66	1.01	0.02	1.19	1.18	0.71	-6.86
M9	# # (L)	7.2	1.84	1.82	1.01	0.02	1.23	1.22	0.67	22.96
M36	# # (L)	10.2	1.97	1.79	1.10	0.16	1.29	1.18	0.66	23.92

Table 4.1: Finite and longitudinal strain results of the Stonyfell Quartzite samples; Ø is the angle between the long axes of the strain markers and maximum extension direction in deformed state; XZ, YZ and XY are the strain ratios in three principal planes of the finite strain elipsoid; K is Flinn parameter; (1+e1), (1+e2), and (1+e3) are the maximum, intermediate, and minimum principal stretches respectively; dL[%] is the value of the finite longitudinal strain in the XZ plane of the finite strain elipsoid (horizontal shortening by internal deformation). Symbols in second column show the location of the samples on HT= hangingwall ductile thrusts to the shear zones, FT= footwall ductile thrusts to the shear zones, T= transitional zone to the shear zones, W= within the shear zones, and L= lower boundary thruts.

The results of the longitudinal strain analysis show that almost all samples collected from the lower boundary thrust to the shear zones underwent a positive line-length change from about 3% to 27%. Samples with about 27% longitudinal strain value also demonstrate higher finite strain magnitudes of about 2.0 (Table 4.1). Nevertheless, samples collected from transitional zones or from the upper limbs of hangingwall associated regional fault-propagation folds show negative line length changes from -2% to -11%, while their finite strain magnitudes are between 1.6 to 1.8 (Table 4.1).

4.4.4. Sources of error

Some general sources of error in the data evaluation that have to be taken into account result from inaccurate digitising and from graphic determination of the ellipse shape from Rf/Ø plots. These errors can be picked up from within the plots (see appendix A). Errors less than 16% which comes from inaccurate procedure of both the digitising process and graphic determination of the ellipse shapes are acceptable (INSTRAIN package by Erslev, 1988). The other specific sources of error might be due to measurements of deformed grains in which their margins were not accurately determined. Similarly, in the case of samples with evidence of dissolution processes, asymmetrical solution of marker grains has the effect of changing the grain shapes. Since measurements were mostly carried out on grains with less deformation and/or marginal dissolution, the effect of these specific errors was relatively low especially with ellipticity in, the both XZ and YZ planes, ranging from only 1.4 to 2.

4.5. Discussion

4.5.1. Thrust system

The balanced cross-sections from the area of study (Fig. 4.1) show several stacked thrust sheets, with basement involved in each sheet. The base of each thrust sheet makes up the lower boundary thrust to the major shear zones at the trailing edges of the sheets. Several ductile thrusts also propagate from the hangingwall or footwall to the lower boundary thrusts. These associated ductile thrusts produce an array of later but progressively propagated thrusts which

on a smaller scale demonstrate the geometry of the major and regional thrust or shear zones which propagated to form the overall imbricate fan.

Measured displacements across the thrust sheets in the cross-sections show that the amounts of displacement of individual thrust sheets increase from the foreland side sheet towards the hindward sheets. The overall geometry and style of the thrust sheets closely resemble a piggy back style of leading imbricate thrust sheets (e.g. Boyer & Elliott 1982, and Gray & Willman 1991). This can be constrained by the geometry of thrust sheets in the sections and increases in the amount of displacement on the fault surface in each section from the forward sheets to the hindward sheets.

Furthermore, taking the results of strain analysis into account, it is possible to infer that the mechanism of thrust emplacement appears not to be a simple imbrication. Rather, it is suggested that the thrust sheets were emplaced as hybrid sheets (Geiser 1988b) by a combination of imbrication, folding, and to a lesser extent layer-parallel shortening.

4.5.2. Restoration of balanced sections and internal deformation

In internally deformed thrust sheets, shortening is mainly partitioned into rigid-body translation (sliding along thrust planes), rigid-body rotation (folding) and distortion (pure shear strain) (Geiser 1988b, Mitra 1994). The proportion of rigid-body translation in relation to other internal deformation which accommodates thrust sheet motion represents a broad spectrum of thrust sheet motions ranging between zero or minimal folding and pure shear strain (e.g. the Lewis Thrust in North American Cordillera, Dahlstrom 1970) to thrust sheets dominated by either rotation or distortion (e.g. the Morcles Thrust sheet in the western Helvetic Alps, Boyer & Elliott 1982).

Most balanced sections have been restored by removing the rigid-body translation component on the fault surface and the rigid-body rotation component, which is represented mainly by large scale dip changes due to fault propagation folding or fault bend folding. Only a few thrust sheets (from different FTBs) have had their strains (distortion component) adequately studied and incorporated into the section balancing and restoration process (Woodward *et al.* 1986,

Mitra 1994). This is mainly because of the lack of sufficient strain markers and the different rheological properties of the lithological units across many fold-thrust belts (Mitra 1994).

Geometrical restorations of the balanced cross-sections in the study area indicate an average of 34% for geometrical shortening. The restoration was carried out by removing the translation component on the faults and the rigid-body rotation component represented mainly by large scale fault-propagation folds. Net orogenic shortening in the upper crust of other fold-thrust belts is approximately estimated as 42% (Dittmar *et al.* 1994). The similarity of values of the geometrical restoration of the sections in the study area to the estimated average shortening of the fold-thrust belts implies that the Adelaide Hills area is deformed mainly by rigid-body translation and rotation. However, this does not obscure the effect of layer parallel shortening (pure shear strain) on the deformation of the thrust sheets. Development of an array of cleavages (especially in less competent units) in the shear zones and along associated ductile thrusts illustrate this effect. However, the low intensity and less penetrative nature of the cleavages rule out a significant effect of layer parallel shortening strain in internal deformation of quartzitic rocks of the thrust sheets.

4.5.3. Finite strain variation across the sheets

Finite strain variation across the area is represented by the graphs shown on top of the cross sections. They show that the average finite strains in the plane of the sections (XZ) across the thrust sheets are 1.6:1 (Fig. 4.1). Toward the basal thrust sheets or lower boundary thrusts to the shear zones and their hangingwall anticlines, this value increases to 2:1. It does, however, decrease further away from the anticlinal hinge zones, but remains fairly constant for the rest of the sheets to the east. This shows that narrow zones of concentrated deformation persist through-out the shear zones and associated ductile thrusts. Similar decreases in the value of strain from basal thrust sheets to upper ones have been seen elsewhere for example in the Appalachian Valley and Ridge sheets (Wojtal 1986). This concentration of higher strain, together with increases in the intensity of the deformed fabrics and structures toward the lower boundary thrusts to the shear zones (refer to chapter 3 for more detail), suggest that simple shear deformation was also probably effective at the base of the sheets during, or at the early

stages of, thrusting. Therefore, subsequent and/or continued deformation appears to have been concentrated into these narrowly confined zones. Such narrow zones were controlled either by mechanisms of strain localisation (e.g. White *et al.* 1986) and/or increasing brittleness during exhumation and cooling of the thrust sheets (e.g. Dittmar *et al.* 1994). Microstructural studies should further constrain this concept (see chapters 5 & 6).

4.5.4. Finite longitudinal strain components

Calculation of the layer-parallel finite longitudinal strain of the samples (the amounts of dL% in Table 4.1) in the plane of cross sections (XZ) shows that these values vary significantly. They vary from negative for most samples from the upper limbs of the hangingwall anticlines and the remainder of each sheet to the east, to positive for almost all samples from the narrower zones near the lower boundary thrusts or the overturned limbs of their hangingwall anticlines, where deformation was also concentrated (Fig. 4.1).

Regional finite strain analysis of the Stonyfell Quartzite across the SAF-TB (Flöttmann & James 1997) shows that these rocks undergo almost no line-length change (< -1%), therefore the higher negative to positive values of the samples from the upper transitional zones toward the lower boundary thrusts to the shear zones in the area of study are significant. The low negative values of the samples from the upper transitional zones may further constrain the result of the regional study but on the other hand may show that the shortening in the Adelaide Hills area is accommodated mainly by rigid-body rotation (folding) rather than by layer parallel shortening. The positive values of the line-length change of the samples from the lower boundary thrusts indicate that at these boundaries the main deformation was accommodated by shearing and would further constrain the localisation of deformation at these boundaries possibly by process of shearing.

The differences in the values of the finite longitudinal strains across the shear zones imply that the shear zones have suffered a most complex strain history that requires partitioning of finite strain components. The different distribution of finite longitudinal strains across the sheets leads to a model of strain components in which shortening was superposed by layer parallel

shearing during localisation of strain and/or development of the shear zones. Very frequent veins parallel to bedding and/or shear planes, the presence of asymmetric extensional shear bands and substantially high positive values of longitudinal strain at the lower boundary thrusts provides further positive constraining evidences to this argument.

4.5.5. Shortening and volume loss across the sheets

The apparent flattening strains recorded by the finite strain analysis (Fig. 4.3) could be the result of a true tectonic flattening strain, volume loss during deformation or a combination of both (Bailey *et al.* 1994). Volume loss in the order of 15-50% depending on lithology and metamorphic grade has been cited for slate belts in general (e.g. Wright & Henderson 1992). Geochemical analysis shows volume losses in the range of 10-20% (Gessner 1996 in Flöttmann & James 1997) for the same type of lithology as in the area of study. The ubiquitous presence of mineralised veins containing quartz and/or chlorite and pressure shadows around competent grains of detrital quartz and mica in the shear zones and associated ductile thrust seems to lead some support to the occurrence of volume loss.

As a hypothetical concept, if the thrust sheets were allowed to undergo a volume loss of 20%, then the line of plane strain on the Flinn diagram would shift along the abscissa toward the right (Fig. 4.4). This places the strain data from the transitional zone, or outside the shear zones of the sheets, near to the adjusted line of plane strain (black triangles in Fig. 4.4). Samples from the lower boundary thrusts, however, still plot in the field of flattening (black diamonds in Fig. 4.4). A 40% volume loss would shift the line of plane strain further to the right, and then samples from the lower boundary thrusts would plot along the plane strain line. No extensive evidence of cleavage development nor compaction has been observed or detected to justify such volume loss strain. Therefore it is suggested that such apparent flattening strain results more from true tectonic flattening strain. If material were not only to be transported toward the foreland during thrust displacement but also was allowed to expand laterally, which is more likely during localisation of strain along lower boundary thrusts and/or loading, then it would be a possible explanation for the development of regional flattening strain.

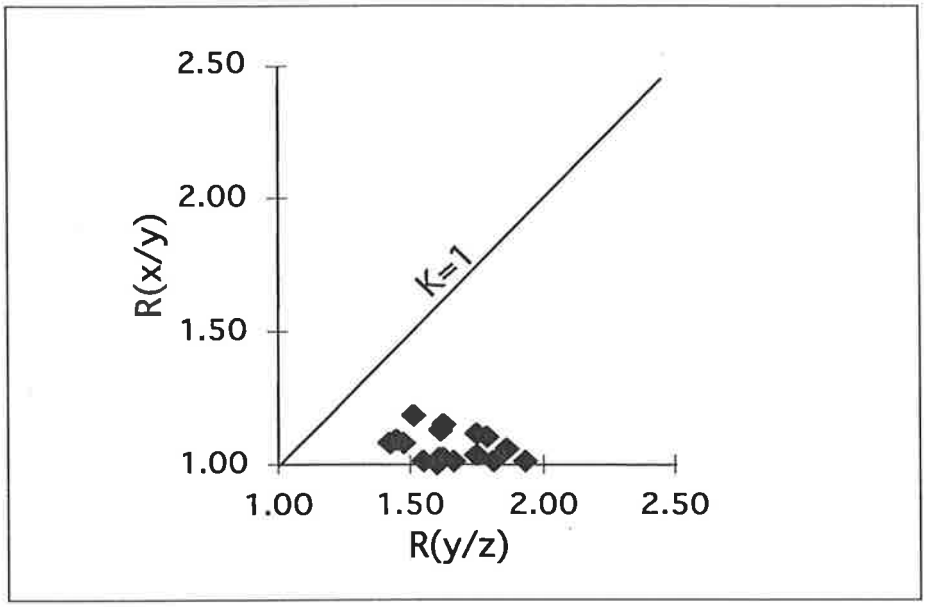

Fig. 4.3: Flinn diagram for finite strain geometry of the Stonyfell Quartzite samples across the shear zones in the Adelaide Hills area.

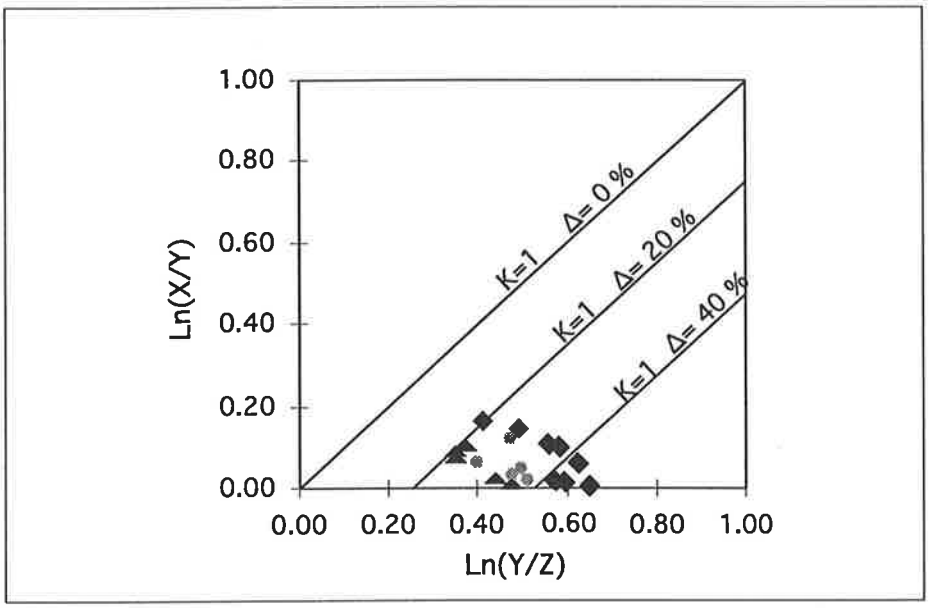

Fig. 4.4: Logarithmic Flinn diagram of the Stonyfell Quartzite data. Lines of plane strain hypothetically adjusted for possible volume changes within the samples across the shear zones.

The fact that the process of shearing is intensely developed towards the hindward shear zones (see discussion in chapter 3) and that the substantially high positive values of longitudinal strain in samples from the lower boundary thrusts to the shear zones in contrast to negative values of longitudinal strain on the rest of the sheets (Table 4.1) may imply that "extensional shear zones" (Passchier 1991) were superposed on earlier shortening. This also produces coaxial deformation leading to development of apparent flattening strain.

4.5.6. Out-of-section strain

As mentioned in section 4.4.1, strain measurements were carried out in competent layers of the Stonyfell Quartzite. This was mainly because of a lack of suitable outcrops of all other lithological units within the shear zones. This use of a single rock type also avoids data incompatibility between the very different lithological units across the area.

As was discussed in the previous section, samples from the transitional zones and from within the shear zones show a maximum of 20% volume loss, which would account for approximately 20% out-of-section strain in balanced cross sections.

Chapter 5

MICROSTRUCTURES OF CLEAVAGES IN THE SHEAR ZONES

5.1. Introduction

Microstructure refers to grain shapes, arrangement of grains, preferred orientation of grains, grain boundary configuration, and the internal features of grains in rocks (Hobbs, *et al.* 1976). The study of microstructures in shear zones provides information regarding the variations of grain scale microstructures (e.g. Passchier & Trouw, 1995), the environmental conditions of deformation (e.g. Boullier 1980 and Hirth & Tullis 1992), the deformation history (e.g. Schmid 1982 and Tullis *et al.* 1982), and the kinematics during thrusting and shearing (e.g. Simpson & Schmid 1983, Hanmer & Passchier 1991).

Analysis of the microstructure or microfabric of a rock can be used in two major fields. It can be applied to understand rock deformation conditions and metamorphism and/or it can be used to reconstruct the structural and geometric evolution of a given rockmass. Microstructural studies have also been used to reconstruct the spatial development of the shear zones in the study area by dealing with fabric development on the microscopic scale (microfabric study). In addition, thin section studies have provided a tool to identify the relative movement of the flow (Simpson & Schmid 1983, and Hanmer & Passchier 1991).

A tectonothermal rock fabric (e.g. Sander 1930 in Turner & Weiss 1963, Hobbs *et al.* 1976) includes the complete spatial and geometrical configuration of all those components that make up a rock. The parts that make up the fabric, also known as fabric elements (e.g. Passchier & Trouw 1995), are generally penetratively and repeatedly developed throughout a volume of rock (e.g. Turner & Weiss 1963). On the microscopic scale, microfabric elements may include grain shape, grain boundary configuration, deformation lamellae, aggregates of

inequidimensional grains with similar shape and lattice preferred orientations (e.g. Suppe 1985, and Passchier & Trouw 1995). Many microstructures in rocks are defined by the preferred orientation of minerals. Cleavages which are one of these microstructures are mainly defined by preferred orientation of planar minerals (e.g. Turner & Weiss 1963). The study of cleavages in thin sections, including the interpretation of the metamorphic and deformational conditions during their formation, is an important tool to elucidate the tectonic and metamorphic evolution of an area.

Detailed structural mapping across the Adelaide Hills area reveals the development of a variety of cleavages from regional slaty cleavage (S_{1a}) outside the shear zones and/or the upper transitional zones to the shear zones, to fault related cleavages and/or crenulation cleavages (S_{1b}) within the shear zones and toward the lower boundary thrusts (see chapter 3 for more detail). In this chapter the microstructural development of these cleavages within pelitic and psammitic rocks ~~are~~ is studied in detail. This was carried out to further investigate the development of mesoscopic cleavages in the shear zones and also to document their spatial development. Similarly, the deformation mechanisms that have been operating within the rocks, and are revealed by development of cleavages, were also investigated and discussed. In addition, microscopic study of shear sense indicators was also carried out to provide more detail of the kinematic evolution of the shear zones.

For convenience the description of microstructures of the samples is divided into three parts based upon the different characteristics of three sub-zones associated with the shear zones. A sketch of the typical location of each sub-zone from within the shear zones is shown in figure 5.1. As can be seen, sub-zone I is in the upper transitional and/or outside the shear zones but approaching the margins of the shear zones, sub-zone II is in the middle part of the shear zones and sub-zone III is closer to, or at the lower boundary thrusts, to the shear zones. All thin sections were cut parallel to the local stretching lineations and perpendicular to regional (S_{1a}) cleavages (XZ plane of the local finite strain ellipsoid).

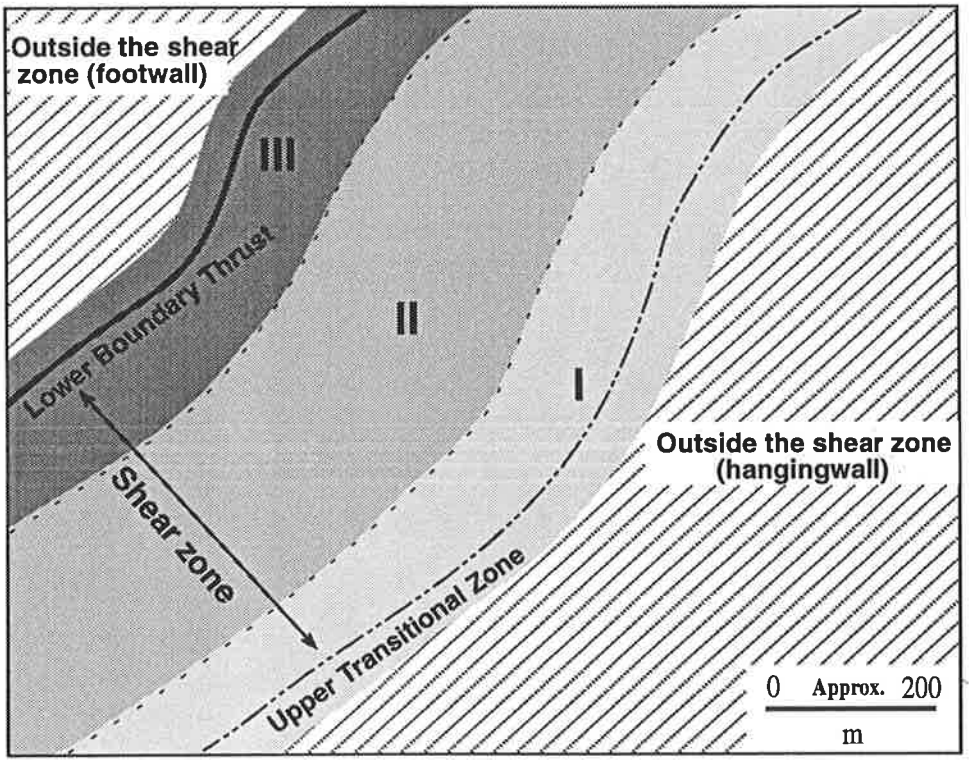

Fig. 5.1: Sketch showing general location of sub-zones in the shear zones; sub-zone I covers the upper transitional zones/outside shear zones, sub-zone II is located within shear zones, and sub-zone III covers the areas around the lower boundary thrusts.

5.2. Mineralogy and microstructure of psammites

5.2.1 Introduction

Microstructural development of cleavages in psammitic rocks in general has been extensively studied in the last two decades (e.g. Durney 1972, Dennis 1972, Means 1975, Gray 1978, Onasch 1983, Becker 1995, and Holl & Anatasio 1995). Such cleavages have been referred to as fracture cleavage (e.g. Durney 1972), slaty cleavage (e.g. Means 1975) and rough cleavage (e.g. Dennis 1972) (Fig. 5.2). The term rough cleavage is preferred here for the development of cleavages in psammites due to the non genetic meaning of the term (see also Gray 1978). The development of microstructures in psammites in the shear zones from the upper transitional zones toward the lower boundary thrusts was carried out. This was done to define the gradation of the spatial development of cleavages in psammites from within the shear zones and also to determine the mechanisms of formation of the cleavage.

The term psammite as used in this study refers to a medium-grained (50 μm to 1500 μm) weakly metamorphosed clastic sedimentary rock (a sandstone), composed of abundant rounded or angular fragments which were cemented by matrix material (see Figs 5.3 a & b). The matrix consists of smaller (about 10 μm) silt and clay enclosing or filling the interstices between the larger grains. Using the classification of Gray (1978), which is based on the relative proportions of grains and matrix, psammites in the shear zones vary from arenites (less than 15% matrix) (Fig. 5.3a) to wackestones (greater than 15% matrix) (Fig. 5.3b). The psammitic textures are also classified into two main types which are termed P domains and Q domains. P domains are commonly referred to as cleavage domains and mainly composed of detrital grains and phyllosilicates, whereas Q domains are mainly composed of quartz grains and are commonly referred to microlithons (e.g. Stephens *et al.* 1979, Onasch 1983, and Waldron & Sandiford 1988).

5.2.2 Description of cleavage types in psammites

Cleavage morphology of all psammites from the shear zones in the area of study ~~are~~ is similar. In

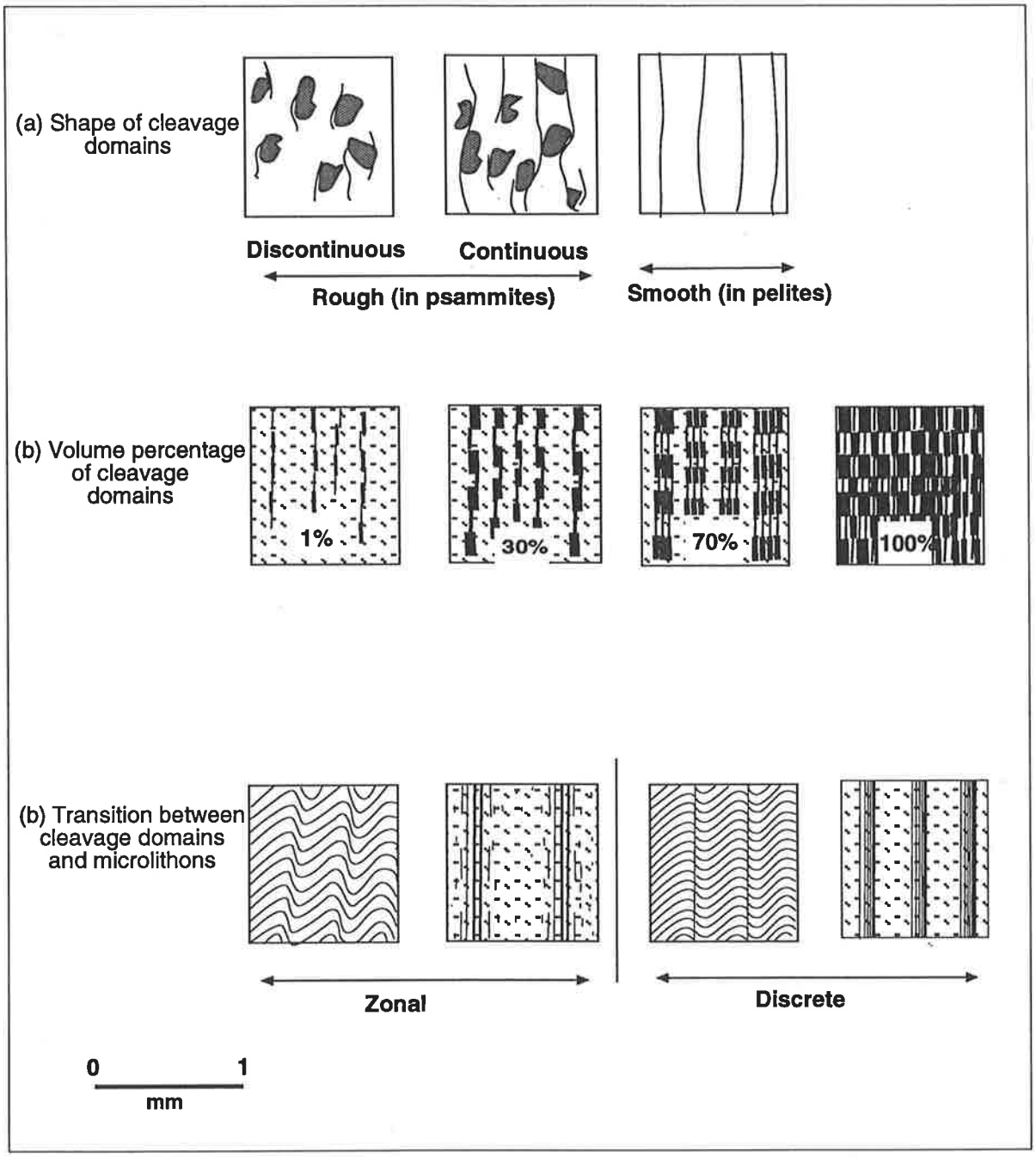

FIG. 5.2: Morphological classification of cleavages using an optical microscope. Modified after Gray (1978), Powell (1979), and Borradaile *et al* (1982).

all samples, the shape of cleavage (P) domains is an irregular, anastomosing rough cleavage (Fig. 5.2a) (see also Gray 1978, and Borradile *et al.* 1982) defined by the relative concentration of phyllosilicates and quartz. The cleavage domains consist of oriented flakes of phyllosilicates (mainly white micas) and sometimes chlorite. In the rocks where the cleavage domains are not well developed, the rough cleavage is discontinuous (Fig. 5.3a) but in rocks where the cleavage domains are well developed the rough cleavage is continuous (Fig. 5.2a). In the latter, the rough cleavage wraps around or truncates detrital grains (Fig. 5.3b). The volume percentage of cleavage domains varies from 1% to more than 30% (Fig. 5.2b), depending mainly upon the cleavage development during deformation and/or upon the amount of phyllosilicate present which varies from brown to green biotites, muscovite, and chlorite. The width of the individual cleavage domains vary from 10 μm to 50 μm and may be as little as 100 μm in length (Fig. 5.3a) or as much as the length of an entire thin section (Fig. 5.3b).

In Q domains or microlithons, grains comprise mainly quartz (>70% of rock volume) and to a lesser extent mica. Detrital quartz grains which range from 100-400 μm in size along the maximum dimension, are ovoid to slightly elongate subparallel to the cleavage direction and to the needle-like white micas (e.g. see Fig. 5.3b). In most samples, elongate detrital grains are usually truncated by the cleavage domains. The amount of this truncation varies significantly between grains. Two end-member groups of quartz grains can be identified. Grains of the first group display the highest degree of dissolution and have smooth sides aligned parallel to the cleavage domains (Fig. 5.3c and also see Fig. 5.4c). Grains of the second group are almost equant with only slightly modified detrital shapes and have tails of beard-like overgrowths (Fig. 5.3b).

Mica and to a lesser extent chlorite that have crystallised or recrystallised in beards or mica films are an important component of many rough cleavage fabrics (e.g. Gray 1978). Quartz and white mica in beards, which taper off one or both ends of detrital grains in a direction subparallel to the rough cleavage, exist in some samples. Both minerals, which are sometimes perpendicularly aligned at the margin of grains, become more parallel to cleavage direction

Figures opposite:

Fig. 5.3a: Weakly developed rough cleavage in psammites of the Woolshed Flat Shale from the upper transitional zone of the Mt. Bold shear zone. Cleavage domains or P domains are short, discontinuous seams "DS" spaced at about 300-500 μm and sometimes truncate grain boundaries "T"; crossed polars; width of view=8 mm.

Fig. 5.3b: Well developed rough cleavages in psammites of the Woolshed Flat Shale from within the Mt. Bold shear zone. Here, the cleavage domains are more closely spaced (100-300 μm), more continuous, and thicker seams. Quartz grain boundaries are either planar truncated "T" or irregularly sutured "S". Overgrowing mica beards "B" have also developed on larger and more spherical grains; crossed polars; width of view=8 mm.

Fig. 5.3c: Very thin, flattened presolved quartz grains "F" and less modified detrital grains "M" with development of beards of overgrowth "B"; crossed polars; width of view=2.4 mm.

Fig. 5.3d: Overgrowths of quartz and small-scale mica in shadows of bent detrital mica oriented sub-orthogonal to the cleavage; crossed polars; width of view=1.2 mm.

Fig. 5.3e: Detrital mica oriented sub-parallel to the cleavage domains. Note the deformation of the mica along the (001) cleavage; crossed polars; width of view=2 mm.

Fig. 5.3f: Deformation band and to a lesser extent subgrain formation in detrital quartz grains from the lower boundary thrust to the Mt. Bold shear zone; crossed polars; width of view=2.4 mm.

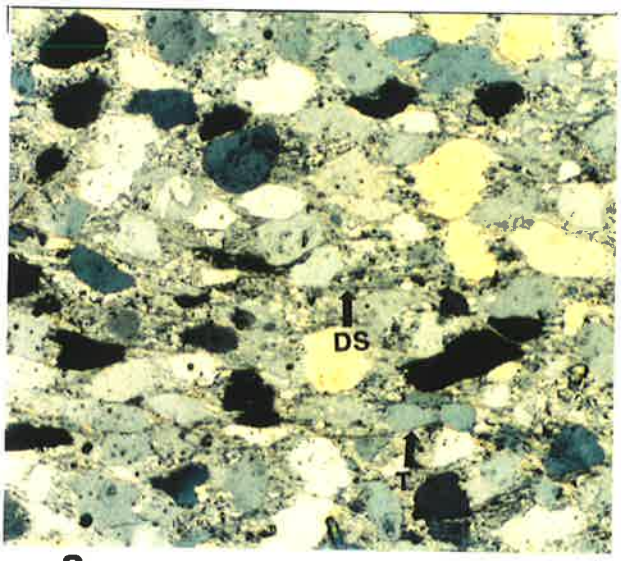

a

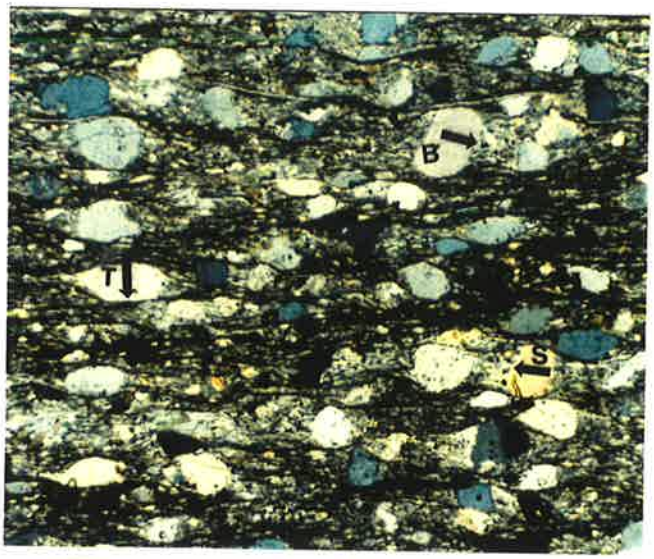

b

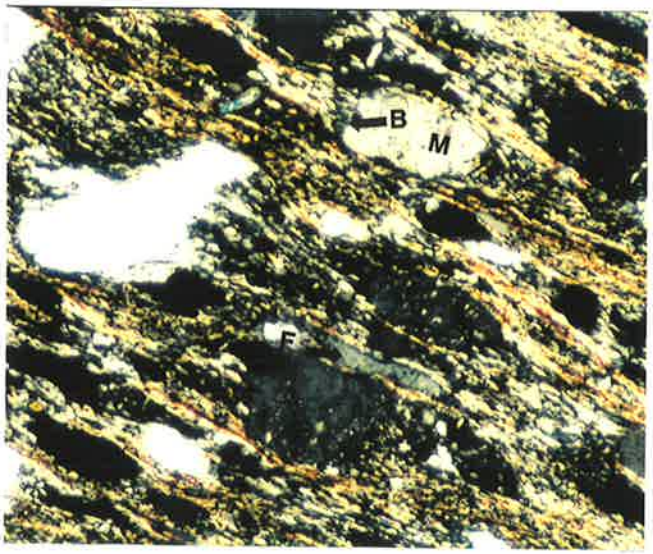

c

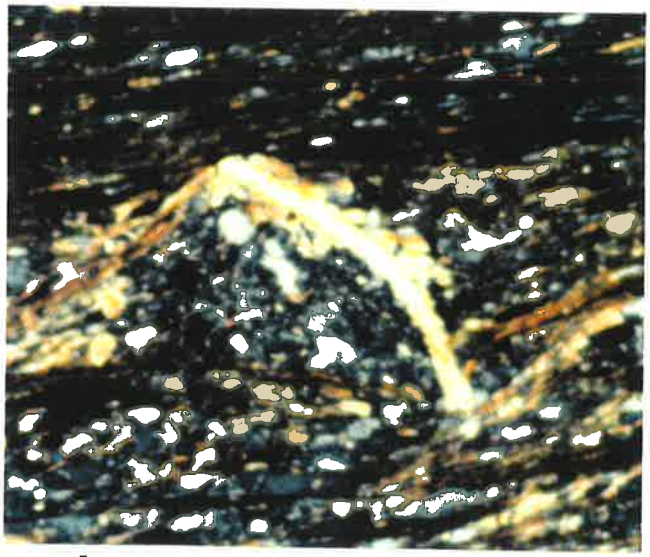

d

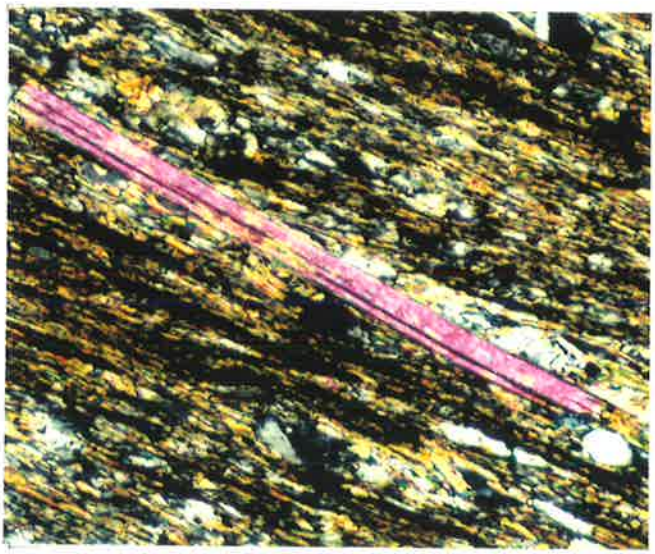

e

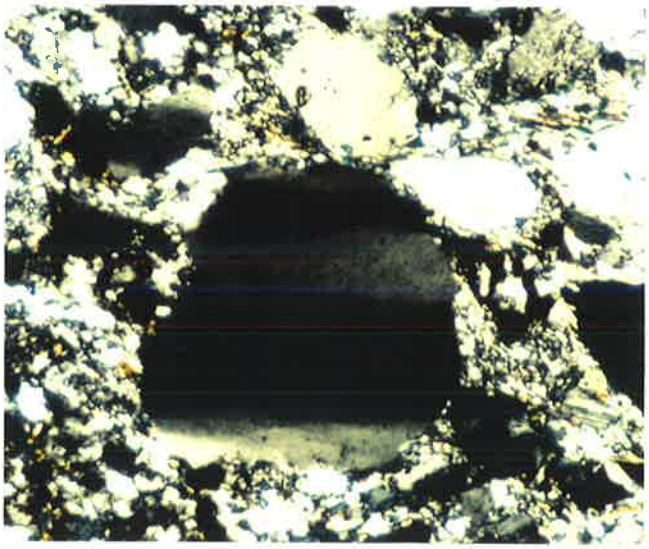

f

farther from the margins.

Mica grains are different in origin, size, and orientation with respect to the rough cleavage but it seems that they can be classified into two distinct groups. Group one micas are defined by coarse grains almost all long (100 μm to 500 μm) with length:width ratio up to 10:1. They are commonly deformed by slip on (001) planes (e.g. Passchier & Trouw 1995) (Fig. 5.7d), undulose extinction, and kinking and folding (Wilson 1980, Lister & Snoke 1984, and Bell *et al.* 1986). The orientation of this mica group with respect to the rough cleavage, varies from sub-orthogonal to sub-parallel. The sub-orthogonal micas are more deformed and exhibit undulose extinction, folding, and kinking with the kink axes often randomly oriented. The folded mica grains have also fringes of quartz and small needle-like mica (Fig. 5.3d). The sub-parallel micas (Fig. 5.3e) are also deformed, with deformation taken up along the basal (001) planes, leading to the development of fish-like structures (mica fish of Lister & Snoke 1984) (Fig. 5.7d). These group one micas are considered as pre-cleavage and most likely detrital in origin.

Group two micas are defined by fine-grained (<60 μm long) young needle-like white micas with high birefringence in cross polars and length:width ratios usually greater than 10:1. They are oriented parallel to subparallel to gross rough cleavage folia (see for example Fig. 5.3c) and show no evidence of intracrystalline deformation features. They are also seen around the edge of sutured detrital quartz grains and in pressure shadows. Unlike group one, group two micas are considered syn-deformational grains and seem to have formed during cleavage development or as precipitated product of dissolved soluble grains (e.g. Stephens *et al.* 1979).

5.2.3. Microstructural development of rough cleavages in psammites from within the shear zones

The progressive microstructural development of rough cleavage in psammite of the Mt. Bold shear zone from the upper transitional zones (sub-zone I) toward the lower boundary thrusts (sub-zone III) was studied and is shown in figure 5.4. In all three samples studied, based on

the classification of Gray (1978), matrix makes up less than 15% of the rocks and thus they are mostly arenites. The matrix mainly comprises quartz grains, needle-like white mica, and in rocks with more intensely developed cleavage, dark folia or seams. Grains which made up more than 85% of the rock volume comprise quartz, feldspar (mainly albite), and mica's of the two main groups previously described.

Three main microstructural features are developed across the shear zone from sub-zone I toward sub-zone III (compare Figs 5.4a, b & c). The grain sizes of detrital quartz grains decreases from 200-600 μm to 50-500 μm. Concomitantly, the amount of group two white mica, which produces the rough cleavage, also increases. In the sample from sub-zone I, the folia or seams which produce cleavage domains or rough cleavages are rare or occupy less than 1% of the rock volume (Fig. 5.4a). In the sample from sub-zone II, the intensity of the folia or rough cleavage increases to produce discontinuous cleavage (e.g. Gray 1978), where the cleavage domains comprise about 10- 20% of the rock volume (Fig. 5.4b). In a sample from sub-zone III, the cleavage is well developed (Fig. 5.4c) to form continuous rough cleavage (Fig. 5.2a). This rough cleavage generally extends across the entire thin section and occupies about 30% of the rock volume (Figs 5.2a & 5.3b). Here, in the cleavage domains, detrital mica needles are also aligned along the trend of the foliation (Fig. 5.4c), and/or truncate parallel sided quartz grain boundaries. This detrital mica, as shown in figure 5.4c, is also deformed to form mica fish microstructures (Simpson & Schmid 1983, Lister & Snoke 1984).

The other main microstructural features, developed across the upper transitional zone (sub-zone I) towards the lower boundary thrust (sub-zone III), is an increase in the amount of intracrystalline deformation features in detrital quartz grains. Quartz grains in samples from sub-zone I show only weak undulatory extinction (Fig. 5.4a). However, samples from sub-zones II and III show evidence of sweeping undulatory extinction, deformation bands (Fig. 5.3f) and in grains with higher dislocation density even subgrain formation and small recrystallised grains (Fig. 5.4b).

Figures opposite:

Fig. 5.4: Microstructural development of rough cleavages in the Mt. Bold shear zone; all crossed polars with width of view=3 mm.

Fig. 5.4a: The upper transitional zone to the shear zone. Note the less modified quartz grains with mostly low intensity of intracrystalline deformation and weakly developed syndeformational white mica defining the rough cleavage.

Fig. 5.4b: From within the shear zone, showing development of discontinuous rough cleavage, increase in the amount of intracrystalline deformation features in quartz grains and decrease in the size of the quartz grains. Note also the development of subgrains "SU" and small recrystallised grains "RS" in the detrital grains.

Fig. 5.4c: Continuous rough cleavage along the lower boundary thrust. Syndeformational white micas are more frequently developed forming cleavage zones. Note orientation of detrital muscovite which shows mica fish-like structure.

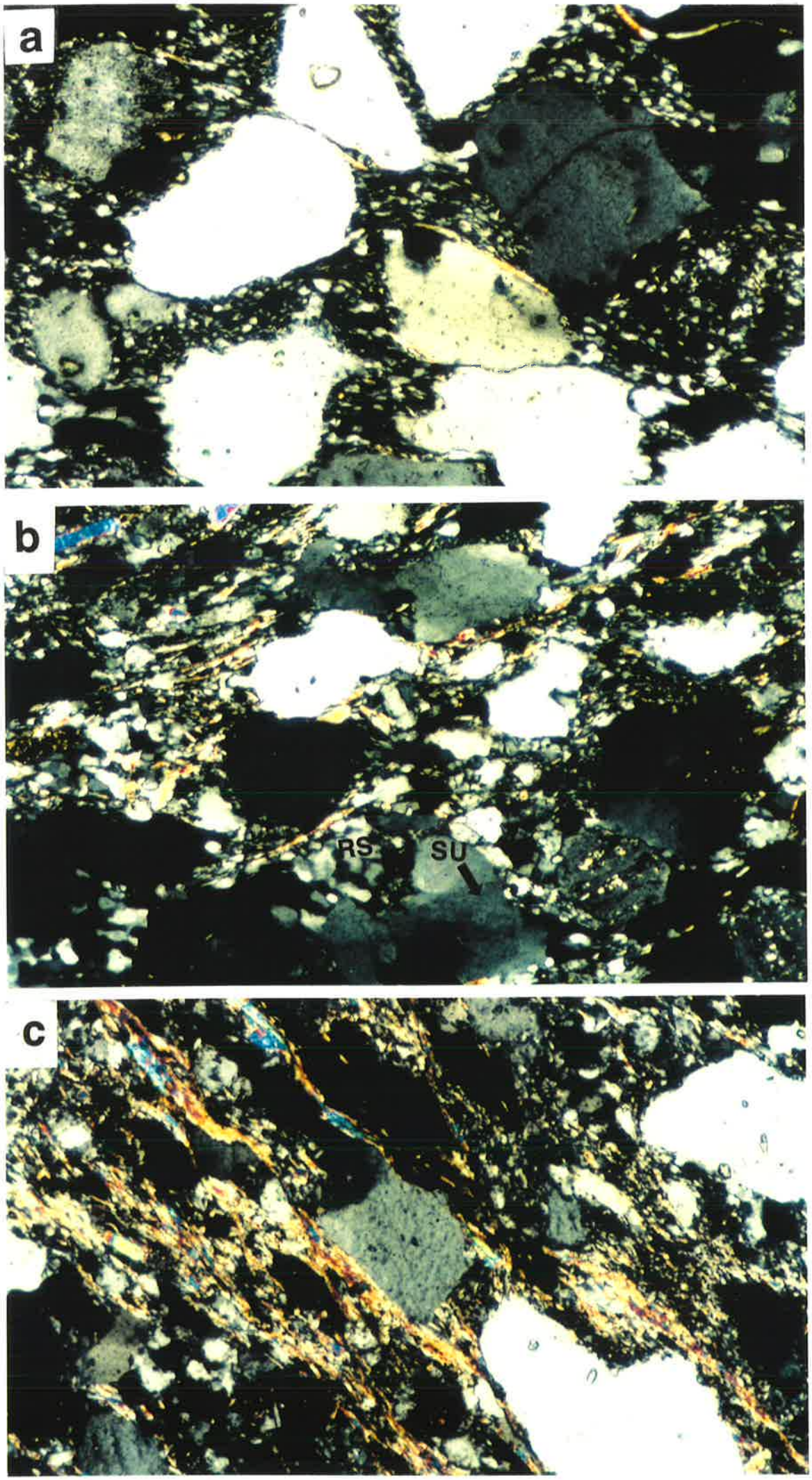
a
b
RS
SU
c

5.3. Mineralogy and microstructure of pelites

5.3.1 Introduction

The development of microstructures in pelites in the shear zones from the upper transitional zones toward the lower boundary thrusts was carried out. This was performed in order to define the gradation of the spatial development of cleavages in pelites from within the shear zones and also to determine the possible mechanisms of formation of the cleavages. The operating processes leading to the development of the cleavages in pelites have been considered to be due to the effect of pressure solution (William 1972, Cosgrove 1976, Gray 1979, Walderon & Sandiford 1988, and Holl & Anastasio 1995) and/or syntectonic crystallisation or recrystallisation of micas in cleavage domains (White & Knipe 1978, Knipe 1981, and Lee *et al.* 1986). These effects are thought to be mainly temperature dependent, because pressure solution occurs more readily at lower grades than syntectonic crystallisation and recrystallisation (Kanagawa 1991).

5.3.2 Description of cleavage microstructure types in pelites

Pelites and phyllites from the Woolshed Flat Shale and Saddleworth Formation are mainly comprised of phyllosilicates (micas and chlorite; more than 45 % of the rock volume), quartz (more than 50% of rock volume), and to a lesser extent feldspars (mostly albite; less than 5% of rock volume). Microscopic examination of the rocks reveals that cleavage in the pelites and phyllites are dominated by a strong dimensional preferred orientation of both elongate quartz and phyllosilicates (Fig. 5.5a). Beard structures and pressure shadows on framboidal pyrite grains are also developed. Framboidal pyrite grains contain pressure shadows of straight, thin interlocking fibres of quartz and occasionally white micas. Shadows have tapered form but the fibres are all subparallel to the cleavage fabric in the pelites (see Fig. 5.7a).

Following the classification of Powell (1979) and Borradaile *et al.* (1982) the cleavages in pelites and phyllites are smooth in shape (Fig. 5.2a) and the mica grains with a preferred orientation are homogenously distributed to form continuous cleavages (Fig. 5.5a). Biotite and

Figures Opposite:

Fig. 5.5a: Continuous cleavage in the pelites from the Woolshed Flat Shale defined by fine-grained micaceous material. Note the existence of deformed white mica of type one (M_1) sub-orthogonal to the cleavage which is comprised of type two "M_2" syndeformational mica; crossed polars; width of view=1.2 mm.

Fig. 5.5b: Development of cleavage domains in sandy pelites of the Woolshed Flat Shale. Inhomogenous distribution of phyllosilicates in cleavage domains spaced at 100-200 μm and also note the truncation of the quartz grains by needle-like micas; crossed polars; width of view=1.2 mm.

Fig. 5.5c: Transposition cleavage in sandy unit of a pelite of the Woolshed Flat Shale which is parallel to the continuous cleavage described in the text; crossed polars; width of view=8 mm.

Fig. 5.5d: Discrete crenulation cleavage (subhorizontal dark traces) overprinting an early slaty cleavage (steep crenulated mica and quartz grains) in pelites of the Clarendon shear zone; crossed polars; width of view=2.4 mm.

Fig. 5.5e: Development of zonal crenulation cleavage by concentration of phyllosilicates in cleavage domains (subhorizontal traces). Note the differences in composition of the cleavage domains and microlithons and the gradual transition between both; crossed polars; width of view=2.4 mm.

Fig. 5.5f: Development of discrete crenulation cleavages (solution seams where the micas are also oriented in parallel) in sandy pelites from the Mt. Bold shear zone. In the upper left side of the photograph, the cleavage is more like the zonal type but towards the finer grained silty unit (in the lower and right parts) the cleavage is transitional to the discrete type where the apparent offset of the crenulated silty unit can also be seen; crossed polars; width of view=8 mm.

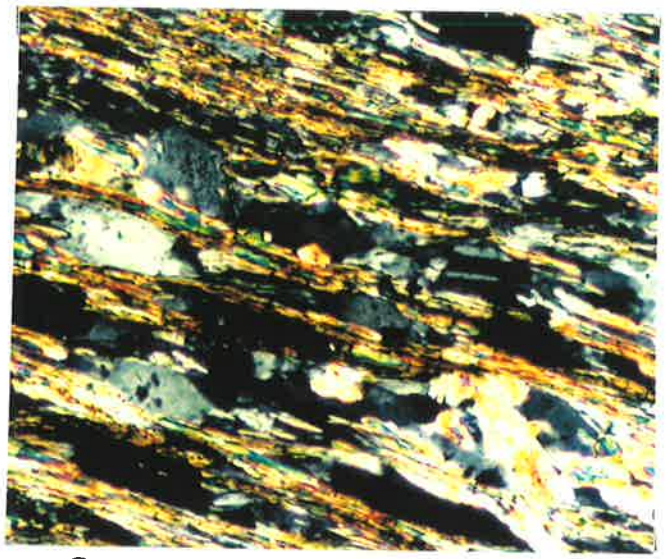

a

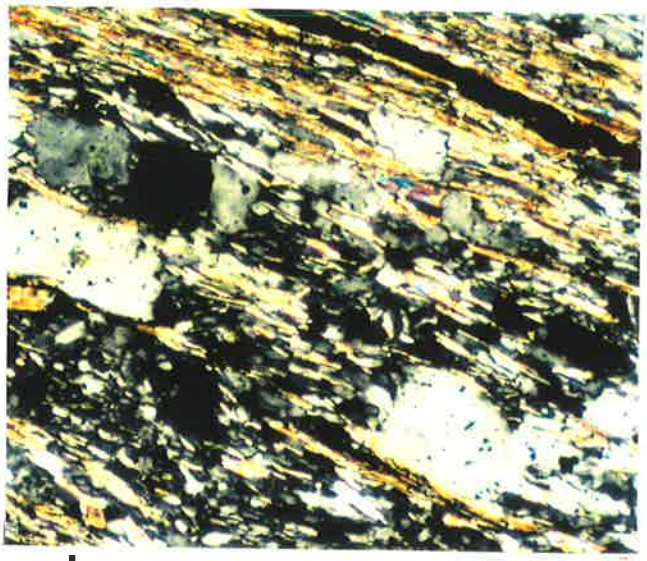

b

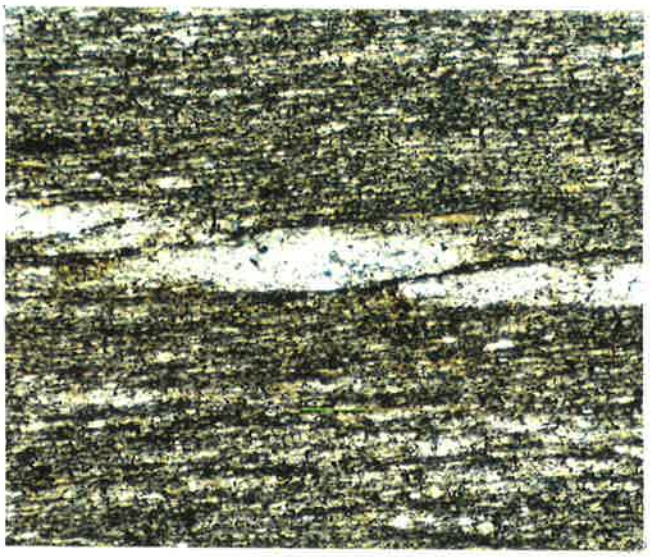

c

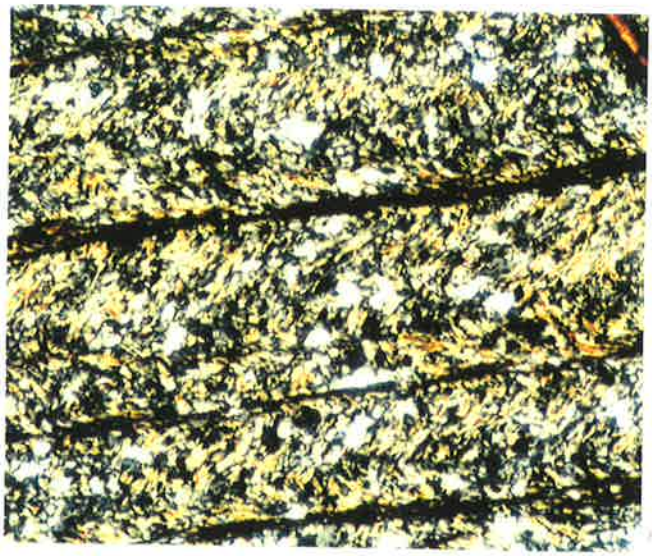

d

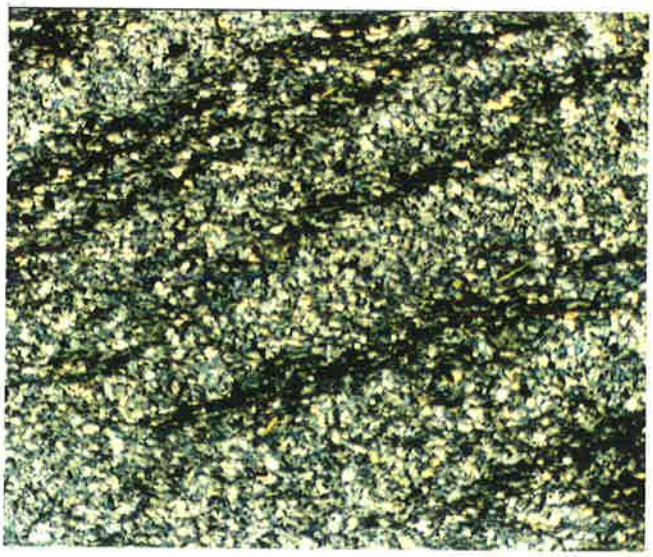

e

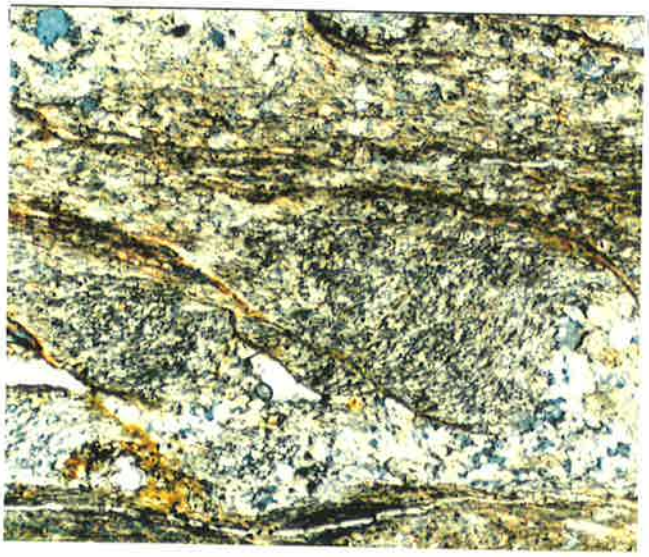

f

white mica and to a lesser extent chlorite are the main fabric elements of the cleavage domains. In more sandy or silty pelites, which comprise alternately layered phyllosilicates and quartz, the cleavage domains are spaced at approximately 100-200 μm (Fig. 5.5b) and occupy about 70% of the rock volume (Fig. 5.2b). These cleavage domains which contain needle-like mica are well oriented but inhomogeneously distributed within discontinuous layers parallel to the slaty cleavage (Fig. 5.5b). Within this domainal fabric, there is pronounced alignment of needle-like elongate white micas, where both long axes and (001) traces of the micas are subparallel to cleavage domain boundaries. Elongate quartz grains within quartz-rich layers are truncated against the needle-like micas (Fig. 5.5b). In thicker sandy units of intensely deformed pelites, especially in sub-zone III, intense transposition cleavage parallel to the slaty cleavage fabrics cut the sandy beds at low angles (<10°) (Fig. 5.5c). Micas in pelites and phyllites, like the psammites, occur mainly in two groups. Group one mica is pre-cleavage and is considered to be detrital in origin while group two micas are metamorphic and interpreted to have grown syn-cleavage development (see Fig. 5.5a).

5.3.3 Microstructural development of continuous cleavages in pelites from within the shear zones

A detailed study of microstructural development of continuous cleavages in pelites within the shear zones (and from sub-zones I toward sub-zones III), reveals three main microstructural changes. Firstly, there is a significant increase in the amount of micas and their parallelism in orientation which results in the intense development of continuous cleavages at the lower boundary thrust (sub-zone III). At this boundary, the mica fabric is observed as a tendency for the whole thin section to go to extinction at the same time. Such an increase in the amount of mica has been considered to be due mainly to the removal of quartz and feldspar (mostly albite) from pressure solution zones and/or the addition of phyllosilicate (e.g. Stephens *et al.* 1979, Groshong 1988).

Secondly, the less abundant development of group two deformed micas, which are mostly suborthogonal to the cleavage, from sub-zone III is another microstructural change within the shear zones. This indicates that micas in cleavage domains have been rotated more and therefore become more subparallel to the continuous cleavage and/or have recrystallised or crystallised by syntectonic recrystallisation or crystallisation to achieve their preferred orientations (e.g. White & Knipe 1978, Lee *et al.* 1986).

The third microstructural change is the change in the shape of quartz grains. Quartz grains in samples from sub-zone I are relatively equant when not in contact with the cleavage laminae, but in samples from sub-zones II and III they are corroded against syn-cleavage mica (Fig. 5.5b) or deformed and elongated subparallel to cleavage. The quartz grains are usually dimensionally oriented but not necessarily crystallographically oriented. The elongation of quartz grains can be explained by removal of the grain margins normal to cleavage laminae by pressure solution. Therefore the width of the grains normal to cleavage is reduced, but their length parallel to cleavage remains unchanged (e.g. Williams 1972, Lisle 1977) (Fig. 5.5b).

5.3.4. Microstructures of crenulation cleavages in the shear zones

In more intensely deformed pelites and phyllites from within the shear zones (sub-zone II) and from the lower boundary thrusts (sub-zone III), the cleavage domains or slaty cleavages are often deformed to produce crenulation cleavages (Fig. 5.5d). Crenulation cleavages are spaced cleavages which generally form in phyllosilicate-rich rocks by small-scale harmonic folding of pre-existing cleavages (e.g. Williams 1972, Cosgrove 1976, Gray 1977, 1979). Both morphologically distinct types (Fig. 5.2c), that is, zonal (Fig. 5.5e) and discrete (Figs 5.5d &f) crenulation cleavage types (Cosgrove 1976, Gray 1978, Powell 1979, Borradaile *et al.*, Swager 1985, and Passchier & Trouw 1995) have been recognised. These two types of crenulation cleavage are seen in the shear zones and sometimes occur together though the discrete crenulation cleavage type is more abundant.

Zonal crenulation cleavages are zones of laminated domains rich in phyllosilicates and are well developed in phyllites and phyllosilicate rich pelites. This cleavage is defined by a concentration

of phyllosilicates in spaced cleavage domains (Fig. 5.5e). The transition between these zonal crenulation domains and the microlithons as shown in figure 5.5e is gradational. The zonal crenulation cleavages commonly change to discrete cleavages at their terminations (Fig. 5.5f).

Discrete crenulation cleavages, however, are thinner than the zonal crenulation cleavages with dark planar discontinuities which have distinct boundaries that truncate the crenulated preexisting slaty cleavages (Fig. 5.5d). This planar discontinuity is a thin (<50 μm) differentiated zone in which an aggregation of opaque and very fine clay minerals are interspersed with the phyllosilicates which are parallel to the cleavage trace. Discrete crenulation cleavages almost always truncate and offset layering (Figs 5.5f & 5.6b). There is no evidence of cracking or fracturing at the terminations of these discrete crenulation cleavages and quartz grains immediately adjacent to the truncated segments show no increase in intracrystalline deformation features (see also Gray 1979). Therefore, the truncation of layers, as shown in figure 5.6b, seems to occur as a result of a marked reduction of quartz and a relative increase in phyllosilicates, opaques and/or carbonate matter in the cleavage zones.

5.3.5 Development of crenulation cleavages in the shear zones

The study of shear zones in low grade metamorphic rocks reveals that crenulation cleavages are developed progressively during shearing (e.g. Tobisch & Paterson 1988 and Burks & Mosher 1996). The spatial development of crenulation cleavages in the shear zones and their increasing intensity towards the lower boundary thrusts in all shear zones studied imply their progressive development during thrusting/shearing. Figure 5.6 shows in detail microstructural development of the crenulation cleavages in the shear zones. The crenulations of the slaty cleavages are initiated at sub-zone I where bedding and slaty cleavages are at a low angle (<20°), (Fig. 5.6a).

Over about 100-200 m from sub-zone I, but within the shear zones (in sub-zone II) a strong crenulation cleavage develops (Fig. 5.6b). In sub-zone III and especially at the lower boundary thrust, where the most intense deformed fabrics and structures are developed, the crenulation cleavages are completely transposed into a new continuous cleavage (Fig. 5.6c). The formation of this cleavage can be distinguished from a relict of the crenulation in microlithons (Fig. 5.6c).

Figures opposite:

Fig. 5.6: Photomicrographs and sketches showing development of crenulation cleavages in the shear zones, all crossed polars and width of view=3 mm.

Fig. 5.6a: shows initiation of crenulation cleavage (S_{1b}) in pelites from the upper transitional zone. Note the crenulation (S_{Cr}) of the early (S_{1a}) slaty cleavage which is at a low angle to bedding (S_0).

Fig. 5.6b: Development of stylolitic discrete crenulation cleavages (S_{Cr}) in pelites from within the shear zone. The apparent offset of the microlithons along the cleavage is considered to be due to solution processes (see text for more information).

Fig. 5.6c: Transposition cleavage (S_T) developed from the intense deformation of crenulation cleavages at the lower boundary thrust. A relict of crenulation cleavage in microlithons of the sandy unit can be seen in the middle part of the photograph.

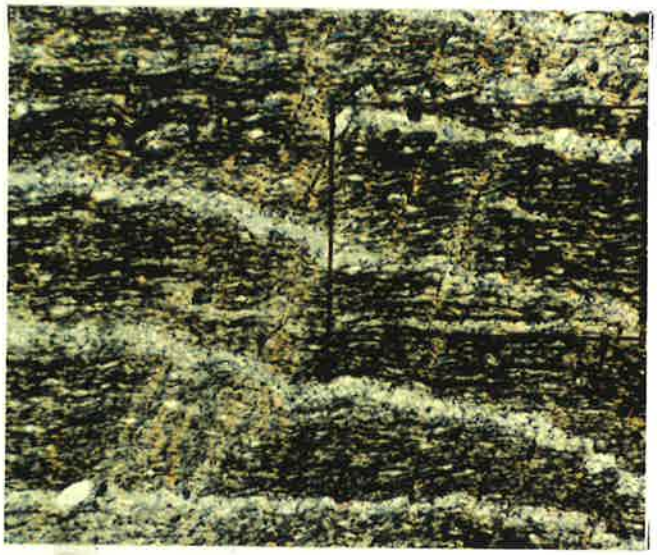

a

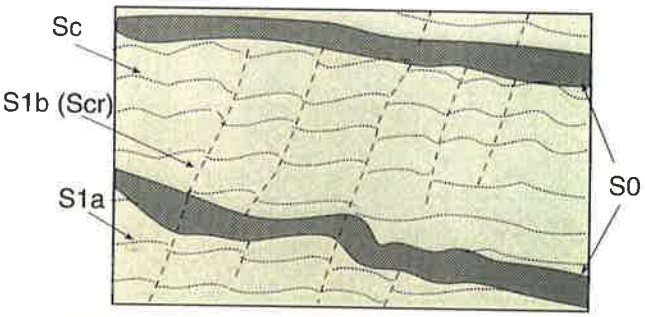
Sc
S1b (Scr)
S1a
S0

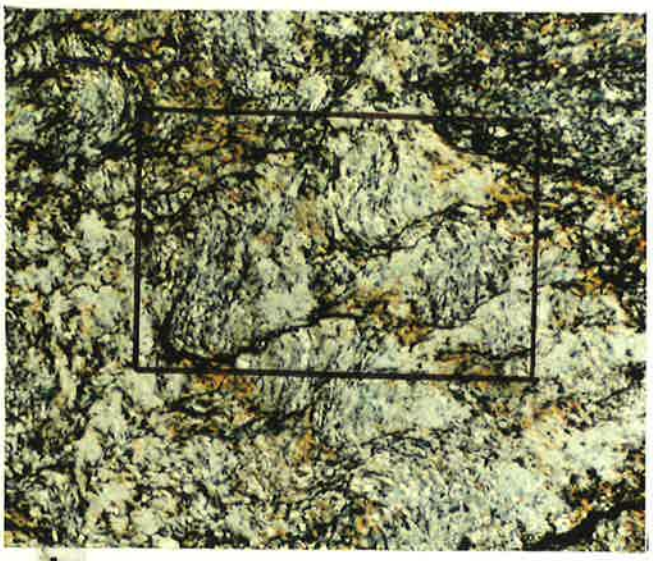

b

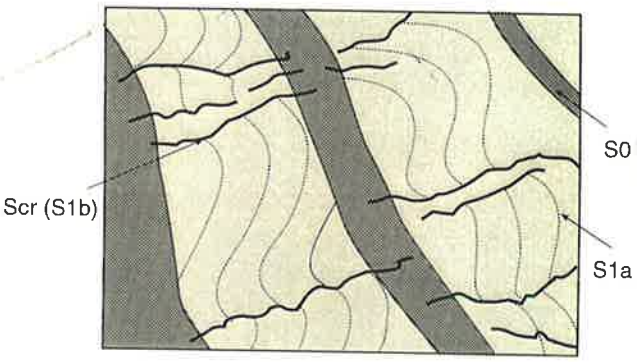
S0
Scr (S1b)
S1a

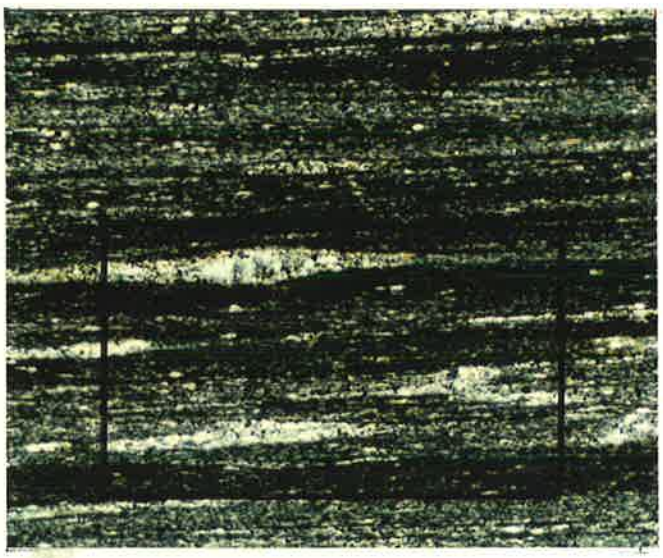

c

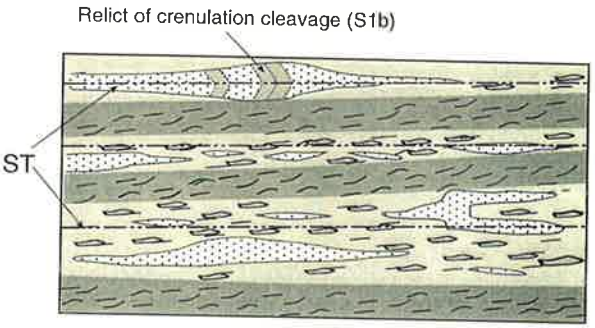
Relict of crenulation cleavage (S1b)
ST

Thus, in samples from the lower boundary thrusts, three cleavage components can be distinguished: the original continuous cleavages, where developed/preserved; a new continuous cleavage; and quartz-rich domains which contain a relict crenulation morphology (Fig. 5.6c). All of these cleavage components are subparallel to each other which makes it difficult to distinguish them, especially in hand specimens and in the field, from samples outside the shear zones. Such progressive microstructural development of crenulation cleavage in the shear zones is comparable with the concept of composite foliation development considered by Tobisch and Paterson (1988) for progressive deformation of ductile shear zones.

5.4. Microscopic shear sense indicators

Kinematic indicators provide the best evidence to define the direction and the nature of the flow in shear zones. Shear sense indicators are a subset of kinematic indicators which show the sense of shear or the vorticity of flow in progressively noncoaxially deformed material (Hanmer & Passchier 1991). In general the criteria that have been found to be the most useful for the determination of the sense of shear are asymmetric augen structures, composite planar fabrics, asymmetric pressure fringes, displaced broken grains and crystallographic fabric asymmetry (Simpson & Schmid 1983, Lister & Snoke 1984, Boullier 1986, Etchecopar & Malavieille 1987, and Hanmer and Passchier 1991).

A detailed study of thin sections cut parallel to the stretching lineations and perpendicular to cleavages from within the shear zones in the area of study reveals that asymmetric pressure fringes, displaced broken grains, curved and displaced fibre veins, and asymmetric microscopic shear folds provide evidence to deduce the sense of shear in the shear zones.

5.4.1. Asymmetric pressure fringes

Pressure fringes (e.g. Durney & Ramsay 1973, Ramsay & Huber 1983, and Passchier & Trouw 1995) are elongate volumes of quartz or calcite crystallised adjacent to stiff crystals or aggregate in fine grained rocks. The asymmetric pressure fringes are one of the most useful criteria for determining the sense of shear in shear zones (Simpson & Schmid 1983, Etchecopar

& Malavieille 1987, Hanmer & Passchier 1991, and Aerden 1996). These structures are the most common shear sense indicators within the shear zones of the study area, especially in samples from the lower boundary thrusts. They can be seen in pelites, sandy pelites and psammites of both the Woolshed Flat Shale and Saddleworth Formations and in almost all cases, the pressure fringes are pyrite type fringes (Ramsay & Huber 1983) with either spherical or cubic cores (see Passchier & Trouw 1995, pp. 141) (Figs 5.7a & b).

Thin section studies reveal that the pyrite grains have asymmetric, dynamically recrystallised quartz fringes subparallel to the matrix cleavage. The internal geometry of the fringes, as shown in figure 5.5b, indicates that at least two crystal growth patterns can be identified in each tail representing increments of strain. Growth of fringes closer to the core of the objects are oriented at low angles (about 30°) to the orientation of cleavage in the matrix, while growth fringes far from the core of the objects tend to be subparallel to the cleavage in the matrix (Fig. 5.7a). This geometry is considered to form by a progressive simple shear in which flow in the matrix tends to draw the previous growth increments of fringes away from the core of the objects. The object cores undergo a rigid body rotation while the fringes undergo a rotation and possibly a shape change (Hanmer & Passchier 1991).

Etchecopar & Malavieille (1987) produced a model for the development of pressure fringes during noncoaxial deformation. In their model an increment of fibres forms during an increment of deformation and an increment of growth. During the increment of deformation, flow in the matrix draws the pressure fringe away from the inclusion. After several increments of rotation and growth, the average fibre orientation from segment to segment describes an asymmetric curvature. In more mature samples especially the ones from the lower boundary thrusts, the overall geometry of the fringes tends toward an asymmetrical "hook" shape (Hanmer & Passchier 1991), where the overall asymmetric curvature marks the sense of rotation of the structure. Using this criteria, the top to the NW sense of shear can be confirmed from all samples studied in the shear zones (e.g. Figs 5.7a & b, and also see Fig. 2.2 for the shear direction).

Figures opposite:

Fig. 5.7: Microscopic shear sense indicators in samples from within the shear zones.

Fig. 5.7a: Pressure fringes developed in silty pelites of the Woolshed Flat Shale in the Clarendon shear zone; showing NW (to the left) sense of shear; crossed polars; width of view=8 mm.

Fig. 5.7b: Pressure fringes in psammites from within the Mt. Bold shear zone; showing again NW (to the left) sense of shear; crossed polars; width of view=1.2 mm.

Fig. 5.7c: Displaced broken feldspar in quartzite from within the Mt. Bold shear zone; note that the feldspar is displaced along a microshear parallel to the mesoscopic shear plane and indicates NW (to the left) sense of displacement; crossed polars; width of view=1.2 mm.

Fig. 5.7d: Antithetic microfaults developed in the basal (001) cleavage and displaced the mica fragments oblique to the mesoscopic shear plane and orientation of cleavage in matrix; the sense of shear is to NW (to the left); crossed polars; width of view=0.6 mm.

Fig. 5.7e: Asymmetric sheared folds in a sandy unit of the Woolshed Flat Shale from within the Pole Road shear zone; the top to NW (to the left) sense of asymmetry defines the sense of shear in the shear zone; crossed polars; width of view=8 mm.

Fig. 5.7f: Curved fibre quartz veins in dolomites of the Montacute Dolomites from within the Mt. Bold shear zone; the curved geometry of the fibres defines the sense of displacement in the shear zone which is to the NW (to the left); crossed polars; width of view=2.4 mm.

W

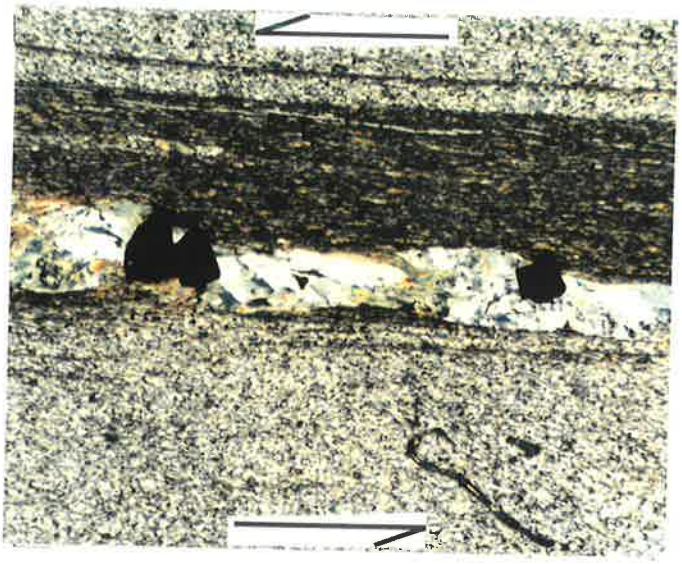

a

E

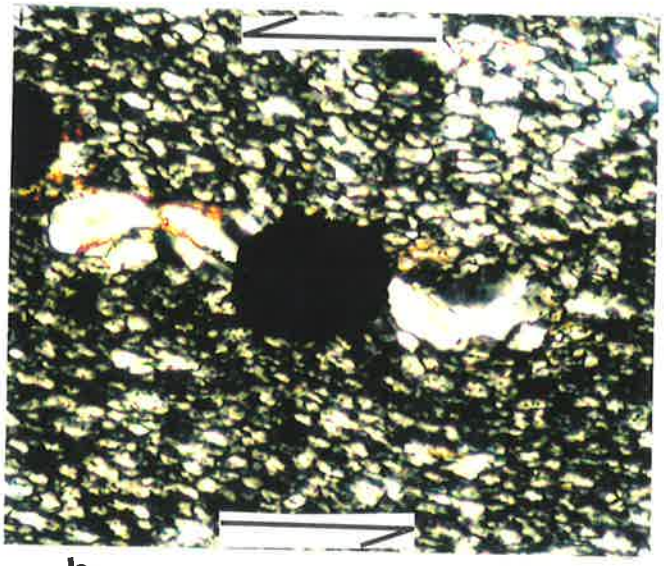

b

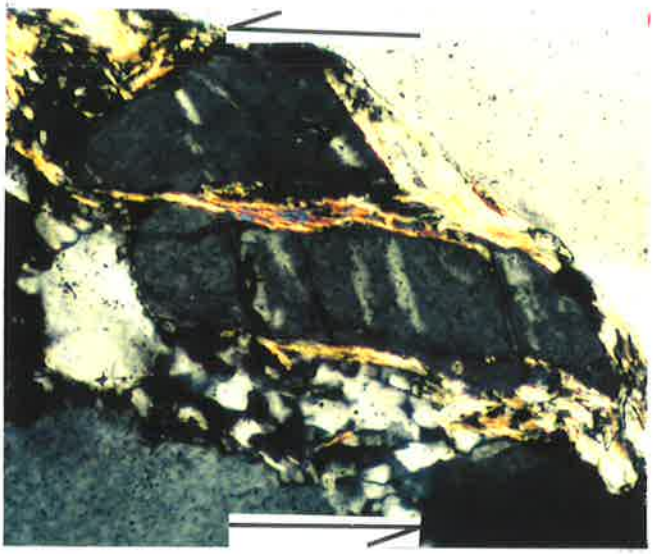

c

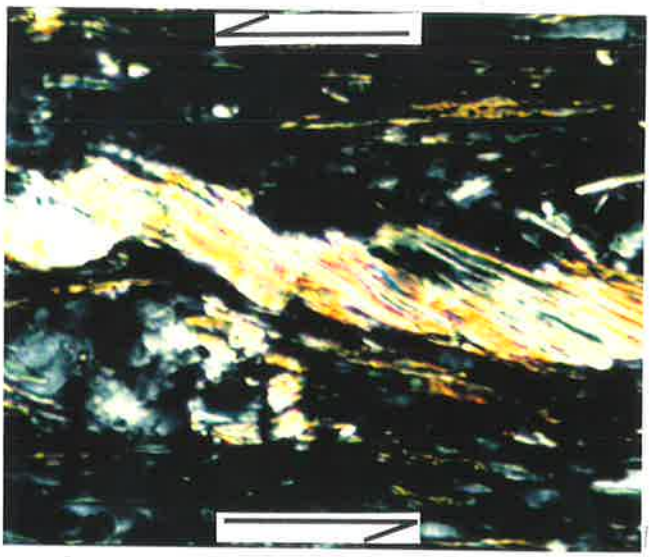

d

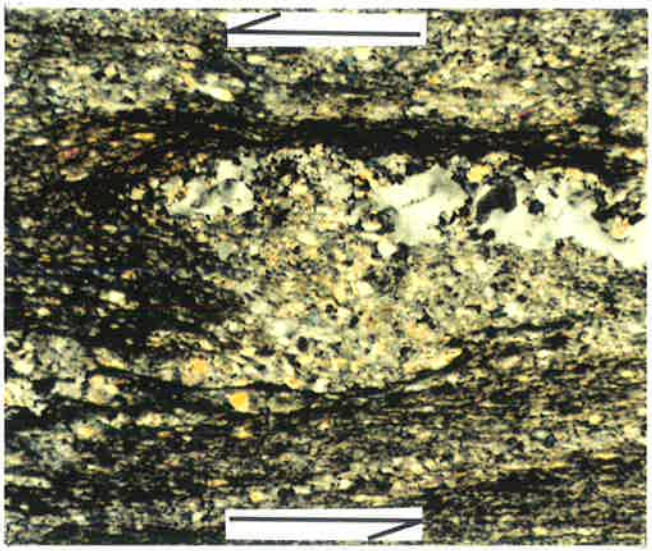

e

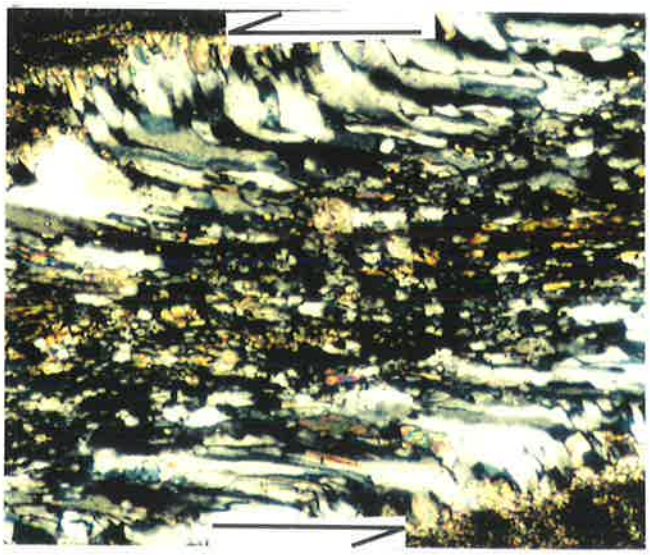

f

5.4.2. Displaced broken grains

Displaced broken grains of feldspar (Fig. 5.7c) and mica (Fig. 5.7d) are very common microstructures in the shear zones. These structures cause relative displacements of the fragments which occur frequently in sheared rocks and have elsewhere been used to determine the overall shear sense in rocks (Simpson & Schmid 1983). However, it is also considered that they should not be used alone to deduce the sense of shear (Hanmer & Passchier 1991). The sense of movement of the fragments can be antithetic or synthetic, and depends not only on the bulk shear sense, but also on the shape of the original clasts, on the kinematic vorticity number of flow, and on the initial orientation of the microfaults which may be partly controlled by crystallographic direction (Passchier & Trouw 1995).

Detailed microscopic study of fractured feldspars and displaced mica show that they are commonly displaced by micro-shear zones or faults. Feldspars are transected by microshears parallel to the shear plane (Fig. 5.7c), whereas micas are displaced oblique to the shear plane (Fig. 5.7d). Therefore, feldspars are displaced towards the NW by synthetic microshear zones (Simpson & Schmid 1983, Hanmer & Passchier 1991, Pryer 1993, and Simpson 1994) whereas the micas are offset to the SE by antithetic microshear zones (e.g. Simpson & Schmid 1983, and Passchier & Trouw 1995), though they still indicate the sense of shear towards the NW. These results are consistent with the sense of shear deduced from the pressure fringes.

5.4.3. Other criteria used to deduce the sense of shear in the shear zones

Asymmetric sheared folds (Fig. 5.7e) are common structures in psammites and sandy pelites of the Woolshed Flat Shale and Saddleworth Formation. They can be used to deduce the sense of shear in the shear zones but should be used more carefully as is indicated in the published literature (Simpson 1986, Hanmer & Passchier 1991). These microscopic asymmetric shear-fold-like structures are considered to develop due to enhanced perturbations in the layering during shearing (Hudleston 1977). From the asymmetric sense of these structures the sense of shear can be deduced, and is consistently top to the NW in the shear zones (Fig. 5.7e).

Quartz veins with curved fibres (Fig. 5.6f) are another source which allows deduction of the sense of shearing in the shear zones. The geometry of these veins, as shown in figure 5.7f, is similar to those described by Ramsay and Huber (1983) as displacement-controlled fibre veins. Like the pressure fringes they can also be used to deduce the sense of shearing. As can be seen in figure 5.7f, the veins were formed by continuous growth of fibres from vein walls towards the vein centre, that is, they exhibit a syntaxial curve (Ramsay & Huber 1983). During shearing, the old fibres are displaced in the direction of shearing while the new fibres grow at the vein walls. After several increments of rotation and growth, the average fibre orientation describes a curvature reflecting the rotation of the fibres in the direction of the shear zone movement and indicating the shear sense of flow which is to the NW in all of the shear zones (Fig. 5.7f, and also see Fig. 2.2 for the shear direction).

5.5. Discussion

5.5.1. The mechanism of formation of cleavages in psammites from within the shear zones

Almost all aspects of the microstructural development of the cleavages in the psammites from the shear zones can be best explained by the process of dissolution deformation. The existence of insoluble residues in folia or solution seams, sutured grain boundaries, truncation of detrital quartz grains against folia and offset across folia, all demonstrate that pressure solution was an important, if not the dominant mechanism of cleavage formation (e.g. Durney 1972, Elliott 1973, Groshong 1976, Gray 1978, Onasch 1983, Waldron & Sandiford 1988, Twiss & Moores 1992, and Tan *et al.* 1995). This can be further constrained by evidence for the contemporaneous increase in the amount of pressure solution and enhancement in the development of rough cleavage from the discontinuous type to the continuous type from sub-zone I to III within all of the shear zones. During the pressure solution process, the more soluble grains such as quartz have been sutured at the margins or dissolved from the matrix. Insoluble grains like mica, however, were passively concentrated along the folia.

Although the rough cleavages were probably entirely a product of pressure solution, the abundant evidence of intracrystalline deformation in quartz grains such as deformation bands, sweeping undulatory extinction and occasional subgrain formation implies that intracrystalline deformation has also contributed to the development of rough cleavages (e.g. Stephens 1979). It has also affected the modification of quartz grain shapes and thus the total strain.

The size reduction of quartz grains within the shear zones and from sub-zone I towards sub-zone III (see Fig. 5.4) is likely to be either a function of grain boundary dissolution processes (e.g. Gray 1978, Onasch 1983) and/or development of intracrystalline deformation features during increasing temperature or decrease in strain rate (e.g. Knipe & White 1979, Hirth & Tullis 1992). Like the products of pressure solution, the amount of intracrystalline deformation features also increase in the shear zones from sub-zone I to III.

The simultaneous development of intracrystalline deformation features with rough cleavage formation suggests that strain was partitioned between pressure solution and intracrystalline deformation during the cleavage formation. Considering the fact that the amount of finite strain measured from quartzite samples (see chapter 4) increases within the shear zones, particularly at the lower boundary thrusts, it is likely that microstructural development of the psammites in the shear zones was accomplished coevally by proportional development of continuous rough cleavages and intracrystalline deformation features during the localisation of deformation and/or strain at the lower boundary thrusts to the shear zones. Such localisation of strain occurs due to the process of thrust zone softening (Wojtal & Mitra 1988) at the lower boundary thrusts to the shear zones which in turn causes strain to concentrate along these boundaries (e.g. Mitra 1984, Wojtal & Mitra 1986). This happens more readily when the strain rate becomes low and/or when temperature increases in shear zones as is the case closer to the hinterland.

5.5.2. The mechanism of formation of crenulation cleavages in the pelites from within the shear zones

Almost all aspects of microstructural development of crenulation cleavages at lower greenschist facies have been explained by processes of solution transfer (Williams 1972, Gray 1977, 1979,

and Passchier & Trouw 1995). Microscopic study of crenulation cleavages in pelites from within the shear zones of the study area shows that there are similarities in the development of these cleavages in the shear zones. At the upper transitional zone or outside the shear zones (sub-zone I), the cleavage is dominantly slaty (Fig. 5.5a & also see Fig. 5.6a). Within the shear zones (sub-zone II), the continuous cleavages crenulate to form small-scale folds and to develop new cleavage or spaced cleavage (Fig. 5.6b). As a result, the hinge area of these microfolds becomes enriched in the more soluble components (mainly quartz and feldspar) to form generally lighter-coloured microlithon domains, whereas the limbs are enriched in the more insoluble components (mainly mica and opaques) to develop dark cleavage domains characteristic of domainal crenulation cleavages (see also Fig. 5.5e). From this mineralogical differentiation, it is clear that there has been a mass transfer of chemical components during the formation of the cleavage (e.g. William 1972, Cosgrove 1976, Gray 1979, Gray & Durney 1979). The absence of intragranular deformation such as undulose extinction, subgrain formation or recrystallisation in the component minerals of the cleavage zones suggests that the most dominant deformation mechanism is one of intergranular diffusion (e.g. Gray 1977, Mancktelow 1994).

In samples from within sub-zone III, the crenulation cleavages are more intensely developed and cause apparent offset of the bedding (Fig. 5.6b). Pressure solution (Cosgrove 1976, Gray & Durney 1979, Groshong 1988, and Wright & Henderson 1992) has been mostly invoked to explain such disrupted-offset and missing parts of lithological units cut by crenulation cleavages. Such apparent offset of the microlithon along the crenulation cleavages were considered to be a result of preferential reduction in volume along the cleavage and possibly representing 0-20% volume loss (e.g. Gray 1979, Cox & Etheridge 1989, Tan *et al.* 1995). At the lower boundary thrusts to the shear zones, the intense deformation of the crenulation cleavages cause development of new continuous cleavage defined by Tobisch & Patterson (1988) as transposition cleavage (see Fig. 5.6c).

Chapter 6

QUANTITATIVE/STATISTICAL ANALYSIS OF QUARTZITE MICROSTRUCTURES IN THE SHEAR ZONES

6.1. Introduction

The importance of detailed studies of microstructures of quartz (and quartzite) in rocks within and adjacent to thrust faults and shear zones of orogenic belts is well recognised (e.g. Bailey *et al.* 1994 and Kirschner *et al.* 1995). This is because quartz is a sensitive indicator of variations of strain orientation and intensity as well as of the rate controlling deformation mechanisms operating (e.g. Etheridge & Wilkie 1979 and O'Hara 1988 & 1990). It may also reveal important information regarding the temperature, fluid activity and strain rate during deformation (e.g. Simpson 1986, Urai *et al.* 1986 and Hirth & Tullis 1992). These features along with the ability of these rock types to easily pick up even small amounts of deformation make them some of the most reliable rocks to analyse and document the deformational history from within the fold-thrust belts (e.g. Law *et al.* 1984, Law *et al.* 1987, and Dunlap *et al.* 1995).

A study of quartzite microstructures has been carried out on selected samples of quartzofeldespathic rocks of the Stonyfell Quartzite, along the structural transects from outside the shear zones towards the lower boundary thrusts of the shear zones. Oriented specimens were collected and cut parallel to the stretching lineation and perpendicular to cleavage (the XZ plane of the local finite strain). These samples are also those that were used for the determination of finite strain in chapter 4 (also see appendix A for their localities). The aim was to investigate the deformation processes operating in the quartzites, which were affected mainly by grain-scale microstructural changes across the shear zones. These microstructural changes were also compared with possible changes in conditions of deformation across the shear zones. It was also planned to integrate analysis of deformation mechanisms with geometrical evolution of fabrics

and structures.

In this chapter the deformational behaviour and microstructural development of individual grains of quartz and feldspar from the selected transects are presented and discussed to determine deformation mechanisms acting on the shear zones and possible changes across them. Subsequently, a statistical analysis of grain-scale microstructures is also presented to quantitatively analyse deformation processes that have been operating. Finally, the deformation conditions and history of the quartzite rocks discussed are used to demonstrate and document the spatial and temporal evolution of the shear zones.

6.2. The deformational behaviour of quartz and feldspar from within the shear zones

The microstructural development and deformation behaviour of quartz (e.g. Bell & Etheridge 1973, White 1976, Voll 1976, Linker *et al.* 1984, Simpson 1985 and Hirth & Tullis 1992) and feldspar (e.g. Tullis & Yund 1985, 1987, and White & Mawer 1986) has been extensively studied in experimental and in naturally deformed rocks. In spite of this and although quartz is one of the most common minerals in the crust, its deformation behaviour is still not completely understood. This is mainly due to the complex role that water plays in the deformation of quartz where pressure solution is very important, especially at low temperatures and low strain rates (Passchier & Trouw 1995). The deformational behaviour of feldspar is, however, also strongly dependent on metamorphic (i.e. pressure and temperature) conditions (e.g. Tullis & Yund 1991 and Pryer 1993).

In this section the deformational behaviour of quartz and feldspar is examined in selected samples of the Stonyfell Quartzite units from weakly deformed rocks, from outside and/or in the upper transitional zones (sub-zone I), to more deformed and strained rocks near the lower boundary thrusts (sub-zone III) to the shear zones (see Fig. 5.1 for the location of each subzone across the shear zones). Because of the similarities of microstructures from the different shear zones, only three of the recognised shear zones (which have the best outcrops) are studied in more detail and described here. These are (from SE to NW) the Mt. Bold, Pole Road and Morialta shear zones

(Fig. 2.2). Some detailed microstructural description of the other shear zones is also tabulated and presented in table 6.1.

6.2.1. Mt. Bold shear zone

The samples studied were collected from the shear zone (T_2) and its footwall ductile thrust (T_1) (see Fig. 3.14 for their locations). Because of poor outcrops of the Stonyfell Quartzite in the hangingwall ductile thrust (T_3) (Fig. 3.14), no samples of this thrust sheet have been analysed. Here, only detailed microstructures from within the shear zone are presented and discussed and some detailed microstructures from the footwall thrust sheet (T_1) are given in table 6.1.

The modal analyses of quartzite samples collected from within the Mt. Bold shear zone are from the main three sub-zones (samples # M17, M9 & M9I respectively, see appendix A for their locations) and comprise quartz (~85%), feldspar (~15%) and very small amounts of white mica (~0.5%). The sample collected from within the shear zone or sub-zone II (# M9) was located about 200m from the sample collected from the upper transitional zone or sub-zone I (# M17) and about 100m from the sample collected from the lower boundary thrust or sub-zone III (# M9I). Detailed microstructures of each sample are described individually as follows:

Sub-zone I (# M17): in this sample, quartz grains are almost equant (with 890 μm mean grain size) and slightly elongate with lobate and serrated grain boundaries. The grains exhibit patchy to slightly undulatory extinction and grain boundary serration in which small (~20 μm) white mica grains are located. Evidence of recovery in the form of deformation bands is also seen in grains with higher dislocation density (Fig. 6.1a). Feldspar grains are of both, plagioclase (mostly albite) and potassium feldspar (mostly microcline and orthoclase) with approximately the same grain size as the quartz grains. They are almost all fractured and partly altered to white mica or zoisite (see bottom right corner of Fig. 6.1a). They also show weak undulatory extinction.

Sub-zone II (# M9): in this sample, the original quartz grains have a mean grain size of 680 μm and are more elongate than those of sub-zone I, and their grain boundaries are sutured. They show intracrystalline deformation features like sweeping undulatory extinction, deformation

Table opposite:

Table 6.1: General description of the microstructures of quartz and feldspars in quartzite from within the shear zones. Labels; Qtz: quartz, F: feldspar, DB: deformation bands; GBMR: grain boundary migration recrystallisation; SRR: subgrain rotation recrystallisation; SS: subgrain structures, SUE: sweeping undulatory extinction, and SMT: solution mass-transfer. **I, II,** and **III** are the sub-zones of the shear zones.

Shear Zones	Specimens & Sub-zones	Main Mineralogy	Grain Size (μm)		Microstructures	
			Qtz & F	Mica	Quartz	Feldspars
Mt. Bold	M17 (I) Fig. 6.1a	Quartz (~85%), Feldspar (~15%) & White Mica (~0.5%)	890	~20	Patchy to slight undulatory extinction and grain boundary bulging	Interacrystalline fracturing on which feldspars are partly altered to white mica
	M9 (II) Fig. 6.1b	Quartz (~85%), Feldspar (~15%) & White Mica (~0.5%)	680	~20	SUE, DB, SS and GBMR in grains with greater dislocation densities	Slight undulatory extinction (UE) and intracrystalline fractures with little offsets
	M9I (III) Fig. 6.1c	Quartz (~85%), Feldspar (~15%) & White Mica (~0.5%)	790	~20	Increase in the amount of SUE, DB, SS and more evidence of GBMR and in some grains SRR to develop core & mantle structure	Slight UE, intracrystalline fracturing to splitting of the grains into elongate book shape fragments
	M11 (II)	Quartz (~90%), Feldspar (~10%) & White Mica (~0.5%)	870	~20	SUE, DB, SS and development of grain boundary bulging at the margin of some grains which show initiation of GBMR	Slight undulatory extinction and intracrystalline fractures with little offsets along them
	M36 (III)	Quartz (~90%), Feldspar (~10%) & White Mica (~0.5%)	820	~20	SUE, DB, SS, more evidence of GBMR than sub-zone II and in some grains SRR to develop core & mantle structure	Slight undulatory extinction and intracrystalline fractures in which small white mica are precipitated
Pole Road	U10 (I) Fig. 6.2a	Quartz (85-90%), Feldspar (~10-15%) & White Mica (~1%)	570	~30	Random extinction but in some grains slight undulatory extinction & SS	Little evidence of intracrystalline fractures with almost no undulatory extinction
	AC3 (II) Fig. 6.2b	Quartz (85-90%), Feldspar (~10-15%) & White Mica (1-2%)	480	~50	Slightly SUE, DB, SS and on grains with more dislocation density SRR	Slight intracrystalline fracturing and their margins recrystallised to small white mica
	AC2 (III) Fig. 6.2c	Quartz (85-90%), Feldspar (~10-15%) & White Mica (~2%)	440	~200	SUE, DB, SS. Grain boundaries of some grains are sutured to produce SRR and/or with less developed GBMR or are truncated by white mica	Intracrystalline fractures and margin of grains are also truncated by white mica
Norton Summit	G6 (II)	Qurtz (~85%), Feldspar (~15%) & White Mica (~1%)	667	~20	SUE, DB, SS, GB bulging and development of misorientation of subgrains to produce SRR	Slight undulatory extinction and intracrystalline fractures
	G7 (III)	Quartz (~85%), Feldspar (~15%) & White Mica (~1%)	600	~20	SUE, DB, SS and development of core & mantle structure due to SRR and, in less degree, GBMR	Extensive intracrystalline fractures and undulatory extinction
Greenhill	H8 (II)	Quartz (~80%), Feldspar (~10%) & White Mica (~10%)	1100	100-300	In phyllosilicate layers pressure solution products, in quartz rich layers, intracrystalline deformation and recovery such as patchy to SUE, SS	Intracrystalline fracturing on in which feldspars are partly altered to white mica
	H9 (III)	Quartz (~80%), Feldspar (~10%) & White Mica (~10%)	800	100-300	Like sub-zone II but in solution zone grains are ribbon in shape & on the other parts SRR and in less developed GBMR produce core & mantle structures.	Slight undulatory extinction and intracrystalline fracturing on which feldspars are partly altered to white mica
Morialta	MO1 (I) Fig. 6.3a	Quartz (~85%), Feldspar (~10%) & White Mica (~5%)	640	~100	Patchy to slight UE, DB in some grains. Grain boundary serration & bulging and growth of small white mica on the margin of grains	Intracrystalline fracturing and growth of white mica on truncated grain margins
	MO5 (II) Fig. 6.3b	Quartz (~80-85%), Feldspar (~10%) & White Mica (5-10%)	600	100-300	Patchy to slight UE, DB & SS in some grains. Grain boundaries are truncated by flakes of mica. Some grains show beards of small quartz & mica	Evidence of intracrystalline fracturing and growth of white mica on truncated grain margins
	MO4 (III) Fig 6.3c & d	Quartz (~80%), Feldspar (~10%) & White Mica (~10%)	500	~400	Large evidence of SMT such as beards of small quartz & mica, corrosion and truncation of grains by large mica. On some original grains SUE, SS, DB & recrystallised small grains due to SRR	More evidence of intracrystalline fracturing and growth of white mica on truncated grain margins and in intracrystalline fractures

bands and subgrain structures (Fig. 6.1b). Evidence of minor grain boundary migration and recrystallised small grains are also seen around the boundaries of the grains which have greater dislocation density. Feldspar grains as in sub-zone I show slightly undulatory extinction and intracrystalline fractures (middle right side of Fig. 6.1b). Some feldspars show offset along these fractures.

Sub-zone III (# M9I): the mean grain size of this sample is 790 μm and unlike sub-zone II grains are more equant. Two main microstructural changes from the quartz grains of sub-zone II are observed. They are: (i) an increase in the frequency of recrystallised small grains on the margins of original grains, which show the initiation of core and mantle structure, more likely to develop during grain boundary migration recrystallisation (White 1976, Urai *et al.* 1986, and Simpson 1994), and (ii) an increase in the amount of sweeping undulatory extinction and deformation bands (Fig. 6.1c). Evidence of subgrain rotation recrystallisation can also be seen on the margins of some grains. As the microstructures from this sample indicate, it appears that at the lower boundary thrust recrystallisation is achieved by development of subgrain rotation and grain boundary migration representing the dislocation creep regime (Simpson 1985, Urai *et al.* 1986 and Hirth & Tullis 1992). The unexpected slight increase in the value of the mean grain size and the presence of more equant grains with respect to the sample from sub-zone II might show a response to grain boundary surface energy constraints due to annealing recrystallisation (Simpson 1994).

The feldspar grains are almost all fractured and typically display extension and shear fractures, which result in the production of angular and elongate fragments. The feldspar grains as shown in figure 5.6d are split into elongate tabular fragments which have their upper halves offset to the left with respect to their lower halves along synthetic low-angle normal microfractures (Pryer 1993, and Simpson 1994). As mentioned earlier in chapter 5, these microstructures indicate overall top to the NW sense of shear movement for the Mt. Bold shear zone.

Figures opposite:

Fig. 6.1: Photomicrographs of quartzite collected from the Mt. Bold shear zone. Thin sections cut parallel to the stretching lineation and perpendicular to the cleavage; all photomicrographs crossed polars and their width of view=3 mm.

Fig. 6.1a: Slightly deformed quartzite from sub-zone I. Note weak intracrystalline deformation and grain boundary bulge.

Fig. 6.1b: More deformed quartzite from sub-zone II. Note greater development of intracrystalline features like deformation bands (DB) and subgrains (SG).

Fig. 6.1c: More highly deformed quartz from sub-zone III. Note widespread development of recrystallised small grains at the margin of original grains.

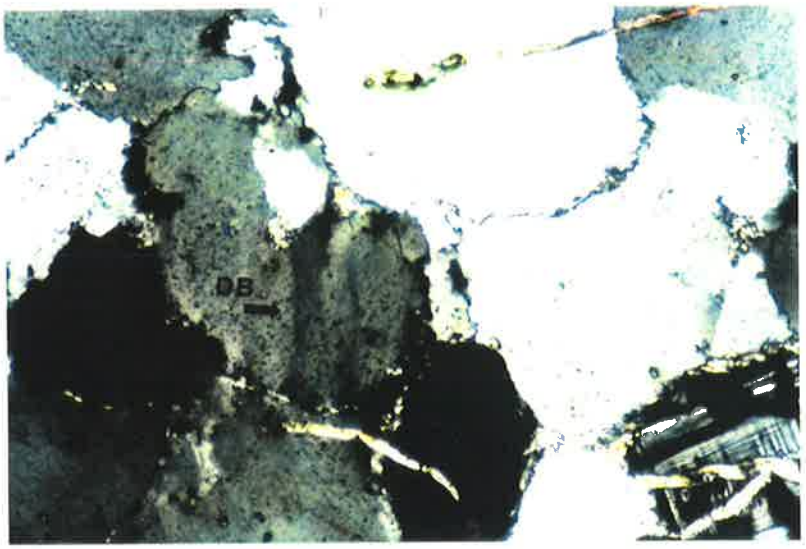

a

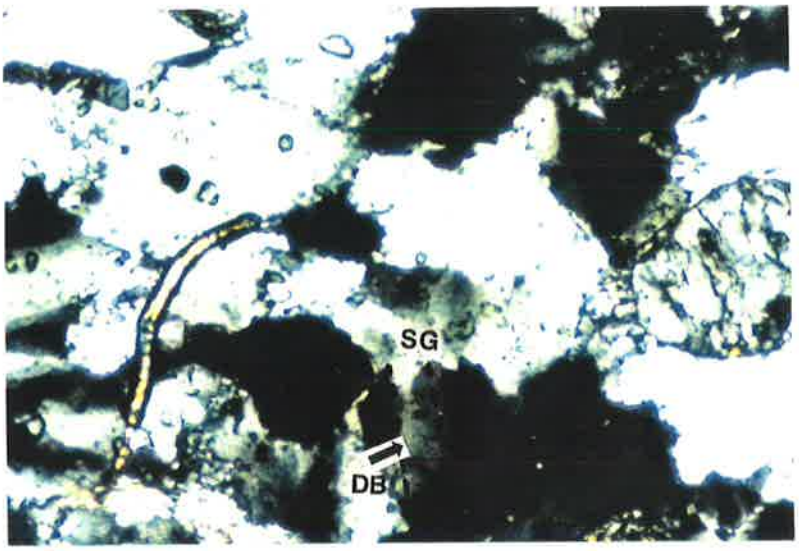

b

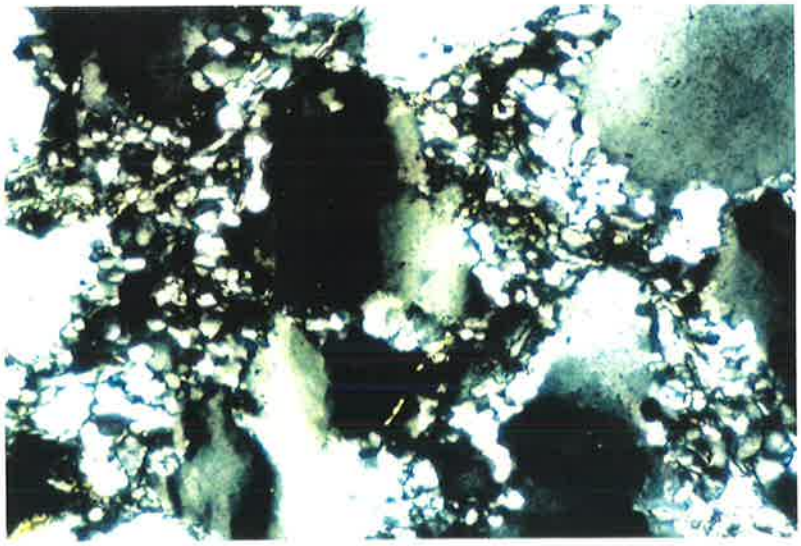

c

6.2.2. Pole Road shear zone

Three samples of the Stonyfell Quartzite were collected from three sub-zones of the Pole Road shear zone (see appendix A for their locations). Two were from the Ackland Hill Road from within the shear zone (#'s AC3 & AC2) and the other one from outside but approaching the transitional zone (sub-zone I) (# U10). Mineral assemblages of the three samples are almost identical and comprise quartz (85-90%), feldspar (~15%) and small flakes of white mica (~1%).

In **Sub-zone I** (# U10), quartz grains are almost equant and polygonal to slightly elongate with a mean grain size of 570 μm. Grain boundaries are lobate to slightly serrated with the development of overgrowths (see arrows in Fig. 6.2a). Random extinction is a characteristic feature of these grains though grains with greater dislocation densities display slightly undulatory extinction and subgrains (see for example the grain labelled with "UN" in Fig. 6.2a). Feldspars show little evidence of intracrystalline fracture with almost no undulatory extinction.

In **Sub-zone II** (# AC3), a sample was collected from within the shear zone but closer (about 100 m) to the transitional zone. Quartz grains, with a mean grain size of 480 μm are polygonal to slightly elongate and their boundaries are serrated. Evidence of intracrystalline deformation is indicated by undulatory extinction, deformation bands and subgrain formation, which are seen in almost all grains. Grains with higher dislocation density exhibit sutured grain boundaries and development of small (~50 μm in diameter) recrystallised grains on the margin of original grains (see the grains labelled with "RE" in the middle of Fig. 6.2b). Small (~50 μm in length) white micas are also developed on the margins of original quartz grains (Fig. 6.2b). Feldspars, which are almost all K-feldspars, show slight intracrystalline fracturing (~100 μm in size) and are almost entirely marginally recrystallised to small (~30 μm) white micas.

In **sub-zone III** (# AC2), a sample was collected from near the lower boundary thrust (about 20m away). Quartz grains are more elongate than those of sub-zone II. The grain size is also decreased to a mean value of 400 μm. Sweeping undulatory extinction, deformation bands and subgrain formation are seen in all quartz grains. Grain boundaries of some grains are almost all

Figures opposite:

Fig. 6.2: Photomicrographs of quartzite collected from the Pole Road shear zone. Thin sections cut parallel to the stretching lineation and perpendicular to the cleavage; all photomicrographs crossed polars and their width of view=3 mm.

Fig. 6.2a: Undeformed to slightly deformed quartzite from sub-zone I. Note random intracrystalline extinction (UN) and development of overgrowths (arrows).

Fig. 6.2b: More deformed quartzite from sub-zone II. Here, quartz grains are more deformed to develop small recrystallised grains (RE) which shows initiation of core and mantle structures.

Fig. 6.2c: More highly deformed quartz from sub-zone III. Note greater development of core and mantle structure and also development of phyllosilicates to form spaced cleavage.

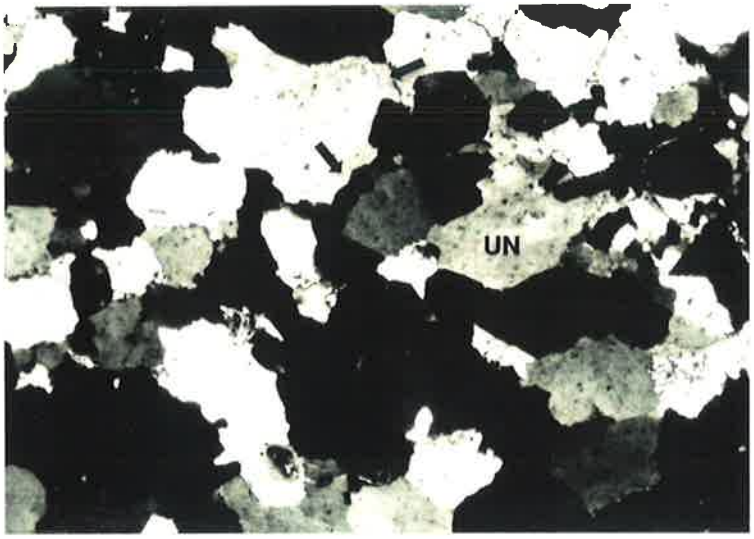

a

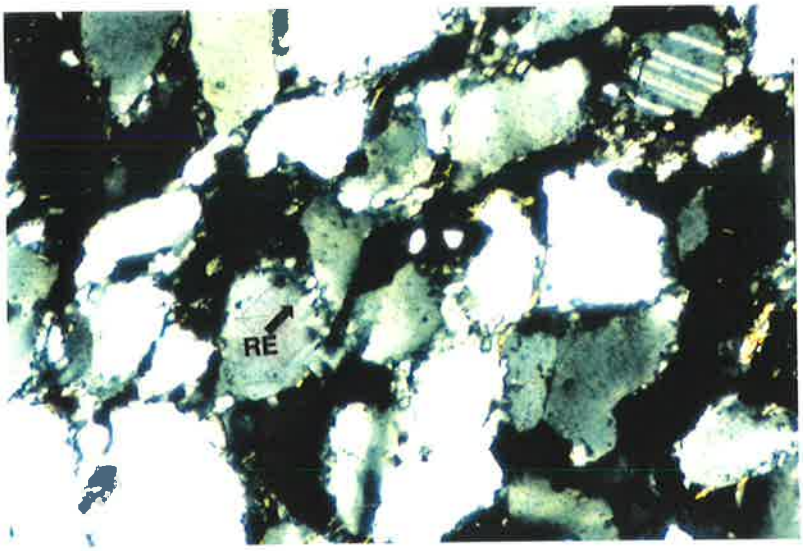

b

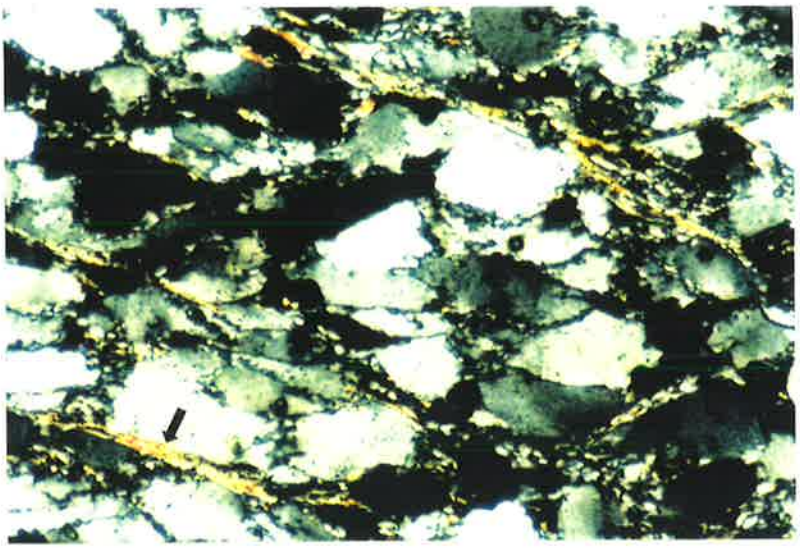

c

entirely sutured and small recrystallised quartz grains are also seen on the margin of original grains, showing the initiation of core and mantle structures (e.g. Simpson 1985, Urai *et al.* 1986, and Hirth & Tullis 1992). These small (~50 μm in diameter) recrystallised grains (Fig. 6.2c) were mostly produced by subgrain rotation recrystallisation (Simpson 1994). Larger white micas, with respect to sub-zone II, with a grain size of about 200 μm, are also seen in this sample. These grains are almost all aligned parallel to the alignment of elongate quartz grains and define the cleavage zones. Where these white micas exist, they truncate quartz grain margins (arrow in Fig. 6.2c) and show microstructural evidence similar to microstructures found within the psammites (Fig. 5.3c) being developed by the solution mass-transfer deformation mechanism (e.g. Eliott 1973, Gray 1978, and Simpson 1994). Feldspars show evidence of intracrystalline fractures in which small white mica flakes also grew.

6.2.3. Morialta shear zone

Like the Mt. Bold shear zone the Morialta shear zone also has good outcrops of the Stonyfell Quartzite unit from sub-zone I through to sub-zone III. The locations of three samples collected from within these three sub-zones of the shear zone, are shown in appendix A. The mineral grains of the samples comprise quartz (~80-85%), feldspar (~10%) and white mica (5-10%). The amount of white mica in sub-zone I is less than that in sub-zone III.

The overall microstructural development within this shear zone is similar to that of the Pole Road shear zone. However, an increase in the amount of white mica, (which is most likely due to sample impurities) produces different microstructures in this shear zone, where evidence of solution mass-transfer microstructures is substantially increased.

In **sub-zone I** (# MO1), a sample was collected from the upper transitional zone. Quartz grains are polygonal to slightly elongate with a mean grain size of 640 μm. They show evidence of intracrystalline deformation features like patchy to slightly undulatory extinction and, in grains with higher dislocation density, there are deformation bands. Grain boundary serration and bulging as well as growth of small white mica on the margins of original grains are also seen (Fig. 6.3a). These small white micas are aligned subparallel to slightly elongate quartz grains and

Figures opposite:

Fig. 6.3: Photomicrographs of deformed quartzite collected from within the Morialta shear zone and associated hangingwall ductile thrust. Thin sections cut parallel to the stretching lineation and perpendicular to the cleavage; all photomicrographs crossed polars and their width of view=3 mm.

Fig. 6.3a: Slightly deformed quartzite from sub-zone I. Note low intensity of intracrystalline deformation and weak development of phyllosilicates which define initiation of a spaced cleavage.

Fig. 6.3b: More deformed quartzite with greater development of pressure solution products from sub-zone II. Note development bearded overgrowths (BO) and truncation of grains boundaries (T) by oriented phyllosilicates.

Fig. 6.3c: More highly developed pressure solution process in phyllosilicate rich layer of a sample from sub-zone III. Note increasing development of cleavage domains and bearded overgrowths (BO).

Fig. 6.3d: Highly deformed quartz grains in quartz rich layer of a sample from sub-zone III. Note development of small recrystallised grains due to subgrain rotation recrystallisation (SRR) around the margin of original grains.

Fig. 6.3e: Fractured feldspar with development of slight intracrystalline deformation in sample from sub-zone III.

Fig. 6.3f: Intracrystalline fracturing in quartz from the hangingwall ductile thrust of the shear zone. These fractures are not much later fractures because there is no evidence of this type of fracture in samples from within the shear zones.

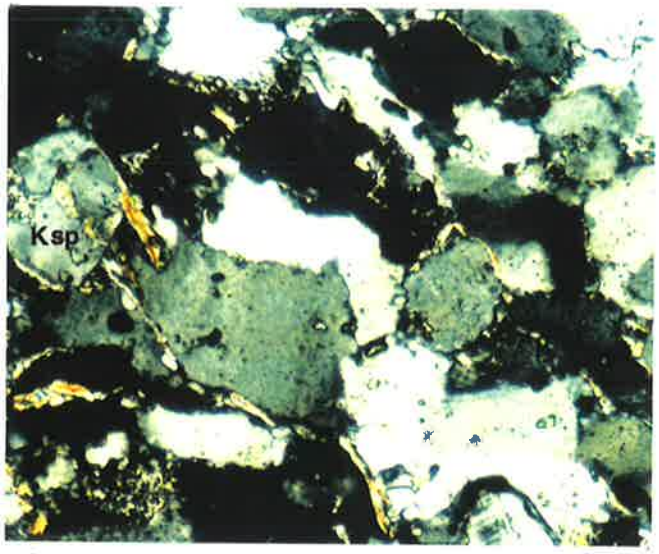

a

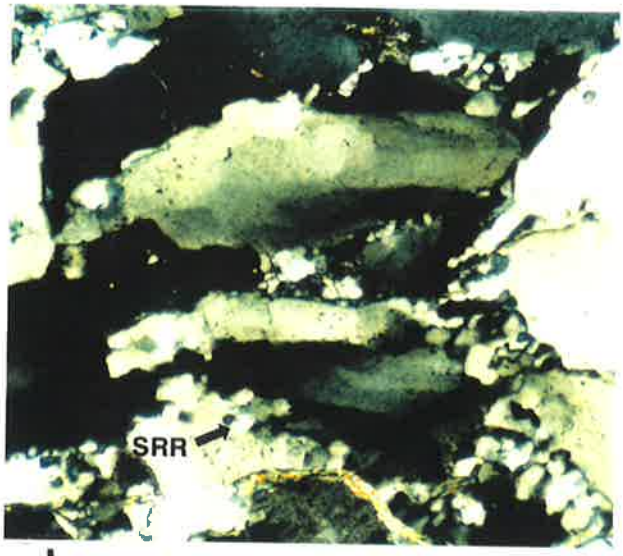

d

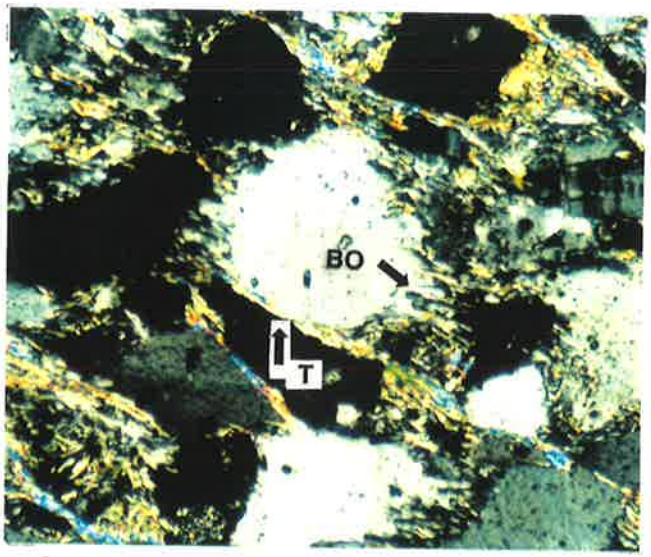

b

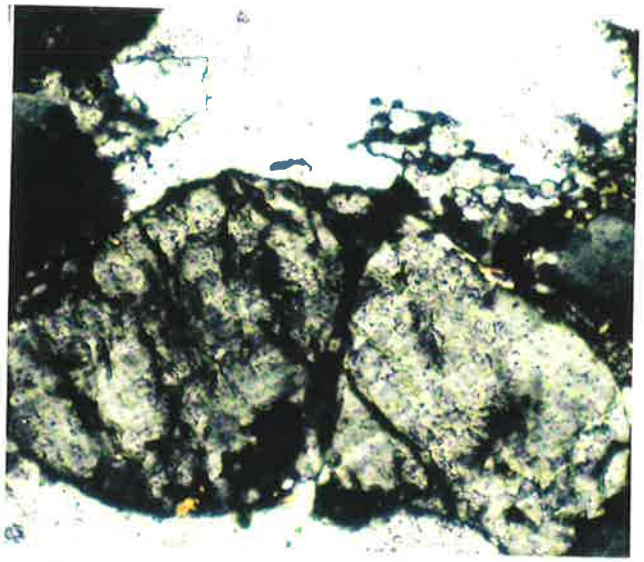

e

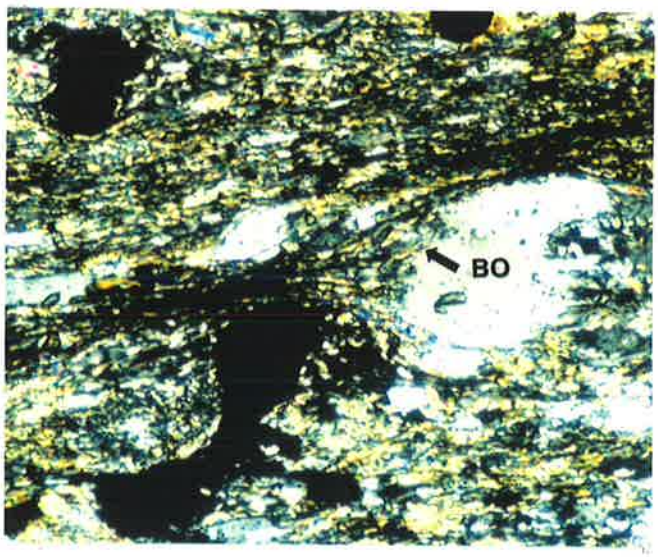

c

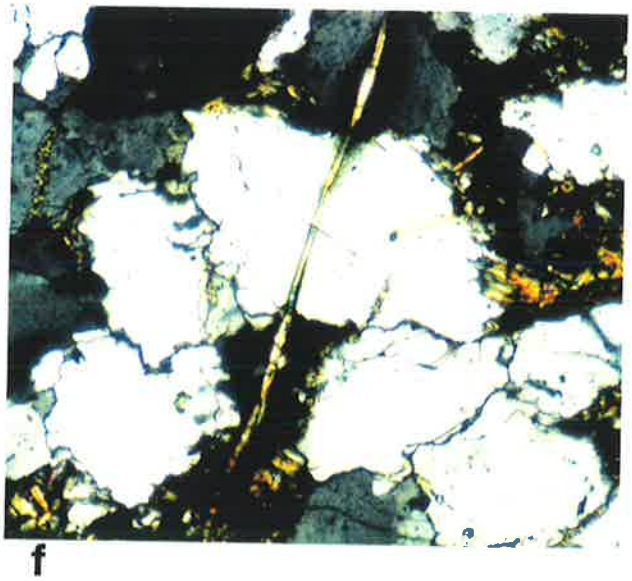

f

may define the cleavage. Feldspars show intracrystalline fractures in which the white mica grains are almost entirely located (see the grain at the left middle side of Fig. 6.3a, labelled with "Ksp").

In **sub-zone II** (# MO5), a sample was collected from within the shear zone at a distance of about 150m from the lower boundary thrust. Like sub-zone I, quartz grains are polygonal to slightly elongate with a mean grain size of 600 μm. They also show evidence of intracrystalline deformation features such as patchy to slightly undulatory extinction and, in grains with greater dislocation density, deformation bands and subgrains. Where there are increased impurities in the quartzite, the amount of intracrystalline deformation of quartz grains decreases and their grain boundaries are sutured to develop beard-like overgrowths or are truncated by flakes of white mica (Fig. 6.3b). Truncations are seen on the margin of most grains, which are sub-parallel to the white mica flakes. On the other margins, however, small (50 μm in average) 'beards' of white mica and small (~50 μm) recrystallised quartz grains are also located (see white quartz grain in the middle part of Fig. 6.3b).

In **sub-zone III** (# MO4), from the sample collected, quartz grains have a mean grain size of about 500 μm. Grain sizes of quartz in layers associated with phyllosilicates (Fig. 6.3c) are smaller than in quartz rich layers (Fig. 6.3d). Like the sample in sub-zone II, the quartzite is impure and it is actually a micaceous quartzite. The presence of more impurities in the sample from this subzone than from the sample of sub-zone II, cause the impure parts to be much more influenced by microstructures similar to the microstructures develop in psammites (Fig. 5.3c) due to the solution mass-transfer process (compare Fig. 6.3c with Fig. 6.3b). In micaceous quartzite layers the margins of quartz grains are sometimes truncated by larger (up to 400 μm in length) mica flakes and/or are broadly corroded where 'beards' of small recrystallised quartz grains and white mica are located (Fig. 6.3c). In more pure quartzite layers, subgrain formation, sweeping undulatory extinction and grain boundary serration are also seen on these quartz grains. In quartz grains with higher dislocation density, recrystallised small grains formed due to subgrain rotation recrystallisation (Hirth & Tullis 1992 and Simpson 1994) are also developed (Fig. 6.3d). In coarser grained layers (with less phyllosilicate), quartz grains may enclose mica and may also pin quartz grain boundaries. Feldspars, some of which are perthitic orthoclase, are

also truncated and marginally recrystallised to small quartz grains and mica. Intracrystalline fracturing is also seen in feldspar grains (Fig. 6.3e).

6.2.4. Summary of the deformational behaviour of quartz and feldspar in the shear zones

The detailed study of microstructures from the Stonyfell Quartzite adjacent to and within the shear zones show that from sub-zone I to sub-zone III, ie. from outside through the upper transitional zone and toward the lower boundary thrust to all of the shear zones, the amount of deformation revealed by microstructural changes increases (see also Table 6.1 for comparison). This change in deformational behaviour is more evident in quartz grains while the feldspar grains almost all display intracrystalline fracturing. The amount of intracrystalline fracturing of feldspar grains also increases within the shear zone from sub-zone I to sub-zone III and across the shear zones from the Morialta to the Mt. Bold shear zones (compare microstructures of feldspars across the shear zones in table 6.1).

In sub-zone I, quartz grains show equant polygonal to slightly elongate grains and their boundaries are bulged or misoriented. Growth of small white micas on the margins of quartz grains, especially in the Morialta shear zone, are also seen (Fig. 6.1a). The grains also exhibit intracrystalline deformation features like patchy to slight undulatory extinction. The types of quartz microstructures from within this sub-zone are coincident with microstructural development of experimentally deformed quartz at the first stage of shearing (Simpson 1994) or in regime one of Hirth and Tullis (1992).

In sub-zone II, quartz grains exhibit sweeping undulatory extinction, deformation bands, subgrain formation and small recrystallised grains on the margin of original grains with increased dislocation density (Fig. 6.1b). Such microstructures show that the rate of dislocation climb becomes more effective in sub-zone II and the amount of dislocation climb may be sufficiently rapid to accommodate the recovery. This type of microstructure is similar to the microstructures developed in regime two of the experimentally deformed quartzites of Hirth and Tullis (1992), in which a subgrain rotation microstructure is suggested to be responsible for recovery at moderate

temperatures or slow strain rates (Urai *et al.* 1986, Hirth and Tullis 1992, and Simpson 1994). In the Morialta shear zone, truncation of quartz grain boundaries against flakes of white mica and the existence of small beards of white mica and small recrystallised quartz grains show that a solution mass-transfer process is also active in this shear zone. The amount of intracrystalline fracturing in feldspar also increases in this sub-zone, while displacements across these fractures are rare.

In sub-zone III, the amount of recrystallised small grains on the margins of original grains is enhanced (Fig. 6.1c) and leads to development of core and mantle structures (White 1976). In naturally and experimentally deformed quartzite, progressive misorientation of subgrains or subgrain rotation recrystallisation and grain boundary migration recrystallisation is considered to be responsible for development of core and mantle structures (Urai *et al.* 1986, Hirth & Tullis 1992, Simpson 1994, Passchier & Trouw 1995, and Kirschner *et al.* 1995). These microstructures are almost identical to microstructures developed in regime three of Hirth and Tullis (1992) in experimentally deformed quartzites in which dislocation climb is sufficiently high to control recovery at high temperature or lower strain rate.

Comparison of microstructures from the Mt. Bold and Morialta shear zones (Table 6.1) shows that the core and mantle structure in the Morialta shear zone is achieved by greater subgrain rotation recrystallisation than in the Mt. Bold shear zone. Similarly, general evidence of solution mass-transfer deformation mechanisms such as beards containing white mica and small quartz grains is also seen in the Morialta shear zone. Feldspar grains show increasing amounts of intracrystalline fractures in which the margins of feldspars are displaced to produce bookshelf structures (Passchier 1982, and Pryer 1993) (for example see Fig. 5.6c).

6.3. Qualitítive analysis of microstructural quartz grain geometry

A study of the variation of grain size, grain shape (aspect ratio) and shape preferred orientation (ø) has been made to demonstrate and tentatively quantify development of microstructures from within the Stonyfell Quartzite unit in the Adelaide Hills shear zones (Figs. 6.4 & 6.5). The comparison of these parameters has also been performed across the Mt. Bold, the Pole Road and

the Morialta shear zones to integrate the results with these microstructural analyses. Measurement of the parameters was carried out on photomicrographs which were taken from the oriented (XZ) thin sections. These thin sections were the ones that were also used for finite strain analyses and studies of the deformational behaviour of the quartz and feldspar grain microstructures from within the Stonyfell Quartzite unit (see appendix C for more detail of the method and measurement).

6.3.1. Grain size analysis

The histograms of log-normal grain size (Figs 6.4a & b) show the distributions of the values of mean and median grain size of each sample across the shear zones. In almost all the shear zones this value decreases from sub-zone I toward sub-zone III. It can also be seen that there is a general tend to a decrease in grain size from the Mt. Bold toward the Morialta shear zones (see also Table 6.1).

Scatter graphs of long axis versus short axis length for each sub-zone across most of the shear zones were constructed and their regression lines and R^2 (the goodness-of-fit statistic which is often used to convey the quality of a regression line) were also calculated (Figs 6.4a & b). These graphs demonstrate: (1) the distribution and proportion of grain size reduction between larger and smaller detrital grains and (2) the variation in distribution of long axis and short axis length. As can be seen on figures 6.4a & b, across all the shear zones from sub-zone I to sub-zone II, the larger grains appear to undergo greater grain size reduction than the smaller ones. For instance, in the Pole Road shear zone, from sub-zone I to sub-zone II the values of log-long axis (L) and log-short axis (W) of most of the larger grains is reduced (by about 10% in size), while of the smaller grains remain constant. Continuing to sub-zone III, however, the size of the smaller grains is also decreased (by about 15% in size) (e.g. see the graphs of the Pole Road shear zone in Fig. 6.4a and of the Morialta shear zone in Fig. 6.4b).

Similarly, the range of distribution of the values of long axis versus short axis lengths from sub-zone I to sub-zone III across most of the shear zones varies systematically. This can be

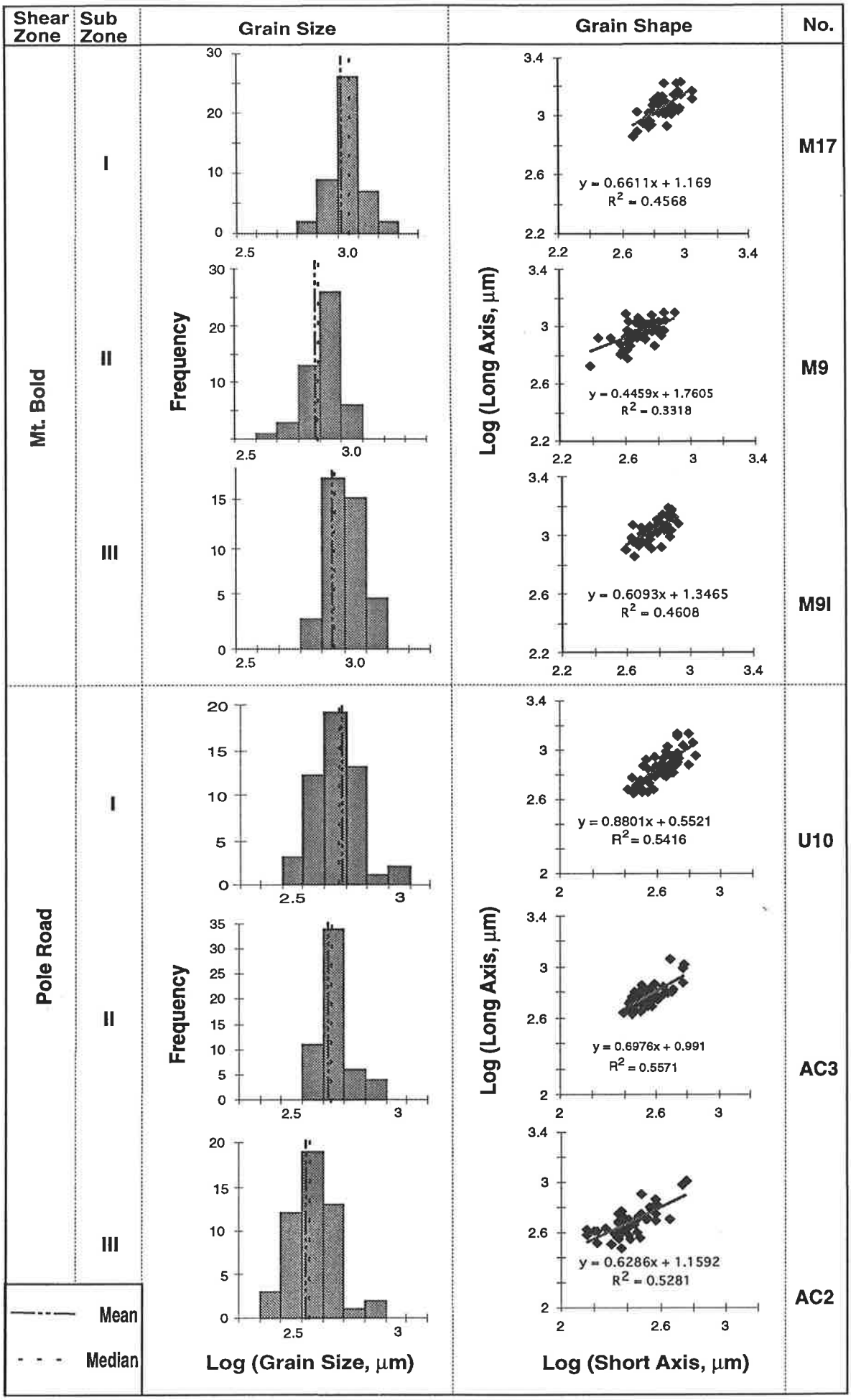

Fig. 6.4a: Histograms and scattergrams of the distribution of grain sizes and grain shapes of the quartzite from within the Mt. Bold and Pole Road shear zones. Note decrease in the mean value of grain sizes from sub-zone I to sub-zone III in each shear zone.

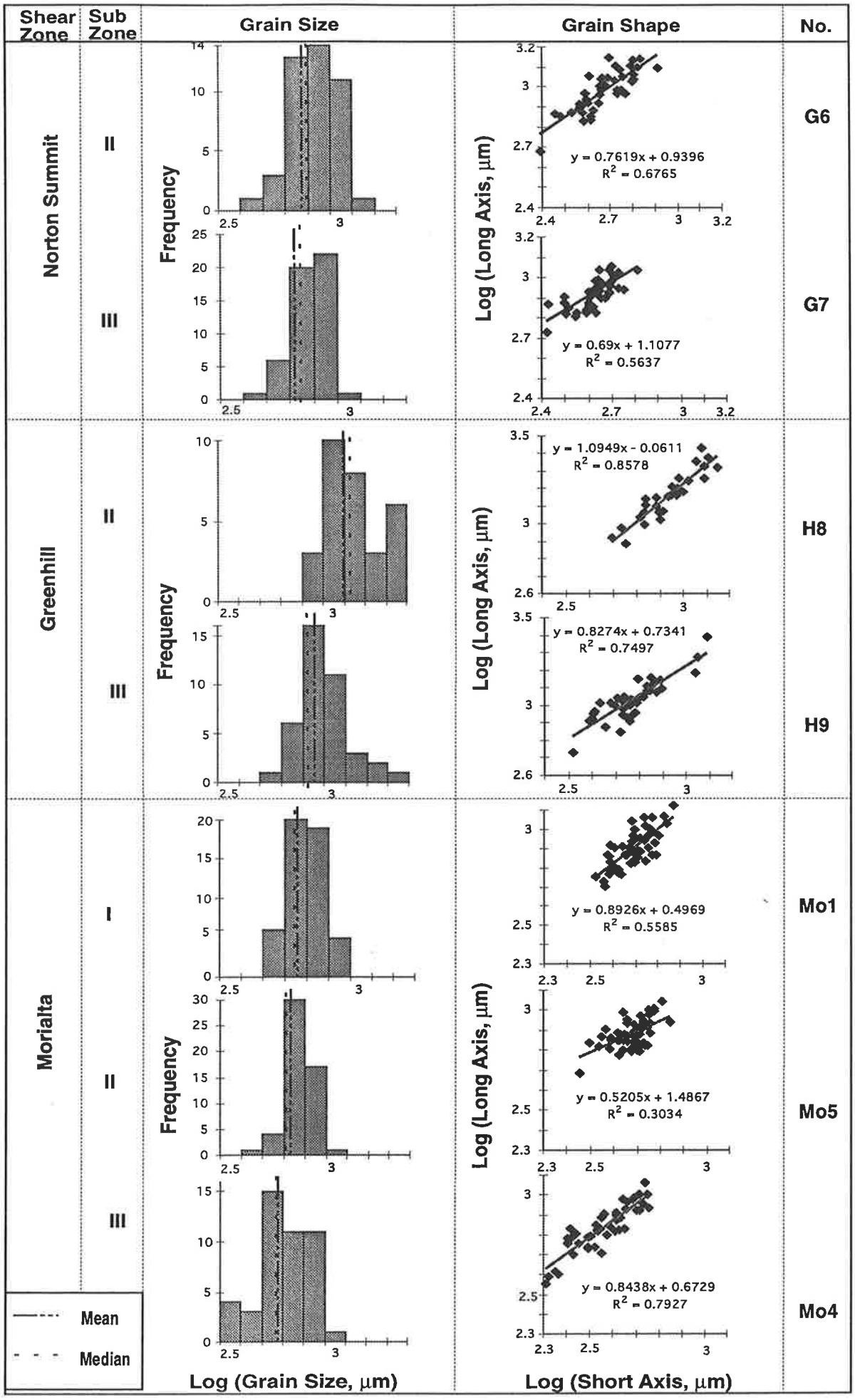

Fig. 6.4b: Histograms and scattergrams of the distribution of grain sizes and grain shapes of the quartzite from within the Norton Summit, Greenhill, and Morialta shear zones. Note decrease in the mean value of grain sizes from sub-zone I to sub-zone III in each shear zone.

demonstrated by a decrease in the value of "b" (gives the gradient of the regression line) and an increase in the value of "a" (gives the intercept of the regression line on the y axis) in the calculated and constructed regression line functions (Y=bX + a, the equation of the best fit regression line), which cause a decreases in the slope of the regression lines (Figs 6.4a & b). For example, in samples from Pole Road shear zone (Fig. 6.4a) the value of "b" decrease from 0.8801 in sub-zone I to 0.6286 in sub-zone III. Considering reduction of the grain size across the shear zones from sub-zone I to sub-zone III, the decrease in the slope of the trend lines implies that the values of short axes decreases more than the values of the long axes.

6.3.2. Grain shape (aspect ratio) analysis

The grain shape distributions (Figs 6.5a & b) show that the aspect ratio of grains increases from sub-zone I to sub-zone III in each shear zone and all samples have an average range varying between 1.6 to 2.0. It also shows that across all the sub-zone III's of the shear zones this average is almost invariant. The slightly higher value for the aspect ratio in samples from sub-zone I (e.g. the Mt. Bold shear zone) may be due either to regional deformation or to a shape effect of the original grains due to synsedimentary compaction.

6.3.3. Shape-preferred orientation (Ø) analysis

The histograms of figures 6.5 (a & b) display the distribution of the values of Ø (the angle between long axes of grains and the reference frame) across the shear zones. These values in all samples were measured with respect to bedding. As can be seen in figures 6.5 (a & b), in almost all samples especially in samples from the Morialta, Pole Road, and Mt. Bold shear zones there is a variation in the degree of shape-preferred orientation of the grains across the shear zones from sub-zone I to III. Similarly, long axis orientation of the grains in most samples (e.g. samples from the Pole Road shear zone and especially the ones from sub-zone III) show a symmetrical distribution about the plane of the tectonic fabric. However, samples with a weak long axis orientation about the plane of tectonic fabric may be interpreted as: (a) representing a pre-existing sedimentary fabric (# M17, Fig. 6.5a) or (b) recording a slightly greater intensity of deformation (possibly # M9I, Fig. 6.5a) or (c) a combination of both of the above (probably #

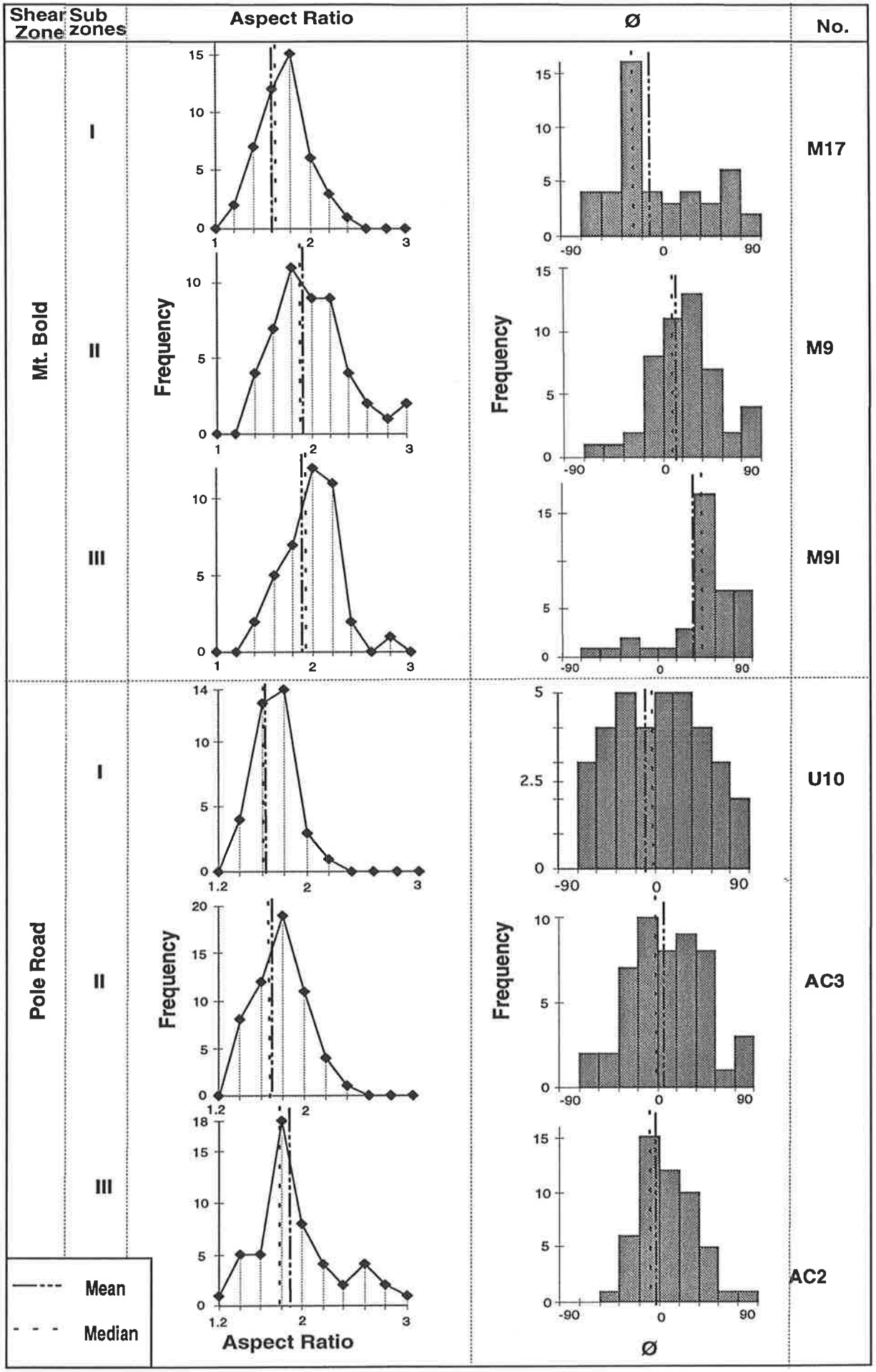

Fig. 6.5a: Linegraphs of the aspect ratio of the grains and histograms of the shape-preferred orientation of the grains in samples of quartzite from sub-zones I to sub-zones III within the Mt. Bold and Pole Road shear zones.

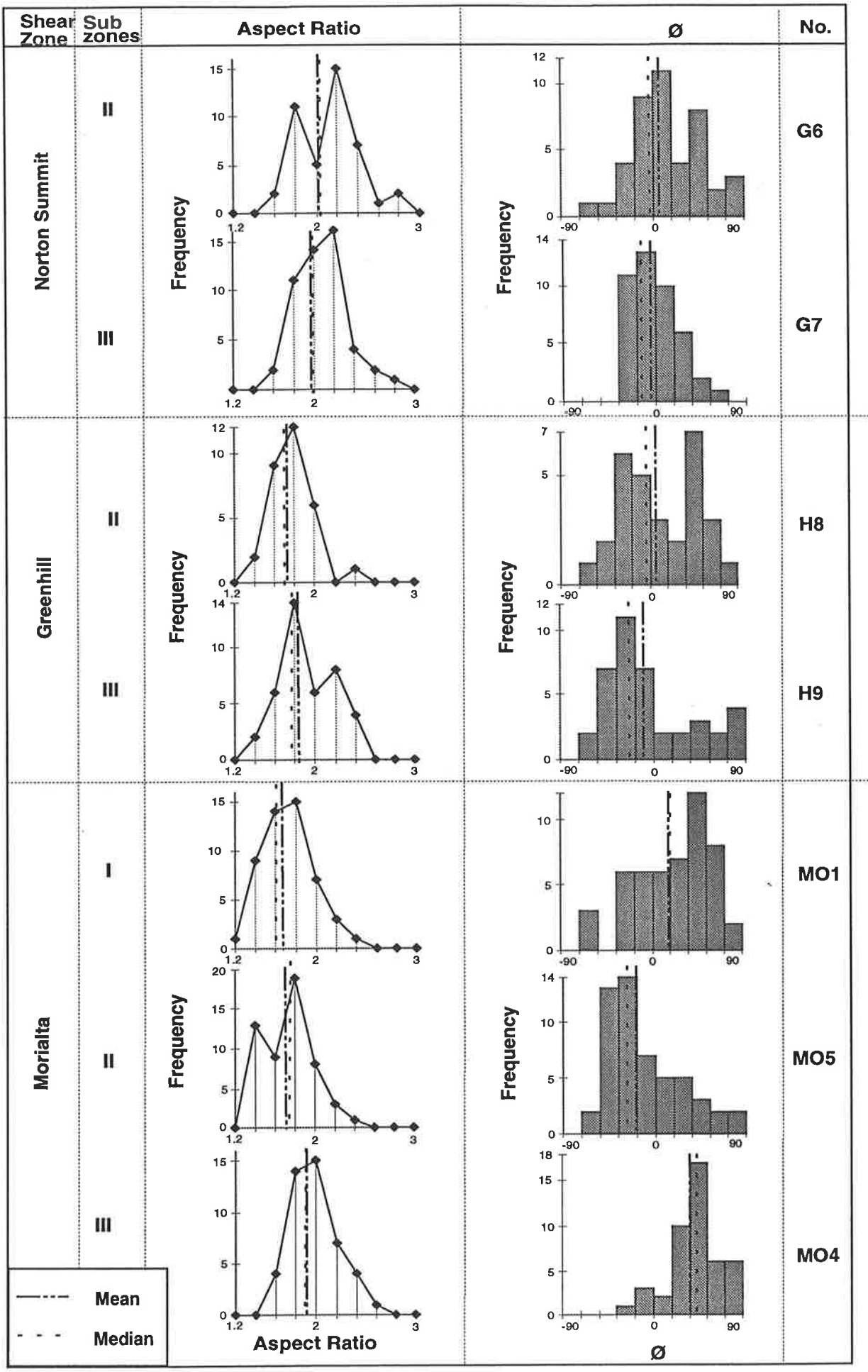

Fig. 6.5b: Linegraphs of the aspect ratio of the grains and histograms of the shape-preferred orientation of the grains in samples of quartzite from sub-zones I to sub-zones III within the Norton Summit, Greenhill, and Morialta shear zones.

H9, Fig. 6.5b).

6.4. Quantitative statistical analysis of the quartz grain configuration data

Evaluation of the grain configuration data was carried out on a number of samples from sub-zone I to sub-zone III across the shear zones. From these qualitative analyses it is concluded that across the shear zones from the outside/transitional zones toward the lower boundary thrusts: (1) the grain size is reduced, (2) the aspect ratio is increased and (3) the shape-preferred orientation of grains is changed. This information was obtained from a few samples from within each shear zone. This is not a complete documentation to allow full decisions to be made about the entire population of the grain configuration variations in each shear zone. It is obviously impossible (because of outcrop limitations) to obtain grain configuration data from the entire population (see also Davis 1986, p 59). To make a rational decision/interpretations about the grain configuration development in each shear zone based on a few samples, which contain only a small portion of the elements in the population, some statements are required about the parameters of a population which are called as statistical hypotheses (Swan & Sandilands 1995, p 91). The way in which these hypotheses are tested and parameters are estimated constitute the subject of statistical inference.

A statistical inference can be made by assuming a scientific hypothesis such as grain configuration development in each shear zone. While it is impossible to evaluate directly the scientific hypothesis (grain configuration development) by observing all members of population, it should be possible to do this indirectly by statistical inference using random sampling of the normal population. To do such a statistical inference, the scientific hypothesis must be first expressed in the form of a statistical hypothesis and then it must be tested by a statistical test. The testing of a statistical hypothesis is the application of an explicit set of rules for deciding whether to accept the "null hypothesis" or to reject it in favour of the "alternative hypothesis". The null hypothesis is the one whose tenability is actually tested while the alternative hypothesis is the statement whose truth we would like to establish (Swan & Sandilands 1995, p 109).

In this section, a test is performed as to whether or not there is any difference between the means of the values of grain size, aspect ratio, and shape preferred orientation within the samples collected from sub-zone I toward sub-zone III of the shear zones. It is necessary to test the null hypothesis that the difference between two population means is equal to 0, with the restriction that in all likelihood the population variances are not known. In fact we compare statistics of two samples against one another, therefore the appropriate test is t-test statistic (Davis 1986, p 64). T-tests are useful for establishing the likelihood that a given sample could be a member of a population with specified characteristics, or testing hypotheses about equivalence of two samples (Davis 1986, p 64, and Kirk 1990, p 378).

Three shear zones (Mt. Bold, Pole Road, and Morialta, where samples were collected from all the sub-zones) were chosen for statistical testing. In all cases, the mean values of grain size, aspect ratio and shape preferred orientations were tested. An f-test was carried out at first to define the population variances of each sample. The f-test is a test for equality of variances for independent samples and is based on a probability distribution (Kirk 1990, p 410). This is the theoretical distribution of values that would be expected by randomly sampling from a normal population (Davis 1986, p 67). The results of the f-tests are shown in appendix D indicating that the samples came from different populations having different variance. Then, a null hypothesis H_0: $\mu_1=\mu_2$, that is, the mean values are equal, was proposed and tested against the alternative hypothesis H_1: $\mu_1\neq\mu_2$, that is, the mean values are not equal. The Microsoft Excel programme (version 5) was used to test the statistical data. The value of the test statistic was calculated using the programme which tells what action to take for each possible outcome for each of the samples. The test procedure, therefore, partitions the possible values of the test statistic into two subsets: an acceptance region for H_0 and a rejection region for H_1, called the critical region. When the value of the test statistic falls in the critical region, then the null hypothesis would be rejected and a final decision regarding the hypothesis would be inducted. This means that there is no significant relationship between the tested samples. The size of a critical region is just the probability (α) which is called the value of significance of the test (e.g. Davis 1986). The value

Grain Size Analysis of the Mt. Bold Shear Zone

Descriptive Statistics

Samples	*M17*	*M9*	*M9l*
Sub-zones	**I**	**II**	**III**
Mean	2.9533118	2.82012125	2.90121248
Standard Error	0.011552	0.01199607	0.01196659
Median	2.9566801	2.82870155	2.90079733
Mode	#NUM!	#NUM!	#NUM!
Standard Deviation	0.0783497	0.08311118	0.07568333
Sample Variance	0.0061387	0.00690747	0.00572797
Kurtosis	-0.023796	1.09877182	-0.7401665
Skewness	-0.1768871	-0.6181919	-0.1197381
Range	0.3451135	0.44298673	0.27851394
Minimum	2.7615952	2.55599978	2.74749959
Maximum	3.1067087	2.9989865	3.02601353
Sum	135.85234	135.36582	116.048499
Count	46	48	40
Confidence Level(95.0%)	0.023267	0.02413295	0.02420468

t-Test: Two-Samples

Samples	*M17- M9*	*M17- M9l*	*M9- M9l*
Hypothesized Mean Difference	0	0	0
df	93	84	87
t Stat	8.0046616	3.12468681	-4.7223619
P(T<=t) two-tail	3.314E-12	0.00244356	8.8663E-06
t Critical two-tail	1.9857998	1.98861017	1.98760972

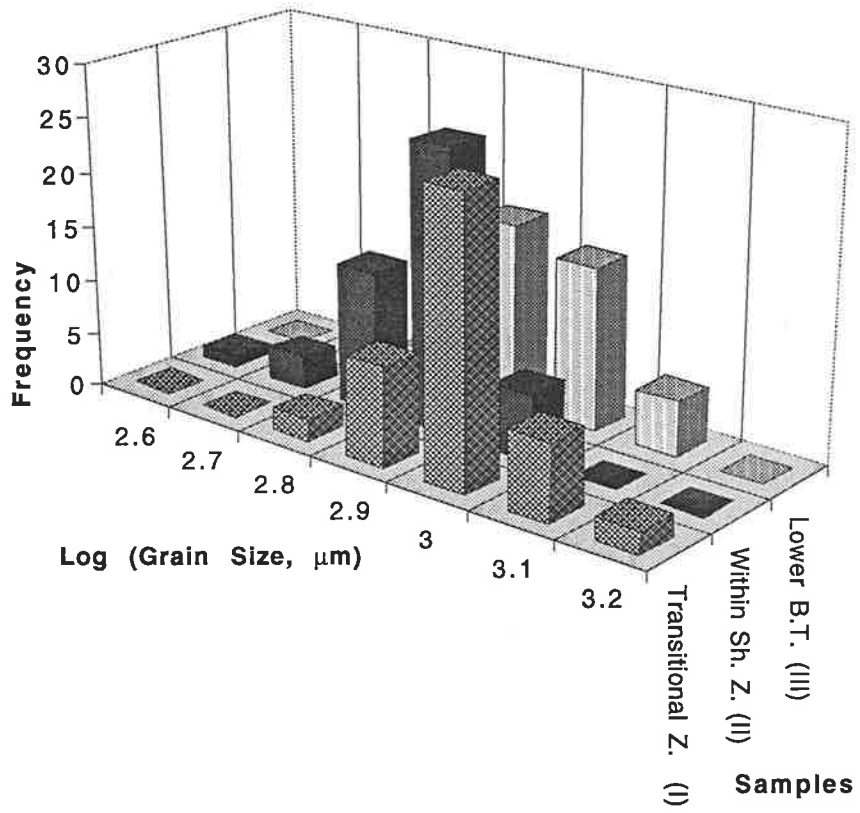

Fig. 6.6a: Descriptive statistics and 3-D histogram of the grain size variations along with the results of the statistical test (t-Test) on grain size variations for samples from the Mt. Bold shear zone.

Grain Size Analysis of the Pole Road Shear Zone

Descriptive Statistics

Samples	*U10*	*AC3*	*AC2*
Sub-zones	*I*	*II*	*III*
Mean	2.746027313	2.655140131	2.55158099
Standard Error	0.014530594	0.01102886	0.015965865
Median	2.740996606	2.640878343	2.541049786
Mode	#NUM!	#NUM!	#NUM!
Standard Deviation	0.103769195	0.081792217	0.112895717
Sample Variance	0.010768046	0.006689967	0.012745443
Kurtosis	-0.52071825	1.707313483	0.905181463
Skewness	0.063622367	1.175234203	0.757127161
Range	0.416532742	0.38171774	0.51891518
Minimum	2.549917758	2.515374105	2.366784489
Maximum	2.9664505	2.897091845	2.885699669
Sum	140.047393	146.0327072	127.5790495
Count	51	55	50
Confidence Level(95.0%)	0.029185568	0.022111553	0.032084588

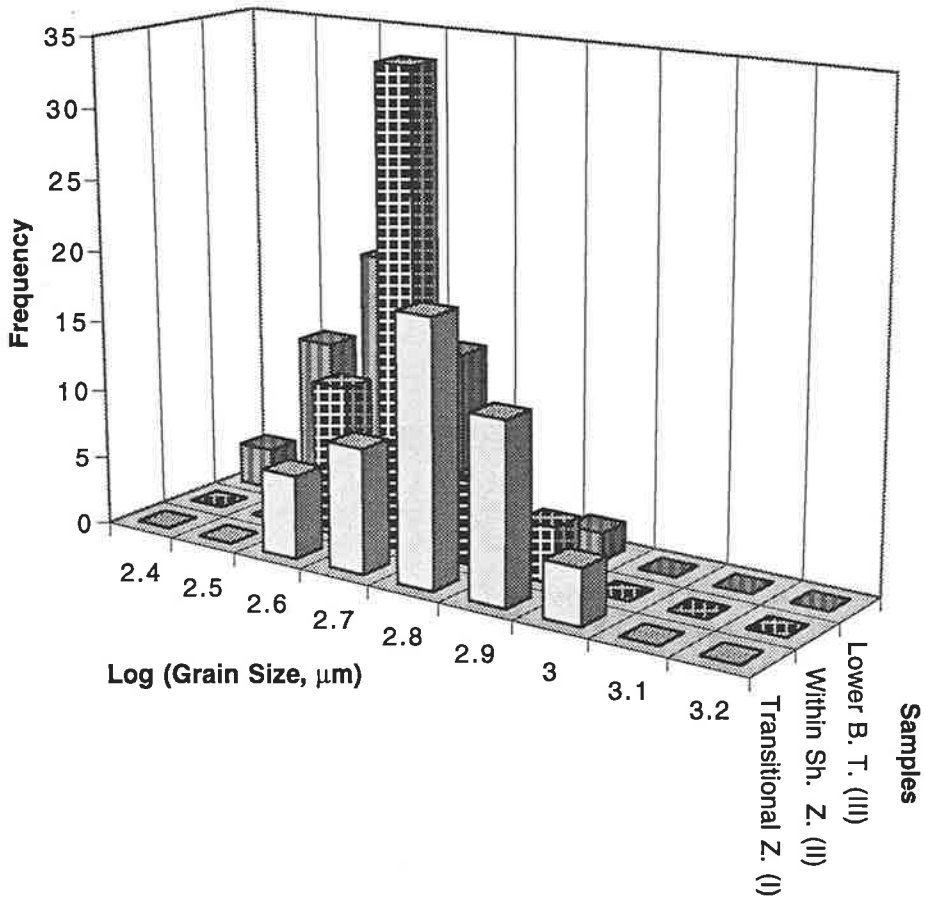

t-Test: Two-Samples

Samples	*U10-AC3*	*U10- AC2*	*AC3-AC2*
Hypothesized Mean Difference	0	0	0
df	104	103	98
t Stat	5.02682172	5.417359619	-9.00709767
P(T<=t) two-tail	2.08628E-06	3.98806E-07	1.72666E-14
t Critical two-tail	1.983034963	1.983262337	1.984467417

Fig. 6.6b: Descriptive statistics and 3-D histogram of the grain size variations along with the results of the statistical test (t-Test) on grain size variations for samples from the Pole Road shear zone.

Grain Size Analysis of the Morialta Shear Zone

Descriptive Statistics

Samples	*MO1*	*MO5*	*MO4*
Sub-zones	*I*	*II*	*III*
Mean	2.795821254	2.775823631	2.698562558
Standard Error	0.011619283	0.008765201	0.017408212
Median	2.793718197	2.766142632	2.713622793
Mode	#NUM!	#NUM!	#NUM!
Standard Deviation	0.082160738	0.063811624	0.116777835
Sample Variance	0.006750387	0.004071923	0.013637063
Kurtosis	-0.257573896	1.243742008	-0.411668057
Skewness	0.08367893	-0.173062406	-0.384736539
Range	0.360705706	0.356246788	0.46989615
Minimum	2.635923502	2.570400193	2.431595462
Maximum	2.996629208	2.926646981	2.901491612
Sum	139.7910627	147.1186524	121.4353151
Count	50	53	45
Confidence Level(95.0%)	0.023349809	0.01758865	0.035083944

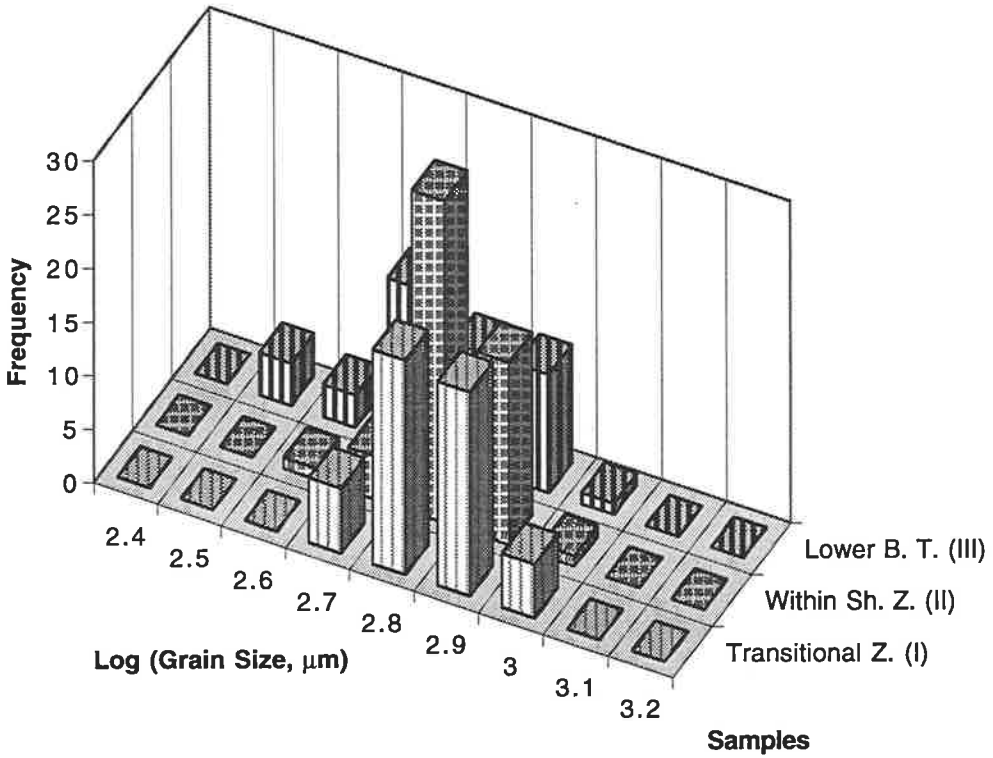

t-Test: Two-Samples

	MO1-MO5	*MO1-MO4*	*MO5-MO4*
Hypothesized Mean Difference	0	0	0
df	92	93	41
t Stat	1.373972401	4.731199427	2.195268425
P(T<=t) two-tail	0.172788584	7.94295E-06	0.033861729
t Critical two-tail	1.986086318	1.985799827	2.01954208

Fig. 6.6c: Descriptive statistics and 3-D histogram of the grain size variations along with the results of the statistical test (t-Test) on grain size variations for samples from the Morialta shear zone.

of α=0.05 is conducted in all the tests which means that 5% decision error, or 95% confidence, is accepted.

6.4.1. Results

6.4.1.1. Grain size

The distribution of grain size variation across the shear zones and the results of the descriptive statistics and statistical tests (t-Test) are shown in figures 6.6 (a, b & c). In each shear zone, the statistical test has been done between samples of sub-zones I-II, sub-zones I-III and sub-zones II-III. As can be seen in figures 6.6 (a, b & c), in all tests the value of test statistics (t Stat) falls in the critical region. This indicates that there is significant difference between the mean values of grain size in the entire population of samples from within the shear zones. This provides supporting evidence to conclude that the reduction of grain size in the shear zones is statistically significant. The very small probability that the values of test statistic [P(T<=t)] less or equal to the critical values confirms that the decision is taken with little risk of error (less than 8%).

6.4.1.2. Grain shape (aspect ratio)

The distributions of mean values across the shear zones (Figs. 6.7a, b & c) shows that the aspect ratios of grains changes and in almost all cases increases from sub-zone I to sub-zone III. Similarly, the value of the test statistic in most tested samples falls into the critical region (Figs 6.7a, b & c). The very low probability that the values of test statistic [P(T<=t)] are less than or equal to the critical values substantially supports the decision that in each shear zone the value of the aspect ratio increases toward the lower boundary thrusts. The values of the test statistic of some samples, however, do not fall in the critical region. In all the cases this happens between samples from adjacent sub-zones. For instance, it occurs between sub-zones II & III in the Mt. Bold shear zone and between sub-zone I & II in the Pole Road and Morialta shear zones. In the case of the Pole Road shear zone, because of the low probability that the value of the test statistic is equal to or less than the critical value, i.e. only 0.15, this low probability was not accepted and a decision was made, with 85% probability, that there are significant differences between the

Aspect Ratio Analysis of the Mt. Bold Shear Zone

Descriptive Statistics

Samples	*M17*	*M9*	*M9l*
Sub-zones	**I**	**II**	**III**
Mean	1.61306522	1.9141571	1.861355
Standard Error	0.03741345	0.0577017	0.04454836
Median	1.63475	1.8679	1.90495
Mode	#NUM!	#NUM!	#NUM!
Standard Deviation	0.25375034	0.4039119	0.28174855
Sample Variance	0.06438924	0.1631448	0.07938224
Kurtosis	-0.1387718	1.3480458	0.92419801
Skewness	0.22935346	0.9531034	0.24291895
Range	1.1253	1.8744	1.4265
Minimum	1.1244	1.2308	1.2739
Maximum	2.2497	3.1052	2.7004
Sum	74.201	93.7937	74.4542
Count	46	49	40
Confidence Level(95.0%)	0.07535455	0.116017	0.09010747

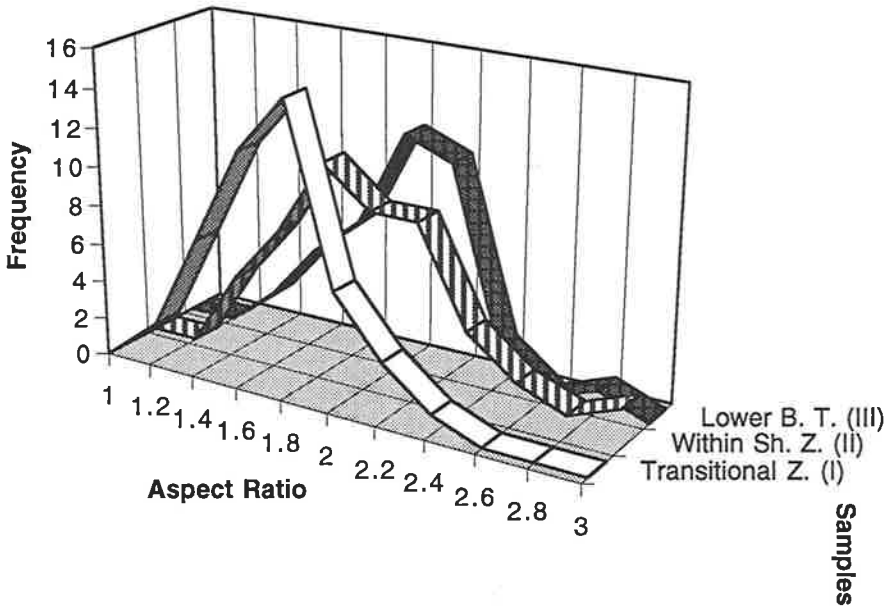

t-Test: Two-Samples

	M17-M9	*M17-M9l*	*M9-M9l*
Hypothesized Mean Difference	0	0	0
df	93	79	85
t Stat	-4.3180425	-4.2679862	0.72433431
P(T<=t) two-tail	3.9317E-05	5.436E-05	0.47084956
t Critical two-tail	1.98579983	1.9904519	1.9882691

Fig. 6.7a: Descriptive statistics and 3-D histogram of the grain shape (aspect ratio) variation analysis along with the results of the statistical test (t-Test) on aspect ratio variations for samples from the Mt. Bold shear zone.

Aspect Ratio Analysis of the Pole Road Shear Zone

Descriptive Statistic

Samples	*U10*	*AC3*	*AC2*
Sub-zone	*I*	*II*	*III*
Mean	1.6153771	1.68274364	1.85823
Standard Error	0.0316688	0.0328211	0.05656761
Median	1.6028	1.6785	1.77645
Mode	#NUM!	#NUM!	#NUM!
Standard Deviation	0.1873551	0.24340779	0.39999341
Sample Variance	0.0351019	0.05924735	0.15999472
Kurtosis	0.206714	0.08108123	0.16167245
Skewness	0.404676	0.38214663	0.70543945
Range	0.8255	1.0804	1.7578
Minimum	1.2512	1.2784	1.1358
Maximum	2.0767	2.3588	2.8936
Sum	56.5382	92.5509	92.9115
Count	35	55	50
Confidence Level(95.0%)	0.0643587	0.0658024	0.1136768

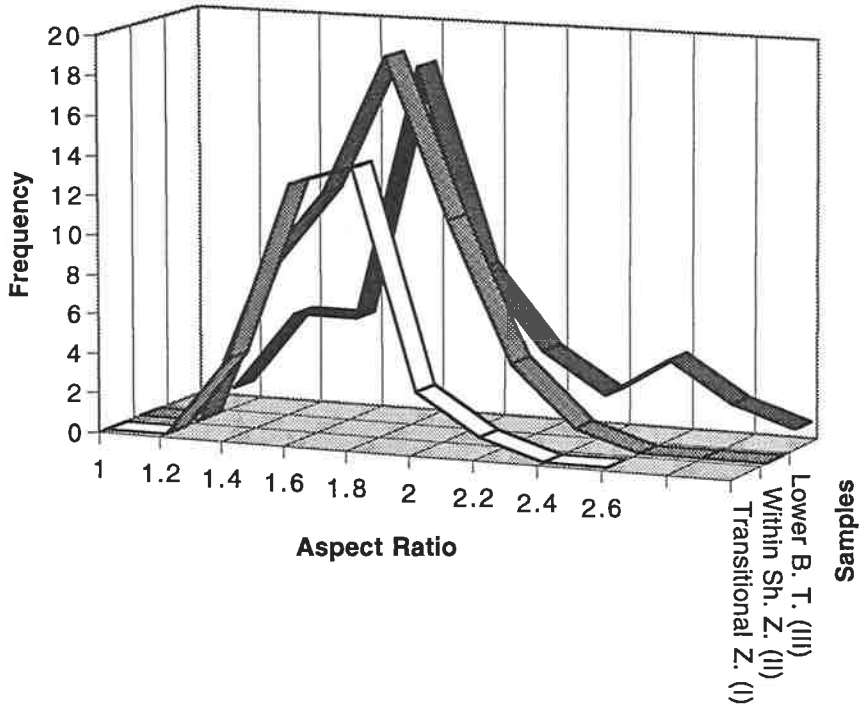

t-Test: Two-Samples

	U10-AC3	*U10-AC2*	*AC2-AC3*
Hypothesized Mean Difference	0	0	0
df	85	83	103
t Stat	-1.4770594	-3.3401874	-2.74325943
P(T<=t) two-tail	0.1433553	0.00125615	0.00717636
t Critical two-tail	1.9882691	1.98896032	1.98326234

Fig. 6.7b: Descriptive statistics and 3-D histogram of the grain shape (aspect ratio) variation analysis along with the results of the statistical test (t-Test) on aspect ratio variations for samples from the Pole Road shear zone.

Aspect Ratio Analysis of the Morialta Shear Zone

Descriptive Statistics

Samples	*MO1*	*Mo5*	*Mo4*
Sub-zones	*I*	*II*	*III*
Mean	1.631338	1.6220415	1.88931778
Standard Error	0.0344975	0.0354834	0.03728316
Median	1.6042	1.6522	1.8846
Mode	#NUM!	#NUM!	#NUM!
Standard Deviation	0.2439342	0.2583232	0.25010301
Sample Variance	0.0595039	0.0667309	0.06255152
Kurtosis	-0.169486	-0.141104	0.24113458
Skewness	0.4851982	0.4042087	0.55461
Range	1.0721	1.0486	1.1537
Minimum	1.1962	1.2117	1.4292
Maximum	2.2683	2.2603	2.5829
Sum	81.5669	85.9682	85.0193
Count	50	53	45
Confidence Level(95.0%)	0.0693253	0.0712027	0.07513926

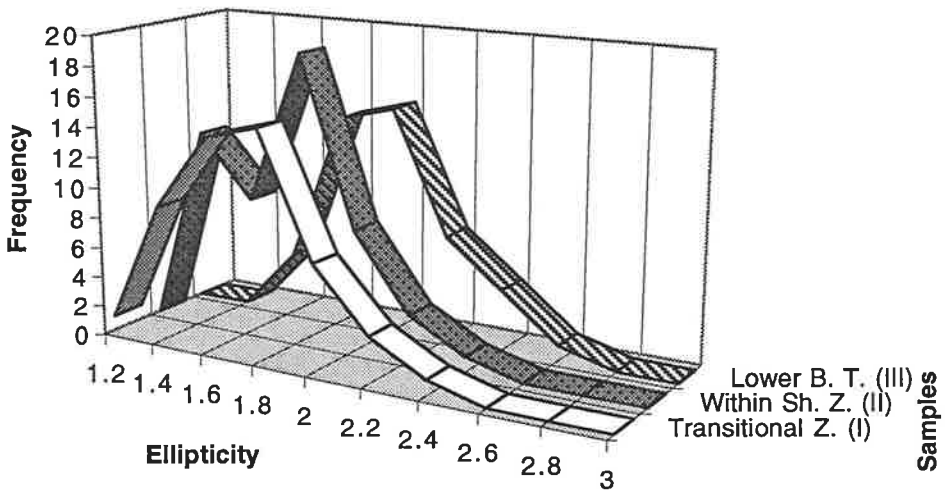

t-Test: Two-Samples

	MO1-MO5	*MO1-MO4*	*MO5-MO4*
Hypothesized Mean Difference	0	0	0
df	101	91	96
t Stat	0.18785	-5.078862	-5.1790801
P(T<=t) two-tail	0.8513711	2.007E-06	1.2275E-06
t Critical two-tail	1.9837307	1.9863774	1.98498583

Fig. 6.7c: Descriptive statistics and 3-D histogram of the grain shape (aspect ratio) variation analysis along with the results of the statistical test (t-Test) on aspect ratio variations for samples from the Morialta shear zone.

mean values of the aspect ratio of the samples. In the case of the Mt. Bold shear zone, as the qualitative analysis of the microstructures showed, the original quartz grains in sub-zone III become larger and more equant than the ones in sub-zone II, which might be due to an increase in the temperature after the stress is removed (Simpson 1994). The Morialta shear zone, however, is the only case where the test displays significant relationships between the samples. The possible reason which can be demonstrated here is that because there are a few mapped ductile thrusts in the hangingwall of the Morialta shear zone (see Figs 2.2 & 3.1), the sample # MO1 of sub-zone I might have been collected from one of these existing but unmapped ductile thrusts and therefore does not show the aspect ratio of typical upper transitional zone sample.

6.4.1.3. Shape-preferred orientation

The mean values of the shape-preferred orientations (Ø) of the quartz grains in each shear zone, as shown by the analysis of the descriptive statistics in figure 6.8 (a, b & c), is different. Similarly, the distributions of the values of the test statistic ["P(T<=t)" in Fig. 6.8a & c) and the values of the critical region ("t Critical" in Fig. 6.8a & c) for the Mt. Bold and Morialta shear zones display significant difference between the samples tested (Figs. 6.8a & c). This demonstrates the effect of shearing processes on changes in the shape-preferred orientation of the grains from within the shear zones. Nevertheless, the statistical test from the Pole Road shear zone, however, shows that there are no significant differences between its samples (Fig. 6.8b), despite a grain size reduction and an aspect ratio increase across the shear zone (refer to Figs 6.6b & 6.7b). The value of Kurtosis, however, changes from negative to positive across the shear zone which demonstrates that toward the lower boundary thrust shape-preferred orientation of the quartz grains is concentrated more about the plane of the tectonic fabric (Ø=0) (Fig. 6.8b).

6.5. Discussion

6.5.1. Microstructural development within quartzites in the shear zones

The microstructural development of each shear zone from the transitional zone to the lower

Shape-Prefered Orientation Anlysis of the Mt. Bold Shear Zone

Descriptive Statistics

Samples	*M17*	*M9*	*M9l*
Sub-zones	*I*	*II*	*III*
Mean	-12.34789	12.51859	37.664415
Standard Error	6.9790725	4.8260873	6.1586034
Median	-30.8031	10.4969	45.0231
Mode	-38.1078	#NUM!	45.0231
Standard Deviation	47.334372	33.782611	38.9504279
Sample Variance	2240.5428	1141.2648	1517.13583
Kurtosis	-0.818258	0.8196914	2.63902821
Skewness	0.5526232	-0.1063713	-1.57151457
Range	170.1191	168.2992	179.4381
Minimum	-84.2355	-82.2771	-89.7178
Maximum	85.8836	86.0221	89.7203
Sum	-568.0028	613.4109	1506.5766
Count	46	49	40
Confidence Level(95.0%)	14.056573	9.7034931	12.4569389

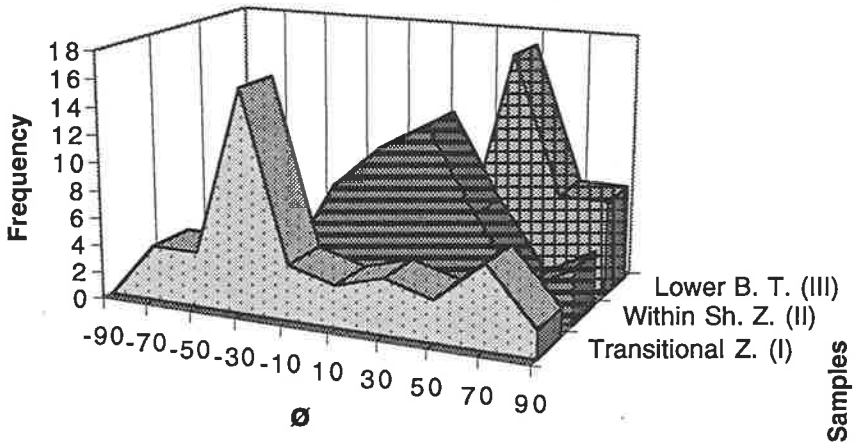

t-Test: Two-Samples

	M17-M9	*M17-M9l*	*M9-M9l*
Hypothesized Mean Differe	0	0	0
df	81	84	78
t Stat	-2.930571	-5.3006125	-3.21381559
P(T<=t) two-tail	0.004395	9.159E-07	0.00190554
t Critical two-tail	1.9896879	1.9886102	1.99084752

Fig. 6.8a: Descriptive statistics and 3-D histogram of the shape-preferred orientation analysis along with the results of the statistical test (t-Test) on shape-preferred orientation variations for samples from the Mt. Bold shear zone.

Shape-Prefered Orientation Analysis of the Pole Road Shear Zone

Descriptive Statistics

Samples	*U10*	*AC3*	*AC2*
Sub-zone	*I*	*II*	*III*
Mean	-3.31725429	0.508902	-0.53551176
Standard Error	7.791058843	5.4213604	4.061863744
Median	-1.6374	-1.7132	-6.6167
Mode	#NUM!	#NUM!	#NUM!
Standard Deviation	46.09252571	38.334807	29.00750921
Sample Variance	2124.520926	1469.55743	841.4355907
Kurtosis	-1.00679763	-0.20688013	0.007695478
Skewness	0.052908017	-0.00052676	0.528041102
Range	171.5621	174.9591	132.926
Minimum	-85.8835	-89.3706	-51.3658
Maximum	85.6786	85.5885	81.5602
Sum	-116.1039	25.4451	-27.3111
Count	35	50	51
Confidence Level(95.0%)	15.83332615	10.894625	8.158496764

t-Test: Two-Samples

Samples	U10-AC3	U10-AC2	AC3-AC2
Hypothesized Mean Difference	0	0	0
df	83	52	91
t Stat	-0.41645244	-0.31659945	0.15417505
P(T<=t) two-tail	0.678153947	0.75281507	0.877813126
t Critical two-tail	1.988960321	2.00664545	1.986377356

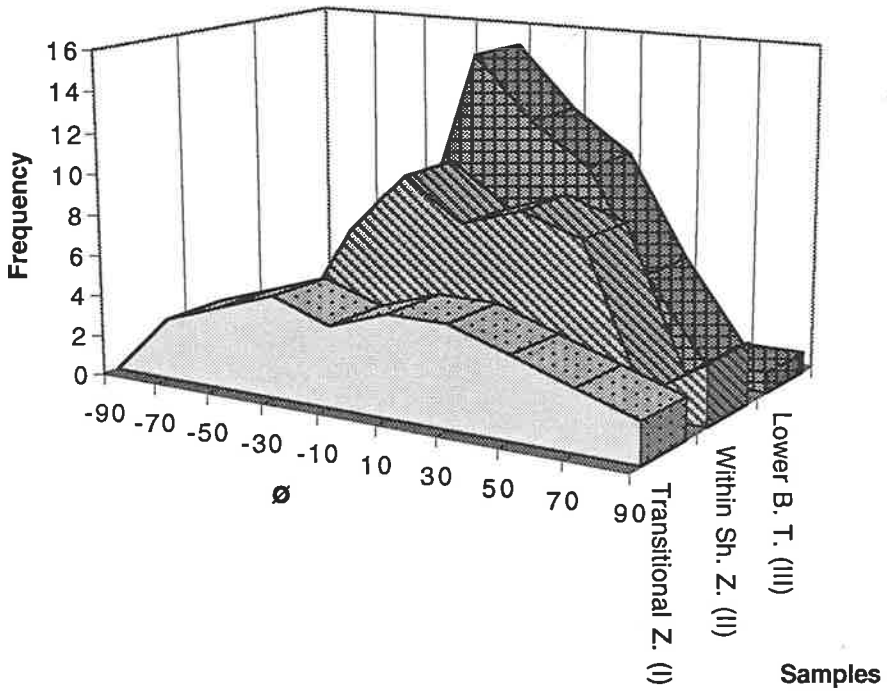

Fig. 6.8b: Descriptive statistics and 3-D histogram of the shape-preferred orientation analysis along with the results of the statistical test (t-Test) on shape-preferred orientation variations for samples from the Pole Road shear zone.

Shape-Prefered Orientation Analysis of the Morialta Shear Zone

Descriptive Statistic

Samples	*A1045Mo1*	*A1045Mo5*	*A1045MO4*
Sub-zone	*I*	*II*	*III*
Mean	13.060266	-21.158951	35.870453
Standard Error	5.9787338	5.78041895	4.1123531
Median	14.3729	-32.8159	39.5703
Mode	#NUM!	#NUM!	#NUM!
Standard Deviation	42.276032	42.0820851	27.586503
Sample Variance	1787.2629	1770.90189	761.01515
Kurtosis	-0.35379	0.16897349	0.2039601
Skewness	-0.488578	0.90321557	-0.5222417
Range	170.9919	174.9113	113.0941
Minimum	-84.8481	-88.2908	-31.9333
Maximum	86.1438	86.6205	81.1608
Sum	653.0133	-1121.4244	1614.1704
Count	50	53	45
Confidence Level(95.0%)	12.014708	11.5992514	8.2879027

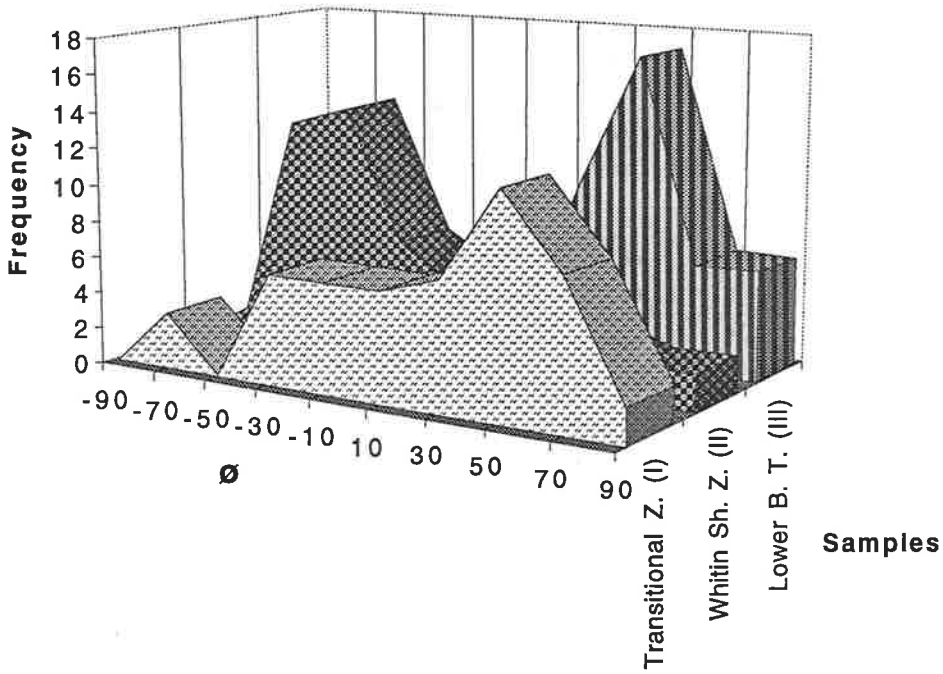

t-Test: Two-Samples

Samples	*MO1-MO5*	*MO1-MO4*	*MO5-MO4*
Hypothesized Mean Difference	0	0	0
df	101	85	91
t Stat	4.1153429	-3.1434171	-8.0391156
P(T<=t) two-tail	7.905E-05	0.00229983	3.178E-12
t Critical two-tail	1.9837307	1.9882691	1.9863774

Fig. 6.8c: Descriptive statistics and 3-D histogram of the shape-preferred orientation analysis along with the results of the statistical test (t-Test) on shape-preferred orientation variations for samples from the Morialta shear zone.

boundary thrust, that is from sub-zone I to sub-zone III, shows that the dynamic recrystallisation process is likely to be the dominant process in the development of the shear zones. The accumulation of dynamic recovery products such as grain boundary migration recrystallisation (GBMR) and sub-grain rotation recrystallisation (SRR) at the lower boundary thrusts to the shear zones demonstrates that toward these boundaries, it is likely that the temperature increases or the strain rate decreases (Hirth & Tullis 1992, Lloyd & Freeman 1994). Similarly, an increase in the relative proportion of SRR to GBMR towards the Morialta shear zone also shows that toward this shear zone the temperature becomes moderate to low or strain rate slows further (e.g. Hirth & Tullis 1992 and Kirschner *et al.* 1995). This therefore is further supporting evidence that temperature decreases or strain rate increases within the shear zones closer to the foreland relative to the shear zones closer to the hinterland.

6.5.2. Environment conditions and deformation mechanisms of the shear zones

It has been shown that feldspar in the shear zones deformed consistently by cataclasis with fragments separated by mica flakes (for example Fig 5.6d). No evidence for subgrain development, deformation twinning or recrystallisation along grain boundaries or cracks was found. This suggests that within feldspars crystal plastic processes were not substantially active and deformation temperatures were below 450 °C (e.g. Tullis 1983, Simpson 1985, O'Hara 1990, and Bailey *et al.* 1994). The parallelism of the mica flakes to syntectonic fractures or microshears in feldspars (Fig. 5.6c) suggests that feldspar dissolution with concurrent reaction to form white mica occurred along these movement planes.

Quartz grains in the shear zones on the other hand are obviously deformed and exhibit overwhelming evidence of crystal plastic deformation mechanisms, such as sweeping undulatory extinction, deformation bands, subgrain formation and core and mantle texture. These microstructures indicate that rotational recrystallisation is more active than dislocation glide. Crystal plastic deformation becomes effective in quartz at temperatures near 300°C, whereas lack of complete recovery suggests deformation temperatures within the greenschist facies (e.g. Voll 1976, Simpson 1983, 1985, and Bailey *et al.* 1994). Since there is no extensive evidence of

quartz ribbon grains, deformation in the shear zones is most likely to have occurred at lower greenschist facies (e.g. Simpson 1985, and Bailey *et al.* 1994).

The above considerations suggest that deformation took place between 350-450°C, with quartz grains deformed by crystal plastic deformation mechanism, while feldspars deformed by cataclastic fracturing. From the Mt. Bold shear zone toward the Morialta shear zone the amounts of intracrystalline fracture of feldspar, and deformation bands and core and mantle textures of quartz decreases, while the amount of dissolution products such as corrosion of quartz grains and beards of small quartz and mica increases. An increase in the amount of dynamic recovery products is expected at higher temperatures or slower strain rates, since recovery involves the thermally activated climb of dislocations. Therefore, a decrease in the amount of crystal plastic deformation products toward the Morialta shear zone might possibly be due to a decrease in the temperature or an increase in fluid activity (Simpson 1985) toward the NW. These microstructures are recognised to occur in association with conditions of brittle-ductile transition (Simpson 1985, and Bailey *et al.* 194).

The semi-brittle nature of the deformation would facilitate significant amounts of dissolution in feldspar and quartz. A substantial increase in the amount of dissolution in quartz and to a lesser extent in feldspar from the Pole Road shear zone toward the Morialta shear zone further constrains the transitional nature of deformation from ductile to brittle-ductile across the shear zones. Such a transition from ductile to brittle-ductile deformation can also be seen in quartz veins across the shear zones. In the Mt. Bold shear zone, almost all quartz veins are deformed by ductile deformation to produce folded and boudinaged veins (Figs 3.13c and 3.16f), while in the Morialta shear zone the quartz veins are deformed by semi-ductile deformation to produce en-echelon tension gash structures (Fig. 3.2e). This transition in the formation of quartz veins across the shear zones provides further support that the brittle-ductile transition conditions of deformation were prevalent in the shear zones.

Processes of dissolution may have taken place either by grain-boundary diffusion or by solution in the presence of an advecting fluid. If the latter case was more important, large volume losses

would be implied to have occurred (O'Hara 1988, 1990 and Bailey *et al.* 1994). Volume losses up to 20% are considered to be more effective in foreland fold-thrust belts (Tan *et al.* 1995, and Gessner 1996 in Flöttmann & James 1997). Analysis of cleavage development in the shear zones (chapter 5) and also in other low grade metamorphic rocks has documented that development of cleavages by pressure solution generally involves mass redistribution with only small volume losses (0-20%) (see also Cox & Etheridge 1989, Waldron & Sandiford 1989, and Tan *et al.* 1995). Similarly, the results of balancing and restoration of the cross sections and finite strain analysis across the shear zones (see chapter 4) show that the amount of pure strain leading to the development of volume losses are not substantially higher than this amount of 0-20% volume losses. Therefore, it is suggested that dissolution process took place either by grain boundary diffusion during a decrease in temperature or an increased presence of impurities in quartzite.

6.5.3. Statistical interpretation of the microstructural data

Grain size is an important variable in fault zone deformation and formation of fault rocks in shear zones generally involves a reduction in grain size (White 1979, Etheridge & Wilkie 1979, Newman & Mitra 1993, and Michibayashi 1996). Statistical analysis of the grain size distributions from sub-zone I toward III, i.e., from the upper transitional zone toward the lower boundary thrust, in almost all the shear zones, show a substantial reduction in grain size (see Figs 6.4 & 6.7). It is widely accepted that such reduction might be due to the development of microstructures involving increasing shear strain during dynamic recovery and/ or recrystallisation (Bell & Etheridge 1973, 1976, White 1973, 1976, 1977, Etheridge & Wilkie 1979, Evans & White 1984, and Newman & Mitra 1993).

The proportion of reduction in grain size is not equally partitioned between larger and smaller grains. As can be seen on scatter graphs of figures 6.4 (a & b), from sub-zone I to II, the sizes of the larger grains are reduced while the smaller ones remain almost unchanged. The progression to sub-zone III, however shows that the amount of ductile deformation increases, and all grains are reduced in size. It is assumed that microfracturing, without significant dilation, is the initial deformation mechanism of the shear zone's development (Knipe & White 1979).

Such fracturing can be seen mostly in samples from sub-zone I, and in samples from the associated ductile thrusts (Fig. 6.3f). It is considered that this fracturing might be responsible for grain size reduction of original detrital grains in sub-zone II prior to dynamic recovery and/or recrystallisation, a process which occurred more at the lower boundary thrust to the shear zones or in sub-zones III.

A marked reduction in grain size is also observed from the Mt. Bold shear zone toward the Morialta shear zone (Figs 6.4a & b and Table 6.1). This reduction might not only be due to an increase in the amount of shear strain or ductile deformation but also, more likely, because of the presence of phyllosilicate minerals, many of which grow by processes of solution mass-transfer. Taking into account the qualitative study of microstructures of the shear zones (see Table 6.1 for more detail), it now can be ascertained that in the Mt. Bold and Norton Summit shear zones, the grain size reduction is more likely due only to crystal plastic deformation mechanisms but in the Pole Road and Morialta shear zones further reduction of grain size might be due to both crystal plastic and solution mass-transfer deformation mechanisms. These shear zones are thought to have been generated at higher crustal levels, possibly during their imbrication and emplacement as described elsewhere, for example, by Evans and White (1984).

Similarly, variations in the range of distribution of the values of long axes versus short axes across almost all of the shear zones shows that toward sub-zone III the values of the lengths of the short axes decrease more than the elongation of long axes. Thus during grain size reduction the short axis lengths reduced more than the long ones. This can be seen by decreases in the values of "b" and increases in the values of "a" in the trend line functions (Fig. 6.4) across each shear zone. This suggests that towards the lower boundary thrusts the grains are more flattened due to accommodation of tectonic flattening strains at these boundaries. The results of finite strain analyses in which all samples plot on the field of apparent flattening strain (Fig. 4.3) further support this argument.

The statistical data show that grain size also has an effect on the grain shape and the shape-preferred orientation. The relationship between grain size and aspect ratio in the shear zones from

sub-zone I towards sub-zone III is shown in figure 6.9. As can be seen, toward sub-zone III, across each shear zone, the proportion of the aspect ratio between the larger grains and smaller ones is not constant and it is the smaller grains which show mostly higher aspect ratios. This is in accordance with the observation that smaller grains are affected more by the processes of dynamic recovery and recrystallisation during shear zone development. This is because crystal plastic processes produce flattened and or elongate grain shapes with higher aspect ratios (Passchier & Trouw 1995). In the Morialta shear zone, however, there are smaller grains whose aspect ratios are not as high as their counterparts in the other shear zones (compare samples from the sub-zones III in Fig. 6.9). The possible reason is that in this shear zone, the aspect ratios of these grains are not increased although their sizes are reduced due to the greater effects of the solution-mass transfer processes than the crystal plastic process.

In addition, the detailed study of the statistical data calculated for the shape-preferred orientation of the grains (Figs. 6.8a, b & c) shows that crystal plastic deformation processes have also some effect on shape-preferred orientation (refer also to Passchier & Trouw 1995). As can be seen in figure 6.8, in all the shear zones, the value of kurtosis changes from negative (Platykurtic, when distribution of data is flatter than the normal distribution) to positive (Leptokurtic, when distribution of data is more peaked than the normal distribution). These variations in distribution of the value of kurtosis, however, are different across the shear zones. For instance, across the Mt. Bold shear zone, this value is -0.8 in sub-zone I, 0.8 in sub-zone II and 2.63 in sub-zone III while in the Morialta shear zone the values are -0.4, 0.2 and 0.2 respectively. Thus as shown, in the Morialta shear zone, these values are not increased as in the Mt. Bold shear zone, which is more likely due to a decrease in effects of crystal plastic deformation processes in the Morialta shear zone.

The results of the statistical analyses show that there is also a positive correlation between the increase in aspect ratio of grains and the development of shape-preferred orientations.

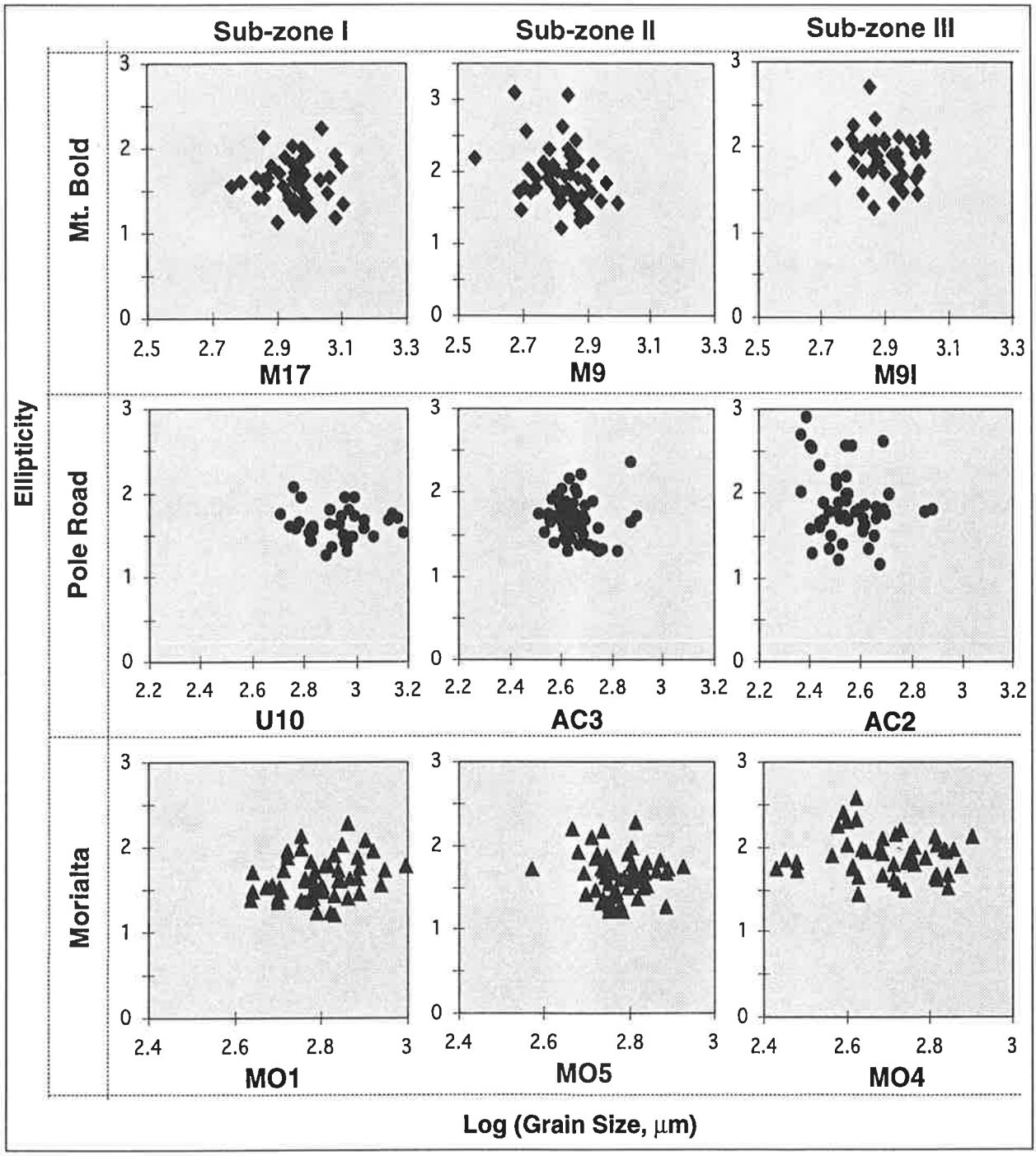

Fig. 6.9: Scattergrams showing the relationship between aspect ratio (ellipticity) and grain size in samples from sub-zone I towards sub-zone III from within the Mt. Bold, Pole Road and Morialta shear zones.

6.5.4. Temporal evolution of the shear zones

The geometric and kinematic analysis of the shear zones (chapter 3) shows that they have experienced only one major, but progressive, deformational event. Therefore, the microstructural transformation of sheared Stonyfell Quartzite within the shear zones must have developed during this progressive event. Based on the geometric and kinematic analysis, and balancing and restoration of the cross sections, the temporal evolution of the structures in the shear zones in the Adelaide Hills area is considered to have developed by the foreland propagation of a décollement thrust from within the basement at depth (see also Evans 1989, and Hatcher & Hooper 1992).

Structures and microstructures from the quartzites in each shear zone would initially have resembled the microstructures currently observed in sub-zone I during the early stages of propagation of the shear zones. With propagation of the shear zones toward the foreland, the deformation rates in the shear zones closer to the hinterland become lower whilst conversely the temperature is higher. Therefore, quartzite microstructures of the hindward shear zones develop microstructures similar to microstructures of sub-zone II and III. At such slower strain rates, dynamic recovery/ recrystallisation is accomplished by both grain boundary migration and sub-grain rotation recrystallisation (Simpson 1985, Urai *et al.* 1986, Hirth & Tullis 1992, and Passchier & Trouw 1995) and develops core and mantle structure (White 1977). Continuation of propagation of the shear zones toward the foreland causes strain to become more localised along the lower boundary thrusts of the shear zones, especially in those closer to the hinterland where dynamic recovery/recrystallisation products are also more intensely developed. Microstructural comparison of the quartz grains between the samples from the Mt. Bold (hindward) shear zone and from the Morialta (forward) shear zones support this argument (compare Fig. 6.1c with Figs 6.3c & d).

The changes in microstructural development from the Mt. Bold to the Morialta shear zones may provide estimates of a smooth increase in flow stress toward the foreland. In addition, a transition in deformation mechanisms of the quartzite, from a region dominated mainly by disorientation of sub-grains and grain boundary migration to one dominated mostly by solution-

mass transfer also occurs toward the foreland. This transition could have happened due to propagation of the shear zones and the major décollement thrust to a lower structural level (e.g. Simpson 1985, and Bailey *et al.* 1994).

Microstructural similarities between the minor imbricate-propagating ductile thrusts with those from sub-zone I in the shear zones (for instance compare Figs 6.3f and 6.1a) indicate that the deformation and microstructural development of the shear zones initiate from these ductile imbricate thrusts. Such development began with the shear zone propagation as imbricate thrusts from a basement décollement at depth to a final strain and deformation localisation at their lower boundary thrusts. The change in size, aspect ratio and shape-preferred orientation of grains across the shear zones from sub-zones I to sub-zones III support such localisation of deformation during the process of shearing. Development of microfractures in quartz grains from within the ductile thrusts in study area, with no significant dilation, which is considered to be the initial mechanism of shear zone development prior to dynamic recovery/ recrystallisation (Knipe & White 1979) further support the development of the shear zones from the ductile thrusts.

Microstructural evolution of the quartzite in the shear zones of the Adelaide Hills area is similar to the other examples of foreland imbrication of thrust sheets (see for instance Voll 1976, Simpson 1985, Bailey *et al.* 1994, and Kirschner *et al.* 1995).

Chapter 7

PRESSURE AND TEMPERATURE CONDITIONS OF THE SHEAR ZONES

7.1. Introduction

Several studies have suggested that ductile shear zones in the continental crust have been infiltrated syntectonically by large volumes of fluid (e.g. Reynolds & Lister 1987, O'Hara 1988). Fluid inclusion studies are playing an increasingly important role in understanding the fluid-rock interaction in such zones (e.g. Roedder 1984, Shepherd *et al.* 1985, and Sisson & Hollister 1990). The relationship between microstructural evidence and fluid inclusion data may provide a reference frame to interpret the fluid inclusion data (e.g. O'Hara & Haak 1992, and Gonzalez-Casado *et al.* 1995). The ability to relate fluid inclusion data and fluid inclusion densities to deformation behaviour provides the opportunity to utilise fluid inclusion data for geobarometry and geothermometry in order to analyse the P-T conditions during deformation in naturally deformed rocks (e.g. Boullier *et al.* 1991, and Alderton & Bevins 1996).

P-T constraints form important data in understanding the temporal, spatial and kinematic (dynamic) evolution of orogenic belts, and in particular fold-and-thrust belts (Karabinos 1988, Karabinos & Ketcham 1988, and Barr & Dahlen 1989). This data also provides a powerful tool to recognise the burial and exhumation history of rocks during episodes of continental thickening (e.g. Vityk *et al.* 1996). Since the fluid inclusion data are not an independent source to constrain the amount of pressure during deformation, an independent geobarometric source is necessary to provide the pressure at the time of peak metamorphism. This, however, can be achieved using pelites which contain the assemblage biotite-muscovite-chlorite-quartz, an assemblage considered as a good geobarometer in low-grade metamorphic rocks (e.g. Powell & Evans 1983, Bucher-Nurminen 1987).

7.2. Fluid inclusion analysis

The study of fluid inclusions was carried out on samples of quartz collected from deformed and boudinaged quartz veins contained within the four major shear zones (Mt. Bold, Pole Road, Norton Summit, and Morialta shear zones; see appendix A for their localities) in order to complement microstructural studies on quartzite from within the shear zones. This study was also conducted to correlate the spatial relationship between the temperature at the time of formation of fluid inclusions with the microstructural development and to determine P-T conditions, based on density and salinity of inclusions, from the shear zones.

7.2.1. Microstructure of quartz veins

All the quartz veins investigated are bedding parallel and of variable thicknesses (1-15 cm) and variable lateral extent (up to 3m). The abundance of veins in a given outcrop generally increases toward the lower boundary thrust of the shear zones (see also section 3.7.1.3 for more detail), from where most samples were collected. Quartz veins adjacent to this boundary are deformed by boudinage and folding (Figs 7.1a & 3.13c).

Microstructural observations in thin sections show that quartz veins have undergone grain size reduction by intracrystalline plasticity from patchy to sweeping undulatory extinction and subgrain formation. They also show evidence for grain size reduction by fracturing. In more deformed grains, especially in samples from the Mt. Bold shear zone, quartz grains show evidence for crystal plastic deformation which cause grain size reduction by syntectonic recrystallisation via grain boundary migration recrystallisation.

The quartz samples are almost all milky quartz. This may be due to the presence of numerous minute fluid inclusions and the development of high dislocation densities (i.e. due to crystal plastic deformation) in quartz, which are scattering the light when they are examined under the microscope, thus giving the milky appearance (see also Gonzoles-Casad *et al.* 1995 and Barker 1995). Some grains show weak elongation parallel to the foliation, but the length-width ratios are generally < 2:1.

Figures opposite

Fig. 7.1a: Photograph of folded and boudinaged quartz veins in the phyllonites of the Woolshed Flat Shale from within the Clarendon shear zone. The coin diameter is 2 cm.

Fig. 7.1b: Type I and III fluid inclusions in quartz veins collected from the Pole Road shear zone; width of view 160 μm.

Fig. 7.1c: Rounded (R) to negative crystal (NC) Type II fluid inclusions in quartz vein sample from the Mt. Bold shear zone; width of view 160 μm.

Fig. 7.1d: Type II fluid inclusion with negative crystal (NC) shape along sub-grain boundaries; width of view 300 μm. Note the bigger size of these inclusion with respect to figure 7.1c where the inclusions are smaller and enriched more in CO_2 phases.


a

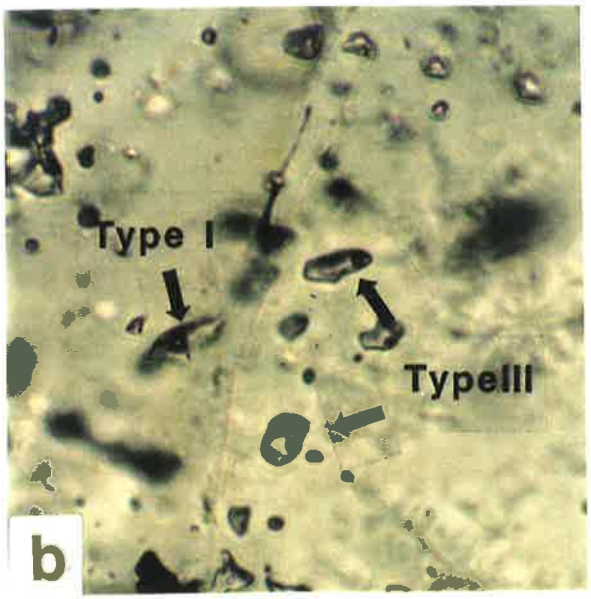
Type I
TypeIII
b

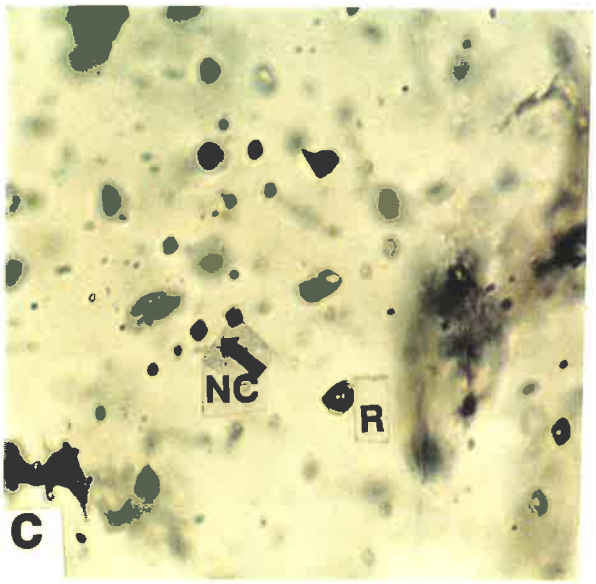
NC
R
C

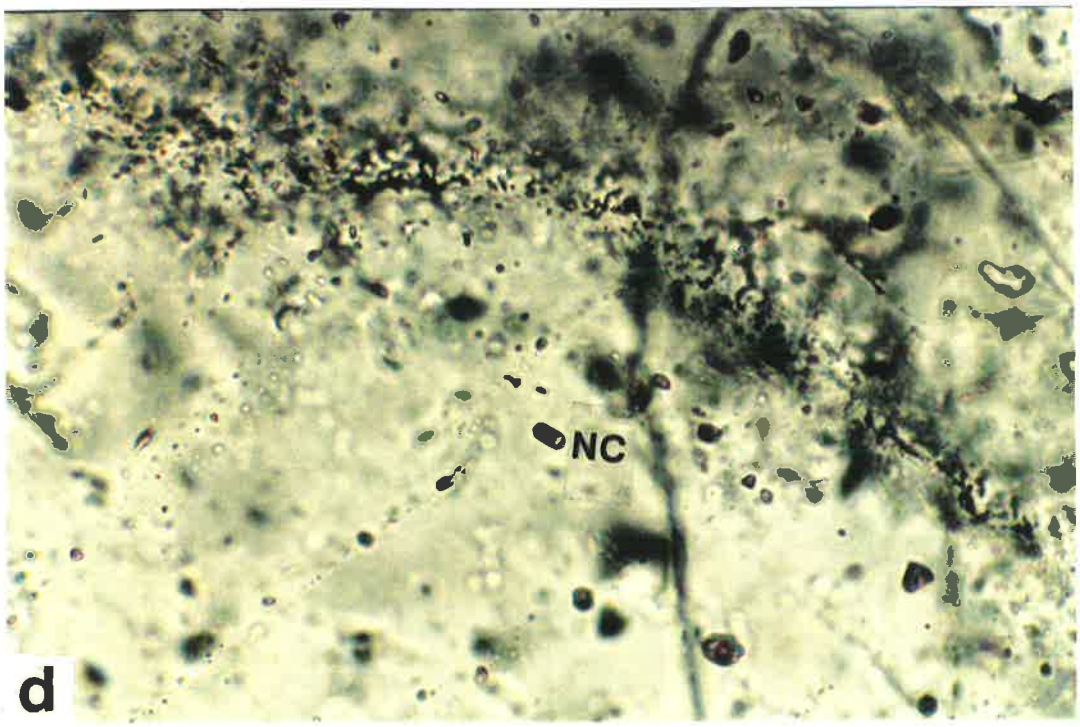
NC
d

The similarity of the quartz vein microstructures to quartz microstructures in the fault zones and the increase in veining-abundance toward the lower boundary thrusts suggests that the veins are genetically related to thrusting and shearing.

7.2.2. Types of fluid inclusions

Fluid inclusions are normally trapped at different times over an extended period of time resulting in a family of genetically related inclusions that formed at different steps. The quartz veins in the shear zones show a family of fluid inclusions which contain two principal types of fluid inclusion phases: (a) an H_2O-CO_2-NaCl phase and (b) two phases of aqueous inclusions. The fluid inclusions were classified using the combined scheme of Roedder (1984) and Shepherd *et al.* (1985). The criterion of Shepherd *et al.* (1985) was also used to define the primary or secondary nature of fluid inclusions. Primary fluid inclusions are those formed during initial crystal growth and are identified by euhedral to rounded shapes and sometimes necked forms. They are randomly distributed along subgrain and grain boundaries or as isolated inclusions within them. Secondary fluid inclusions form post-crystallisation and appear to fill healed microfractures, cutting all primary fluid inclusions and grain boundaries.

In this study four main types of fluid inclusion have been identified based on their origin as primary or secondary, type and amount of liquid phase, shape, size, and proportion of vapour. They are (Fig. 7.2): (1) Type I are H_2O-CO_2-NaCl phase inclusions and occur as isolated large inclusions (6-12 μm in diameter). The content of CO_2 phase in this type of inclusion is less than 20% by weight; (2) Type II are also H_2O-CO_2-NaCl phase inclusions but are more enriched in CO_2 content and usually occur as smaller inclusions than Type I; (3) Type III are two phase aqueous inclusions and like Type I form isolated large inclusions; and (4) Type IV which are two phase aqueous inclusions, almost always occur as healed microfractures.

Type I and III fluid inclusions usually occur within grains and along grain boundaries and subgrain boundaries. Abundant smaller fluid inclusions can also be seen along grain and subgrain boundaries. Because of the difficulty in measurement of these types of fluid inclusions, all measurements were done on inclusions within the grains. Types I and III fluid inclusions are both irregular to rounded in shape, although the shapes of Type III inclusions are

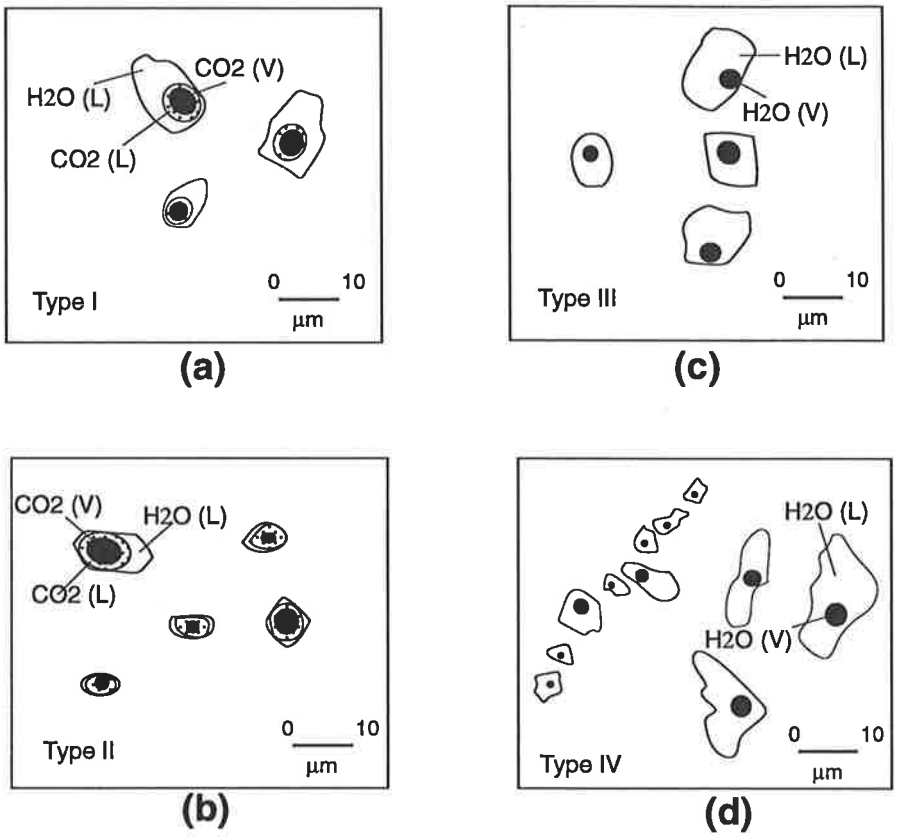

Type *I* : H2o-Co2-Nacl system

Type *II* : H2o-Co2-Nacl system

Type *III* : H2o-Nacl syatem

Type *IV* : H2o-Nacl system

Fig. 7.2: Sketches of main fluid inclusion types: (**a**) Type I carbonic inclusions with regular shapes; (**b**) Type II CO2-rich carbonic inclusions with small rounded or larger negative crystal forms; (**c**) Type III two-phase aqueous inclusions with different shapes from regular to negative crystals; (**d**) Type IV late aqueous inclusions decorating healed microfractures.

sometimes negative crystal forms (see sketches a & c in Fig. 7.2). Types I and III are almost always found close to each other (Fig. 7.1b) and show textural similarity. This, along with the fact that they have the same homogenisation temperatures (see later section 7.2.3.2), provides good evidence that they were trapped from an immiscible fluid (Roedder 1984) during vein formation, and therefore they are likely to be primary in origin.

Type II fluid inclusions are more equant to idiomorphic in shape than Types I and III, with negative crystal shapes (Figs. 7.1c & d and also sketch b on Fig. 7.2) and are smaller than Types I and III (4-7 μm in diameter). They are enriched in the CO_2 phase (more than 40 wt % CO_2) and have probably experienced CO_2 enrichment from the Type I inclusions during post-crystallisation deformation (e.g. Hollister 1990, Johnson & Hollister 1995). Thus, they are not really primary in origin and are normally referred to as modified pseudo-primary fluid inclusions (Hollister 1990, Barker 1995).

Type IV fluid inclusions are obviously trapped along partially healed fractures (Figs. 7.3a & b and also see their sketches in Fig. 7.2) and are therefore secondary inclusions (Roedder 1984). These types of fluid inclusions are almost all two-phase aqueous inclusions with small vapour size components (0.9-0.95 degree of fill). Their sizes are very variable from small (<6 μm) to very large (>12 μm) (Fig. 7.3a & c and also sketch d in Fig. 7.2). They terminate or cut the grain and subgrain boundaries (Fig. 7.3b) or may be sealed within the grains. Large sutured inclusions with irregular shapes and clear edges are also seen as healed microfractures which also terminate within grains (Fig. 7.3b). They can be clearly distinguished from Type III by their irregular shape, clear margins, and amount of filling (> 95% liquid).

Evidence of necked and decrepitated inclusions of Types I and III are also seen mostly along grain boundaries and healed microfractures (Figs 7.3d & e). As can be seen in figure 7.3e, the decrepitated inclusions are surrounded by a distinctive halo of daughter inclusions. These re-equilibrated inclusions are most common in metamorphic rocks and indicate that the rocks were affected by subsequent events after trapping (Swanenburg 1980, in Shepherd *et al.* 1985).

Figures opposite

Fig. 7.3a: Photomicrograph of Type IV fluid inclusions developed as healed fractures; width of view is 0.3 mm.

Fig. 7.3b: Photomicrograph of Type IV fluid inclusions cutting grain (GB) and sub-grain (SG) boundaries; width of view is 1.5 mm.

Fig. 7.3c: Photomicrograph of Type IV fluid inclusions in a sample from the Morialta shear zone. Note the size of this type of inclusion which are the biggest inclusions; width of view is 0.3 mm.

Fig. 7.3d: Necking in type III inclusions (arrow) along healed microfractures showing reequilibrated fluid inclusions; width of view 0.3 mm.

Fig. 7.3e: Decrepitated inclusions surrounded by a halo of smaller inclusions along grain boundaries in a quartz vein sample from the Mt. Bold shear zone; width of view 0.16 mm.

Fig. 7.3f: Showing arrangement of fluid inclusions along grain and subgrain boundaries; width of view 1.5 mm.

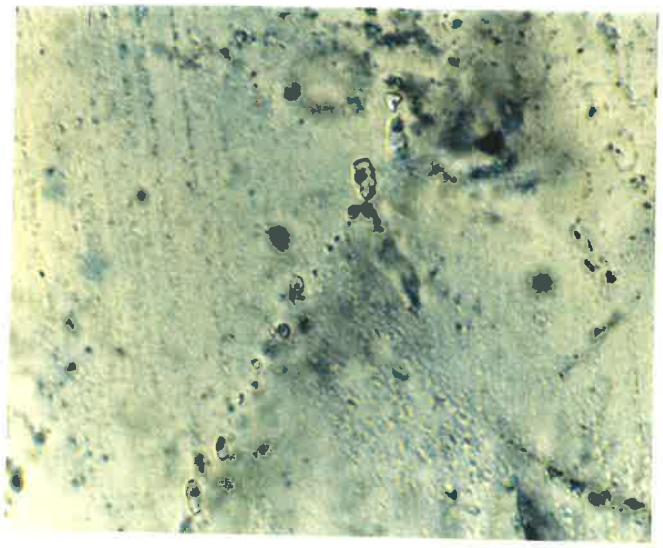

a

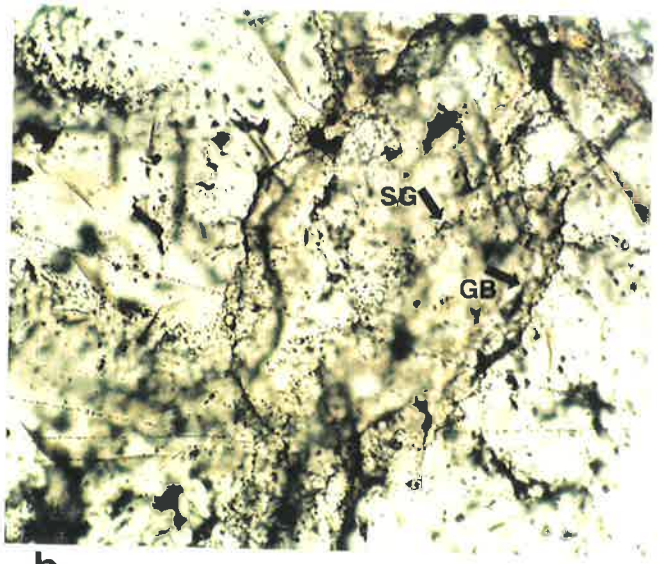

b

c

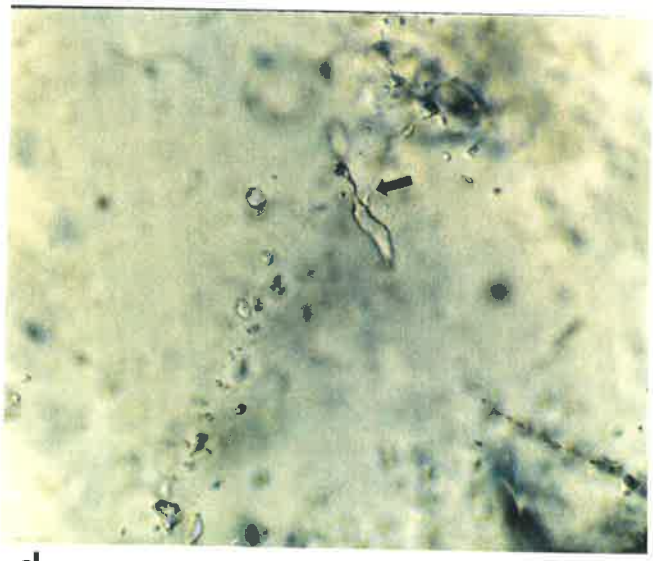

d

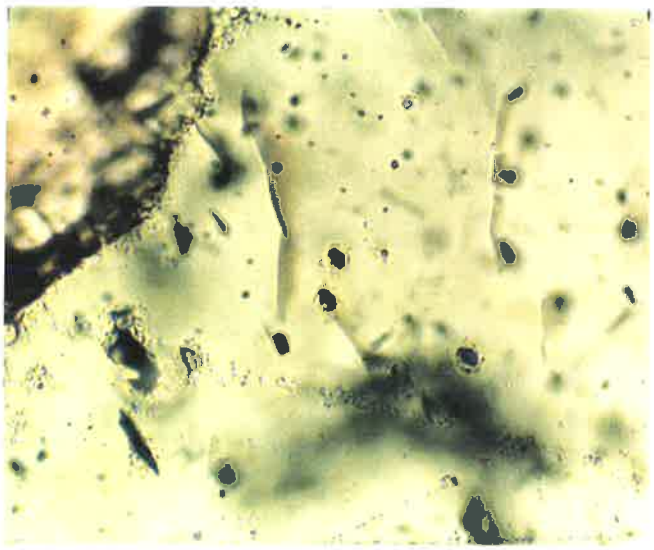

e

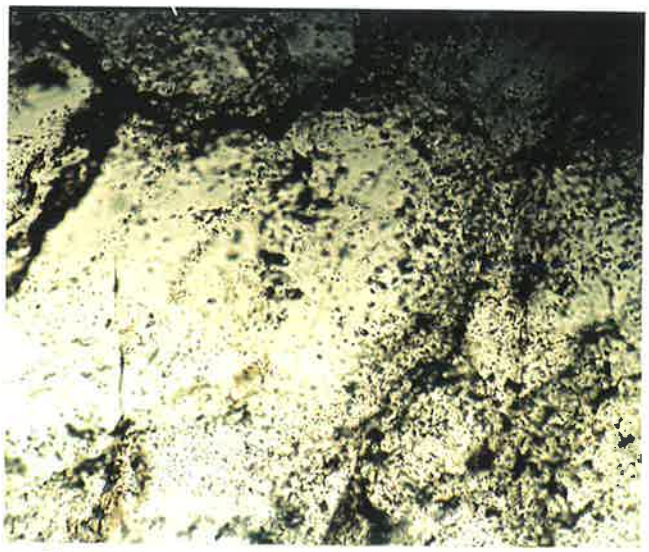

f

7.2.3. Analytical methods

Doubly polished thin sections of quartz veins were prepared as slices about 100 μm thick, mounted in epoxy resin between two thin glass cover slips. They were then examined with a standard petrographic microscope to establish inclusion types present, prior to being broken into smaller samples for microthermometric analysis. The microthermometric method is the most popular and widely used non-destructive analytical technique for fluid inclusion studies. The method relies on careful observation and recognition of the phase changes which take place within the fluid inclusions during heating and cooling processes.

Selected fragments were heated and cooled on a Reynolds Fluid Inclusion Stage. The samples were first supercooled to -110 °C, to achieve freezing of all phases in the inclusions. With the heating steps, the temperature was cycled from -110 °C to +30 °C with heating rates varying from 15 °C min^{-1} over the initial 50 °C to a rate of 1-2 °C min^{-1} during the key phase changes. Repeated cycling back and forth was sometimes necessary to record some of the phase transformations accurately. Heating to a maximum of 410 °C (limitation temperature of the apparatus used) was done and all phase changes below room temperature were investigated. This process involved heating at rates ranging generally from 15 °C min^{-1} to rates down to 2.0 °C min^{-1} over the phase change intervals. The data obtained from fluid inclusions of the shear zones during freezing and heating are presented in table 7.1 and Figures 7.4 and 7.6.

For the purpose of this study, the following abbreviations are used in presenting and discussing the fluid inclusion data:

T_{MCO2} = Temperature of final melting of solid CO_2

T_{FM} = Temperature of first ice melting

T_M = Temperature of final ice melting

T_{clath} = Temperature of CO_2 clathrate melting

T_{HCO2} = Temperature of homogenisation of CO_2-rich phase

T_H = Total homogenisation temperature

T_T = Estimated temperature of trapping

P_T = Estimated pressure of trapping

P_{ov} = Estimated overpressuring.

7.2.3.1. Freezing

Cooling of fluid inclusions was conducted to define the components of the fluid phase, to compute density and salinity of the different types of fluid inclusions, to provide more evidence to constrain the results of homogenisation temperature determination and to gather sufficient data to constrain the P-T conditions during formation of the shear zones.

The data obtained from the freezing and melting processes below room temperature are shown in table 7.1 and in figure 7.4. The value of T_{MCO2} for Types I and II fluid inclusions of the shear zones is close to the observed value in pure CO_2-H_2O phases (e.g. Shepherd *et al* 1985) which possibly shows that there is almost no methane in the fluid. Similarly, the temperature at which first and/or final melting occurs can be used to determine the components of the fluid phase. The mean value of first melting temperature of inclusions in vein quartz, which provides information on the composition of the fluids, range from -22 to -25 °C (table 7.1) indicating no significant presence of salts in addition to NaCl.

The final melting temperatures (T_M in table 7.1 and in Fig. 7.4) were measured to calculate the salinities in terms of NaCl equivalent, using Crawford's (1981) graph (Fig. 7.5). Figure 7.4 shows histograms of the distribution of melting temperatures (T_M) of the various inclusion types. As can be seen, the value of T_M for each type of fluid inclusions does not vary substantially across the shear zones. This value is, however, different between CO_2-phase containing inclusions or carbonic inclusions (Types I & II) and aqueous inclusions (Types III & IV). The mean value of T_M for Types I and II vary from -2 to 1 which corresponds to 1-4 wt % NaCl equivalent, while this value for Types III and IV inclusions ranges from -8 to -13, respectively, which indicates about 12 and 16 wt % NaCl equivalent. This bimodal distribution of salinity between Types I and III fluid inclusions, as reflected in their final melting temperatures (Fig. 7.4), may imply immiscibility during entrapment of these inclusions (Roedder & Bodnar 1980).

The clathrate melting temperatures of CO_2-phase inclusions were also measured and the results are shown in table 7.1 and figure 7.4. These values are less than 10 °C in all samples from

Fluid	Shear Zones	T_{MCo2}			T_{FM}			T_M			T_{Clath}			T_{HCo2}			T_H		
Inclusions		No.	Range	Mean	No.	Range	Mean	No.	Range	Mean	No.	Range	Mean	No.	Range	Mean	No.	Range	Mean
	Morialta	4	-57.6 to -58.1	-57.8	-	-- --	--	4	-1 to 2	1	4	8-10	9	4	23-25	24	4	310-370	337
Type I	Summertown	7	-49.6 to -57.2	-56.6	-	-- --	--	-	-- --	--	8	6-10	8	8	20-30	26	8	280-370	340
	Pole Road	12	-56.4 to -59.6	-56.9	-	-- --	--	-	-- --	--	12	4-8	6	12	21-27	25	14	270-410	353
	Mt. Bold	5	-57.6 to -58.1	-57.8	-	-- --	--	3	-2 to -3	-2	5	7.5-8.5	8	5	20-22	21	5	310-390	360
Type II	Summertown	4	-56.9 to -57.2	-57.0	-	-- --	--	-	-- --	--	4	8-10	9	4	29-30	29.5	4	400->410	410?
	Mt. Bold	22	-56.8 to -57.9	-57.5	-	-- --	--	9	-3 to 1	-1.5	22	4-8	7	22	20-26	24.5	19	290->410	410?
	Morialta	-	-- --	--	10	-24 to -22.5	-23	9	-10 to-13	-12	-	- -	-	-	- -	-	9	270-401	350
Type III	Summertown	-	-- --	--	7	-23 to -28	-25	7	-8 to -11	-9	-	- -	-	-	- -	-	7	340-410	360
	Pole Road	-	-- --	--	8	-26 to -23	-24	8	-9 to -13	-12	-	- -	-	-	- -	-	8	240-350	330
	Mt. Bold	-	-- --	--	2	-20 to -23	-22.5	2	-8 to -8.5	-8	-	- -	-	-	- -	-	2	350-380	365
	Morialta	-	-- --	--	12	-23 to -24	-23.5	12	-11 to -16	-13	-	- -	-	-	- -	-	12	170-250	185
Type IV	Summertown	-	-- --	--	6	-21 to -24	-23	6	-10 to -13	-12	-	- -	-	-	- -	-	6	120-240	170
	Pole Road	-	-- --	--	11	-23 to -26	-24	11	-5 to -14	-10	-	- -	-	-	- -	-	11	170-200	170
	Mt. Bold	-	-- --	--	7	-21 to -24	-23	7	-7.5 to -8.5	-8	-	- -	-	-	- -	-	7	180-220	190

Table 7.1: Summary of fluid inclusion data.

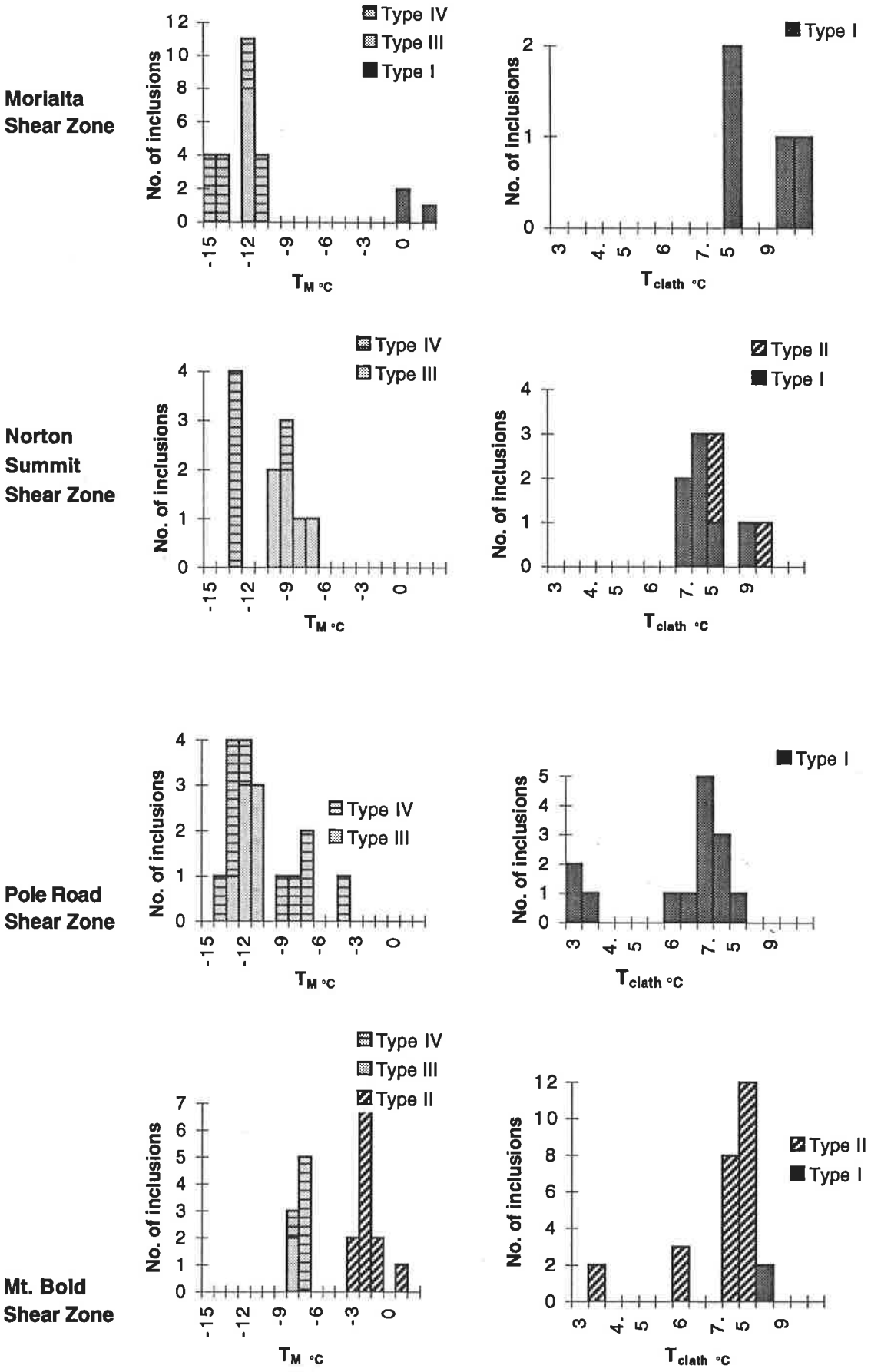

Fig. 7.4: Histograms showing the distribution of last melting temperature (T_M) and CO_2 clathrate melting temperature (T_{clath}) for all fluid inclusion types from within the shear zones.

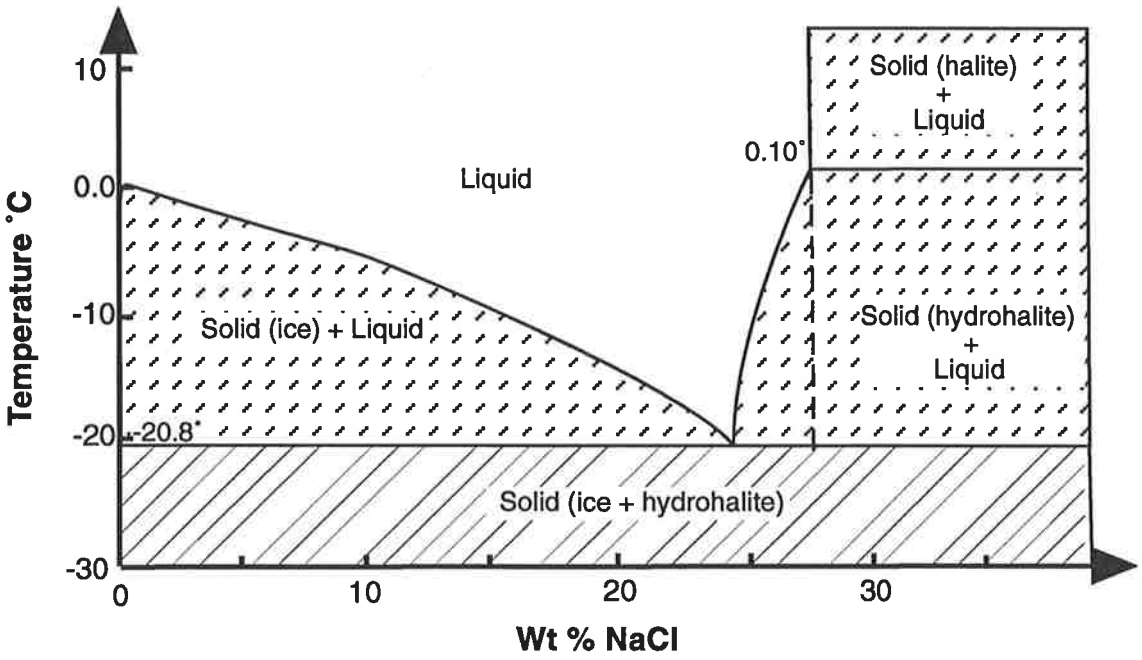

Fig. 7.5: Temperature-composition diagram for the system H2O-NaCl (after Crawford 1981). The amount of salinity of the fluid inclusions in term of NaCl equivalent were measured using this graph.

within the shear zones inferring that a small amount of dissolved salt, approximately 1-5 wt % NaCl equivalent, is present (e.g. Hollister & Burruss 1976). As figure 7.4 shows, temperatures of clathrate melting of carbonic fluid inclusions have bimodal distribution. Such distributions reflect different amounts of CO_2 content of inclusions not only between two different Types I and II fluid inclusions but also from within Type I fluid inclusions (see for example inclusions from the Pole Road shear zone in Fig. 7.4).

7.2.3.2. Heating

Heating experiments were conducted on all the fluid inclusions of different types which were examined during the freezing stage. At lower temperatures (< 40 °C), homogenisation of carbonic inclusions of Types I and II was measured, which almost all occur along with the disappearance of the CO_2 vapour phase. Total homogenisation of all fluid inclusions was also determined, which occurred as a vapour disappearance, liquid disappearance, or decrepitation prior to homogenisation. Since all inclusions have evidence of liquid and vapour and most of them homogenised to liquid, it may imply that the fluid inclusions were trapped from a boiling fluid (Roedder 1984). Since the size of most inclusions examined was relatively large, exact T_H and T_{HCO2} were determined.

Result of T_{HCO2} of Type I and II fluid inclusions are shown in table 7.1 and figure 7.6. As can be seen, values of T_{HCO2} vary between these inclusion types. The mean values of T_{HCO2} for Type I inclusions range from 21 to 26 °C and for Type II from 23.5 to 29.5 °C (table 7.1). This value is also higher for Type II in each shear zone than Type I. The fact that T_{HCO2} affects the bulk density of inclusions, might lead to the conclusion that Type II fluid inclusions have lower density than Type I. The slight variation in the mean value of T_{HCO2} of Type I inclusions across the shear zones (table 7.1 & Fig. 7.6) may also show that the bulk densities of this type of inclusion are roughly constant. This is likely to be a valuable source of information to estimate pressure of entrapment.

Total homogenisation temperatures (T_H) of all types of fluid inclusions are also shown in figure 7.6. The criterion of Shepherd and others (1985) has been applied to classify the T_H of fluid inclusions based on their types. An overall bimodal distribution in homogenisation

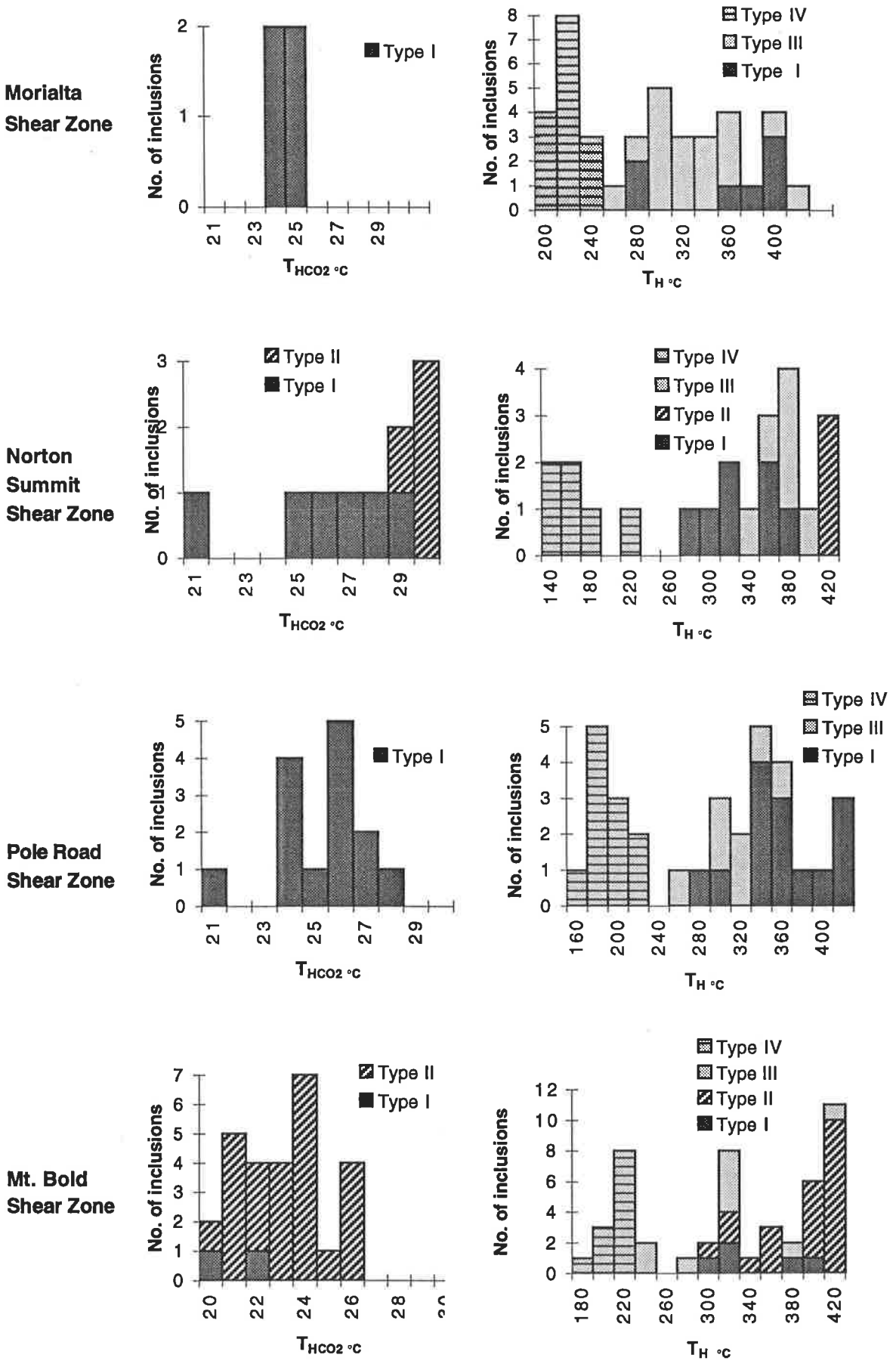

Fig. 7.6: Histograms showing the distribution of CO_2 homogenisation temperature (T_{HCO2}) and total homogenization temperature (T_H) for all fluid inclusion types from within the shear zones.

temperatures of inclusion can be seen in all samples (Fig. 7.6). One grouping can be seen at T_H= 160-240 °C with a mean value of 170-190 °C (table 7.1). The other population grouping is located at T_H= 250->420 °C with a mean value of 330-400 °C (table 7.1). The first group which have higher salinity (12-16 wt % Na-Cl) are late aqueous inclusions of Type IV. As mentioned earlier they also decorate healed microfractures and cut grain boundaries and arrays of primary fluid inclusions, and therefore are likely to be secondary in origin. The second group are all primary fluid inclusions of different Types I, II, and III. The mean value of these Types of inclusions, however, shows that they may be divided into two sub-groups. Types I and III with mean values of T_H=337-365 °C can be defined as one sub-group and Type II with mean homogenisation temperatures of more than 400 °C may be considered as the other sub-group.

7.2.4. Salinity-T_H relationship

Comparison of T_H and salinity, as reflected in the temperature of last melting of ice, from within the fluid inclusions, shows that in contrast to homogenisation temperature, the salinity of inclusions is not sensitive to volume or density changes (Sterner & Bodnar 1989) and provided the inclusions have been trapped in a close system, their salinities are accurate reflections of the fluid salinity at the time of trapping. A scattergram of salinity verses T_H of all types of fluid inclusions (Fig. 7.7) shows that inclusions of Types I and II were trapped at high T_H and as low to moderate salinity fluids, while Type IV inclusions have relatively lower T_H and higher salinity. Type III, however, are different and show both higher T_H and salinity.

The low to moderate salinity of Types I and II with respect to Type III seems to have developed due to higher vapour ratio of gas-rich Types I and II fluid inclusions. Thus, the low ratio of vapour phase of Type III leads to a substantial increase in salinity because salts are strongly partitioned in the liquid phase (Hedenquist & Henley 1985, in: Ahmad 1993). Another possibility for low salinity of the inclusions might be due to metamorphic dehydration reactions near the fault zone. This process could supply low salinity fluid if fluid was focused along the fault zone (O'Hara & Haak 1992). Evidence of chlorite development in the deformed quartz

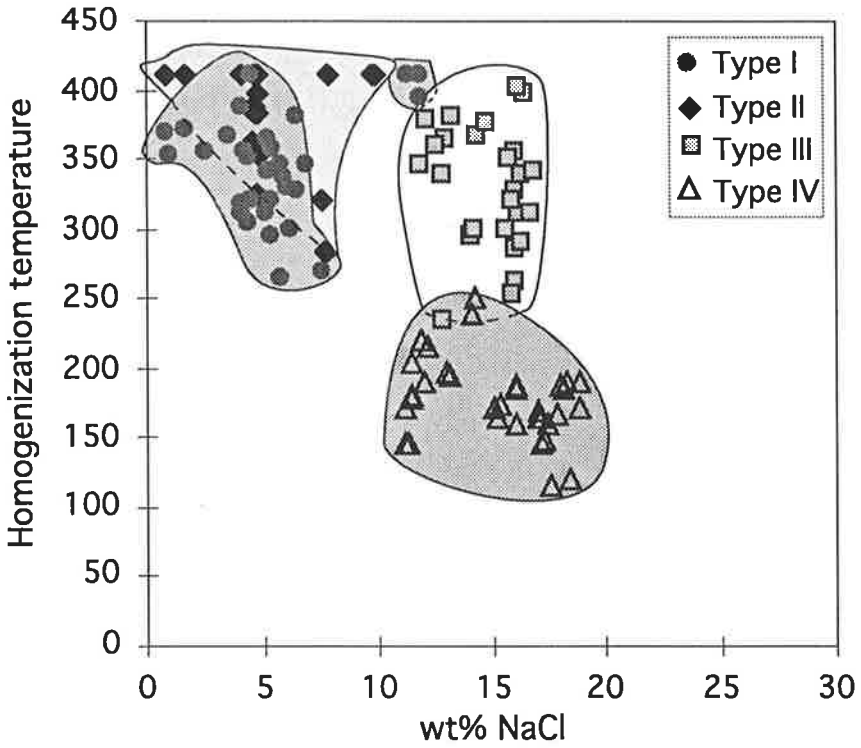

Fig. 7.7: Scattergram of homogenisation temperature vs salinity data of all inclusions. The diagram shows that solubility of salts increases with increasing temperature.

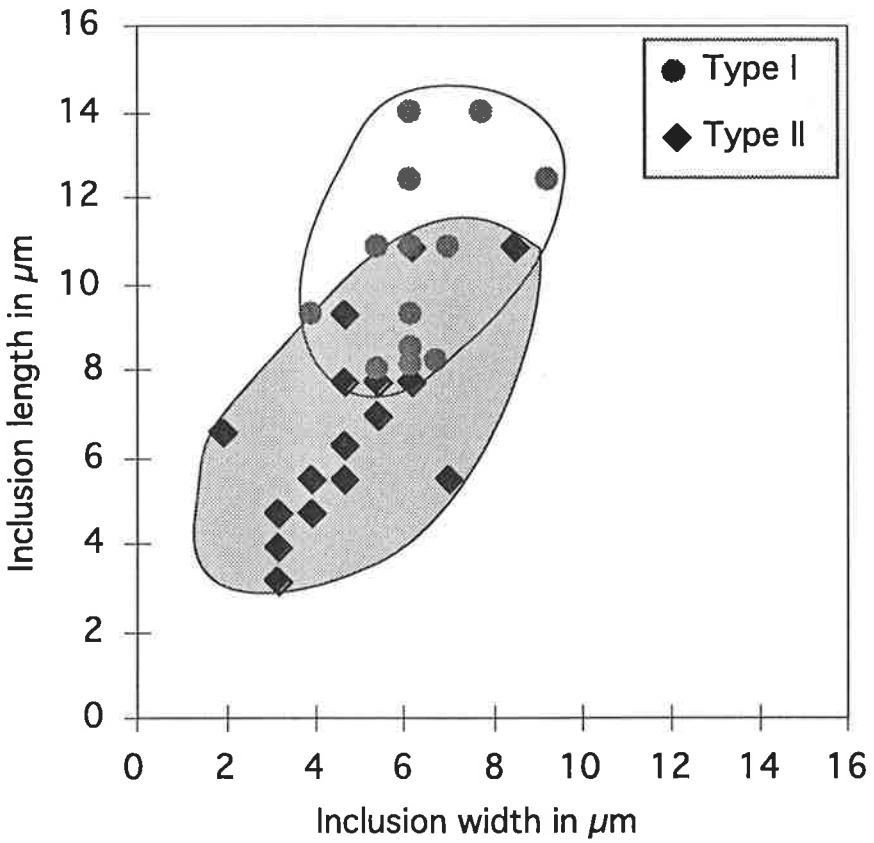

Fig. 7.8: Scattergram of aspect ratio of carbonic fluid inclusions of Types I & II. Note the smaller size of Type II modified inclusions.

veins, however, indicate hydration rather than dehydration and therefore may rule out the second possibility.

High salinity and lower T_H of Type IV inclusions, entrapped along healed microfractures, probably represent late residual fluids. In such fluids, the amount of solutes such as Na^+ and K^+ increased the salinity of the fluids (Crawford *et al.* 1979) and produced lower temperature (and possibility later) inclusions.

As a whole, decrease of fluid inclusion salinity is usually accompanied by an increase in the value of T_H. Since an increase in the amount of crystal plastic deformation process may cause H_2O leakage from fluid inclusions and results in an increase in the amount of CO_2 phase, reduction in salinity and increase in the value of T_H would also occur.

7.2.5. Interpretation of homogenisation temperature

The higher homogenisation temperatures of modified Type II fluid inclusions provides some evidence that the inclusions have been re-equilibrated to lower density. The re-equilibration of inclusions may occur by inelastic volume change, decrepitation or leakage (e.g. O'Hara & Haak 1992). Experimental studies of quartz inclusions also indicate that fluid inclusions can undergo either leakage (Bakker & Jansen 1990) or volume change (Sterner & Bodnar 1989). Extensive evidence of volume change from carbonic inclusions to produce smaller sized inclusions with negative crystal forms (e.g. Figs. 7.1c & d and Fig. 7.8) and/or decrepitation (e.g. Fig. 7.3e) has been detected from all samples. This can be explained by modification of fluid inclusions to be enriched in the CO_2 phase. CO_2 enrichment of fluid inclusions is proposed to have occurred during increases in the amount of crystal plastic deformation at grain boundaries by preferential removal of H_2O phase during grain boundary migration (eg. Hollister 1990 and Johnson & Hollister 1995). This process causes increased T_H and creates smaller inclusions (Giles & Marshall 1994).

Homogenisation temperature of primary Types I and III inclusions also varies from low to high (250->400 °C). The higher value of T_H of Type I inclusions in all samples of the shear zones (Fig. 7.9) might also be due to modification of inclusions to lower density during crystal

plastic deformation processes. Because such modification and enrichment processes were not observed, they have not been classified separately from normal Type I inclusions which have mean and median value of T_H=345 °C (Fig. 7.9).

Similarly, the high value of T_H of Type III inclusions in all samples of the shear zones might have also developed during re-equilibration of these inclusions to lower density. Such re-equilibration can be constrained by a change in the shape of the inclusions to rounded and negative crystal forms, though the content of the CO_2 phase of the inclusions is not substantially developed to support this re-equilibration. The lower values of T_H of Type III inclusions, however, may represent the fluid density during trapping, provided that they were not subsequently modified. Thus, the density of these fluid inclusions can be used to constrain the fluid pressure conditions at the time of trapping (e.g. Roedder & Bodnar 1980).

The very close mean and median values of T_H of Types I and III (335-345 °C, Fig. 7.9), along with the fact that they are primary, may show that they were trapped at the same time during peak metamorphism. The subsequent occurrence of thrusting and shearing with development of recovery and recrystallisation may have caused these fluid inclusions to modify to higher T_H . As Johnson and Hollister (1995) show, an increase in T_H by as much as 30 °C can happen if inclusions are subjected to 1 K bar overpressure.

Scatter in the results of T_H is also considered to be due to necking down of fluid inclusions which occurred near the temperature of original trapping (Roedder 1984). Evidence of necking down of fluid inclusions especially of Type III, which has the most widely scattered values of T_H, is seen in some samples (Fig. 7.3a). Since almost all measured inclusions were chosen from isolated and regular shaped fluid inclusions, the process of necking down of inclusions which is attributed as due to increases in the amount of dislocation density (O'Hara & Haak 1992, and Barker 1995), would not be the case.

Taking these interpretations into account, it is now possible to use the lower values of T_H of primary Type I and III inclusions to estimate temperatures of fluid inclusion trapping.

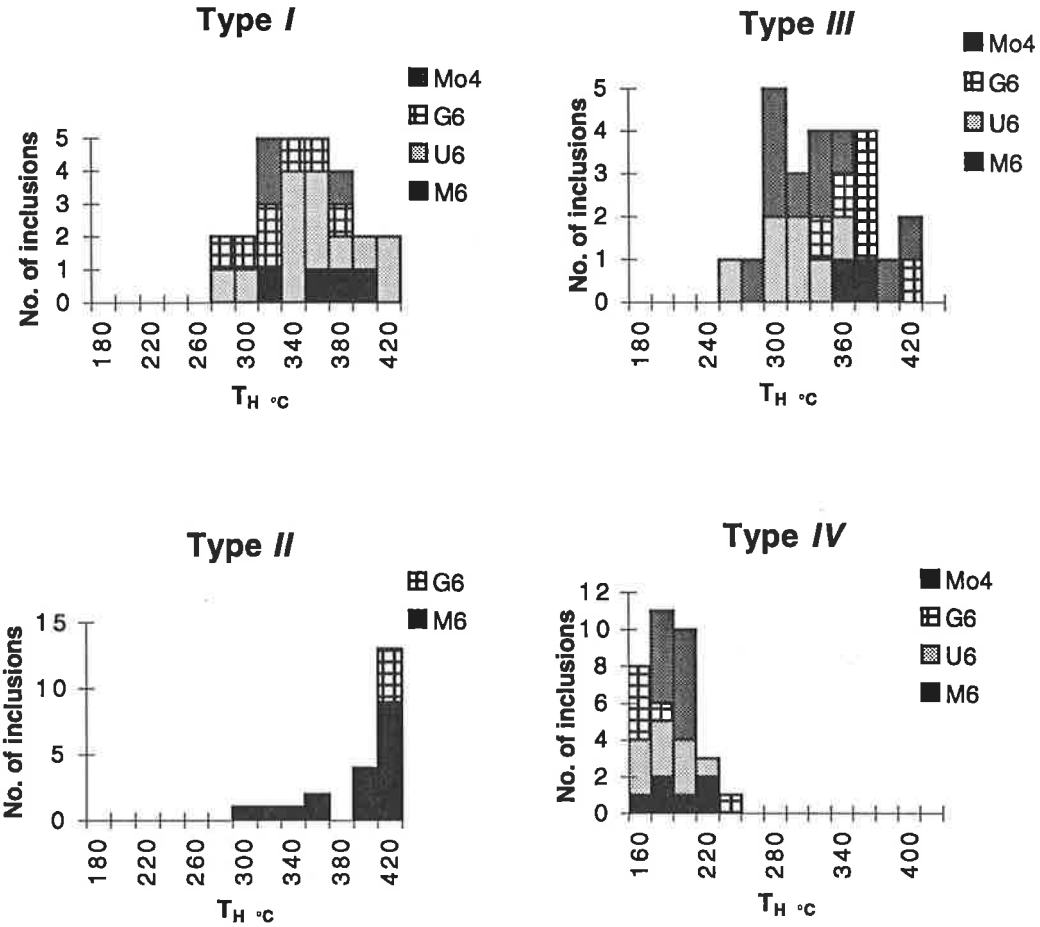

Descriptive Statistics

	Type I	*Type II*	*Type III*	*Type IV*
Mean	344.80645	385.95652	332.741	179.333
Standard Error	6.8110314	7.3013828	8.87385	4.86614
Median	345	401	339	176.5
Mode	410	410	300	165
Standard Deviation	37.922218	35.016202	46.1099	29.1969
Sample Variance	1438.0946	1226.1344	2126.12	852.457
Kurtosis	-0.291946	2.3775968	-0.5051	0.50526
Skewness	-0.119884	-1.725679	-0.3234	0.2377
Range	145	126	176	134
Minimum	265	284	234	117
Maximum	410	410	410	251
Sum	10689	8877	8984	6456
Count	31	23	27	36
Confidence Level(95.0%)	13.909968	15.142157	18.2405	9.87881

Fig. 7.9: Histograms of homogenisation temperature and descriptive statistics for all fluid inclusion types.

7.2.6. Estimation of temperatures of entrapment

The measurement of homogenisation temperature is based upon the assumption that contents of the vacuoles were deposited from an original fluid. Therefore, when the mineral is heated and the liquid expands to fill the vacuole, and thus restores a single phase, the minimum temperature at the time of entrapment of the original fluid can be estimated. The difference between this minimum temperature and the true temperature at the time of trapping is a function of the trapment pressure. A knowledge of the pressure at the time of trapping is important as it may provide information of intrinsic geological significance, but it also provides a means of correcting homogenisation temperatures to obtain true trapping temperature, the so called "pressure correction" of Roedder & Bodnar (1980).

However, when fluid inclusions are trapped from an immiscible fluid or trapped from a boiling fluid, temperatures of homogenisation in a given fluid are equal to temperature of trapping (Roedder & Bodnar 1980, and Roedder 1984) and therefore there is no need for a pressure correction. The existence of carbonic fluid inclusions in samples studied provides data to allow the determination of the conditions of trapping. The coexistence of immiscible H_2O and CO_2 phases in Type I inclusions shows that they were trapped at almost T_H, so the homogenisation temperature is also the temperature of trapping (Roedder 1984). Bimodal salinity of the fluid composition (as evidenced from clathrate melting temperatures and last melting temperatures, Fig. 7.4), the slight difference in ratio of CO_2 content and evidence of higher T_H may further imply immiscibility during entrapment (Roedder & Bodnar 1980).

Primary Type I and III inclusions in all samples occur close to one another and show textural similarity (Fig. 7.1b). This close spatial relationship between these types of inclusions along with the fact that they have close T_H values (Fig. 7.9) may suggest a fluid condition during which a continuously decreasing pressure or increasing salinity can cause almost total loss of CO_2 (e.g. Bowers & Helgeson 1983). Therefore, it is suggested that Type III fluid inclusions resulted from such a mechanism and probably contain minor CO_2, which is not visible or detectable at room temperature especially in the milky quartz vein samples. The rare appearance of minute solid CO_2 upon freezing is consistent with less than 5 wt percent CO_2 being present

(Shepherd *et al.* 1985). Thus, T_H of the Type III inclusion may also show actual trapping temperature and does not require pressure correction.

Type II fluid inclusions may be comparable to the CO_2 rich inclusions described by Johnson and Hollister (1995) as being trapped during recrystallisation-related grain boundary migration, rather than representing primary inclusions. They are actually Type I inclusions modified to lower density and higher T_H and therefore their T_H is greater than T_T (Sterner & Bodnar 1989). Since T_H of most of these inclusions is not measurable due to the limitation of the stage used, the actual T_T is also not easy to calculate but is estimated to be less than 400 °C.

Taking these results along with the homogenisation temperatures of inclusions into account, it is now possible to estimate trapping temperature, based on the values of homogenisation temperature of Type I and III inclusions. As mentioned earlier, since the lower values of T_H of these inclusion types show more precisely the temperature of trapment, therefore the temperature of trapping can be estimated and is about 330-360 °C (see also Fig. 7.9).

Unlike Types I , II and III inclusions, Type IV inclusions are not entrapped from an immiscible fluid, so their T_H do not represent T_T and therefore, pressure correction should be done on their homogenisation temperatures. These inclusions which form healed microfractures, probably sustained minimum pressure as their vapour pressure at any given temperature (Shepherd *et al.* 1985), so the pressures of entrapment of these inclusions are less than lithostatic pressure. However, their pressures are greater than the value that can be defined from the liquid-liquid+vapour curve for the system H_2O-NaCl (see Fig. 7.10 for this curve).

Homogenisation of primary Type I inclusions occurs in CO_2 or H_2O at near identical temperature ranges suggesting entrapment of fluids on the H_2O-CO_2 solvus. The common mean values of T_H (i.e. 337-360 °C, see table 7.1) define a pressure of about 500 bar for a pure H_2O-CO_2 system (Roedder 1984). Addition of salt raises the solvus to a higher temperature and pressure. The existence of 6% NaCl (calculated from T_{clath} using the MacFlinCor program of Brown & Hagemann 1995) in Type I inclusions suggests a pressure of 75 Mpa at a temperature of 350 °C (Bowers & Helgeson 1983). Using data of Potter (1977) a correction of

+50 °C was carried out on T_H of Type IV inclusions (see table 7.2 and spreadsheets of inclusion data in appendix E for more details).

7.2.7. Estimation of pressure of trapping

Pressure of trapment can be estimated based on the salinity and density of fluid inclusions. Using the MacFlinCor program of Brown and Hagemann (1995) the salinity and bulk density of all types of fluid inclusions were calculated from T_M or T_{clath} (depends upon inclusion types), T_{HCO2} and T_H (see appendix E for the result). The pressure was then estimated by applying calculated isochores (lines of constant density) for different densities of the inclusion types. These isochores were computed and extracted from the experimental data of Bowers and Helgeson (1983) for carbonic inclusions and of Zhang and Frantz (1987) for aqueous inclusions (table 7.2 and also appendix E for more details).

Estimation of pressure of trapping for Type I inclusions ranges from 2100 to 3900 bars and for Type III inclusions from 1000-1800 bars (table 7.2). Type I and III inclusions are assumed to be primary inclusions, however, as mentioned earlier, Type III inclusions were developed from the same fluid as Type I but were trapped under lower pressure, which caused the amount of CO_2 to be reduced to less than 5wt %. Type II inclusions with higher T_H and lower density than that of Type I show lower pressure estimates. As expected, such lower pressure is due to the effects of overpressuring, during which crystal plastic deformation occurred. Similarly, some Type III fluid inclusions also display higher T_H and lower density. Since these inclusions display negative crystal forms, it seems that they were also modified to higher T_H and lower density due to overpressuring.

Assuming Type I as primary fluid inclusions, estimated pressure for these inclusions would also show pressure of trapment at peak metamorphism. The fact that T_{HCO2} reflects bulk density of carbonic inclusions and that this value is roughly constant for this type of inclusion across the shear zones (see table 7.1 and Fig. 7.6), implies that the mean bulk density value of Type I inclusions can be used to estimate pressure at the time of peak metamorphism. Using the mean bulk density value of Type I inclusions (table 7.2), a maximum pressure of 3100-3250 bar, equivalent to depths of more than 10 Km has been calculated for all the shear zones by the

Fluid	XNacl			XCO_2			Bulk Density			T_T °C			P_T bar		
Inclusions	No.	Range	Mean	No.	Range	Mean	No.	Range	Mean	No.	Range	Mean	No.	Range	Mean
Type I	31	0.002- 0.04	0.017	31	0.048- 0.17	0.086	31	0.919-1.009	0.95	31	265- 410	345	31	2000- 3900	3120
Type II	22	0.003- 0.03	0.019	22	0.121- 0.2	0.17	22	0.84- 0.95	0.90	22	284-> 410	383	22	1900- 3600	2893
Type III	26	0.38- 0.06	0.05	26	<0.05- <0.05	<0.05	26	0.65- 0.94	0.84	27	240- 410	329	26	900- 1800	1360
Type IV	34	0.024- 0.07	0.05	-	-- --	--	34	0.914- 1.07	0.99	34	167- 290	226	34	220- 800	405

Table 7.2: Summary data of bulk composition (XNacl & XCO2), bulk density and estimated pressure and temperature of trapment of all types of fluid inclusions.

isochor projection of the mean bulk density of the Type I inclusions to maximum estimated temperature of trapping (points T on graphs of Fig. 7.10).

Extensive development of metamorphic biotite in all rock samples from within the shear zones may further constrain this estimate. In any lithostatic pressure environment, the trapping pressure of an inclusion can be considerably less than lithostatic pressure, especially where the country rocks are not completely plastic (Roedder & Bodnar 1980). Pressure may be greater where these rocks undergo high strain deformation which causes fluid inclusions to be overpressured and may increase fluid pressure. Independent geobarometry may be needed to further constrain this estimate.

Liquid rich aqueous Type IV inclusions which occupy healed microfractures and formed at lower temperatures than the other types of inclusions (table 7.1) represent higher density fluids ranging from 0.94 to 1.05 (table 7.2). The estimated pressure for this type of inclusion varies from 400 to 800 bar.

7.3. Geobarometric analysis using electron microprobe data

An electron microprobe analysis study was carried out on selected samples of pelites collected from the Woolshed Flat Shales (samples M30, M2 & U6) and the Saddleworth Formation (samples H19 & H20) from within the Mt. Bold, Pole Road and Morialta shear zones (see appendix A for the sample localities). This was performed to obtain independent geobarometric and geothermometric (P-T) data to further constrain the thrust/shear zone environment.

7.3.1. Sample petrography and microstructures

Deformed pelites in the shear zones show a metamorphic grade of lower greenschist facies (chlorite-biotite zone) with appropriate mineral assemblages ubiquitous in all samples. The mineral assemblage of the samples are biotite + muscovite + chlorite + feldspars and quartz. Muscovite, biotite and chlorite are almost always platy mineral grains of about 300-500 μm in length and 100-150 μm in width. They are almost always preferentially oriented and define a fine pervasive slaty cleavage (S_{1a}). Biotites in pelites of the Woolshed Flat Shale (#'s U6, M2

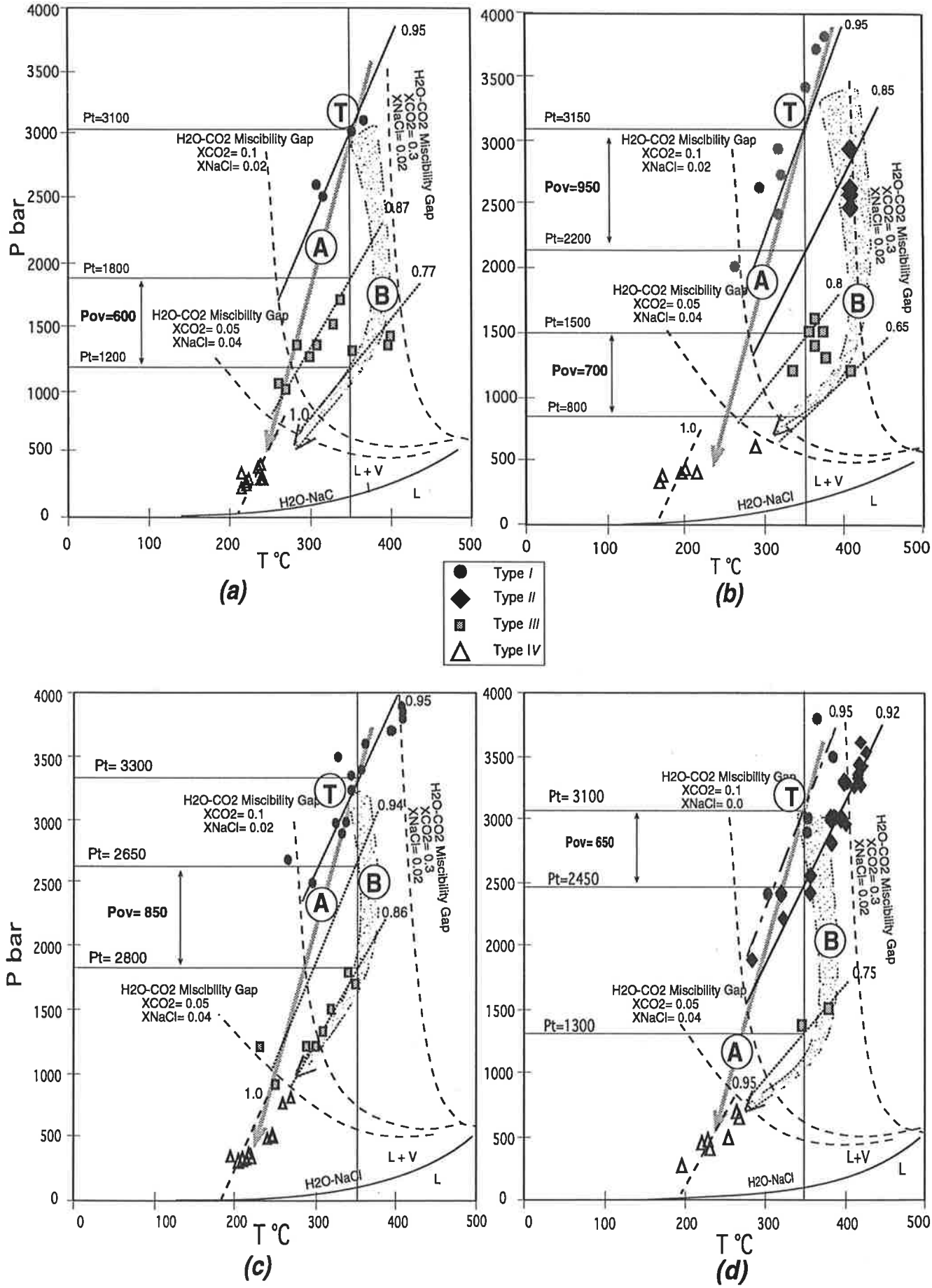

Fig. 7.10: P-V-T graphs and P-T paths of the shear zones. Graphs for: (a) Morialta, (b) Norton Summit, (c) Pole Road, and (d) Mt. Bold shear zones. Symbols: T= estimated pressure and temperatureof trapping, Pt= pressure of trapping, Pov=pressure of overpressuring. Path A shows isochorical development of inclusions, and Path B shows isothermic path for development of inclusions. For more detail see text.

& M30) are all brown (Fig. 7.11a) while in pelites of the Saddleworth Formation (#'s H19 & H20) they are mostly brownish green or green (Fig. 7.11b). Also the amount of chlorite is greatest in samples H19 and H20 (compare Figs 7.11a & b). Quartz grains with a grain size of about 200-400 μm, are more equant than the micas and their grain boundaries are partly dissolved by pressure solution processes (e.g. see Fig. 5.2c). They also show weak evidence of intracrystalline deformation in the form of undulatory extinction. Quartz grains in all samples comprise the bulk of the rocks (about 60%). Feldspars (mostly plagioclase) like quartz are equant with a grain size about 200-300 μm, but are almost always fresh with no evidence of dissolution or intracrystalline deformation.

Spaced overprinting cleavage is common in all samples, cutting the S_{1a} slaty cleavages at a low angle (less than 30°) and creating two different domains, viz cleavage domains or cleavage lamella and microlithons (Fig. 7.11c). In cleavage domains, the micas are more concentrated whereas in the microlithons the quartz and feldspars are more abundant. As mentioned earlier in chapter 5, this spaced cleavage is well developed in samples from the lower boundary thrusts (i.e. samples #'s H20, M2, and U6) and diminishes toward the upper transitional zones.

7.3.2. Mineral chemistry

Mineral compositions were determined for the samples in the CEMMSA (the Center for Electron Microscopy and Microstructure Analysis) of the Adelaide University. This was done on a CAMECA SXS1 microprobe machine with accelerating voltage of 15 Kev. The machine itself has a cold stage and anticontaminator for low Z analysis. It also has a NORAN EDS detector and Mourun software analysis packages. The "miscmica" analysis package was used for the analysis of the micas and "miscfp" package was also used for the analysis of plagioclases. A total of 167 analyses were performed, and representative analyses of mineral phases of each sample are shown in table 7.3.

Figures opposite

Fig. 7.11a: Photomicrograph and backscatter image of the phyllosilicate aggregates from within the Morialta shear zone, showing a cluster of green biotite (bold circle in the image) and chlorite (white cross in the image); width of view in photomicrograph is 1.2 mm.

Fig. 7.11b: Photomicrograph and backscatter image of a sample from within the Mt. Bold shear zone, showing clusters of brown biotite (white cross in the image); width of view in photomicrograph is 2.4 mm.

Fig. 7.11c: Cleavage domains in pelites from the lower boundary thrust to the Pole Road shear zone; width of view is 2.4 mm. Note the low angle between early slaty cleavage (E) and new spaced cleavage (N) or cleavage domains.

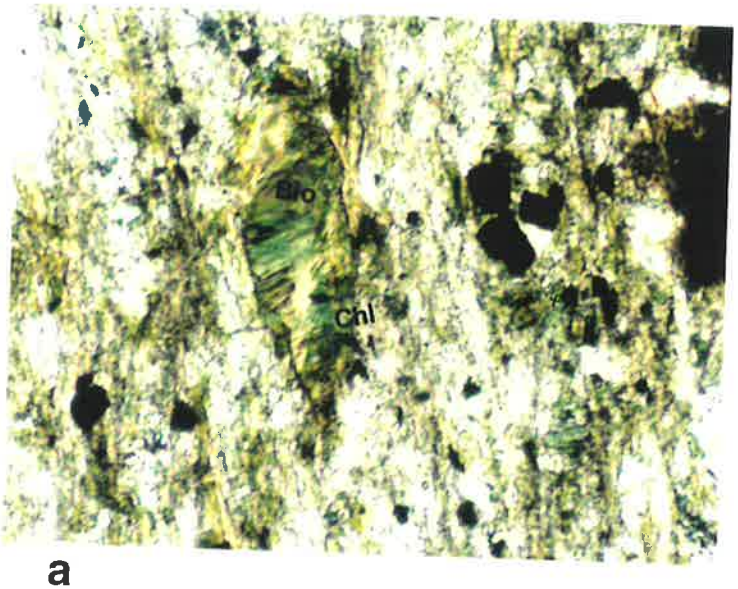

a

b

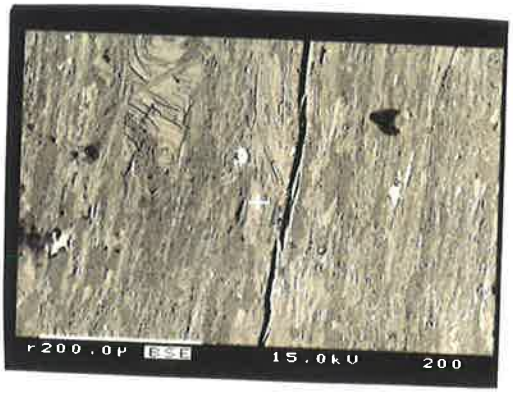

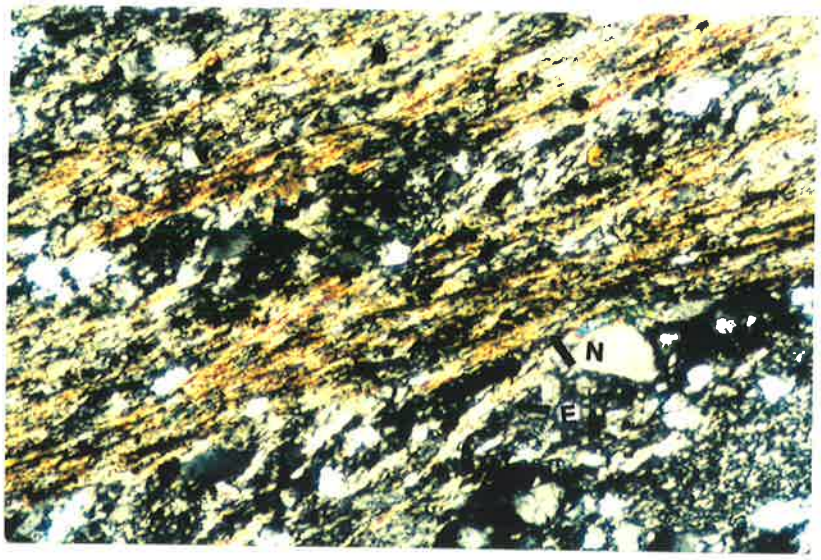

c

Mineral	bi					mu					chl					ab				
No.	H20	H19	U6	M2	M30	H20	H19	U6	M2	M30	H20	H19	U6	M2	M30	H20	H19	U6	M2	M30
SiO2	37.51	38.80	40.38	37.38	38.01	47.24	48.11	48.23	47.83	47.58	25.82	27.05	27.45	26.08	26.25	68.78	69.18	68.88	69.68	68.78
TiO2	2.08	1.81	1.65	2.00	1.45	0.70	0.32	0.45	0.95	0.79	0.08	0.08	0.23	0.15	0.03	0.00	0.00	0.00	0.00	0.00
Al2O3	14.24	14.38	16.75	15.37	15.50	35.06	35.87	35.44	31.65	33.79	19.55	18.75	18.92	20.63	20.72	19.08	18.88	19.08	19.48	19.08
Cr2O3	0.02	0.02	0.00	0.01	0.03	0.04	0.00	0.04	0.06	0.10	0.01	0.03	0.02	0.00	0.01	0.01	0.01	0.01	0.01	0.01
MgO	13.10	12.85	10.56	11.11	14.78	1.00	0.84	0.55	1.46	0.93	18.19	18.83	17.93	14.55	19.98	0.00	0.00	0.00	0.00	0.00
CaO	0.00	0.12	0.05	0.02	0.19	0.02	0.02	0.05	0.02	0.00	0.01	0.02	0.04	0.03	0.09	0.06	0.06	0.06	0.06	0.06
MnO	0.07	0.10	0.07	0.06	0.07	0.06	0.00	0.04	0.00	0.00	0.19	0.10	0.19	0.06	0.04	0.05	0.04	0.05	0.05	0.05
FeO	18.03	16.76	15.96	18.08	13.33	2.18	1.23	2.49	4.41	4.09	20.42	19.44	20.63	22.85	16.86	0.16	0.16	0.06	0.16	0.16
ZnO	0.08	0.01	0.05	0.21	0.17	0.00	0.00	0.00	0.02	0.04	0.11	0.17	0.14	0.17	0.06	0.00	0.00	0.00	0.00	0.00
BaO	0.00	0.00	0.00	0.00	0.00	0.10	0.25	0.07	0.10	0.08	0.00	0.00	0.15	0.02	0.08	0.10	0.10	0.10	0.10	0.10
Na2O	0.00	0.12	0.07	0.05	0.07	0.32	0.67	1.15	0.17	0.44	0.04	0.03	0.02	0.03	0.00	10.44	10.44	10.44	10.24	10.44
K2O	9.89	9.21	8.71	9.00	9.22	10.97	10.03	8.81	10.95	10.59	0.00	0.08	1.10	0.36	0.06	0.10	0.10	0.10	0.10	0.10
Total	95.37	94.52	94.69	93.63	93.29	97.75	97.33	97.47	97.63	98.44	84.50	84.61	86.83	84.94	84.20	98.79	98.79	98.79	99.39	98.79
Si	5.68	5.85	5.96	5.73	5.71	6.17	6.24	6.24	6.33	6.22	4.34	4.51	4.51	4.41	4.33	8.32	8.32	8.32	8.32	8.32
Ti	0.24	0.20	0.18	0.23	0.16	0.07	0.03	0.04	0.09	0.08	0.01	0.01	0.03	0.02	0.00	0.00	0.00	0.00	0.00	0.00
Al	2.54	2.55	2.92	2.78	2.75	5.40	5.48	5.40	4.94	5.21	3.87	3.68	3.67	4.11	4.03	2.72	2.72	2.72	2.72	2.72
Cr	0.00	0.00	0.00	0.00	0.00	0.00	0.00	0.00	0.01	0.01	0.00	0.00	0.00	0.00	0.00	0.00	0.00	0.00	0.00	0.00
Mg	2.96	2.89	2.32	2.54	3.31	0.19	0.16	0.11	0.29	0.18	4.55	4.67	4.39	3.67	4.91	0.00	0.00	0.00	0.00	0.00
Ca	0.00	0.02	0.01	0.00	0.03	0.00	0.00	0.01	0.00	0.00	0.00	0.00	0.01	0.00	0.02	0.01	0.01	0.01	0.01	0.01
Mn	0.01	0.01	0.01	0.01	0.01	0.01	0.00	0.00	0.00	0.00	0.03	0.01	0.03	0.01	0.01	0.01	0.01	0.01	0.01	0.01
Fe	2.28	2.11	1.97	2.32	1.67	0.24	0.13	0.27	0.49	0.45	2.87	2.71	2.84	3.23	2.33	0.02	0.02	0.02	0.02	0.02
Zn	0.01	0.00	0.01	0.02	0.02	0.00	0.00	0.00	0.00	0.00	0.01	0.02	0.02	0.02	0.01	0.00	0.00	0.00	0.00	0.00
Ba	0.00	0.00	0.00	0.00	0.00	0.01	0.01	0.00	0.01	0.00	0.00	0.00	0.01	0.00	0.01	0.00	0.00	0.00	0.00	0.00
Na	0.00	0.04	0.02	0.01	0.02	0.08	0.17	0.29	0.04	0.11	0.01	0.01	0.01	0.01	0.00	2.45	2.45	2.45	2.45	2.45
K	1.91	1.77	1.64	1.76	1.77	1.83	1.66	1.45	1.85	1.77	0.00	0.02	0.23	0.08	0.01	0.01	0.01	0.01	0.01	0.01
Total	15.63	15.44	15.04	15.40	15.46	14.00	13.90	13.82	14.04	14.03	15.70	15.65	15.74	15.56	15.65	13.54	13.54	13.54	13.54	13.54

Table 7.3: Representative probe analyses of minerals in samples from the Morialta shear zone (H20 & H19), Pole Road shear zone (U6), and Mt. Bold shear zone (M2 & M30). Symbols: **bi**=Biotite, **mu**= Muscovite, **chl**= Chlorite and **ab**= Albite.

The mineral chemistry of each mineral is generally constant across the samples except for small changes in the content of Fe or Al cations in muscovite and biotite. In the biotites, the amount of Al cation decreases from 2.92 in samples from the Woolshed Flat Shale to 2.54 in samples from the Saddleworth Formation (table 7.3). The amount of Fe cation increases from 1.67 in samples of the Woolshed Flat Shale from within the Mt. Bold shear zone to 2.28 in samples from the Saddleworth Formation from within the Morialta shear zones. In the Mt. Bold shear zone, the amount of Fe cation also increases from 1.67 in sample #M30 to 2.32 in sample #M2, that is, from within the shear zone toward the lower boundary thrust.

For the muscovite, however, the amount of Fe cation decreases from a mean value of 0.47 in the Mt. Bold shear zone to a mean value of 0.18 in the Morialta shear zone. Similarly, within both shear zones the amount of Fe cation also increases from within the shear zones toward the lower boundary thrusts, that is, from 0.47 to 0.49 in the Mt. Bold shear zone and from 0.13 to 0.24 in the Morialta shear zone.

7.3.3 Estimation of pressures and temperatures

The mineral assemblage described in the previous section has considerable potential for the estimation of deformation conditions using the THERMOCALC computer program and the approach of Powell and Holland (1988), with the expanded internally consistent thermodynamic dataset of Holland and Powell (1990). The procedures from which the electron probe data were calculated and prepared for the program are presented in appendix F.

7.3.3.1 Estimation of average pressures

To calculate pressure using THERMOCALC an estimate of the temperature for any given sample is required. This is because the pressures calculated for an independent set of reactions are based on an estimated temperature. These pressures are the result of involving all mineral end-members which are shared between an equilibrium mineral assemblage and the data set. Therefore, the calculations maximise the information available in a mineral assemblage.

Analyses of the microstructures and fluid inclusions show that the temperature is in excess of 350 °C (see sections 6.5.3 & 7.2.6). Therefore, based on this information the maximum temperature of 400 °C was considered and used for the analysis of all samples by the program to find out the average pressures. A temperature of 400 °C was used for the rocks because this is actually the highest temperature that can be assumed based on the T_H of primary fluid inclusions but, in any case, the calculations turn out to be temperature insensitive. The result of the fluid inclusion analysis, which shows that the rock fluids are not pure H_2O, but have at least 20% CO_2, was also used in the calculations.

The result of an average pressure analysis for the rocks is shown in table 7.2. Samples from the Morialta shear zone give P= 2.4± 1 kbar (#H20, table 7.4a) equivalent to depth of 8-9 Km and P= 2.9± 1 kbar (#H19, table 7.4b) equivalent to depth of 9-10 Km assuming T= 400 °C. The very low fit (f= 0.3) for sample #H20 suggests that the P= 1.9± 1 kbar (equivalent to depth of 7 Km) is a better value. Similarly, although the sample from the Pole Road shear zone gives P= 2.3± 1 kbar (equivalent to depth of 8 Km) assuming T= 400 °C (table 7.4c), the lower f= 0.8 implies that P< 2.3± 1 kbar. Samples from the Mt. Bold shear zone give P= 2.5± 1 kbar (equivalent to depth of 8-9 Km) for #M2 (table 7.4d) and P= 2.3± 1 kbar (equivalent to depth of 8 Km) for #M30 (table 7.4e) assuming T= 400 °C.

Although the temperature of 400 °C for the calculation is assumed to be a maximum, the lower fit in the calculation of some samples (table 7.4a & c) suggests that an optimal temperature is less than 400 °C for at least those samples and in fact should be closer to 380 °C. Therefore it is considered necessary to calculate the average temperatures for the samples to further constrain the results of the average pressure calculations.

Table 7.4: Average pressure calculations on samples from the Morialta shear zone (#'s H20 & H19), Pole Road shear zone (#U6) and Mt. Bold shear zone (#'s M2 & M30), using the approach of Powell & Holland (1988) with the expanded, internally consistent dataset of Holland & Powell (1990). To see in detail the activity data and reactions for the end-members refer to appendix E.

Table 7.4a: Average pressure calculations on the interpreted peak assemblage for rock *#H20.*

T°C	360	380	400	420	440
av P	1.3	1.9	2.4	3.1	3.7
sd	1.05	1.07	1.09	1.11	1.13
f	0.4	0.3	0.4	0.5	0.6

Table 7.4b: Average pressure calculations on the interpreted peak assemblage for rock *#H19.*

T°C	360	380	400	420	440
av P	1.7	2.3	2.9	3.6	4.3
sd	1.06	1.08	1.10	1.13	1.15
f	0.9	0.8	0.8	0.8	0.9

Table 7.4c: Average pressure calculations on the interpreted peak assemblage for rock *#U6.*

T°C	360	380	400	420	440
av P	1.1	1.7	2.3	2.9	3.6
sd	1.04	1.06	1.08	1.09	1.13
f	0.9	0.8	0.9	0.9	1.0

Table 7.4d: Average pressure calculations on the interpreted peak assemblage for rock *#M2.*

T°C	360	380	400	420	440
av P	-	1.6	2.5	3.4	4.4
sd	1.47	1.49	1.52	1.54	1.56
f	0.9	0.9	0.8	0.8	0.8

Table 7.4e: Average pressure calculations on the interpreted peak assemblage for rock *#M30.*

T°C	360	380	400	420	440
av P	1.2	1.7	2.1	2.7	3.2
sd	1.15	1.17	1.19	1.20	1.21
f	0.7	0.6	0.5	0.5	0.5

7.3.3.2 Estimation of average temperatures

An estimation of the average temperature was carried out to further constrain the results of the average pressure calculations and to see whether or not the mineral assemblages could be used as a good geothermometer. The result of the average temperature calculations using the THERMOCALC program is shown in table 7.5. Samples from the Morialta shear zone give T= 395± 24 °C for #H20 (table 7.5a) and T= 393± 24 °C for #H19 (table 7.5b) assuming P= 2.5 kbar for both calculations. However, since the optimal average pressure of P= 1.9± 1 kbar (table 7.4a) is shown to be a more acceptable value for the average pressure, thus, a temperature between 365°C and 389°C can be considered preferable. The same modification can also be made for the sample from the Pole Road shear zone which gives T= 396± 24 °C assuming P= 2.5± 1 kbar. Samples from the Mt. Bold shear zone give T= 403± 26 °C for sample #M2 (table 7.5d) and T= 415± 24 °C for sample #M30 (table 7.5e) assuming P= 2.5±1 kbar.

The results of the average temperature analyses for a pressure of 2.5±1 kbar, show that the calculated temperature for samples from within the Mt. Bold shear zone are in excess of 400 °C while for the samples from the Pole Road and Morialta shear zones they are less than 400 °C, although the difference is not great. This analysis also shows that there is a general trend of temperature increase from the samples within the Morialta shear zone toward the samples within the Mt. Bold shear zone (table 7.5), that is, from more forelandward shear zones to more hindward shear zones (see also Fig. 7.12). Thus, this analysis constrains the mineral assemblage of the rocks as a good geothermometer as well as a good geobarometer. Furthermore, this analysis shows that temperatures in the area of study are relatively high compared with average pressures of about 2.5 kbar (e.g. Thompson & England 1984).

Table 7.5: Average temperature calculations on samples from the Morialta shear zone (#'s H20 & H19), Pole Road shear zone (#U6) and Mt. Bold shear zone (#'s M2 & M30), using the approach of Powell & Holland (1988) with the expanded, internally consistent dataset of Holland & Powell (1990). To see in detail the activity data and reactions for the end-members refer to appendix E.

Table 7.5a: Average temperature calculations on the interpreted peak assemblage for rock *#H20.*

P	1.5	2.0	2.5	3.0	3.5
av T	365	389	395	404	414
sd	20	20	24	24	23
f	0.4	0.5	0.5	0.5	0.6

Table 7.5b: Average temperature calculations on the interpreted peak assemblage for rock *#H19.*

P	1.5	2.0	2.5	3.0	3.5
av T	378	386	393	401	410
sd	20	20	21	21	21
f	0.8	0.8	0.8	0.8	0.8

Table 7.5c: Average temperature calculations on the interpreted peak assemblage for rock *#U6.*

P	1.5	2.0	2.5	3.0	3.5
av T	363	389	396	406	419
sd	18	20	24	24	24
f	0.8	0.8	0.9	0.9	1.0

Table 7.5d: Average temperature calculations on the interpreted peak assemblage for rock *#M2.*

P	1.5	2.0	2.5	3.0	3.5
av T	379	396	403	412	421
sd	22	22	26	26	27
f	0.9	0.8	0.8	0.8	0.8

Table 7.5e: Average temperature calculations on the interpreted peak assemblage for rock *#M30.*

P	1.5	2.0	2.5	3.0	3.5
av T	387	405	415	427	442
sd	26	30	30	29	28
f	0.5	0.5	0.5	0.5	0.5

7.3.3.3 Estimation of average pressure and temperature

The THERMOCALC program can also estimate the average pressure and temperature of any given sample based on an independent set of reactions (see Holland & Powell 1990). This provides constraints on the result of average pressure and temperature calculations. Table 7.6 demonstrates the results of this analysis and shows that average pressure ranges from P= 1.8 kbars equivalent to a depth of 7 km (table 7.6c) to P= 3.0 kbars equivalent to a depth of 10 km (table 7.6d). It also shows that the average temperature ranges from T= 383 °C (table 7.6c) to T=416 °C (table 7.6d). Although the values of standard deviations and fits of the calculations are higher than the individually calculated average pressures and temperatures, the calculated amounts of average pressure and temperature for each sample are consistent with the amount of average pressure and temperature which were individually calculated earlier in the study and constrain the estimated pressure and temperature for each sample (compare data on tables 7.4 & 7.5 with table 7.6).

7.3.4. Estimation of pressure and temperature of peak metamorphism

The assemblage biotite+ muscovite+ chlorite+ feldspar+ quartz suggests the metamorphism is of lower greenschist facies within the biotite or biotite-chlorite zone. For the estimation of average pressure and temperature determined by the internally consistent dataset of Powell and Holland (1988), an average pressure of 2.5± 1 kbar (equivalent to a depth of 8-9 km) and average temperature of 400± 25 °C (tables 7.4, 7.5, & 7.6) was considered to be the best estimate for the condition of peak metamorphism. Under the given pressure of 2.5± 1 kbar the estimated temperature of 400± 25 °C is high and calls for a further discussion.

Table 7.6: Average temperature and pressure calculations on samples from the Morialta shear zone (#'s H20 & H19), Pole Road shear zone (#U6) and Mt. Bold shear zone (#'s M2 & M30), using the approach of Powell & Holland (1988) with the expanded, internally consistent dataset of Holland & Powell (1990). To see in detail the activity data and reactions for the end-members refer to appendix E.

Table 7.6a: Average temperature and pressure calculations on the interpreted peak assemblage for rock *#H20*.
T = 386°C, sd = 36,
P = 2.0 kbars, sd = 1.7, cor = 0.783, f = 0.38

Table 7.6b: Average temperature and pressure calculations on the interpreted peak assemblage for rock *#H19*.
T = 398°C, sd = 36,
P = 2.9 kbars, sd = 1.8, cor = 0.786, f = 0.87

Table 7.6c: Average temperature and pressure calculations on the interpreted peak assemblage for rock *#U6*.
T = 383°C, sd = 35,
P = 1.8 kbars, sd = 1.7, cor = 0.790, f = 0.94

Table 7.6d: Average temperature and pressure calculations on the interpreted peak assemblage for rock *#M2*.
T = 412°C, sd = 51,
P = 3.0 kbars, sd = 2.7, cor = 0.880, f = 0.90

Table 7.6e: Average temperature and pressure calculations on the interpreted peak assemblage for rock *#M30*.
T = 412°C, sd = 51,
P = 3.0 kbars, sd = 2.7, cor = 0.880, f = 0.90

7.4. Discussion

7.4.1. Microstructure analysis and fluid inclusions data

Microstructural analyses of quartz in quartzite rocks from within the shear zones shows that although dynamic recrystallisation of quartz was not extensive, the temperature was sufficient to allow dislocation creep processes. Microstructural studies of quartz veins also indicate that dislocations were mobilised into sub-grain arrays, giving rise to polygonal textures (Fig. 7.3b). On the basis of observations on naturally deformed rocks, this suggests a temperature in excess of 300 ℃ (Voll 1976). This can also be seen from the brittle-ductile transition critical isotherm for quartz-rich rocks assumed by, for example, Sibson *et al.* (1979), White and White (1983), and Simpson (1985). Reductions in the amount of grain boundary migration recrystallisation across the shear zones from the Mt. Bold shear zone toward the Morialta shear zone suggest temperature variations are likely to have occurred on this scale. This is in accordance with the results of experimental analysis which argues that grain boundary migration recrystallisation in quartz develops due to an increase in the temperature of deformation (Hirth & Tullis 1992). Therefore a reduction in the amount of recrystallisation products across the shear zones more likely reflects a temperature variation.

The fluid inclusion homogenisation temperatures also increase for certain types of inclusions across the shear zones (Fig. 7.9). As can be seen in figure 7.9 and table 7.1, mean values of T_H of primary inclusions (Types I & III) increases from the Mt. Bold shear zone toward the Morialta shear zone, which would support a reduction in the degree of ductile deformation of quartz in this direction across the shear zones. Similarly, the shear zones in which recrystallisation of quartz (to produce core and mantle structures) is substantially developed exhibit evidence of fluid inclusions with higher T_H values (Type II). Such higher values of T_H are in accordance with modification or re-equilibration of CO_2-content inclusions to be enriched in CO_2 during which grain boundary migration deformation may have operated.

Overall, a reduction in the value of homogenisation temperature together with reduction in the amount of modified CO_2-rich fluid inclusions from the Mt. Bold to the Morialta shear zones

provides an insight into the conditions of shearing. It is suggested that recrystallisation products and homogenisation temperature across the shear zones decreases along with a decline in the amount of dislocation creep in quartz at the lower boundary thrusts to the shear zones. On the other hand, this might also be because of the development of thrusting and shearing at higher crustal levels from the SE toward the foreland to the NW.

7.4.2. P-T paths and conditions of deformation based on fluid inclusion data

Fluid inclusions in quartz veins from low temperature metamorphic rocks are assumed to have retained a constant composition and volume since the time of trapping (e.g. Mullis 1987). Therefore each inclusion represents a small amount of the fluid phase, present in the rocks at a specific time. Several generations of inclusions within a crystal may thus record the evolution of fluid composition. Similarly, detailed fluid inclusion studies also show that changes in shape and size of inclusions during recrystallisation (e.g. Giles & Marshall 1994 and Johnson & Hollister 1995), and in density of inclusions because of re-equilibration (e.g. Hollister 1990 and Barker 1995), can occur due to changes in physical conditions (that is, pressure and temperature) of the rocks. Recognition of fluid inclusion re-equilibration or modification during recrystallisation provides a constraint on the conditions of deformation and the determination of P-T paths (e.g. Boullier *et al.* 1991, and Barker 1995).

To establish the conditions of deformation and P-T paths from within and between the shear zones, representative isochors for different types of fluid inclusions have been statistically calculated and plotted in figure 7.10. Physical conditions during peak metamorphism in the area have been estimated at 330-360 °C, based on microstructural evidence and T_T of the primary fluid inclusions (refer to section 7.2.6.1). Considering 350 °C as a temperature for trapping, the pressure of 3100-3300 bars can be estimated from the mean value of bulk density of Type I primary inclusions (Fig. 7.10).

The presence of modified Type II inclusions indicates that these inclusions and their possible formative fluid events occurred post entrapment. Homogenisation temperatures of these inclusions are also higher than the trapment temperatures (Sterner & Bodnar 1989). Similarly,

Type III inclusions show scatter values for T_H and their density implies re-equilibration of some inclusions. Isochor projection of maximum and minimum density of these inclusions to estimated temperature of trapping (Fig. 7.10) yields apparent P_T=2200-2450 bars for Type II and P_T=1300-2650 bars for Type III inclusions. Computed amounts of overpressuring for samples from the shear zones show 600-900 bars for Type II and 600-850 bars for Type III inclusions (Fig. 7.10). Overpressuring of greater than 300-400 bars is necessary to have modified inclusions (Bodnar *et al.* 1989). Evidence of negative crystal forms, leaking, necking and/ or decrepitation of inclusions, which are common in all samples across the shear zones (eg. Figs. 5a & b) indicate the possibility of this.

Following the re-equilibration event, a further episode of fluid infiltration is recognised on the basis of inclusion types and lower homogenisation temperatures. These inclusions (Type IV) have consistent vapour/ liquid ratios, have decorated healed microfractures, and show no signs of modification. These aqueous inclusions seem to be a result of infiltration of fluid passing through the veins via microfracturing after their initial formation. This may happen when the rock passes through the ductile-brittle transitional zone to more brittle behaviour which occurs during exhumation. The presence of fractured quartz in quartz veins across the shear zones along with the high salinity of this type of inclusion shows that they formed during brittle deformation. Evidence of development of such inclusions from residual fluids during late stage of deformation has also been reported elsewhere (e.g. Craw 1988, Craw & Norris 1993 and Johnson & Hollister 1995).

Possible P-T paths for development of the fluid inclusions are shown on figure 7.10. The path A shows the development of inclusions which experienced little differential pressure due to re-equilibration. These inclusions were formed at temperatures and pressures of trapment (point T) and later cooled isochorically along path A and therefore are volumetrically representative of the fluid present at the time of trapping. However, Type II and most of Type III inclusions are situated along path B which shows inclusions which formed at pressures and temperatures of trapping and which were then uplifted under nearly isothermal conditions. These inclusions encounter substantial internal overpressuring. Internal overpressure and decrepitation within

fluid inclusions are a response to reduction of confining pressure plus the cohesion of the host mineral by an amount sufficient to rupture the inclusions. As this results in a decrease in the bulk density of contained phases (e.g. Hollister *et al.* 1979; Sterner & Bodnar 1989), it suggests that samples studied experienced exhumation in the period after inclusion trapping. Evidence for such overpressure other than the fluid inclusion data is sparse in the area of study.

An overall reduction of the significance of overpressuring from the Mt. Bold shear zone toward the Morialta shear zone, as indicated by the amount of overpressuring of Type III inclusions, might probably suggest that the shear zones in the Adelaide Hills area developed in piggy-back fashion. This required increases in the amount of exhumation on the structurally higher shear zones, that is, to the SE and toward the Mt. Bold shear zone.

7.4.3. Pressure and temperature conditions of peak metamorphism

The distribution of calculated pressures and temperatures of peak metamorphism using microprobe data (Tables 7.4, 7.5, and 7.6) across the area shows that from the Morialta shear zone toward the Mt. Bold shear zone the pressures and temperatures increase (Fig. 7.12). This increase is not substantial but considering the fact that this occurs within a distance of 20 km across the strike of the shear zones, it is significant and gives an indication that from the more forward to more hindward shear zones both the pressure and temperature increase. This evidence which is consistent with the increase in microstructures and finite strain of quartzite, suggesting that the hindward shear zones accommodated more shortening and thickening, a situation which is common in active fold-and-thrust belts.

A temperature of about 300°C is generally expected from the pressure of 2.5 kbar which is equivalent to a depth of 8-9 km, (see for example Sandiford *et al.* 1990). The estimated temperature of peak metamorphism from all the samples in the study area is higher than 300°C (390-410 °C, Table 7.5) at the given pressure of 2.5±1 kbar. In the more internal portions of the southern Adelaide Fold-Thrust Belt, where there is an extensive occurrence of granitic activity, evidence of high temperature low pressure conditions of peak metamorphism have

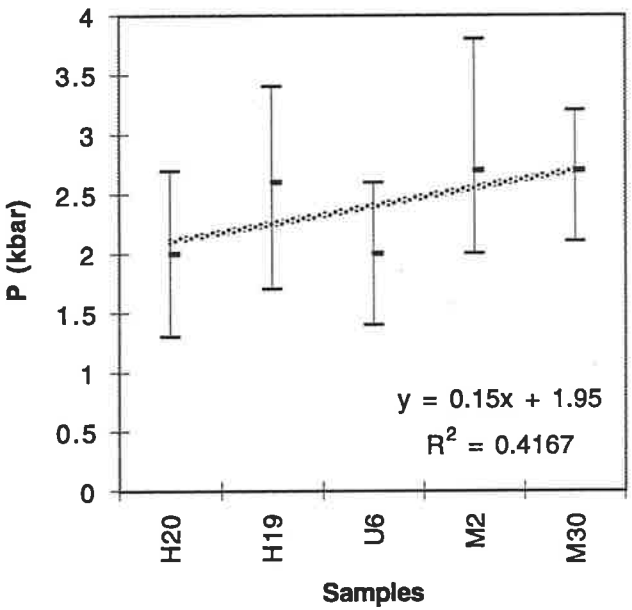

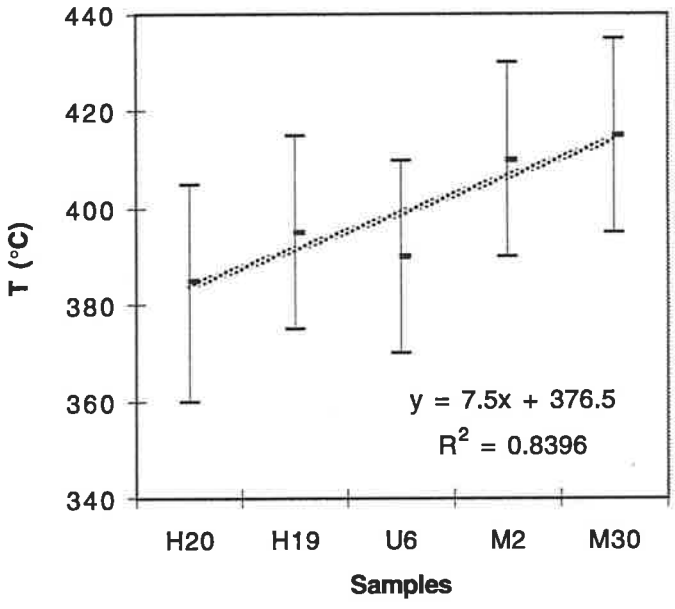

Fig. 7.12: Diagrams showing the distribution of minimum, maximum and average temperatures and pressures of peak metamorphism in samples from the shear zones. For their localities refer to appendix A.

been reported (Mills 1964, Offler & Fleming 1968, Mancktelow 1979, and Sandiford *et al.* 1990). High temperature perturbation of the thermal regime during orogenesis may theoretically be influenced by three major factors: (1), magma input (2) deformation and (3) metamorphic fluid flow. In the internal portion of the belt (Eastern Mt. Lofty Ranges) the occurrence of high temperatures is recorded as a clear manifestation of a "Buchan Style" terrain (e.g. Offler & Fleming 1968, Abbas 1972, Mancktelow 1979, and Sandiford *et al.* 1990). Recently, more detailed analysis of the thermal processes contributing to the formation of this terrain has lead to the proposition that high temperature low pressure metamorphism may be generated during crustal thickening with significant heat advected within the crust, as for example may occur during the segregation of granitic melts (e.g. Sandiford & Powell 1991, and Sandiford *et al.* 1995).

In the external parts of orogens where the temperature comes mainly from the burial of the rock masses, the high temperature and low pressure of the rocks are particularly significant. The study area, which is located in the transition from the more internal portion to the external portion of the southern Adelaide Fold-Thrust Belt, has a distance of about 70 km from the closest outcrop of the magmatic activity from within more internal portion of the belt (refer to Fig 1.3 for the location of magmatic activity). Therefore, the effect of magmatic advection of heat might be significant on raising the temperatures of peak metamorphism from 300 °C to about 400 °C. Thus, it is considered that the high temperatures of peak metamorphism recognised here are more likely to have developed due to advection during that magmatic activity.

Nevertheless, the study of active fold-thrust belts reveals that the main parameters controlling the thermal structure of the fold-thrust belts are the accretion and erosion rates within the wedge, undisturbed geothermal gradients at the toe, and the amount of frictional heating at the basal décollement of the wedge (Barr & Dahlen 1989, and Barr *et al.* 1991). In such fold-thrust belts, it is proposed that metamorphism is not due only to burial of rock masses but also due to the amount of frictional heating both on the basal décollement fault and within the deforming

brittle wedge (Barr *et al.* 1991). If there were no frictional heating, rocks incorporated into the fold-thrust belt would not experience any increase in temperature, and thus they would not show any evidence of syntectonic metamorphism (Barr & Dahlen 1989). Frictional heating has been considered to be responsible for raising temperatures from the 250 °C which has been proposed for typical fold-thrust belts up to 400 °C (e.g. Barr *et al.* 1991). Therefore, it is also likely that much of the higher temperature in the present area has resulted from such frictional heating produced mainly on the décollement fault/shear zone (see balanced sections in Fig. 4.1 for its proposed location) in the basement at depth. However, the extensive evidence of ductile deformation within the shear zones lessens the importance of the possible effect of frictional heating which is proposed for such deforming brittle wedges (Barr *et al.* 1991).

7.5. Conclusions

Fluid inclusion studies show that fluids formed at three different stages during exhumation of the shear zones along their lower boundary thrusts. This process began with fluid entrapment within quartz veins during peak metamorphism (probably biotite grade) followed by inclusion modification which decorates grain boundaries and records the end of ductile crystal plastic processes. Finally a stage of late aqueous inclusion entrapment is associated with late stage brittle fractures. Samples for the present study indicate fluid inclusion trapping at approximately T=330-360 °C and P=3.1-3.3 kbar. Similarly, the results of the calculation of average pressure and temperature using electron probe data show an average temperature of peak metamorphism of around 400°C and an average pressure of about 2.5±1 kbar. These represent deformation conditions at or near the brittle-ductile transition (BDT), a position at which deformation mechanisms in quartz rocks show major changes (Simpson 1985).

From integration and comparison of the results of the fluid inclusion studies and microstructural analysis of quartzite across the shear zones (refer to chapter 6 for more detail), it can be concluded that the shear zones in the Adelaide Hills area developed close to the brittle-ductile transition. In addition, the shear zones closer to the hinterland (including the Mt. Bold

shear zone) behaved in a more ductile manner while ones further to the west and closer to the foreland tend to display greater brittle deformation behaviour. This is in accordance with changes in microstructure of quartzite from grain boundary migration recrystallisation in the Mt. Bold shear zone to the development of recovery products in the Morialta shear zone. Decrease in the amount and ratio of carbonic inclusions (which are argued to represent a decrease in the amount of crystal plastic deformation) and their T_H, together with a decrease in the estimated amount of pressure and temperature from hindward toward forelandward shear zones further supports the brittle-ductile deformation conditions of the shear zones.

The higher temperature of peak metamorphism in the area was considered to be the effect of heat advection of magmatic activity which was emplaced extensively in more internal parts of the southern Adelaide Fold-Thrust belt. In addition, an increase in the accretion and erosion rates resulted from the propagation of the décollement fault at depth toward the foreland or NW which also increased the temperature and heat flow because of the increased advective influx of hot rocks at the toe, as well as due to the influence of increased frictional heating.

Chapter 8

DISCUSSION OF STRUCTURAL EVOLUTION, DEFORMATION MECHANISMS, AND P/T CONDITIONS OF THE SHEAR ZONES

8.1 Introduction

The general geological characteristics of the Southern Adelaide Fold-Thrust belt and in particular the study area (southern Mt. Lofty Ranges/Adelaide Hills area) along with detailed structural mapping and interpretation of seven major transects, which lead to the identification of six major stacked parallel shear zones and many minor associated ductile thrusts, were presented in the first two chapters (see Fig 2.2 for more detail). The sequential development of the main geometrical features of the shear zones, from a number of small areas (refer to Fig. 2.2 for the areas), has also been studied and synthesised (see chapter 3) in order to provide an understanding of the geometric and kinematic evolution of the shear zones.

In addition, microstructural analysis of the shear zones and associated ductile thrusts were also studied using qualitative and quantitative analyses to document the existence of the shear zones and also to determine and to further discuss (refer to section 8.5 in this chapter) possible deformation mechanisms acting within the shear zones. Similarly, conditions and history of the deformation from within the shear zones (P-T conditions) and their possible changes were also presented and discussed (refer to sections 7.4.1 & 7.4.2) to obtain a better understanding of the spatial and temporal evolution of the shear zones.

This chapter provides a summary discussion of the following:

- The structural geometry of the shear zones.
- The relative significance of ductile thrusts versus the shear zones.
- Strain and displacement of the shear zones.
- Deformation mechanisms operating during the development of the shear zones.

- Temperature variations within the shear zones.
- Ductile-brittle transition conditions of the shear zones.
- Exhumation of the shear zones.

The results of these discussions are then used to examine the possible mechanisms of formation of the shear zones in the area of study and in the southern Adelaide Fold-Thrust belt as such.

8.2. Structural geometry of the shear zones

Many studies of the natural deformation of the earth's upper-middle crust have recognised that anomalously high deformation is often localised in narrow, subparallel sided planar shear zones (Ramsay 1980) that accommodate relative movement of mostly rigid wallrock blocks (Hanmer & Passchier 1991). Deformation in such high strain zones usually contains a rotational component, reflecting lateral displacement of wallrock segments with respect to each other (Passchier & Trouw 1995).

Shear zone types are subdivided into brittle shear zones or faults, brittle-ductile shear zones, and ductile shear zones. Major shear zones which transect the crust or upper mantle may have both brittle and ductile segments (Ramsay 1980, and Passchier & Trouw 1995). Deformation fields within the shear zones lead to the development of characteristic fabrics and structures (Naruk 1986, Malavieille 1987), and mineral assemblages that reflect ambient P-T conditions (Passchier & Trouw 1995). The nature of the shear zone flow type as coaxial or non coaxial (Hanmer & Passchier 1991, and Passchier 1991), and movement sense and history in the shear zones (Simpson & Schmid 1983, Lister & Snoke 1984, and Hanmer & Passchier 1991) may also be revealed.

The geometrical analysis of shear zones is basically concerned with the spatial analysis of structures (folds and veins) and fabrics (foliations, lineations, and shear bands) (Hanmer & Passchier 1991). Description of these structures and fabrics from outside of and into a shear zone not only defines the characteristics of the shear zone boundary (Coward 1976) but also qualitatively shows the intensity of shearing (Naruk 1986, Gaudemer & Tapponier 1987, Malavieille 1987, and Hanmer & Passchier 1991).

The geometrical features of the shear zones and associated ductile thrusts in the study area, and in particular the characteristics of their fabrics and minor structures from a number of small areas has been described and analysed and presented in detail in chapter 3. The study has revealed that bedding (S_0) and to lesser extent macroscopic folds and a regional cleavage (S_{1a}) are the main structures and fabrics found outside of the shear/thrust zones. Within the shear zones and adjacent to associated ductile thrusts, however, a concentration of deformation fabrics (stretching lineations, fault-related cleavage/crenulation cleavage, transposition cleavage, and extensional crenulation cleavages or shear bands) and a new array of minor structures (minor folds, transposed layering, and folded and boudinaged quartz veins) comprise the main geometrical features (Fig. 8.1). As is shown in figure 8.1, these fabrics and structures developed progressively and increase in spacing and intensity within the shear zones and towards their basal thrusts (i.e. from A to B, and to C in Fig. 8.1).

The S_{1a} fabric in pelites and phyllites from outside of the shear zones is deformed into an incipient crenulation cleavage at the upper transitional zones (Fig. 3.3a, and step A in Fig. 8.1). This crenulation of S_{1a} then progressively develops by becoming tighter to form crenulation cleavages (S_{1b}) within the shear zones (Fig. 3.3c, and step B in Fig. 8.1) and finally to develop new continuous and/or transposed cleavages (S_{1c}) (Fig. 5.5c, and step C in Fig. 8.1) along the lower boundary thrusts. Unlike S_{1a} which dips shallow to moderately (28- 30° SE), S_{1b} has steeper dips (40- 45° SE) (see also Figs 3.1, 3.6, and 3.14). Such progressive development of the cleavages within the shear zones of the study area (i.e. from steps A to C in Fig. 8.1) has been reported elsewhere and is generally considered to show progressive development of ductile deformation within thrusts/shear zones (e.g. Tobisch & Paterson 1989, Mawer & Williams 1991, and Gray 1995).

In psammites and to a lesser extent in quartzite, the S_{1b} or fault related cleavages also have steeper dips with spaced geometry. Where interlayered pelites and psammites are present, the psammite bands are transposed to form transposition fabrics which are subparallel to fault related cleavages or S_{1b} (refer to section 3.2.1 and Fig. 3.5a for more detail).

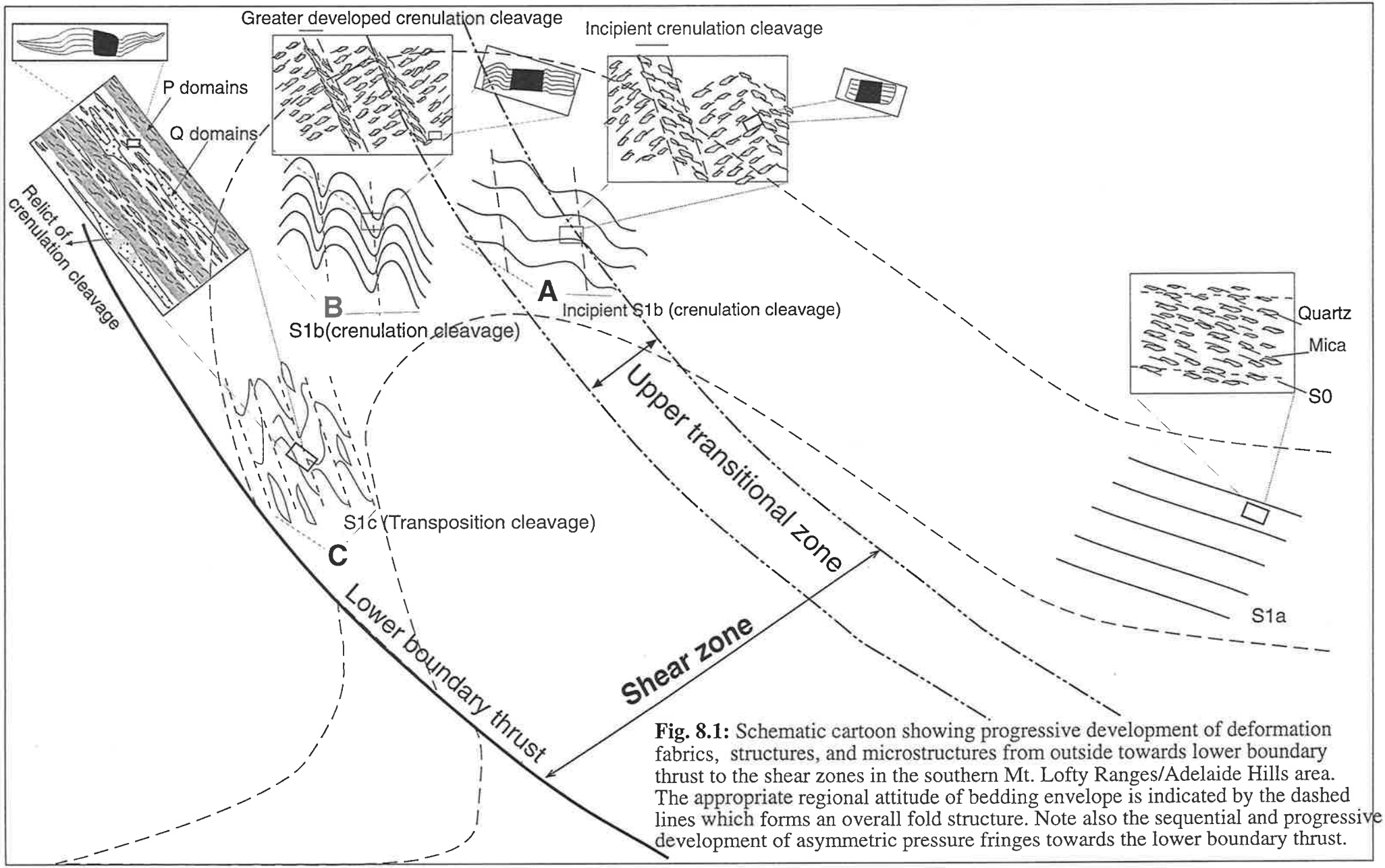

Fig. 8.1: Schematic cartoon showing progressive development of deformation fabrics, structures, and microstructures from outside towards lower boundary thrust to the shear zones in the southern Mt. Lofty Ranges/Adelaide Hills area. The appropriate regional attitude of bedding envelope is indicated by the dashed lines which forms an overall fold structure. Note also the sequential and progressive development of asymmetric pressure fringes towards the lower boundary thrust.

The stretching lineation which is a prominent fabric element in the shear zones, plunges shallowly (<30°), but its trend varies, by about 20-30°, between competent and incompetent units (see for example Fig. 3.4). Analyses of the vergence directions (Bell 1981) of selected pairs of S_0 and S_{1a} from outside of, and on selected pairs of S_{1a} and S_{1b} from within, the shear zones (crenulation cleavage/fault related cleavage) (Fig. 3.18), show that there is consistency of average vergence direction towards the west-northwest. These results are also in accordance with the west-northwest sense of movement obtained from the asymmetric minor folds, asymmetric pressure fringes (for example Fig. 5.6), and shear bands (Fig. 3.13d). The slight change in trend of the mean value of the vergence direction from the W towards the NW and from the older fabrics to younger ones (Fig. 3.18) is due to progressive development of the fabrics during thrusting/shearing.

The oblique (Type II) to sub-parallel (Type I) orientation of minor folds with respect to the orientation of stretching lineations implies that some of the minor folds in the shear zones of the study area were at least modified after their initiation. A strong anisotropy due to the presence of interlayered competent and incompetent rocks, suggests that buckling was most likely to be the cause of fold initiation. It is considered that such modification of the earlier buckle folds resulted from passive rotation of the folds during non-coaxial flow (e.g. Sanderson 1973, Escher & Waterson 1974). The general non-coaxial nature of shear zone deformation, which is considered for example by Hanmer & Passchier (1991), Passchier (1991), and Stock (1992) to be the cause for the formation of extensional crenulation cleavages, further supports the suggestion of the passive rotation of pre-existing folds during thrusting/shearing.

8.3. The relative significance of ductile thrusts versus shear zones

The shear zones and associated imbricate ductile thrusts are the most notable structural elements within the study area (Fig. 2.2). Characteristically, the geometry and kinematics of these shear zones and ductile thrusts are similar. However, there are significant differences in the spatial and temporal development of their deformation fabrics, structures, and microstructures which are discussed below.

The shear zones with their lower boundary thrusts form the base of the major thrust sheets (Fig. 4.1), where most of the ductile deformation is localised (see also Schmid 1975, and Wojtal 1986). This ductile deformation is localised in narrow (from about 150 m to about 600 m in thickness, Fig. 2.2) subparallel zones at the base of wider thrust sheets (6-8 km in outcrop width, Figs 2.2 & 4.1) (Geiser 1988b). Ductile thrusts, however, are narrower (from <1m to about 20 m thick) zones of ductile deformation which are developed either within the shear zones or both in the footwall and hangingwall to the shear zones, forming propagating imbricate fans verging to the NW (Figs 2.2 & 4.1).

Within the ductile thrusts, deformation fabrics (Lx, S_{1a}, and S_{1b}) and structures (minor to macroscopic folds & veins) with the same geometry and kinematics as the shear zones were developed. The intense localisation of ductile deformation, however, is only developed within the shear zones. Such localisation of ductile deformation within thrust/shear zones is also reported elsewhere from for example the southern Appalachians (Wojtal & Mitra 1986) and in the Alps (Travarnelli 1997) and is considered to develop during strain-softening processes (Mitra 1984, and Wojtal & Mitra 1988). The process of localisation of ductile deformation causes development of core and mantle microstructure (White 1976) in quartzite (e.g. Fig. 6.1c) along the lower boundary thrusts to the shear zones in contrast to the development of intracrystalline fracturing in quartzite from within the ductile thrusts (e.g. Fig. 6.3f). In addition, extensional crenulation cleavage (ECC-fabrics, Passchier 1991), which confirms the general non-coaxial nature of the shear zones (Hanmer & Passchier 1991, Stock 1992) is also developed only within the shear zones and no evidence of this structure has been found from within the ductile thrusts. Similarly, the extensive development of asymmetric pressure fringes (e.g. Fig. 5.6a & b) at these boundaries implies that a significant amount of non-coaxial deformation has occurred.

Both shear zones and associated ductile thrusts are accompanied by macroscopic to minor folding in their hangingwalls, which in most cases reveal a geometry similar to the geometry of fault-propagation folds (Suppe 1983, 1985). Macroscopic folds, many of which are anticlines with overturned west limbs, characteristically were mainly developed in the hangingwalls of the lower boundary thrusts to the shear zones. In almost all cases, the shear zones developed on the steep to

overturned limbs of these macroscopic folds (see for example Figs 4.2 & 8.1) and show the dominance of cut-through fault-propagation fold geometry (Elliott 1976, Suppe 1985, Mitra 1990, and Suppe & Medwedeff 1990) (refer also to section 4.2).

Development of minor folds adjacent to the associated ductile thrusts is also considered to be similar to the geometry of fault-propagation folds (see Figs 3.9a & 8.2). As can be seen in figure 8.2a, the initiation of ductile thrusting at depth is considered to have caused the beds to bulge at the tip of the thrust to develop an antiformal structure. As the thrust continued to propagate, the fold continued to grow at the fault tip to produce asymmetric folds with a consistent sense of asymmetry to the movement direction of the thrust (Fig 8.2b). As is shown, the forelimb is attenuated and the interlimb angle is reduced to less than 50°. Further propagation of the thrust tip toward the attenuated forelimb causes the fold to be sheared off and a ductile deformation zone develops. The fold geometry is characterised by progressive tightening of the fold hinge and overturning of the anticlinal fore limb (Fig. 8.2). This process for the propagation of ductile thrusts is similar to those shown by Suppe (1985), Mitra (1990) and McClay (1992) in which the fault propagates through the overturned forelimb of an anticline, a scenario which is common in fault propagation folding. Note that during this process, the hinge zone also migrates towards the thrust propagation direction (Fig. 8.2) at each stage of fold growth (Tavarnelli 1994, 1997) and develops a geometry close to that of fault propagation folds formed by migrating hinge kinematics (Suppe 1985, Fischer *et al.* 1992). The evidence of hinge migration of the folds during meso- and macroscopic fold growth supports the proposal that the tip-line folding model (Elliott 1976, Williams & Chapman 1983) seems appropriate to describe the thrust fold interaction in the area of study.

Based on these observations it is proposed that ductile thrusts and shear zones in the area of study did not propagate instantaneously as brittle fractures (e.g. Hubbert & Ruby 1959 and Hsü 1980) but rather they propagated gradually as slip accumulated along them. This provides a better explanation for the common association of asymmetric folds, with steep to overturned forelimbs, in the hangingwalls of the shear zones and adjacent to ductile thrusts (see also Suppe & Medwedeff 1990).

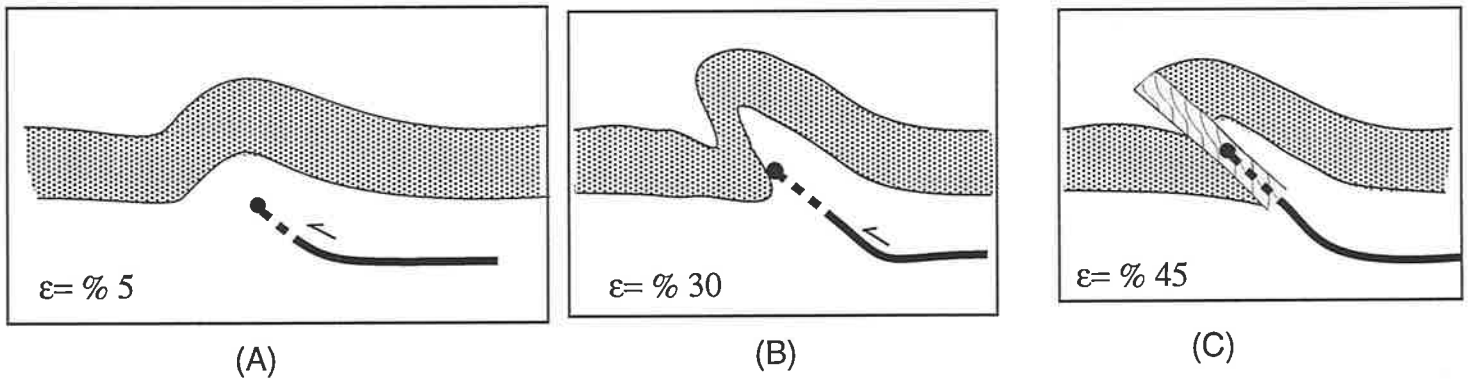

Fig. 8.2: Sketches showing development of fault propagation folds along the ductile thrusts in the Adelaide Hills area. A: the initiation of a thrust at depth causes bulging of quartzite unit (stippled layer); B: propagation of the thrust upwards causes development of an antiform and synform pair in the quartzite layer; C: greater propagation of thrust tip into overturned limb causes this limb to be sheared-off which produces a geometry similar to the geometry of a fault propagation fold. Sketch C is drawn from figure 3.9a. The amount of shortening was also geometrically measured, using a line length balance, and is shown on the bottom left hand side of each sketch. The scale of these sketches can be from minor (like Fig. 3.8c) to macroscopic (like Fig. 3.8).

Overall, the geometries of the ductile thrusts are quite similar to the geometries of the shear zones. This can be further constrained by the similarities between the geometry of minor asymmetric folds formed within the ductile thrusts (Figs 3.9a & 8.2) and the geometry of macroscopic folds which occur in the hangingwall of the shear zones (Fig. 2.2 and also refer to Fig. 3.8). Similarly, the coincidence in orientations of the stretching lineations along the ductile thrusts and within the shear zones provides evidence that the kinematics of the ductile thrusts are also the same as for the shear zones. These geometric and kinematic similarities further demonstrate that the ductile thrusts are more likely to be developed by the same process as the process of development of the shear zones (but on a smaller scale and lower intensity). This may also suggest that the ductile thrusts most likely resemble the early stages in the development of the major shear zones.

8.4. Strain and displacement of the shear zones

Analysis of finite strains from quartzite within the upper transitional zones and toward the lower boundary thrusts of the shear zones (Table 4.1) reveals that samples from the lower boundary thrusts have the highest finite strain magnitude whereas the magnitude of finite strain in samples from the upper transitional zones are approximately similar to those from outside the shear zones (see also Table 4.1). This is in accordance with an increase in the concentration of deformational fabrics and structures at the lower boundary thrusts (Fig. 8.1) and suggests that strain was mainly localised at these boundaries.

Similarly, the results of finite longitudinal strain estimates in quartzite parallel to bedding, using the Rf/Ø method, from within the shear zones (refer to section 4.4.3 for the measurement method and to Table 4.1 for the results) also show that there is a variation in the magnitude of bedding parallel finite strain from negative values (outside/upper transitional zones) to positive values (lower boundary thrusts) across the shear zones. The very low and negative values of finite longitudinal strain values in samples from the upper transitional zones is in accordance with the results of a regional study conducted on similar rocks which shows that quartzite undergoes about -1% line-length change (Flöttmann & James 1997). These negative values are not substantial but show that the rocks outside the shear zones are most likely deformed by a layer parallel shortening component of strain (see also Fig. 3.21). The substantially higher positive values of finite

longitudinal strain from the lower boundary thrusts, however, show that at these boundaries the rocks were most likely deformed by layer parallel extension/shearing during the development of the shear zones. The development of this extensional strain component along the lower boundary thrusts to the shear zones leads to the consideration that extensional shear zones (Passchier 1991) have been superposed on earlier and regional layer parallel shortening (see also Figs 3.21 & 3.22 and section 3.8.5). The development of a layer parallel extensional component of strain along the lower boundary thrusts to the shear zones is further supported by the development of an apparent flattening strain at these boundaries (see Fig. 4.3). The relatively low values of layer parallel shortening component of strain with respect to the layer parallel extension leads to the argument that the shortening in the southern Mt. Lofty Ranges/Adelaide Hills area is accommodated mainly by rigid-body rotation (i.e. folding, Mitra 1994) rather than by pure strain.

From the construction of balanced cross-sections across the shear zones (Fig. 4.1) it is evident that the amounts of transitional displacement along the lower boundary thrusts, in the plane of these sections, of individual shear zones increases from about 900 m near the foreland to about 1400 m toward the hinterland. This is compatible with the results of finite longitudinal strain measurements and confirms that the amount of strain and displacement decreases toward the foreland.

8.5. Deformation mechanisms operative during development of the shear zones

Deformation mechanisms which operated during development of the shear zones can be inferred from the observation of deformation microstructures made on quartzites, psammites, and pelites from within the shear zones. From these observations it appears that strain and displacement along the shear zones was accommodated by the dislocation creep (crystal plastic) deformation mechanism (e.g. Knipe 1989) in quartzites, while in pelites and psammites it was mainly accommodated by pressure solution (e.g. Beach 1979 and Rutter 1983).

Observations on the deformational behaviour of quartz and feldspar grains in the Stonyfell Quartzite from within the shear zones show that quartz grains exhibit mainly intracrystalline deformation features while feldspar grains show mainly internal fracturing. However, quartz

grains with greater dislocation density show evidence of dynamic recrystallisation and feldspar grains display weak intracrystalline deformation features like sweeping undulatory extinction. The intensity of intracrystalline deformation features, like sweeping undulatory extinction and deformation bands in quartz grains increases from the upper transitional zones towards the lower boundary thrusts. Along the lower boundary thrusts, softening mechanisms reduced the work-hardening process and increased the ductility of the quartzite (White *et al.* 1980 and Schmid 1982). This can be evidenced by the development of core and mantle structures (White 1976) in quartzite (Fig. 6.1c) and by the development of both continuous rough cleavage (Gray 1979) and intracrystalline deformation features in psammites (Fig. 5.2c).

The softening mechanisms lead to localisation of deformation features along the lower boundary thrusts, where core and mantle structures (White 1976) are mainly developed. These microstructures are illustrated by undeformed cores surrounded by mantles of finely recrystallised new grains mainly showing subgrain rotation recrystallisation and/or grain boundary migration recrystallisation (e.g. Urai *et al.* 1986, and Hirth & Tullis 1992). A distinguishing factor between subgrain rotation recrystallisation (SRR) and grain boundary migration recrystallisation (GBMR) is grain size. SRR grains have the same size as adjacent subgrains, whereas GBMR grains are usually much smaller than any subgrain present (Simpson 1994). The core and mantle structure in quartz grains from the lower boundary thrust of the Mt. Bold shear zone (see Fig. 2.2 for the location of this shear zone) is mainly developed by grain boundary migration recrystallisation, while in quartz grains from the lower boundary thrust to the Norton Summit shear zone, which is located further towards the foreland (see Fig. 2.2 for the location of this shear zone), the core and mantle structure is mainly developed by subgrain rotation recrystallisation (see also Table 6.1 for the comparison).

Core and mantle structures, however, are not well developed in quartz grains from the lower boundary thrusts to the Morialta shear zone (Fig. 2.2), which is the shear zone closest to the foreland in the study area, (compare Figs 6.1c and 6.3e for a description of the development of core and mantle structures). The decrease in the degree of development of core and mantle structures from the hinterland towards the foreland shear zones, along with the changes in the

form of recrystallisation products from grain boundary migration recrystallisation to subgrain rotation recrystallisation show that the degree of crystal plastic deformation mechanisms decrease in this direction.

Overall, observation on the development of these microstructural features in quartz grains within quartzites is interpreted as evidence for dislocation creep (crystal plastic) deformation mechanism (e.g. White 1976, Schmid *et al.* 1980, and Vernon 1981). Moreover, the greater reduction in the lengths of short axes of quartz grains with respect to their long axes (i.e. increase in shape ratio) along the lower boundary thrusts (Fig. 6.4a & b) might be mainly due to greater elongation of grains at these boundaries. Crystal plastic deformation mechanisms are considered to produce more flattened and elongated grain shapes (e.g. Passchier & Trouw 1995). Therefore the higher aspect ratios of the grains (Fig. 6.7) along the lower boundary thrusts is most likely due to the greater influence of the crystal plastic deformation mechanisms along these boundaries.

In contrast to the quartzites, observation of the microstructural development of cleavages in pelites shows that these fine grained rocks mainly exhibit deformation features indicative of the pressure solution/diffusion process. Within the shear zones, the pressure solution process, which is considered to be a dominant deformation mechanism in fine grained rocks (e.g. Knipe 1989), caused marginal removal of quartz and feldspar (mostly albite) grains and addition of phyllosilicates (e.g. Stephens *et al.* 1979, and Groshong 1988). This can be explained by the elongation of quartz grains parallel to the continuous rough cleavage due to reduction of their lengths normal to the cleavage (Williams 1972, and Lisle 1977) (Fig. 5.4b). A similar reduction in the proportion of the quartz grains and a relative increase in the amount of phyllosilicate in pelites from within the shear zones can also be seen from within the microstructures of discrete crenulation cleavages in the shear zones (Figs 5.4f & 5.5b). These observations further support the interpretation that pelites in the shear zones were affected dominantly by pressure solution deformation mechanism (Williams 1972, Gray 1979, Groshong 1988, and Passchier & Trouw 1995).

Similarly, the microstructural study of the development of cleavages in psammites from within the shear zones revealed that these cleavages also developed by pressure solution processes. This is

supported by the presence of sutured quartz grain boundaries, truncation of detrital quartz grains against folia comprised of insoluble phyllosilicate grains (e.g. Fig. 5.3), and offset across folia (see also Elliott 1973 and Gray 1978). However, the abundant evidence of intracrystalline deformation features in quartz grains, including deformation bands (e.g. Fig. 5.2f), sweeping undulatory extinction and sometimes subgrain formation (e.g. Fig. 5.3), implies that intracrystalline deformation has also contributed to microstructural development of psammites. Such intracrystalline deformation features are well developed mainly in psammites from the lower boundary thrusts.

Simultaneous development of intracrystalline deformation features with development of pressure solution products in psammites from the lower boundary thrusts to the shear zones is considered to be due to the localisation of deformation and/or strain at these boundaries. This is further supported by the localisation of deformation features (i.e. core and mantle structures) in quartzites at these boundaries.

8.6. Temperature variations of the shear zones

The extensive microstructural evidence which includes sweeping undulatory extinction, deformation bands, subgrain formation, and in grains with higher dislocation densities core and mantle structure in quartzites, from within the shear zones suggest that deformation temperature was in excess of 300 °C (see also Voll 1976, Simpson 1985, and Bailey *et al.* 1994). Similarly, lack of recrystallisation along grain boundaries of feldspars also suggest that the deformation temperature was below 450 °C (see also Tullis 1983, Simpson 1985, and O'Hara 1990). Therefore, based on these observations the temperature of deformation is considered to be somewhere between 350-450°C. Furthermore, it is also interpreted that the temperature at the time of deformation across the shear zones varies and generally decreases from the hinterland, where grain boundary migration recrystallisation is dominant, towards the foreland, where subgrain rotation recrystallisation is more effective (see also Hirth & Tullis 1992).

Analysis of primary fluid inclusions (Type I) in quartz veins from within the shear zones shows that homogenisation temperatures of these inclusions occurred at between 337-360 ± 30 °C (see

Table 7.1). As homogenisation temperature is recognised as being less than the temperature of inclusion trapment (Roedder 1984), it can be inferred that the temperature of fluid inclusion trapment or peak metamorphism was in excess of 350 °C, which is compatible with the temperature of deformation obtained from the microstructural observations. However, the higher homogenisation temperature of modified Type II fluid inclusions, which are enriched in CO_2 phases, indicates that the temperature of deformation increased during the development of the shear zones. The spatially preferred location of Type II fluid inclusions along the lower boundary thrusts of the shear zones closer to the hinterland, and the decrease in the frequency of these inclusions towards the foreland further supports the result of the microstructural study that the temperature of deformation decreased in the shear zones closer to foreland (see also Table 7.1 and Fig. 7.12 for more detail).

8.7. Ductile-brittle transition conditions in the shear zones

The fact that the quartz grains in quartzites deformed in a ductile manner whereas feldspar grains show brittle deformation features implies that the shear zones developed under brittle-ductile transition conditions (see also Simpson 1985 and Bailey *et al.* 1994). The transition from ductile to brittle-ductile bulk rock behaviour in quartz rich rocks is thought to be determined by the response of quartz to changes in applied stress and temperature (e.g. Sibson 1983). The overall decrease in the degree of crystal plastic microstructures from the Mt. Bold towards the Morialta shear zones (see Fig 2.2 for the location of the shear zones, and Table 6.1 for the comparison of the microstructural changes), together with the change in microstructural features from dominant grain boundary migration recrystallisation to subgrain rotation recrystallisation has been interpreted to occur due to gradual changes in temperature (see also Hirth & Tullis 1992). Therefore it is interpreted that these microstructural variations were developed within the shear zones under brittle-ductile transition conditions (i.e. 8-10 km depth, Sibson 1983). Such brittle-ductile transition conditions of deformation can be further supported by the change in the geometry of quartz veins across the shear zones. In the Mt. Bold shear zone, quartz veins were deformed by ductile deformation to produce folded and boudinaged veins (Hanmer 1986, Malavieille 1988, and Swanson 1992) (Figs 3.13c and 3.16f), while in the Morialta shear zone

quartz veins were deformed by brittle-ductile deformation to produce en-echelon tension gash structures (Ramsay 1980) (Fig. 3.2e).

In the external part of fold-and-thrust belts, it is considered that rocks deform in a brittle wedge above a basal detachment which separates the wedge from the underlaying basement (Davis *et al.* 1983, and Barr & Dahlen 1989). The main deformation mechanism in this part of orogens is the solution transfer deformation mechanism (Elliott 1973). In the internal part of fold-and-thrust belts where magmatic activity can be present and metamorphic conditions are moderate to high, crystal plasticity is recognised as the dominant deformation mechanism (Wojtal & Mitra 1988). Typically, in this part of the orogen, rocks deformed under ductile conditions and basement can be also involved (Rathbone *et al.* 1983, Platt & Behrmann 1986). Based on these definitions and due to the lack of moderate to high metamorphic conditions and magmatic activity, the study area is in fact not a typical internal part of the SAFT-B. However, the involvement of basement rocks in the deformation (Fig. 4.1), the relatively higher temperature of deformation than the typical foreland fold-and-thrust belts (e.g. the Appalachian foreland fold-thrust belt, Karabinos 1988, and Taiwan fold-and-thrust belt, Barr & Dahlen 1989), and extensive evidence of fluid activity (the presence of fluid inclusions, folded and boudinaged quartz veins, and pressure fringes) suggest that the study area is not a typical example of the external part of a fold-and-thrust belt either. Based on the geometrical changes of deformed quartz veins, observation of microstructures, and involvement of basement into the thrusting and shearing , it is rather interpreted that the study area is a type of transitional zone between the more internal parts of fold-and-thrust belts and the classical external part. Therefore, the shear zones are especially significant as they developed dominantly in such a transitional zone. The involvement of the basement in the thrusting and shearing supports the idea that the study area forms part of crystalline thrust system but with thin-skinned tectonic behaviour (Hatcher & Hooper 1992) where the rocks from within the shear zones were deformed under brittle-ductile transition conditions.

8.8. Exhumation of the shear zones

The calculation of the average pressure of peak metamorphism from within the shear zones from the assemblage of biotite, muscovite, chlorite and feldspar (albite) using the THERMOCALC

computer program and internally consistent data set of Powell & Holland (1988) (Table 7.3) has provided an average pressure of 2.5±1 kbar (equivalent to a depth of 8-9 km). Similarly, an average pressure of about 3.0 kbar (equivalent to a depth of 10 km) was also estimated for the trapping of primary fluid inclusions (Type I) (Table 7.2), which is compatible with the pressure calculation of peak metamorphism.

Modified Type II fluid inclusions, however, show trapping pressures with a lower average of 2.8 kbar (equivalent to a depth of 9-10 km. Furthermore, Type IV fluid inclusions, which formed as healed microfractures, show average pressure of trapment at about 0.5 kbar (equivalent to depths of less than 2 km). The existence of several generations of fluid inclusions within a crystal record the evolution of the fluid (e.g. Shepherd *et al.* 1985). Each fluid inclusion is assumed to have retained a constant composition and volume since the time of trapment. Therefore, the presence of different types of fluid inclusions in the shear zones of the study area imply that they were trapped at different times and with possibly different compositions.

Similarly, it is broadly considered that changes in shape and size of fluid inclusions during recrystallisation (e.g. Giles & Marshall 1994, and Johnson & Holister 1995), and that change in density of fluid inclusions because of re-equilibration (e.g. Holister 1990, and Barker 1995), can occur due to changes in physical conditions (that is, pressure and temperature) of the rocks. Based on the detailed study of homogenisation temperature and salinity of the fluid inclusions (see Tables 7.1 & 7.2), it is proposed that modified Type II and III inclusions were developed from the same fluid as primary Type I but were then modified to lower densities (See Table 7.2). This situation may have occurred when the shear zones were exhumed to higher crustal levels (lower depth). Evidence of negative crystal forms, leaking, necking down, and decrepitation of Type II and III inclusions show that fluid inclusions have suffered overpressuring most likely during the exhumation of the shear zones. The calculated amount of overpressuring reveals values of 0.6-0.9 kbar for Type II and 0.6-0.85 kbar for Type III inclusions (Fig. 7.10). The amount of overpressuring of these fluid inclusions as indicated in figure 7.10 decreases from the shear zones closer to the hinterland towards the shear zones closer to the foreland (see the decrease in the value of overpressuring for Type I inclusions from Pov= 0.85 kbar in the Pole Road shear zone to a

value of Pov= 0.6 kbar in the Morialta shear zone in Fig. 7.10). This also indicates that the amount of exhumation of the shear zones decreases towards the foreland.

The fact that thrusting/shearing in the area of study and in general in the southern Adelaide Fold-Thrust belt was attributed to the Delamerian Orogeny (Flöttmann *et al.* 1995, 1997), provides evidence that fluid inclusion formation and modification has also occurred during this orogeny. Therefore, it is considered that the exhumation of the shear zones in the area of study occurred most likely during the late Delamerian Orogeny.

8.9. Mechanisms of formation of the shear zones

Construction of balanced and restored cross sections (Fig. 4.1) show that the general geometry of the shear zones closely resembles the piggy back style of hinterland dipping imbricate fans commonly formed in leading imbricate thrust sheets (e.g. Boyer & Elliott 1982). The decrease in the intensity and amount of deformation fabrics (e.g. ECC-fabrics) and structures (e.g. isoclinal recumbent folds of Type I fold geometry) in the shear zones (see also Fig. 3.22 and section 3.8.5) from the hinterland (Mt. Bold) towards the foreland (Morialta); together with the reduction in the amount of displacement, measured from the sections (figure 4.1), as shown by Dunlap *et al.* (1995) further supports a piggy back style of development for the shear zones. The relatively low displacement values (i.e. less than 3000 m of overall displacement, Fig. 4.1) and low internal strain (i.e. about 2.00, Table 4.1) within the shear zones is similar to that reported from other frontal imbricate thrust systems (e.g. southern Appalachian thrust belt, Wojtal & Mitra 1988). The steeper dip of the S_{1b} cleavage compared to S_{1a} within the shear zones, and especially along the lower boundary thrusts (e.g. Figs 3.6 & 3.10) is compatible with the consideration that layer boundary parallel shortening (Sanderson 1982) was most effective, that is, thrust sheets were shortened in the direction of shear. This implies that subhorizontal compression was more likely a relevant process for the formation of the shear zones than was gravitational spreading.

The mechanisms of development of the shear zones in the study area and overall in the external parts of the southern Adelaide Fold-Thrust Belt can be best explained by a critical-taper wedge model (Davis *et al.* 1983) (Fig. 8.3a). The critical-taper wedge model is now generally considered

to be the main mechanism for interpreting the evolution of fold-thrust belts (Davis *et al.* 1983, Barr & Dahlen 1989, De Celles & Mitra 1995, Boyer 1995, and Mitra & Sussman 1997). Based on this model, an active fold-thrust belt is analogous to a wedge of soil or snow which forms in front of a moving bulldozer. This wedge deforms internally by shortening and thickening untill reaches a critical taper (Davis *et al.* 1983, and Dahlen 1990). The rate of erosion and the accretionary influx rate of fresh material controls the width of a critically-tapered wedge and produces a steady state fold-and-thrust belt (Dahlen & Suppe 1988, and Barr & Dahlen 1989).

The model is considered to be generally applicable based on the qualitative compatibility between spatial and temporal patterns of thrusting/shearing in orogens (e.g. Boyer & Geiser 1987, Geiser & Boyer 1987, Boyer 1995, and DeCelles & Mitra 1995). However, it has been argued that the model has limited applicability to fold-and-thrust belts because of mechanical and deformational incompatibilities between the geologic record and the model (e.g. Woodward 1987, Bombolakis 1994). According to Woodward (1987), shortening seen in the deformed thrust-belt cross sections is not predominantly a result of shortening within the wedge as suggested by Davis *et al.* (1983), therefore, Woodward (1987) maintained that the wedge model requires high internal strains. Consequently, the frequent presence of low internal strains and lack of out-of-sequence thrusting would appear to reflect shortcomings in the critical wedge model. Nevertheless, study of sedimentary basin taper (the dip of underlaying basement) by Boyer (1995) shows that strains need not to be as high as previously thought. Boyer (1995) also points out that the use of the critical-wedge model in explaining structural variation in fold-thrust belts does not constitute proof of the model. Similarly, Mitra and Sussman (1997) consider that continued duplexing at the rear of the wedge results in the shortening and thickening of the rear wedge to maintain the taper.

The general structural variation of the Adelaide Hills shear zones (e.g. Fig. 3.22), the decrease in the amount of crystal plastic deformation microstructures from the hinterland towards the foreland (e.g. Table 6.1), the spatial distribution of pressure and temperature across the shear zones (e.g. Table 7.2 and Fig. 7.12), and the decrease in the exhumation of the shear zones towards the foreland (e.g. Fig. 7.10) which have been presented and discussed in previous sections are

considered to be most likely compatible with a critical-taper wedge model. More detailed supporting evidence of such compatibility is presented and discussed below.

As described earlier (see section 3.8.5 and Fig. 3.22), during the reactivation of the Neo-Proterozoic Adelaidean Supergroup and Cambrian Normanville/Kanmantoo Groups (Flöttmann *et al.* 1994), a master crystalline décollement fault within the Barossa Complex basement propagated toward the foreland. The propagation of such a basement décollement created an orogenic wedge where the dip of the décollement decreased from about 9° in the hinterland to about 3° towards the foreland (Figs 8.4a & 8.5a). In the rear part of this tapered wedge, which is closer to the hinterland, an initial thrust/shear zone was formed. The first thrust/shear zone is most likely to have initiated in the region of maximum décollement dip (Figs 8.4a & 8.5a) where less internal deformation is required to build the taper and thus the least amount of work will be expended (Boyer 1995). As this first sheet advanced, it loaded the foreland (Fig. 8.4b) and increased the dip on the basement décollement which in turn led to the development of the next thrust/shear zone (Figs 8.4c & 8.5b). This process of initiation of thrust/shear zones continued towards the foreland until the taper became subcritical and where greater deformation was required to a create critical taper (Boyer 1995) (Fig. 8.5d).

The spacing of the thrust/shear zones which varies from 4 to 6 km (see Fig. 2.2) may have been controlled by the basal strength of the basement décollement. As the basal décollement of the wedge is developed within the strong basement, the basal strength of the wedge is relatively high. Thus, the wedge builds up a taper and propagates toward the foreland by means of relatively closely spaced thrusts/shear zones (see also Figs 2.2 & 4.1) involving basement rocks (e.g. DeCelles & Mitra 1995). The thrust advance may also have been controlled by erosion, which in turn also affects tectonic loading of thrusts/shear zones and basement décollement subsidence. If erosion rates are less than uplift rates, the taper may become supercritical and lead to the accretion of additional frontal thrust/shear zones in the foreland (e.g. Dahlen & Barr 1989 and DeCelles & Mitra 1995).

Overall, it is considered that the Mt. Bold shear zone (Fig. 8.5b) was initiated first. Loading of this shear zone caused initiation of the next shear zone (Figs 8.4c & 8.5c). Loading of this second

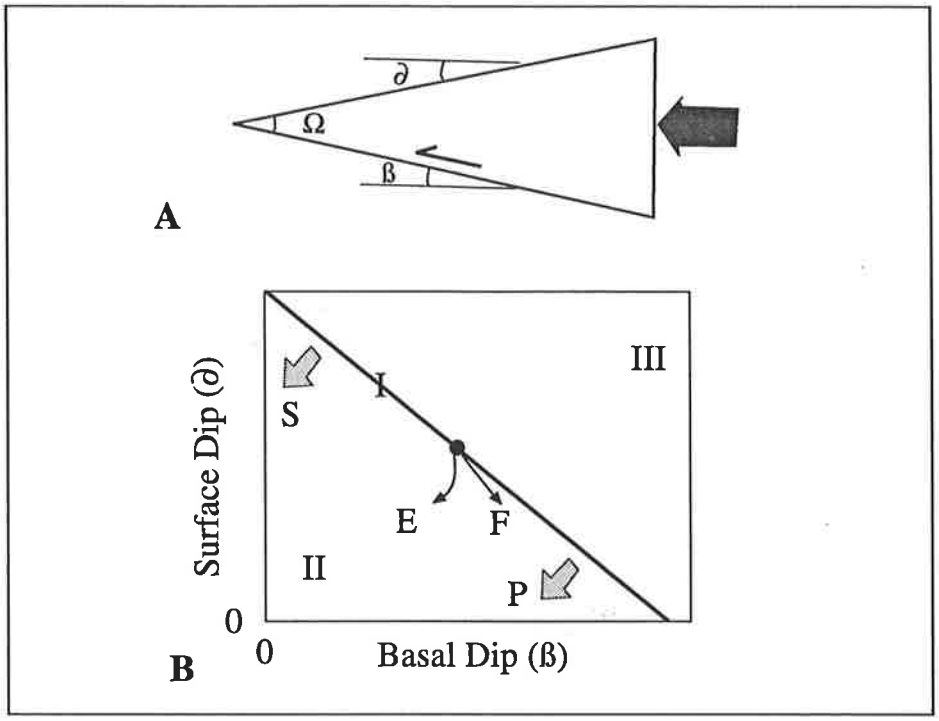

Fig. 8.3: (A) Schematic diagram showing the geometry of a tapered orogenic wedge (after Mitra & Sussman 1997). Wedge taper (Ω) is the sum of the surface slope (∂) and the dip angle of the basement décollement (ß). (B) Behavior of a Coulomb wedge in ∂-ß space in response to changes in certain geologic parameters. Labelled fields are: I- Critical, wedge deforms internally and advances in self-similar form; II- Subcritical, wedge stalls due to insufficient taper; III- Supercritical, wedge can slide forward on a basement décollement thrust. Increase in wedge strength (S) and increased pore pressure at base (P) or decreased basal strength shifts the critical taper line (I) downwards. A critically taper wedge (filled circle) may change its taper as shown as a result of surface erosion (E), or flexural subsidence (F).

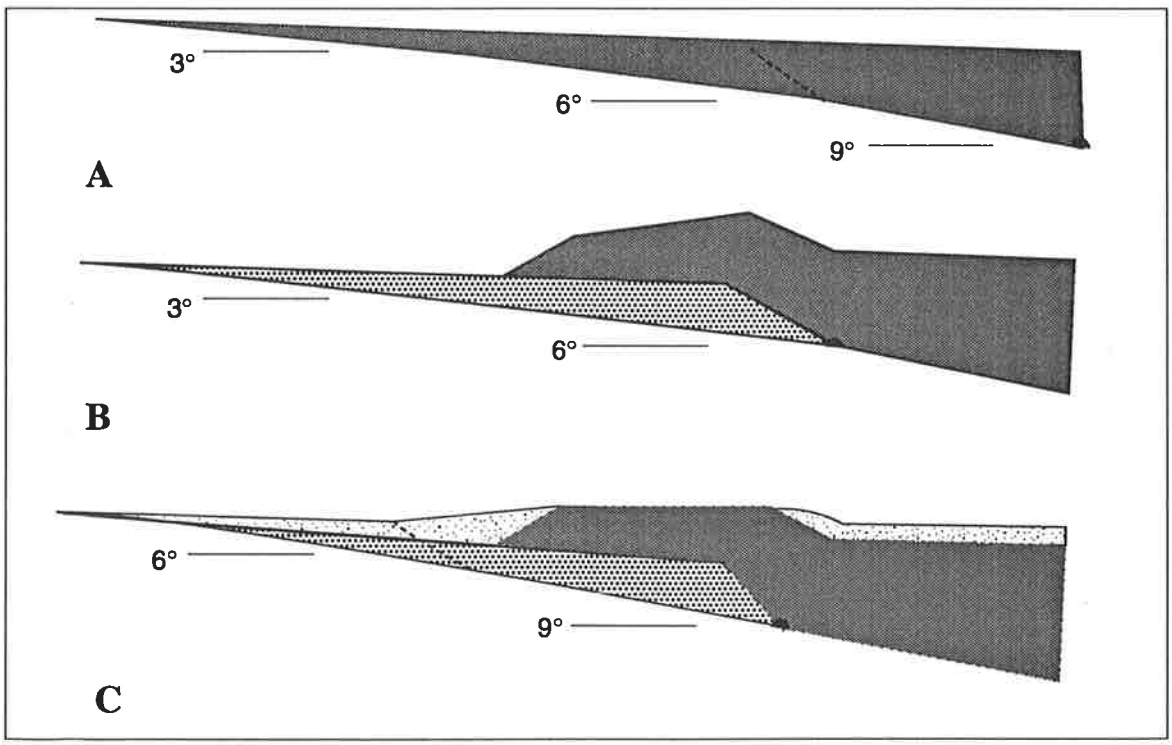

Fig. 8.4: Initiation of thrust sheets in regions of high basin taper (after Boyer 1995). (A) A cross section of a basin in which the basement décollement dip decreases in a convex up fashion from 9° in the hinterland to 3°in the foreland. (B) Development of a thrust in the region of maximum basement décollement dip. (C) The tectonic load of the initial thrust sheet depresses the crust, bring in additional portions of the foreland basement to a critical taper angle, thus leading to the initiation of the next thrusts.

shear zone not only caused formation of the third shear zone, i.e. the Morialta shear zone (Fig. 8.5d) but also increased the exhumation of the first shear zone, i.e. the Mt. Bold shear zone, (Fig. 8.5d). The process of thrust/shear zone formation continued until the taper wedge became subcritical (Fig. 8.5d).

With the advance of each new thrust/shear zone (Fig. 8.5c), the deformation in previous thrust/shear zones (i.e. Mt. Bold shear zone in Fig. 8.5c) decreased and deformation was more localised along the base of the thrust sheet, leading to development of each shear zone, due to strain-softening processes (Mitra 1984, Wojtal & Mitra 1988). Thus along the newly developed thrust/shear zone closer to foreland (thrust/shear zone III in Fig. 8.5) the deformation was relatively higher intensity than thrust/shear zone I and the softening process was not developed as it was along thrust/shear zone I. Increases in the intensity of deformed fabrics and structures together with increases in the intensity of crystal plastic deformation in quartz grains from the Morialta shear zone towards the Mt. Bold shear zone support this argument (see also Figs 3.22 & 8.1).

Decrease in the amount of shear zone exhumation (see section 8.8 and Fig. 7.10) from the Mt. Bold shear zone towards the Morialta shear zone together with the relatively higher temperature and moderate pressure of peak metamorphism for the rocks from the study area can also be best explained using the critical-wedge taper model. As shown in figure 8.6, rocks that enter first into the wedge are buried at greater depths (i.e. 7 km for path *a* in Fig. 8.6c) and remain at higher temperatures (300 °C) and pressures (about 3.0 kbar) before being exhumed (path *a* in Fig. 8.6c). Rocks that enter later are buried to lesser depths (i.e. 3 km for path *c* in Fig. 8.6c) and therefore exhibit lower pressures (1.5 kbar) and temperatures (about 200 °C) before being uplifted to the surface (path *c* in Fig. 8.6). Thus, the shallowest entering rock experiences little burial and shows minimal increase in pressure and temperature.

All of the trajectories of the rocks that experience burial are clockwise (Barr *et al.* 1989) (Fig. 8.6). P-T path analysis of the shear zones based on fluid inclusion data (Fig. 7.10) also show clockwise trajectories of the inclusion development after trapment (points T in Fig. 7.10) during

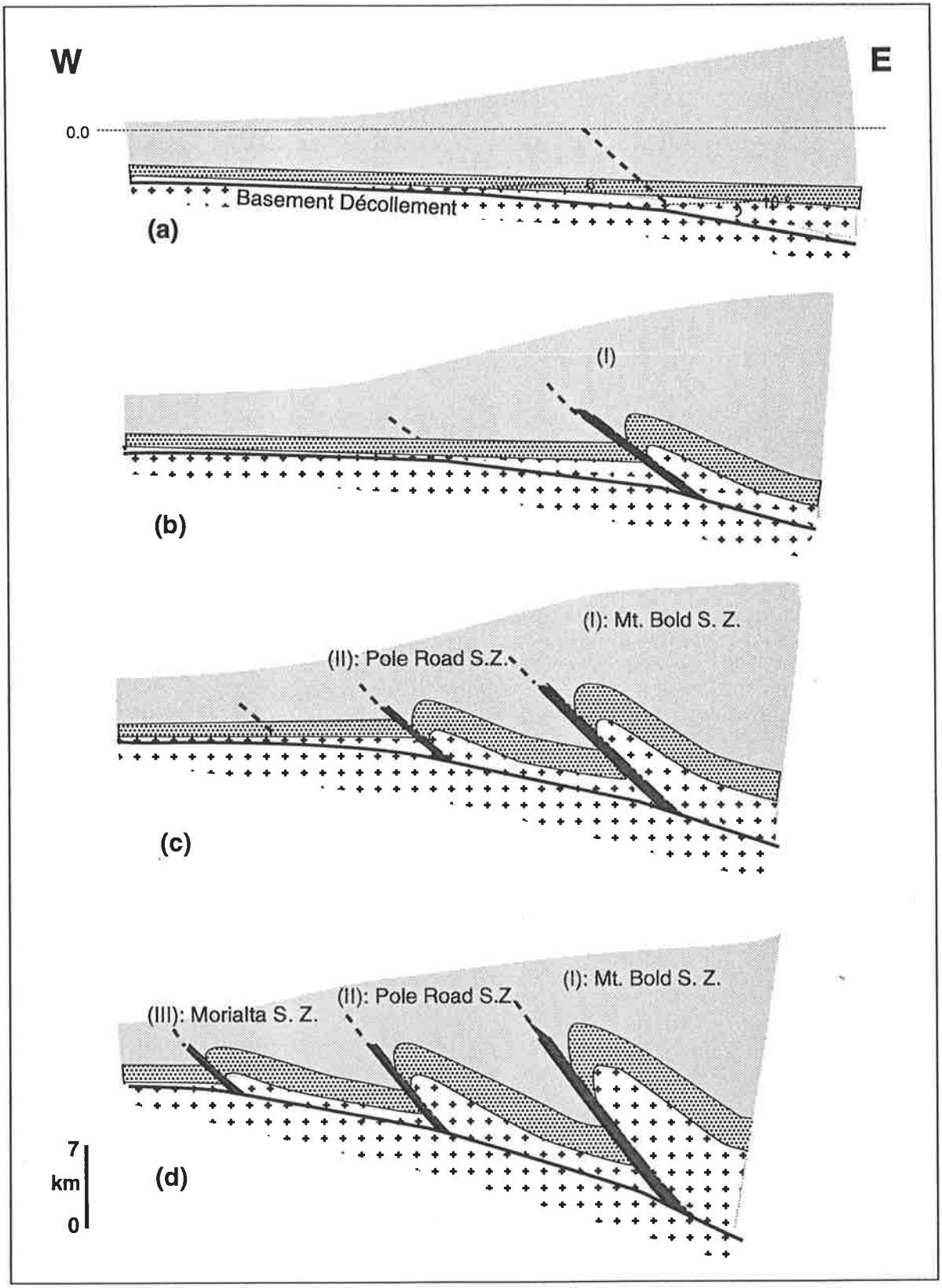

Fig. 8.5: Sketches showing evolution of thrust/shear zones in the southern Mt. Lofty Ranges/ Adelaide Hills wedge. The geometry of folds are drawn based on the geometry of the mesoscopic folds in the area shown in figures 4.1 and 4.2. Basement rocks are white with cross pattern and cover is represented with the gray pattern. (a): proposed Adelaide Hills basin, in which the basement décollement dip decreases toward the foreland due to loading. (b) Initiation of first thrust/shear zone in the region of maximum décollement dip. (c): Loading of first thrust/shear zone causes the décollement to dip more steeply and provide the requirement for the initiation of second thrust/shear zone. (d): Final stage in which loading of the second thrust/shear zone cause the décollement dip to steepen with occurence of the third thrust/shear zone. See text for more information.

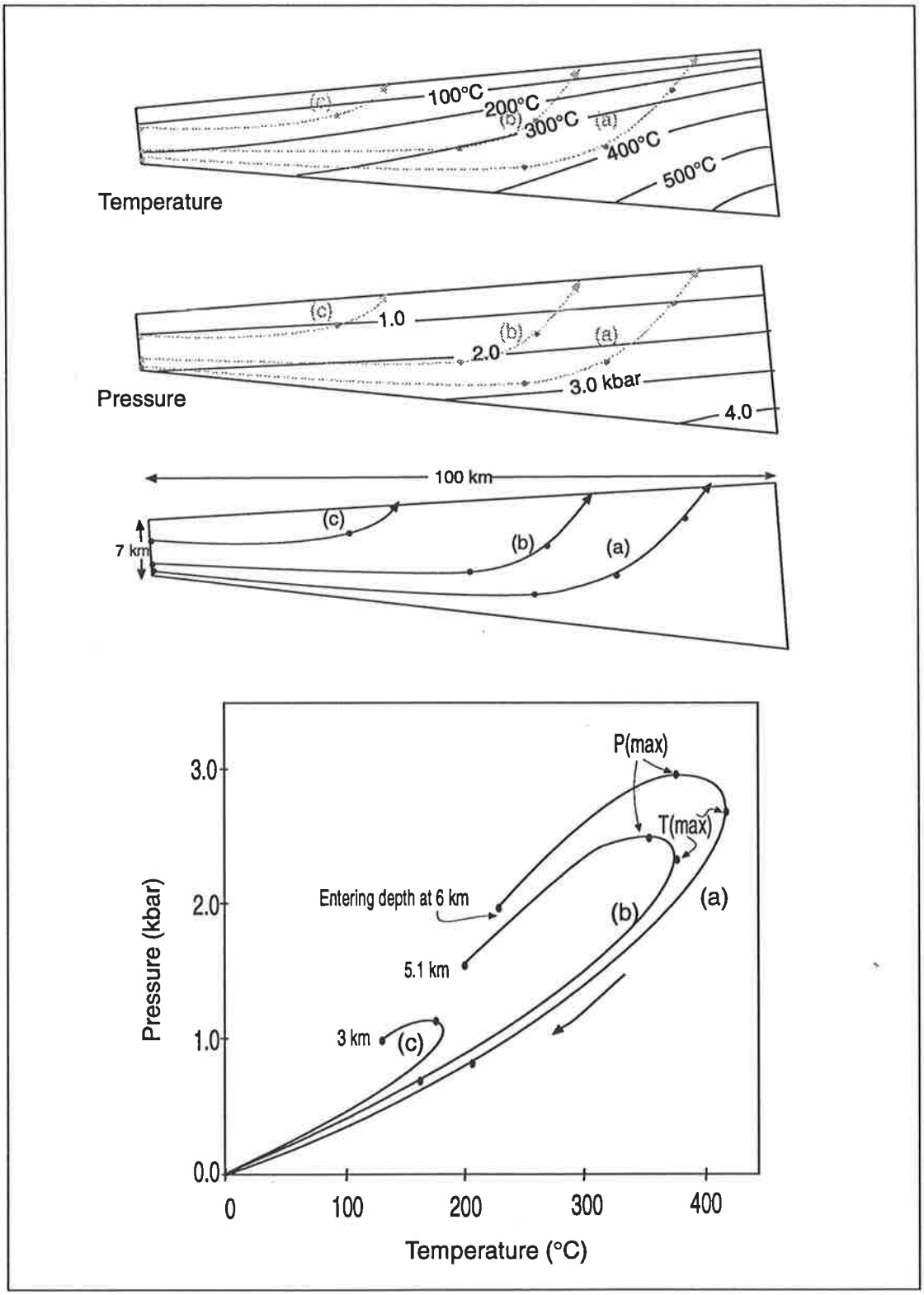

Fig. 8.6: Trajectories of three rocks from three main shear/thrust zones in the southern Adelaide Fold-Thrust belt (modified after Barr & Dahlen 1989). Path "a" represents a rock from the Mt. Bold shear zone, path "b" represents a rock from the Morialta shear zone, and path "c" represents a rock from an unknown shear zone to the NW of the area of study towards the foreland.

the exhumation (paths B in Fig. 7.10). A decrease in the temperature of peak metamorphism from 416± 37°C in the hinterland side shear zones (Mt. Bold) to 386± 36°C in the foreland side shear zones (Morialta) (Table 7.6) is consistent with the decrease in the amount of exhumation (Fig. 7.10) from the Mt. Bold toward the Morialta shear zones and further supports the proposed P-T trajectories (Fig. 8.6).

Similarly, the temperature also slightly increases within the shear zones and from samples collected at about 200 to 300 m above the lower boundary thrusts to samples collected along the lower boundary thrusts. For example, in the Mt. Bold shear zone, temperature in sample # M2 which was collected from about 100m away from the lower boundary thrust is 403°C whereas in sample #M30 which was collected from the lower boundary thrust it is 415°C assuming a pressure of 2.5 kbar for both samples. Although the differences between temperature of these samples is not substantially significant, this may, however, indicate the effect of shear heating at the lower boundary thrusts to the shear zones during the formation of the shear zones in the tapered basin of the SAF-TB.

8.10: Conclusions

In this thesis the location of the mapped shear zones and associated ductile thrusts in the southern Mt. Lofty Ranges/Adelaide Hills area has been shown. The existence of such high deformation zones was documented based on the sequential development of the main geometrical features from within the shear zones, microstructural development and analysis of grain configuration geometry, and development and modification of fluid inclusions from the deformed quartz veins. Similarly, based on the geometric and kinematic analyses of the shear zones, balanced and restored cross-sections, finite strain analysis, microstructural development and deformation mechanisms, and spatial and temporal development of pressure and temperature of the deformation across the shear zones the possible mechanisms for the formation of the shear zones were also examined.

The main conclusions to be drawn are:

• Shear zones in the study area are spatially concentrated zones including an array of fabrics and minor structures. These fabrics and structures are incipiently developed at the upper transitional zones to the shear zones and then develop greater within the shear zones and finally intensify along the lower boundary thrusts which make up the base to the shear zones. The presence and intensity of these fabrics and structures (for example shear bands) decrease from the shear zones closer to the hinterland towards the shear zones closer to the foreland.

• Study of macroscopic and microscopic kinematic indicators like shear bands, asymmetric minor folds, asymmetric pressure fringes, and displaced broken grains show that the shear zones were propagated and overthrust towards W-NW.

• All the shear zones are associated with ductile thrusts which show the same geometry and kinematics as the shear zones. However, the narrower zones of deformation along the ductile thrusts and the absence of shear bands and curvilinear folds together with the lack of dynamic recrystallisation microstructures from within the ductile thrusts show that unlike the shear zones localisation of ductile deformation was not well developed along these ductile thrusts. The geometric and kinematic similarities of the shear zones and ductile thrusts indicates that the ductile thrusts are more likely to be developed by the same process as the process of development of the shear zones but at the early stages due to lack of shear bands and dynamic recrystallisation.

• The results of finite strain analysis on quartzites show that samples from outside/the upper transitional zones have lower magnitude than those from within the shear zones. Estimation of layer parallel finite longitudinal strain also indicates a variation in the magnitude from negative values (in samples from outside/the upper transitional zones) to positive (in samples from within the shear zones). The relatively high positive values of finite longitudinal strain in samples from within the shear zones along with the spatial development of curvilinear folds and shear bands in the shear zones leads to the consideration that the shortening in the study area was largely accomplished by shearing/thrusting (rigid-body rotation component of strain) along the shear zones.

• Observation of microstructural development of cleavages in pelites and psammites shows that cleavages are well developed within the shear zones by the process of pressure solution. In pelites, this is supported by a reduction in the proportion of quartz grains and a relative increase in the amount of phyllosilicates within the shear zones. In psammites, the presence of sutured quartz grain boundaries, truncation of detrital quartz grains against cleavage domains comprised of insoluble phyllosilicates further indicate that the pressure solution process is dominant in pelites and psammites from within the shear zones. The progressive development of cleavages from a regional fine slaty cleavage outside the shear zones to an intense crenulation cleavage within the shear zones implies that they progressively developed during thrusting/shearing.

• Detailed studies of quartz grain microstructures in quartzites from outside/the upper transitional zones to within the shear zones show that in the upper transitional zones, quartz grains exhibit mainly intracrystalline deformation like undulatory extinction while within the shear zones the intensity of these intracrystalline deformation features increases and shows evidence of shear bands, subgrains and in grains with greater dislocation densities dynamic recrystallisation in the form of core and mantle structures. These microstructures exhibit overwhelming evidence of crystal plastic deformation mechanisms across the shear zones. Based on the decrease in intensity and development of the core and mantle structures, the amount of this deformation mechanism decreases from the shear zones closer to the hinterland towards the shear zones on the foreland side where evidence of pressure solution deformation mechanisms were also seen in quartzites. This confirms the brittle-ductile transition condition of deformation within the shear zones.

• Quantitative/statistical analyses of quartz grain configuration from outside towards the shear zones show that all quartz grains are reduced in size. Crystal plastic deformation mechanisms are considered to be responsible for this reduction. Further reduction of quartz grains in samples from the foreland-side shear zones is recognised to be due to both the effects of crystal plastic and pressure solution deformation mechanisms. Similarly, the analyses confirm that the aspect ratios of the quartz grains are increased, and their shape preferred orientations are also changed. These

reorganisation of quartz grain configurations within the shear zones are considered to be due to the process of thrusting/shearing.

• Analyses of primary fluid inclusions in deformed quartz veins from within the shear zones show that the temperatures of fluid inclusion trapment were in excess of 350 °C. Similarly, the result of the calculation of average temperature of peak metamorphism using electron probe data also show an average temperature of around 400 °C. These data represent deformation conditions of the shear zones at or near the brittle-ductile transition zone.

• The calculation of the average pressure of peak metamorphism has shown an average pressure of 2.5±1 kbar which is compatible with the estimated pressure of 3.0 kbar for the trapping of primary fluid inclusions. Modified secondary fluid inclusions, however, show average pressure of trapment of less than 0.5 kbar. Such decrease in pressure of fluid inclusion trapping along with evidence of negative crystal forms, leaking, necking down, and decrepitation of fluid inclusions indicates that they have suffered overpressuring during the exhumation of the shear zones. Calculation of overpressuring of fluid inclusions across the shear zones demonstrate that the amount of exhumation of the shear zones decreases towards the foreland.

• The critical-wedge taper model is considered as a more compatible model for the mechanisms of formation of the shear zones. This is based on the observation of microstructural variations and the spatial distribution of pressures and temperatures across the shear zones, the decrease in the amount of exhumation of the shear zones toward the foreland, and the piggy back style of hinterland dipping imbricate fans which is considered for the general geometry of the shear zones.

• It is considered that the thrust/shear zones closer to the hinterland was initiated first by propagation from a basement décollement. Loading of this first thrust/shear zone caused propagation of the next thrust/shear zone towards the foreland. Loading of this second thrust/shear zone not only caused formation of the first thrust/shear zone but also increase its exhumation. During the continuation of propagation of the thrust/shear zones, the deformation decreased along the previous thrust/shear zones and become more localised along the base of each

shear zone, leading to the development of shearing due to the strain-softening process. Therefore this process was not well developed in the younger shear zones closer to the foreland.

• Rocks in the first propagated and generated thrust/shear zones were buried at greater depths and remained at higher temperatures and pressures before being exhumed. However, rocks in the later propagated and generated thrust/shear zones were buried to lesser depths and therefore suffered lower pressures and temperatures before being uplifted.

REFERENCES

Aerden, D. G. A. M. (1996) The pyrite-type strain fringes from Lourdes (France): indicators of Alpine thrust kinematics in the Pyrenees.*Journal of Structural Geology* **18;** 75-91.

Ahmad, M. (1993) The origin of tin deposits in the Mount Wells region, Pine Creek Geosyncline, Northern Territory. *Australian Journal of Earth Sciences* **40**; 5, 427-443.

Alderton, D. H. M. and Bevins, R. E. (1996) P-T conditions in the South Wales Coalfield; evidence from coexisting hydrocarbon and aqueous fluid inclusions. *Journal of the Geological Society of London* **153**, Part 2; 265-275.

Aller, J. and Bastida, F. (1993) Anatomy of the Mondoñedo Nappe basal shear zone (NW Spain). *Journal of Structural Geology* **15;** 1405-1419.

Anderson, J. A. (1975) Structural and strain analysis of the nose of the Myponga-Little Gorge inlier, Fleurieu Peninsula, South Australia. The University of Adelaide, Adelaide,

Bailey, C. M., Simpson, C. and De Paor, D. G. (1994) Volume loss and tectonic flattening strain in granitic mylonites from the Blue Ridge province, central Appalachians. *J. Struct. Geol.* **16;** 1403-1416.

Bakker, R. J. and Jansen, B. H. (1990) Preferential water leakage from fluid inclusions by means of mobile dislocations. *Nature* **345;** 58-60.

Barker, A. J. (1995) Post-entrapment modification of fluid inclusions due to overpressure; evidence from natural samples. *Journal of Metamorphic Geology* 13; 6, 737-750.

Barr, T. D. and Dahlen, F. A. (1989) Brittle frictional mountain building, 2, Thermal Structure and Heat Budget. *J. Geophys. Res.* **94;** 3923-3947.

Barr, T. D., Dahlen, F. A. and McPhail, D. C. (1991) Brittle frictional mountain building; 3, Low-grade metamorphism. *Journal of Geophysical Research, B, Solid Earth and Planets* **96**; 6, 10,319-10,338.

Batchelor, G. K. (1967) An introduction to fluid dynamics. Cambridge University Press, 615.

Beach, A. (1979) Pressure solution as a metamorphic process in deformed terrigenous sedimentary rocks. *Lithos* **12**; 1, 51-58.

Becker, A. (1995) Quartz pressure solution: influence of crystallographic orientation *Journal of Structural Geology* **17;** 1395-1405.

Bell, A. M. (1981) Vergence; an evaluation. *Journal of Structural Geology* **3;** (3), 197-202.

Bell, I. A., Wilson, C. J. L., McLaren, A. C., *et al.* (1986) Kinks in mica; role of dislocations and (001) cleavage. *Tectonophysics* 127; 1-2, 49-65.

Bell, T. H. and Etheridge, M. A. (1973) Microstructure of mylonites and their descriptive terminology. *Lithos* **6;** 337-348.

Bell, T. H. and Etheridge, M. A. (1976) The deformation and recrystallization of quartz in a mylonite zone, central Australia. *Tectonophysics* 32; 3-4, 235-267.

Berberian, M. (1983). Continental deformation in the Iranian plateau, *Geo. Surv. of Iran.*

Bodnar, R. J., Binns, P. R. and Hall, D. L. (1989) Synthetic fluid inclusions; VI, Quantitative evaluation of the decrepitation behaviour of fluid inclusions in quartz at one atmosphere confining pressure. *Journal of Metamorphic Geology* 7; 2, 229-242.

Bombolakis, E. G. (1994) Applicability of critical-wedge theories to foreland belts. *Geology (Boulder)* 22; 6, 535-538.

Borradile, J. G., Bayly, M. B. and Powell, C. M. (1982) Atlas of deformational metamorphic rock fabrics. Springer-Verlag, 551.

Boullier, A. M. (1980) A preliminary study on the behaviour of brittle minerals in a ductile matrix; example of zircons and feldspars. *Journal of Structural Geology* **2;** 1/2, 211-217.

Boullier, A. M. (1986) Sense of shear and displacement estimates in the Abeibara-Rarhous Late Pan-African shear zone, Adrar des Iforas, Mali. *Journal of Structural Geology* **8;** 47-58.

Boullier, A. M., France, L. C., Dubessy, J., *et al.* (1991) Linked fluid and tectonic evolution in the High Himalaya mountains (Nepal). *Contributions to Mineralogy and Petrology* 107; 3, 358-372.

Bowers, T. S. and Helgeson, H. C. (1983) Calculation of the thermodynamic and geochemical consequences of non ideal mixing in the system H (sub 2) O-CO (sub 2) -NaCl on phase relations in geologic systems; metamorphic equilibria at high pressures and temperatures. *American Mineralogist* 68; 11-12, 1059-1075.

Boyer, S. E. (1978). Structure and origin of Grandfather Mountain window, North Carolina, John Hopkins Univ.

Boyer, S. E. (1992) Sequential development of the southern Blue Ridge Province of North Carolina ascertained from the relationships between penetrative deformation and thrusting. Structural geology of fold and thrust belts. S. Mitra and G. W. Fisher. John Hopkins Uni. Press, Baltimore. 161-188.

Boyer, S. E. (1995) Sedimentary basin taper as a factor controlling the geometry and advance of thrust belts. *American Journal of Science* 295; 10, 1220-1254.

Boyer, S. E. and Elliott, D. (1982) Thrust systems. *AAPG Bulltein* **66;** 1196-1230.

Boyer, S. E. and Geiser, P. A. (1987) Sequential development of thrust belts; implications for mechanics and cross section balancing. *Abstracts with Programs Geological Society of America* 19; 7, 597.

Brown, P. E. and Hagemann, S. G. (1995) MacFlinCor and its application to fluids in Archean lode-gold deposits. *Geochimica et Cosmochimica Acta* **59;** (19), 3943-3952.

Bucher, N. K. (1987) A recalibration of the chlorite-biotite-muscovite geobarometer. *Contributions to Mineralogy and Petrology* 96; 4, 519-522.

Buhrer (1995) The structure of the Myponga River-Carickalinga Creek area, southern Adelaide Fold Belt, Fleurieu Peninsula, South Australia. The University of Adelaide, Adelaide, 35.

Burks, R. and Mosher, S. (1996) Multiple crenulation cleavages as kinematic and incremental strain indicators. *Journal of Structural Geology* 18; 5, 625-642.

Butler, R. W. H. (1982) The terminology of structures in thrust belts. *Journal of Structural Geology* **4;** 239-245.

Campana, B., Wilson, R. B. and Whittle, A. W. G. (1954). Geological Atlas of South Australia, Yankalilla sheet. Adelaide, Geological Survey of South Australia.

Chapple, W. M. (1978) Mechanics of thin-skinned fold-thrust belts. *Geol. Soc. of Am. Bull.* **89;** 1189-1198.

Clarke, G. L. and Powell, R. (1989) Basement cover interaction in the Adelaide Fold Belt, South Australia: the development of an arcuate fold Belt. *Tectonophysics* **158;** 209-226.

Cobbold, P. R. and Quinquis, H. (1980) Development of sheath fold in shear regimes *Journal of Structural Geology* **2;** 119-126.

Coogan, J. C. (1993) Structural evolution of piggyback basins in the Wyoming-Idaho-Utah thrust belt. Regional Geology of Eastern Idaho & Western Wyoming. P. K. Link, M. A. Kuntz and L. B. Platt. Geol. Soc. of Am. Mem., **179:** 55-81.

Cooper, J. A., Jenkins, R. J. F., Compston, W., *et al.* (1992) Ion-probe zircon dating of a mid-Early Cambrain tuff in South Australia. *J. geol. Soc. Lond.* **149;** 185-192.

Cosgrove, J. W. (1976) The formation of crenulation cleavage. *Jl. geol. Soc. Lond.* **132;** 155-178.

Cosgrove, J. W. (1993) The interplay between fluids, folds and thrusts during the deformation of a sedimentary succession. *Journal of Structural Geology* **15;** 491-500.

Coward, M. P. (1976) Strain whitin ductile shear zones. *Tectonophysics* **34;** 181-197.

Coward, M. P. (1984) The strain and textural history of thin-skinned tectonic zones: examples from the Assynt region of the Moine thrust zone, NW Scotland. *Journal of Structural Geology* **6;** 89-99.

Coward, M. P. (1988) The Moine thrust and the Scottish Caledonides. *Geol. Soc. Am.* **222;** 1-16.

Coward, M. P., Nell, P. R. and Talbot, J. (1992) An analysis of the strains associated with the Moine thrust zone, Assynt, Northwest Scotland. Structural Geology of Fold and Thrust Belts. S. Mitra and G. W. Fischer. John Hopkins University Press, Baltimore. 105-122.

Cox, S. F. and Etheridge, M. A. (1989) Coupled grain-scale dilatancy and mass transfer during deformation at high fluid pressures; examples from Mount Lyell, Tasmania. *Journal of Structural Geology* **11**; 1-2, 147-162.

Craw, D. (1988) Shallow-level metamorphic fluids in a high uplift rate metamorphic belt; Alpine Schist, New Zealand. *Journal of Metamorphic Geology* **6**; 1, 1-16.

Craw, D. and Norris, R. J. (1993) Grain boundary migration of water and carbon dioxide during uplift of garnet-zone Alpine Schist, New Zealand. *Journal of Metamorphic Geology* **11**; 3, 371-378.

Crawford, M. L. (1981) Phase equilibria in aqueous fluid inclusions. Short course in fluid inclusions: applications to petrology. L. S. Hollister and M. L. Crawford. Mineralogical Association of Canada, **6:** 75-100.

Crawford, M. L., Kraus, D. W. and Hollister, L. S. (1979) Petrologic and fluid inclusion study of calc-silicate rocks, Prince Rupert, British Columbia. *American Journal of Science* **279**; 10, 1135-1159.

Dahlastrom, C. D. (1969) Balanced cross-sections. *can. J. Earth. Sci.* **6;** 743-753.

Dahlastrom, C. D. (1970) Structural geology in the eastern margin of the Canadian Rocky Mountains. *Bull. can. Petrol. Geol.* **18;** 332-406.

Dahlen, F. A. (1984) Noncohesive critical Coulomb wedges: An exact solution. *J. Geophys. Res.* **89;** (10), 125-133.

Dahlen, F. A. (1990) Critical taper model of fold-and-thrust belts and accretionary wedges. *Annual Review of Earth and Planetary Sciences* **18**; 55-99.

Dahlen, F. A. and Barr, T. D. (1989) Brittle frictional mountain building, 1, Deformation and mechanical energy budget. *J. Geophys. Res.* **94;** (10), 3906-3922.

Dahlen, F. A. and Suppe, J. (1988) Mechanics, growth and erosion of mountain belts. *Geol. Soc Amer. Spec. Pap.* **218;** 161-178.

Dahlen, F. A., Suppe, J. and Davis, D. (1984) Mechanics of fold-and-thrust belts and accretionary wedges: Cohesive Coulomb theory. *J. Geophys. Res.* **89;** (10), 87-101.

Daily, B. and Milnes, A. R. (1973) Stratigraphy, structure and metamorphism of the Kanmantoo Group (Cambrian) in its type section east of Tunkalilla Beach, South Australia. *Trans. R. Soc. S. Aust.* **97;** 213-242.

Dalziel, I. W. D. (1991) Pacific margins of Laurentia and East Antractica-Australia as a conjugate rift pair: Evidence and implications for Eocambrian supercontinent. *Geology* **19;** 598-601.

Davis, D., Suppe, J. and Dahlen, F. A. (1983) Mechanics of fold-and-thrust belts and accretionary wedges. *J. Geophys. Res.* **88;** 1153-1172.

Davis, D. M. and Engelder, T. (1985) The role of salt in fold-thrust-belts. *Tectonophysics* **119;** 67-89.

Davis, J. C. (1986) Statistics and data analysis in geology. 646.

DeCelles, P. G. and Mitra, G. (1995) History of the Sevier orogenic wedge in terms of critical taper models, northeast Utah and southwest Wyoming. *Geol. Soc Amer. Bull.* **107;** 454-467.

Dennis, D. W. (1972) Structural geology. The Ronald Press Company, New York, 532.

DePaor, D. G. (1988) Balanced sections in thrust belts, Part 1: Construction. *AAPG Bull.* **72;** 73-90.

DIGITIZE (1989). Digitizing software for macintosh, Rockeare, Inc.

Dittmar, D., Meyer, W., Oncken, O., *et al.* (1994) Strain Partitioning across a fold and thrust belt: the Rhenish Massif, Mid-European Variscides. *Journal of Structural Geology* **16;** 1335-1352.

Drexel, J. F., Preiss, W. V. and Parker, A. J. (1993) The geology of South Australia; Volume 1, The Precambrian. Bulletin, Geological Survey of South Australia, 242.

Dunlap, W. J., Teyssier, C., McDougall, I., *et al.* (1995) Thermal and structural evolution of the intracratonic Arltunga Nappe Complex, central Australia. *Tectonics* **14;** 1182-1204.

Dunnet, D. (1969) A technique of finite strain analysis using elliptical particles. *Tectonophysics* **7;** 117-136.

Durney, D. W. (1972) Solution-transfer, an Important Geological Deformation Mechanism. *Nature (London)* **235**; 5337, 315-317.

Durney, D. W. and Ramsay, J. G. (1973) Incremental Strains Measured by Syntectonic Crystal Growths. Gravity and Tectonics. John Wiley & Sons, New York. 67-96.

Dymoke, P. and Sandiford, M. (1992) Phase relationships in Buchan Facies Series pelitic assemblages: Calculations with applications to andalusite-staurolite paragenesis in the Mount Lofty Ranges, South Australia. *Contrib. Mineral. Petrol.* **110;** 121-132.

Elliott, D. (1973) Diffusion flow laws in metamorphic rocks. *GSA Bull.* **84;** 2645-2664.

Elliott, D. (1976) The energy balance and deformation mechanisms of thrust sheets. *Royal Soc. London Philos. Trans.* **283;** (Ser. A), 289-312.

Elliott, D. (1983) The construction of balanced cross-sections. *Journal of Structural Geology* **5**; 2, 101.

Elliott, D. and Johnson, M. R. W. (1980) Structural evolution in the northern part of the Moine thrust belt, NW Scotland. *Trans. Royal Soc. of Edinburgh* **71;** 69-96.

England, P. C. and Thompson, A. B. (1984) Pressure-temperature-time paths of regional metamorphism; I, Heat transfer during the evolution of regions of thickened continental crust. *Journal of Petrology* **25**; 4, 894-928.

Erslev, E. (1988) INSTRAIN, an integrated fabric analysis program for the Macintosh. Rockware, Inc., 99.

Escher, A. and Watterson, J. (1974) Stretching fabrics, folds and crustal shortening. *Tectonophysics* **22;** 223-231.

Etchecopar, A. and Malavieille, J. (1987) Computer models of pressure shadows: a method for strain measurement and shear-sense determination. *Journal of Structural Geology* **9;** 667-677.

Etheridge, M. A. and Wilkie, J. C. (1979) Grainsize reduction, grain boundary sliding and the flow strength of mylonites. *Tectonophysics* **58;** 159-178.

Evans, D. J. and White, S. H. (1984) Microstructural and fabric studies from the rocks of the Moine Nappe, Eriboll, NW Scotland. *Journal of Structural Geology* **6;** (4), 369-389.

Evans, M. A. (1989) The structural geometry and evolution of foreland thrust system, northern Virginia. *Geol. Soc. Am. Bull* **101;** 339-354.

Fischer, M. P., Woodward, N. B. and Mitchell, M. M. (1992) The kinematics of break-thrust folds. *Journal of Structural Geology* **14;** (4), 451-460.

Fitches, W. R., Cave, R., Craig, J., *et al.* (1986) Early veins as evidence of detachment in the lower Palaeozoic rocks of the Welsh Basin. *Journal of Structural Geology* **8;** (6), 607-620.

Flinn, D. (1962) On folding during three-dimensional progressive deformation. *Q. J. Geological Soc. London* 385-433.

Flöttmann, T. and James, P. (1997) Influence of basin architecture on the style of inversion and fold-thrust belt tectonics; the southern Adelaide Fold-Thrust Belt, South Australia *Journal of Structural Geology* **19;** (8), 1093-1110.

Flöttmann, T., James, P., Menpes, R., *et al.* (1995) The structure of Kangaroo Island, South Australia: strain and kinematic partitioning during Delamerian basin and platform reactivation. *Aust. J. Earth. Sci.* **42;** 35-49.

Flöttmann, T. and James, P. R. (1993). The Southern Adelaide Fold-and-Thrust Belt, a revised architecture based on balanced cross sections and strain analysis, Department of Geology and Geophysics, Adelaide University, S.A., Australia.

Flöttmann, T., James, P. R., Rogers, J., *et al.* (1994) Early Palaeozoic foreland thrusting and basin reactivation at the Palaeo-Pacific margin of the southern Australian Precambrian Craton: a reappraisal of the structural evolution of the Southern Adelaide Fold-Thrust Belt. *Tectonophysics* **234;** 95-116.

Foden, J. D., Turner, S. P. and Morrison, R. S. (1990) Tectonic implications of Delamerian magmatism in South Australia and western Victoria. The evolution of a Late Precambrian-Early Palaeozoic Rift Complex: The Adelaide Geosyncline. J. B. Jago and P. S. Moore. **16:** 465-482.

Forbes, B. G. (1983). Noarlunga Map Sheet. Adelaide, Department of Mines, S.A.

Forbes, B. G. C. (1979). Onkaparinga map sheet. Adelaide, Department of Mines, S.A.

Forbes, B. G. C. (1980). Adelaide map sheet. Adelaide, Department of Mines, S.A.

Gaudemer, Y. and Tapponnier, P. (1987) Ductile and brittle deformations in the northern Snake Range, Nevada. *Journal of Structural Geology* **9;** 159-180.

Geiser, P. A. (1988a) The role of kinematics in the construction and analysis of geological cross sections in deformed terranes. Geometry and mechanism of faulting with special reference to the Appalachians. G. Mitra and S. Wojtal. *Spec. Pap. Geol. Soc. Am.*, **222:** 47-76.

Geiser, P. A. (1988b) Mechanisms of thrust propagation; some examples and implications for the analysis of overthrust terranes. *Journal of Structural Geology* **10;** (8), 829-845.

Geiser, P. A. and Boyer, S. E. (1987) The paradox of the orogenic wedge and a model for crustal recycling. *Abstracts with Programs Geological Society of America* 19; 7, 674.

Giles, A. D. and Marshall, B. (1994) Fluid inclusion studies on a multiply deformed, metamorphosed volcanic-associated massive sulfide deposit, Joma Mine, Norway. *Economic Geology and the Bulletin of the Society of Economic Geologists* **89**; 4, 803-819.

Gilotti, J. and Kumpulanien, R. (1986) Strain-softening induced ductile flow in the Särv thrust sheet, Scandinavian Caledonides; A description. *Journal of Structural Geology* **8;** (3/4), 441-455.

Gonzalez, C. J. M., Casquet, C., Martinez, M. J. M., *et al.* (1995) Retrograde evolution of quartz segregations from the Dos Picos shear zone in the Nevado-Filabride Complex (Betic chains, Spain); evidence from fluid inclusions and quartz c-axis fabrics. *Geologische Rundschau* **84**; 1, 175-186.

Gray, D. (1978) Cleavages in deformed psammitic rocks from southeastern Australia; their nature and origin. *Geological Society of America Bulletin* 89; **4**, 577-590.

Gray, D. R. (1977) Morphologic classification of crenulation cleavage. *Journal of Geology* **85**; 2, 229-235.

Gray, D. R. (1979) Microstructure of crenulation cleavages: an indicator of cleavage origin. *Am. J. Sci.* **279;** 97-128.

Gray, D. R. (1995) Thrust kinematics and transposition fabrics from a basal detachment zone, eastern Australia. *Journal of Structural Geology* **17;** 1637-1654.

Gray, D. R. and Durney, D. W. (1979) Investigations on the mechanical significance of crenulation cleavage. *Tectonophysics* **58;** 35-79.

Gray, D. R. and Willman, C. E. (1991) Thrust-related strain gradients and thrusting mechanisms in a chevron-folded sequence, southeastern Australia. *Journal of Structural Geology* **13;** (6), 691-710.

Groshong, R. H., Jr. (1976) Strain and pressure solution in the Martinsburg Slate, Delaware Water Gap, New Jersey. *American Journal of Science* **276**; 9, 1131-1146.

Groshong, R. H., Jr. (1988) Low-temperature deformation mechanisms and their interpretation. *Geological Society of America Bulletin* 100; 9, 1329-1360.

Hanmer, S. (1986) Asymmetrical pull-aparts and foliation fish as kinematic indicators. *Journal of Structural Geology* **8;** (2), 111-122.

Hanmer, S. and Passchier, C. (1991) Shear-sense indicators: a review. *Geol. Surv. Pap. Can.* **90-17;**

Hansen, E. (1971) Strain Facies. Springer-Verlag, 207.

Harris, L. D. and Milici, R. C. (1977). Characteristic of thin-skinned style of deformation in the southern Applachians and potential hydrocarbon traps. U.S. Geological Survey Professional Paper, U.S. Geological Survey Professional Paper. **1018:** 40.

Hatcher, R. D. and Hooper, R. J. (1992) Evolution of crystalline thrust sheets in the internal parts of mountain chains. Thrust Tectonics. K. R. McClay. Chapman & Hall, 217-234.

Henderson, J. R., Henderson, M. N. and Wright, T. O. (1990) Water-sill hypothesis for the origin of certain veins in the Meguma Group, Nova Scotia, Canada. *Geology (Boulder)* **18**; 7, 654-657.

Hirth, G. and Tullis, J. (1992) Dislocation creep regimes in quartz aggregates. *Journal of Structural Geology* **14;** (2), 145-159.

Ho, N. C., Peacor, D. R. and van, d. P. B. A. (1996) Contrasting roles of detrital and authigenic phyllosilicates during slaty cleavage development. *Journal of Structural Geology* **18**; 5, 615-623.

Hobbs, B. E., Means, W. D. and Williams, P. F. (1976) An outline of structural geology. Wiley International Edition, U.S.A.,

Holdsworth, R. E. (1989) The geology and structural evolution of a Caledonian fold and ductile thrust zone, Kyle of Tongue region, Sutherland, northern Scotland. *J. geol. Soc. london* **146;** 809-823.

Holdsworth, R. E. (1990) Progressive deformation structures associated with ductile thrusts in the Moine Nappe, Sutherland, N. Scotland. *Journal of Structural Geology* **12;** (4), 443-452.

Holl, J. E. and Anastasio, D. J. (1995) Cleavage development within a foreland fold and thrust belt, southern Pyrenes, Spain. *Journal of Structural Geology* **17**; 3, 357-369.

Holland, T. J. B. and Powell, R. (1990) An enlarged and updated internally consistent thermodynamic dataset with uncertainties and correlations; the system K (sub 2) O-Na (sub 2) O-CaO-MgO-MnO-FeO-Fe (sub 2) O (sub 3) -Al (sub 2) O (sub 3) -TiO (sub 2) -SiO (sub 2) -C-H (sub 2) -O (sub 2). *Journal of Metamorphic Geology* **8**; 1, 89-124.

Hollister, L. S. (1990) Enrichment of CO2 in fluid inclusions in quartz by removal of H2O during crystal-plastic deformation. *Journal of Structural Geology* **12;** (7), 895-901.

Hollister, L. S. and Burruss, R. C. (1976) Phase equilibria in fluid inclusions from the Khtada Lake metamorphic complex. *Geochimica et Cosmochimica Acta* **40**; 2, 163-175.

Hollister, L. S., Burruss, R. C., Henry, D. L., *et al.* (1979) Physical conditions during uplift of metamorphic terranes, as recorded by fluid inclusions. *Bulletin de Mineralogie* 102; 5-6, Mineraux et Minerais, 555-561.

Holst, T. B. (1985) Implications of a large flattening for the origin of a bedding-parallel foliation in the Early Proterozoic Thomson Formation, Minnesota. *J. Struct. Geol.* **7;** 375-383.

Hsü, K. J. (1969) Preliminary analysis of the statics and kinetics of the Glarus overthrust. *Eclogae geologicae Helvetiae* **62;** (1), 143-154.

Hsü, K. J. (1980) Thin-skinned plate tectonics and orogenic uplift. *Pages 60* 1980.

Hsü, K. J. (1982) Mountain building processes. Academic Press, New York,

Hubbert, M. K. and Rubey, W. W. (1959) Role of fluid pressure in mechanics of overthrust faulting. *Geol. Soc. of Am. Bull.* **70;** (115-166),

Hudleston, P. J. (1973) The analysis and interpretation of minor folds developed in the Moine rocks of Monar, Scotland. *Tectonophysics* **17;** 89-132.

Hudleston, P. J. (1977) Similar folds, recumbent folds, and gravity tectonics in ice and rocks. *J. of Geol.* **85;** 113-122.

Hudleston, P. J. (1986) Extracting information from folds in rocks. *J. Geol. Ed.* **34;** 237-245.

Hudleston, P. J. and Lan, L. (1993) Information from fold shapes. *Journal of Structural Geology* **15;** 253-264.

James, P. R. (1989). Field excursion guided, structural geology of the Fleurieu Peninsula. Specialist group in Tectonics and Structural Geology, Adelaide, SA, Australia, Geological Society of Australia.

Jamison, W. R. (1987) Geometric analysis of fold development in overthrust terranes. *Journal of Structural Geology* **9;** (2), 207-219.

Jenkins, R. J. F. (1990) The Adelaide Fold Belt: Tectonic reappraisal. The evolution of Late Precambrian-Early Palaeozoic Rift Complex: The Adelaide Geosyncline. J. B. Jago and P. S. Moore. *Geol. Soc. Aust., Spec. Publ.*, **16:** 395-420.

Jenkins, R. J. F. and Sandiford, M. (1992) Observations on the tectonic evolution of the southern Adelaide Fold Belt. *Tectonophysics* **214;** 27-36.

Jessell, M. W., Willman, C. E. and Gray, D. R. (1994) Bedding parallel veins and their relationship to folding. *Journal of Structural Geology* **16;** 753-767.

Johnson, E. L. and Hollister, L. S. (1995) Syndeformational fluid trapping in quartz; determining the pressure-temperature conditions of deformation from fluid inclusions and the formation of pure CO (sub 2) fluid inclusions during grain-boundary migration. *Journal of Metamorphic Geology* **13**; 2, 239-249.

Kanagawa, K. (1991) Change in dominant mechanisms for phyllosilicate preferred orientation during cleavage development in the Kitakami slates of NE Japan. *Journal of Structural Geology* **13**; 8, 927-943.

Kapetas, J. (1993) The structure of the Clarendon-Mt. Bold region, southern Adelaide Fold Belt, Fleurieu Peninsula, South Australia. The University of Adelaide, Adelaide, 30.

Karabinos, P. (1988) Heat transfer and fault geometry in the Taconian thrust belt, western New England. *Special Paper Geological Society of America* **222**; 35-45.

Karabinos, P. and Ketcham, R. (1988) Thermal structure of active thrust belts. *Journal of Metamorphic Geology* **6**; 5, 559-570.

Kelley, S. P. and Powell, D. (1985) Relationships between marginal thrusting and movement on major, internal shear zones in the northern Highland Caledonides, Scotland. *Journal of Structural Geology* **7;** (2), 161-174.

Kirk, R. E. (1990) Statistics; an introduction. 711.

Kirschner, D. L. and Teyssier, C. (1992) Deformation history of the White Range duplex, central Australia, with implications for fold reorientation. *Australian Journal of Earth Sciences* **39;** (4), 441-456.

Kirschner, D. L., Teyssier, C., Gregory, R. T., *et al.* (1995) Effect of deformation on oxygen isotope exchange in the Heavitree Quartzite, Ruby Gap duplex, central Australia. *Journal of Structural Geology* **17;** 1407-1423.

Knipe, R. J. (1981) Deformation and metamorphism in slates. *Journal of Structural Geology* **3**; 3, 336.

Knipe, R. J. (1989) Deformation mechanism-recognition from natural tectonites. *J. Struct. Geol.* **11;** 127-146.

Knipe, R. J. and White, S. H. (1979) Deformation in low grade shear zones in the Old Red Sandstone, S.W. Wales. *Journal of Structural Geology* **1;** (1), 53-66.

Lacassin, R. (1988) Large-scale foliation boudinage in gneisses. *Journal of Structural Geology* **10;** (6), 643-647.

Law, R. D., Casey, M. and Knipe, R. J. (1987) Kinematic and tectonic significance of microstructures and crystallographic fabrics within quartz mylonites from the Assynt and Eriboll regions of the Mione thrust zone, NW Scotland. *Trans. Edinburgh Geol. Soc.* 99-125.

Law, R. D., Knipe, R. J. and Dayan, H. (1984) Strain path partitioning within thrust sheets; microstructural and petrofabric evidence from the Moine thrust zone at Loch Eriboll, Northwest Scotland. *Journal of Structural Geology* **6;** (5), 477-497.

Lee, J. H., Peacor, D. R., Lewis, D. D., *et al.* (1986) Evidence for syntectonic crystallisation for the mudstone to slate transition at Lehigh Gap, Pennsylvania, U.S.A. *Journal of Structural Geology* **8**; 7, 767-780.

Lemon, N. M. and Mc Gowran, B. M. (1989). Structural development of the Willunga embayment, St Vincent Basin, South Australia. University of Adelaide, University of Adelaide.

Linker, M. F., Kirby, S. H., Ord Alison, *et al.* (1984) Effects of compression direction on the plasticity and rheology of hydrolytically weakened synthetic quartz crystals at atmospheric pressure. *Journal of Geophysical Research.*

Lisle, R. J. (1977) Estimation of the tectonic strain ratio from the mean shape of deformed elliptical markers. *Geologie en Mijnbouw* **56**; 2, 140-144.

Lister, G. S. and Snoke, A. W. (1984) S-C Mylonites. *J. Struct. Geol.* **6;** 617-638.

Lloyd, G. E. and Freeman, B. (1994) Dynamic recrystallization of quartz under greenschist conditions. *Journal of Structural Geology* **16;** 867-881.

Malavieille, J. (1987) Kinematics of compressional and extensional ductile shearing deformation in a metamorphic core complex of the Northeastern of Basin and Rang. *Journal of Structural Geology* **9;** 541-554.

Mancktelow, N. S. (1979) The development of slaty cleavage, Fleurieu Peninsula, South Australia. *Tectonophysics* **58;** 1-20.

Mancktelow, N. S. (1981) Variation in fold axis geometry and slaty cleavage microfabrics associated with a major fold arc, Fleurieu

Peninsula, South Australia. *J. Geol. Soc. Aust.* **28;** 1-12.

Mancktelow, N. S. (1990) The structure of the southern Adelaide Fold Belt, South Australia. The evolution of a Late Precambrian-Early Palaeozoic Rift Complex: The Adelaide Geosyncline. J. B. Jago and P. S. Moore. *Geol. Soc. Aust., Spec. Publ.*, **16:** 369-395.

Marshak, S. and Flöttmann, T. (1996) Structural Geometry of the Adelaide Fold Thrust Belt, South Australia: Orocline and arc formation along an irregular cratonic margin. *Journal of Structural Geology* **18;** 891-908.

Marshak, S. and Mitra, G. (1989) Basic method of structural geology. Prentice Hall, 446.

Marshak, S. and Woodward, N. (1989) Introduction to cross-section balancing. Basic methods of structural geology. S. Marshak and G. Mitra. 446.

Marshak, S. and Woodward, N. B. (1989) Introduction to cross-section balancing. Basic method of structural geology. S. Marshak and G. Mitra. Prentice Hall, 446.

Martino, R. D., Simpson, C. and Law Richard, D. (1993) Taconic- (Ocloyic-) age west-directed ductile thrusts in basement rocks of the Sierras Pampeanas, Argentina. *Abstracts with Programs Geological Society of America* **25**; 6, 233.

Mawer, C. K. (1987) The formation of gold-bearing quartz veins, Nova Scotia, Canada. *Tectonophysics* **115;** 99-119.

Mawer, C. K. and Williams, P. F. (1991) Progressive folding and foliation development in a sheared, coticule-bearing phyllite. *Journal of Structural Geology* **13**; 5, 539-555.

Mawson, D. and Sprigg, R. C. (1950) Subdivision of the Adelaide System. *Aus. J. Sci.* **13;** 69-72.

McClay, K. R. (1992) Thrust Tectonics. Chapman & Hall, 447.

McNulty, B. A. (1995) Shear zone development during magmatic arc construction; the Bench Canyon shear zone, central Sierra Nevada, California. *Geological Society of America Bulletin* **107**; 9, 1094-1107.

Means, W. D. (1975) Natural and experimental microstructures in deformed micaceous sandstones. *Geological Society of America Bulletin* **86**; 9, 1221-1229.

Means, W. D. (1984) Shear zones of types I and II and their significance for reconstruction of rock history. *Abstracts with Programs Geological Society of America* **16**; 1, 50.

Michibayashi, K. (1996) The role of intragranular fracturing on grain size reduction in feldspar during mylonitization. *Journal of Structural Geology* **18;** 1-17.

Mills, K. (1964). The structural geology of an area east of Springton, University of Adelaide.

Mills, K. J. (1973) The structural geology of the Warren National Park and the western portion of the Mount Crawford State Forrest, South Australia. *Trans. R. Soc. S. Aust.* **94;** 281-315.

Milnes, A. R., Compston, W. and Daily, B. (1977) Pre- to syntectonic emplacement of early Palaeozoic granites in south-eastern South Australia. *J. Geol. Soc. Aus* **24;** 87-106.

Mitra, G. (1978) Ductile deformation zones and mylonites: The mechanical processes involved in the deformation of crystalline basement rocks. *Am. J. of Sci.* **278;** 1057-1084.

Mitra, G. (1984) Brittle to ductile transition due to large strains along the White Rock Thrust, Wind River Mountains, Wyoming. *Journal of Structural Geology* **6**; 1-2, 51-61.

Mitra, G. (1994) Strain variation in thrust sheets across the Sevier fold-and-thrust belt (Idaho-Utah-Wyoming); implications for section restoration and wedge taper evolution. *Journal of Structural Geology* **16**; 4, 585-602.

Mitra, G. and Sussman, A. J. (1997) Structural evolution of connecting splay duplexes and their implications for critical taper; an example based on geometry and kinematics of the Canyon Range culmination, Sevier Belt, central Utah. *Journal of Structural Geology* **19**; 3-4, 503-521.

Mitra, G. and Wojtal, S. F. (1988) Geometries and mechanism of thrusting; with special reference to Appalachian. Special Paper Geological Society of America, 222.

Mitra, S. (1990) Fault-propagation folds; geometry, kinematic evolution, and hydrocarbon traps. *AAPG Bulletin* **74**; 6, 921-945.

Mitra, S. and Fisher, G. W. (1992) Structural geology of fold and thrust belts. John Hopkins Univ. Press, 254.

Moores, E. M. (1991) Southwest U.S.-East Antarctic (SWEAT) connection: A hypothesis. *Geology* **19;** 425-428.

Muller, W. H. and Hsü, K. J. (1980) Stress distribution in overthrusting slabs and mechanical Jura deformation mountain building processes. *Rock Mechanics Supplement* **9;** 219-232.

Mullis, J. (1987) Fluide inschluss-Untersuchungen in den Nagra-Bohrungen der Nordschweiz Translated Title: Study of fluid inclusions in the Nagra boreholes, northern Switzerland. *Eclogae Geologicae Helvetiae* **80**; 2, 553-568.

Naruk, S. J. (1986) Strain and displacement across the Pinaleno Mountains shear zone, Arizona, U.S.A. *Journal of Structural Geology* **8;** 35-46.

Newman, J. and Mitra, G. (1993) Lateral variations in mylonite zone thickness as influenced by fluid-rock interactions, Linville Falls Fault, North Carolina. *Journal of Structural Geology* **15**; 7, 849-863.

O'Hara, K. (1988) Fluid flow and volume loss during mylonitization; an origin for phyllonite in an overthrust setting, North Carolina, U.S.A. *Tectonophysics* **156;** (1-2), 21-36.

O'Hara, K. (1990) State of strain in mylonites from the western Blue Ridge Province, Southern Appalachians; the role of volume loss. *Journal of Structural Geology* **12**; (4), 419-430.

O'Hara, K. and Haak, A. (1992) A fluid inclusion study of fluid pressure and salinity variations in the footwall of the Rector Branch Thrust, North Carolina, U.S.A. *Journal of Structural Geology* **14**; 5, 579-589.

Offler, R. and Fleming, P. D. (1968) A synthesis of folding and metamorphism in the Mt. Lofty Ranges, South Australia. *J. Geol. Soc. Aus.* **15;** 245-266.

Onasch, C. M. (1983) Origin and significance of microstructures in sandstones of the Martinsburg Formation, Maryland. *American Journal of Science* **283**; 9, 936-966.

Passchier, C. W. (1982) Pseudotachylyte and the development of ultramylonite bands in the Saint-Barthelemy Massif, French Pyrenees. *Journal of Structural Geology* **4**; 1, 69-79.

Passchier, C. W. (1991) Geometric constraints on the development of shear bands in rocks. *Geologie en Mijinbouw* **70;** 203-211.

Passchier, C. W. and Trouw, R. A. J. (1995) Microtectonics. Springer, 289.

Platt, J. P. (1984) Secondary cleavages in ductile shear zones. *Journal of Structural Geology* **6;** (4), 439-442.

Platt, J. P. and Behrmann, J. H. (1986) Structures and fabrics in a crustal-scale shear zone, Betic Cordillera, SE Spain. *Journal of Structural Geology* **8**; 1, 15-33.

Platt, J. P. and Vissers, R. L. M. (1980) Extensional structures in anisotropic rocks *Journal of Structural Geology* **2;** (4), 397-410.

Potter, R. and Brown, D. (1977) The volumetric properties of aqueous sodium chloride solutions from 0 to 500 C at pressures up to 2000 bars based on a regression of available data in the literature. Geological survey bulletin, S.

Powell, C. M. (1979) A morphological classification of rock cleavage. *Tectonophysics* **58;** 21-34.

Powell, R. and Evans, J. A. (1983) A new geobarometer for the assemblage biotite-muscovite-chlorite-quartz. *Journal of Metamorphic Geology* **1**; 4, 331-336.

Powell, R. and Holland, T. J. B. (1988) An internally consistent dataset with uncertainties and correlations; 3, Applications to geobarometry, worked examples and a computer program. *Journal of Metamorphic Geology* **6**; 2, 173-204.

Preiss, W. V. (1987) The Adelaide Geosyncline - late Proterozoic stratigraphy, sedimentation, palaeontology and tectonics. *Geol. Survey S. Aust. Bull.* **53;** 1-438.

Preiss, W. V. (1993) Neoproterozoic. The Geology of South Australia. J. F. Drexel, W. V. Preiss and A. J. Parker. Geological Survey of South Australia, Adelaide. **Bull. 54 (Vol.1):** 171-203.

Preiss, W. V. (1995) Delamerian Orogeny. The geology of South Australia. Geol. Surv. S. Aust. Bull., Adelaide. **2:** 45-61.

Price, R. A. (1981) The Cordilleran foreland thrust and fold belt in the southern Canadian Rocky Mountains. Thrust and Nappe Tectonics. K. R. McClay and N. J. Price. Blackwell, Oxford. **9:** 427-448.

Price, R. A. and Mountjoy, E. W. (1970). Geologic structure of the Canadian Rocky Mountains between Bow and Athabaska Rivers, Geological Association of Canada.

Pryer, L. L. (1993) Microstructures in feldspars from a major crustal thrust zone; the Grenville Front, Ontario, Canada. *Journal of Structural Geology* **15**; 1, 21-36.

Ramsay, J. G. (1967) Folding and fracturing of rocks. McGraw-Hill Book Company, New Yourk,

Ramsay, J. G. (1980) Shear zone geometry; a review. *Journal of Structural Geology* **2**; 1/2, 83-99.

Ramsay, J. G. and Graham, R. H. (1970) Strain variation in shear belts. *Can. J. Earth. Sci.* **7;** 786-813.

Ramsay, J. G. and Huber, M. (1983) The technique of modern structural geology; vol.1, strain analysis. Academic Press, London,

Ramsay, J. G. and Huber, M. (1987) The technique of modern structural geology; vol. 2, folds and fractures. Academic Press, London,

Rathbone, P. A., Coward, M. P. and Harris, A. L. (1983) Cover and basement: a contrast in style and fabrics. *Geol. Soci. Am. Mem.* **158;** 213-223.

Rattey, P. R. and Sanderson, D. J. (1982) Patterns of folding within nappes and thrust sheets: examples from the variscan of southwest England. *Tectonophysics* **88;** 247-267.

Reynolds, S. J. and Lister, G. S. (1987) Structural aspects of fluid-rock interactions in detachment zones. *Geology (Boulder)* **15**; 4, 362-366.

Ridley, J. (1986) Parallel stretching lineations and fold axes oblique to a shear displacement direction; a model and observations. *Journal of Structural Geology* **8;** (6), 647-653.

Rodgers, J. (1970) Tectonics of the Appalachians. Wiely, New York, 271.

Rodgers, J. (1987) Chains of basement uplifts within cratons marginal to orogenic belts. *Am. J. Sci.* **287;** 661-694.

Rodgers, J. (1990) Fold-and-thrust belts in sedimentary rocks. Part 1: typical examples. *Am. J. Sci.* **290;** 321-359.

Rodgers, J. (1991) Fold-and-thrust belts in sedimentary rocks. Part 2: other examples, especially variants. *Am. J. Sci.* **291;** 825-886.

Roedder, E. (1984) Fluid Inclusions: Reviews in Mineralogy. Mineralogical Society of America,

Roedder, E. and Bodnar, R. J. (1980) Geologic pressure determinations from fluid inclusion studies. *Annual Review of Earth and Planetary Sciences* **8**; 263-301.

Roeder, D., Gilbert, O. C. and Witherspoon, W. D. (1978). Evolution and macroscopic structure of Valley and Ridge thrust belt, Tennessee and Virginia, Uni. Tennessee Dept. Geol. Sci.

Roering, C. and Smit, C. A. (1987) Bedding-parallel shear, thrusting and quartz vein formation in Witwatersrand quartzites. *Journal of Structural Geology* **9;** (4), 419-427.

Rutter, E. H. (1983) Pressure solution in nature, theory and experiment. *Journal of the Geological Society of London* **140**; 5, 725-740.

Sanderson, D. J. (1973) The development of fold axes oblique to the regional trend. *Tectonophysics* **16;** 55-70.

Sanderson, D. J. (1982) Models of strain variation in nappes and thrust sheets: a review. *Tectonophysics* **88;** 201-233.

Sandiford, M., Fraser, G., Arnold, J., *et al.* (1995) Some causes and consequences of high-temperature, low-pressure metamorphism in the eastern Mt Lofty Ranges, South Australia. *Australian Journal of Earth Sciences* **42**; 3, 233-240.

Sandiford, M., Oliver, R. L., Mills, K. J., *et al.* (1990) A cordierite-staurolite-muscovite association, east of Springton, Mt Lofty Ranges; implications for the metamorphic evolution of the Kanmantoo Group. *Special Publication Geological Society of Australia* **16**; 483-495.

Sandiford, M. and Powell, R. (1991) Some remarks on high-temperature-low-pressure metamorphism in convergent orogens. *Journal of Metamorphic Geology* **9**; 3, 333-340.

Schmid, S. M. (1975) The Glarus overthrust; field evidence and mechanical model. *Eclogae Geologicae Helvetiae* **68**; 2, 247-280.

Schmid, S. M. (1982) Microfabric studies as indicators of deformation mechanisms and flow laws operative in mountain building. 95-110.

Schmid, S. M. (1983) Experimental deformation of calcite rocks in simple shear. *Abstracts with Programs Geological Society of America* **15**; 6, 680.

Schmid, S. M., Paterson, M. S. and Boland, J. N. (1980) High temperature flow and dynamic recrystallization in Carrara Marble. *Tectonophysics* **65**; 3-4, 245-280.

Shepherd, T. J., Rankin, A. H. and Alderton, D. H. M. (1985) A practical guide to fluid inclusion studies. Blackie & Son Ltd, 239.

Sibson, R. H. (1977) Fault rocks and fault mechanism. *J. geol. Soc. Lond.* **133;** 191-213.

Simpson, C. (1985) Deformation of granitic rocks across the brittle-ductile transition. *Journal of Structural Geology* **7;** (5), 503-511.

Simpson, C. (1986) Determination of movement sense in mylonites. *J. Feol. Ed.* **34;** 246-261.

Simpson, C. (1994). 100 photomicrographs of microstructures, Earth'nWare Inc. & Industrial Association of George Washington Uni.: 27.

Simpson, C. and Schmid, S. M. (1983) An evaluation of criteria to deduce the sense of movement in sheared rocks. *Bull. Geol. Soc. Am.* **94;** 1281-1288.

Sisson, V. B. and Hollister, L. S. (1990) A fluid-inclusion study of metamorphosed pelitic and carbonate rocks, south-central Maine. *American Mineralogist* **75**; 1-2, 59-70.

Smith, A. G. (1981) Subduction and coeval thrust belts, with particular reference to North America. Thrust and Nappe Tectonics. K. R. McClay and N. J. Price. Geological Society of London, 111-124.

Sprigg, R. C. (1946) Reconnaissance geological survey of portion of the western escarpment of the mount lofty ranges. *Roy. Soc. S. Aust.* **70;** 313-347.

Sprigg, R. C., Whittle, A. W. G. and Campana, B. (1951). Adelaide map sheet. Adelaide, Geological Survey of South Australia.

Steinhardt, C. (1991) The microstructural anatomy of a major thrust zone on Fleurieu Peninsula, South Australia. *Aust. J. Earth Sci.* **38;** 139-150.

Stephens, M. B., Glasson, M. J. and Keays, R. R. (1979) Structural and chemical aspects of metamorphic layering development in metasediments from Clunes, Australia. *Am. J. Sci.* **279;** 129-160.

Sterner, S. M. and Bodnar, R. J. (1989) Synthetic fluid inclusion; VII, Re-equilibration of fluid inclusions in quartz during laboratory simulated metamorphic burial and uplift. *Journal of Metamorphic Geology* **7**; 2, 243-260.

Stock, P. (1992) A strain model for antithetic fabric rotation in shear band structures. *Journal of Structural Geology* **14**; 10, 1267-1275.

Suppe, J. (1983) Geometry and kinematics of fault-bend folding. *Am. J. Sci.* **283;** 684-721.

Suppe, J. (1985) Principles of structural geology. Prentice-Hall Inc., Englewood Cliffs, New Jersey,

Suppe, J. (1987) The active Taiwan mountain belt. The anatomy of Mountain Ranges. J. P. Schaer and R. J. Princeton University Press, Princeton, N.J. **283:** 277-293.

Suppe, J. and Medwedeff, D. A. (1990) Geometry and kinematics of fault-propagation folding. *Eclogae Geologicae Helvetiae* **83**; 3, 409-454.

Swager, N. (1985) Solution transfer, mechanical rotation and kink-band boundary migration during crenulation-cleavage development. *Journal of Structural Geology* **7;** 421-429.

Swan, A. R. and Sandilands, M. (1995) Introduction to geological data analysis. Blackwell Science, 446.

Swanson, M. T. (1992) Late Acadian-Alleghenian transpressional deformation; evidence from asymmetric boudinage in the Casco Bay area, coastal Maine. *Journal of Structural Geology* **14;** (3), 323-341.

Tan, B. K., Gray, D. R. and Stewart, I. (1995) Volume change accompanying cleavage development in graptolitic shales from Gisborne, Victoria, Australia. *Journal of Structural Geology* **17;** 1387-1394.

Tanner, P. W. G. (1989) The flexural-slip mechanism. *Journal of Structural Geology* **11**; 6, 635-655.

Tavarnelli, E. (1994) Map analysis techniques and fold kinematics in the Umbrian Apennines, Italy. *Eclogae Geologicae Helvetiae* **87**; 1, 33-46.

Tavarnelli, E. (1997) Structural evolution of a foreland fold-and-thrust belt; the Umbria-Marche Apennines, Italy. *Journal of Structural Geology* **19**; 3-4, 523-534.

Thompson, A. B. and England, P. C. (1984) Pressure-temperature-time paths of regional metamorphism; II, Their inference and interpretation using mineral assemblages in metamorphic rocks. *Journal of Petrology* **25**; 4, 929-955.

Thomson, B. P. (1969) Precambrian crystalline basement. Handbook of South Australian Geology. L. W. Parkin. Geological Survey of South Australia, 21-48.

Tobisch, O. T. and Paterson, S. R. (1988) Analysis and interpretation of composite foliations in areas of progressive deformation. *Journal of Structural Geology* **10;** (7), 745-754.

Tullis, J. (1983) Deformation of feldspars. Feldspar mineralogy. P. H. Ribbe. Mineral. Soc. Am. Rev. Mineral., **2:** 297-323.

Tullis, J., Snoke, A. W. and Todd, V. R. (1982) Significance and petrogenesis of mylonitic rocks. *Geology* **10;** 227-230.

Tullis, J. and Yund, R. A. (1985) Dynamic recrystallization of feldspar; a mechanism for ductile shear zone formation. *Geology (Boulder)* **13**; 4, 238-241.

Tullis, J. and Yund, R. A. (1987) Transition from cataclastic flow to dislocation creep of feldspar; mechanisms and microstructures. *Geology (Boulder)* **15**; 7, 606-609.

Tullis, J. and Yund, R. A. (1991) Diffuse creep in feldspar aggregates; experimental evidence. *Journal of Structural Geology* **13**; 9, 987-1000.

Tullis, T. E. (1980) The use of mechanical twinning in minerals as a measure of shear stress magnitudes. *Jgr* Journal of Geophysical Research.

Turner, F. J. and Weiss, L. E. (1963) Structural analysis of metamorphic tectonites. McGraw Hill Company,

Twiss, R. J. and E.M., M. (1992) Structural geology. W.H. Freeman & Company, 532.

Urai, J. L., Means, W. D. and Lister, G. S. (1986) Dynamic recrystallization of minerals. *Geophysical Monograph* **36**; 161-199.

Vernon, R. H. (1976) Metamorphic process. Allen & Unwin, London,

Vernon, R. H. (1981) Optical microstructure of partly recrystallised calcite in some naturally deformed marbles. *Tectonophysics* **78**; 1-4, 601-612.

Vityk, M. O., Bodnar, R. J. and Dudok, I. V. (1996) Fluid inclusions in "Marmarosh Diamonds": evidence for tectonic history of the Folded Carpathian Mountains, Ukraine. *Tectonophysics* **255;** 163-174.

Voll, G. (1976) Recrystallization of Quartz, Biotite and Feldspars from Erstfeld to the Leventina Nappe, Swiss Alps, and its geological significance. *Schweiz. mineral. petrogr. Mitt.* **56;** 641-647.

Von Winterfeld, C. and Oncken, O. (1995) Non-plane strain in section balancing; calculation of restoration parameters. *Journal of Structural Geology* **17**; 3, 447-450.

Waldron, H. M. and Sandiford, M. (1988) Deformation volume and cleavage development in metasedimentary rocks from the Ballarat slate belt. *Journal of Structural Geology* **10;** (1), 53-62.

Webb, A. W., Thompson, B. P., Blissett, A. H., *et al.* (1987) Geochronology of the Gawler Craton, South Australia. *Aus. J. Earth Sci.* **33;** 119-143.

White, J. C. and Mawer, C. K. (1986) Extreme ductility of feldspars from a mylonite, Parry Sound, Canada. *Journal of Structural Geology* **8**; 2, 133-143.

White, J. C. and White, S. H. (1983) Semi-brittle deformation within the Alpine fault zone, New Zealand. *Journal of Structural Geology* **5**; 6, 579-589.

White, S. (1973) Syntectonic Recrystallization and Texture Development in Quartz. *Nature (London)* **244**; 5414, 276-278.

White, S. (1976) The effects of strain on the microstructures, fabrics, and deformation mechanisms in quartzites. *Philosophical Transactions of the Royal Society of London, Series A: Mathematical and Physical Sciences* 283; 1312, A discussion on natural strain and geological structure, 69-86.

White, S. (1977) Geological significance of recovery and recrystallization processes in quartz. *Tectonophysics* **39**; 1-3, 143-170.

White, S. (1979) Grain and sub-grain size variation across a mylonite zone. *Contrib. Mineral. Petrol.* **70;** 193-202.

White, S. H., Bretan, P. G. and Rutter, E. H. (1986) Fault-zone reactivation: kinematics and mechanisms. *Phil. Tran. R. Soc. Lond.* **A317;** 81-97.

White, S. H., Burrows, S. E., Carreras, J., *et al.* (1980) On mylonites in ductile shear zones. *Journal of Structural Geology* **2**; 1/2, 175-187.

White, S. H. and Knipe, R. J. (1978) Microstructure and cleavage development in selected slates. *Contributions to Mineralogy and Petrology* **66**; 2, 165-174.

Williams, G. and Chapman, T. (1983) Strains developed in the hangingwalls of thrusts due to their slip/ propagation rate; a dislocation model. *Journal of Structural Geology* **5**; 6, 563-571.

Williams, P. F. (1972) Development of metamorphic layering and cleavage in low grade metamorphic rocks at Bermagui, Australia. *American Journal of Science* **272**; 1, 1-47.

Wilson, C. J. L. (1980) Shear zones in a pegmatite; a study of albite-mica-quartz deformation. *Journal of Structural Geology* **2**; 1/2, 203-209.

Wojtal, S. (1986) Deformation within foreland thrust sheets by populations of minor faults. *Journal of Structural Geology* **8**; 3-4, 341-360.

Wojtal, S. and Mitra, G. (1986) Strain hardening and strain softening in fault zones from foreland thrusts. *Geological Society of America Bulletin* **97**; 6, 674-687.

Wojtal, S. F. and Mitra, G. (1988) Nature of deformation in some fault rocks from Appalachian thrusts. *Special Paper Geological Society of America* **222**; 17-33.

Woodward, N. B. (1987) Geological applicability of critical-wedge thrust-belt models. *Geol. Soc Amer. Bull.* **99;** 827-832.

Woodward, N. B., Boyer, S. E. and Suppe, J. (1985). An outline of balanced cross-sections, University of Tennessee.

Woodward, N. B., Boyer, S. E. and Suppe, J. (1989) Balanced geological cross-sections: an essential technique in geological research and exploration. Am. Geophys. Un. Short Course in Geology,

Woodward, N. B., Gray, D. R. and Spears, D. B. (1986) Including strain data in balanced cross-sections. *Journal of Structural Geology* **8**; 3-4, 313-324.

Wright, T. O. and Henderson, J. R. (1992) Volume loss during cleavage formation in the Meguma Group, Nova Scotia, Canada. *Journal of Structural Geology* **14**; 3, 281-290.

Yonkee, W. A. and Bruhn, R. L. (1989) Chemical, mineralogical, and textural changes during growth of shear zones. *Abstracts with Programs Geological Society of America* **21**; 6, 224.

Zhang, Y. G. and Frantz, J. D. (1987) Determination of the homogenization temperatures and densities of supercritical fluids in the system NaCl-KCl-CaCl (sub 2) -H (sub 2) O using synthetic fluid inclusions. *Chemical Geology* **64**; 3-4, 335-350.

Appendix A: Sample (quartzites, pelites, and quartz veins) location map

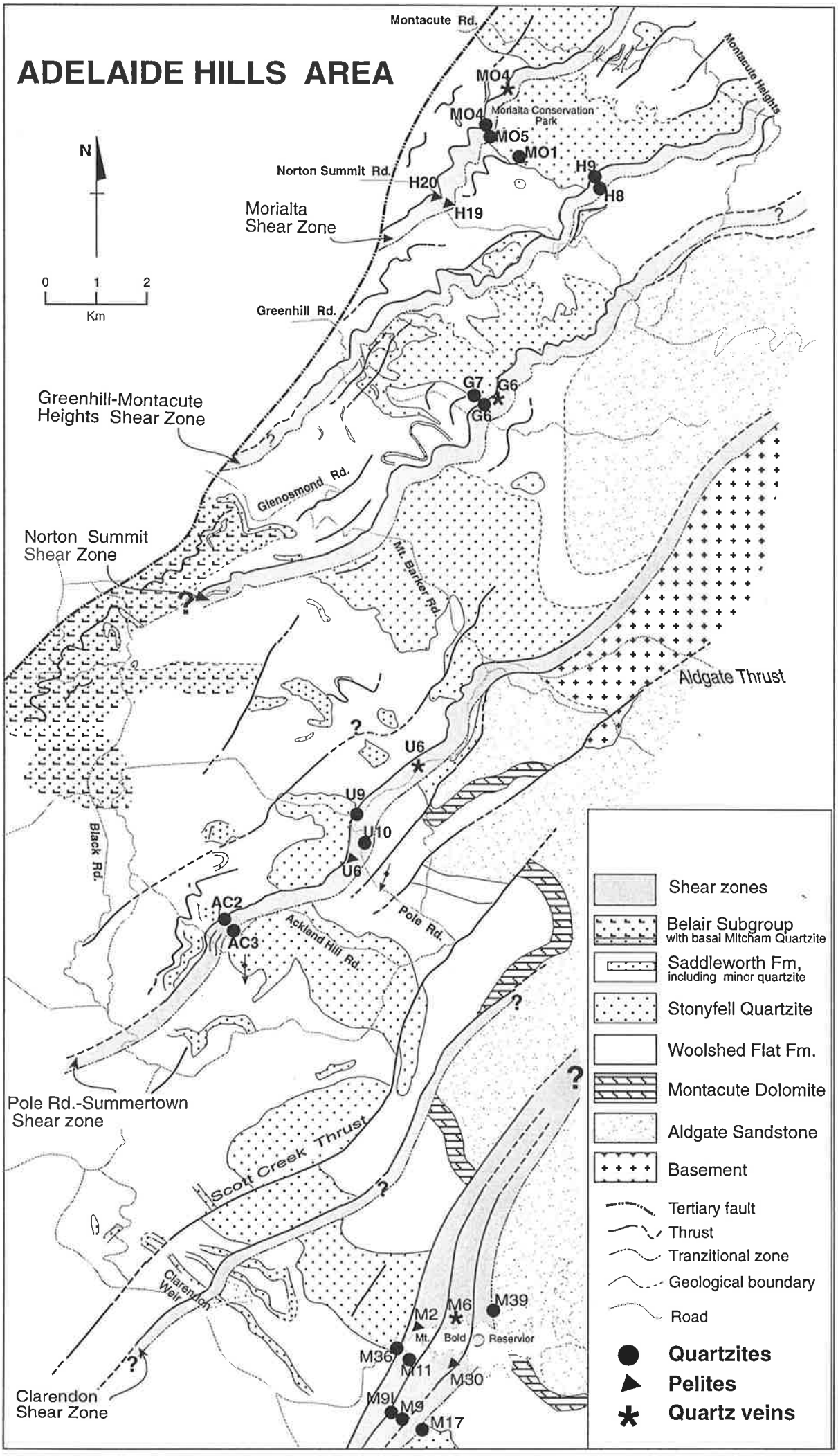
ADELAIDE HILLS AREA
N
0 1 2
Km
Montacute Rd.
Montacute Heights
MO4
MO4
Morialta Conservation Park
MO5
MO1
H9
H8
Norton Summit Rd.
H20
H19
Morialta Shear Zone
Greenhill Rd.
G7
G6
G6
Greenhill-Montacute Heights Shear Zone
Glenosmond Rd.
Norton Summit Shear Zone
Mt. Barker Rd.
Aldgate Thrust
U6
U9
U10
U6
Black Rd.
AC2
AC3
Ackland Hill Rd.
Pole Rd.
Pole Rd.-Summertown Shear zone
Scott Creek Thrust
Clarendon Weir
Clarendon Shear Zone
M2
M6
M39
Mt. Bold Reservior
M36
M11
M30
M9l
M9
M17
Shear zones
Belair Subgroup
with basal Mitcham Quartzite
Saddleworth Fm,
including minor quartzite
Stonyfell Quartzite
Woolshed Flat Fm.
Montacute Dolomite
Aldgate Sandstone
Basement
Tertiary fault
Thrust
Tranzitional zone
Geological boundary
Road
Quartzites
Pelites
Quartz veins

Appendix B: Graphical Rf/Ø plots of quartzites from the Stonyfell Quartzite

INSTRAIN 2.5: INTEGRATED STRAIN ANALYSIS

Project: Morialta Shear Zone
Data File: Mo4-XZ-Rf/O
Number of Objects: 45 defined by 4 points each.

Sample ID: A1045Mo4
Surface Orientation: XZ

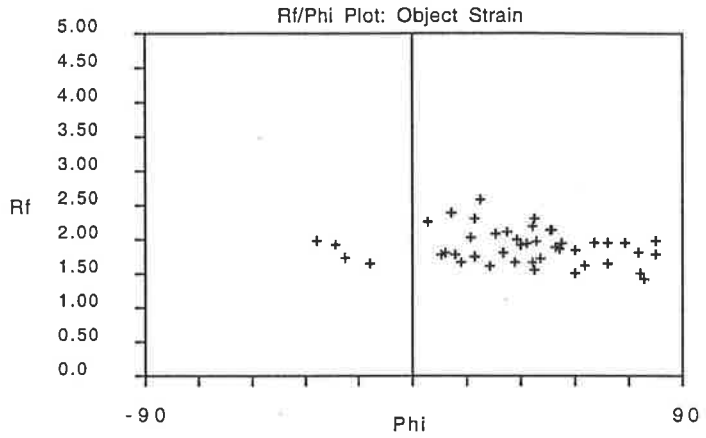

Ellipticity Range: 1.429 to 2.583

MEANS (+/- 1 STD)

Phi (degrees) : 35.870 +/- 27.587
X/Y (n = 45)
Arithmetic 1.889 +/- 0.250
Harmonic 1.858

Mean Object Ellipse: X/Y = 1.630 Phi = 28.83
Average error: 15.72 %

INSTRAIN 2.5: INTEGRATED STRAIN ANALYSIS

Project: Morialta Shear Zone
Data File: Mo4-Yz-text
Number of Objects: 52 defined by 4 points each.

Sample ID: A1045Mo4
Surface Orientation: YZ

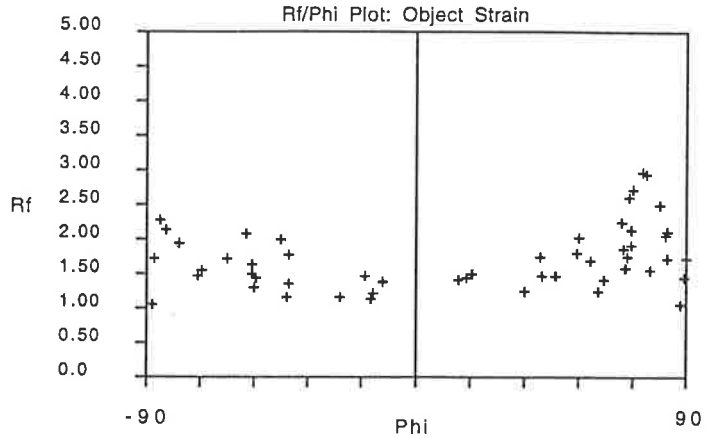

Ellipticity Range: 1.048 to 2.979

MEANS (+/- 1 STD)

Phi (degrees) : 14.103 +/- 62.053
X/Y (n = 52)
Arithmetic 1.729 +/- 0.463
Harmonic 1.623

Mean Object Ellipse: X/Y = 1.455 Phi = 79.64
Average error: 17.46 %

INSTRAIN 2.5: INTEGRATED STRAIN ANALYSIS

Project: Morialta Shear Zone
Data File: Mo5-XZ-Rf/O
Number of Objects: 53 defined by 4 points each.

Sample ID: A1045Mo5
Surface Orientation: XZ

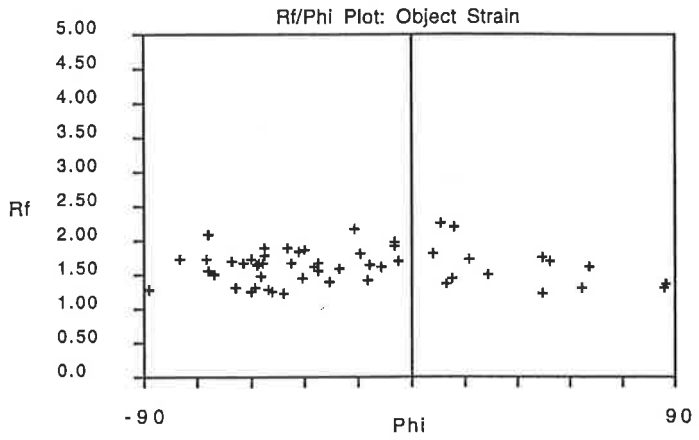

Ellipticity Range: 1.212 to 2.260

MEANS (+/- 1 STD)

Phi (degrees) : -21.159 +/- 42.082
X/Y (n = 53)
Arithmetic 1.622 +/- 0.258
Harmonic 1.583

Mean Object Ellipse: X/Y = 1.292 Phi = -33.94
Average error: 16.43 %

INSTRAIN 2.5: INTEGRATED STRAIN ANALYSIS

Project: Morialta Shear Zone
Data File: Mo5-Yz-text
Number of Objects: 49 defined by 4 points each.

Sample ID: A1045MO5
Surface Orientation: YZ

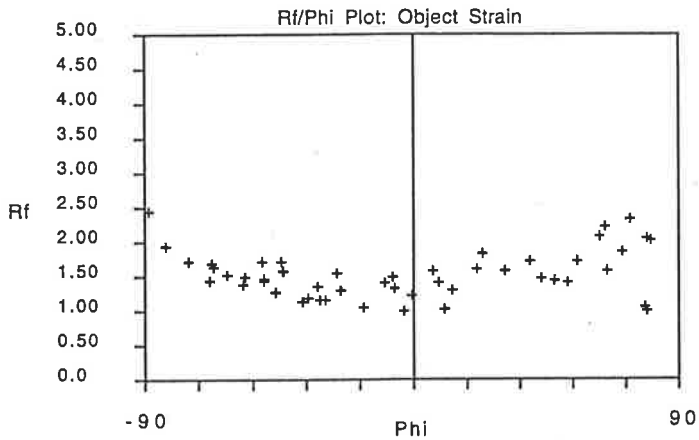

Ellipticity Range: 1.002 to 2.452

MEANS (+/- 1 STD)

Phi (degrees) : -3.340 +/- 51.315
X/Y (n = 49)
Arithmetic 1.535 +/- 0.343
Harmonic 1.465

Mean Object Ellipse: X/Y = 1.167 Phi = 87.32
Average error: 17.32 %

INSTRAIN 2.5: INTEGRATED STRAIN ANALYSIS

Project: Morialta Shear Zone
Data File: Mo1-Rf/O
Number of Objects: 50 defined by 4 points each.

Sample ID: A1045Mo1
Surface Orientation: XZ

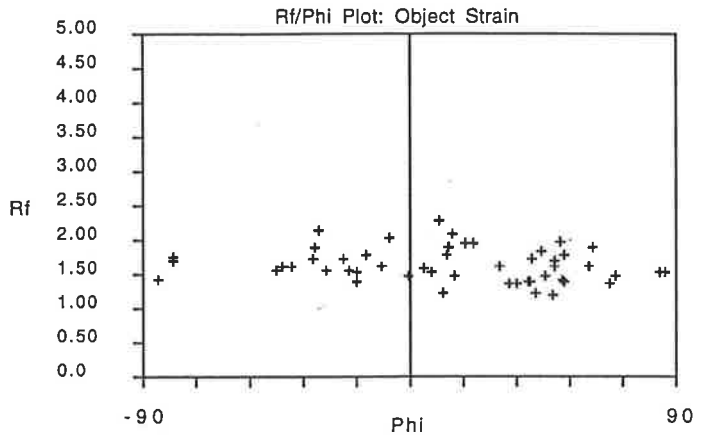

Ellipticity Range: 1.196 to 2.268

MEANS (+/- 1 STD)

Phi (degrees) : 13.060 +/- 42.276
X/Y (n = 50)
Arithmetic 1.631 +/- 0.244
Harmonic 1.597

Mean Object Ellipse: X/Y = 1.269 Phi = 10.79
Average error: 17.25 %

INSTRAIN 2.5: INTEGRATED STRAIN ANALYSIS

Project: Morialta Shear Zone
Data File: Mo1-Yz-text
Number of Objects: 52 defined by 4 points each.

Sample ID: A1045M01
Surface Orientation: YZ

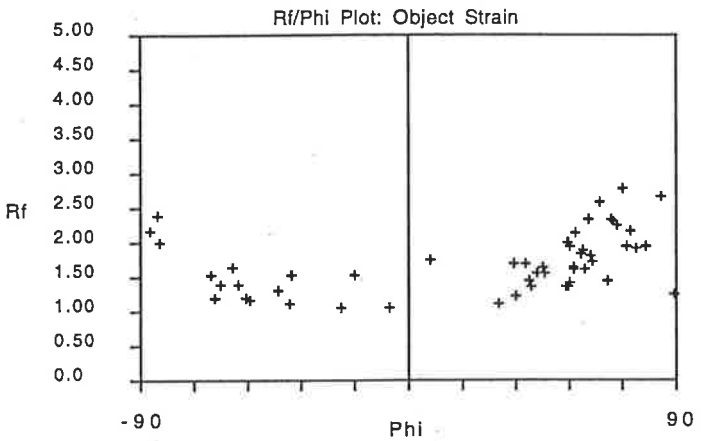

Ellipticity Range: 1.042 to 2.772

MEANS (+/- 1 STD)

Phi (degrees) : 23.128 +/- 54.339
X/Y (n = 52)
Arithmetic 1.709 +/- 0.437
Harmonic 1.606

Mean Object Ellipse: X/Y = 1.531 Phi = 68.31
Average error: 15.46 %

INSTRAIN 2.5: INTEGRATED STRAIN ANALYSIS

Project: Greenhill Shear Zone
Data File: H9-Rf/O
Number of Objects: 40 defined by 4 points each.

Sample ID: A1045H9
Surface Orientation: XZ

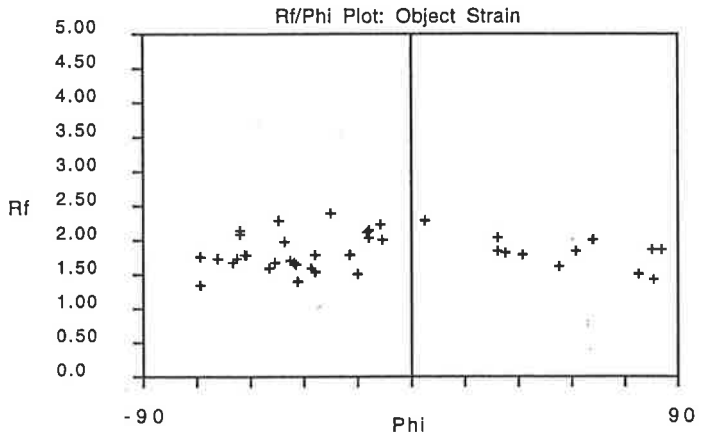

Ellipticity Range: 1.333 to 2.392

MEANS (+/- 1 STD)

Phi (degrees) : -12.287 +/- 47.234
X/Y (n = 40)
Arithmetic 1.819 +/- 0.259
Harmonic 1.783

Mean Object Ellipse: X/Y = 1.226 Phi = -42.14
Average error: 21.48 %

INSTRAIN 2.5: INTEGRATED STRAIN ANALYSIS

Project: Greenhill Shear Zone
Data File: H9-Yz-text
Number of Objects: 50 defined by 4 points each.

Sample ID: A1045H9
Surface Orientation: YZ

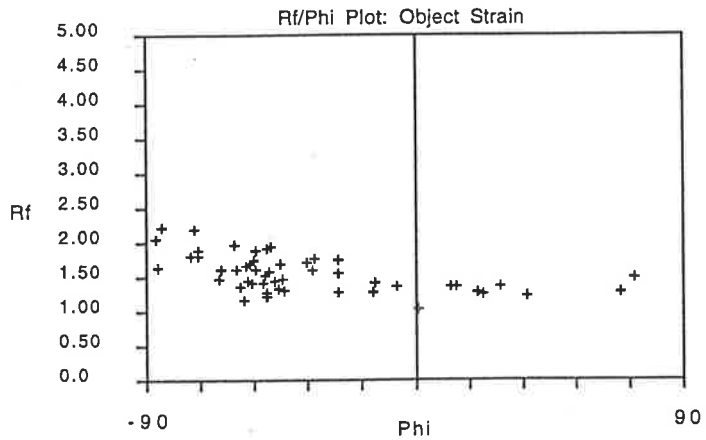

Ellipticity Range: 1.029 to 2.215

MEANS (+/- 1 STD)

Phi (degrees) : -36.248 +/- 37.360
X/Y (n = 50)
Arithmetic 1.557 +/- 0.273
Harmonic 1.512

Mean Object Ellipse: X/Y = 1.412 Phi = -60.13
Average error: 11.86 %

INSTRAIN 2.5: INTEGRATED STRAIN ANALYSIS

Project: Greenhill Shear Zone
Data File: H8-XZ-Rf/O
Number of Objects: 30 defined by 4 points each.

Sample ID: A1045H8
Surface Orientation: XZ

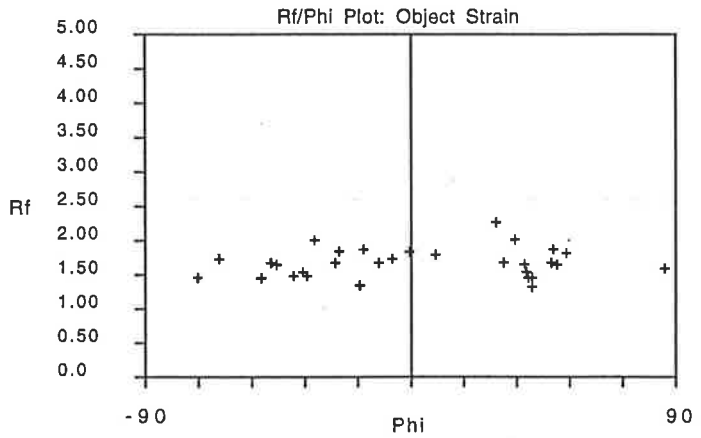

Ellipticity Range: 1.304 to 2.251

MEANS (+/- 1 STD)

Phi (degrees) : 2.072 +/- 42.290
X/Y (n = 30)
Arithmetic 1.664 +/- 0.209
Harmonic 1.640

Mean Object Ellipse: X/Y = 1.243 Phi = 0.87
Average error: 19.04 %

INSTRAIN 2.5: INTEGRATED STRAIN ANALYSIS

Project: Greenhill Shear Zone
Data File: H8-YZ-Rf/Phi
Number of Objects: 40 defined by 4 points each.

Sample ID: A1045H8
Surface Orientation: YZ

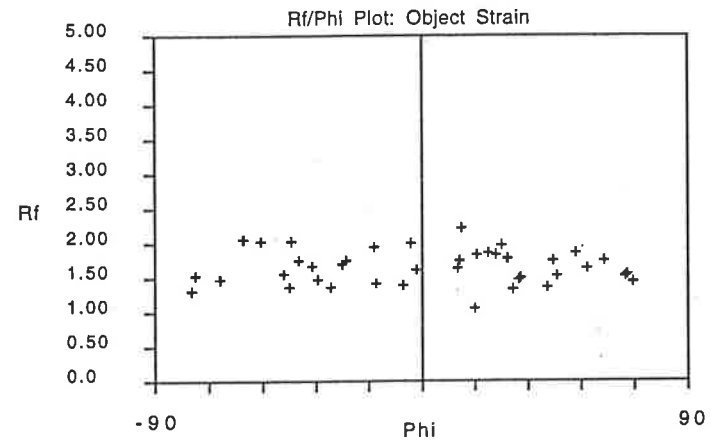

Ellipticity Range: 1.051 to 2.221

MEANS (+/- 1 STD)

Phi (degrees) : 1.755 +/- 43.452
X/Y (n = 40)
Arithmetic 1.652 +/- 0.250
Harmonic 1.614

Mean Object Ellipse: X/Y = 1.200 Phi = -2.10
Average error: 19.09 %

INSTRAIN 2.5: INTEGRATED STRAIN ANALYSIS

Project: Summertown Shear Zone
Data File: G7-XZ-Rf/O
Number of Objects: 50 defined by 4 points each.

Sample ID: A1045G7
Surface Orientation: XZ

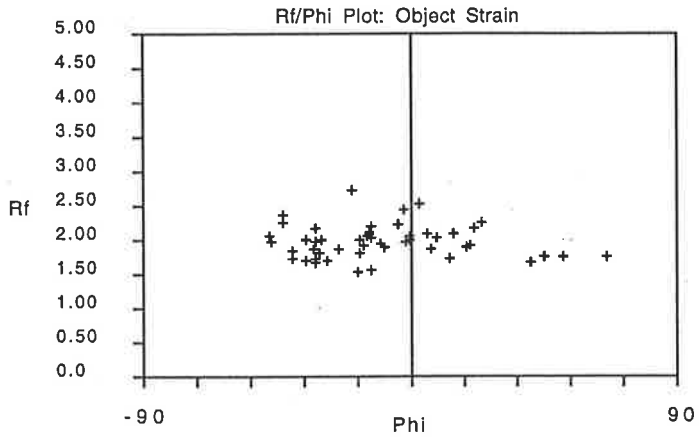

Ellipticity Range: 1.527 to 2.714

MEANS (+/- 1 STD)

Phi (degrees) : -9.751 +/- 26.233
X/Y (n = 50)
Arithmetic 1.972 +/- 0.242
Harmonic 1.945

Mean Object Ellipse: X/Y = 1.698 Phi = -14.13
Average error: 16.24 %

INSTRAIN 2.5: INTEGRATED STRAIN ANALYSIS

Project: Norton Summit Shear Zone
Data File: G7-YZ-Rf/Phi
Number of Objects: 51 defined by 4 points each.

Sample ID: A1045G7
Surface Orientation: YZ

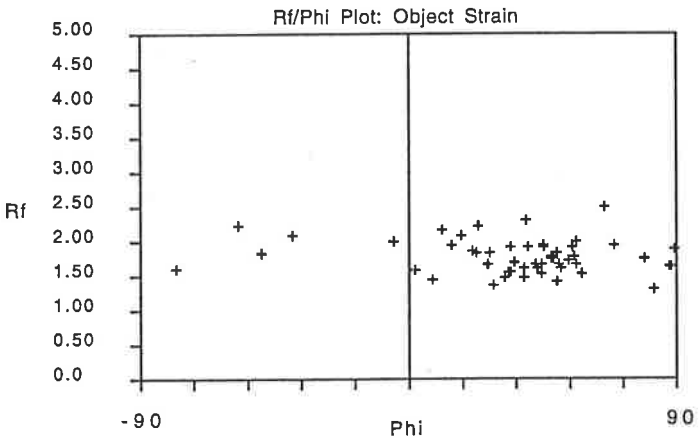

Ellipticity Range: 1.295 to 2.505

MEANS (+/- 1 STD)

Phi (degrees) : 35.277 +/- 34.216
X/Y (n = 51)
Arithmetic 1.779 +/- 0.250
Harmonic 1.746

Mean Object Ellipse: X/Y = 1.412 Phi = 34.85
Average error: 15.93 %

INSTRAIN 2.5: INTEGRATED STRAIN ANALYSIS

Project: Summertown Shear Zone
Data File: G6-XZ-Rf/O
Number of Objects: 43 defined by 4 points each.

Sample ID: A1045G6
Surface Orientation: XZ

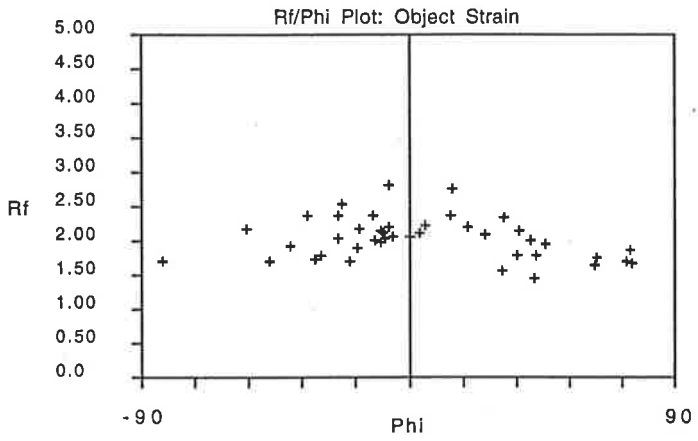

Ellipticity Range: 1.454 to 2.794

MEANS (+/- 1 STD)

Phi (degrees) : 4.975 +/- 36.748
X/Y (n = 43)
Arithmetic 2.030 +/- 0.303
Harmonic 1.987

Mean Object Ellipse: X/Y = 1.467 Phi = -2.94
Average error: 22.08 %

INSTRAIN 2.5: INTEGRATED STRAIN ANALYSIS

Project: Norton Summit Shear Zone
Data File: G6-YZ-Rf/Phi
Number of Objects: 47 defined by 4 points each.

Sample ID: A1045G6
Surface Orientation: YZ

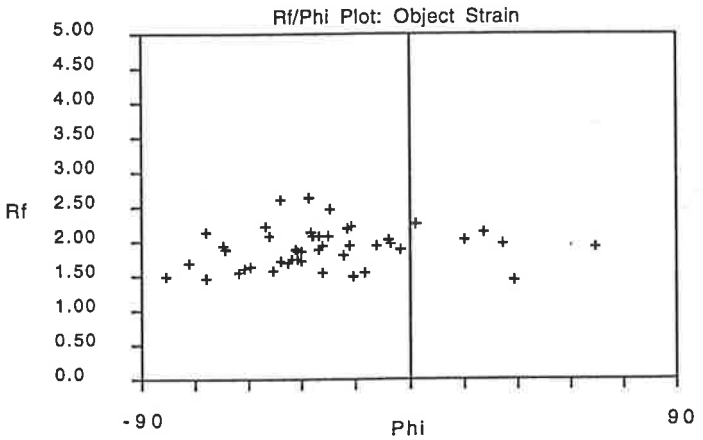

Ellipticity Range: 1.450 to 2.629

MEANS (+/- 1 STD)

Phi (degrees) : -28.742 +/- 29.035
X/Y (n = 47)
Arithmetic 1.908 +/- 0.283
Harmonic 1.869

Mean Object Ellipse: X/Y = 1.549 Phi = -34.65
Average error: 16.83 %

INSTRAIN 2.5: INTEGRATED STRAIN ANALYSIS

Project: Pole Road Shear Zone
Data File: U9-XZ-Rf/O
Number of Objects: 51 defined by 4 points each.

Sample ID: A1045U9
Surface Orientation: XZ

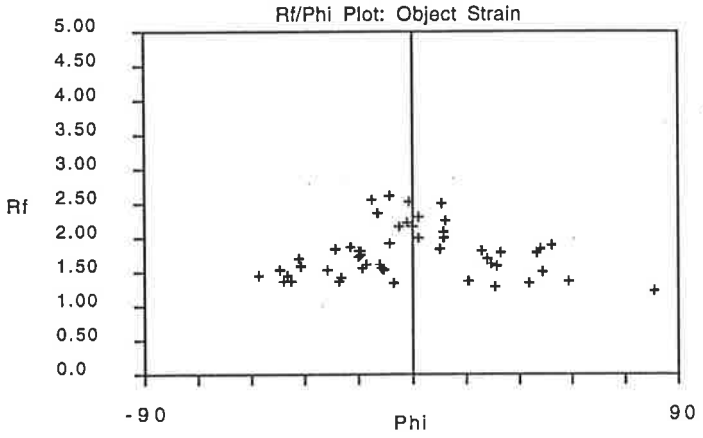

Ellipticity Range: 1.226 to 2.599

MEANS (+/- 1 STD)

Phi (degrees) : 0.536 +/- 29.008
X/Y (n = 51)
Arithmetic 1.771 +/- 0.363
Harmonic 1.704

Mean Object Ellipse: X/Y = 1.663 Phi = -3.45
Average error: 14.23 %

INSTRAIN 2.5: INTEGRATED STRAIN ANALYSIS

Project: Pole Road Shear Zone
Data File: U9-YZ-Rf/Phi
Number of Objects: 55 defined by 4 points each.

Sample ID: A1045U9
Surface Orientation: Yz

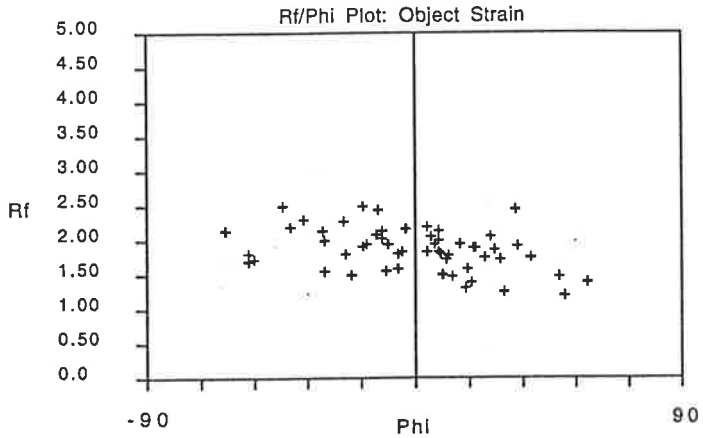

Ellipticity Range: 1.204 to 2.491

MEANS (+/- 1 STD)

Phi (degrees) : 0.977 +/- 28.032
X/Y (n = 55)
Arithmetic 1.868 +/- 0.313
Harmonic 1.813

Mean Object Ellipse: X/Y = 1.658 Phi = -10.92
Average error: 15.74 %

INSTRAIN 2.5: INTEGRATED STRAIN ANALYSIS

Project: Pole Road Shear Zone
Data File: AC2-XZ-Rf/O
Number of Objects: 50 defined by 4 points each.

Sample ID: A1045AC2
Surface Orientation: XZ

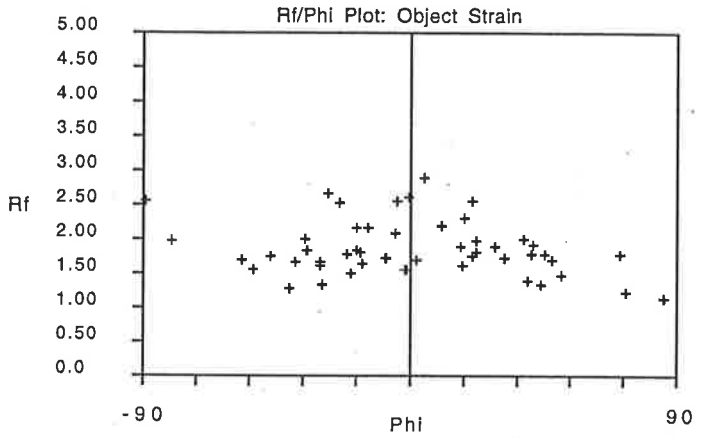

Ellipticity Range: 1.136 to 2.894

MEANS (+/- 1 STD)

Phi (degrees) : 0.509 +/- 38.335
X/Y (n = 50)
Arithmetic 1.858 +/- 0.400
Harmonic 1.780

Mean Object Ellipse: X/Y = 1.405 Phi = -5.83
Average error: 20.22 %

INSTRAIN 2.5: INTEGRATED STRAIN ANALYSIS

Project: Pole Road Shear Zone
Data File: AC2-YZ-Rf/Phi
Number of Objects: 60 defined by 4 points each.

Sample ID: A1045AC2
Surface Orientation: YZ

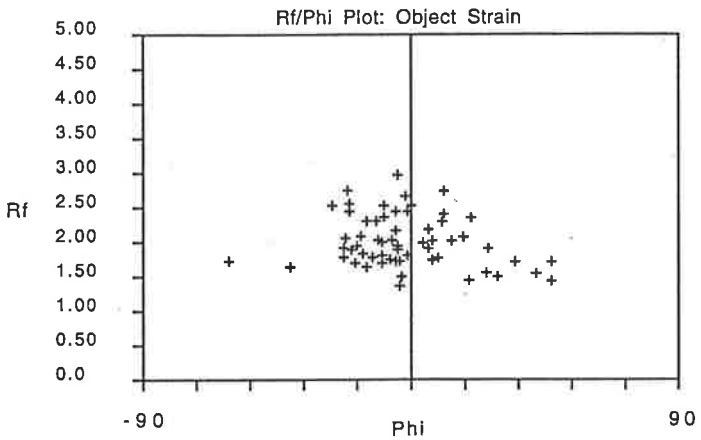

Ellipticity Range: 1.368 to 2.979

MEANS (+/- 1 STD)

Phi (degrees) : -2.305 +/- 19.818
X/Y (n = 60)
Arithmetic 2.009 +/- 0.374
Harmonic 1.944

Mean Object Ellipse: X/Y = 1.893 Phi = -6.16
Average error: 12.89 %

INSTRAIN 2.5: INTEGRATED STRAIN ANALYSIS

Project: Pole Road Shear Zone
Data File: AC3-XZ-Rf/O
Number of Objects: 55 defined by 4 points each.

Sample ID: A1045AC3
Surface Orientation: XZ

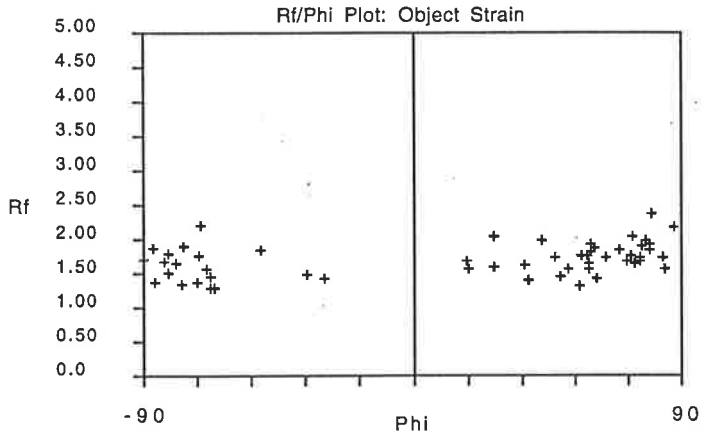

Ellipticity Range: 1.278 to 2.359

MEANS (+/- 1 STD)

Phi (degrees) : 12.633 +/- 65.806
X/Y (n = 55)
Arithmetic 1.683 +/- 0.243
Harmonic 1.649

Mean Object Ellipse: X/Y = 1.515 Phi = 70.98
Average error: 13.48 %

INSTRAIN 2.5: INTEGRATED STRAIN ANALYSIS

Project: Pole Road Shear Zone
Data File: AC3-YZ-Rf/Phi
Number of Objects: 52 defined by 4 points each.

Sample ID: A1045AC3
Surface Orientation: YZ

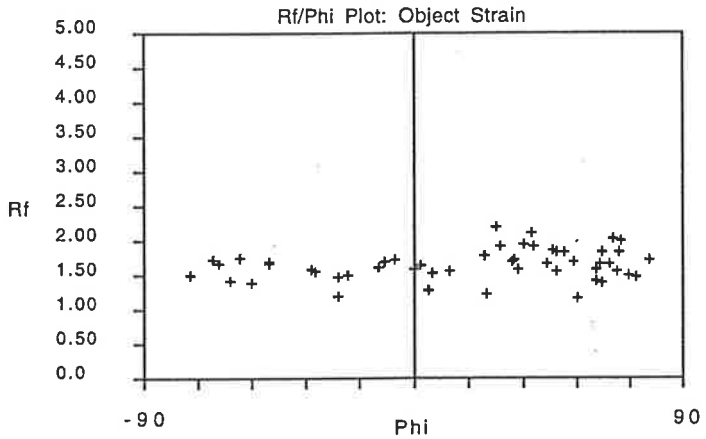

Ellipticity Range: 1.177 to 2.207

MEANS (+/- 1 STD)

Phi (degrees) : 18.262 +/- 45.014
X/Y (n = 52)
Arithmetic 1.646 +/- 0.219
Harmonic 1.617

Mean Object Ellipse: X/Y = 1.230 Phi = 34.82
Average error: 18.17 %

INSTRAIN 2.5: INTEGRATED STRAIN ANALYSIS

Project: Pole Road Shear Zone
Data File: U10-XZ-Rf/0
Number of Objects: 35 defined by 4 points each.

Sample ID: A1045U10
Surface Orientation: XZ

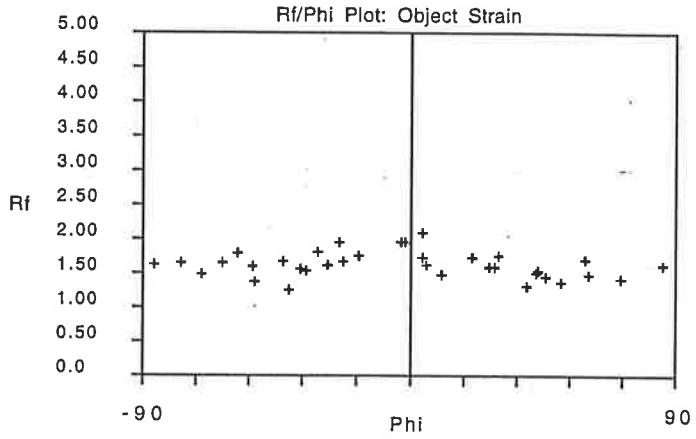

Ellipticity Range: 1.251 to 2.077

MEANS (+/- 1 STD)

Phi (degrees) : -3.317 +/- 46.093
X/Y (n = 35)
Arithmetic 1.615 +/- 0.187
Harmonic 1.595

Mean Object Ellipse: X/Y = 1.180 Phi = -12.66
Average error: 18.58 %

INSTRAIN 2.5: INTEGRATED STRAIN ANALYSIS

Project: Polr road Shear Zone
Data File: U10-YZ-Rf/Phi
Number of Objects: 42 defined by 4 points each.

Sample ID: A1045U10
Surface Orientation: YZ

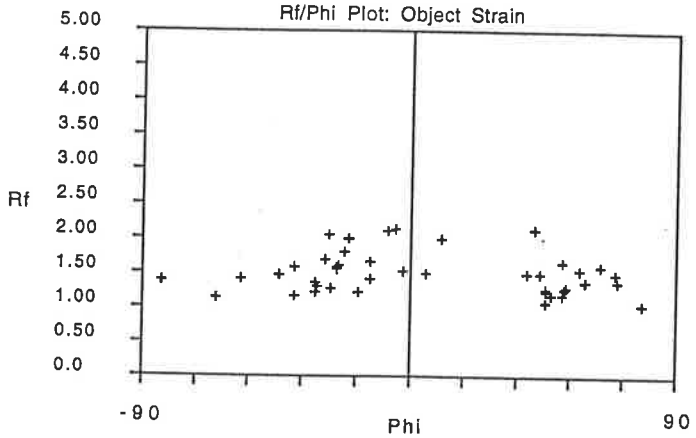

Ellipticity Range: 1.054 to 2.144

MEANS (+/- 1 STD)

Phi (degrees) : 6.066 +/- 43.504
X/Y (n = 42)
Arithmetic 1.502 +/- 0.295
Harmonic 1.450

Mean Object Ellipse: X/Y = 1.243 Phi = 0.55
Average error: 15.01 %

INSTRAIN 2.5: INTEGRATED STRAIN ANALYSIS

Project: Mt. Bold Shear Zone
Data File:
Number of Objects: 40 defined by 4 points each.

Sample ID: A1045M9I
Surface Orientation: XZ

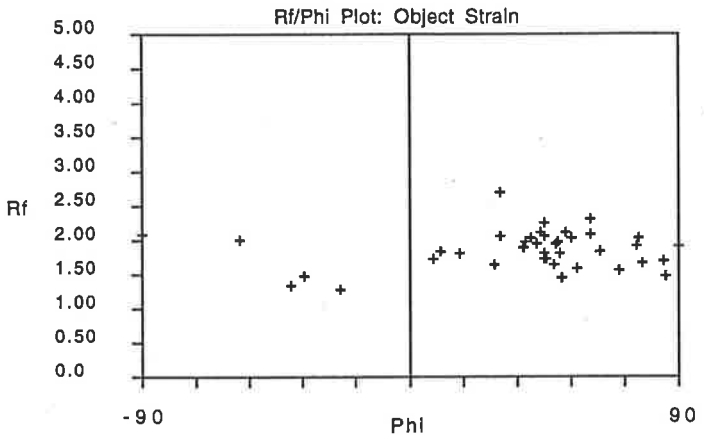

Ellipticity Range: 1.274 to 2.700

MEANS (+/- 1 STD)

Phi (degrees) : 37.664 +/- 38.950
X/Y (n = 40)
Arithmetic 1.861 +/- 0.282
Harmonic 1.819

Mean Object Ellipse: X/Y = 1.545 Phi = 46.00
Average error: 16.09 %

INSTRAIN 2.5: INTEGRATED STRAIN ANALYSIS

Project: Mt.Bold Shear Zone
Data File: M9I-YZ-Rf/Phi
Number of Objects: 40 defined by 4 points each.

Sample ID: A1045M9I
Surface Orientation: Yz

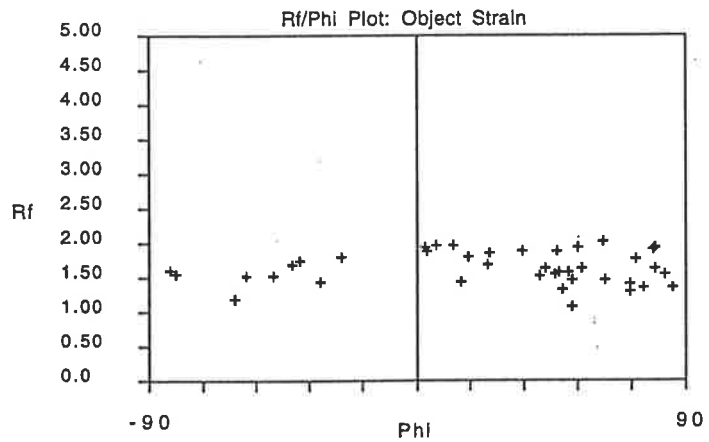

Ellipticity Range: 1.091 to 2.031

MEANS (+/- 1 STD)

Phi (degrees) : 25.871 +/- 48.777
X/Y (n = 40)
Arithmetic 1.642 +/- 0.236
Harmonic 1.607

Mean Object Ellipse: X/Y = 1.251 Phi = 39.35
Average error: 17.47 %

INSTRAIN 2.5: INTEGRATED STRAIN ANALYSIS

Project: Mt. Bold Shear Zone
Data File:
Number of Objects: 46 defined by 4 points each.

Sample ID: A1045M17
Surface Orientation: XZ

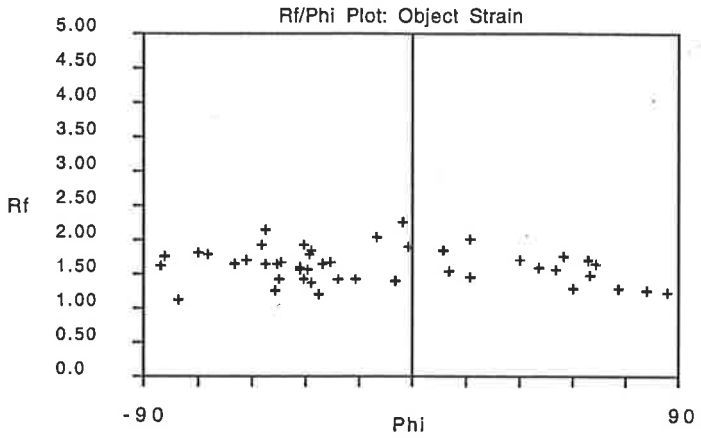

Ellipticity Range: 1.124 to 2.250

MEANS (+/- 1 STD)

Phi (degrees) : -12.348 +/- 47.334
X/Y (n = 46)
Arithmetic 1.613 +/- 0.254
Harmonic 1.574

Mean Object Ellipse: X/Y = 1.173 Phi = -38.56
Average error: 18.03 %

INSTRAIN 2.5: INTEGRATED STRAIN ANALYSIS

Project: Mt. Bold Shear Zone
Data File: m17-yz-Rf
Number of Objects: 50 defined by 4 points each.

Sample ID: A1045M17
Surface Orientation: YZ

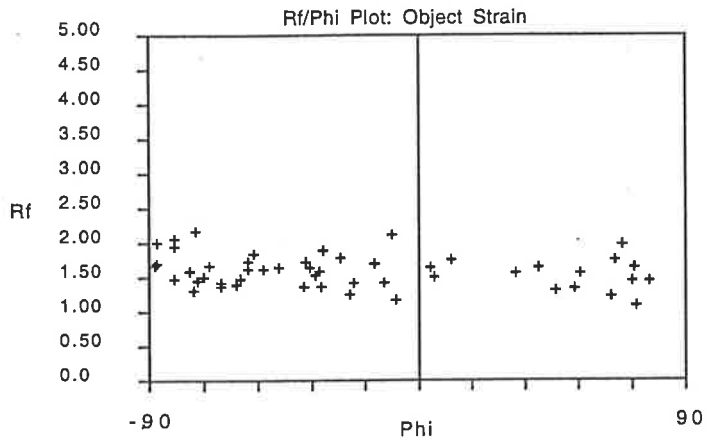

Ellipticity Range: 1.083 to 2.175

MEANS (+/- 1 STD)

Phi (degrees) : -21.836 +/- 53.336
X/Y (n = 50)
Arithmetic 1.587 +/- 0.245
Harmonic 1.550

Mean Object Ellipse: X/Y = 1.233 Phi = -69.17
Average error: 16.49 %

INSTRAIN 2.5: INTEGRATED STRAIN ANALYSIS

Project: Mt. Bold Shear Zone
Data File:
Number of Objects: 49 defined by 4 points each.

Sample ID: A1045M9
Surface Orientation: XZ–

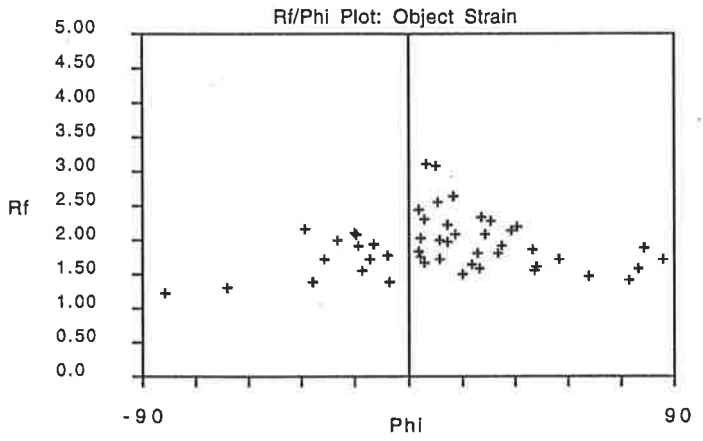

Ellipticity Range: 1.231 to 3.105

MEANS (+/- 1 STD)

Phi (degrees) : 12.519 +/- 33.783
X/Y (n = 49)
Arithmetic 1.914 +/- 0.404
Harmonic 1.839

Mean Object Ellipse: X/Y = 1.598 Phi = 7.16
Average error: 17.56 %

INSTRAIN 2.5: INTEGRATED STRAIN ANALYSIS

Project: Mt. Bold Shear Zone
Data File: m9-yz-Rf
Number of Objects: 51 defined by 4 points each.

Sample ID: A1045M9
Surface Orientation: YZ

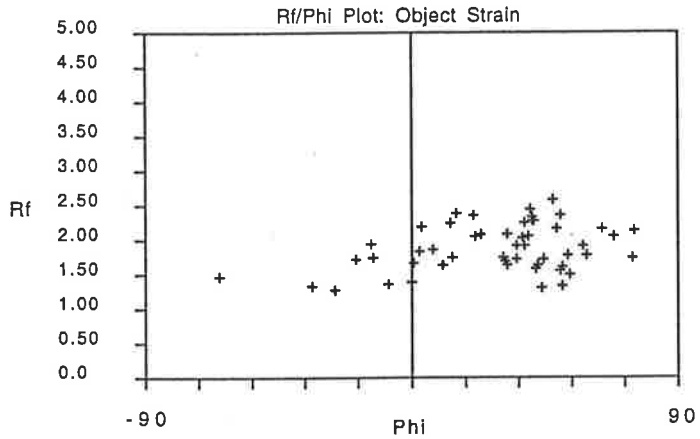

Ellipticity Range: 1.274 to 2.582

MEANS (+/- 1 STD)

Phi (degrees) : 28.256 +/- 28.876
X/Y (n = 51)
Arithmetic 1.876 +/- 0.335
Harmonic 1.816

Mean Object Ellipse: X/Y = 1.702 Phi = 27.67
Average error: 15.13 %

INSTRAIN 2.5: INTEGRATED STRAIN ANALYSIS

Project: Mt. Bold Shear Zone
Data File:
Number of Objects: 47 defined by 4 points each.

Sample ID: A1045M11
Surface Orientation: XZ

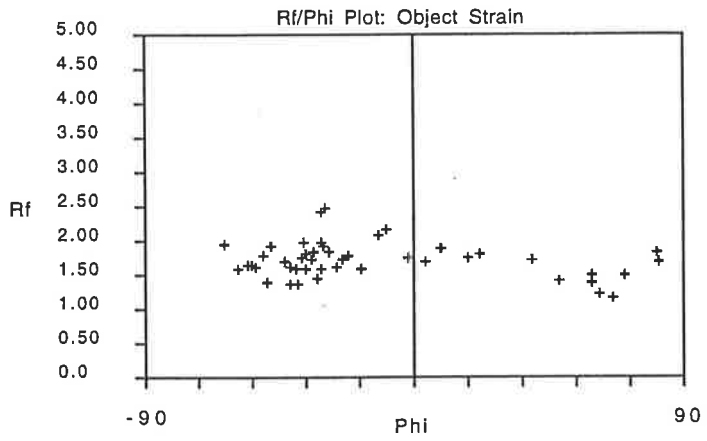

Ellipticity Range: 1.176 to 2.459

MEANS (+/- 1 STD)

Phi (degrees) : -12.391 +/- 41.658
X/Y (n = 47)
Arithmetic 1.713 +/- 0.261
Harmonic 1.676

Mean Object Ellipse: X/Y = 1.355 Phi = -36.40
Average error: 16.78 %

INSTRAIN 2.5: INTEGRATED STRAIN ANALYSIS

Project: Mt. Bold Shear Zone
Data File: M11-YZ-Rf/Phi
Number of Objects: 41 defined by 4 points each.

Sample ID: A1045M11
Surface Orientation: YZ

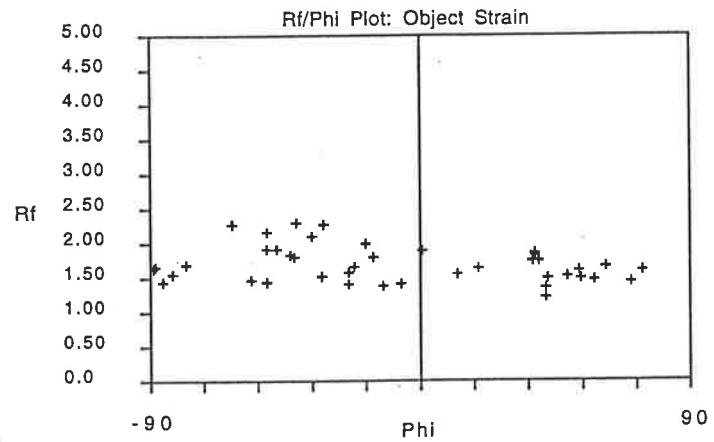

Ellipticity Range: 1.230 to 2.298

MEANS (+/- 1 STD)

Phi (degrees) : -8.833 +/- 49.440
X/Y (n = 41)
Arithmetic 1.697 +/- 0.267
Harmonic 1.659

Mean Object Ellipse: X/Y = 1.126 Phi = -40.58
Average error: 20.91 %

INSTRAIN 2.5: INTEGRATED STRAIN ANALYSIS

Project: Mt. Bold Shear Zone
Data File:
Number of Objects: 40 defined by 4 points each.

Sample ID: A1045M36
Surface Orientation: XZ

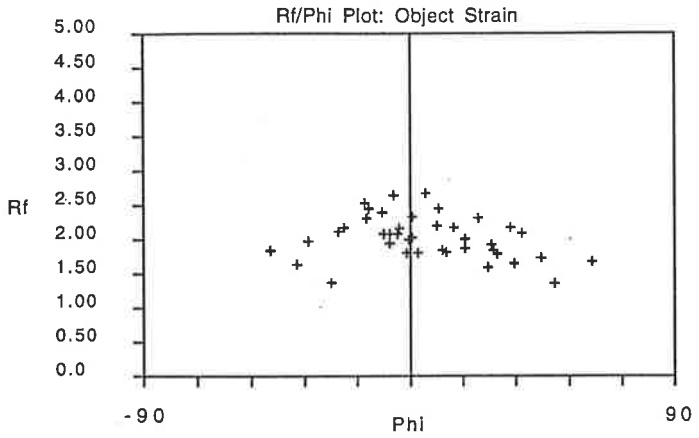

Ellipticity Range: 1.364 to 2.654

MEANS (+/- 1 STD)

Phi (degrees) : 5.267 +/- 24.686
X/Y (n = 40)
Arithmetic 2.019 +/- 0.312
Harmonic 1.970

Mean Object Ellipse: X/Y = 1.840 Phi = 0.20
Average error: 15.63 %

INSTRAIN 2.5: INTEGRATED STRAIN ANALYSIS

Project: Mt. Bold Shear Zone
Data File: M36-YZ-Rf/Phi
Number of Objects: 50 defined by 4 points each.

Sample ID: A1045M36
Surface Orientation: YZ

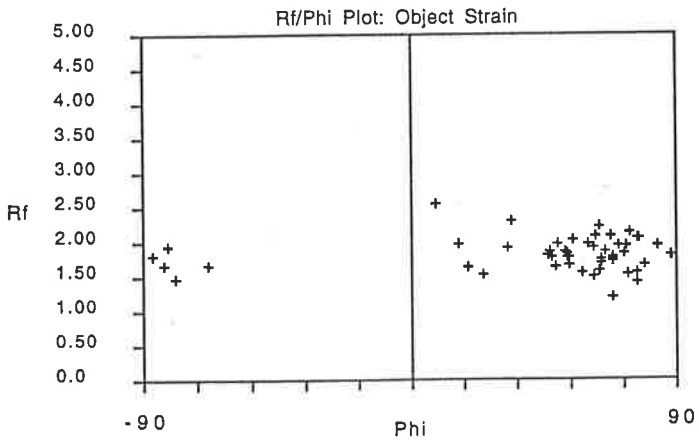

Ellipticity Range: 1.199 to 2.567

MEANS (+/- 1 STD)

Phi (degrees) : 45.070 +/- 45.398
X/Y (n = 50)
Arithmetic 1.822 +/- 0.244
Harmonic 1.790

Mean Object Ellipse: X/Y = 1.694 Phi = 54.53
Average error: 12.31 %

Appendix C:

Method of quantitative analysis of microstructural quartz grain geometry

A study of the variation of grain size, grain shape (aspect ratio), and shape preferred orientation (ø) has been made to demonstrate and tentatively quantify development of quartz grain geometry from within microstructures of the Stonyfell Quartzite in the Adelaide Hills shear zones.

As described in section 6.3, measurement of the quartz grain geometry was carried out on photomicrographs of oriented (XZ) thin sections using digitising software (DIGITIZE 1989). These samples are those which were also used to study the finite strain (chapter 4) and the deformation behaviour of quartz and feldspars (section 6.2). Parameters measured during this study were the length of grains (L), the width of grains (W-perpendicular to the length), and the relative orientation that length of grains (L) makes with the reference frame (Ø), in this case bedding planes. Over 35 detrital quartz grains and quartz grains with a core and mantle structure whose outline could be clearly distinguished, were measured from each thin section. The results were converted into a Word document format (Microsoft Word) and read into a commercial spread sheet package (Microsoft Excel). Frequency histograms of log-normal grain size and long axis orientation (Ø) were constructed separately for each sample. Plots of log-normal long axis versus short axis length and graphs of the aspect ratio (R= L/W) which described the shape of individual grains, were also constructed for each sample (refer to Figs. 6.6 & 6.7). The area (grain size) of individual grains (d) was determined by: $d=(LW)^{1/2}$ (e.g. Masuda 1982, and Michibayashi 1996).

Appendix D: Results of the f-test statistic

F-test two-sample for variances of grain size within the Mt. Bold shear zone

Sub-zone I	*Sub-zone II*	*Sub-zone III*
M17	M9	M9I
2.979691514	2.849826424	2.803377828
2.903516347	2.855667449	2.828852837
2.90691954	2.899624348	2.946060813
3.080616292	2.807682236	2.942028733
2.956368854	2.825025168	3.006202397
2.860797877	2.707626993	2.848830103
3.106708695	2.826437679	2.994755329
3.005790436	2.744569629	3.021928252
2.845101175	2.843309401	2.872391695
2.994352716	2.870036937	2.944062683
2.955373053	2.808419127	2.74749959
3.060505923	2.793629474	2.95629054
2.972239656	2.874359386	2.901905694
2.956991263	2.998986503	2.902851659
2.858738487	2.694872027	2.946215001
2.950964737	2.901869094	2.794310877
3.083271771	2.814949044	2.981135637
2.99597401	2.555999776	2.857687455
2.791158387	2.76596346	2.863532247
3.033383291	2.676167196	2.998407759
2.869007236	2.794921811	2.802087963
2.887082774	2.858555238	2.958578355
2.953776005	2.686854038	2.868446452
2.937035997	2.86344644	2.885410913
2.977584018	2.764985722	2.853048657
2.835268225	2.852529208	2.749272692
2.996098441	2.787230566	2.879328467
2.761595166	2.745506003	2.899688972
2.972328848	2.899695358	2.933100722
2.965911906	2.81835673	3.025096237
3.042198215	2.918936266	3.000897644
2.980955556	2.78888886	2.827515427
2.929335902	2.780013045	2.924658506
2.862193557	2.878592498	2.942189899
2.951826286	2.720904165	2.870180585
2.982642599	2.830965414	3.026013531
2.96063492	2.715547663	2.878482309
2.985870506	2.91458996	2.92821601
2.87054278	2.841955337	2.80700604
2.871015152	2.724406818	2.83095261
2.94932633	2.844222038	
2.940607988	2.847837616	
2.993254923	2.964834176	
2.919060865	2.944657292	
3.101439008	2.819843403	
3.057283857	2.887906172	
	2.877836739	
	2.876780292	
	2.871007411	

F-Test Two-Sample for Variances

	M17	*M9*
Mean	2.95331176	2.82115975
Variance	0.00613867	0.00681641
Observations	46	49
df	45	48
F	0.90057232	
P(F<=f) one-tail	0.63992111	
F Critical one-tail	0.61542682	

F-Test Two-Sample for Variances

	M17	*M9I*
Mean	2.95331176	2.90121248
Variance	0.00613867	0.00572797
Observations	46	40
df	45	39
F	1.07170118	
P(F<=f) one-tail	0.41492824	
F Critical one-tail	1.68243908	

F-Test Two-Sample for Variances

	M9	*M9I*
Mean	2.82115975	2.90121248
Variance	0.00681641	0.00572797
Observations	49	40
df	48	39
F	1.19002234	
P(F<=f) one-tail	0.28952915	
F Critical one-tail	1.67329617	

F-test two-sample for variances of grain size within the Pole Road shear zone

U10-(I)	AC3-(II)	AC2-(III)
2.917436547	2.682768337	2.664488118
2.720781591	2.555997033	2.366784489
2.843863974	2.640606059	2.36895021
2.705137756	2.630057234	2.412916298
2.774768247	2.594895461	2.547185097
2.927621898	2.614148476	2.513597154
2.851151553	2.535225818	2.479025187
2.820299082	2.567810804	2.389525545
2.728849427	2.683132641	2.459201431
2.818070673	2.606441787	2.510257747
2.740996606	2.697525633	2.407455913
2.805420149	2.605983167	2.545989723
2.631128794	2.640878343	2.476948112
2.595191136	2.673040823	2.566942538
2.593727114	2.749631906	2.693128235
2.899166946	2.878452133	2.885699669
2.835419391	2.897091845	2.529951883
2.825447463	2.573977517	2.414614569
2.598299411	2.55734258	2.579132759
2.660749424	2.648471951	2.539954825
2.732946243	2.675954631	2.552044007
2.730104107	2.875672054	2.511779066
2.754149108	2.761039357	2.512171886
2.695648227	2.686336593	2.630307666
2.580904099	2.664235995	2.489550538
2.549917758	2.68989233	2.715922005
2.55170485	2.634594612	2.544375225
2.940722653	2.622850204	2.51470102
2.745567722	2.609924754	2.542144747
2.754080271	2.580149319	2.679701004
2.624805204	2.634514644	2.521663677
2.728494891	2.613500167	2.609672488
2.640163572	2.614611255	2.657962494
2.732526995	2.605550107	2.597325945
2.716571849	2.746656525	2.699602155
2.9664505	2.601369201	2.530790911
2.759649556	2.556742565	2.456733393
2.761656044	2.699712888	2.445198914
2.752107895	2.724761679	2.403609074
2.784078857	2.641101899	2.609176683
2.714922455	2.645309238	2.616630379
2.800164897	2.626517732	2.446176417
2.688589041	2.656334661	2.509885297
2.718176601	2.660812738	2.608471475
2.843440191	2.642829671	2.550929325
2.821424936	2.583025922	2.44429739
2.836997391	2.619574513	2.661191368
2.89755025	2.564357825	2.617474411
2.691329831	2.515374105	2.853656434

F-Test Two-Sample for Variances

	U10-(I)	*AC3-(II)*
Mean	2.74602731	2.65514013
Variance	0.01076805	0.00668997
Observations	51	55
df	50	54
F	1.60958134	
P(F<=f) one-tail	0.04387059	
F Critical one-tail	1.58152424	

F-Test Two-Sample for Variances

	U10 (I)	*Ac2 (III)*
Mean	2.55158099	2.74602731
Variance	0.01274544	0.01076805
Observations	50	51
df	49	50
F	1.18363566	
P(F<=f) one-tail	0.2773163	
F Critical one-tail	1.60235381	

F-Test Two-Sample for Variances

	AC3-(II)	*AC2-(III)*
Mean	2.65514013	2.55158099
Variance	0.00668997	0.01274544
Observations	55	50
df	54	49
F	0.52489089	
P(F<=f) one-tail	0.98819831	
F Critical one-tail	0.62735239	

F-test two-sample for variances of grain size within the Morialta shear zone

Mo1 (I)	*Mo5 (II)*	*Mo4 (III)*
2.90080233	2.7494878	2.61283997
2.77763699	2.79653129	2.81083514
2.70184042	2.6792665	2.90149161
2.93520201	2.80529678	2.74258889
2.85967311	2.72024948	2.81697071
2.82934534	2.75148093	2.7186275
2.7523128	2.76614263	2.84413925
2.78629773	2.86408139	2.78996563
2.80199369	2.81597056	2.83718975
2.82907946	2.89100327	2.74032839
2.6740351	2.74390041	2.61501075
2.77022591	2.75686188	2.62261056
2.81886533	2.87535666	2.76333445
2.7555626	2.75061562	2.48142149
2.88170714	2.83602029	2.43159546
2.76077873	2.88504678	2.68722881
2.77588645	2.66659193	2.59299542
2.79783819	2.92664698	2.73105458
2.76342533	2.70968856	2.60172237
2.88363896	2.78717984	2.62716213
2.80101309	2.75268126	2.83292041
2.76361995	2.73421125	2.68721833
2.6359235	2.77003737	2.75486991
2.64402022	2.77690727	2.87413567
2.78959821	2.69742447	2.81564021
2.83155669	2.73947143	2.81481964
2.88781669	2.73391249	2.67598506
2.8639766	2.75070398	2.63899832
2.72179438	2.84298793	2.76048586
2.70956156	2.80613584	2.71559132
2.91923361	2.82053754	2.45414967
2.69852217	2.80721229	2.67718977
2.84126681	2.74965727	2.62768516
2.7808721	2.83183368	2.7245047
2.86278103	2.72346561	2.56526724
2.71148788	2.7484264	2.85878517
2.99662921	2.76239466	2.5797701
2.81741445	2.57040019	2.48198067
2.83844844	2.82994505	2.60335588
2.78299461	2.78501102	2.64571557
2.75164433	2.73815682	2.71362279
2.94842898	2.77904379	2.68612602
2.72117389	2.77728096	2.62189374
2.84972571	2.79553675	2.81307125
2.88668016	2.88943707	2.84241975
2.80908171	2.81034071	
2.84038459	2.81482809	
2.68570007	2.69509069	
2.7035298	2.73628271	

F-Test Two-Sample for Variances

	Mo1	*Mo5*
Mean	2.79582125	2.77582363
Variance	0.00675039	0.00407192
Observations	50	53
df	49	52
F	1.6577883	
P(F<=f) one-tail	0.03718996	
F Critical one-tail	1.59304747	

F-Test Two-Sample for Variances

	Mo1	*Mo4*
Mean	2.79582125	2.69856256
Variance	0.00675039	0.01363706
Observations	50	45
df	49	44
F	0.49500299	
P(F<=f) one-tail	0.99030541	
F Critical one-tail	0.6115064	

F-Test Two-Sample for Variances

	Mo5	*Mo4*
Mean	2.77582363	2.69856256
Variance	0.00407192	0.01363706
Observations	53	45
df	52	44
F	0.2985924	
P(F<=f) one-tail	0.99996338	
F Critical one-tail	0.61454042	

F-test two-sample for variances of grain shape within the Mt. Bold shear zone

M17 (I)	*M9 (II)*	*M9I (III)*
1.2834	2.268	2.2416
1.1244	2.0843	1.7111
1.7069	1.8679	1.8014
1.1935	1.9908	1.9321
1.7068	2.6371	1.7096
1.4245	1.7925	2.0638
1.3482	1.7113	1.9318
1.2528	1.7679	2.1188
1.4254	1.7408	2.0557
1.2236	2.4335	2.104
1.4028	1.7331	1.6366
1.6498	1.8002	1.4608
1.5322	1.9174	2.0394
1.2771	1.5476	2.0868
2.1253	1.4801	1.8136
1.8284	1.3783	2.0948
1.9244	1.5665	2.0675
1.2536	2.1975	1.7117
1.6033	2.1389	1.9248
1.6355	3.1052	1.6315
1.5838	2.0968	1.8147
1.7916	1.6064	1.6721
1.582	1.7171	1.2739
1.4498	1.6611	1.8297
1.6577	2.1091	2.7004
1.6477	1.981	2.0324
1.9081	2.3215	1.9009
1.5527	1.9172	1.6961
1.8438	1.3844	1.5712
1.7656	1.5913	1.9626
2.2497	2.0967	1.4462
2.0032	2.0096	1.979
1.8905	1.9027	1.909
1.6435	1.509	1.544
2.0295	2.0188	2.3172
1.7463	1.934	2.0343
1.7435	2.5534	1.821
1.6878	1.7213	1.3466
1.6707	2.2979	2.0057
1.5693	1.7322	1.4598
1.634	3.0695	
1.3904	2.2228	
1.4109	1.8347	
1.5496	1.5805	
1.8002	1.2308	
1.4772	1.6435	
	1.4167	
	1.3034	
	2.1714	

F-Test Two-Sample for Variances

	M17	*M9*
Mean	1.61306522	1.91415714
Variance	0.06438924	0.16314481
Observations	46	49
df	45	48
F	0.39467536	
P(F<=f) one-tail	0.99908135	
F Critical one-tail	0.61542682	

F-Test Two-Sample for Variances

	M17	*M9I*
Mean	1.61306522	1.861355
Variance	0.06438924	0.07938224
Observations	46	40
df	45	39
F	0.81112897	
P(F<=f) one-tail	0.74629781	
F Critical one-tail	0.59437522	

F-Test Two-Sample for Variances

	M9	*M9I*
Mean	1.93265652	1.861355
Variance	0.15841215	0.07938224
Observations	46	40
df	45	39
F	1.99556151	
P(F<=f) one-tail	0.01486107	
F Critical one-tail	1.68243908	

F-test two-sample for variances of grain shape within the Pole Road shear zone

U10	*AC3*	*AC2*
1.3654	2.1965	1.838
1.5979	1.7385	2.6789
1.6615	1.6241	2.0088
1.2512	1.2897	2.5201
1.9511	1.9148	2.2013
1.6474	1.4426	1.2111
1.5253	1.5	1.3395
1.3613	1.9129	2.8936
1.9444	1.5537	1.6615
1.5195	1.8221	1.7854
1.6607	1.6646	2.5669
1.792	1.6454	2.5469
1.6875	1.4353	1.7675
1.6351	1.3596	2.5507
1.7296	1.2784	1.7901
1.4853	1.6377	1.7984
1.4817	1.7176	1.3862
1.6028	1.3912	1.289
1.7439	1.6785	1.7646
1.7309	1.8664	1.7311
1.4115	1.5502	1.986
1.502	2.3588	2.0948
1.5778	1.3057	2.1602
1.4837	1.4835	1.3434
1.2991	1.9745	1.4773
1.6064	1.6674	1.9806
1.5427	2.1637	1.9874
1.5798	1.7973	1.8824
1.57	1.8624	1.9118
2.0767	1.7205	1.1358
1.9343	1.5652	1.7035
1.4326	1.5631	1.6847
1.7842	1.6702	1.4905
1.617	2.0374	1.7969
1.7459	1.5715	1.7479
	1.8225	1.7347
	1.7124	1.881
	1.834	2.3104
	1.8761	1.5651
	1.7586	1.5645
	1.5565	1.8424
	1.425	1.6348
	2.0398	2.1743
	1.7469	1.5429
	1.7855	1.6624
	1.9689	1.6017
	1.405	1.7023
	1.6485	1.6108
	1.739	1.763
	1.7134	2.6084

F-Test Two-Sample for Variances

	U10	*AC2*
Mean	1.615377143	1.85823
Variance	0.035101937	0.15999472
Observations	35	50
df	34	49
F	0.21939434	
P(F<=f) one-ta	0.999999175	
F Critical one-t	0.599801098	

F-Test Two-Sample for Variances

	U10	*AC3*
Mean	1.615377143	1.68274364
Variance	0.035101937	0.05924735
Observations	35	55
df	34	54
F	0.592464245	
P(F<=f) one-ta	0.958072272	
F Critical one-t	0.607785822	

F-Test Two-Sample for Variances

	AC3	*AC2*
Mean	1.682743636	1.85823
Variance	0.059247351	0.15999472
Observations	55	50
df	54	49
F	0.370308152	
P(F<=f) one-ta	0.99971321	
F Critical one-t	0.627352392	

F-test two-sample for variances of grain shape within the Morialta shear zone

Mo1 (I)	*Mo5 (II)*	*Mo4 (III)*
2.0859	1.8585	1.7429
1.8363	1.8876	2.1294
1.355	1.927	2.1205
1.5528	1.967	1.8037
1.3969	1.8295	1.6234
1.1962	1.2117	2.1509
1.387	1.6617	1.6628
1.7018	1.6989	1.8647
1.4704	2.2603	1.9401
1.4128	1.7178	1.4987
1.5205	1.6241	1.7647
1.3868	1.283	2.3125
1.2361	1.8118	1.9823
1.9824	1.3177	1.7253
1.6155	1.6605	1.7287
1.6078	1.674	1.9125
1.6097	2.1896	2.3868
1.5345	1.7353	2.1865
1.6136	2.0864	2.3058
1.8778	1.6131	1.6454
1.5321	1.7749	1.9662
1.357	1.7116	2.0883
1.365	1.4371	1.9051
1.4726	1.2458	1.7737
1.2255	1.4211	2.0136
1.8947	1.3571	1.658
1.4606	1.3164	1.9374
1.621	1.2742	1.9619
1.8862	1.5103	1.7844
1.4698	1.6522	1.7969
1.9376	1.3675	1.838
1.4031	1.7532	1.9357
1.6006	1.5458	1.4292
1.389	1.4955	1.5642
2.2683	1.8829	1.8846
1.7346	1.3123	1.9546
1.7847	1.3772	2.2392
1.7858	1.7059	1.8103
1.7339	1.6351	2.0265
1.5441	1.2158	1.9428
2.1252	1.694	1.6241
1.7248	1.293	1.6606
1.9381	1.5824	2.5829
2.0156	1.4799	1.6468
1.7535	1.2595	1.5067
1.7802	1.5558	
1.592	1.607	
1.5577	1.6754	
1.5255	2.1753	

F-Test Two-Sample for Variances

	Mo1	*Mo5*
Mean	1.631338	1.62204151
Variance	0.05950389	0.0667309
Observations	50	53
df	49	52
F	0.8916992	
P(F<=f) one-tail	0.65836724	
F Critical one-tail	0.6277272	

F-Test Two-Sample for Variances

	Mo1	*Mo4*
Mean	1.631338	1.88931778
Variance	0.05950389	0.06255152
Observations	50	45
df	49	44
F	0.95127811	
P(F<=f) one-tail	0.56504745	
F Critical one-tail	0.6115064	

F-Test Two-Sample for Variances

	Mo5	*Mo4*
Mean	1.62204151	1.88931778
Variance	0.0667309	0.06255152
Observations	53	45
df	52	44
F	1.06681503	
P(F<=f) one-tail	0.41534455	
F Critical one-tail	1.62723168	

F-test two-sample for variances of prefered orientation of grains within the Mt. Bold shear zone

ø- M17	*ø- M9*	*ø- M9I*
53.7173	27.6901	45.0231
-78.38	-17.0578	44.7198
-55.7411	41.568	45.0231
-31.4726	10.4969	48.9854
35.9281	14.8043	8.0132
-19.1348	23.3561	30.084
-33.7777	50.8277	42.6845
-46.2019	-7.1921	43.9745
-24.7559	4.117	44.7728
85.8836	2.9455	52.3859
-44.7723	86.0221	48.3914
61.7481	30.4353	85.1937
12.1465	31.4803	54.22
69.2632	-15.744	-89.7178
-49.3456	61.2208	49.9759
10.3941	-6.4772	60.6505
-36.3931	42.7314	44.8287
79.0648	36.4633	45.5907
-84.2355	34.9374	76.0932
-30.1336	5.8937	28.1743
-38.1078	15.263	16.623
-69.0498	43.2688	77.7203
42.1828	-13.1791	-23.3294
19.2483	5.2334	63.6303
-44.585	-17.7365	30.4812
-59.8045	12.9447	40.6735
-50.5028	24.2217	37.8309
-35.3109	-16.4254	84.9152
-34.0364	-32.0214	56.0458
-34.7321	23.9282	38.5203
-3.4354	25.7336	50.5814
19.0627	-23.666	49.5543
-1.2953	79.9803	89.7203
-45.5958	17.8003	70.1716
-11.9558	3.5465	60.6185
-83.1754	-11.3156	76.4267
51.0235	9.6169	10.4428
59.4276	-28.1488	-40.121
-27.4602	5.0345	-57.4937
-38.1078	10.3585	-35.5023
-49.4956	9.3146	
-5.8965	13.0823	
-36.759	3.0302	
48.3913	77.9928	
-71.8835	-82.2771	
60.049	21.1032	
	74.2661	
	-61.1042	
	-34.9534	

F-Test Two-Sample for Variances

	M17	M9
Mean	-12.347887	12.5185898
Variance	2240.54281	1141.2648
Observations	46	49
df	45	48
F	1.96321029	
P(F<=f) one-tail	0.01140309	
F Critical one-tail	1.62488867	

F-Test Two-Sample for Variances

	M17	M9I
Mean	-12.347887	37.664415
Variance	2240.54281	1517.13583
Observations	46	40
df	45	39
F	1.47682413	
P(F<=f) one-tail	0.10828671	
F Critical one-tail	1.68243908	

F-Test Two-Sample for Variances

	M9	M9I
Mean	-12.347887	12.5185898
Variance	2240.54281	1141.2648
Observations	46	49
df	45	48
F	1.96321029	
P(F<=f) one-tail	0.01140309	
F Critical one-tail	1.62488867	

F-test two-sample for variances of prefered orientation of grains within the Pole Road shear zone

Ø-U10	*Ø-AC3*	*Ø-AC2*
-51.9078	-34.7124	9.3241
85.6786	-27.9109	-51.3658
-42.5453	-35.2897	-11.3849
-40.3847	-23.6937	-38.1442
-3.4964	10.1805	-16.5126
-77.2991	72.9353	-7.5069
43.0472	-29.4903	8.6908
50.6804	4.54	0
-1.6374	-38.5196	-1.3329
-34.7633	-21.4874	-44.3636
-22.6732	20.7831	-43.3613
-30.9793	-89.3706	-11.2244
59.3733	70.7019	27.6274
-63.2997	-4.4995	-9.3396
3.9472	40.5601	29.4912
-70.0521	21.8126	-7.5985
60.3255	38.9763	28.345
4.8555	-40.4819	-20.8094
29.4515	45.0233	-6.6167
20.5666	31.4066	24.8766
71.2716	-80.2064	-28.3538
42.5748	-4.8328	-18.1128
26.5786	-17.6932	52.7017
10.4289	43.9419	10.0741
38.9582	50.7371	-23.9743
-27.9375	21.7166	-13.2914
-36.4405	37.9619	-15.2626
-52.9534	28.0871	-17.6165
27.9815	41.1335	-36.996
4.0877	85.5885	-40.1896
-23.7614	-56.8215	23.2982
45.6897	2.1487	-41.703
-58.0238	-20.1676	-10.4967
-85.8835	-16.6392	46.8253
-17.5623	20.4329	43.1257
	-8.4934	-2.1932
	16.6157	18.4441
	18.1622	1.7235
	-1.1941	-25.476
	-2.2323	10.1919
	-17.8048	-17.0713
	-16.0987	43.6421
	-14.4279	26.5788
	-53.0063	-24.3532
	-30.2714	-18.0524
	-30.426	1.6143
	47.7084	81.5602
	17.5347	39.1341
	-46.9985	10.8138

F-Test Two-Sample for Variances

	U10	*AC3*
Mean	-3.3172543	0.508902
Variance	2124.52093	1469.55743
Observations	35	50
df	34	49
F	1.44568758	
P(F<=f) one-ta	0.11714763	
F Critical one-t	1.66721748	

F-Test Two-Sample for Variances

	U10	*AC2*
Mean	-3.3172543	-0.5355118
Variance	2124.52093	841.435591
Observations	35	51
df	34	50
F	2.52487647	
P(F<=f) one-ta	0.00142477	
F Critical one-t	1.66248526	

F-Test Two-Sample for Variances

	AC3	*AC2*
Mean	12.6330564	0.508902
Variance	4330.46171	1469.55743
Observations	55	50
df	54	49
F	2.94677951	
P(F<=f) one-ta	9.5035E-05	
F Critical one-t	1.5939996	

F-test two-sample for variances of prefered orientation of grains within the Morialta shear zone

ø-Mo1	*Ø-Mo5*	*Ø-Mo4*
13.9636	-35.9001	20.5666
44.3643	-41.9101	46.5536
67.5143	-5.7135	31.4827
-45.0226	-5.9237	11.0759
51.9191	-37.8472	25.85
47.9232	-42.8692	45.4415
-17.9054	-56.4776	34.2665
-80.0321	-4.3705	48.839
69.422	9.6568	49.2182
-84.8481	-68.784	76.0844
86.1438	-32.8159	14.2446
39.6167	-88.2908	20.3583
10.9107	6.7571	-31.9333
50.7035	57.9625	42.6025
48.6185	-51.7003	-22.287
-39.8917	-49.8781	-25.8242
30.38	13.9099	12.8607
6.827	19.4123	39.5703
-9.8047	-68.0429	40.257
61.8531	-10.2665	-14.3473
84.2365	-49.6411	40.9832
35.8814	-77.6835	27.878
33.2922	13.5235	36.1947
-0.7077	-47.026	9.8416
42.6687	-14.8157	34.5889
-32.0214	11.3158	39.8605
45.5963	-52.7915	70.4053
60.7398	-48.3905	80.7012
12.6487	25.5905	81.1608
14.7822	-51.8687	75.212
21.4479	86.6205	54.2168
51.3667	44.3932	60.2434
-43.1936	-67.8304	77.4139
40.5069	-66.1169	40.1766
9.6938	-49.8191	47.5692
-22.3305	85.9165	38.0126
51.9013	-27.8243	5.1971
12.1612	47.2271	30.3121
40.8934	-14.1496	19.45
-20.5076	44.2271	64.9497
-30.9003	-60.6147	57.2941
-32.5372	-59.2555	15.804
18.9344	-24.3314	22.5017
-7.1753	-50.6658	65.0492
-79.6025	-54.2874	54.2738
-14.6837	-31.6233	
4.3345	60.3995	
-27.9761	-40.4296	
-17.8689	-19.1886	

F-Test Two-Sample for Variances

	Mo1	*Mo5*
Mean	13.060266	-21.158951
Variance	1787.26287	1770.90189
Observations	50	53
df	49	52
F	1.00923878	
P(F<=f) one-tail	0.48592116	
F Critical one-tail	1.59304747	

F-Test Two-Sample for Variances

	Mo1	*Mo4*
Mean	13.060266	35.8704533
Variance	1787.26287	761.015154
Observations	50	45
df	49	44
F	2.34852468	
P(F<=f) one-tail	0.00237622	
F Critical one-tail	1.635307	

F-Test Two-Sample for Variances

	Mo5	*Mo4*
Mean	-21.158951	35.8704533
Variance	1770.90189	761.015154
Observations	53	45
df	52	44
F	2.32702579	
P(F<=f) one-tail	0.00240465	
F Critical one-tail	1.62723168	

Appendix E: Spreadsheets of fluid inclusion data

Fluid Inclusion data of quartz vein sample #Mo4 from within the Morialta shear zone

No.	*%V*	L	W	*D*	*Phase*	$T_{FM(ice)}$	$T_{FM(co2)}$	$T_{M(ice)}$	T_{clath}	T_{Hco2}	T_H	L-V	wt%Nacl	XNacl	Mo. Nacl	XCo2	Co2 De.	Bul.De.	T_T	P_T(Bar)*
1	0.25	10.85	6.2	8.202	I		-57.8	1.3	9.5	24.8	352		1.024	0.003	0.177	0.09	0.715	0.927	352	3000
3	0.35	7.75	5.425	6.484	I		-57.6	1.2	9.6	23.2	369		0.825	0.002	0.142	0.115	0.737	0.919	369	3100
10	0.25	13.95	7.75	10.4	I		-57.8	-0.3	7.9	23.3	310		4.074	0.012	0.727	0.092	0.735	0.951	310	2600
11	0.25	9.3	9.3	9.3	I		-58.1	-0.3	7.9	24.2	318		4.074	0.012	0.727	0.09	0.723	0.948	318	2500
2	0.25	5.425	3.1	4.101	III	-23.5					294								294	
5	0.1	6.975	4.65	5.695	III	-23.2		-10.2			300		14.2	0.05	2.82	<0.05		0.88	300	1250
12	0.2	17.05	7.75	11.5	III	-23.8		-12.1			261		16.1	0.06	3.27	<0.05		0.93	261	1050
16	0.5	13.95	7.75	10.4	III	-23.1		-12.1			328		16.1	0.06	3.27	<0.05		0.86	328	1500
17	0.1	12.4	9.3	10.74	III	-22.8		-12.3			310		16.2	0.06	3.32	<0.05		0.88	310	1350
18	0.3	13.95	6.2	9.3	III	-22.9		-12.2			354		16.1	0.06	3.3	<0.05		0.83	354	1300
19	0.4	15.5	10.85	12.97	III	-22.7		-12.5			397		16.4	0.06	3.36	<0.05		0.77	397	1350
20	0.2	10.85	6.2	8.202	III	-23.1		-12.4			338		16.3	0.06	3.34	<0.05		0.85	338	1700
21	0.3	7.75	7.75	7.75	III	-22.7		-12.2			285		16.1	0.06	3.3	<0.05		0.91	285	1350
22	0.2	7.75	4.65	6.003	III	-22.5		-12.3			401		16.24	0.056	3.317	<0.05		0.76	401	1400
4	0.05	5.425	2.325	3.551	III	-23.5		-10.3			251		14.3	0.05	2.85	<0.05		0.93	270	1000
6	0.05	23.25	6.975	12.73	IV	-24		-11.2			165		15.2	0.05	3.06			1.01	215	350
7	0.05	15.5	4.65	8.49	IV	-24.1		-11.1			171		15.1	0.05	3.04			0.97	221	270
8	0.05	13.95	7.75	10.4	IV	-24.2		-11.2			165		15.2	0.05	3.06			0.96	215	220
9	0.05	15.5	9.3	12.01	IV	-24		-11.3			174		15.3	0.05	3.09			0.98	224	290
13	0.1	7.75	4.65	6.003	IV	-23.7		-12			189		16	0.06	3.25			1	239	420
15	0.07	15.5	6.975	10.4	IV	-23.4		-12			185		16	0.06	3.25			1	235	400
23	0.1	9.3	6.2	7.593	IV	-23.7		-15.2			190		18.8	0.07	3.96			1.02	240	300
25	0.1	17.05	4.65	8.904	IV	-22.7		-14.6			191		18.3	0.07	3.83			1.02	241	300
27	0.05	6.2	5.425	5.8	IV	-23.3		-14.5			186		18.2	0.06	3.81			1.02	239	300
28	0.1	11.63	6.975	9.005	IV	-23.3		-14.3			188		18	0.06	3.76			1.02	238	300
30	0.1	9.3	4.65	6.576	IV	-23.2		-15.2			172		18.8	0.07	3.96			1.04	222	260

*: Pressuer corection has been done for types I and III based on Bowers and Helgeson (1983) and for type IV based on Potter and Brown (1977).

Fluid inclusion data of quartz vein sample #G6 from within the Summertown shear zone

NO.	%V	L	W	D	Phase	$T_{FM(co2)}$	$T_{FM(ice)}$	$T_{M(Ice)}$	T_{clath}	T_{Hco2}	T_{H}	L-V	wt%Nacl	XNacl	Mo.Nacl	XCo2	Co2MV	Co2 De.	Bul. De	Bul.MV	T_{T}	P_{T} (Bar)*
1	0.1	14	6.2	9.3	I	-57.2			9.2	28.7	370	V	1.615	0.005	0.281	0.06	68.85	0.639	0.929	21.32	370	3700
2	0.1	14	7.75	10.4	I	-57			7	26.3	265	D	5.681	0.018	1.031	0.07	63.75	0.69	0.966	21.16	265	2000
8	0.1	10.9	6.98	8.7	I				7.2	20.1	295	V	5.331	0.017	0.964	0.1	56.92	0.773	0.968	21.82	295	2600
12	0.1	7.75	5.43	6.48	I	-49.6			6.6	28.5	380	V	6.371	0.021	1.164	0.06	68.29	0.644	0.96	21.26	380	3800
14	0.1	8.53	6.2	7.27	I	-57.1			7.4	27.5	324	I	4.976	0.016	0.896	0.08	65.93	0.667	0.938	22.16	324	2700
22	0.1	12.4	6.2	8.77	I	-57			8.7	24.6	355		2.58	0.008	0.453	0.09	61.34	0.718	0.937	22.03	355	3400
25	0.1	10.9	6.2	8.2	I	-57.2			7.2	25.7	320	L	5.331	0.017	0.964	0.07	62.82	0.701	0.965	21.14	320	2900
16	0.1	12.4	9.3	10.7	I	-57			7.7	29.5	320	D	4.438	0.014	0.795	0.08	71.56	0.615	0.921	22.32	320	2400
9	0.1	7.75	6.2	6.93	II				9.6	29.4	410	L	0.825	0.003	0.142	0.12	71.17	0.618	0.864	24.6	410	2900
10	0.1	6.98	5.43	6.15	II	-57.2			7.9	29.1	410	L	4.074	0.013	0.727	0.15	70.09	0.628	0.863	25.83	410	2600
11	0.1	6.98	5.43	6.15	II	-57			7.9	29.5	410	L	4.074	0.013	0.727	0.15	71.56	0.615	0.858	25.89	410	2550
13	0.1	7.75	5.43	6.48	II	-56.9			9.2	28.9	410	V	1.615	0.005	0.281	0.18	69.44	0.634	0.836	27.23	410	2450
23	0.1	9.3	6.2	7.59	III		-27.6	-10.4			367	V	14.364	0.049	2.87	<0.05			0.786	25.46	367	1400
24	0.2	10.1	6.2	7.9	III		-28	-10.8			375	V	14.775	0.051	2.966	<0.05			0.779	25.78	375	1500
4	0.1	14	7.3	10.5	III		-23	-9			339	V	12.855	0.043	2.524	<0.05			0.808	24.44	339	1200
5	0.1	10.9	6.2	8.2	III		-23.3	-9.1			365	V	12.967	0.044	2.549	<0.05			0.768	25.78	365	1600
6	0.1	10.9	9.3	10	III		-23.6	-8.7			360	V	12.516	0.042	2.448	<0.05			0.778	25.34	360	1500
7	0.1	10.9	7.75	9.17	III		-23.9	-7.8			410	V	11.464	0.038	2.215	<0.05			0.652	29.99	410	1200
26	0.2	12.4	6.98	9.3	III		-25.1	-9.4			380	V	13.298	0.045	2.624	<0.05			0.747	26.55	380	1300
17	0.1	14	7.75	10.4	IV		-24.1	-14.8			120	L	18.452	0.065	3.872				1.066	19.37	170	390
18	0.1	15.5	9.3	12	IV		-24	-13.8			117	L	17.598	0.062	3.654				1.06	19.36	167	330
19	0.1	14	6.2	9.3	IV		-21.2	-13.1			165	L	16.977	0.059	3.499				1.018	20.05	215	410
20	0.1	9.3	6.2	7.59	IV		-21	-13.3			146	L	17.156	0.06	3.544				1.033	19.78	196	400
21	0.1	7.75	4.65	6	IV		-23.2	-13.4			148	L	17.246	0.06	3.566				1.033	19.8	198	400
3	0.1	10.9	6.2	8.2	IV		-21.2	-10.2			240	L	14.156	0.048	2.822				0.938	21.27	290	600

*: Pressure correction has been done for types I, II and III based on Bowers and Helgeson (1983) and for type IV based on Potter and Brown (1977)

Fluid Inclusion data of quartz vein sample #U6 from within the Pole Road shear zone

NO.	%V	L	W	D	Phase	$T_{FM(co2)}$	$T_{FM(ice)}$	$T_{M(Ice)}$	T_{clath}	T_{Hco2}	T_H	L-V	wt%Nacl	XNacl	Mo.Nacl	XCo2	Co2 MV	Co2 De	Bul.De	Bul MV	T_T	P_T (Bar)*
1	0.1	12.4	7.75	9.8	I	-57.1			7.7	26	410	V	4.438	0.014	0.795	0.067	63.273	0.696	0.959	21.16	410	3900
2	0.1	7.75	4.65	6	I	-57.2			3.4	24	410	V	11.334	0.038	2.187	0.069	60.616	0.726	1.009	21.06	410	3850
3	0.1	6.98	4.65	5.7	I	-57			3	25.3	410	V	11.885	0.04	2.308	0.068	62.255	0.707	1.008	21.11	410	3800
4	0.1	7.75	5.43	6.48	I	-57			6.3	27.2	345	L	6.878	0.022	1.264	0.065	65.334	0.674	0.969	21.19	345	3250
5	0.1	4.65	3.1	3.8	I	-57.1			3	26.1	395	V	11.885	0.04	2.308	0.067	63.428	0.694	1.005	21.14	395	3700
15	0.1	9.3	4.65	6.58	I	-57.4			5.9	21	270	D	7.54	0.025	1.395	0.052	57.653	0.763	1.008	20.17	270	2700
23	0.1	10.9	6.2	8.2	I				7.3	26	364	L	5.154	0.016	0.93	0.067	63.273	0.696	0.963	21.15	364	3600
25	0.1	6.98	4.65	5.7	I				7	26	345	V	5.681	0.018	1.031	0.067	63.273	0.696	0.967	21.15	345	3350
26	0.1	4.65	4.65	4.65	I	-59.6			7.2	27	358	L	5.331	0.017	0.964	0.065	64.957	0.678	0.961	21.19	358	3400
28	0.1	12.4	7.75	9.8	I	-56.8			7.3	24	340	L	5.154	0.016	0.93	0.091	60.616	0.726	0.955	21.97	340	3000
29	0.1	6.2	5.43	5.8	I	-56.4			6.9	24.1	336	L	5.855	0.019	1.064	0.09	60.733	0.725	0.958	21.97	336	2900
30	0.1	9.3	3.88	6	I	-56.9			6.8	26	330	L	6.028	0.019	1.098	0.048	63.273	0.696	0.986	20.3	330	3500
31	0.1	12.4	12.4	12.4	I	-56.7			6.7	23.8	300	D	6.2	0.02	1.131	0.091	60.387	0.729	0.962	21.96	300	2500
32	0.1	10.9	7.75	9.17	I	-57.1			6.6	23.5	328	L	6.371	0.021	1.164	0.07	60.054	0.733	0.979	21.05	328	3000
7	0.1	14	6.2	9.3	III		-24.3	-9			234	L	12.855	0.043	2.524	<0.05			0.934	21.15	234	1200
10	0.1	7.75	4.65	6	IV		-24	-4.6			210	L	7.25	0.024	1.337				0.914	20.77	260	750
11	0.1	9.3	4.65	6.58	IV		-23.4	-7.8			219	L	11.464	0.038	2.215				0.937	20.86	270	800
19	0.1	8.53	4.65	6.3	III		-24.1	-11.8			350	L	15.764	0.055	3.202	<0.05			0.829	24.41	350	1700
20	0.2	10.1	7.75	8.84	III		-23.9	-11.6			300	L	15.57	0.054	3.155	<0.05			0.889	22.72	300	1200
21	0.1	7.75	4.65	6	III		-23.6	-11.9			252	L	15.86	0.055	3.225	<0.05			0.94	21.54	252	900
22	0.1	10.9	6.2	8.2	III		-24.1	-12			320	L	15.956	0.055	3.248	<0.05			0.87	23.28	320	1500
34	0.1	4.65	3.1	3.8	III		-25.9	-12.8			310	L	16.704	0.058	3.431	<0.05			0.888	22.93	310	1300
35	0.2	7.75	6.2	6.93	III		-25.8	-12.4			290	L	16.333	0.057	3.34	<0.05			0.906	22.42	290	1200
36	0.1	10.9	4.65	7.1	III		-24.7	-13			340	L	16.886	0.059	3.476	<0.05			0.855	23.87	340	1800
6	0.1	14	6.2	9.3	IV		-24.1	-9.1			197	L	12.967	0.044	2.549				0.967	20.48	247	500
8	0.1	12.4	5.43	8.2	IV		-22.4	-9.2			194	L	13.078	0.044	2.574				0.97	20.41	247	500
9	0.1	14	6.2	9.3	IV		-23.1	-8.2			191	L	11.938	0.04	2.32				0.964	20.36	241	480
12	0.1	7.75	6.2	6.93	IV		-24.2	-7.7			145	L	11.343	0.038	2.189				0.994	19.67	195	350
13	0.1	10.9	7.75	9.17	IV		-24.6	-14.1			168	L	17.859	0.063	3.72				1.022	20.13	218	370
14	0.1	9.3	4.65	6.58	IV		-24.6	-13.3			165	L	17.156	0.06	3.544				1.019	20.06	215	330
16	0.1	7.75	4.65	6	IV		-24.5	-13.6			160	L	17.423	0.061	3.61				1.025	19.99	210	320
17	0.1	7.75	6.2	6.93	IV		-22.7	-13.1			169	L	16.977	0.059	3.499				1.014	20.11	219	335
33	0.1	9.3	6.2	7.59	IV		-26.1	-12.1			159	L	16.051	0.056	3.272				1.015	19.97	209	330

*: Pressure correction has been done for type I and III based on Bowers and Helgeson (1983) and for type IV based on Potter and Brown (1977).

Fluid Inclusion data of quartz vein sample #M6 from within the Mt. Bold shear zone

NO.	%V	L	W	D	L/W	Phase	$T_{FM(co2)}$	$T_{FM(ice)}$	$T_{M(Ice)}$	T_{clath}	T_{Hco2}	T_{H}	L-V	wt%Nacl	XNacl	Mo.Nacl	XCo2	Co2 De.	Bul. De.	T_{T}	P_{T}(Bar)*
30	0.1	9.3	3.875	5.48	2.4	I	-57.6		-2.1	7.7	21.5	355	D	4.44	0.01	0.8	0.17	0.76	0.919	355	2900
31	0.1	10.9	5.425	7.1	2	I	-57.7		-2	7.8	20.7	305	D	4.26	0.01	0.76	0.17	0.77	0.921	305	2400
32	0.1	9.3	6.2	8.2	1.5	I	-57.9		-2.1	7.7	20.6	357	L	4.44	0.01	0.8	0.17	0.77	0.923	357	3000
28	0.25	7.75	6.2	6.93	1.25	I	-58			8.1	22	387	L	4.07	0.01	0.73	0.09	0.75	0.955	387	3500
29	0.25	7.75	6.2	6.93	1.25	I	-58.1			8.2	19.9	366	L	3.52	0.01	0.62	0.1	0.78	0.958	366	3800
1	0.15	4.65	3.875	4.24	1.2	II	-57.6			7.5	24.1	396	L	4.8	0.02	0.86	0.14	0.73	0.922	396	3000
2	0.1	6.2	4.65	5.37	1.33	II	-57.9			7.6	25.5	382	L	4.62	0.02	0.83	0.16	0.7	0.897	382	2800
3	0.2	7.75	4.65	6	1.67	II	-57.5			7.6	25.6	388	L	4.62	0.02	0.83	0.16	0.7	0.897	388	2800
4	0.15	5.43	3.875	4.58	1.4	II	-57.6			7.6	25.6	356	L	4.62	0.02	0.83	0.16	0.7	0.897	356	2400
7	0.15	3.88	3.1	3.47	1.25	II	-57.1		-3.1	7.5	23.8		L	4.8	0.02	0.86	0.17	0.73	0.908		
8	0.15	4.65	3.1	3.8	1.5	II	-57		-2.8	7.6	23.6		L	4.62	0.02	0.83	0.17	0.73	0.909		
9	0.15	3.88	3.1	3.47	1.25	II	-56.8			7.7	22.5	386	L	4.44	0.01	0.8	0.17	0.75	0.914	386	3000
10	0.15	3.1	3.1	3.1	1	II	-57			7.5	22.5	401	L	4.8	0.02	0.86	0.17	0.75	0.915	401	3300
11	0.15	3.1	3.1	3.1	1	II	-57.1			7.6	21.2		L	4.62	0.02	0.83	0.17	0.76	0.921		
12	0.15	5.43	3.875	4.58	1.4	II	-56.8			7.5	21.2	401	L	4.8	0.02	0.86	0.17	0.76	0.922	401	3400
14	0.12	10.9	6.2	8.2	1.75	II	-57.2			7.5	23.4	324	D	4.8	0.02	0.86	0.2	0.73	0.896	324	2200
15	0.2	4.65	3.1	3.8	1.5	II	-57.1			7.5	23.3	382	L	4.8	0.02	0.86	0.17	0.74	0.911	382	3000
16	0.1	7.75	6.2	6.93	1.25	II	-57.2		-3.2	7.6	23.6	356	L	4.62	0.02	0.83	0.17	0.73	0.909	356	2550
17	0.2	3.88	3.1	3.47	1.25	II	-57.2			7.6	23.4	401	L	4.62	0.02	0.83	0.14	0.73	0.924	401	3600
18	0.15	9.3	4.65	6.58	2	II	-57.2		-2	5.9	21	320	D	7.54	0.03	1.4	0.15	0.76	0.95	320	2400
19	0.1	10.9	8.525	9.62	1.27	II	-56.9		-1.2	5.8	23.5	284	D	7.7	0.03	1.43	0.17	0.73	0.924	284	1900
20	0.1	4.65	3.875	4.24	1.2	II	-57.1		-1.4	3.4	20.8	401	L	9.89	0.03	1.88	0.17	0.77	0.948	401	3300
21	0.1	6.51	1.938	3.55	3.36	II	-57.5			5.7	25.7	401	L	7.87	0.03	1.46	0.16	0.7	0.911	401	2950
22	0.1	7.75	6.2	6.93	1.25	II	-57.3		0.8	3.4	20	401	L	9.74	0.03	1.85	0.18	0.77	0.951	401	3400
33	0.1	5.43	6.975	8.05	0.78	II	-57.7		-2.1	7.6	20.1	401	L	4.62	0.02	0.83	0.18	0.77	0.926	401	3550
34	0.1	5.43	4.65	5.02	1.17	II	-57.7		-2.2	7.5	22.8	401	L	4.8	0.02	0.86	0.17	0.74	0.914	401	3300
35	0.1	5.43	4.65	5.02	1.17	II	-57.6			7.5	22.7	401	L	4.8	0.02	0.86	0.17	0.74	0.914	401	3300
13	0.1	6.2	3.1	4.38	0.1	III		-20.4	-8.1			345	L	11.8	0.04	2.29	<0.05		0.79	345	1350
36	0.1	9.3	6.2	5.8	0.1	III		-22.7	-8.3			379	L	12.1	0.04	2.35	<0.05		0.73	379	1500
5	0.2	4.65	3.1	3.8	1.5	IV		-20.6	-8.2			220	L	11.9	0.04	2.32			0.94	270	650
6	0.3	9.3	6.2	7.59	1.5	IV		-20.1	-8.3			215	L	12.1	0.04	2.35			0.95	265	700
23	0.1	7.75	4.65	6	1.67	IV		-21	-7.5			146	L	11.1	0.04	2.14			0.97	196	270
24	0.1	4.65	3.875	4.24	1.2	IV		-23.8	-7.6			171	L	11.2	0.04	2.16			0.97	221	450
25	0.1	3.88	3.1	3.47	1.25	IV		-23	-7.8			179	L	11.5	0.04	2.22			0.96	229	470
26	0.1	4.65	3.875	4.24	1.2	IV		-22.6	-7.8			182	L	11.5	0.04	2.22			0.95	232	400

*: Pressuer corection has been done for types I, II and III based on Bowers Helgeson (1983) and for type IV based on Potter and Brown (1977).

Descriptive statistic of bulk density and estimated P and T of trappment of all inclusion types.

Type I	T_H	*XNacl*	*XCo2*	*Bul.De.*	T_T ℃	P_T bar
Mean	344.806452	0.01677419	0.08609677	0.95787097	344.806452	3120.96774
Standard Error	6.81103143	0.00167185	0.00570292	0.00478792	6.81103143	93.3479499
Median	345	0.016	0.078	0.959	345	3000
Mode	410	0.01	0.09	0.919	410	3000
Standard Deviation	37.9222181	0.00930845	0.03175254	0.02665801	37.9222181	519.739389
Sample Variance	1438.09462	8.6647E-05	0.00100822	0.00071065	1438.09462	270129.032
Kurtosis	-0.2919456	1.61927088	2.88605852	-0.3444839	-0.2919456	-0.9491992
Skewness	-0.1198842	1.12956407	1.78112467	0.36568439	-0.1198842	-0.1634882
Range	145	0.038	0.122	0.09	145	1900
Minimum	265	0.002	0.048	0.919	265	2000
Maximum	410	0.04	0.17	1.009	410	3900
Sum	10689	0.52	2.669	29.694	10689	96750
Count	31	31	31	31	31	31
Confidence Level(95.0%)	13.9099676	0.00341436	0.01164691	0.00977823	13.9099676	190.641751

Type II	T_H	*XNacl*	*XCo2*	*Bul.De.*	T_T ℃	P_T bar
Mean	383.045455	0.01976	0.16476	0.90716	383.045455	2893.18182
Standard Error	7.29361853	0.00142042	0.00308344	0.0055865	7.29361853	100.015987
Median	401	0.02	0.17	0.911	401	2925
Mode	401	0.02	0.17	0.897	401	3300
Standard Deviation	34.2101033	0.00710211	0.0154172	0.02793248	34.2101033	469.116559
Sample Variance	1170.33117	5.044E-05	0.00023769	0.00078022	1170.33117	220070.346
Kurtosis	2.45833236	0.6787695	2.28770504	0.89588163	2.45833236	-0.7667548
Skewness	-1.7493035	-0.5186082	-0.7656715	-0.8218341	-1.7493035	-0.2935624
Range	126	0.027	0.079	0.115	126	1700
Minimum	284	0.003	0.121	0.836	284	1900
Maximum	410	0.03	0.2	0.951	410	3600
Sum	8427	0.494	4.119	22.679	8427	63650
Count	22	25	25	25	22	22
Confidence Level(95.0%)	15.1679127	0.00293161	0.00636391	0.01152996	15.1679127	207.994666

Type III	T_H	*XNacl*	*XCo2*	*Bul.De.*	T_T ℃	P_T bar
Mean	329.259259	0.05246154	0.05	0.83688462	329.962963	1355.76923
Standard Error	9.3585728	0.00143176	0	0.01456406	9.15651831	42.4560336
Median	338	0.055	0.05	0.8525	338	1350
Mode	300	0.06	0.05	0.88	300	1500
Standard Deviation	48.6285707	0.00730058	0	0.07426241	47.5786648	216.484144
Sample Variance	2364.73789	5.3298E-05	0	0.00551491	2263.72934	46865.3846
Kurtosis	-0.7886952	-1.0617735	-2.173913	-0.2208037	-0.7781752	-0.0670409
Skewness	-0.2412769	-0.5852809	-1.0622957	-0.535605	-0.2009351	0.04310313
Range	176	0.022	0	0.288	176	900
Minimum	234	0.038	0.05	0.652	234	900
Maximum	410	0.06	0.05	0.94	410	1800
Sum	8890	1.364	1.3	21.759	8909	35250
Count	27	26	26	26	27	26
Confidence Level(95.0%)	19.2368345	0.00294877	0	0.02999522	18.8215053	87.4397768

Type IV	T_H	*XNacl*	*XCo2*	*Bul.De.*	T_T ℃	P_T bar
Mean	176.029412	0.05208824	#DIV/0!	0.9935	226.235294	405.441176
Standard Error	4.49548898	0.00196873	0	0.00644063	4.52228761	23.5661617
Median	173	0.053	#NUM!	1	223	380
Mode	165	0.04	#NUM!	0.97	215	400
Standard Deviation	26.21298	0.01147954	#DIV/0!	0.03755501	26.3692415	137.413155
Sample Variance	687.120321	0.00013178	#DIV/0!	0.00141038	695.336898	18882.3752
Kurtosis	0.57257158	-0.6588419	#NUM!	-0.7899917	0.51519591	1.87829859
Skewness	-0.0246824	-0.3132954	#NUM!	-0.1166328	-0.031084	1.42727855
Range	123	0.046	0	0.152	123	580
Minimum	117	0.024	0	0.914	167	220
Maximum	240	0.07	0	1.066	290	800
Sum	5985	1.771	0	33.779	7692	13785
Count	34	34	0	34	34	34
Confidence Level(95.0%)	9.14614836	0.0040054	#NUM!	0.01310357	9.20067062	47.9457545

Appendix F: Representitive P-T estimates using Thermocalc Program and the approch of Powell and Holland (1988) with the expanded, internally consistent dataset of Holland and Powell (1990).

Appendix F-I: calculations of average pressure

(a) Average pressure calculations on the interpreted peak assmblage for rock #H20 from within the Morialta shear zone.

(i) The activity data for mineral end-members in the rock

	clin	daph	ames	mu	pa	cel	ab	phl
a	0.0743	0.00737	0.0202	0.707	0.426	0.0452	0.990	0.116
sd(a)/a	0.31753	0.58376	0.44142	0.10000	0.09888	0.37199	0.05000	0.26128

	ann	east	naph	q	H2O
a	0.0530	0.0216	0.00276	1.00	0.800
sd(a)/a	0.35079	0.43674	3.61894	0	

(ii) An independent set of reactions involving mineral end-members.

1) clin + 4pa + phl + q = 2ames + mu + 4ab
2) 6clin + 14pa + 2phl = 9ames + 2mu + 14ab + 2H2O
3) 2clin + 4pa + east + q = 3ames + mu + 4ab
4) 2clin + 4pa + phl + q = 3ames + cel + 4ab
5) 8clin + 20pa + 5ann + 5q = 3daph + 10ames + 5mu + 20ab
6) 14pa + 6cel + 5ann + 3q = 3daph + 11mu + 12ab + 2naph

(iii) Calculated pressures for the given activity data and at T = 400°C and for x(CO2) = 0.2 and x(H2O) = 0.8.

	P(T)	sd(P)	a	sd(a)	b	c	ln_K	sd(ln_K)
1	2.0	1.91	5.09	6.70	-0.02110	4.720	-0.015	1.075
2	2.0	1.88	128.04	23.55	-0.20929	18.822	-4.069	4.705
3	1.5	2.39	-8.52	7.30	-0.00107	4.824	0.365	1.598
4	1.8	2.34	13.49	6.86	0.00092	4.828	-4.065	1.600
5	2.1	2.19	14.26	33.94	-0.06262	22.006	-3.106	6.103
6	4.5	4.06	-28.21	21.89	-0.16389	12.510	14.770	8.185

(iv) Average pressure calculated from the intercepts of the reactions (for x(CO2) = 0.2 and x(H2O) = 0.8)

T°C	360	380	400	420	440
av P	1.3	1.9	2.4	3.1	3.7
sd	1.05	1.07	1.09	1.11	1.13
f	0.4	0.3	0.4	0.5	0.6

==========

Appendix F-I: continued

(b) Average pressure calculations on the interpreted peak assmblage for rock #H19 from within the Morialta shear zone.

(i) The activity data for mineral end-members in the rock

	phl	ann	east	naph	mu	pa	cel	clin
a	0.100	0.0423	0.0259	0.0223	0.519	0.282	0.0702	0.0550
sd(a)/a	0.28056	0.38208	0.42236	0.44767	0.10000	0.15483	0.32420	0.35153

	daph	ames	ab	q	H2O
a	0.00654	0.0176	0.800	1.00	0.800
sd(a)/a	0.59488	0.45137	0.05000	0	

(ii) An independent set of reactions involving mineral end-members.

1) naph + 3pa + clin + q = 2ames + 4ab
2) 5phl + 3daph = 5ann + 3clin
3) 5ann + 2mu + 3ames = 5east + 2cel + 3daph
4) 4naph + 3mu + q = phl + 2east + clin + 4ab
5) 14naph + 12mu = 3phl + 9east + 3clin + 14ab + 2H2O
6) phl + 5ann + 3naph + 9pa + 3q = 6east + 3daph + 12ab

(iii) Calculated pressures for the given activity data and at T = 400°C and for x(CO2) = 0.2 and x(H2O) = 0.8.

	P(T)	sd(P)	a	sd(a)	b	c	ln_K	sd(ln_K)
1	1.3	2.16	-3.96	6.88	-0.01542	4.425	1.530	1.181
2	3.7	11.58	11.20	5.59	-0.04289	1.596	2.090	3.149
3	6.4	13.28	73.67	14.45	-0.01320	-1.897	-9.420	3.686
4	2.6	4.86	-3.89	11.37	-0.03845	3.334	3.774	2.062
5	2.4	4.36	123.83	42.51	-0.31006	13.762	9.489	7.582
6	1.6	3.18	58.60	26.33	-0.12354	11.061	1.240	4.176

(iv) Average pressure calculated from the intercepts of the reactions (for x(CO2) = 0.2 and x(H2O) = 0.8)

T°C	360	380	400	420	440
av P	1.7	2.3	2.9	3.6	4.3
sd	1.06	1.08	1.10	1.13	1.15
f	0.9	0.8	0.8	0.8	0.9

Appendix F-I: continued

(c) Average pressure calculations on the interpreted peak assmblage for rock #U6 from within the Pole Road shear zone.

(i) The activity data for mineral end-members in the rock

	clin	daph	ames	phl	ann	east	naph	mu
a	0.110	0.00261	0.0358	0.0523	0.0320	0.0320	0.00919	0.765
sd(a)/a	0.26837	0.66935	0.39445	0.35693	0.41906	0.40441	1.08808	0.10000

	pa	cel	ab	q	H2O
a	0.638	0.0315	0.990	1.00	0.800
sd(a)/a	0.05000	0.40598	0.05000	0	

(ii) An independent set of reactions involving mineral end-members.

1) clin + naph + 3pa + q = 2ames + 4ab
2) 6clin + 2naph + 12pa = 9ames + 14ab + 2H2O
3) clin + phl + 4pa + q = 2ames + mu + 4ab
4) 2clin + phl + 4pa + q = 3ames + cel + 4ab
5) 2clin + east + 4pa + q = 3ames + mu + 4ab
6) 8clin + 5ann + 20pa + 5q = 3daph + 10ames + 5mu + 20ab

(iii) Calculated pressures for the given activity data and at T = 400°C and for x(CO2) = 0.2 and x(H2O) = 0.8.

	P(T)	sd(P)	a	sd(a)	b	c	ln_K	sd(ln_K)
1	1.3	2.35	-3.96	6.88	-0.01542	4.425	1.550	1.393
2	2.0	1.91	109.93	23.69	-0.19794	18.232	-2.070	4.559
3	2.0	1.81	5.09	6.70	-0.02110	4.720	-0.008	0.955
4	2.1	2.19	13.49	6.86	0.00092	4.828	-4.318	1.435
5	2.7	2.21	-8.52	7.30	-0.00107	4.824	-0.638	1.394
6	3.5	2.09	14.26	33.94	-0.06262	22.006	-8.808	5.553

(iv) Average pressure calculated from the intercepts of the reactions (for x(CO2) = 0.2 and x(H2O) = 0.8)

T°C	360	380	400	420	440
av P	1.1	1.7	2.3	2.9	3.6
sd	1.04	1.06	1.08	1.09	1.13
f	0.9	0.8	0.9	0.9	1.0

==========

Appendix F-I: continued

(d) Average pressure calculations on the interpreted peak assmblage for rock #M30 from within the Mt. Bold shear zone.

(i) The activity data for mineral end-members in the rock

	clin	daph	ames	ab	phl	ann	east	naph
a	0.110	0.00261	0.0358	0.990	0.156	0.0201	0.0484	0.0268
sd(a)/a	1.09091	0.66935	0.39445	0.05000	0.21961	0.47721	0.36498	0.37378

	mu	pa	cel	q	H2O
a	0.611	0.494	0.0398	1.00	0.800
sd(a)/a	0.10000	0.07687	0.38442	0	

(ii) An independent set of reactions involving mineral end-members.

1) clin + naph + 3pa + q = 2ames + 4ab
2) 6clin + 2naph + 12pa = 9ames + 14ab + 2H2O
3) 3clin + 5ann = 3daph + 5phl
4) 2clin + 3daph + 5east = 5ames + 5ann
5) ames + naph + cel = clin + phl + pa
6) 36daph + 70naph + 60mu = 6clin + 45ames + 70ab + 60ann + 10H2O

(iii) Calculated pressures for the given activity data and at T = 400°C and for x(CO2) = 0.2 and x(H2O) = 0.8.

	P(T)	sd(P)	a	sd(a)	b	c	ln_K	sd(ln_K)
1	1.7	3.28	-3.96	6.88	-0.01542	4.425	1.245	2.286
2	1.7	4.23	109.93	23.69	-0.19794	18.232	-1.157	13.111
3	7.6	25.11	-11.20	5.59	0.04289	-1.596	-0.978	7.091
4	5.5	17.00	-56.87	14.54	0.05724	2.112	1.215	5.868
5	4.4	31.18	-17.45	2.25	-0.01635	-0.403	5.404	2.207
6	1.1	3.71	140.88	191.36	-1.16379	92.604	99.014	51.046

(iv) Average pressure calculated from the intercepts of the reactions (for x(CO2) = 0.2 and x(H2O) = 0.8)

T°C	360	380	400	420	440
av P	1.2	1.7	2.1	2.7	3.2
sd	1.15	1.17	1.19	1.20	1.21
f	0.7	0.6	0.5	0.5	0.5

==========

Appendix F-I: continued

(e) Average pressure calculations on the interpreted peak assmblage for rock #M2 from within the Mt. Bold shear zone.

(i) The activity data for mineral end-members in the rock

	mu	pa	cel	clin	daph	ames	phl	ann
a	0.718	0.484	0.0549	0.0231	0.0123	0.0144	0.0731	0.0439
sd(a)/a	0.10000	1.40496	0.35172	0.43164	0.53265	0.46461	0.31945	0.37707

	east	naph	ab	q	H2O
a	0.0303	0.0149	0.990	1.00	0.800
sd(a)/a	0.40926	0.67156	0.05000	0	

(ii) An independent set of reactions involving mineral end-members.

1) 3pa + clin + naph + q = 2ames + 4ab
2) 2clin + 3daph + 5east = 5ames + 5ann
3) 3daph + 2phl + 3east = 3ames + 5ann
4) 4pa + 2cel + phl + q = 3mu + clin + 4ab
5) 14pa + 9cel + 2phl = 11mu + 3clin + 14ab + 2H2O
6) 20pa + 8cel + 5ann + 5q = 13mu + 3daph + 2ames + 20ab

(iii) Calculated pressures for the given activity data and at T = 400°C and for x(CO2) = 0.2 and x(H2O) = 0.8.

	P(T)	sd(P)	a	sd(a)	b	c	ln_K	sd(ln_K)
1	1.2	5.77	-3.96	6.88	-0.01542	4.425	1.634	4.394
2	5.0	12.76	-56.87	14.54	0.05724	2.112	1.390	4.054
3	7.8	10.60	-29.64	9.80	0.01719	1.905	0.570	3.157
4	4.2	7.24	-11.71	6.84	-0.06514	4.505	6.517	5.701
5	4.2	6.42	52.45	24.35	-0.40749	17.854	26.408	20.017
6	2.9	7.69	-52.93	34.26	-0.23879	21.146	27.166	28.410

(iv) Average pressure calculated from the intercepts of the reactions (for x(CO2) = 0.2 and x(H2O) = 0.8)

T°C	360	380	400	420	440
av P	-	1.6	2.5	3.4	4.4
sd	1.47	1.49	1.52	1.54	1.56
f	0.9	0.9	0.8	0.8	0.8

==========

Appendix F-II: calculations of average tempreature

(a) Average temperature calculations on the interpreted peak assmblage for rock #H20 from within the Morialta shear zone.

(i) The activity data for mineral end-members in the rock

	clin	daph	ames	mu	pa	cel	ab	phl
a		0.0743	0.00737	0.0202	0.707	0.426	0.0452	0.990	0.116
sd(a)/a		0.31753	0.58376	0.44142	0.10000	0.09888	0.37199	0.05000	0.26128

	ann	east	naph	q	H2O
a	0.0530	0.0216	0.00276	1.00	0.800
sd(a)/a	0.35079	0.43674	3.61894	0	

(ii) An independent set of reactions involving mineral end-members.

1) clin + east = ames + phl
2) ames + cel = clin + mu
3) 2clin + 3daph + 5east = 5ames + 5ann
4) 6clin + 14pa + 2phl = 9ames + 2mu + 14ab + 2H2O
5) 4pa + 3cel + east + q = clin + 4mu + 4ab
6) 8clin + 10ab + 5ann = 3daph + 5east + 10naph + 20q + 10H2O

(iii) Calculated temperatures for these reactions, for the given activity data at P = 2.5 kbar (for x(CO2) = 0.2 and x(H2O) = 0.8)

	T(P)	sd(T)	a	sd(a)	b	c	ln_K	sd(ln_K)
1	303	248	-13.61	2.68	0.02001	0.104	0.380	0.745
2	471	176	-8.41	1.04	-0.02201	-0.108	4.050	0.666
3	252	470	-56.75	14.54	0.05698	2.124	4.930	4.023
4	451	168	126.31	23.55	-0.21073	19.533	-4.069	4.705
5	341	167	-35.54	7.57	-0.06459	4.528	12.515	1.376
6	269	260	710.09	28.98	-0.79183	3.630	-57.244	36.432

(iv) Average temperatures calculated from the intercepts of the reactions (for x(CO2) = 0.2 and x(H2O) = 0.8)

P	1.5	2.0	2.5	3.0	3.5
av T	365	389	395	404	414
sd	20	20	24	24	23
f	0.4	0.5	0.5	0.5	0.6

==========

Appendix F-II: continued

(b) Average temperature calculations on the interpreted peak assmblage for rock #H19 from within the Morialta shear zone.

(i) The activity data for mineral end-members in the rock

	phl	ann	east	naph	mu	pa	cel	clin
a	0.100	0.0423	0.0259	0.0223	0.519	0.282	0.0702	0.0550
sd(a)/a	0.28056	0.38208	0.42236	0.44767	0.10000	0.15483	0.32420	0.35153

	daph	ames	ab	q	H2O
a	0.00654	0.0176	0.800	1.00	0.800
sd(a)/a	0.59488	0.45137	0.05000	0	

(ii) An independent set of reactions involving mineral end-members.

1) phl + ames = east + clin
2) east + cel = phl + mu
3) 5phl + 3daph = 5ann + 3clin
4) east + naph + cel = 2phl + pa
5) 2phl + naph + 3pa + q = 2east + clin + 4ab
6) 8phl + 3daph + 8ab = 5ann + 8naph + 3mu + 9q + 4H2O

(iii) Calculated temperatures for these reactions, for the given activity data at P = 2.5 kbar (for x(CO2) = 0.2 and x(H2O) = 0.8)

	T(P)	sd(T)	a	sd(a)	b	c	ln_K	sd(ln_K)
1	340	252	13.61	2.68	-0.02001	-0.104	-0.210	0.764
2	579	2200	-22.01	2.75	-0.00199	-0.004	3.350	0.610
3	322	429	11.29	5.59	-0.04308	1.604	2.090	3.149
4	545	1863	-30.75	3.42	0.00328	-0.310	4.238	0.907
5	460	209	21.75	8.58	-0.05333	4.235	1.110	1.268
6	413	103	304.31	20.92	-0.33955	0.380	-12.896	4.995

(iv) Average temperatures calculated from the intercepts of the reactions (for x(CO2) = 0.2 and x(H2O) = 0.8)

P	1.5	2.0	2.5	3.0	3.5
av T	378	386	393	401	410
sd	20	20	21	21	21
f	0.8	0.8	0.8	0.8	0.8

Appendix F-II: continued

(c) Average temperature calculations on the interpreted peak assmblage for rock #U6 from within the Pole Road shear zone.

(i) The activity data for mineral end-members in the rock

	clin	daph	ames	phl	ann	east	naph	mu
a	0.110	0.00261	0.0358	0.0523	0.0320	0.0320	0.00919	0.765
sd(a)/a	0.26837	0.66935	0.39445	0.35693	0.41906	0.40441	1.08808	0.10000

	pa	cel	ab	q	H2O
a	0.638	0.0315	0.990	1.00	0.800
sd(a)/a	0.05000	0.40598	0.05000		0

(ii) An independent set of reactions involving mineral end-members.

1) ames + cel = clin + mu
2) east + cel = phl + mu
3) 6clin + 2naph + 12pa = 9ames + 14ab + 2H2O
4) 2clin + 3daph + 5east = 5ames + 5ann
5) ames + naph + cel = clin + phl + pa
6) clin + 10ann + 5naph + 15pa + 5q = 6daph + 10east + 20ab

(iii) Calculated temperatures for these reactions, for the given activity data at P = 2.5 kbar (for x(CO2) = 0.2 and x(H2O) = 0.8)

	T(P)	sd(T)	a	sd(a)	b	c	ln_K	sd(ln_K)
1	354	168	-8.41	1.04	-0.02201	-0.108	4.310	0.634
2	497	2361	-22.01	2.75	-0.00199	-0.004	3.680	0.682
3	455	174	108.83	23.69	-0.20018	18.922	-2.070	4.559
4	223	475	-56.75	14.54	0.05698	2.124	5.620	4.085
5	293	457	-17.15	2.25	-0.01673	-0.414	5.867	1.306
6	352	372	86.19	44.31	-0.18047	17.965	-3.491	9.015

(iv) Average temperatures calculated from the intercepts of the reactions (for x(CO2) = 0.2 and x(H2O) = 0.8)

P	1.5	2.0	2.5	3.0	3.5
av T	363	389	396	406	419
sd	18	20	24	24	24
f	0.8	0.8	0.9	0.9	1.0

==========

Appendix F-II: continued

(d) Average temperature calculations on the interpreted peak assmblage for rock #M30 from within the Mt. Bold shear zone.

(i) The activity data for mineral end-members in the rock

	clin	daph	ames	ab	phl	ann	east	naph
a	0.110	0.00261	0.0358	0.990	0.156	0.0201	0.0484	0.0268
sd(a)/a	1.09091	0.66935	0.39445	0.05000	0.21961	0.47721	0.36498	0.37378

	mu	pa	cel	q	H2O
a	0.611	0.494	0.0398	1.00	0.800
sd(a)/a	0.10000	0.07687	0.38442	0	

(ii) An independent set of reactions involving mineral end-members.

1) clin + east = ames + phl
2) east + cel = phl + mu
3) 6clin + 2naph + 12pa = 9ames + 14ab + 2H2O
4) 2clin + 3daph + 5east = 5ames + 5ann
5) ames + naph + cel = clin + phl + pa
6) 9daph + 5ames + 20naph + 15cel + 5q = 19clin + 20ab + 15ann

(iii) Calculated temperatures for these reactions, for the given activity data at P = 2.5 kbar (for x(CO2) = 0.2 and x(H2O) = 0.8)

	T(P)	sd(T)	a	sd(a)	b	c	ln_K	sd(ln_K)
1	381	621	-13.61	2.68	0.02001	0.104	0.047	2.170
2	451	2140	-22.01	2.75	-0.00199	-0.004	3.900	0.582
3	486	385	108.83	23.69	-0.20018	18.922	-1.157	13.111
4	494	630	-56.75	14.54	0.05698	2.124	1.215	5.868
5	372	750	-17.15	2.25	-0.01673	-0.414	5.404	2.207
6	382	540	-250.65	54.76	-0.44665	20.817	90.216	41.950

(iv) Average temperatures calculated from the intercepts of the reactions (for x(CO2) = 0.2 and x(H2O) = 0.8)

P	1.5	2.0	2.5	3.0	3.5
av T	387	405	415	427	442
sd	26	30	30	29	28
f	0.5	0.5	0.5	0.5	0.5

==========

Appendix F-II: continued

(e) Average temperature calculations on the interpreted peak assmblage for rock #M2 from within the Mt. Bold shear zone.

(i) The activity data for mineral end-members in the rock

	mu	pa	cel	clin	daph	ames	phl	ann
a		0.718	0.484	0.0549	0.0231	0.0123	0.0144	0.0731	0.0439
sd(a)/a		0.10000	0.41322	0.35172	0.43164	0.53265	0.46461	0.31945	0.37707

	east	naph	ab	q	H2O
a	0.0303	0.0149	0.990	1.00	0.800
sd(a)/a	0.40926	0.67156	0.05000	0	

(ii) An independent set of reactions involving mineral end-members.

1) cel + east = mu + phl
2) clin + east = ames + phl
3) 3cel + 3ames + 5ann = 3mu + 3daph + 5phl
4) 4pa + 3phl + q = mu + clin + 2east + 4ab
5) 14pa + 8phl = 2mu + 3ames + 6east + 14ab + 2H2O
6) 3mu + 6cel + 5ann + 12naph + 3q = 3daph + 14phl + 12ab

(iii) Calculated temperatures for these reactions, for the given activity data at P = 2.5 kbar (for x(CO2) = 0.2 and x(H2O) = 0.8)

	T(P)	sd(T)	a	sd(a)	b	c	ln_K	sd(ln_K)
1	552	2255	-22.01	2.75	-0.00199	-0.004	3.450	0.635
2	297	266	-13.61	2.68	0.02001	0.104	0.410	0.820
3	435	883	-36.51	6.40	-0.02294	-1.929	9.780	3.436
4	404	250	30.50	8.44	-0.05860	4.540	-0.383	2.135
5	442	145	207.96	27.95	-0.33081	18.909	-3.412	6.964
6	387	775	-156.78	31.23	-0.08136	8.323	34.574	9.796

(iv) Average temperatures calculated from the intercepts of the reactions (for x(CO2) = 0.2 and x(H2O) = 0.8)

P	1.5	2.0	2.5	3.0	3.5
av T	379	396	403	412	421
sd	22	22	26	26	27
f	0.9	0.8	0.8	0.8	0.8

Appendix F-III: Calculations of average temperature and pressure

(a) Average temperature and pressure calculations on the interpreted peak assmblage for rock #H20 from within the Morialta shear zone.

(i) The activity data for mineral end-members in the rock

	clin	daph	ames	mu	pa	cel	ab	phl
a	0.0743	0.00737	0.0202	0.707	0.426	0.0452	0.990	0.116
sd(a)/a	0.31753	0.58376	0.44142	0.10000	0.09888	0.37199	0.05000	0.26128

	ann	east	naph	q	H2O
a	0.0530	0.0216	0.00276	1.00	0.800
sd(a)/a	0.35079	0.43674	3.61894	0	

(ii) An independent set of reactions involving mineral end-members.

1) 4clin + 6pa = 5ames + 6ab + 2q + 2H2O
2) clin + 4pa + phl + q = 2ames + mu + 4ab
3) 2clin + 4pa + east + q = 3ames + mu + 4ab
4) 2clin + 4pa + phl + q = 3ames + cel + 4ab
5) 12pa + 9cel + 2naph = 3clin + 9mu + 14ab + 2H2O
6) 8clin + 20pa + 5ann + 5q = 3daph + 10ames + 5mu + 20ab

(iii) Calculated pressures for these reactions,for the given activity data and for x(H2O) = 0.8.

	P(T)	sd(P)	a	sd(a)	b	c	ln_K	sd(ln_K)
1	2.0	1.79	119.75	10.21	-0.17357	10.036	-4.038	2.632
2	2.0	1.90	3.28	6.70	-0.01858	4.748	-0.015	1.075
3	1.5	2.38	-10.32	7.30	0.00143	4.852	0.365	1.598
4	1.8	2.32	11.69	6.86	0.00343	4.857	-4.065	1.600
5	1.0	2.90	33.18	24.45	-0.39823	17.948	38.836	8.198
6	2.1	2.17	5.12	33.94	-0.04982	22.138	-3.106	6.103

(iv) Average temperature and pressure calculated from the intercepts of the reactions (for x(CO2) = 0.2 and x(H2O) = 0.8).

T = 386°C, sd = 36,
P = 2.0 kbars, sd = 1.7, cor = 0.783, f = 0.38

Appendix F-III: Continued

(b) Average temperature and pressure calculations on the interpreted peak assmblage for rock #H19 from within the Morialta shear zone.

(i) The activity data for mineral end-members in the rock

	phl	ann	east	naph	mu	pa	cel	clin
a	0.100	0.0423	0.0259	0.0223	0.519	0.282	0.0702	0.0550
sd(a)/a	0.28056	0.38208	0.42236	0.44767	0.10000	0.15483	0.32420	0.35158

	daph	ames	ab	q	H2O
a	0.00654	0.0176	0.800	1.00	0.800
sd(a)/a	0.59488	0.45137	0.05000	0	

(ii) An independent set of reactions involving mineral end-members.

1) naph + 3pa + clin + q = 2ames + 4ab
2) 2naph + 12pa + 6clin = 9ames + 14ab + 2H2O
3) 5phl + 3daph = 5ann + 3clin
4) 5ann + 3ames = 2phl + 3east + 3daph
5) 4naph + 3mu + q = phl + 2east + clin + 4ab
6) 5ann + 12pa + 6cel + 3q = 2phl + 9mu + 3daph + 12ab

(iii) Calculated pressures for these reactions,for the given activity data and for x(H2O) = 0.8.

	P(T)	sd(P)	a	sd(a)	b	c	ln_K	sd(ln_K)
1	1.3	2.15	-5.21	6.88	-0.01366	4.440	1.530	1.181
2	1.2	1.97	108.70	23.69	-0.19930	18.754	0.726	5.069
3	3.8	11.53	11.27	5.59	-0.04305	1.603	2.089	3.149
4	1.5	10.80	29.55	9.80	-0.01700	-1.914	-2.720	3.254
5	2.6	4.88	-4.37	11.37	-0.03765	3.320	3.773	2.062
6	3.7	2.56	-50.96	21.27	-0.14601	11.980	18.676	3.944

(iv) Average temperature and pressure calculated from the intercepts of the reactions (for x(CO2) = 0.2 and x(H2O) = 0.8).

T = 398°C, sd = 36,
P = 2.9 kbars, sd = 1.8, cor = 0.786, f = 0.87

Appendix F-III: Continued

(e) Average temperature and pressure calculations on the interpreted peak assmblage for rock #M2 from within the Mt. Bold shear zone.

(i) The activity data for mineral end-members in the rock.

	mu	pa	cel	clin	daph	ames	phl	ann
a	0.718	0.384	0.0549	0.0231	0.0123	0.0144	0.0731	0.0439
sd(a)/a	0.10000	0.52083	0.35172	0.43164	0.53265	0.46461	0.31945	0.37707

	east	naph	ab	q	H2O
a	0.0303	0.0149	0.990	1.00	0.800
sd(a)/a	0.40926	0.67156	0.05000	0	

(ii) An independent set of reactions involving mineral end-members.

1) 3cel + 3ames + 5ann = 3mu + 3daph + 5phl
2) 4pa + 2cel + phl + q = 3mu + clin + 4ab
3) 14pa + 9cel + 2phl = 11mu + 3clin + 14ab + 2H2O
4) 4pa + 3cel + east + q = 4mu + clin + 4ab
5) 3pa + 2cel + naph + q = 2mu + clin + 4ab
6) 20pa + 10cel + 5ann + 5q = 15mu + 2clin + 3daph + 20ab

(iii) Calculated pressures for these reactions,for the given activity data and for x(H2O) = 0.8.

	P(T)	sd(P)	a	sd(a)	b	c	ln_K	sd(ln_K)	
1	1.4	10.52	-36.48	6.40	-0.02298	-1.927	9.780	3.436	
2	3.1	3.21	-13.23	6.84	-0.06302	4.528	7.443	2.292	
3	3.2	2.82	50.65	24.35	-0.40807	18.390	29.648	8.184	
4	4.0	3.46	-35.24	7.57	-0.06501	4.523	10.893	2.451	
5	3.3	3.03	-22.02	7.00	-0.05767	4.224	8.408	1.911	
6	2.3	3.46	-77.42	34.65	-0.27204	21.035	37.875	11.445	

(iv) Average temperature and pressure calculated from the intercepts of the reactions (for x(CO2) = 0.2 and x(H2O) = 0.8).

T = 412°C, sd = 51,
P = 3.0 kbars, sd = 2.7, cor = 0.880, f = 0.90